

# The development of a quasi-dimensional model for dual fuel combustion in engine cycle-simulation

---

**Taritaš, Ivan**

**Doctoral thesis / Disertacija**

**2018**

*Degree Grantor / Ustanova koja je dodijelila akademski / stručni stupanj:* **University of Zagreb, Faculty of Mechanical Engineering and Naval Architecture / Sveučilište u Zagrebu, Fakultet strojarstva i brodogradnje**

*Permanent link / Trajna poveznica:* <https://urn.nsk.hr/urn:nbn:hr:235:150800>

*Rights / Prava:* [In copyright / Zaštićeno autorskim pravom.](#)

*Download date / Datum preuzimanja:* **2024-04-24**

*Repository / Repozitorij:*

[Repository of Faculty of Mechanical Engineering and Naval Architecture University of Zagreb](#)





University of Zagreb  
FACULTY OF MECHANICAL ENGINEERING  
AND NAVAL ARCHITECTURE

Ivan Taritaš

**THE DEVELOPMENT OF A QUASI-DIMENSIONAL  
MODEL FOR DUAL FUEL COMBUSTION IN ENGINE  
CYCLE-SIMULATION**

DOCTORAL THESIS

Zagreb, 2018



Sveučilište u Zagrebu  
FAKULTET STROJARSTVA I BRODOGRADNJE

Ivan Taritaš

**RAZVOJ KVAZIDIMENZIJSKOGA MODELA  
DVOGORIVOGA IZGARANJA U SIMULACIJAMA  
RADNOGA CIKLUSA MOTORA**

DOKTORSKI RAD

Zagreb, 2018.



University of Zagreb  
FACULTY OF MECHANICAL ENGINEERING  
AND NAVAL ARCHITECTURE

Ivan Taritaš

# **THE DEVELOPMENT OF A QUASI-DIMENSIONAL MODEL FOR DUAL FUEL COMBUSTION IN ENGINE CYCLE-SIMULATION**

DOCTORAL THESIS

Supervisor:  
Darko Kozarac, PhD, associate professor

Zagreb, 2018





Sveučilište u Zagrebu  
FAKULTET STROJARSTVA I BRODOGRADNJE

Ivan Taritaš

**RAZVOJ KVAZIDIMENZIJSKOGA MODELA  
DVOGORIVOGA IZGARANJA U SIMULACIJAMA  
RADNOGA CIKLUSA MOTORA**

DOKTORSKI RAD

Mentor:  
Prof. dr. sc. Darko Kozarac

Zagreb, 2018.

## BIBLIOGRAPHY DATA

UDC	621.43
Keywords:	dual fuel engine, turbulence, combustion, cycle-simulation
Scientific area:	Technical sciences
Scientific field:	Mechanical engineering
Institution:	Faculty of Mechanical Engineering and Naval Architecture (FMENA), University of Zagreb
Supervisor:	Darko Kozarac, PhD, associate professor
Number of pages:	375
Number of figures:	223
Number of tables:	51
Number of references:	152
Date of public defense:	15 <sup>th</sup> January 2018
Committee members:	Zoran Lulić, PhD, full professor
	Milan Vujanović, PhD, assistant professor
	Reinhard Tatschl, PhD, (AVL List GmbH, Graz)
Archive:	Faculty of Mechanical Engineering and Naval Architecture (FMENA), University of Zagreb, Croatia

## **Author's Originality Statement**

I hereby declare that the new ideas as well as the improvements and extensions that were made to the existing models are originally mine, and are a result of the work and knowledge that I gained during my studies at the Faculty of Mechanical Engineering and Naval Architecture. All of the findings, especially regarding the fundamental physical phenomena that are modeled, have been appropriately cited. Likewise, the models that were not originally developed during this research and have been used to describe some of the in-cylinder phenomena, have been appropriately cited.

## Acknowledgments

At the beginning, I would like to thank my doctoral supervisor, Darko Kozarac, PhD, associate professor for his guidance and support during my research that has resulted with this doctoral thesis.

I am grateful to the doctoral thesis defense committee members Zoran Lulić, PhD, full professor, Milan Vujanović, PhD, assistant professor and Reinhard Tatschl, PhD for their comments that have significantly improved this thesis.

The research that is presented in this thesis was funded by the Croatian Science Foundation and AVL AST d.o.o. Croatia; this help is gratefully appreciated. In this regards I am very grateful to the AVL AST d.o.o. Croatia director, Mr. Goran Mirković.

I would like to thank Momir Sjerić, PhD, assistant professor for numerous advices regarding 0-D combustion modeling and for numerous programing tips. I am also very grateful to AVL AST team in Graz (Reinhard Tatschl, PhD, Henrik Schuemie, Christoph Poetsch, PhD and Peter Priesching, PhD) for numerous advices regarding the combustion model development.

The experiments that were used to validate the 0-D combustion model were done during my stay at UC Berkeley. In this regards I am grateful to Robert Dibble, PhD, full professor, for giving me the opportunity to come and work at UC Berkeley, and to David Vuilleumier, PhD, Miguel Sierra Aznar and Mislav Blažić for their help in conducting the experiments.

I would also like to thank my colleagues from the Chair of IC Engines and Motor Vehicles, Ivan Mahalec, PhD, full professor, Krunoslav Ormuž, Josipa Kancir, Marija Mihalić, Rudolf Tomić, PhD, Petar Ilinčić, PhD, Goran Šagi, PhD, Ante Vučetić, Mladen Božić, Mario Sremec, Ognjen Tošanović and Denis Grgić for creating a very nice working atmosphere.

The writing of this doctoral thesis was finalized when I was already a part of the KF Finanace d.o.o. team. Therefore, I am very grateful to partners at KF Finance d.o.o., Ivan Fabijančić and Luka Mrkonjić and to director at KF Finance d.o.o., Lovro Plejić for giving me some free time to finish this doctoral thesis.

The 3-D CFD simulations that were used to validate the 0-D  $k-\varepsilon$  turbulence model were provided by Zvonimir Petranović, PhD and I am very grateful for his help. I also have to thank another colleague from the Faculty of Mechanical Engineering and Naval Architecture in Zagreb, Marko Ban, PhD for his help regarding the chemical kinetics and its tabulation methods.

I am also very grateful to all of my friends and family (my grandmothers, aunts, uncles, cousins, mother in law, father in law and Hugo) for their support all these years. In the end, the biggest appreciation goes to my beloved parents Ana and Zlatko, my brother Fran and my wife Ema for their unconditional love and support.

Ivan Taritaš  
Zagreb, January 2018

# Contents

Preface .....	vii
Summary .....	viii
Sažetak .....	ix
Prošireni sažetak.....	x
List of Figures .....	xxvi
List of Tables.....	xxxvii
Nomenclature .....	xxxix
Abbreviations .....	xlix
1. Introduction .....	1
1.1. Combustion Process in the IC Engines.....	1
1.2. Dual fuel IC engines .....	7
1.3. Numerical Simulation in the IC Engine Development Process.....	11
1.4. State of the art.....	14
1.5. Objective and hypotheses of research .....	16
2. Zero-dimensional dual fuel combustion model.....	18
2.1. Model features .....	18
2.2. Thermodynamic properties.....	21
2.3. Zero-dimensional single zone formulation.....	22
2.4. Zero-dimensional multi zone formulation .....	27
2.4.1. Temperature and pressure derivatives.....	28
2.5. Quasi-dimensional approach to combustion modeling .....	30
2.6. Zone formation and evolution .....	33
3. Sub-models of 0-D dual fuel combustion model .....	43
3.1. In-cylinder flow and turbulence .....	43
3.1.1. Physical background .....	43
3.1.2. Overview of the k- $\epsilon$ turbulence model in 0-D environment .....	47
3.1.3. Modeling of the injection effect on in-cylinder turbulence level.....	52
3.1.4. Characteristic turbulence scales calculation.....	54
3.2. Heat transfer .....	57
3.2.1. Physical background .....	57
3.2.2. Heat transfer in IC engines.....	60
3.2.3. Wall heat transfer model .....	61
3.2.4. Zone heat transfer model.....	64

3.3.	Diesel fuel spray development process and combustion .....	65
3.3.1.	Physical background .....	66
3.3.2.	Overview of the 0-D spray combustion model .....	70
3.3.3.	Spray zone evolution modeling.....	72
3.3.4.	Spray ignition and combustion model.....	84
3.4.	Ignition delay and chemical reaction rate tabulation .....	87
3.4.1.	Physical background – chemical kinetics.....	89
3.4.2.	0-D tabulation code .....	92
3.4.3.	Autoignition times definition .....	101
3.4.4.	Reaction rate time definition .....	106
3.5.	Flame propagation combustion modeling .....	113
3.5.1.	Physical background .....	113
3.5.2.	Overview of the 0-D flame propagation combustion models .....	120
3.5.3.	Overview of the fractal combustion model .....	122
3.5.4.	Overview of the turbulent flame speed combustion model.....	128
3.5.5.	Start of the flame propagation calculation .....	130
3.5.6.	Transition from laminar to fully developed turbulent flame calculation .....	132
3.5.7.	Calculation of the wall-combustion phase .....	134
3.6.	Laminar flame speed calculation .....	136
3.6.1.	Influence of the initial state and composition on the laminar flame speed .....	137
3.7.	Flame surface area calculation model .....	141
3.7.1.	Piston position matrix generation.....	144
3.7.2.	In-cylinder volume matrix generation.....	145
3.7.3.	Flame radius matrix generation.....	145
3.7.4.	Flame surface data matrices generation .....	147
3.7.5.	Instantaneous flame surface values calculation .....	167
3.8.	Pollutants formation models .....	167
3.8.1.	Pollutant formation background.....	167
3.8.2.	Overview if the emissions models .....	171
3.9.	Knock calculation model .....	175
3.9.1.	Physical background .....	175
3.9.2.	Knock model .....	176
4.	Validation of the developed 0-D combustion model .....	181
4.1.	Comparison between the 0-D and 3-D CFD turbulence results .....	181
4.1.1.	3-D CFD simulation model .....	182
4.1.2.	0-D simulation model.....	185
4.1.3.	Results .....	187

4.2.	Validation of the 0-D dual fuel combustion model .....	188
4.2.1.	Experimental setup .....	189
4.2.2.	Sensitivity analysis of the DFMZCM to its parameters .....	195
4.2.3.	Validation of the model with the measured data .....	238
4.2.4.	Validation with a single set of model parameters .....	255
5.	Application of the 0-D dual fuel model .....	269
5.1.	The effect of the engine geometry and of the operating settings on the performance and exhaust gas emissions .....	270
5.1.1.	The effect of change in the compression ratio .....	270
5.1.2.	The effect of the change in the intake pressure .....	272
5.1.3.	The effect of the change in the intake temperature .....	275
5.1.4.	The effect of the change in the mass fraction of combustion products at the start of high pressure cycle .....	277
5.1.5.	The effect of change in the direct fuel injection timing .....	279
5.1.6.	The effect of change in the direct fuel injection rail pressure .....	282
5.1.7.	The effect of change in the Diesel fuel substitution ratio .....	285
5.2.	Full conventional dual fuel IC engine simulation .....	288
5.2.1.	Engine model and simulation settings .....	289
5.2.2.	Simulation results .....	294
6.	General Overview and Conclusions .....	299
6.1.	Original scientific contribution .....	307
6.2.	Possible directions of further work .....	307
	References .....	309
	Curriculum Vitae in English .....	317
	Curriculum Vitae in Croatian .....	319

## Preface

This doctoral thesis presents an overview of the research that was conducted at the Chair of IC Engines and Motor Vehicles that is a part of the Faculty of Mechanical Engineering and Naval Architecture, University of Zagreb. This research has been conducted in the collaboration with AVL List GmbH, Graz, Austria and Croatian Science Foundation (*HrZZ*). The newly developed 0-D dual fuel combustion model, kinetically-controlled spray combustion calculation method and multiple flame propagation calculation method as well as the modified and extended in-cylinder turbulence, spray combustion, zone heat transfer, flame propagation and knock models have been integrated within the AVL cycle-simulation software.

Ivan Taritaš

Zagreb, January 2018



## Summary

The research presented within this thesis gives an overview of the process of development, validation and application of a quasi-dimensional combustion model for the cycle-simulations in the conventional dual fuel internal combustion (IC) engines. The newly developed combustion model is called the Dual Fuel Multi Zone Combustion Model (DFMZCM), and has been integrated within the AVL cycle-simulation software (AVL Boost)

Dual fuel engine is a term which is used for an IC engine that operates with two fuels simultaneously. However, this term is usually used to describe an IC engine that operates in the compression-ignition mode and is powered by a combination of the high and low reactivity fuels, mainly Diesel fuel and natural gas (methane). A conventional dual fuel engine operates with the port injected low reactivity fuel (natural gas) and directly injected high reactivity fuel (Diesel fuel). The combustion process in a conventional dual fuel engine shares characteristics with the combustion in the conventional compression-ignited and spark-ignited engines. In the initial stages the combustion in a conventional dual fuel IC engine is driven by the chemistry of the prepared fuel/air mixture, while in the later stages it is driven by both the fuel/ air/ combustion products mixing process and the flame propagation through the premixed mixture.

The DFMZCM is a zero-dimensional (0-D) model, which means that only the time discretization is accounted for, while the spatial heterogeneities of composition and of the state are neglected. In order to introduce more physical description of the phenomena which occur inside the engine's combustion chamber, a multi-zone and quasi-dimensional approach to combustion modeling are used. Quasi-dimensional approach to the 0-D combustion modeling enables the inclusion of various geometrical effects in the calculation of the burning rate. Multi-zone approach to the 0-D combustion modeling enables the prediction of in-cylinder composition and temperature heterogeneity. The DFMZCM accounts for the in-cylinder turbulence, zone and wall heat transfer, spray process and mixing-controlled combustion process, the process of flame propagation through the premixed mixture, harmful exhaust gas emissions formation, and knock in the end gas. The validation and application of newly developed DFMZCM reveal that the model is predictive, and that with this model it is possible to achieve a good fit between the experimentally measured and simulated results.

**Keywords:** dual fuel engine, turbulence, combustion, cycle-simulation

## Sažetak

U okviru ovog doktorskog rada prikazan je razvoj, validacija te primjena kvazidimenzijskoga modela dvogorivoga izgaranja u simulacijama radnog ciklusa motora s unutarnjim izgaranjem (MSUI). Novo razvijeni model izgaranja naziva se engl. *Dual Fuel Multi Zone Combustion Model* (DFMZCM).

Dvogorivi (engl. *dual fuel*) MSUI su motori s kompresijskim paljenjem koji koriste kombinaciju visokoreaktivnog i niskoreaktivnog goriva. Kao visoko-reaktivno gorivo najčešće se koristi dizelsko gorivo dok se kao nisko-reaktivno gorivo najčešće koristi prirodni plin. U dvogorivim motorima, prirodni plin se ubrizgava u usisnu cijev dok se dizelsko gorivo ubrizgava pod visokim tlakom izravno u cilindar motora. Sam proces izgaranja u dvogorivim MSUI je kombinacija dvaju procesa izgaranja koji su karakteristični za klasične motore s kompresijskim (Dieselovi MSUI) te sa stranim paljenjem (Ottovi MSUI). U početnom dijelu, proces izgaranja vođen je brzinom kemijskih reakcija u pripremljenoj smjesi goriva i zraka. Nakon te inicijalne faze dolazi do „paljenja“ te početka širenja plamena kroz predmiješanu smjesu goriva i zraka tako da je u toj fazi izgaranje istovremeno vođeno širenjem plamena kroz prostor izgaranja te miješanjem između neizgorjelog goriva, zraka i vrućih produkata izgaranja.

DFMZCM model izgaranja se ubraja u bezdimenzijske modele (0-D) te je ugrađen u postojeći programski paket za proračun radnog ciklusa MSUI kojeg je razvila tvrtka AVL iz Graza. U 0-D modelima izgaranja u danom vremenskom trenutku smjesa i stanje unutar cilindra motora su homogeni. Dakle u tim modelima razmatraju se samo vremenske promjene u sastavu smjese i termodinamičkim značajkama u cilindru MSUI. Kako bi se točnije opisale stvarne fizikalne pojave koje se odvijaju u cilindru MSUI, u ovom modelu korišteni su takozvani kvazidimenzijski i višezonski pristupi u 0-D modeliranju izgaranja. Kroz kvazidimenzijski pristup u modeliranju izgaranja moguće je uključiti utjecaj geometrije prostora izgaranja i samog plamena na brzinu oslobađanja topline, dok je kroz višezonski pristup moguće opisati heterogenost sastava smjese i temperature u cilindru MSUI. Unutar DFMZCM modela ugrađeni su podmodeli kojima se opisuju pojave koje se odvijaju u cilindru dvogorivih MSUI (turbulencija, izmjena topline, sprej dizelskog goriva, širenje plamena kroz prostor izgaranja, stvaranje štetnih tvari u produktima izgaranja te predviđanje detonantnog izgaranja). Validacija i primjena novo razvijenog DFMZCM modela pokazale su da je dani model prediktivan te da je njime moguće postići rezultate koji se dobro podudaraju s rezultatima eksperimentalnih ispitivanja.

**Ključne riječi:** dvogorivni motor, turbulencija, izgaranje, simulacija radnog ciklusa

## Prošireni sažetak

Glavni cilj istraživanja koje je prikazano ovom doktorskom disertacijom bilo je definirati te razviti fizikalni, prediktivni i brzi simulacijski alat za proučavanje utjecaja različitih radnih i geometrijskih parametara MSUI na ukupni stupanj djelovanja, performanse i emisije štetnih tvari u ispušnim plinovima konvencionalnog dvogorivog MSUI. U tu svrhu razvijen je kvazidimenzijski model dvogorivoga izgaranja, skraćenog naziva DFMZCM (engl. *Dual Fuel Multi Zone Combustion Model*), čiji su razvoj, validacija te primjena u simulaciji radnoga ciklusa motora s unutarnjim izgaranjem (MSUI) prikazani u okviru ove doktorske disertacije. Budući da kvazidimenzijski modeli pripadaju tzv. bezdimenzijskim (0-D) modelima, DFMZCM se ubraja u kategoriju 0-D modela izgaranja. Pojedini dijelovi istraživanja koji su prikazani u okviru ove doktorske disertacije, već su objavljeni u nekim od znanstvenih časopisa te na nekim od znanstvenih konferencija iz područja istraživanja [1]-[4].

Motivacija za ovaj rad proizlazi iz potrebe za smanjenjem štetnog utjecaja MSUI na okoliš. Kao što će biti prikazano u idućih nekoliko poglavlja ovog dokorskog rada, prenamjenom ili zamjenom postojećih Diesellovih motora konvencionalnim dvogorivim MSUI moguće je značajno smanjiti udio nekih od štetnih tvari u ispušnim plinovima MSUI uz zadržavanje visokog stupnja djelovanja motora (na razini postojećih Diesellovih motora). Međutim, kako bi se optimirali radni parametri takvih MSUI potrebno je provesti detaljna ispitivanja, a upravo simulacijski alati mogu značajno ubrzati taj cijeli proces. Štoviše, pregledom područja istraživanja utvrđeno je da postoji potreba za fizikalnim, prediktivnim modelom 0-D izgaranja pomoću kojeg bi se na odgovarajući način moglo opisati pojavu izgaranja u konvencionalnom dvogorivom MSUI.

### Proces izgaranja u motorima s unutarnjim izgaranjem

Izgaranje je kemijski proces u kojem reakcija goriva i kisika dovodi do oslobađanja velike količine energije (topline). U MSUI se u većini slučajeva kao gorivo koristi određena mješavina ugljikovodika, a kisik za proces izgaranja dolazi iz zraka (izuzetak je takozvani proces oks-i-zgaranja koji koristi čisti kisik). S obzirom na proces izgaranja, odnosno način paljenja, MSUI se mogu podijeliti na:

1. MSUI s kompresijskim paljenjem (Dieselovi motori);
2. MSUI s stranim paljenjem (Ottovi motori).

Osnova razlika između ova dva motora je u samoj vrsti izgaranja u cilindru motora. U Ottovim motorima izgaranje je vođeno turbulentnim širenjem plamena kroz predmiješanu

smjesu. Ova vrsta izgaranja često se naziva turbulentni predmiješani plamen. U Diesellovim motorima izgaranje je vođeno turbulentnim miješanjem goriva i zraka. Ova vrsta izgaranja često se naziva turbulentni nepredmiješani plamen.

Rezultat procesa izgaranja bilo koje vrste goriva i kisika (čisti kisik ili zrak) je smjesa plinova koji se nazivaju produktima izgaranja. U motorima, produkti izgaranja sastoje se prvenstveno od sljedećih spojeva i tvari:

1. Ugljikov dioksid ( $\text{CO}_2$ ), koji je ujedno i staklenički plin te vodena para ( $\text{H}_2\text{O}$ ). Ove dvije tvari nastaju kao rezultat potpunog procesa izgaranja ugljikovodika.
2. Dušik ( $\text{N}_2$ ) koji dolazi iz zraka, kisik ( $\text{O}_2$ ) koji se javlja u slučaju rada motora sa siromašnom smjesom te dušikovi oksidi ( $\text{NO}_x$ ) koji nastaju reakcijom dušika i kisika pri visokim temperaturama u cilindru motora.
3. Neizgorjele čestice, ugljikov monoksid ( $\text{CO}$ ) te ne izgorjeli ugljikovodici (UHC) koji nastaju kao posljedica nepotpunog procesa izgaranja ugljikovodika.

Produkti izgaranja sadrže određene količine štetnih tvari te se uglavnom ispuštaju u atmosferu. Štetnim tvarima u produktima izgaranja MSUI nazivaju se tvari koje imaju negativan utjecaj na ljudsko zdravlje i okoliš; te štetne tvari su:  $\text{CO}_2$ , (koji je ujedno i staklenički plin),  $\text{CO}$ , UHC,  $\text{NO}_x$  te neizgorjele čestice. Negativni učinci cjelokupnog onečišćenja zraka na ljudsko zdravlje, koje je velikim dijelom uzrokovano upotrebom MSUI u transportnim sredstvima zabilježeni su u brojnim radovima i izvještajima. Tako Anderson i Thundiyil [6] navode da kod ljudi koji su dulje vrijeme izloženi emisiji čestica dolazi do većeg broja preranih smrtnih slučajeva; Kampa i Castanas [7] navode da onečišćenje zraka ima negativan utjecaj na ljudsko zdravlje, dok Kim i sur. [8] navode da je potrebno strože regulirati dozvoljene količine policikličnih aromatskih ugljikovodika u atmosferi.

Svjetska zdravstvena organizacija (WHO) objavila je 2014. godine šokantno izvješće [9] u kojem navode kako je 7 milijuna preranih smrtnih slučajeva u 2012. godini povezano upravo s onečišćenjem zraka.

Iz pregleda globalnih emisija stakleničkih plinova po sektorima vidljivo je da je sektor prometa jedan od glavnih zagađivača jer je 14% ukupnih emisija stakleničkih plinova uzrokovano upravom prometom [10]. Imajući u vidu veliko povećanje broja registriranih vozila, broja vozila po osobi te povećanje globalne proizvodnje vozila iz godine u godinu [11], vidljivo je da je nužno smanjiti štetni utjecaj prometa na okoliš. Stoga su vlade diljem svijeta nametnule niz propisa koji za cilj imaju smanjenje emisija štetnih tvari iz vozila.

Tako su uvedene tzv. EURO norme (trenutno je na snazi EURO VI norma iz 2014. godine) kojom se ograničavaju dopuštene emisije štetnih tvari ( $\text{CO}$ , UHC,  $\text{NO}_x$  te neizgorjele čestice)

u ispušnim plinovima MSUI [13]. S druge strane, po pitanju štetne emisije stakleničkih plinova ( $\text{CO}_2$ ) iz cestovnih vozila; za 2020. godinu EU postavila je cilj od 95 g/km kao prosjek flote za nove automobile [12].

Upravo ovi propisi i norme usmjerili su razvoj MSUI prema optimizaciji procesa izgaranja, primjeni različitih modernih sustava u upravljanju radnim parametrima motora, primjeni sustava za obradu ispušnih plinova te primjeni nekonvencionalnih, „čišćih“ goriva.

U kontekstu uporabe „čišćih“ goriva, gorivo koje se zbog svojih pozitivnih karakteristika sve češće koristi u MSUI je prirodni plin. Prirodni plin može se koristiti kao pogonsko gorivo i u Ottovim i u Dieselovim motorima [16], a sve češće se koristi zbog svojih brojnih pozitivnih karakteristika, odnosno prednosti u odnosu na konvencionalna tekuća goriva:

1. Budući da je u plinovitom stanju, lakše i potpunije se miješa sa zrakom čime je smjesa unutar cilindra homogenija. Homogenija smjesa unutar cilindra dovodi do potpunijeg, odnosno čisteg izgaranja čime se smanjuje količina UHC u ispušnim plinovima MSUI [17].
2. Budući da od svih ugljikovodika ima najveći omjer vodika u odnosu na ugljik, u teoriji omogućuje smanjenje emisija  $\text{CO}_2$  za skoro 25 % u usporedbi s konvencionalnim tekućim gorivima [18].
3. Ima višu temperaturu samozapaljenja te je otporniji na detonaciju u odnosu na konvencionalna tekuća goriva. To znači da MSUI pogonjen s prirodnim plinom može raditi s većim kompresijskim omjerom čime raste stupanja djelovanja motora [16].

Pri upotrebi u Ottovim motorima, prirodni plin u potpunosti zamjenjuje benzin. Iako je zbog prethodno nabrojanih prednosti moguće ostvariti nešto veći stupanja djelovanja u odnosu na Ottove motore pogonjene benzinom, stupanja djelovanja je i dalje uglavnom niži u odnosu na Dieslove motore (izuzetak su veliki plinski Ottovi motori). To je posljedica brojnih poznatih nedostataka Ottovih motora (rad sa stehiometrijskom smjesom, gubitci uslijed izmjene radnog medija, itd.). S druge strane pri upotrebi u Dieselovim motorima, prirodni plin ne može u potpunosti zamijeniti dizelsko gorivo. Razlog tome je njegova otpornost na samozapaljenje koja onemogućuje da se prirodni plin zapali u uvjetima tlaka i temperature u cilindru MSUI u okolini gornje mrtve točke (GMT) [16]. Stoga se u Dieselovim motorima prirodni plin koristi u takozvanom dvogorivom konceptu MSUI [16], [18]. U dvogorivim motorima kao osnovno pogonsko gorivo koristi se prirodni plin, koji se pali s malom količinom dizelskog goriva koje se ubrizgava izravno u cilindar motora u okolini GMT [19].

## Dvogorivi motori s unutarnjim izgaranjem

Dvogorivi (engl. *dual fuel*) MSUI su motori s kompresijskim paljenjem koji rade s kombinacijom visoko-reaktivnog i nisko-reaktivnog goriva. Kao visokoreaktivno gorivo najčešće se koristi dizelsko gorivo dok se kao niskoreaktivno gorivo najčešće koristi prirodni plin. U procesu dvogorivog izgaranja, relativna količina prirodnog plina obično se definira kao omjer zamjene dizelskog goriva, što predstavlja omjer energije dobivene od prirodnog plina i ukupne energije dobivene od oba goriva [2]. S obzirom na sam proces izgaranja, postoje tri vrste dvogorivih MSUI [2]:

1. MSUI u kojima se prirodni plin i dizelsko gorivo ubrizgavaju pod visokim tlakom izravno u cilindar motora. Takvi motori nazivaju se HPDI motri (engl. *High Pressure Direct Injection*) [20].
2. MSUI u kojima su oba goriva (prirodni plin i dizelsko gorivo) predmiješani, tj. oba se goriva ubrizgavaju u usisnu cijev motora. Takvi motori nazivaju se dvogorivi HCCI motori (engl. *Homogeneous Charge Compression Ignition*) [21].
3. MSUI kod kojih se primarno gorivo (prirodni plin) ubrizgava u usisnu cijev dok se sekundarno gorivo (dizelsko gorivo) koje služi isključivo kao izvor paljenja ubrizgava pod visokim tlakom izravno u cilindar motora. Takvi motori nazivaju se konvencionalni dvogorivi motori [19], a modeliranje izgaranje u ovakvim motorima je predmet ovog doktorskog rada.

Izgaranje u HPDI motorima vođeno je turbulentnim miješanjem goriva, zraka i vrućih produkata izgaranja (tzv. turbulentni ne predmiješani plamen). U ovakvim motorima oba se goriva ubrizgavaju izravno u cilindar kroz dvije odvojene brizgaljke, ili kroz jedinstvenu brizgaljku posebne konstrukcije. Više o HPDI izgaranju te o performansama i emisijama štetnih tvari u ispušnim plinovima takvih motora može se pronaći u [22].

Eksperimentalna i numerička ispitivanja dvogorivog HCCI izgaranja prikazana su u [21]. Budući da su u takvim motorima oba goriva predmiješana, u njima je izgaranje vođeno brzinom kemijskih reakcija u smjesi. Iako takav način izgaranja dovodi do visokog stupnja djelovanja cijelog MSUI uz niske emisije štetnih tvari u ispušnim plinovima, sama kontrola početka i faze izgaranja je prilično zahtjevna te zahtjeva ugradnju kompleksnih sustava s preciznim upravljanjem na sam motor [2].

Glavna prednost konvencionalnog u odnosu na HPDI i HCCI dvogorivi način rada MSUI je mogućnost jednostavne prenamjene postojećih Diesellovih motora u dvogorive motore te mogućnost motora da radi isključivo s dizelskim gorivom u slučaju da se potroši sav prirodni

plin [2], [18]. Obzirom da su velika vozila (kamioni, autobusi, kombi vozila te razna velika rada vozila) uglavnom pogonjena Dieslovim motorima, njihovom prenamjenom u dvogorive motore ostvarila bi se značajna smanjenja ukupne emisije stakleničkih plinova iz prometnog sektora. Princip rada konvencionalnog dvogorivog MSUI sastoji se od sljedećih faza:

1. Prirodni plin ubrizgava se u usisnu cijev svakog cilindra gdje se miješa sa zrakom te u taktu usisa uvlači u cilindar motora.
2. Mješavina prirodnog plina i zraka komprimira se u taktu kompresije. Budući da prirodni plin ima visoku otpornost na samozapaljenje, ne može se zapaliti u uvjetima tlaka i temperature u cilindru motora u okolici GMT.
3. Stoga se u okolici GMT u cilindar izravno ubrizgava mala količina dizelskog goriva.
4. Dizelsko gorivo se razbija na niz kapljica koje prodiru duboko u prostor izgaranja te postepeno isparavaju. Pare dizelskog goriva miješaju se sa okolnom smjesom (smjesa prirodnog plina i zraka), čime dolazi do stvaranja zapaljive smjese, koja se u jednom trenutku zapali. Vrijeme koje protekne od izravnog ubrizgavanja goriva do paljenja smjese u cilindru naziva se zakašnjenje paljenja.
5. Zapaljena smjese djeluje kao „svjećica“, odnosno izvor paljenja koji dovodi do širenja plamena kroz predmiješanu smjesu prirodnog plina i zraka.

Iz gore prikazanog rada konvencionalnog dvogorivog motora, vidljivo je da je proces izgaranja u takvom motoru kombinacija izgaranja vođenog miješanjem i izgaranja vođenog širenjem plamena kroz predmiješanu smjesu; tj. kombinacija turbulentnog predmiješanog plamena i turbulentnog nepredmiješanog plamena. Na temelju podataka iz literature [23], [24], kao i vlastitih eksperimentalnih istraživanja [2], izgaranje u konvencionalnim dvogorivnim motorima moguće je podijeliti na sljedeće faze [2]:

1. Početna faza izgaranja koja je kontrolirana brzinom kemijskih reakcija u pripremljenoj smjesi dizelskog goriva, prirodnog plina i zraka. Vrući produkti ove faze izgaranja dovode do početka širenja plamena kroz predmiješanu smjesu prirodnog plina i zraka te izmiješanog, a ne zapaljenog dizelskog goriva.
2. Kombinacija izgaranja vođenog širenjem plamena kroz predmiješanu smjesu te izgaranja vođenog miješanjem između ne izgorjelog dizelskog goriva, zraka i vrućih produkata izgaranja u područjima bogatim dizelskim gorivom. U toj fazi izgaranja javljaju se predmiješani turbulentni plamen, kao i ne predmiješani turbulentni plamen.
3. Završni dio vođen miješanjem između neizgorjelog goriva i smjese u cilindru, nakon što se plamen proširio kroz čitavi cilindar motora.

Königsson [18] navodi da u konvencionalnom dvogorivom motoru dolazi do istovremenog širenja više plamenova kroz prostor izgaranja te da je broj plamenova jednak broju mlaznica na brizgaljci za ubrizgavanje dizelskog goriva.

Do paljenja smjese (dizelsko gorivo / prirodni plin / zrak) dolazi u području koje je bogato dizelskim gorivom, tj. u području cilindra gdje su postignuti odgovarajući uvjeti za paljenje smjese. Shah i sur. [25] pokazali su da dodavanje prirodnog plina produljuje ukupno vrijeme zakašnjenja paljenja smjese. Do ovog fenomena dolazi iz dva razloga:

1. Termodinamički razlog; dodavanjem prirodnog plina u predmiješanu smjesu dolazi do smanjenja omjera specifičnih toplinskih kapaciteta smjese, što dovodi do smanjenja tlaka i temperature u GMT. Upravo smanjenje tlaka i temperature u cilindru dovodi do produljenja zakašnjenja paljenja.
2. Kemijski razlog; dodavanje prirodnog plina smanjuje reaktivnost smjese goriva što dovodi do produljenja zakašnjenja paljenja [26].

Zbog različitih zahtjeva (masa dizelskog goriva) kao i različitog zakašnjenja paljenja, kod konvencionalnog dvogorivog motora postavke izravnog ubrizgavanja (trenutak ubrizgavanja, tlak ubrizgavanja kao i trajanje ubrizgavanja) su različite u odnosu na Dieslove motore. Utjecaj promjena postavki izravnog ubrizgavanja na stupanj djelovanja i štetne emisije konvencionalnog dvogorivog motora prikazane su u [2], gdje je zaključeno da trenutak paljenja ovisi o lokalnom sastavu i stanju smjese u području spreja dizelskog goriva.

U isto vrijeme kada se plamen širi kroz prostor izgaranja, neizgorjelo dizelsko gorivo koje se nalazi unutar plamena miješa se s okolnim zrakom i vrućim produktima izgaranja, te izgara. Ovisno o opterećenju i omjeru dizelskog goriva i prirodnog plina, izgaranje će većim dijelom biti vođeno ili širenjem plamena kroz predmiješanu smjesu, ili miješanjem između goriva, zraka i toplih produkata izgaranja [2].

Autori u [18], [27], [28] uspoređivali su konvencionalni dvogorivi i Dieslov način rada MSUI pri različitim opterećenjima i omjerima zamjene dizelskog goriva. Zaključak tih istraživanja je da konvencionalni dvogorivi način rada MSUI dovodi do smanjenja emisija  $\text{NO}_x$ , ne izgorjelih čestica kao i  $\text{CO}_2$  uz zadržavanje visokog stupnja djelovanja kao i kod Dieslovih MSUI. Međutim, u tim istraživanjima zabilježeno je da dolazi do povećanja štetnih emisija CO i UHC u usporedbi s Dieslovim načinom rada. Također, zabilježeno je da konvencionalni dvogorivi način rada ima niski stupanj djelovanja kod nižih opterećenja što je posljedica lokalnog gašenja plamena zbog siromašne gorive smjese.



## Upotreba simulacija u procesu razvoja motora s unutarnjim izgaranjem

Prof. Dibble je jednom rekao [29]: „*Eksperiment je ustvari simulacija koja sve pojave u cilindru motora računa savršeno točno te ih računa u realnom vremenu*“. Iako je ova izjava savršeno točna, problem s detaljnim eksperimentalnim ispitivanjima je da ona dugo traju i da su iznimno skupa te da ne daju sve potrebne rezultate za ocjenu procesa izgaranja. Štoviše, ponekad je iznimno teško, ako ne i nemoguće unutar eksperimentalnog istraživanja izolirati utjecaj pojedinog parametra na sam proces izgaranja. Stoga se u zadnje vrijeme u svim razvojnim fazama MSUI sve više koriste simulacije, tj. numerički proračuni.

Simulacije bazirane na tro-dimenzijskim proračunima metodom konačnih volumena (3-D CFD) daju najdublji uvid u fizikalne procese u cilindru motora te shodno tome u usporedbi s eksperimentom daju najtočnije rezultate fizikalnih pojava u cilindru motora. Problem s takvim simulacijama je da dugo traju te su stoga nepogodne za detaljne analize utjecaja pojedinog radnog parametra na sam proces izgaranja u MSUI.

Na drugom kraju po pitanju vremena trajanja proračuna nalaze se takozvani 0-D ili termodinamički modeli [30], [31]. Ovakvi modeli često se u literaturi nazivaju modelima za simulaciju radnog ciklusa motora stoga što u relativno kratkom vremenu omogućuju izračun stotina radnih ciklusa motora. Za razliku od 3-D CFD modela, u 0-D modelima sadržaj u cilindru diskretizira se samo u vremenu, a prostorne varijacije u sastavu i termodinamičkim svojstvima se zanemaruju. To znači da je u danom vremenskom trenutku cijela masa u cilindru homogena (isti tlak, temperatura te sastav smjese). Iako takva početna pretpostavka dovodi do određenih pogrešaka, ukoliko se odgovarajućim modelima na ispravan način opišu pojave u cilindru motora, 0-D modelima može se ostvariti jako dobro podudaranje između izmjerenih i izračunatih rezultata. Upravo to je vidljivo iz brojnih radova u kojima je prikazana usporedba između izmjerenih i izračunatih (pomoću 0-D modela) rezultata procesa izgaranja u Ottovim, Dieselovim, kao i konvencionalnim dvogorivim MSUI [32]-[35]. Budući da su 0-D modeli izgaranja u MSUI iznimno brzi, isti se mogu koristiti za analizu performansi cijelog motora, kao i pri optimizaciji radnih parametara motora što je prikazano u [21], [36], [37]. Štoviše, kao takvi, mogu se koristiti i za proučavanje temeljnih aspekata određenog procesa izgaranja.

Nejednolikost temperature i sastava smjese koji predstavljaju negativni aspekt osnovnih 0-D modela, djelomično se mogu simulirati primjenom višezonskog i kvazidimenzijskoga pristupa u 0-D modeliranju. Višezonski pristup u 0-D modeliranju omogućuje opisivanje heterogenosti sastava smjese i temperature u cilindru MSUI čime se povećava točnost proračuna paljenja,

izgaranja te emisije štetnih tvari u ispušnim plinovima MSUI. Kvazidimenzijski pristup u 0-D modeliranju izgaranja omogućuje uključivanje utjecaja geometrijskih značajki motora na brzinu oslobađanja topline. Također, kako bi se pomoću 0-D modela na odgovarajući način izračunala brzina oslobađanja topline, potrebno je odgovarajućim matematičkim modelima opisati fizikalne pojave koje se javljaju u cilindru MSUI, a koje uključuju:

1. Turbulentno strujanje u cilindru MSUI.
2. Izmjenu topline između zona, kao i između smjese u cilindru i stijenci cilindra.
3. Proces formiranja i razvoja spreja dizelskog goriva koji uključuje raspad tekućeg goriva na kapljice te njihovo isparavanje; miješanje para dizelskog goriva s okolnom smjesom te paljenje gorive smjese.
4. Izgaranje vođeno miješanjem.
5. Izgaranje vođeno širenjem plamena kroz predmiješanu smjesu.
6. Pojava detonantnog izgaranja ispred fronte plamena.
7. Formiranje štetnih spojeva u izgorjeloj smjesi u cilindru MSUI.

### **Pregled područja istraživanja**

Pregledom područja istraživanja utvrđeno je da postoji niz 3-D CFD modela izgaranja dvogorivih motora. Singh i sur. [38] usporedili su rezultate 3-D CFD simulacijskog modela konvencionalnog dvogorivog motora s eksperimentalno dobivenim rezultatima. Utvrdili su da je potrebno na odgovarajući način obuhvatiti izgaranje vođeno širenjem plamena kroz predmiješanu smjesu kako bi uopće bilo moguće simulirati konvencionalni dvogorivi način izgaranja te je razvoj 3-D CFD modela širenja plamena prikazan u [39]. U nedavno objavljenom radu [41], autori su koristili 3-D CFD simulacije kako bi usporedili performanse i emisije štetnih tvari u ispušnim plinovima Dieselvog, konvencionalnog te HPDI dvogorivog motora te su otkrili kako dvogorivi način rada omogućuje istovremeno smanjenje emisija čestica i  $\text{NO}_x$  uz povećanje stupnja djelovanja motora.

Jednako tako razvijen je i niz 0-D modela izgaranja u konvencionalnim dvogorivim motorima. Hountalas i Papagiannakis [35] su 2000. godine razvili i prikazali 0-D model izgaranja u konvencionalnom dvogorivom MSUI. U ovom modelu sprej dizelskog goriva opisan je pomoću jednadžbi za stacionarni mlaz, dok se brzina spreja računa pomoću Hiroyasuovog izraza [42]. Izgaranje počinje kada se pilot gorivo (dizelsko gorivo) zapali; zakašnjenje paljenja računa se pomoću empirijske korelacije. Brzina izgaranja dizelskog goriva i prirodnog plina također se računaju pomoću empirijskih korelacija te se samo dio plinovitog goriva koje je ušlo u područje spreja zapali i izgara. Ovaj model uključuje pod-

modele za izračun stvaranja štetnih spojeva u ispušnim plinovima. Isti su autori u [43], [44] nadogradili model iz [35]. Nadograđeni model obuhvaća i pojavu širenja plamena kroz prostor izgaranja. Tim modelom [43], [44] se razmatra širenje samo jednog plamena kroz prostor izgaranja; širenje plamena kreće od vanjskog ruba spreja te plamen ima oblik konusa. Pomoću odgovarajuće konstante (iznos konstante ovisi o brzini vrtnje motora), danim modelom [43], [44] uključuje se i utjecaj turbulencije na brzinu širenja plamena. Model koji je izvorno izveden u [44], dodatno je doradio Papagiannakis u [45]. U novom modelu, oblik plamene plohe promijenjen je iz konusnog u sferni te se površina plamena računa geometrijskim modelom koji se temelji na radijusu plamena i udaljenosti čela klipa od glave cilindra (razmatra se samo cilindrični oblik komore izgaranja). U ovom modelu, turbulentna brzina plamena računa se na temelju laminarne brzine plamena i intenziteta turbulencije koji se računa pomoću empirijskog izraza.

Krishnan i Srinivasan [46] razvili su prediktivni 0-D model kojim je moguće opisati niskotemperaturni proces izgaranja u konvencionalnim dvogorivim motorima. U ovom modelu, pojave u spreju dizelskog goriva računaju se s dobro poznatim Hiroyasuovim pristupom [42], dok je proces širenja plamena kroz predmiješanu smjesu opisan s jednim poznatim 0-D modelom turbulentnog predmiješanog plamena (*Turbulent Entrainment Model*) [47]. Kao i kod prethodnog modela [45] i u ovom modelu se zakašnjenja paljenja računa putem empirijske korelacije. Utjecaj pojave širenja više plamenova kroz prostor izgaranja obuhvaćen je s empirijskom jednadžbom. Nakon izrade modela, isti je korišten za proučavanje utjecaja temperature zraka na usisu motora, količine dizelskog goriva i kvalitete predmiješane smjese na performanse i emisije štetnih tvari u ispušnim plinovima konvencionalnog dvogorivog motora.

U [48], Mikulski i sur. razvili su empirijski 0-D model izgaranja u konvencionalnim dvogorivnim motorima. U danom modelu se brzina oslobađanja topline računa pomoću Vibeove funkcije, što dovodi do potrebe za prilagođavanjem parametara modela kako se mijenjaju radni parametri motora (brzina vrtnje i opterećenje motora, tlak i temperature na usisu motora, te postavke izravnog ubrizgavanja).

U [49], Cernik i sur. razvili su prediktivni 0-D model za opis procesa izgaranja u 2-taktnom konvencionalnom dvogorivom motoru. Danim modelom moguće je opisati i fazu izgaranja kontroliranog miješanjem, kao i fazu izgaranja kontroliranog širenjem plamena kroz predmiješanu smjesu. Ovaj model sadrži i pojednostavnjeni pod-model za izračun turbulentne kinetičke energije u cilindru motora; pod-modelom turbulencije rješava se samo diferencijalna

jednadžba za turbulentnu kinetičku energiju. Kako bi se obuhvatile heterogenosti u cilindru motora (sastav smjese i temperatura), sadržaj u cilindru je podijeljen na više zona.

Preglednom literature utvrđeno je da je razvijen određeni broj prediktivnih 0-D modela kojima je moguće simulirati proces izgaranja u konvencionalnim dvogorivim motorima (Papagiannakisov model [45], Krishnanov model [46] te Cernikov model [49]). Jednako tako, pregledom područja istraživanja utvrđeno je da s dosad razvijenim modelima nisu obuhvaćene sve fizikalne pojave koje se javljaju u dvogorivim motorima. Također, utvrđeno je da neke od fizikalnih pojava nisu opisane na odgovarajući, prediktivan način. Sukladno tome, potrebno je raditi na sljedećim aspektima 0-D modela izgaranja; tj. na modelima i podmodelima kojima je moguće opisati:

1. Kvazidimenzijski pristup u proračunu izgaranja u dvogorivim motorima; 0-D modelom moraju se obuhvatiti utjecaji različitih geometrija prostora izgaranja, različitog broja plamenova koji se šire kroz prostor izgaranja, kao i geometrijskih značajki brizgaljke za dizelsko gorivo (brizgaljka kojom se dizelsko gorivo ubrizgava izravno u cilindar motora).
2. Turbulenciju u motorima s izravnim ubrizgavanjem goriva u cilindar; model mora obuhvatiti i utjecaj procesa ubrizgavanja na razinu turbulencije u cilindru motora.
3. Utjecaj zahvaćenog prirodnog plina na izgaranje u spreju dizelskog goriva. U tom modelu potrebno je obuhvatiti i kemijski utjecaj prirodnog plina na paljenje i izgaranje smjese u području spreja dizelskog goriva.
4. Pojavu širenja većeg broja plamenova kroz predmiješanu smjesu (kroz prostor izgaranja).
5. Vezu između izgaranja u spreju dizelskog goriva i izgaranja vođenog širenjem plamena kroz predmiješanu smjesu; poglavito utjecaj spreja na ranu fazu širenja plamena kroz prostor izgaranja.
6. Interakcije između istovremenog izgaranja vođenog turbulentnim miješanjem (izgaranje u spreju dizelskog goriva) te izgaranja vođenog turbulentnim širenjem plamena kroz predmiješanu smjesu.
7. Pojavu detonantnog izgaranja u ne izgorjeloj zoni (zona koja se nalazi ispred plamena).

Sve ove pojave, kao i ostale pojave koje se javljaju u cilindru dvogorivih motora, uzete su u obzir prilikom formulacije DFMZCM modela izgaranja.

## Ciljevi i hipoteza istraživanja

Osnovni cilj ovog doktorskog rada je razvoj i izrada simulacijskoga modela izgaranja dvogorivoga motora s unutarnjim izgaranjem te njegova ugradnja u postojeći programski paket za proračun radnog ciklusa motora. Kako bi se ostvario zadani cilj, bilo je potrebno ostvariti nekoliko međusobno povezanih ciljeva:

1. Razvoj višezonskog modela izgaranja spreja dizelskog goriva koji uključuje predmiješani prirodni plin.
2. Poboljšanje modela turbulencije koji će uključiti utjecaj spreja dizelskog goriva.
3. Izrada modela opisa geometrije višestrukog širenja plamena.
4. Nadogradnja postojećih modela zakašnjenja paljenja smjese goriva i zraka, te brzine oslobađanja topline koji će uključiti utjecaj predmiješanog prirodnog plina.
5. Razvoj modela za određivanje uvjeta početka širenja plamena

Hipoteze ovog doktorskog rada uvjetovane su i određene upravo u skladu s ciljevima istraživanja te glase:

1. Moguće je definirati i razviti odgovarajuće matematičke modele za 0-D proračun izgaranja dvogorivoga motora s unutarnjim izgaranjem te iste implementirati u postojeći programski paket za proračun radnog ciklusa takvih motora
2. Primjenom novog modela izgaranja u simulacijama radnog ciklusa dvogorivoga motora moguće je postići rezultate koji se dobro podudaraju s rezultatima eksperimentalnih ispitivanja.

## Pregled doktorskoga rada

U **prvom poglavlju** ovog doktorskog rada dan je uvod koji sadrži motivaciju za ovo istraživanje, ciljeve, hipotezu te znanstveni doprinos rada. Unutar tog poglavlja dan je pregled literature iz područja istraživanja.

U **drugom poglavlju** opisan je simulacijski model izgaranja dvogorivoga motora s unutarnjim izgaranjem. Na početku poglavlja dan je opis i izvod općih jednadžbi za proračune izgaranja u 0-D okruženju. Zatim je shematski prikazana i matematički opisana podjela 0-D proračunske domene na više zona te su opisane interakcije, odnosno izmjena mase i energije između pojedinih zona.

Nadograđeni i novo razvijeni pod-modeli opisani su u **trećem poglavlju** doktorskog rada. Ovo poglavlje moguće je tematski podijeliti na osam (8) dijelova. Na početku svakog dijela dan je opis fizikalne pojave koja se opisuje danim matematičkim modelom. U **prvom dijelu** dan je detaljan opis modela turbulencije. U **drugom dijelu** dan je opis modela izmjene topline

između pojedinih zona, kao i izmjene topline između smjese u cilindru i stijenci cilindra. U trećem dijelu dan je opis svih pod-modela vezanih za sprej dizelskog goriva. U četvrtom dijelu dan je opis načina na koji su kreirane tablice za izračun zakašnjenja paljenja i brzine kemijskih reakcija. Predmetne tablice koriste se za proračun početka izgaranja i brzine oslobađanja topline u spreju kao i za proračun početka i intenziteta detonantnog izgaranja. U petom dijelu dan je opis modela izgaranja vođenog širenjem plamena kroz predmiješanu smjesu. U šestom dijelu dan je opis modela za proračun površine plamena u slučaju širenja većeg broja plamenova kroz prostor izgaranja. U sedmom dijelu dan je opis modela za izračun emisija štetnih tvari u ispušnim plinovima. Dok je u osmom dijelu dan opis modela detonantnog izgaranja.

Validacija razvijenog modela izgaranja u dvogorivim motorima prikazana je u četvrtom poglavlju disertacije. Validacija modela turbulencije provedena je s dostupnim 3-D CFD rezultatima, dok je cijeli model validiran s prikupljenim eksperimentalnim rezultatima. Osim validacije provedena je i analiza osjetljivosti na parametre modela te je prikazana validacija modela s jedinstvenim setom konstanti.

Prikaz primjene novo razvijenog modela izgaranja u simulacijama suvremenih dvogorivih motora dan je u petom poglavlju disertacije. U tom poglavlju provedena je analiza utjecaja raznih geometrijskih i radnih parametara motora na performanse, stupanj djelovanja te emisije štetnih tvari u ispušnim plinovima konvencionalnih dvogorivih motora. Također, u tom poglavlju dan je primjer optimizacije trenutka početka izravnog ubrizgavanja dizelskog goriva u konvencionalnom dvogorivom MSUI s aspekta stupnja djelovanja motora i emisije štetnih tvari u ispušnim plinovima.

U zadnjem, šestom poglavlju doktorskog rada izvedeni su zaključci te je dan znanstveni doprinos i smjernice za daljnja poboljšanja razvijenog modela izgaranja u dvogorivim motorima s unutarnjim izgaranjem

### **Pregled DFMZCM modela izgaranja**

Novo razvijeni DFMZCM je višezonski, kvazidimenzijski 0-D model kojim je moguće opisati cijeli proces izgaranja u konvencionalnim dvogorivim motorima. Značajke novo razvijenog 0-D modela izgaranja su:

1. Višezonski pristup u 0-D modeliranju, kojim se prostor izgaranja dijeli na:
  - a. Ne izgorjelu zonu.
  - b. N zona spreja.
  - c. Zonu plamena.

2. Kvazidimenzijski pristup u 0-D modeliranju, kojim se omogućuje opis utjecaja geometrijskih parametara na brzinu oslobađanja topline:
  - a. Utjecaj geometrije prostora izgaranja.
  - b. Utjecaj geometrije brizgaljke za izravno ubrizgavanje dizelskog goriva (broj i orijentacija te lokacija mlaznica na brizgaljci).
  - c. Praćenje položaja svake od zona spreja čime se omogućuje točan izračun centra spreja te lokacije početka širenja plamena kroz predmiješanu smjesu.
  - d. Utjecaj broja plamenova koji se šire kroz predmiješanu smjesu.
  - e. Utjecaj raznih interakcija između plamenova kao i između pojedinog plamena i stijenki prostora izgaranja.
3. Opis turbulencije u cilindru motora.
4. Opis izmjene topline između pojedinih zona, kao i između smjese u cilindru i stijenki prostora izgaranja.
5. Opis procesa koji se odvijaju u spreju dizelskog goriva:
  - a. Ubrižgavanje goriva.
  - b. Proces raspada goriva na kapljice.
  - c. Zahvaćanje predmiješane smjese u zone spreja.
  - d. Zagrijavanje i isparavanje kapljica tekućeg goriva.
  - e. Paljenje smjese u zonama te izgaranje vođeno miješanjem.
  - f. Izračun formiranja štetnih tvari u zonama spreja.
6. Opis procesa širenja plamena kroz predmiješanu smjesu:
  - a. Izračun početka širenja plamena kroz predmiješanu smjesu.
  - b. Izračun laminarne brzine širenja plamena na temelju trenutnog tlaka i temperature te sastava smjese u ne izgorjeloj zoni.
  - c. Izračun ukupne površine plamene plohe na temelju broja plamenova koji se šire kroz prostor izgaranja te na temelju pozicije centra pojedinog plamena.
  - d. Izračun turbulentne brzine oslobađanja topline.
  - e. Izračun formiranja štetnih tvari unutar zone plamena
7. Izračun emisije UHC ispred fronte plamena (unutar ne izgorjele zone).
8. Izračun pojave i intenziteta detonantnog izgaranja ispred fronte plamena (unutar ne izgorjele zone).

Pojava turbulencije opisana je 0-D  $k-\varepsilon$  modelom turbulencije koji je razvijen i validiran u [32]. U okviru ovog istraživanja taj model je dodatno proširen kako bi se obuhvatile sljedeće pojave:

1. Utjecaj izravnog ubrizgavanja na razinu turbulentne kinetičke energije, na veličinu turbulentnih vrtloga koji naboravaju frontu plamena te na vrijeme raspada turbulentnih vrtloga koji definiraju tranziciju iz laminarnog u turbulentni predmiješani plamena te trajanje izmjene topline između pojedinih zona u cilindru.
2. Utjecaj geometrije na veličinu turbulentnih vrtloga koji naboravaju frontu plamena. Budući da je vrijeme raspada vrtloga u funkciji veličine turbulentnog vrtloga, ovim proširenjem poboljšana je i izračun vremena raspada turbulentnih vrtloga.

Izmjena topline između smjese koja se nalazi u cilindru te stijenki cilindra opisana je s poznatom Woschnijevom korelacijom za konvektivni prijenos topline [75]. Izmjena topline između pojedinih zona u cilindru temelji se na pristupu koji je razvijen u [34] i bazira se na pretpostavci da će nakon što protekne odgovarajuće vrijeme (tzv. vrijeme izmjene topline) cijeli sadržaj cilindra biti na istoj temperaturi. Međutim, suprotno originalnom modelu [34] u kojem je vrijeme izmjene topline bilo zadano kao parametar, u DFMZC-u je vrijeme izmjene topline povezano s vremenom raspada turbulentnih vrtloga.

Pojave u spreju dizelskog goriva opisane su na temelju poznatog Hiroyasuovog modela spreja [42], koji je ugrađen u AVL Boost kroz istraživanje koje je predstavljeno u [33]. Budući da se u dvogorivim motorima dodatno gorivo miješa u sprej dizelskog goriva te da to dodatno gorivo ima veliki utjecaj na paljenje smjese kao i na izgaranje u spreju koje je vođeno miješanjem, u okviru ovog istraživanja bilo je potrebno nadograditi postojeći model spreja. Jednako tako, budući da izgaranje u spreju ima veliki utjecaj i povezano je s kasnijim širenjem plamena kroz prostor izgaranja, bilo je potrebno razviti dodatne pod-modele kako bi se mogla opisati ta interakcija. Nadograđeni i novo razvijeni podmodeli spreja obuhvaćaju sljedeća poboljšanja i pojave:

1. Utjecaj dodatnog goriva na stanje unutar svake zone spreja.
2. Novi način izračuna brzine ubrizgavanja goriva.
3. Izračun pozicije svake zone u cilindru te izračun pozicije centra spreja.
4. Novi pristup u izračunu zakašnjenja paljenja (početka izgaranja), kroz koji su obuhvaćeni sastav gorive smjese te utjecaj umiješanog prirodnog plina.
5. Novi pristup u izračunu brzine oslobađanja topline uslijed izgaranja vođenog miješanjem kroz koji su obuhvaćeni kvaliteta gorive smjese (brzina kemijskih reakcija) te utjecaj umiješanog prirodnog plina.

Zakašnjenje paljenja i brzina kemijskih reakcija računaju se na temelju podataka iz tablica (tablice zakašnjenja paljenja i brzine kemijskih reakcija). Te su tablice generirane posebnim novo razvijenom kodom unutar kojeg se za niz različitih početnih uvjeta (tlak, temperatura,



sastav smjese), u zatvorenom adijabatskom reaktoru konstantnog volumena, izračunavaju visoko-temperaturno i nisko-temperaturno zakašnjenje paljenja, udio energije oslobođene za vrijeme nisko-temperaturnih kemijskih reakcija te sama brzina kemijskih reakcija. Tablice zakašnjenja paljenja i brzine kemijskih reakcija koriste se kod izračuna pojava u spreju dizelskog goriva (paljenje i brzina oslobađanja topline) te kod izračuna pojave i intenziteta detonantnog izgaranja.

Pojava širenja plamena kroz predmiješanu smjesu može se izračunati sa dva različita 0-D modela:

1. Postojećim fraktalnim modelom (FCM) koji je korišten za opis procesa širenja plamena u 0-D modelima izgaranja u [32]
2. Novo ugrađenim turbulentnim modelom (TCM) koji je baziran na izračunu turbulentne brzine plamena prema izrazu iz [56]. Isti izraz za izračun turbulentne brzine plamena primjenjuje se kod izračuna brzine izgaranja vođenog širenjem plamena kroz predmiješanu smjesu u 3-D CFD programskom paketu AVL Fire.

Kako bi se na odgovarajući način opisao rani razvoj plamena kao i tranzicija predmiješanog plamena iz laminarnog u turbulentni, razvijeni su novi pod-modeli inicijacije plamena kao i novi pod-model za izračun tranzicije iz laminarnog u turbulentni plamen. Također, s ciljem točnijeg opisa završne faze izgaranja razvijen je novi pod-model za izračun završne faze dogorijevanja uz stjenke cilindra.

Trenutačna laminarna brzina širenja plamena računa se posebno razvijenim i novo ugrađenim tablicama. Ove tablice dobivene su od partnera u istraživanju, tvrtke AVL List GmbH. Trenutačna glatka površina plamena računa se iz tablica koje se kreiraju na početku proračuna. U svrhu izrade tih tablica koje uključuju i efekt istovremenog širenja većeg broja plamenova kroz prostor izgaranja kao i mogućnost da se centri plamena nalaze na bilo kojoj poziciji unutar cilindra, razvijen je posebni matematički model koji je također ugrađen u programski paket AVL Boost.

Za izračun stvaranja štetnih spojeva unutar zone plamena i zona spreja korišteni su postojeći modeli koji su dostupni unutar programskog paketa AVL Boost.

Pojava detonantnog izgaranja u zoni ispred fronte plamena računa se na temelju postojećeg modela koji je razvijen i integriran u programski paket AVL Boost kroz istraživanje koje je predstavljeno u [58]. Slično kao i kod modela turbulencije i izgaranja u spreju, kako bi se poboljšao opis stvarnih fizikalnih procesa koji dovode do pojave detonantnog izgaranja, postojeći je model nadograđen i proširen te sada uključuje:

1. Izračun nisko-temperaturnog i visoko-temperaturnog zapaljenja smjese od početka visoko-tlačnog dijela ciklusa. Uvođenjem ovakvog načina proračuna moguće je obuhvatiti efekt samozapaljenja smjese prije početka širenja plamena kroz prostor izgaranja.
2. Zakašnjenje paljenja kao i intenzitet detonantnog izgaranja računaju se na temelju novih kemijskih tablica.

## **Zaključak i doprinos rada**

U validacijskom dijelu ove doktorske disertacije utvrđeno je da se novo razvijenim 0-D modelom izgaranja mogu na zadovoljavajući način opisati pojave u konvencionalnom dvogorivom motoru. Također je utvrđeno da se proračunski rezultati jako dobro poklapaju s rezultatima eksperimentalnih ispitivanja.

U završnom dijelu doktorske disertacije unutar kojeg je pokazana primjena novo-razvijenog 0-D modela izgaranja utvrđeno je da je s DFMZCM modelom na odgovarajući način moguće pratiti promjene koje se javljaju u izgaranju kao i u performansama, stupnju djelovanja i emisiji štetnih tvari u ispušnim plinovima kao posljedica promjena geometrijskih i radnih parametara motora. Također, u tom je dijelu pokazana i primjena DFMZCM modela u optimiranju jedne radne točke suvremenog motora u vidu performansi, stupnja djelovanja i emisija štetnih tvari u ispušnim plinovima.

Znanstveni doprinosi predstavljenog dokorskog istraživanja u sklopu kojeg je razvijen i izrađen simulacijski model izgaranja dvogorivoga motora, te je isti ugrađen u postojeći programski paket za proračun radnog ciklusa motora s unutarnjim izgaranjem, su:

1. novi podmodeli za opis geometrije višestrukog širenja plamenova kroz prostor izgaranja, za interakciju spreja dizelskog goriva i predmiješanog plamena u prostoru izgaranja te za izračun zakašnjenja paljenja i brzine oslobađanja topline mješavine dizelskog goriva i prirodnog plina;
2. integracija razvijenih podmodela u novi model izgaranja dvogorivih motora;
3. proračun heterogenosti u pogledu temperature i sastava smjese omogućuje kvalitativni izračun emisija štetnih plinova dvogorivih motora i promjene trenutka početka izgaranja s obzirom na promjenu radnih parametara te izračun trajanja i intenziteta pojedine faze izgaranja;
4. numerička analiza utjecaja i optimizacija radnih parametara dvogorivoga motora s unutarnjim izgaranjem s obzirom na kriterije emisija, učinkovitosti te ostvarenih snaga motora.

## List of Figures

Figure 1. Global GHG emissions by gas; data taken from [10] .....	3
Figure 2. Global GHG emissions by economic sector; data taken from [10] .....	3
Figure 3. Worldwide trends in the number and production of motor vehicles, and number of motor vehicles per 1000 people in the U. S.; data taken from [11].....	4
Figure 4. Conventional dual fuel engine operating principle .....	9
Figure 5. Conventional dual fuel engine rate of heat release (ROHR) and mass fraction burned (MFB) traces .....	10
Figure 6. Types of simulation model (model complexity .vs. computational time curve) .....	12
Figure 7. Zero-dimensional calculation approach in the IC engine combustion modeling .....	12
Figure 8. Schematic overview of the tracked species .....	21
Figure 9. Schematic presentation of the gas exchange process in 0-D calculation.....	23
Figure 10. Schematic presentation of the high-pressure cycle in 0-D calculation .....	23
Figure 11. Schematic presentation of the interaction between the zones.....	27
Figure 12. Presentation of the injector geometry; $z_{tip}$ (m) – injector nozzle hole depth; $\varphi_{nozzl}$ (rad) – injector nozzle hole angle; $\alpha_{nozzl}$ (rad) – angle between the two neighboring injector nozzles .....	31
Figure 13. Schematic presentation of the spray angle; $\varphi_{spray}$ (rad) – spray angle .....	31
Figure 14. Schematic presentation of the possible combustion chamber designs .....	32
Figure 15. Schematic presentation of possible flame center locations and number of flames that propagate through the combustion chamber .....	32
Figure 16. Schematic presentation of the zone created inside the cylinder at the intake valve closure moment .....	33
Figure 17. Schematic presentation of the zones inside the cylinder during injection of Diesel fuel .....	34
Figure 18. Schematic presentation spray zones formation.....	34
Figure 19. Schematic presentation of the interaction between one spray zone and the unburned zone before flame propagation through the premixed mixture has started.....	35
Figure 20. Schematic presentation of the process of mass transfer from the unburned spray region the unburned zone at the start of flame propagation moment .....	36
Figure 21. Schematic presentation of the zones inside the cylinder during spray combustion and flame propagation through the premixed charge .....	37
Figure 22. Schematic presentation of the interaction between the zones after the flame propagation has started .....	38
Figure 23. Scheme of the zone formation and evolution process (mass transfer between the zones).....	38

Figure 24. Various types of turbulent flows in real life and engineering applications (flow around a cyclist, flow around a car, flow in the compressor, flow that cools various hardware components); figures taken from [64].....	44
Figure 25. The schematic presentation of the energy cascade mechanism; reproduced from [32].....	45
Figure 26. Types of in-cylinder charge motion; images taken from [67], [68].....	46
Figure 27. Scheme of the zone evolution in the turbulence model .....	48
Figure 28. Presentation of the single zone turbulence approach.....	48
Figure 29. Presentation of the two-zone turbulence approach .....	50
Figure 30. Turbulent kinetic energy (Total and Unburned Zone).....	51
Figure 31. Difference in turbulent kinetic energy level between a case with and without direct fuel injection .....	53
Figure 32. Schematic presentation of the turbulent integral length scale in particular zones..	55
Figure 33. Distance between piston and cylinder head for two considered combustion chamber geometries .....	56
Figure 34. 1-D conductive heat transfer between two neighboring regions .....	58
Figure 35. Schematic of the convective heat transfer .....	59
Figure 36. Schematic of the radiative heat transfer.....	59
Figure 37. Wall heat transfer.....	61
Figure 38. Zone heat transfer principle .....	64
Figure 39. Fuel spray development process .....	66
Figure 40. DI CI engine rate of heat release curve.....	68
Figure 41. Schematic of the non-premixed (diffusion) flame.....	69
Figure 42. Non-premixed (diffusion) flame structure; reproduced from [50], [51].....	70
Figure 43. Injector and spray geometry properties .....	81
Figure 44. Zone position tracking .....	82
Figure 45. Schematic presentation of the of the wall hit conditions .....	83
Figure 46. Schematic presentation of the spray center location.....	84
Figure 47. Exothermic reaction energy profile; reproduced from [93].....	91
Figure 48. Schematic of the 0-D chemistry tabulation code .....	100
Figure 49. Normalized released energy, ROHR and 2 <sup>nd</sup> derivative of temperature traces for a case that exhibits LTHR.....	102
Figure 50. Normalized released energy, ROHR and 2 <sup>nd</sup> derivative of temperature traces for a case that does not exhibits LTHR .....	103
Figure 51. Influence of temperature on autoignition time for various n-heptane/methane fuel blends at three different pressure levels .....	104
Figure 52. Influence of pressure, equivalence ratio and combustion products mass fraction on autoignition time for various n-heptane/methane fuel blends .....	105

Figure 53. Normalized released energy traces for a case with LTHR event (left figure) and a case without LTHR event (right figure).....	107
Figure 54. Verification principle for the chemical reaction rate time calculation approach..	108
Figure 55. Verification of the chemical reaction rate time calculation approach .....	110
Figure 56. Influence of temperature on chemical reaction rate time for various n-heptane/methane fuel blends at three different pressure levels .....	111
Figure 57. Influence of pressure, equivalence ratio and combustion products mass fraction on chemical reaction rate time for various n-heptane/methane fuel blends .....	112
Figure 58. Schematic of the laminar propagating (premixed) flame .....	114
Figure 59. Laminar propagating (premixed) flame structure; reproduced from [85] .....	114
Figure 60. Regime diagram for premixed turbulent combustion according to [105]; reproduced from [51] .....	115
Figure 61. Presentation of the flamelet regime, which is characteristic for turbulent premixed combustion in IC engine; picture taken from [32] .....	117
Figure 62. Schematic of the turbulent propagating (premixed) flame .....	118
Figure 63. Typical MFB and normalized ROHR traces for a combustion process which governed by the flame propagation through the premixed mixture.....	119
Figure 64. Measured area vs. measuring scale for a surface that is fractal in its nature; reproduced from [55] .....	124
Figure 65. Measured area vs. measuring scale for a surface that is fractal in its nature and has inner and outer cutoffs; Reproduced from [55] .....	124
Figure 66. Fractal dimension as a function of the ratio of turbulence intensity to laminar flame speed; reproduced from [115].....	126
Figure 67. Schematic of the early combustion phase (spray ignition) and later combustion phase (spray combustion & flame propagation that occur at the same time).....	130
Figure 68. Schematic of the flame initiation after the start of spray combustion; partial mass transfer from the non-ignited spray zones to the unburned zone.....	131
Figure 69. Schematic of the transition from laminar to the fully developed turbulent flame	132
Figure 70. Shape of the under-relaxation function that is used in modeling the transition from laminar to the fully developed turbulent flame .....	133
Figure 71. Schematic of the transition from the fully developed turbulent flame to the wall-combustion phase.....	134
Figure 72. Shape of the under-relaxation function that is used in the wall-combustion phase modeling .....	135
Figure 73. Influence of the equivalence ratio and temperature on the laminar flame speed .	138
Figure 74. Influence of the equivalence ratio and pressure on the laminar flame speed .....	138
Figure 75. Influence of the equivalence ratio and EGR mass fraction on the laminar flame speed .....	139

Figure 76. Influence of the equivalence ratio and temperature on the surface area specific laminar mass burning rate.....	140
Figure 77. Influence of the equivalence ratio and pressure on the surface area specific laminar mass burning rate.....	140
Figure 78. Influence of the equivalence ratio and EGR mass fraction on the surface area specific laminar mass burning rate .....	141
Figure 79. Schematic presentation of the combustion chamber section (top two figures) and considered combustion chamber geometry types (bottom two figures) .....	142
Figure 80. Schematic of the flame location within the combustion chamber and its relative position to the combustion chamber walls and calculation domain boundaries....	146
Figure 81. Schematic of the division of the numerical calculation of the sphere volume and surface area (division into slices).....	148
Figure 82. Schematic of the possible flame – combustion chamber walls interactions .....	149
Figure 83. Schematic of the sections within the combustion chamber .....	150
Figure 84. Schematic of the division of the flame surface data calculation in two parts.....	150
Figure 85. Schematic of the free flame arc, interaction arc, flame slice surface area.....	151
Figure 86. Schematic of the flame center location relative to the combustion chamber geometry .....	153
Figure 87. Schematic of the specific interaction in the case of the 1 <sup>st</sup> type of the relative location between the flame center and the domain walls .....	154
Figure 88. Schematic of the specific interaction in the case of the 2 <sup>nd</sup> type of the relative location between the flame center and the domain walls .....	155
Figure 89. Schematic of the specific interaction in the case of the 3 <sup>rd</sup> type of the relative location between the flame center and the domain walls .....	156
Figure 90. Schematic of the specific interaction in the case of the 4 <sup>th</sup> type of the relative location between the flame center and the domain walls .....	157
Figure 91. Schematic of the specific interaction in the case of the 5 <sup>th</sup> type of the relative location between the flame center and the domain walls .....	159
Figure 92. Schematic of the specific interaction in the case of the 6 <sup>th</sup> type of the relative location between the flame center and the domain walls .....	160
Figure 93. Schematic of the 1 <sup>st</sup> type of the flame slice – wall interaction .....	161
Figure 94. Schematic of the 2 <sup>nd</sup> type of the flame slice – wall interaction .....	162
Figure 95. Schematic of the 3 <sup>rd</sup> type of the flame slice – wall interaction.....	163
Figure 96. Schematic of the 4 <sup>th</sup> type of the flame slice – wall interaction .....	164
Figure 97. Schematic of the 5 <sup>th</sup> type of the flame slice – wall interaction .....	165
Figure 98. Schematic of the 6 <sup>th</sup> type of flame slice – wall interaction.....	166
Figure 99. The occurrence of autoignition in engines which operate with the premixed mixture .....	176

Figure 100. Schematic presentation of the unburned zone temperature stratification sub-model .....	177
Figure 101. Schematic of the mesh that was used in the 3-D CFD simulation.....	183
Figure 102. Specific TKE and temperature fields inside the cylinder at two specific crank angle positions .....	184
Figure 103. Schematic of the single cylinder Diesel engine model created in the AVL CruiseM .....	185
Figure 104. Comparison of pressure, temperature, ROHR and specific TKE results simulated with 3-D CFD and 0-D DFMZCM for the pure Diesel case; specific experimental results were also added to the charts for comparison .....	187
Figure 105. Schematic of the single cylinder dual fuel IC engine model that was created in the AVL CruiseM .....	188
Figure 106. Schematic of the UC Berkeley IC engine experimental setup.....	190
Figure 107. Micro-Motion Coriolis mass flow meters; figures taken from [150] .....	190
Figure 108. Real piston geometry (figure taken from [151]) vs. modeled piston geometry..	191
Figure 109. VW IC engine cylinder head; figure taken from [151].....	191
Figure 110. Intake and exhaust valve lift profiles .....	192
Figure 111. Schematic of the high pressure fuel (Diesel fuel) delivery system; figure taken from [150] .....	192
Figure 112. Schematic of the port fuel injection system; figure taken from [150] .....	193
Figure 113. Comparison between the measured and simulated CA5, CA10, CA50, CA90 and CA95 values for the base operating point.....	197
Figure 114. Comparison between the measured and simulated in-cylinder pressure, temperature, ROHR and MFB traces for the base operating point.....	198
Figure 115. Comparison between the measured and simulated NO <sub>x</sub> , CO, HC and soot emissions for the base operating point.....	198
Figure 116. Influence of the $S_{in}$ model parameter on the in-cylinder pressure and ROHR traces; FCM flame propagation model .....	200
Figure 117. Influence of the $S_{in}$ model parameter on the in-cylinder pressure and ROHR traces; TCM flame propagation model .....	200
Figure 118. Influence of the $S_{in}$ model parameter on the in-cylinder turbulence quantities ..	201
Figure 119. Influence of the $S_{in}$ model parameter on fractal dimension (FCM) and on the turbulent flame velocity (TCM).....	202
Figure 120. Influence of the $C_{in}$ model parameter on the in-cylinder pressure and ROHR traces; FCM flame propagation model .....	202
Figure 121. Influence of the $C_{in}$ model parameter on the in-cylinder pressure and ROHR traces; TCM flame propagation model .....	203
Figure 122. Influence of the $C_{in}$ model parameter on the in-cylinder turbulence quantities..	203

Figure 123. Influence of the $C_{in}$ model parameter on fractal dimension (FCM) and on the turbulent flame velocity (TCM).....	204
Figure 124. Influence of the $S_{inj}$ model parameter on the in-cylinder pressure and ROHR traces; FCM flame propagation model .....	205
Figure 125. Influence of the $S_{inj}$ model parameter on the in-cylinder pressure and ROHR traces; TCM flame propagation model .....	205
Figure 126. Influence of the $C_{inj}$ model parameter on the in-cylinder pressure and ROHR traces; FCM flame propagation model .....	205
Figure 127. Influence of the $C_{inj}$ model parameter on the in-cylinder pressure and ROHR traces; TCM flame propagation model .....	206
Figure 128. Influence of the $S_{inj}$ model parameter on the in-cylinder turbulence quantities .	206
Figure 129. Influence of the $C_{inj}$ model parameter on the in-cylinder turbulence quantities .	207
Figure 130. Influence of the $S_{inj}$ model parameter on fractal dimension (FCM) and on the turbulent flame velocity (TCM).....	208
Figure 131. Influence of the $C_{inj}$ model parameter on fractal dimension (FCM) and on the turbulent flame velocity (TCM).....	208
Figure 132. Influence of the $C_\varepsilon$ model parameter on the in-cylinder pressure and ROHR traces; FCM flame propagation model .....	210
Figure 133. Influence of the $C_\varepsilon$ model parameter on the in-cylinder pressure and ROHR traces; TCM flame propagation model .....	210
Figure 134. Influence of the $C_\varepsilon$ model parameter on the in-cylinder turbulence quantities ..	211
Figure 135. Influence of the $C_\varepsilon$ model parameter on fractal dimension (FCM) and on the turbulent flame velocity (TCM).....	211
Figure 136. Influence of the $C_{\varepsilon,UZ}$ model parameter on the in-cylinder pressure and ROHR traces; FCM flame propagation model .....	212
Figure 137. Influence of the $C_{\varepsilon,UZ}$ model parameter on the in-cylinder pressure and ROHR traces; TCM flame propagation model .....	213
Figure 138. Influence of the $C_{\varepsilon,UZ}$ model parameter on the in-cylinder turbulence quantities	213
Figure 139. Influence of the $C_{\varepsilon,UZ}$ model parameter on fractal dimension (FCM) and on the turbulent flame velocity (TCM).....	214
Figure 140. Influence of the $C_L$ model parameter on the in-cylinder pressure and ROHR traces; FCM flame propagation model .....	215
Figure 141. Influence of the $C_L$ model parameter on the in-cylinder pressure and ROHR traces; TCM flame propagation model .....	215
Figure 142. Influence of the $C_L$ model parameter on the in-cylinder turbulence quantities ..	216
Figure 143. Influence of the $C_L$ model parameter on fractal dimension (FCM) and on the turbulent flame velocity (TCM).....	216
Figure 144. Influence of the turbulence model parameters on the CA10, CA50 and CA90 for both flame propagation models .....	218



Figure 145. Influence of the $C_{\text{evap,HT}}$ model parameter on the in-cylinder pressure and ROHR traces, as well as on the DFI mass and SZ temperature traces .....	221
Figure 146. Influence of the $C_{\text{evap}}$ model parameter on the in-cylinder pressure and ROHR traces, as well as on the DFI mass and SZ temperature traces .....	221
Figure 147. Influence of the $C_{\text{entrain}}$ model parameter on the in-cylinder pressure and ROHR traces, as well as on the mass entrained into the spray region and on the excess air ratio inside the spray region .....	222
Figure 148. Influence of the $C_{\text{ignition}}$ model parameter on the in-cylinder pressure and ROHR traces .....	223
Figure 149. Influence of the $C_{\text{discr,ax}}$ model parameter on the in-cylinder pressure and ROHR traces .....	224
Figure 150. Influence of the $C_{\text{discr,rad}}$ model parameter on the in-cylinder pressure and ROHR traces .....	224
Figure 151. Influence of the $C_{\text{ZHT,SZ}}$ model parameter on the in-cylinder pressure and ROHR traces, as well as on the spray ROHR and SZ temperature standard deviation traces .....	225
Figure 152. Influence of the spray model parameters on the ignition delay, CA10, CA50 and CA90 .....	226
Figure 153. Influence of the $C_{\text{trans}}$ model parameter on the in-cylinder pressure and ROHR traces; FCM flame propagation model .....	229
Figure 154. Influence of the $C_{\text{trans}}$ model parameter on the in-cylinder pressure and ROHR traces; TCM flame propagation model .....	229
Figure 155. Influence of the $C_{\text{ign,UZ,transf}}$ model parameter on the in-cylinder pressure and ROHR traces; FCM flame propagation model .....	230
Figure 156. Influence of the $C_{\text{ign,UZ,transf}}$ model parameter on the in-cylinder pressure and ROHR traces; TCM flame propagation model .....	230
Figure 157. Influence of the $C_{\text{SOWC}}$ model parameter on the in-cylinder pressure and ROHR traces; FCM flame propagation model .....	231
Figure 158. Influence of the $C_{\text{SOWC}}$ model parameter on the in-cylinder pressure and ROHR traces; TCM flame propagation model .....	232
Figure 159. Influence of the $C_{\text{WC,shp}}$ model parameter on the in-cylinder pressure and ROHR traces; FCM flame propagation model .....	233
Figure 160. Influence of the $C_{\text{WC,shp}}$ model parameter on the in-cylinder pressure and ROHR traces; TCM flame propagation model .....	233
Figure 161. Influence of the $C_{\text{comb}}$ model parameter on the in-cylinder pressure and ROHR traces; FCM flame propagation model .....	234
Figure 162. Influence of the $C_{\text{comb}}$ model parameter on the in-cylinder pressure and ROHR traces; FCM flame propagation model .....	234
Figure 163. Influence of the $C_{\text{EOF}}$ model parameter on the in-cylinder pressure and ROHR traces; FCM flame propagation model .....	235

Figure 164. Influence of the $C_{EOF}$ model parameter on the in-cylinder pressure and ROHR traces; TCM flame propagation model .....	235
Figure 165. Influence of the flame propagation model parameters ( $C_{trans}$ , $C_{WC,shp}$ , $C_{comb}$ ) on the CA10, CA50 and CA90 for both flame propagation models .....	237
Figure 166. Comparison between the measured and simulated in-cylinder pressure, temperature, ROHR and MFB traces for OP1 at 1000 rpm .....	242
Figure 167. Comparison between the measured and simulated in-cylinder pressure, temperature, ROHR and MFB traces for OP2 at 1000 rpm .....	243
Figure 168. Comparison between the measured and simulated in-cylinder pressure, temperature, ROHR and MFB traces for OP3 at 1000 rpm .....	244
Figure 169. Comparison between the measured and simulated in-cylinder pressure, temperature, ROHR and MFB traces for OP4 at 1000 rpm .....	244
Figure 170. Comparison between the measured and simulated IMEPg, peak cylinder pressure and the crank angle at the peak cylinder pressure for all operating points at 1000 rpm .....	245
Figure 171. Comparison between the measured and simulated in-cylinder pressure, temperature, ROHR and MFB traces for OP1 at 1800 rpm .....	249
Figure 172. Comparison between the measured and simulated in-cylinder pressure, temperature, ROHR and MFB traces for OP2 at 1800 rpm .....	249
Figure 173. Comparison between the measured and simulated in-cylinder pressure, temperature, ROHR and MFB traces for OP3 at 1800 rpm .....	250
Figure 174. Comparison between the measured and simulated in-cylinder pressure, temperature, ROHR and MFB traces for OP4 at 1800 rpm .....	250
Figure 175. Comparison between the measured and simulated in-cylinder pressure, temperature, ROHR and MFB traces for OP5 at 1800 rpm .....	251
Figure 176. Comparison between the measured and simulated in-cylinder pressure, temperature, ROHR and MFB traces for OP6 at 1800 rpm .....	251
Figure 177. Comparison between the measured and simulated in-cylinder pressure, temperature, ROHR and MFB traces for OP7 at 1800 rpm .....	252
Figure 178. Comparison between the measured and simulated in-cylinder pressure, temperature, ROHR and MFB traces for OP8 at 1800 rpm .....	252
Figure 179. Comparison between the measured and simulated in-cylinder pressure, temperature, ROHR and MFB traces for OP9 at 1800 rpm .....	253
Figure 180. Comparison between the measured and simulated IMEPg, peak cylinder pressure and the crank angle at the peak cylinder pressure for all operating points at 1800 rpm .....	254
Figure 181. Comparison between the measured and simulated in-cylinder pressure, temperature, ROHR and MFB traces for OP1 at 1000 rpm and the single set of the flame propagation model parameters .....	257

Figure 182. Comparison between the measured and simulated in-cylinder pressure, temperature, ROHR and MFB traces for OP2 at 1000 rpm and the single set of the flame propagation model parameters.....	257
Figure 183. Comparison between the measured and simulated in-cylinder pressure, temperature, ROHR and MFB traces for OP3 at 1800 rpm and the single set of the flame propagation model parameters.....	258
Figure 184. Comparison between the measured and simulated in-cylinder pressure, temperature, ROHR and MFB traces for OP4 at 1800 rpm and the single set of the flame propagation model parameters.....	258
Figure 185. Comparison between the measured and simulated in-cylinder pressure, temperature, ROHR and MFB traces for OP5 at 1800 rpm and the single set of the flame propagation model parameters.....	259
Figure 186. Comparison between the measured and simulated in-cylinder pressure, temperature, ROHR and MFB traces for OP6 at 1800 rpm and the single set of the flame propagation model parameters.....	259
Figure 187. Comparison between the measured and simulated in-cylinder pressure, temperature, ROHR and MFB traces for OP7 at 1800 rpm and the single set of the flame propagation model parameters.....	260
Figure 188. Comparison between the measured and simulated in-cylinder pressure, temperature, ROHR and MFB traces for OP8 at 1800 rpm and the single set of the flame propagation model parameters.....	260
Figure 189. Comparison between the measured and simulated in-cylinder pressure, temperature, ROHR and MFB traces for OP9 at 1800 rpm and the single set of the flame propagation model parameters.....	261
Figure 190. Comparison between the measured and simulated IMEPg for the operating points that were simulated with the single set of the flame propagation model parameters.....	261
Figure 191. Comparison between measured and simulated pressure, temperature, ROHR and MFB traces for OP1 at 1000 rpm and the single set of all model parameters	263
Figure 192. Comparison between the measured and simulated in-cylinder pressure, temperature, ROHR and MFB traces for OP2 at 1000 rpm and the single set of all model parameters.....	264
Figure 193. Comparison between the measured and simulated in-cylinder pressure, temperature, ROHR and MFB traces for OP3 at 1800 rpm and the single set of all model parameters.....	264
Figure 194. Comparison between the measured and simulated in-cylinder pressure, temperature, ROHR and MFB traces for OP4 at 1800 rpm and the single set of all model parameters.....	265
Figure 195. Comparison between the measured and simulated in-cylinder pressure, temperature, ROHR and MFB traces for OP5 at 1800 rpm and the single set of all model parameters.....	265

Figure 196. Comparison between the measured and simulated in-cylinder pressure, temperature, ROHR and MFB traces for OP6 at 1800 rpm and the single set of all model parameters .....	266
Figure 197. Comparison between the measured and simulated in-cylinder pressure, temperature, ROHR and MFB traces for OP7 at 1800 rpm and the single set of all model parameters .....	266
Figure 198. Comparison between the measured and simulated in-cylinder pressure, temperature, ROHR and MFB traces for OP8 at 1800 rpm and the single set of all model parameters .....	267
Figure 199. Comparison between the measured and simulated in-cylinder pressure, temperature, ROHR and MFB traces for OP9 at 1800 rpm and the single set of all model parameters .....	267
Figure 200. Comparison between the measured and simulated IMEPg for the operating points that were simulated with the single set of all model parameters .....	268
Figure 201. Comparison between the simulated in-cylinder pressure, temperature, ROHR and DFI mass traces for the three different compression ratios .....	271
Figure 202. Comparison between the simulated emissions, ignition delay time and combustion phasing (CA50) for the three different compression ratios.....	271
Figure 203. Comparison between the simulated in-cylinder pressure, temperature, ROHR, DFI mass, liquid fuel SMD and laminar flame velocity traces for the three different intake pressure levels .....	273
Figure 204. Comparison between the simulated emissions, ignition delay time and combustion phasing (CA50) for the three different intake pressure levels .....	274
Figure 205. Comparison between the simulated in-cylinder pressure, temperature, ROHR and DFI mass traces for the three different intake temperature levels .....	275
Figure 206. Comparison between the simulated emissions, ignition delay time and combustion phasing (CA50) for the three different intake temperature levels.....	276
Figure 207. Comparison between the simulated in-cylinder pressure, temperature, ROHR and the laminar flame velocity traces for the three cases that feature different mass fraction of the combustion products at the IVC.....	277
Figure 208. Comparison between the simulated emissions, ignition delay time and combustion phasing (CA50) for the three cases that feature different mass fraction of the combustion products at the IVC.....	278
Figure 209. Comparison between the simulated emissions, ignition delay time and combustion phasing (CA50) for the six cases that feature different direct fuel injection timing .....	279
Figure 210. Comparison between the simulated in-cylinder pressure, temperature, ROHR, DFI mass, entrained mass and mean spray excess air ratio traces for the six cases that feature different direct fuel injection timing .....	280

Figure 211. Comparison between the simulated in-cylinder pressure, temperature, ROHR, liquid fuel SMD, DFI mass, entrained mass and mean spray excess air ratio traces for the four cases that feature different direct fuel injection pressure.....	283
Figure 212. Comparison between the simulated emissions, ignition delay time and combustion phasing (CA50) for the four cases that feature different direct fuel injection pressure .....	284
Figure 213. Comparison between the simulated in-cylinder pressure, temperature, ROHR, DFI mass, entrained mass and mean spray excess air ratio traces for the three cases that feature different Diesel fuel substitution ratio.....	286
Figure 214. Comparison between the simulated emissions, ignition delay time and combustion phasing (CA50) for the three cases that feature different Diesel fuel substitution ratios.....	287
Figure 215. Comparison between the measured and simulated in-cylinder pressure, temperature, ROHR and MFB traces.....	291
Figure 216. Comparison between the measured and simulated CA5, CA10, CA50, CA90 and CA95 values .....	292
Figure 217. Schematic of the full conventional dual fuel IC engine model that was created in the AVL Boost.....	292
Figure 218. Comparison between the simulated in-cylinder pressure, temperature, ROHR, DFI mass, entrained mass and mean spray excess air ratio traces for the seven full engine cases that feature different direct fuel injection timing .....	294
Figure 219. Comparison between the ignition delay time and combustion phasing (CA50) for the seven full engine cases that feature different direct fuel injection timing .	295
Figure 220. Engine load and NO <sub>x</sub> emissions for the seven full engine cases that feature different direct fuel injection timing.....	295
Figure 221. Engine and turbocharger efficiencies and the VGT position for the seven full engine cases that feature different direct fuel injection timing.....	296
Figure 222. Intake and exhaust pressure, and the exhaust temperature for the seven full engine cases that feature different direct fuel injection timing.....	296
Figure 223. Simulated soot emissions for the seven full engine cases that feature different direct fuel injection timing.....	298

## List of Tables

Table 1. European emissions standard for road vehicles propelled by SI engine [13] .....	5
Table 2. European emissions standard for road vehicles propelled by Diesel engine (CI engine) [13].....	5
Table 3. European emissions standard for trucks and buses (heavy duty engines [13] .....	5
Table 4. Typical composition of natural gas [15] .....	6
Table 5. Tabulation parameters (initial mixture properties) used for chemistry table generation .....	88
Table 6. Data for verification of the chemical reaction rate time calculation approach .....	109
Table 7. Tabulation parameters (initial mixture properties) used for the laminar flame speed table generation.....	137
Table 8. Geometry and operating parameters of the engine used in the turbulence model validation .....	182
Table 9. In-cylinder turbulence model parameters for turbulence validation model .....	186
Table 10. Spray and heat transfer model parameters for turbulence validation model.....	186
Table 11. Engine geometry parameters .....	189
Table 12. Base operating point parameters .....	196
Table 13. Turbulence model parameters for the base operating point .....	196
Table 14. Spray and heat transfer model parameters for the base operating point .....	196
Table 15. Flame propagation model parameters for the base operating point .....	197
Table 16. Comparison between the specific measured and simulated parameters for the base operating point .....	199
Table 17. The list of the varied turbulence model parameters .....	199
Table 18. List of the varied spray model parameters .....	220
Table 19. List of the varied FCM parameters .....	228
Table 20. List of the varied TCM parameters .....	228
Table 21. Influence of $C_{ign,UZ,transf}$ model parameter on the main combustion parameters ....	231
Table 22. Influence of $C_{SOWC}$ model parameter on the main combustion parameters .....	232
Table 23. Influence of $C_{EOF}$ model parameter on the main combustion parameters.....	236
Table 24. Operating parameters for the points at 1000 rpm.....	240
Table 25. Spray and zone heat transfer model parameters for the points at 1000 rpm .....	240
Table 26. Flame propagation model parameters for the points at 1000 rpm; the FCM flame propagation model .....	240
Table 27. Flame propagation model parameters for the points at 1000 rpm; the TCM flame propagation model .....	241
Table 28. Operating parameters for the points at 1800 rpm.....	246
Table 29. Spray and zone heat transfer model parameters for the points at 1000 rpm .....	246

Table 30. Flame propagation model parameters for the points at 1000 rpm; the FCM flame propagation model .....	247
Table 31. Flame propagation model parameters for the points at 1000 rpm; the TCM flame propagation model .....	247
Table 32. Operating parameters for the points that were used in the single set of the model parameters simulations .....	255
Table 33. The list of the spray combustion model parameters.....	256
Table 34. The list of the flame propagation model parameters.....	256
Table 35. The list of the spray combustion model parameters.....	262
Table 36. Comparison between the engine output parameters for the three different simulated compression ratios cases .....	272
Table 37. Comparison between the engine output parameters for the three different simulated intake pressure levels .....	274
Table 38. Comparison between the engine output parameters for the three different simulated intake temperature levels.....	276
Table 39. Comparison between the engine output parameters for the three cases that feature different mass fraction of the combustion products at the IVC.....	278
Table 40. Comparison between the engine output parameters for the six cases that feature different direct fuel injection timing.....	280
Table 41. Duration of the direct fuel injection for a given direct fuel injection pressure .....	282
Table 42. Comparison between the engine output parameters for the four cases that feature different direct fuel injection pressure .....	284
Table 43. Duration of the direct fuel injection for a given direct fuel injection pressure .....	285
Table 44. Comparison between the engine output parameters for the three cases that feature different Diesel fuel substitution ratios.....	287
Table 45. Base operating point parameters for the full engine simulation .....	289
Table 46. In-cylinder turbulence model parameters for optimization model.....	290
Table 47. Spray and heat transfer model parameters for optimization model .....	290
Table 48. Flame propagation model parameters for optimization model .....	290
Table 49. Comparison between the specific measured and simulated parameters .....	291
Table 50. Simulated operating points (injection timings) .....	294
Table 51. Optimum cases (injection timing) in terms of the load, efficiency and NO <sub>x</sub> emissions for the simulated operating point .....	298

# Nomenclature

Symbol	Unit	Description
<b><u>Latin letters</u></b>		
$a$	-	Measuring Scale
$A$	-	Reaction Rate Pre-Exponential Factor
$B$	-	Temperature Constant
$A_{\text{flame}}$	$\text{m}^2$	Flame Surface Area
$AFR$	-	Air/ Fuel Ratio
$AF_{\text{ST,D}}$	-	Diesel Fuel Stoichiometric Air/ Fuel Ratio
$AF_{\text{ST,M}}$	-	Methane Stoichiometric Air/ Fuel Ratio
$A_L$	$\text{m}^2$	Laminar Flame Surface Area
$anROHR$	1/s	Average Normalized ROHR
$A_s$	$\text{m}^2$	Surface Area
$AP_i$	J/(kg s)	Replacement Variable
$A_T$	$\text{m}^2$	Turbulent Flame Surface Area
$c$	$\text{kmol}/(\text{m}^3 \text{ s})$	Species Concentration
$c_{p,m}$	J/(kmol K)	Standard State Molar Heat Capacity at Constant Pressure
$c_v$	J/(kgK)	Specific Heat Capacity at Constant Volume
$c_{v,m}$	J/(kmol K)	Standard State Molar Heat Capacity at Constant Volume
$c_{v,\text{mean}}$	J/(kgK)	Specific Heat Capacity at Constant Volume of the Entire Mixture
$C_{\text{axial,SZ,i}}$	-	Axial Correction Parameter
$C_A$	-	Cross Section Area Coefficient
$C_{\text{comb}}$	-	Flame Propagation Model Parameter (Turbulent Flame Speed)
$C_{\text{discr,ax}}$	degCA	Discretization Factor of the Spray in the Axial Direction
$C_{\text{discr,rad}}$	-	Discretization Parameter in the Radial Direction of the Spray
$C_D$	-	Discharge Coefficient
$C_{\text{entrain}}$	-	Spray Combustion Model Parameter (Entrainment)
$C_{\text{evap,HT}}$	-	Spray Combustion Model Parameter (Evaporation Rate)
$C_{\text{head}}$	-	Cylinder Head Surface Area Scaling Factor



<b>Symbol</b>	<b>Unit</b>	<b>Description</b>
$C_{in}$	-	Turbulence Model Parameter (Effect of Intake on the Production of Turbulent Energy Dissipation)
$C_{inj}$	-	Turbulence Model Parameter (Effect of Injection on the Production of Turbulent Energy Dissipation)
$C_{ign,UZ,transf}$	-	Flame Propagation Model Parameter (Spray Zone Mass Transfer)
$C_{liner}$	-	Liner Surface Area Scaling Factor
$C_L$	-	Turbulence Model Parameter
$C_{piston}$	-	Piston Surface Area Scaling Factor
$C_{radial,SZ,i}$	-	Radial Correction Parameter
$C_{soot,form}$	-	Soot Formation Model Parameter
$C_{soot,oxd}$	-	Soot Oxidation Model Parameter
$C_{SOWC}$	-	Flame Propagation Model Parameter (Start of Wall Combustion)
$C_{trans}$	-	Flame Propagation Model Parameter (Flame Transition)
$C_V$	-	Velocity Coefficient
$C_{WC,shp}$	-	Flame Propagation Model Parameter (Wall Combustion Shape)
$C_{ZHT,SZ}$	-	Spray Combustion Model Parameter (Zone Heat Transfer)
$C_\varepsilon$	-	Turbulence Model Parameter (Dissipation Production Parameter)
$C_2$	-	Turbulence Model Parameter (Dissipation Destruction Parameter)
$CR$	-	Compression Ratio
$d$	m	Diameter
$D_{bowl}$	m	Piston Bowl Diameter
$D_{cyl}$	m	Cylinder Bore
$D_3$	-	Fractal Dimension
$E$	J	Energy
$f_{D3,max}$	-	Flame Propagation Model Parameter (Maximum Value of the Fractal Dimension)
$F$	-	Ratio Between the Turbulent and Laminar Flame Speeds
$h$	J/kg	Specific Enthalpy
$h_{bowl}$	m	Piston Bowl Height
$h_{HT}$	W/(m <sup>2</sup> K)	Convection Heat Transfer Coefficient
$h_m$	J/kmol	Standard State Molar Enthalpy

Symbol	Unit	Description
$h_{\text{pis}}$	m	Distance between the Piston Top and the Cylinder Head
$h_{\text{TDC}}$	m	Distance between the Piston Top and the Cylinder Head in TDC
$h_{\text{W}}$	W/(m <sup>2</sup> K)	Wall Heat Transfer Coefficient
$H$	m	Engine Stroke
$H_{\text{flame}}$	m	Flame Height
$i_{\text{axial}}$	-	Number of the Given Spray Zone in the Axial Direction
$i_{\text{pis}}$	-	Characteristic Position of the Piston (Value Inside the Piston Position Vector)
$i_{\text{rad}}$	-	Characteristic Flame Radius (Value Inside the Flame Radius Vector)
$i_{\text{radial}}$	-	Number of the Given Spray Zone in the Radial Direction
$I_{\text{f}}$	-	Under-Relaxation function for the Flame Transition Calculation
$I_{\text{T}}$	-	Under-Relaxation function for the Flame Wall Combustion
$IMEP$	Pa	Indicated Mean Effective Pressure
$IoK$	-	Knock Intensity
$k$	m <sup>2</sup> /s <sup>2</sup>	Turbulent Kinetic Energy
$k_{\text{R}}$	-	Reaction Rate
$Ka$	-	Karlovitz Number
$KI$	-	Knock Integral
$l$	m	Circle Arc
$l_{\text{k}}$	m	Kolmogorov Length Scale
$L_{\text{conrod}}$	m	Conrod Length
$LHV$	J	Lower Heating Value
$L_{\text{I}}$	m	Integral Length Scale (Taylor)
$L_{\text{I,limit}}$	m	Maximum Value of the Integral Length Scale
$L_{\text{I,turb}}$	m	Integral Length Scale Calculated from k-ε Turbulence Model
$LTHR$	-	Relative Amount of the Low-Temperature Heat Released
$m$	kg	Mass
$M$	kg/kmol	Molar Mass
$n$	rpm	Engine speed
$n_{\text{ref}}$	rpm	Referent Engine speed

Symbol	Unit	Description
$n_{\text{axial}}$	-	Total Number of the Spray Zones in the Axial Direction
$n_{\text{pis}}$	-	Number of Possible Piston Positions
$n_{\text{rad}}$	-	Number of Possible Flame Radii
$n_{\text{radial}}$	-	Total Number of the Spray Zones in the Radial Direction
$n_{\text{parcels}}$	-	Number of Parcels in the Axial Direction
$n_{\text{zones,spray}}$	-	Total Number of the Spray Zones
$N$	-	Number
$Nu$	-	Nusselt Number
$p$	Pa	Pressure
$q_{\text{m,in}}$	kg/s	Mean Intake Mass Flow
$q_{\text{m,inj}}$	kg/s	Mean Injection Mass Flow
$Q$	J	Heat
$Q_{\text{R}}$	J	Released Energy
$r_{\text{crank}}$	m	Crank Radius
$r_{\text{f r}}$	m	Flame Radius
$r_{\text{f,ref}}$	m	Referent Flame Radius
$R$	J/(kgK)	Individual gas constant
$R_{\text{bowl}}$	m	Bowl Radius
$R_{\text{cylinder}}$	m	Cylinder Radius
$Re$	-	Reynolds Number
$R_{\text{m}}$	J/(kmolK)	Ideal Gas Constant
$s_{\text{m}}$	J/kmol	Standard State Molar Entropy
$Sh$	-	Sherwood Number
$S_{\text{in}}$	-	Turbulence Model Parameter (Effect of Intake on the Production of Turbulent Kinetic Energy)
$S_{\text{inj}}$	-	Turbulence Model Parameter (Effect of Injection on the Production of Turbulent Kinetic Energy)
$S_{\text{j}}$	kg/s	Species Transformation Source Term
$S_{\text{L}}$	m/s	Laminar flame speed
$S_{\text{T}}$	m/s	Turbulent flame speed
$SMD$	m	Sauter Mean Diameter

Symbol	Unit	Description
$t$	s	Time
$t_{\text{break}}$	s	Liquid Fuel Break-Up Time
$t_{\text{hit}}$	s	Time Elapsed from the Moment that the Spray Hit the Combustion Chamber Wall
$t_{10}$	s	Time when 10% of the Energy Has Been Released
$t_{90}$	s	Time when 90% of the Energy Has Been Released
$T$	K	Temperature
$u$	J/kg	Specific Internal Energy
$u_{\text{in}}$	m/s	Mean Cross Flow Velocity at the Intake Valve
$u_{\text{inj}}$	m/s	Mean Cross Flow Velocity at the Injector Nozzle
$u_{\text{m}}$	J/kmol	Standard State Molar Internal Energy
$u_{\text{T}}$	m/s	Turbulence Intensity
$U$	J	Internal Energy
$v$	m/s	Velocity
$v_{\text{tip}}$	m/s	Spray Tip Velocity
$V$	m <sup>3</sup>	Volume
$V_{\text{D}}$	m <sup>3</sup>	Displacement Volume
$w_{\text{WHT,FZ}}$	Jm <sup>2</sup> K	Wall Heat Transfer Factor for the Flame Zone
$w_{\text{WHT,SZ},i}$	Jm <sup>2</sup> K	Wall Heat Transfer Factor for the $i$ -th Spray Zone
$w_{\text{WHT,UZ}}$	Jm <sup>2</sup> K	Wall Heat Transfer Factor for the Unburned Zone
$W$	J	Work
$W_{\text{flame}}$	m	Flame Width
$X$	-	Species Mass Fraction Vector
$x_{\text{metFV}}$	-	Mass Fraction of Methane Inside the Fuel Vapor
$x_i$	-	Particular Species ( $i$ ) Mass Fraction
$x_{\text{piston}}$	m	Distance Between the Piston Top and Cylinder Head
$x_{\text{SZ},i,\text{front}}$	m	Front Position of the $i$ -th Spray Zone
$x_{\text{SZ},i,\text{medium}}$	m	Medium Position of the $i$ -th Spray Zone
$x_{\text{SZ},i,\text{rear}}$	m	Rear Position of the $i$ -th Spray Zone
$z$	m	Vertical Distance

Symbol	Unit	Description
$z_{tip}$	m	Injector Nozzle Hole Depth
$\Delta Q$	J/(kg s)	Replacement Variable Which is Used in the Pressure and Temperature Derivative Equations (Heat and Work Term)
$\Delta SR$	J/s	Replacement Variable Which is Used in the Pressure and Temperature Derivative Equations (Gas Constant Term)
$\Delta SU$	J/(kg K s)	Replacement Variable Which is Used in the Pressure and Temperature Derivative Equations (Internal Energy Term)
$\Delta t$	s	Time Step (Discretization)
$\Delta t_{10-90}$	s	Time Elapsed between 10% and 90% of the Fuel Burned

### **Greek letters**

$\alpha_{\text{nozzle}}$	rad	Angle Between the Two Neighboring Injector Nozzles
$\beta$	-	Temperature Exponent
$\varepsilon$	$\text{m}^2/\text{s}^3$	Turbulent Kinetic Energy Dissipation
$\varepsilon_{\text{HT}}$	-	Emissivity of the Radiation Source
$\lambda$	$\text{W}/(\text{mK})$	Thermal Conductivity
$\lambda_{\text{crank}}$	-	Crank Mechanism Characteristic Value
$\gamma_{\text{wall}}$	-	Temperature Decrease Rate
$\gamma_{\text{wr}}$	-	Flame Wrinkling Rate
$\mu$	$\text{Pa s}$	Dynamic Viscosity
$\rho$	$\text{kg}/\text{m}^3$	Density
$\varphi$	rad	Spray Zone Angle
$\varphi_{\text{act}}$	rad	Actual Crank Angle
$\varphi_{\text{knock}}$	degCA	Crank Angle at the Start of Knock
$\varphi_{\text{nozzle}}$	rad	Injector Nozzle Hole Angle
$\varphi_{\text{old}}$	rad	Old Crank Angle
$\varphi_{\text{spray}}$	rad	Spray Angle
$\sigma$	$\text{W}/\text{m}^2\text{K}^4$	Stefan – Boltzmann constant
$\tau$	s	Time Scale
$\tau_{\text{reac}}$	s	Reaction Rate Time
$\nu$	$\text{m}^2/\text{s}$	Kinematic viscosity
$\omega$	$\text{kmol}/\text{m}^3\text{s}$	Molar Production Rate
$\Delta\varphi$	rad	Crank Angle Step (Discretization)

### **Subscripts**

act	Actual
aSoFP	After Start of Flame Propagation
avail	Available
AIR	Air
bound	Boundary
B	Burned

BB	Blow-By
BZ	Burned zone
center	Center
charge	Charge (Fuel/ Air/ Combustion Products Mixture)
comb	Combustion
cond	Conduction
conv	Convection
cyl	Cylinder
CP	Combustion Products
det	Knock (Detonation)
D	Diesel Fuel
entr	Entrainment
evap	Evaporation
exh	Exhaust
EOI	End of Injection
flame	Flame (Single Flame)
form	Formed
fresh	Fresh
fuel	Fuel
F	Flame (Surface Area)
FB	Fuel Burned
FP	Flame Propagation
FV	Fuel Vapor
FZ	Flame Zone
head	Head
H	Head (Surface Area)
HC	Hydrocarbon
HT	High-Temperature
i	Zone
id	Ideal

init	Initial
inj	Injection
inner	Inner
int	Intake
IVC	Intake Valve Closure
j	Species
liq	Liquid
loc	Location
L	Laminar
LT	Low-Temperature
liner	Liner
max	Maximum
m	Mean
medium	Medium
min	Minimum
mixed	Mixed
mot	Motored
M	Methane
n	Nozzle
outer	Outer
overall	Overall
oxd	Oxidized
piston	Piston
P	Piston (Surface Area)
PM	Particulate Matter
rad	Radiation
rail	Rail
reac	Reaction
rem	Remaining
R	Reaction (Zone)



satur	Saturation
slice	Slice
soot	Soot
spray	Spray
stoich	Stoichiometric
SHP	Start of High Pressure
SOC	Start of Combustion
SOK	Start of Knock
SZ	Spray Zone
tot	Total
tran	Transition
transf	Transfer
T	Turbulence
TDC	Top Dead Center
UZ	Unburned zone
wall	Wall
WC	Wall Combustion
WHT	Wall Heat Transfer
ZHT	Zone Heat Transfer

## Abbreviations

Mark	Description
aTDC	After Top Dead Center
BMEP	Brake Mean Effective Pressure
bTDC	Before Top Dead Center
CFD	Computational Fluid Dynamics
CA5	Crank Angle at which 5% of Energy has been Released
CA10	Crank Angle at which 10% of Energy has been Released
CA50	Crank Angle at which 50% of Energy has been Released
CA90	Crank Angle at which 90% of Energy has been Released
CA95	Crank Angle at which 95% of Energy has been Released
CO	Carbon Monoxide
CO <sub>2</sub>	Carbon Dioxide
DFMZCM	Dual Fuel Multi-zone Combustion Model
DI-CI	Direct Injection Compression Ignition
DOI	Duration of Injection
ECFM-3Z	Extended Coherent Flame Model – Three Zone
EGR	Exhaust Gas Recirculation
EOC	End of Combustion
EoFP	End of Flame Propagation
EVO	Exhaust Valve Opening
FCM	Fractal Combustion Model
FTDC	Firing Top Dead Center
H	Hydrogen Atom
HCCI	Homogeneous Charge Compression Ignition
HP	High Pressure
HPDI	High Pressure Direct Injection
H <sub>2</sub>	Hydrogen
H <sub>2</sub> O	Water Vapor

IC	Internal Combustion
IMEP	Indicated Mean Effective Pressure
IMEP <sub>g</sub>	Gross Indicated Mean Effective Pressure
IVC	Intake Valve Closure
LMEP	Loss Mean Effective Pressure
LP	Low Pressure
NO <sub>x</sub>	Nitrogen Oxides
N	Nitrogen Atom
N <sub>2</sub>	Nitrogen Molecule
NMHC	Non Methane Hydrocarbons
O	Oxygen Atom
OH	Reaction Radical
O <sub>2</sub>	Oxygen Molecule
PAH	Polycyclic Aromatic Hydrocarbons
PPCI	Partially Premixed Compression Ignition
RCCI	Reactivity Controlled Compression Ignition
RHS	Right Hand Side
ROHR	Rate of Heat Release
SHP	Start of High Pressure
SI	Spark Ignition
SOC	Start of Combustion
SoFP	Start of Flame Propagation
SOI	Start of Injection
StD	Standard Deviation
TCM	Turbulent Flame Speed Combustion Model
TDC	Top Dead Center
TED	Turbulent Energy Dissipation
THC	Total Hydrocarbons
TKE	Turbulent Kinetic Energy
UHC	Unburned Hydrocarbons

VVA	Variable Valve Actuator
VGT	Variable Geometry Turbocharger
0-D	Zero-dimensional
1-D	One-dimensional
2-D	Two-dimensional
3-D	Three-dimensional

# 1. Introduction

This thesis presents the development of a quasi-dimensional combustion model for the cycle-simulations in conventional dual fuel internal combustion (IC) engines. The main objective of this research was to create a predictive, but still computationally cheap simulation tool for studying the influence of various engine operating and geometry parameters on the overall conventional dual fuel engine performance, and some of the initial findings of this research have already been published in [1]–[4].

Quasi-dimensional models are a part of zero-dimensional (0-D) models, which means that this is a 0-D model. In order to describe the heterogeneities that occur in an IC engine combustion chamber, in this combustion model the combustion chamber is divided into a number of zones, which makes this model a multi-zone model. Onwards, the overall model will be referred to with an abbreviation, DFMZCM (Dual Fuel Multi-Zone Combustion Model).

The motivation for this work comes from the fact that there is a need to reduce the impact of IC engines on the environment. As will be shown in the next few chapters of this thesis, if properly adjusted the conventional dual fuel IC engine offers a reduction of greenhouse gas emissions, while retaining high, Diesel-like efficiency. However, in order to properly adjust an IC engine in the process of conversion from a conventional Diesel engine, few steps have to be performed and simulation tools can aid in this process. In order to use simulation tools they have to be able to simulate dual fuel combustion.

The overview of the research field showed that there is a need for a physically based, predictive 0-D combustion model that can simulate combustion process in a conventional dual fuel IC engine.

## 1.1. Combustion Process in the IC Engines

Combustion is a chemical process that involves a reaction of the fuel and oxygen and results in the release of a large amount of energy (heat). In the case of the IC engines the fuels that are used in the majority of applications are mixtures of hydrocarbons; while the oxygen comes from air; the exception is a so-called oxy-combustion process, which uses pure oxygen. Depending on the combustion process, the conventional IC engines can be divided into:

1. Spark-ignition (SI) engines that usually operate with gasoline.
2. Compression-ignition (CI) engines that usually operate with the Diesel fuel.

In order to differentiate between the conventional (Diesel) compression ignition engine and the advanced compression ignition concepts, such as homogeneous charge compression ignition (HCCI), when referred to the conventional Diesel engine, the abbreviation DI-CI (Direct Injection Compression-Ignition) will be used. These two IC engine types operate with different combustion concepts. In the SI engines, combustion is governed by the turbulent flame propagation through the premixed mixture, also referred to as the turbulent premixed flame. On the other hand, in the DI-CI engines combustion is governed by the turbulent fuel-air mixing, also referred to as the turbulent non-premixed or diffusion flame.

A result of the combustion process of any sort of fuel and any sort of oxidizer (pure oxygen or various mixtures of oxygen and other species, i.e. air) is a mixture of gases which are called combustion products. These combustion products, mostly emitted into the atmosphere contain a large amount of various harmful substances. These harmful substances are often referred to as the harmful exhaust gas emissions. In IC engines, the combustion products primarily consist of:

1. Carbon dioxide ( $\text{CO}_2$ ) and water vapor ( $\text{H}_2\text{O}$ ), which are a result of the complete hydrocarbon combustion process.
2. Nitrogen ( $\text{N}_2$ ) that comes from air, oxygen ( $\text{O}_2$ ) that comes as a result of the lean combustion mode (in a case of rich combustion mode, there will be no oxygen in the exhaust gases) and nitrous oxides ( $\text{NO}_x$ ) that is formed in the high temperature regions inside the combustion chamber.
3. Particulate matter (PM; usually referred to as soot, since soot is used to indicate the PM emissions formed during the combustion process [5]), carbon monoxide (CO) and unburned hydrocarbon (UHC, sometimes referred to as THC – total hydrocarbons), which are a result of an incomplete hydrocarbon combustion process.

Harmful exhaust gas emission is a collective name for the species inside the exhaust gas of an IC engine that have harmful effect on the human health and on the environment. These harmful species are  $\text{CO}_2$ , CO, UHC (THC),  $\text{NO}_x$  and PM (soot); all of these species, except for  $\text{CO}_2$  and  $\text{NO}_x$  are a result of an incomplete hydrocarbon combustion process.  $\text{NO}_x$  is formed in the in the high temperature regions inside the combustion chamber, while  $\text{CO}_2$ , which is a greenhouse gas is a result of the complete hydrocarbon combustion process.

The negative effects of the overall air pollution on the human health, part of which is a result of the transport and the IC engine as it powertrain, has been reported in numerous studies; Anderson and Thundiyil [6] indicate that there is a higher mortality rate within the population that is subjected to long-term PM exposure. Kampa and Castanas [7] state that air pollution

has both acute and chronic effects on human health, while Kim et al [8] indicate that there is a need to control the amount of polycyclic aromatic hydrocarbons (PAH) in air since PAHs a cancerogenous effect on humans. World Health Organization (WHO) issued a shocking report [9] linking around 7 million premature deaths in 2012 to air pollution.

Greenhouse gases is a collective name for the gases that cause greenhouse effect and thus have a negative influence on our environment and as can be seen from the figure which is given below (Figure 1) the primary constituents of the global greenhouse gas (GHG) emissions are carbon dioxide (76%), and methane (16%), with a significant share of nitrous oxides (6%) [10].

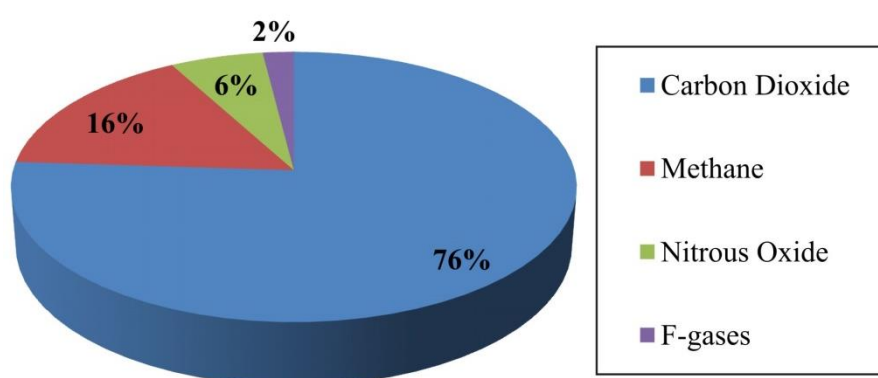


**Figure 1. Global GHG emissions by gas; data taken from [10]**

By looking into the global GHG emissions by sector (Figure 2), it can be seen that the transportation sector is fourth pollutant (14% of the overall GHG emissions by economic sector) [10].

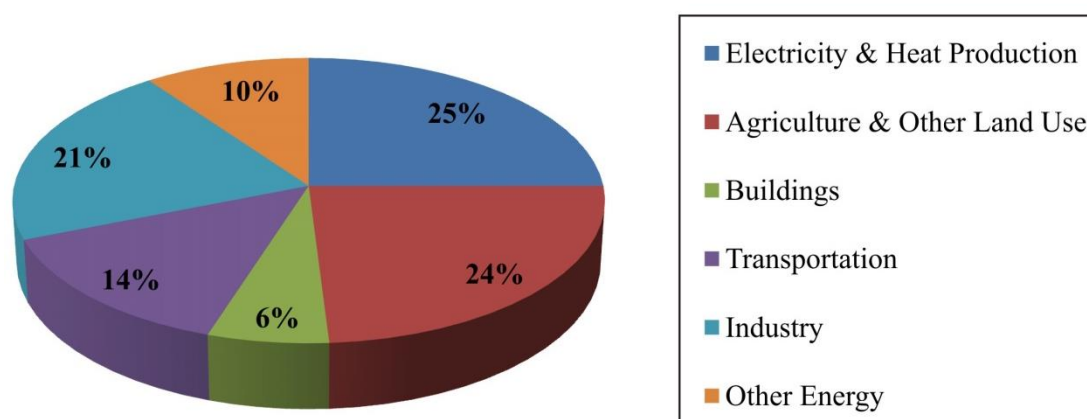


**Figure 2. Global GHG emissions by economic sector; data taken from [10]**

Putting this into the context of a huge increase in the number of registered vehicle, number of vehicles per person and the number of vehicles produced from year to year (Figure 3), it is imperative to reduce the harmful impact of the transport sector on the environment.

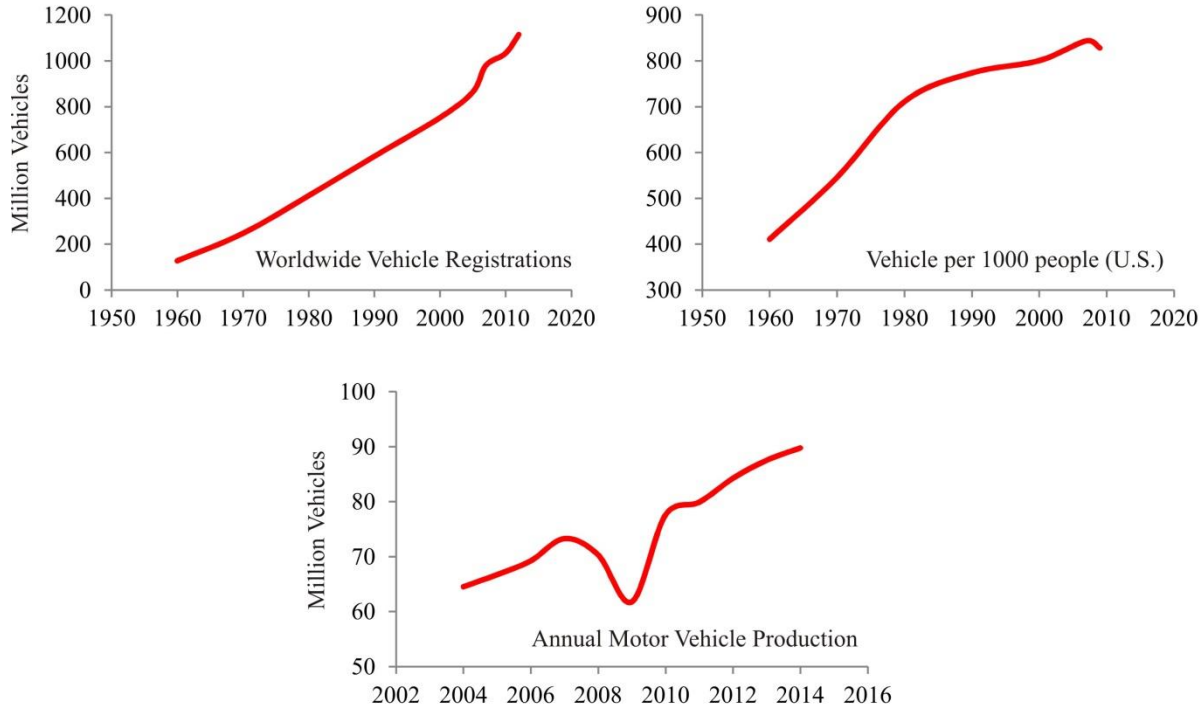


**Figure 3. Worldwide trends in the number and production of motor vehicles, and number of motor vehicles per 1000 people in the U. S.; data taken from [11]**

Therefore, the governments worldwide have imposed a series of regulations that aim at reducing the air pollution (harmful exhaust gas emissions) from the transport sector; i.e. [12]. Regarding the GHG (CO<sub>2</sub>) emissions from road vehicles; for the year 2020, the EU has set a target of 95 g/km as the fleet average for new cars [12]. The allowed mass of other harmful exhaust gas emissions (CO, UHC, NO<sub>x</sub> and PM) is regulated through a well-known European Emissions Standard; EURO I (introduced in 1992) to EURO VI (introduced in 2014). The tables given below (Table 1 – Table 3) present the European emissions standard for road vehicles.

These regulations directed the IC engine research activities towards the optimization of the IC engine combustion process, application of various engine management components and aftertreatment devices, as well as the application of non-conventional, “cleaner” fuels.

Generally, in conventional IC engines (SI and DI-CI combustion types) harmful exhaust gas emissions can be lowered by applying a variety of different engine concepts and aftertreatment devices, some of which have been presented in [14]. A part of harmful exhaust



gas emissions can be cleaned from the exhaust gases by various aftertreatment devices such as:

1. Particulate filter that cleans the PM (soot) emissions from the exhaust gases.
2. Reduction catalyst that cleans the NO<sub>x</sub> emissions from the exhaust gases.
3. Oxidation catalyst that cleans the CO and UHC emissions from the exhaust gases.

**Table 1. European emissions standard for road vehicles propelled by SI engine [13]**

Vehicle Type	European Emissions Standard	CO (g/km)	THC (g/km)	NMHC (g/km)	NO <sub>x</sub> (g/km)	PM (g/km)
Passenger Cars	EURO 4 (January 2005)	1	0.1	-	0.08	-
	EURO 5 (September 2009)	1	0.1	0.068	0.06	0.005
	EURO 6 (September 2014)	1	0.1	0.068	0.06	0.005
Light Commercial Vehicles	EURO 4 (January 2006)	2.27	0.16	-	0.11	-
	EURO 5 (September 2010)	2.27	0.16	0.108	0.082	0.05
	EURO 6 (September 2015)	2.27	0.16	0.108	0.082	0.05

**Table 2. European emissions standard for road vehicles propelled by Diesel engine (CI engine) [13]**

Vehicle Type	European Emissions Standard	CO (g/km)	NO <sub>x</sub> (g/km)	HC + NO <sub>x</sub> (g/km)	PM (g/km)
Passenger Cars	EURO 4 (January 2005)	0.5	0.25	0.3	0.025
	EURO 5a (September 2009)	0.5	0.18	0.23	0.005
	EURO 5b (September 2011)	0.5	0.18	0.23	0.005
	EURO 6 (September 2014)	0.5	0.08	0.17	0.005
Light Commercial Vehicles	EURO 4 (January 2006)	0.74	0.39	0.46	0.06
	EURO 5a (September 2010)	0.74	0.28	0.35	0.005
	EURO 5b (September 2011)	0.74	0.28	0.35	0.005
	EURO 6 (September 2015)	0.74	0.125	0.215	0.005

**Table 3. European emissions standard for trucks and buses (heavy duty engines [13])**

European Emissions Standard	CO (g/km)	HC (g/km)	NO <sub>x</sub> (g/km)	PM (g/km)
EURO 4 (October 2005)	0.5	0.25	0.3	0.025
EURO 5 (October 2008)	0.5	0.18	0.23	0.005
EURO 6 (31 <sup>st</sup> December 2013)	0.5	0.18	0.23	0.005

On the other hand, CO<sub>2</sub> and H<sub>2</sub>O are always left in the exhaust gases and they are emitted into the atmosphere. There are a few steps that can be performed to reduce the CO<sub>2</sub> emissions from an IC engine:

1. Optimization of the entire engine performance through the application of advance control strategies (direct fuel injection, engine downsizing, application of advanced turbomachinery, etc.) and engine design (reduction of friction).
2. Application of advanced combustion strategies, such as homogeneous compression ignition (HCCI) concept or one of its various modifications (partially premixed compression ignition (PPCI), reactivity controlled compression ignition (RCCI)).
3. Application of non-conventional, “cleaner” fuels.

In the context of using “cleaner” fuels, the fuel that has attracted a lot of attention is natural gas. The composition of natural gas is shown in Table 4.

**Table 4. Typical composition of natural gas [15]**

Component	Typical value (mole %)	Range (mole %)
Methane	94.9	87 – 96
Ethane	2.5	1.8 – 5.1
Propane	0.2	0.1 – 1.5
Iso – Butane	0.03	0.01 – 0.3
Normal – Butane	0.03	0.01 – 0.3
Iso – Pentane	0.01	Trace – 0.14
Normal - Pentane	0.01	Trace – 0.04
Hexanes plus	0.01	Trace – 0.06
Nitrogen	1.6	1.3 – 5.6
Carbon Dioxide	0.7	0.1 - 1
Oxygen	0.02	0.01 – 0.1
Hydrogen	Trace	Trace – 0.02

It can be seen that the natural gas is primarily consisted of methane (90%). Natural gas can be used in both SI and DI-CI engines [16]. Even though natural gas is also a fossil fuel, its use has been suggested due to its advantageous properties:

1. It mixes more readily with air compared to conventional liquid fuels thus creating more homogeneous mixture, which eventually leads to cleaner combustion and less UHC emissions [17].

2. It has the highest hydrogen to carbon ratio out of all hydrocarbons, and hence a theoretical potential to reduce the CO<sub>2</sub> emissions by nearly 25% compared to the conventional liquid fuels [18].
3. It has higher autoignition temperature compared to gasoline, which means that the natural gas powered engine can be operated in SI mode with higher compression ratios, which then offers the potential to increase the IC engine's thermal efficiency [16].

When used in SI engines, natural gas can completely substitute the conventional liquid fuel. However, due to their well-known drawbacks (require near stoichiometric operation, pumping losses, lower compression ratios), most SI engines (except from large gas engines) can never reach the DI-CI engine efficiencies, especially at the part load conditions. On the other hand, when used in the CI engines, natural gas can never fully substitute the conventional liquid fuels. The reason for this is its high autoignition temperature, which leads to the inability of natural gas to autoignite at pressure and temperature conditions encountered in DI-CI engines around the top dead center [16]. Therefore in DI-CI engines, natural gas is utilized in a so-called dual fuel concept [16], [18], where natural gas is ignited by a small quantity of the so-called pilot fuel (usually Diesel fuel) [19].

## **1.2. Dual fuel IC engines**

Dual fuel engine is a term which is used for a DI-CI engines in which a large quantity of the main fuel (usually natural gas) is ignited by a small quantity of the pilot fuel (usually Diesel fuel). The relative amount of the natural gas in the combustion process is usually defined as the Diesel fuel substitution ratio, which represents the ratio of the energy supplied by natural gas to the total amount of energy supplied by both fuels [2].

From the combustion process perspective, there are three main types of dual fuel engines [2]:

1. Dual fuel engine that operates with direct injection of both Diesel fuel and natural gas; so called HPDI (High Pressure Direct Injection) dual fuel engines [20].
2. Dual fuel engines that operate with both fuels premixed; so called HCCI dual fuel engines [21].
3. Dual fuel engines that operate with the premixed natural gas and directly injected Diesel fuel; so called conventional dual fuel engines [19].

The HPDI type of dual fuel operation results in the mixing-controlled combustion (turbulent non-premixed or diffusion flame). Such type of operation requires either two separate high pressure direct injectors or a single, specially built injector that injects both fuels at high

pressure directly into the combustion chamber. More on the performance and exhaust gas emission of an HPDI dual fuel engine can be found in the literature, i.e. [22].

The HCCI type of dual fuel operation was studied experimentally and numerically in [21]. In such operation, both fuels are premixed and the combustion is governed by the chemical kinetics of the fuel/air mixture. Even though HCCI combustion process offers quite high efficiency and low NO<sub>x</sub> emissions, the control of combustion phasing is rather challenging [2]. The main benefit of the conventional dual fuel operation compared to the other two operation types is the easy conversion from conventional Diesel engine into a dual fuel one, and the ability of the engine to operate only on Diesel fuel in the case one runs out of natural gas [2], [18]. Considering that the major part of the medium and heavy-duty vehicles are propelled by the conventional Diesel engine, and taking into account that these vehicles represent a large share in the transport of people and goods, the conversion of the existing Diesel engines into the dual fuel engines presents a convenient way to reduce the pollution from the transport sector. The conventional dual fuel operation is presented in Figure 4.

As can be seen, the conventional dual fuel operation can be divided into following six (6) stages:

1. Natural gas is injected into the intake manifold and induced into the cylinder together with air (possibly some recirculated exhaust gases (EGR) as well) during the intake stroke.
2. Natural gas/ air / EGR mixture is compressed during the compression stroke. Since natural gas has a high autoignition temperature it does not ignite at pressure/ temperature conditions that are encountered in the DI-CI engine combustion chamber near the top dead center (end of the compression stroke).
3. Therefore, a small amount of Diesel fuel is injected into the cylinder near the top dead center.
4. Diesel fuel breaks up into a number of droplets, penetrates into the combustion chamber, evaporates and mixes with the surrounding natural gas/ air/ EGR mixture. After appropriate time has passed (known as the ignition delay time), the Diesel fuel/ natural gas/ air/ EGR mixture ignites.
5. Ignited mixture acts as a trigger (can be viewed as a spark plug) that promotes the flame propagation through the premixed natural gas/ air/ EGR mixture. Once the flame propagation has started the combustion process is governed by both the flame propagation (turbulent premixed flame) and mixing-controlled combustion between the Diesel fuel and the surrounding mixture.

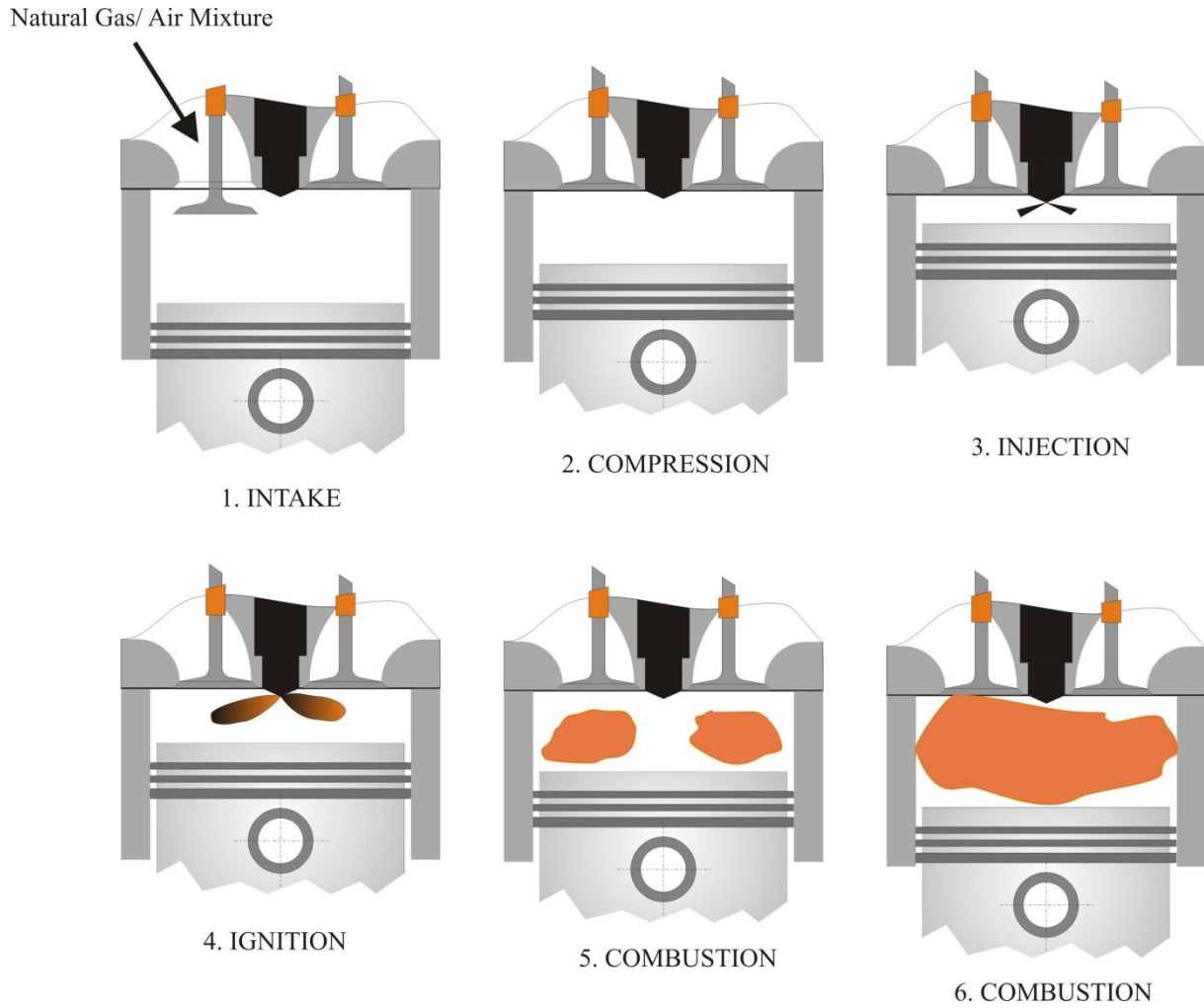


**Figure 4. Conventional dual fuel engine operating principle**

From the elaboration given above it can be seen that the combustion process in a conventional dual fuel engine is quite complex and that it features several stages. Generally speaking this combustion process is a mixture of the mixing-controlled combustion process (characteristic for DI-CI engines) and flame propagation process (characteristic for SI engines) [2]. According to the obtained experimental results and reported combustion chamber images [23] and reported computational fluid dynamics (CFD) studies [24], the following combustion stages can be identified [2], which are also shown in Figure 5:

1. Premixed (chemically controlled) combustion of the Diesel fuel/ natural gas/ air mixture. The products of this combustion phase trigger the flame propagation through the premixed mixture.
2. Combination of the mixing-controlled combustion of Diesel fuel with the surrounding mixture and flame propagation through the premixed Diesel fuel/ natural gas/ air mixture.

3. Final, mixing-controlled combustion of the remaining Diesel fuel after the flame propagated through the entire combustion chamber.

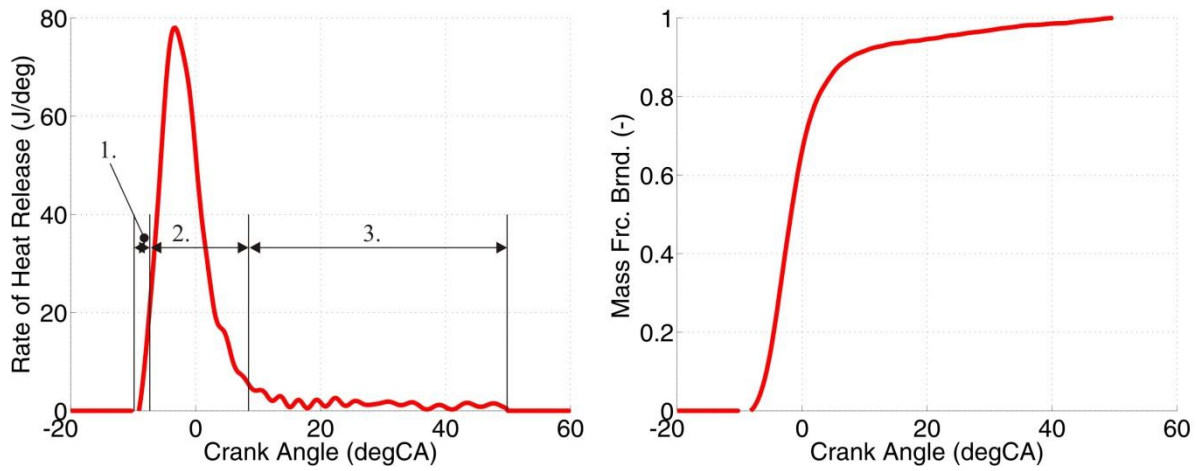


**Figure 5. Conventional dual fuel engine rate of heat release (ROHR) and mass fraction burned (MFB) traces**

As was already mentioned, the fuel mixture (Diesel fuel/ natural gas) is ignited somewhere inside the spray zone where the appropriate condition for the mixture ignition are achieved. The authors in [25] have shown that the addition of natural gas prolongs the overall ignition delay time of the mixture. This was proved in our research and will be presented in the later chapters of this thesis. There are two main reasons for this phenomenon:

1. Thermodynamical reason; the prolonged ignition delay time is a result of the lower in-cylinder pressure and temperature due to the addition of natural gas into the mixture. The addition of natural gas into the premixed mixture lowers the ratio of specific heats thus lowering the in-cylinder pressure and temperature at the end of the compression stroke.
2. Chemical reason; the prolonged ignition delay time is a result of the influence of the premixed natural gas on the overall autoignition process [26].

Due to lower mass that needs to be injected, and prolonged ignition delay time, injection settings (pressure, timing and duration) need to be adjusted for the dual fuel operation. The effect of injection parameters on the dual fuel operation was presented in [2]. Aside from the instantaneous pressure and temperature, the initial, premixed combustion rate is also determined by the local equivalence ratio inside the spray zone and the amount of fuel in the spray region that is prepared for the combustion. Once the part of the mixture has ignited it acts as the trigger for the flame propagation through the premixed mixture. The author in [18] states that in the conventional dual fuel operation there are more flames that propagate

through the combustion chamber at the same time. The number of these flames is equal to the number of nozzles on the Diesel fuel injector [18]. At the same time when the flame propagates through the combustion chamber, the rich Diesel fuel/ natural gas/ air/ EGR mixture that is left unburned inside the spray mixes and burns in the mixing-controlled manner. Depending on the load and on the ratio of the Diesel fuel to natural gas, individual phases contribute more or less to the overall burning rate which either moves the conventional dual fuel combustion process closer to that of the DI-CI engines or closer to that of the SI engines [2].

The authors in [18], [27], [28] compared the conventional dual fuel operation to the conventional Diesel operation at different loads and Diesel substitution ratios. They concluded that the conventional dual fuel operation offers the potential to reduce soot and NO<sub>x</sub> emissions, while maintaining high, Diesel-like efficiencies. However, it has been reported that the CO and UHC emissions tend to increase compared to the conventional Diesel operation and that the conventional dual fuel operation suffers from low efficiency at lower loads due to flame quenching (too lean mixture).

### **1.3. Numerical Simulation in the IC Engine Development Process**

At the beginning of this chapter it would only be appropriate to cite prof. Dibble [29]: *“Experiment is a simulation that calculates all of the physics exactly and in real time”*. Even though one has to agree with this statement, we have to account for the inevitable fact that detailed experimental research is both time and financially demanding. Moreover, experimental research doesn’t reveal all necessary results, and therefore it is necessary to run additional simulations. On top of that, sometimes it is difficult, if not even impossible to isolate a particular part of the overall process in the experiment and to study a specific influence of an isolated parameter on the overall combustion phenomenon. Therefore, numerical simulations are used in all of the IC engine development stages.

Comparing experiment and simulations, detailed 3-D CFD models that feature both spatial and temporal discretization of the computational domain and various detailed physically based sub-models that describe the in-cylinder physics in detail, give the best insight into the real processes that occur in an IC engine. Moreover, such simulation tool offers the best fit between the experiment and simulation. By considering the model complexity vs. calculation time curve (Figure 6) it can be noted that even though 3-D CFD models offer a deep insight into local effects, they are time and thus financially rather expensive. As such they are inconvenient for detailed analysis of various operating parameters that affect the entire engine

operation and for conducting fast combustion calculations in order to study the fundamental aspects of the particular combustion process. In the cases when such, faster, calculations are needed, the 0-D models are used (Figure 7) to calculate the combustion phenomenon in IC engines.

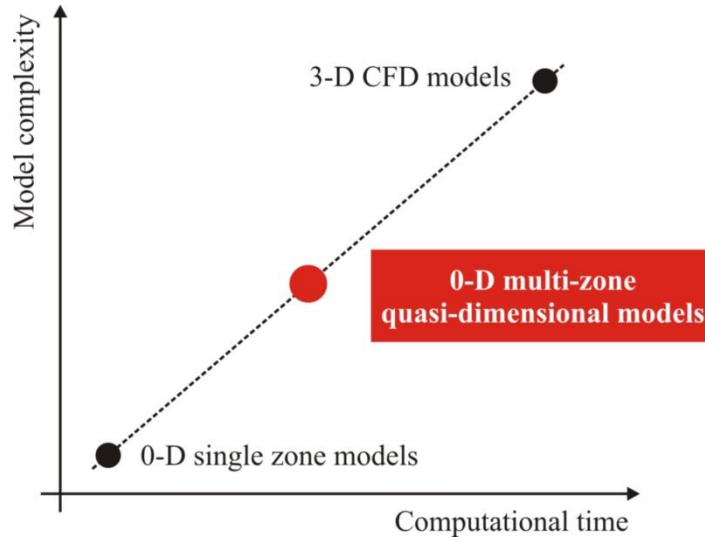


**Figure 6. Types of simulation model (model complexity .vs. computational time curve)**

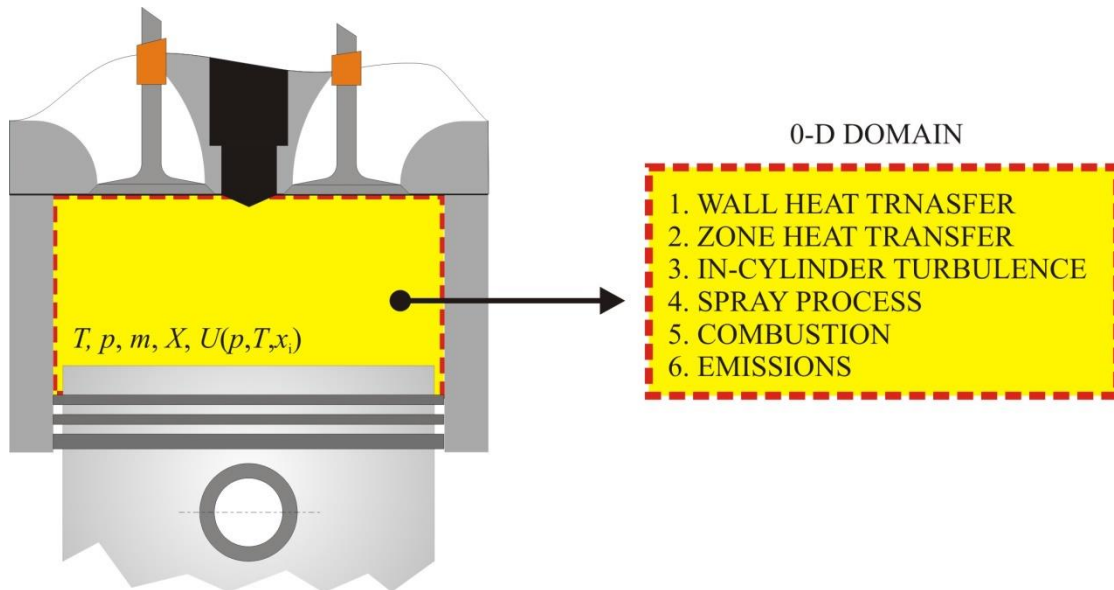


**Figure 7. Zero-dimensional calculation approach in the IC engine combustion modeling**

These models are often referred to as the cycle-simulation or thermodynamic models [30], [31]. The name thermodynamic model, when referring to a 0-D model, comes from the fact that these models are based on the first law of thermodynamics [30], [31]. Contrary to 3-D CFD models, in 0-D models the in-cylinder content is only discretized in time, while the spatial variations in the composition and thermodynamic properties are neglected. This means



that the pressure, temperature and composition homogeneity is assumed in the entire calculation domain (combustion chamber). Although by assuming spatial uniformity of composition and temperature a certain calculation error is introduced, if appropriately developed and used, 0-D models offer a good agreement between the measured and simulated data as can be seen from numerous reported studies on SI, Diesel, HCCI and dual fuel engines [32]–[35]. Moreover, as 0-D models are time efficient and thus financially inexpensive, it is possible to calculate a number of engine cycles in a reasonable amount of time, which means that they can be used in performance analysis of the entire engine system as well as optimization of the engine operating parameters, as has been presented in [21], [36], [37]. Additionally, if properly used, they can be utilized for studying the fundamental aspects of a particular combustion process.

The negative aspects of the basic 0-D models, which are temperature and composition homogeneity, can partially be compensated by the application of multi-zone and quasi-dimensional approach. Multi-zone approach in 0-D modeling enables the description of temperature and mixture in-cylinder heterogeneities, which provides a better description of the actual in-cylinder state, while in the quasi-dimensional 0-D modeling approach the calculation of rate of heat release includes the geometry effects such as piston crown and cylinder head shape, cylinder bore, distance between the piston crown and cylinder head, the location where the flame propagation starts and the number of flames that propagate through the combustion chamber [32].

Regarding the models for conventional dual fuel engines; in order to adequately calculate the combustion rate, various physical phenomena have to be appropriately described. These phenomena include:

1. In-cylinder flow and turbulence.
2. Wall and zone heat transfer.
3. Spray process, which includes liquid fuel break-up, liquid fuel evaporation, charge entrainment and mixing.
4. Spray ignition and combustion.
5. Combustion governed by the flame propagation; multiple flames propagate through the combustion chamber.
6. Knock in the end gas.
7. Formation of the harmful species in the exhaust gases.

## 1.4. State of the art

State of the art on the conventional dual fuel IC engine combustion modeling indicates that a lot of effort was made in the development of 3-D CFD dual fuel models. Singh et al. [38] used a 3-D CFD simulation model to simulate the combustion in a conventional dual fuel IC engine and compared it to the experimentally obtained results. It was found that in order to simulate the conventional dual fuel combustion process it is necessary to appropriately account for the flame propagation phenomenon. The development of a flame propagation model for the 3-D simulations of the conventional dual fuel IC engines has been presented in [39]. Ouellette et al. [40] described the modeling and validation of a 3-D CFD HPDI dual fuel combustion model. In a study that was recently published [41], the authors used a 3-D CFD dual fuel combustion model to compare the conventional Diesel engine to both conventional and HPDI dual fuel IC engines. They found that by dual fueling the engine (both HPDI and conventional operation type) it is possible to simultaneously reduce soot and NO<sub>x</sub> emissions and improve the engine's efficiency. Even though significant effort has been put into the 3-D CFD conventional dual fuel modeling, a certain number of cycle-simulation (0-D) dual fuel models have also been derived.

In 2000., Hountalas and Papagiannakis [35] derived a two-zone 0-D dual fuel combustion model. In this model, Diesel fuel jet is modeled according to the steady jet theory where the jet tip penetration is calculated with Hiroyasu's equation. [42]. The entrainment rate is calculated based on the jet tip velocity and empirically defined cone angle; the entrainment rate calculation model also includes the wall effects (wall jet). Combustion starts once the pilot fuel ignites and the pilot fuel ignition delay time is calculated with an empirical correlation. Only the part of gaseous fuel that has been entrained into the spray region ignites and burns; flame propagation through the premixed mixture is not taken into account. Combustion of pilot fuel and gaseous fuel is treated separately through the respective Arrhenius type equations. This model accounts for the pollutant formation in the exhaust gases. Later, this model was enhanced by the same authors in [43], [44], where a flame propagation model has been added. In these models [43], [44], it is considered that the flame has a conical shape and that only one flame propagates through the combustion chamber. The flame propagates from the outer edges of the burned zone. The effect of in-cylinder turbulence on the flame propagation is taken with a model parameter that depends on the engine speed. The model that was originally presented in [44], was slightly modified by Papagiannakis in [45], where it was assumed that the flame has a spherical, not conical shape.

In this model [45], the flame geometry is calculated with a geometrical model, which is based on the flame radius and combustion chamber height (disc shaped combustion chamber is considered). In this model the turbulent flame velocity is calculated based on the laminar flame velocity and turbulence intensity; turbulence intensity is calculated with an empirical correlation.

Krishnan and Srinivasan [46] derived a predictive 0-D model for the partially premixed low-temperature combustion in pilot-ignited natural-gas engines. After deriving the model, the authors used the model to study the effects of the intake temperature, pilot fuel quantity and natural gas equivalence ratio on the engine performance and harmful exhaust gas emissions. In the model, the spray process is calculated with a well-known Hiroyasu's packet approach [42], while the flame propagation process was modeled with a well-known turbulent entrainment model [47]. Similarly to the previous model [45], in this model the ignition delay time is also calculated with an empirical correlation., while spray combustion of pilot fuel and entrained gaseous fuel are treated separately with appropriate empirical correlations. The effect of multiple ignition sites and hence the occurrence of multiple flames inside the cylinder was accounted for with an empirical equation based on the packet volume and packet burned mass fraction. The second part of the study showed that the intake temperature and pilot quantity increase leads to a faster combustion, increase in the in-cylinder temperature and hence increase in the  $\text{NO}_x$  emissions. The increase of equivalence ratio revealed that only the combustion rate slightly increases, without significantly affecting the peak in-cylinder temperature and  $\text{NO}_x$  emissions.

In [48], Mikulski et al. derived an empirical 0-D conventional dual fuel combustion model. In this model, heat release is calculated with a Vibe function, which leads to the necessity of adjusting the model parameters with the change of engine operating parameters (engine speed, load, intake pressure and temperature, and high pressure direct injection settings).

In [49], Cernik et al. derived a predictive 0-D model for 2-stroke conventional dual fuel engines. The model considers both, pilot fuel combustion inside the spray region as well as the flame propagation through the premixed mixture. In order to capture the in-cylinder temperature and mixture heterogeneities, the in-cylinder content has been divided into a number of zones. In this model, the ignition delay data has been tabulated and the ignition delay time is calculated according to the instantaneous pressure and temperature inside a particular zone. This model also features the in-cylinder turbulence calculation (only turbulent kinetic energy differential equation is solved), while the flame surface is calculated with an empirical correlation.

The literature survey revealed that there are some predictive 0-D conventional dual fuel combustion models (Papagiannakis model [45], Krishnan model [46] and Cernik model [49]). However, this survey also revealed that not all physical aspects of conventional dual fuel combustion have been accounted for. Moreover, the survey also revealed that some of the physics has not been modeled in a predictive way (i.e. some of the spray processes, spray ignition and fuel blend combustion, multiple flame propagation, in-cylinder turbulence, knock in the end gas). Therefore, some more effort needs to be put in order to appropriately capture all aspects of the combustion process in a conventional dual fuel engine. Specifically, some more efforts need to be put into:

1. Quasi-dimensional conventional dual fuel combustion modeling; i.e. the 0-D model needs to account for different combustion chamber geometries, different number of flames that propagate through the combustion chamber as well as injector geometry features.
2. The 0-D modeling of in-cylinder turbulence in DI-CI engines (effect of the injection process on the average turbulence quantities inside the combustion chamber).
3. The 0-D modeling of effect of entrained methane on the spray ignition and combustion process; specifically the chemical effect of natural gas on ignition and combustion inside the spray zones.
4. The 0-D modeling of multiple flame propagation phenomena.
5. The 0-D modeling of the link between spray ignition and early flame development phase.
6. The 0-D modeling of the link between spray combustion and flame propagation.
7. The 0-D modeling of knock in the end gas of a conventional dual fuel engine.

All of these issues (challenges) were considered during the DFMZCM development process that is presented in this thesis.

## **1.5. Objective and hypotheses of research**

The main objective of this doctoral research was to develop a physically based 0-D combustion model for conventional dual fuel (Diesel fuel/ natural gas) engines, and to integrate this model into the commercial AVL cycle-simulation software. In order to achieve these objectives, it was necessary to accomplish several goals:

1. the development of a multizone Diesel spray combustion model which will include the premixed natural gas;
2. the improvement of the turbulence calculation, which will include the injection effect;

3. the development of a multiple flame propagation model;
4. the upgrade of the existing ignition delay and heat release models which will include the effect of the premixed natural gas;
5. the development of a model which calculates the start of flame propagation conditions.

According to the aforementioned objectives and goals of this doctoral research, the hypotheses have been stated as follows:

1. it is possible to define and develop appropriate 0-D mathematical models for the cycle-simulation of combustion of dual fuel internal combustion engine, and to integrate such models into the existing cycle-simulation software;
2. with the new 0-D dual fuel combustion model it will be possible to achieve the calculation results that are in close agreement with the experimentally obtained results.

## 2. Zero-dimensional dual fuel combustion model

In this chapter, the basis of the 0-D modeling is presented, and general equations that are solved for each zone are given.

### 2.1. Model features

The newly developed 0-D combustion model is a multi-zone, quasi-dimensional combustion model which can be used in the cycle-simulation analyses of the conventional dual fuel engines. Since the combustion in the conventional dual fuel engines is a combination of two fundamental combustion types which occur in DI-CI and SI engines, i.e. mixing-controlled combustion and combustion controlled by the flame propagation through the premixed charge [2], [18], the 0-D combustion model (DFMZCM) presented in this thesis can handle both of these combustion processes, and it features:

1. multi-zone approach to combustion modeling with following zones:
  - unburned zone,
  - multiple number of spray zones,
  - flame zone.
2. quasi-dimensional approach to combustion modeling which is apparent by:
  - description of the combustion chamber geometry,
  - description of the injector nozzle orientation and spray angle (injector data),
  - tracking of the spray zone position (deflection of the chamber walls),
  - calculation of the location where flame start to propagate through the premixed mixture,
  - calculation of the multiple flames that propagate through the combustion chamber,
  - calculation of the interactions between the flames and the flame and combustion chamber walls (cylinder head and liner, and piston).
3. in-cylinder turbulence modeling,
4. modeling of the spray processes that includes:
  - injection,
  - liquid fuel break-up,
  - charge entrainment and heat transfer between the zones,
  - liquid fuel heating and evaporation,
  - spray ignition and combustion,
  - calculation of the harmful exhaust gas emissions inside each spray zone.

5. modeling of the flame propagation process that includes:
  - calculation of the start of flame propagation,
  - calculation of the flame surface in case when multiple flames propagate through the combustion chamber,
  - laminar flame speed calculation,
  - calculation of the turbulent burning rate,
  - calculation of the harmful exhaust gas emissions inside the flame zone.
6. calculation of the harmful exhaust gas emissions (HC emissions) in front of the flame (inside the unburned zone),
7. calculation of the knock occurrence and its intensity in in front of the flame (inside the unburned zone).

By dividing the cylinder content into a number of zones (multi-zone approach to combustion modeling) it is possible to account for temperature and charge inhomogeneity, which improves ignition, burning rate and emissions calculations. By applying quasi-dimensional modeling approach, it is possible to account for geometry effects on the spray development process and burning rate calculation. Some of the geometry effects include combustion chamber shape, number of flames that propagates through the combustion chamber, injector characteristics and location where the flame propagation starts. The description of the zone formation and evolution, as well as the description of the geometry features are given in chapters 2.5 and 2.6.

As the interaction between combustion and in-cylinder flow (turbulence) is a well-known fact [50]–[52], as well as the influence of turbulence on heat and mass transfer [53], it is important to calculate the level of in-cylinder turbulence and its characteristic scales. In this work, turbulence is modeled through a well-known  $k$ - $\varepsilon$  model, which is based on two equations [54], one for the turbulent kinetic energy and the other for its dissipation. The reduction of this approach to 0-D space has been shown in [30], while its application in the modeling of the SI engine burning rate has been shown in [32]. The description of this model is given in the chapter 3.1.2.

The basis of the spray process modeling is the Hiroyasu's packet approach first presented in [42], and later used by a number of authors, i.e. [33] in the 0-D simulations of DI-CI engines. Some of the modifications that have been made to this approach in this thesis include:

1. zones entrain both premixed methane and air,
2. calculation of the heat transfer between the spray zones,

3. inclusion of the entrained methane in the spray ignition delay and spray burning rate calculation,
4. calculation of the spray ignition delay through the specially developed ignition delay tables,
5. calculation of the kinetically-controlled condition for spray burning rate through specially developed reaction time tables.

Description of the approach and equations which are used in the calculation of the spray phenomena and burning rate in the case of mixing-controlled (spray) combustion is given in the chapter 3.3.

When calculating the part of combustion governed by the flame propagation through the premixed mixture two different burning rate calculations can be applied:

1. Calculation based on the fractal theory, called the fractal combustion model.
2. Calculation based on the flame turbulent velocity calculation, called the turbulent flame combustion model.

Turbulent flame propagation calculation based on the fractal theory is a well-known calculation approach, which was first presented in [55], later refined and used by a number of authors in modeling the burning rate in the SI engines, i.e. [32]. The other type of turbulent flame propagation calculation is based on the calculation of the turbulent flame velocity as proposed in [56] and applied in modeling of the flame propagation phenomena in 3-D CFD. More on the equations which are used in the calculation of the combustion governed by the flame propagation, as well as on the physical background behind these models is given in the chapter 3.5.

In 0-D combustion model presented in this thesis (DFMZCM), soot (particles), unburned hydrocarbon (HC), carbon monoxide (CO) and nitrogen oxides (NO<sub>x</sub>) emissions are calculated. Harmful exhaust gas emissions calculation is based on the models which are available in the AVL cycle-simulation software [57]. Detail description and equations used in calculating these emissions are given in the chapter 3.8.

Knock occurrence and its intensity in front of the flame (inside the unburned zone) is calculated with the model that was presented in [58]. Detail description and equations which are used in modeling of the knocking combustion in the end gas are given in the chapter 3.9.

Since the composition of both Diesel fuel and natural gas is rather complex and varies, in the DFMZCM most of the properties of Diesel fuel are simulated with n-heptane properties, while the properties of the natural gas are simulated with methane properties. The only Diesel fuel properties that are considered are lower heating value and stoichiometric air to fuel ratio.



## 2.2. Thermodynamic properties

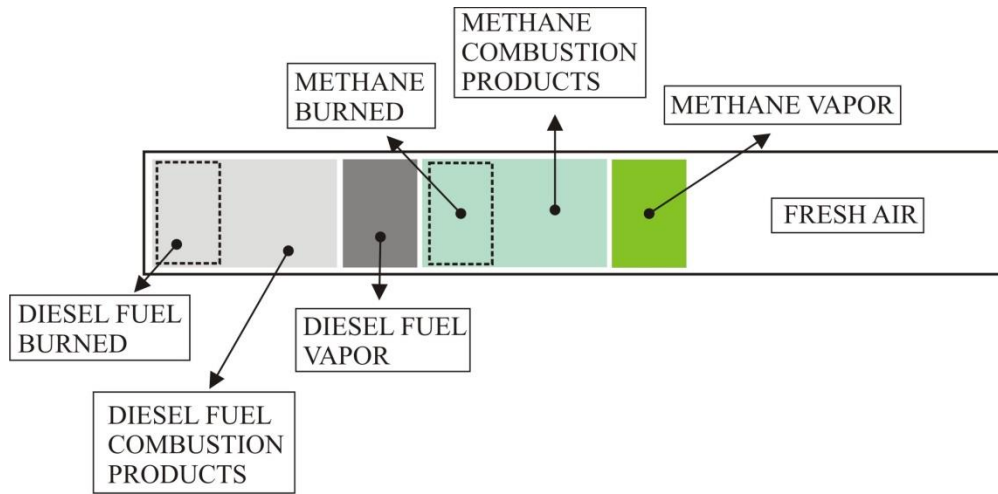


**Figure 8. Schematic overview of the tracked species**

Thermodynamic properties of the in-cylinder charge depend on the temperature, pressure and charge composition. In the DFMZCM, gas properties are calculated in each zone at every time step with the instantaneous zone temperature and composition, and the overall in-cylinder pressure. To speed-up the calculation process, all gas properties are calculated from the look-up tables in which specific internal energy, specific heat capacity at constant volume and specific entropy are mapped as a function of the pressure, temperature and excess air ratio of the mixture. Therefore, in the DFMZCM, only six species are tracked:

1. Diesel fuel burned,
2. Diesel fuel combustion products,
3. Diesel fuel vapor,
4. methane burned,
5. methane combustion products,
6. methane vapor.

The data from the gas properties tables only accounts for the change in the sensible heat; heat of formation, i.e. heat released due to combustion is not included into the tables. This means that the heat generated due to combustion of the fuel/air mixture needs to be calculated with the appropriate models.

Methane and diesel fuel burned mass fractions are calculated from the corresponding fuel burning rates, which will be presented in the following chapters. Corresponding fresh air and combustion products mass fractions are calculated as follows:

$$x_{AIR} = 1 - x_{FV,D} - x_{FV,M} - x_{CP,D} - x_{CP,M} \quad (2.1)$$

$$x_{CP,D} = x_{FB,D} \left( 1 + AF_{stoich,D} \right) \quad (2.2)$$

$$x_{CP,M} = x_{FB,M} \left( 1 + AF_{stoich,M} \right) \quad (2.3)$$

In the equations given above,  $x_{AIR}$  (-) represents the fresh air mass fraction,  $x_{FV,D}$  (-) represents the Diesel fuel vapor mass fraction,  $x_{FV,M}$  (-) represents the methane vapor mass fraction,  $x_{CP,D}$  (-) represents the Diesel fuel combustion products mass fraction,  $x_{CP,M}$  (-) represents the methane combustion products mass fraction,  $x_{FB,D}$  (-) represents the Diesel fuel burned mass fraction,  $x_{FB,M}$  (-) represents the methane burned mass fraction,  $AF_{stoich,D}$  (-) represents the Diesel fuel stoichiometric air/fuel ratio of the combustion products and finally,  $AF_{stoich,M}$  (-) represents the methane stoichiometric air/fuel ratio of the combustion products.

### 2.3. Zero-dimensional single zone formulation

Before introducing the formation of zones in the DFMZCM and the interactions between the zones, it is important to show how the 0-D approach is formulated and what particular equations are solved in a 0-D combustion model.

In the 0-D approach only energy and mass conservation principles are applied, while momentum conservation is neglected [31]. The in-cylinder content is treated as an open thermodynamic system [31], which can exchange both mass and energy with its surrounding. 0-D approach assumes the uniformity of pressure inside the cylinder and this is valid for both the single and multi-zone approach [33]. Since the multi-zone 0-D calculation approach is an extension to the single zone 0-D approach, before presenting the multi-zone 0-D approach equations, the single zone 0-D approach equations are derived.

In the 0-D single zone approach, the entire cylinder content is treated as one zone. Single zone approach is used in the calculation of the gas exchange process and in the simplified, empirical 0-D combustion simulations. The schematic presentation of the interactions during the gas exchange process is given in Figure 9, while the schematic presentation of the interactions during the high-pressure cycle (from intake valve closure till exhaust valve opening) is given in Figure 10.

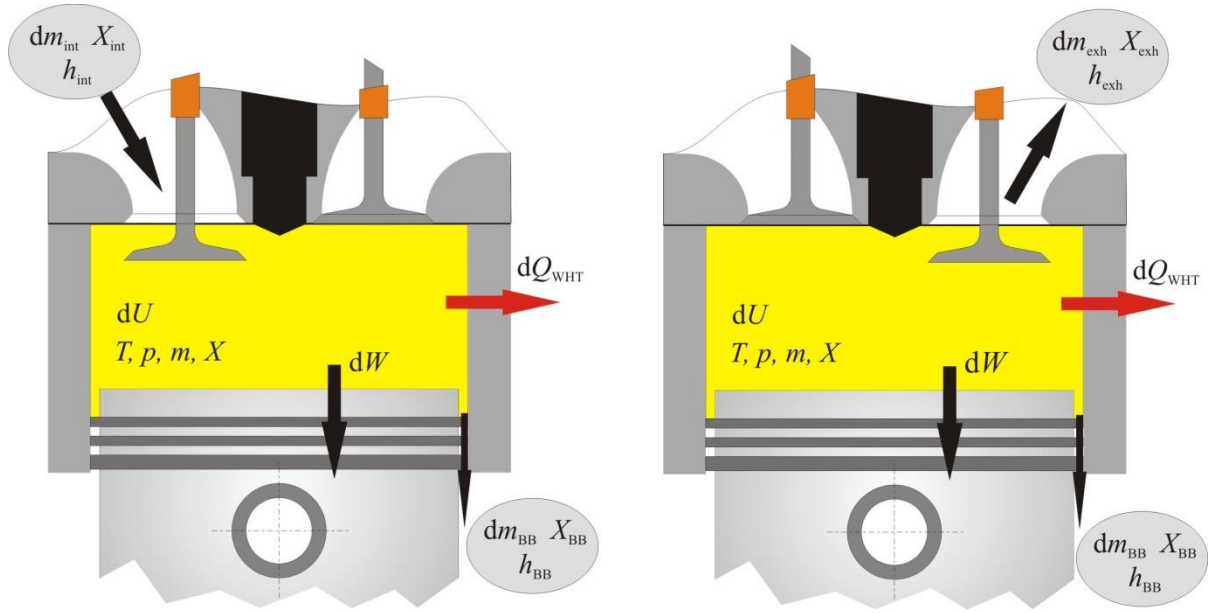


**Figure 9. Schematic presentation of the gas exchange process in 0-D calculation**

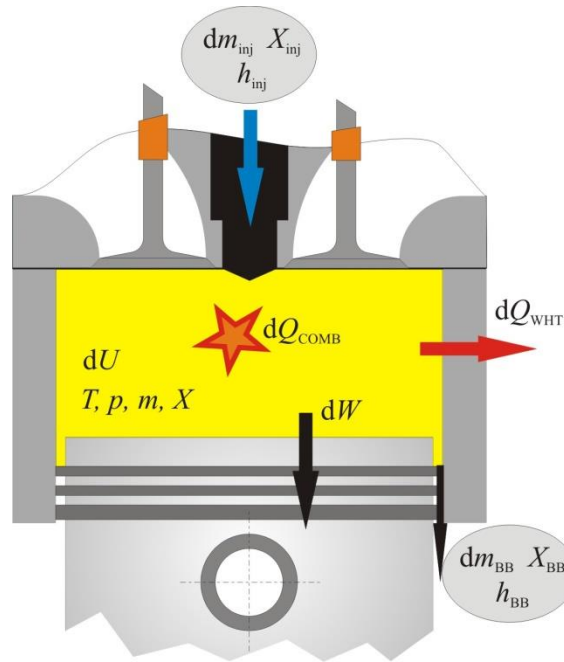


**Figure 10. Schematic presentation of the high-pressure cycle in 0-D calculation**

In both cases the calculation domain represents the volume inside the cylinder (single zone) and for that zone two conservation (energy and mass) and one state equation are solved. As in conventional dual fuel engines the fuel that is injected directly into the cylinder is liquid, the injected fuel increases the liquid fuel mass. The thermodynamic zone's mass (gaseous phase) is then increased through the evaporation process.

The energy conservation equation is given by the first law of thermodynamics and it neglects the in-cylinder kinetic energy [59]. The energy conservation equation can be expressed as (differential):

$$\frac{dE}{dt} = \frac{dU}{dt} = \frac{dQ}{dt} - \frac{dW}{dt} = \frac{dQ}{dt} - p \frac{dV}{dt} \quad (2.4)$$

In the equation given above,  $E$  (J) represents the total energy of the in-cylinder mixture;  $U$  (J) represents the internal energy of the in-cylinder mixture,  $Q$  (J) represents the total amount of the energy (heat) supplied to the in-cylinder mixture, while  $W$  (J) represents the mechanical work supplied to/from the engine piston. The total amount of energy (heat) can be expressed in the following form (differential):

$$\begin{aligned} \frac{dQ}{dt} = & \\ \frac{dQ_{\text{COMB}}}{dt} - \frac{dQ_{\text{EVAP}}}{dt} - \frac{dQ_{\text{WHT}}}{dt} + \frac{dm_{\text{int}}}{dt} h_{\text{int}} - \frac{dm_{\text{exh}}}{dt} h_{\text{exh}} - \frac{dm_{\text{BB}}}{dt} h_{\text{BB}} + \frac{dm_{\text{evap}}}{dt} h_{\text{evap}} \end{aligned} \quad (2.5)$$

In the equation given above,  $Q_{\text{COMB}}$  (J) represents the energy (heat) supplied to the system by the fuel combustion,  $Q_{\text{EVAP}}$  (J) represents the energy (heat) taken away from the system by the process of fuel evaporation (evaporative cooling),  $Q_{\text{WHT}}$  (J) represents the energy (heat) taken away from the system through the process of heat transfer from the system to the surrounding, and finally the last four terms represent the energy (heat) supplied or taken away from the system by either the mass inflow (intake, injection and evaporation) or mass outflow (exhaust, blow-by) from the system. The subscript *int* represents intake, *exh* represents exhaust, *BB* represents blow-by, and *evap* represent evaporation.

Mass fluxes and corresponding heat transfer (intake, exhaust, injection, blow-by and evaporation), as well as the heat generated due to combustion, and heats taken away due to evaporation and heat transfer to the surrounding are calculated by the appropriate models. Details of these models will be presented in chapters 3.3 and 3.5. The internal energy of the in-cylinder mixture can be expressed in the following form (differential):

$$\frac{dU}{dt} = m \frac{du}{dt} + \frac{dm}{dt} u \quad (2.6)$$

Bearing in mind that the internal energy is a function of pressure, temperature and charge composition (species mass fractions), and the correct form of the specific internal energy derivative is:

$$\frac{du}{dt} = \frac{\partial u}{\partial T} \frac{dT}{dt} + \frac{\partial u}{\partial p} \frac{dp}{dt} + \sum_j \frac{\partial u}{\partial x_j} \frac{dx_j}{dt} \quad (2.7)$$

In the above equations,  $u$  (J/kg) represents the specific internal energy of the charge inside the zone,  $m$  (kg) represents the mass of the charge inside the zone,  $T$  (K) represents the temperature of the charge inside the zone,  $p$  (Pa) represents the in-cylinder pressure, while  $x_j$  (-) represent the mass fractions of the species inside the zone. The mass conservation equation when the entire cylinder is treated as one zone can be expressed in the following form (differential):

$$\frac{dm}{dt} = \frac{dm_{\text{int}}}{dt} - \frac{dm_{\text{exh}}}{dt} + \frac{dm_{\text{evap}}}{dt} - \frac{dm_{\text{BB}}}{dt} \quad (2.8)$$

The mass conservation equation for the liquid fuel can be expressed in the following form (differential):

$$\frac{dm_{\text{liq}}}{dt} = \frac{dm_{\text{inj}}}{dt} - \frac{dm_{\text{evap}}}{dt} \quad (2.9)$$

In the equation given above,  $m_{\text{liq}}$  (kg) represents the liquid fuel mass inside the cylinder; this mass is not a part of the thermodynamic zone mass. Conservation of mass of a particular species (species  $j$ ) can be expressed in the following form (differential):

$$\frac{dm_j}{dt} = \frac{dm_{j,\text{int}}}{dt} - \frac{dm_{j,\text{exh}}}{dt} + \frac{dm_{j,\text{inj}}}{dt} \frac{dm_{j,\text{evap}}}{dt} - \frac{dm_{j,\text{BB}}}{dt} + S_j \quad (2.10)$$

In the equation given above,  $S_j$  (kg/s) represents a source term due to transformation of one species into another. For instance, during the combustion process the burned fuel and the combustion products are created, whereas a portion of the fuel vapor and fresh air are destroyed. Now, the energy conservation equation in its differential form for one zone can be written as follows:

$$m \left( \frac{\partial u}{\partial T} \frac{dT}{dt} + \frac{\partial u}{\partial p} \frac{dp}{dt} + \sum_j \frac{\partial u}{\partial x_j} \frac{dx_j}{dt} \right) + \frac{dm}{dt} u = \frac{dQ}{dt} - p \frac{dV}{dt} \quad (2.11)$$

To simplify the notation of the energy conservation equation, the equations representing the total amount of energy (heat) supplied to the zone (2.5) and mass conservation equation (2.8), have not been inserted into the energy conservation equation. The final, third equation (state equation), which describes the relationship between the state variables can be written in the following form (differential):

$$\frac{d}{dt}(pV) = \frac{d}{dt}(mRT) \quad (2.12)$$

In the equation given above,  $R$  (J/kgK) represents the specific gas constant of the gas mixture inside the cylinder (zone). Bearing in mind that the specific gas constant is a function of the composition and temperature inside the zone and pressure inside the entire cylinder, state equation can be expressed in its final differential form as:

$$\frac{dp}{dt}V + p\frac{dV}{dt} = \frac{dm}{dt}RT + mR\frac{dT}{dt} + mT\left(\frac{\partial R}{\partial T}\frac{dT}{dt} + \frac{\partial R}{\partial p}\frac{dp}{dt} + \sum_j \frac{\partial R}{\partial x_j}\frac{dx_j}{dt}\right) \quad (2.13)$$

By combining the equations 2.11 and 2.13; i.e. the energy conservation equation, and state equation respectively, it is possible to calculate the pressure and temperature derivatives for a single zone 0-D model:

$$\frac{dp}{dt} = \frac{\frac{dm}{dt}RT + mT\Delta SR - \frac{R+T}{\frac{\partial u}{\partial T}}(\Delta Q + m\Delta SU) - p\frac{dV}{dt}}{V - mT\frac{\partial R}{\partial p} + \frac{m\frac{\partial u}{\partial p}\left(R+T\frac{\partial R}{\partial T}\right)}{\frac{\partial u}{\partial T}}} \quad (2.14)$$

$$\frac{dT}{dt} = -\frac{\frac{\Delta Q}{m} + \frac{\partial u}{\partial p}\frac{dp}{dt} + \Delta SU}{\frac{\partial u}{\partial T}} \quad (2.15)$$

To simplify the notation of the equations that represent the pressure and temperature derivatives, the following replacement variables are used:

$$\Delta Q = p \frac{dV}{dt} - \frac{dQ}{dt} + \frac{dm}{dt} u \quad (2.16)$$

$$\Delta SU = \sum_j \frac{\partial u}{\partial x_j} \frac{dx_j}{dt} \quad (2.17)$$

$$\Delta SR = \sum_j \frac{\partial R}{\partial x_j} \frac{dx_j}{dt} \quad (2.18)$$

## 2.4. Zero-dimensional multi zone formulation

After derivation of the main equations for the single zone approach, it is possible to extend the 0-D single zone approach to a 0-D multi-zone approach. In the multi-zone approach, each zone is treated as an individual open thermodynamic system which interacts with its surrounding [33]. The main assumptions in a 0-D multi-zone approach are:

1. homogeneity of the temperature inside the zone;
2. homogeneity of the composition inside the zone;
3. uniformity of the pressure inside the entire cylinder.

In the DFMZCM, multi zone approach is used, where the in-cylinder content can be discretized into any number of zones:

1. multiple number of spray zones
2. flame zone
3. unburned zone

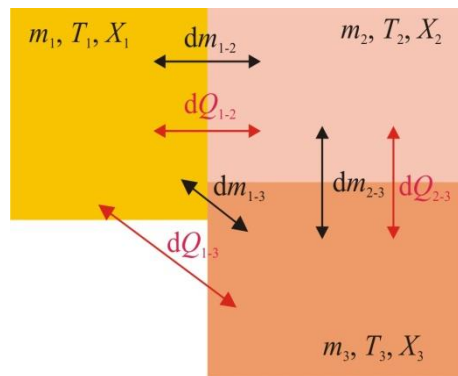


Figure 11. Schematic presentation of the interaction between the zones

All of these zones can exchange both mass and energy between themselves and the surrounding. As has been shown in Figure 11, the exchange of energy with the surrounding is governed by the wall heat transfer, while the exchange of mass with the surrounding is

governed by the blow-by mechanism. The schematic presentation of the heat and mass transfer between the zones is presented in Figure 11.

Since in the 0-D approach there is no pressure difference between the zones, there is no convective flow that could drive the mass transfer from one zone to another. That is why in the 0-D approach the transfer of mass between the zones is specifically modeled. In the DFMZCM, the mass transfer between the zones is modeled in the following ways:

1. the entrainment process of the fresh charge into the spray zones, which is controlled by the spray momentum;
2. the flame propagation process through which the mass is transferred from the unburned into the flame zone.

Heat transfer is partly linked to the mass transfer; if there is mass transfer between two zones, there is also a heat transfer between the zones as enthalpy is transferred from one zone to the other. Other heat transfer models that can be applied include conduction, convection and radiation. More on the mass and heat transfer models between the zones can be found in the chapter 3.2 of this thesis.

It is important to keep in mind that on Figure 11 only the interactions between the zones have been schematically presented. Each of the zones still interacts with the surrounding through energy (heat) and work transfer. In the following chapter the general expression for the temperature and pressure derivative for  $i$ -th zone inside the cylinder is derived. The expressions for the mass and energy fluxes for each of the different zone types will be given later in chapter 2.6, where the zone formation, evolution as well as its interactions with the neighboring zones is presented.

#### 2.4.1. Temperature and pressure derivatives

From the known expressions for the single zone temperature and pressure derivatives (equations 2.14 and 2.15), it is possible to define pressure and temperature derivatives for an arbitrary zone. The energy conservation equation and state equation for an arbitrary zone can be expressed in the following way (differential):

$$m_i \left( \frac{\partial u_i}{\partial T_i} \frac{dT_i}{dt} + \frac{\partial u_i}{\partial p} \frac{dp}{dt} + \sum_j \frac{\partial u_i}{\partial x_{j,i}} \frac{dx_{j,i}}{dt} \right) + \frac{dm_i}{dt} u_i = \frac{dQ_i}{dt} - p \frac{dV_i}{dt} \quad (2.19)$$

$$\frac{dp}{dt} V_i + p \frac{dV_i}{dt} = \frac{dm_i}{dt} R_i T_i + m_i R_i \frac{dT_i}{dt} + m_i T_i \left( \frac{\partial R_i}{\partial T_i} \frac{dT_i}{dt} + \frac{\partial R_i}{\partial p} \frac{dp}{dt} + \sum_j \frac{\partial R_i}{\partial x_{j,i}} \frac{dx_{j,i}}{dt} \right) \quad (2.20)$$



The subscript  $i$  in the above equations denotes  $i$ -th zone.

Assuming there are  $n$  zones ( $n-2$  spray zones + burned zone + unburned zone); there are  $2n + 1$  unknown variables:

1. cylinder pressure,
2.  $n$  zone temperatures,
3.  $n$  zone volumes.

In order to solve such a system, one more equation is needed. This final equation is the equation that states that the sum of zone volumes is equal to the overall cylinder volume and can be expressed in the following way (differential):

$$\frac{dV}{dt} = \sum_i \frac{dV_i}{dt} \quad (2.21)$$

By expressing the zone volume derivative from the zone state equation (2.19), and by combining the energy conservation equation (2.18) and the equation that states that the sum of the zone volumes equals the overall cylinder volume (2.20), it is possible to calculate the pressure and temperature derivatives for every zone in a multi-zone 0-D approach:

$$\frac{dp}{dt} = - \frac{\sum_i \left[ \frac{dm_i}{dt} R_i T_i + m_i T_i \Delta S R_i - \frac{m_i A P_i}{\frac{\partial u_i}{\partial T_i} + \frac{\partial R_i}{\partial T_i} + R_i} \left( R_i + T_i \frac{\partial R_i}{\partial T_i} \right) \right] - p \frac{dV}{dt}}{V + \sum_i \left[ \frac{m_i \left( \frac{\partial u_i}{\partial p} + T_i \frac{\partial R_i}{\partial p} - \frac{R_i T_i}{p} \right)}{\frac{\partial u_i}{\partial T_i} + \frac{\partial R_i}{\partial T_i} + R_i} \left( R_i + T_i \frac{\partial R_i}{\partial T_i} \right) - T_i \frac{\partial R_i}{\partial p} \right]} \quad (2.22)$$

$$\frac{dT_i}{dt} = - \frac{\frac{dp}{dt} \left( T_i \frac{\partial R_i}{\partial p} - \frac{R_i T_i}{p} + \frac{\partial u_i}{\partial p} \right) R_i + \Delta S U_i + T_i \Delta S R_i + \Delta Q_i}{\frac{\partial u_i}{\partial T_i} + \frac{\partial R_i}{\partial T_i} + R_i} \quad (2.23)$$

To simplify the notation of the equations that represent the pressure and temperature derivatives, the following replacement variables are used:

$$\Delta Q_i = \frac{\frac{dm_i}{dt} h_i - \frac{dQ_i}{dt}}{m_i} \quad (2.24)$$

$$\Delta S U_i = \sum_j \frac{\partial u_i}{\partial x_{j,i}} \frac{dx_{j,i}}{dt} \quad (2.25)$$

$$\Delta S R_i = \sum_j \frac{\partial R_i}{\partial x_{j,i}} \frac{dx_{j,i}}{dt} \quad (2.26)$$

$$AP_i = \Delta Q_i + \Delta S U_i + T_i \Delta S R_i \quad (2.27)$$

Once the in-cylinder pressure and the temperature of each zone are obtained zone volume can be calculated from the zone state equation. Energy and mass fluxes for spray, flame and unburned zones will be presented in the chapter 2.6.

## 2.5. Quasi-dimensional approach to combustion modeling

Since the 0-D modeling does not account for the geometry effects [60], and both spray combustion and combustion governed by the flame propagation through the premixed mixture are influenced by the geometry of the combustion chamber, it is necessary to apply the so-called quasi-dimensional 0-D modeling approach, which enables the inclusion of the geometry effects in the calculation of the fuel burning rates. The DMZCM presented in this thesis accounts for the following geometrical effects:

- Injector design (Figure 12 and Figure 13):
  - nozzle tip depth,
  - nozzle orientation (nozzle angle),
  - nozzle number.
- Combustion chamber design (Figure 14):
  - flat cylinder head,
  - flat piston top,
  - piston with cylindrically shaped bowl.
- Flame propagation
  - number of flames that propagate through the combustion chamber,
  - location of the flame centers,
  - interaction between the flames,

- interaction between flame and the combustion chamber walls.

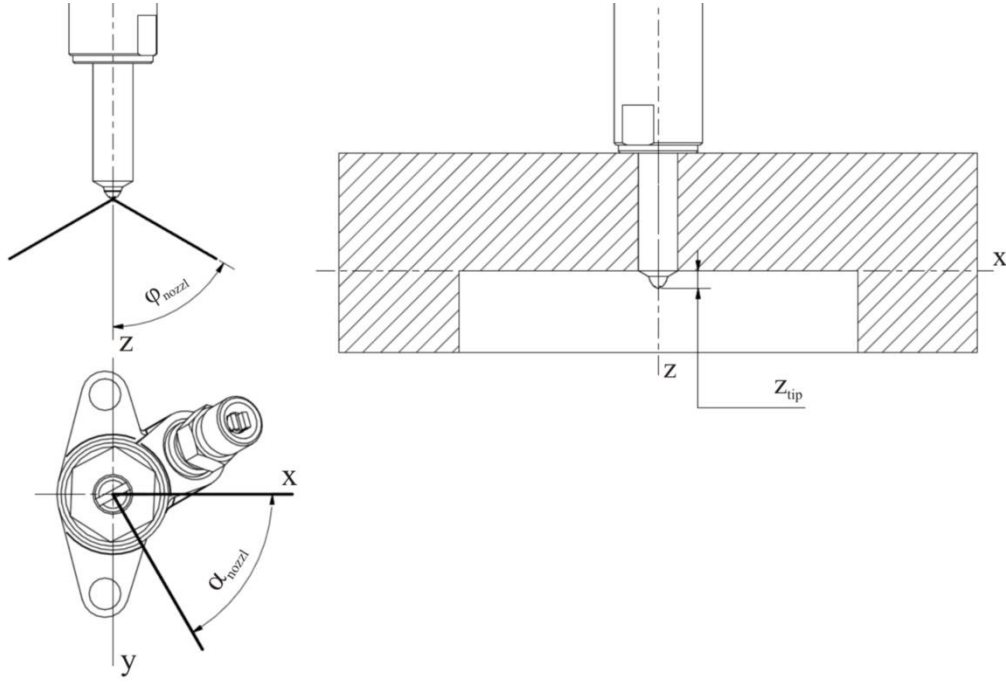


**Figure 12. Presentation of the injector geometry;  $z_{tip}$  (m) – injector nozzle hole depth;  $\varphi_{nozz}$  (rad) – injector nozzle hole angle;  $\alpha_{nozz}$  (rad) – angle between the two neighboring injector nozzles**

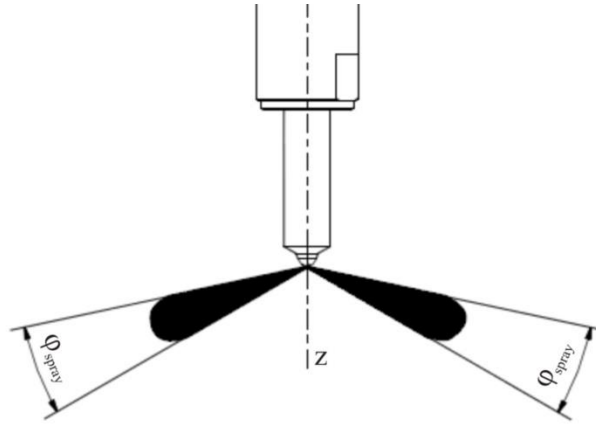


**Figure 13. Schematic presentation of the spray angle;  $\varphi_{spray}$  (rad) – spray angle**

The injector design and its features have a profound effect on the way how spray processes and hence spray combustion is governed. The inclusion of the geometrical description of the nozzle features enables calculation of the spray orientation, which enables calculation of the spray center, its impact with the combustion chamber walls and finally the location where flame propagation starts.

In the DFMZCM, the geometry of only two combustion chamber types that are specific for the conventional Diesel (DI-CI) engines has been developed (Figure 14). Such geometrical

description of the combustion chamber enables the accurate calculation of the spray impact and deflection from the combustion chamber walls, which improves the calculation of the location where the flame propagation starts. Moreover, this enables more accurate calculation of the interaction between the flames and specific flame and combustion chamber walls, which improves the laminar flame surface calculation and hence the flame propagation burning rate calculation (Figure 15).

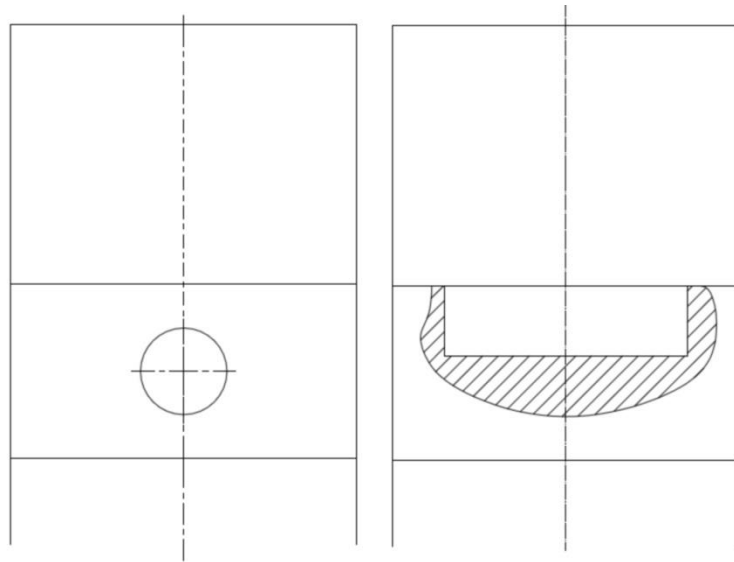


**Figure 14. Schematic presentation of the possible combustion chamber designs**

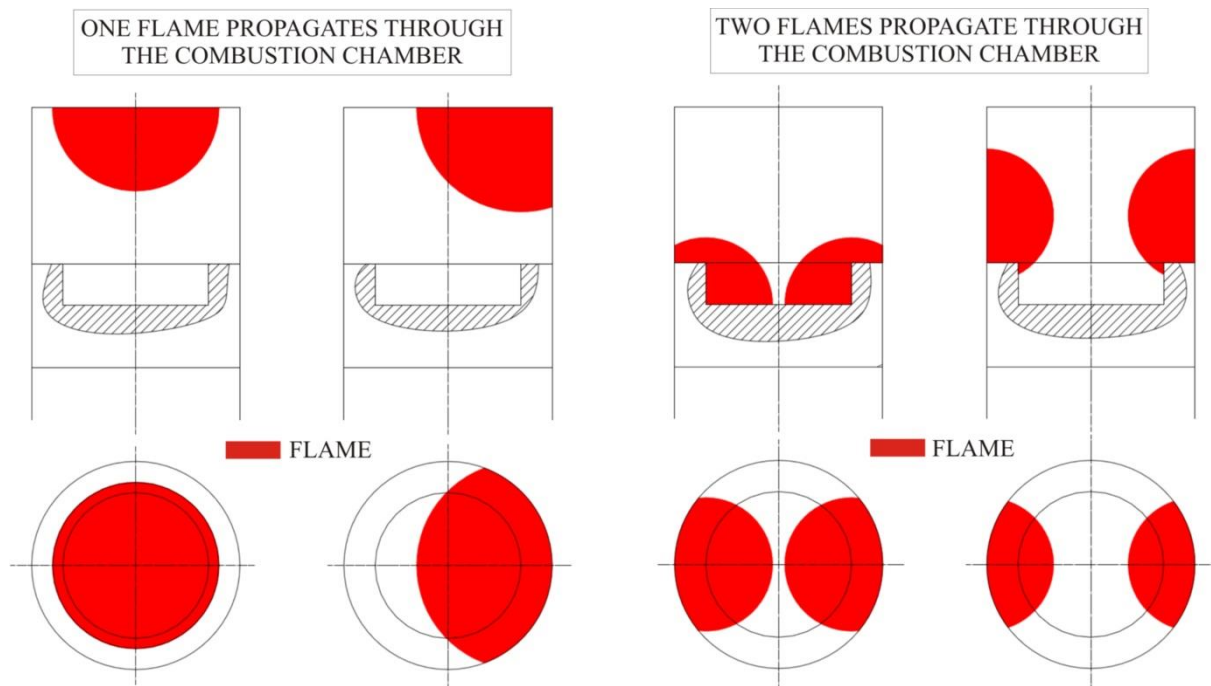


**Figure 15. Schematic presentation of possible flame center locations and number of flames that propagate through the combustion chamber**

Since it was found [18], [61] that in the conventional dual fuel IC engines multiple flames propagate through the combustion chamber, and that their number coincides with the number of nozzles on the Diesel fuel injector, with this 0-D model it is possible to calculate the interactions between any number of flames that propagate through the premixed mixture. Moreover, it is possible to account for any possible location of the flame center within the combustion chamber. More on the model that is used in the calculation of the flame front in the case when multiple flames propagate through the combustion chamber is given in chapter 3.7.

## 2.6. Zone formation and evolution

In this section, the formation of zones in the DFMZCM model is described and it is presented how a particular zone evolves in time. Moreover, the interactions between particular zones are also presented.

The 0-D combustion model presented in this thesis (DFMZCM) is only applied during the high-pressure cycle calculation of the conventional dual fuel IC engine. The high-pressure cycle of the IC engine last from the moment of the intake vale closure to the moment when the exhaust valve opens, and it is consisted of the compression and the expansion strokes. At the end of the gas exchange stroke, when the intake valve closes, the 0-D model is initiated and one zone that features the entire cylinder content is formed (Figure 16 and Figure 23).

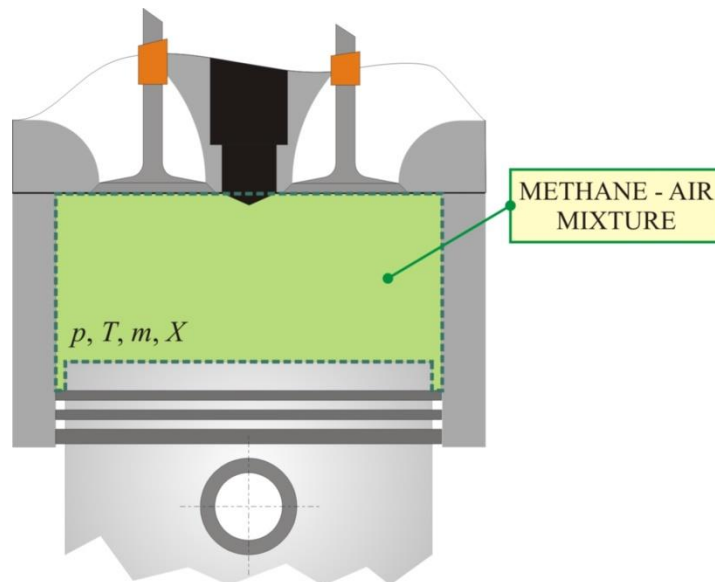


**Figure 16. Schematic presentation of the zone created inside the cylinder at the intake valve closure moment**

This zone (unburned zone) has uniform temperature and pressure, and all its properties are calculated every time-step during the compression stroke. When the injection of Diesel fuel starts, spray zones are created (Figure 17 and Figure 23). Spray is discretized in its axial and radial direction (Figure 18).

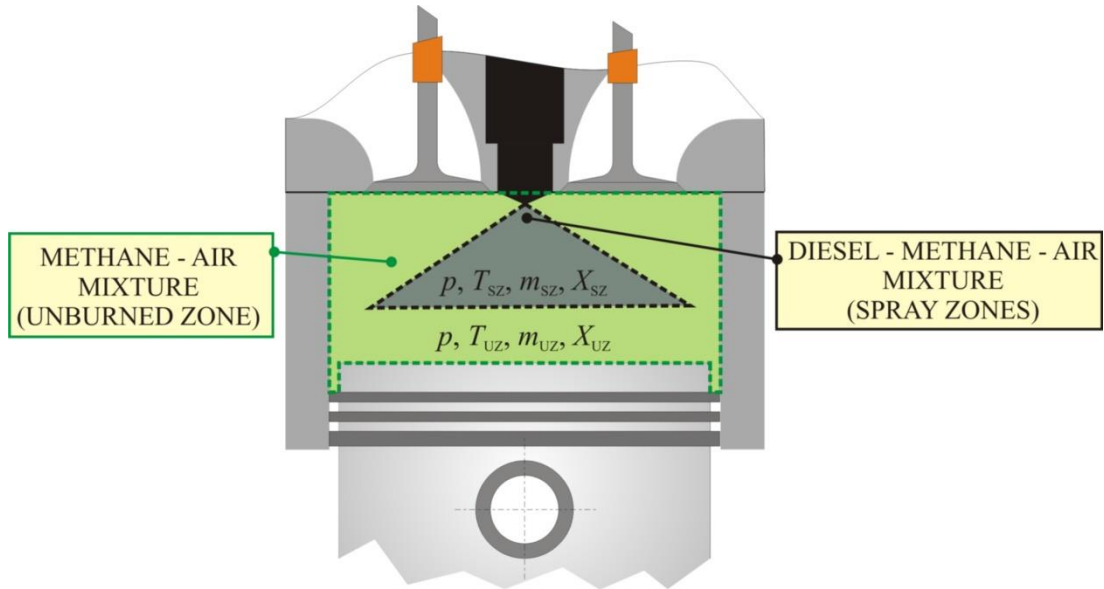


**Figure 17. Schematic presentation of the zones inside the cylinder during injection of Diesel fuel**

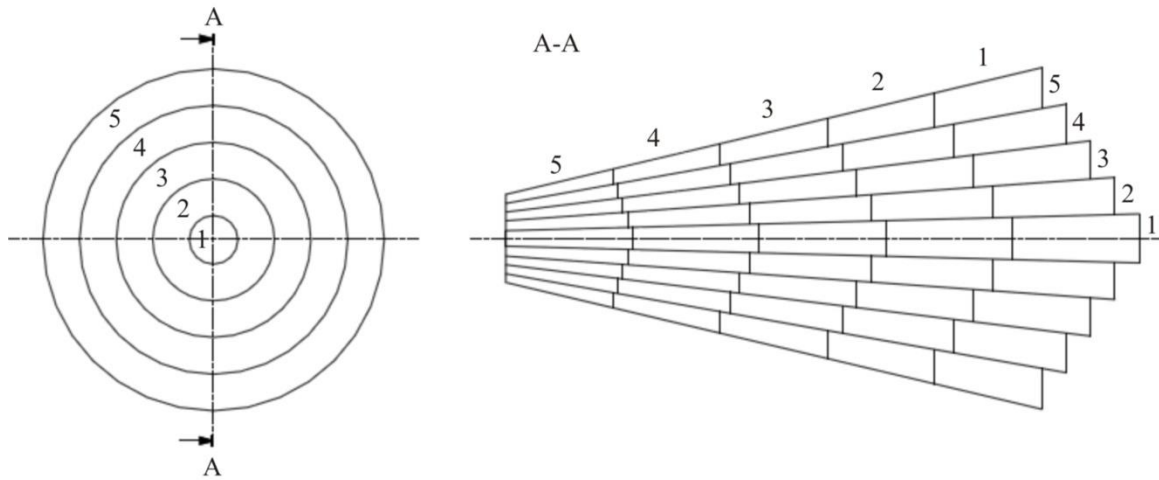


**Figure 18. Schematic presentation spray zones formation**

The number of parcels in axial direction depends on the selected discretization of the spray in the axial direction. In the case of a predefined setting, one axial parcel is created every degree crank angle during the injection process, and in this case the coarsest spray grid in axial direction is created. On the other hand, the finest grid in axial direction is created in the case

when one axial parcel is created every time-step (predefined value of 0.1 degCA) during the Diesel fuel injection process. The total number of axial parcels of the spray equals:

$$n_{\text{parcels}} = \frac{DOI}{C_{\text{discr,ax}}} \quad (2.28)$$

In the equation given above,  $n_{\text{parcels}}$  (-) represents the number of parcels in the axial direction,  $DOI$  (degCA) represents the duration of injection, while  $C_{\text{discr,ax}}$  (degCA) represents the discretization factor of the spray in the axial direction and it ranges from 0.1 to 1. Discretization of each axial parcel in the radial direction is a user-defined parameter and it usually ranges from 3 – 5. Finally, the overall number of spray zones is given with the following equation:

$$n_{\text{zones,spray}} = n_{\text{parcels}} \cdot C_{\text{discr,rad}} \quad (2.29)$$

In the equation given above,  $n_{\text{zones,spray}}$  (-) represents the total number of the spray zones,  $C_{\text{discr,rad}}$  (-) represents the discretization parameter in the radial direction of the spray for every axial parcel.

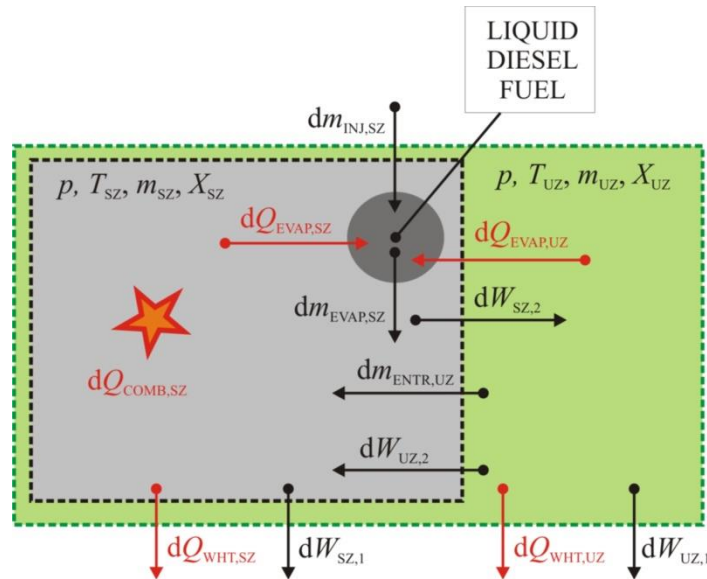


**Figure 19. Schematic presentation of the interaction between one spray zone and the unburned zone before flame propagation through the premixed mixture has started**

During the process of spray formation and evolution, every spray zone entrains fresh charge from the unburned zone (Figure 19 and Figure 23). Each of the spray zones consists of 2 phases:

- liquid phase: liquid Diesel fuel,
- gaseous phase: mixture of various gases:
  - Diesel fuel vapor,
  - methane
  - combustion products (contain burned methane and Diesel fuel)
  - fresh air.

Part of the energy for liquid fuel heat up and evaporation comes from the spray zone, while the other part comes from the zones that surround the spray (Figure 19 and Figure 22). Unburned and spray zones exchange both mass and energy. Part of the energy transfer is connected to the enthalpy of the transferred mass, while the other part is a result of the heat transfer through the zone boundary. The only interaction between the spray zones is the heat transfer between the zones; there is no mass transfer between the spray zones. Once the model defines that specific spray zone ignites, the spray combustion of the prepared gaseous mixture starts. Fuel combustion and consequent energy release in the spray zones lead to an increase in the in-cylinder pressure and temperature, especially in the spray region where the temperature raises to above 2000 K. Ignited spray acts as a high energy source that triggers the flame propagation through the premixed mixture is triggered. The flame propagation through the premixed mixture can only start if:

1. spray has ignited,
2. premixed mixture is within the flammability limits.

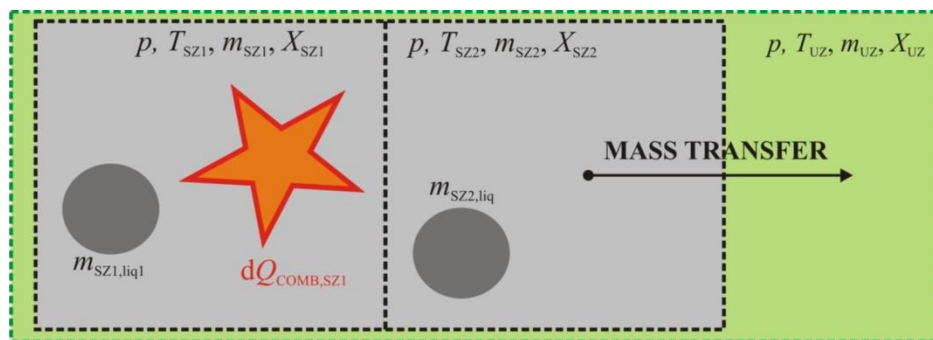


**Figure 20. Schematic presentation of the process of mass transfer from the unburned spray region to the unburned zone at the start of flame propagation moment**

Flame is considered to have a spherical shape and it starts to propagate from the outer surfaces of the spray zones that have ignited. Spray can essentially be viewed as a spark plug that triggers the flame propagation through the premixed mixture once the conditions (pressure and temperature) for the start of flame propagation are satisfied. As the flame starts



to propagate from the outer surfaces of the warm spray zones that have ignited, from the physical stand point flame will propagate through both the premixed methane/air charge (unburned zone) and the other spray zones that have not yet ignited. This is why at this moment a part of the content of the spray zones that have not ignited is transferred into the unburned region (Figure 20 and Figure 23).

Once the flame propagation has started a new zone called “flame zone” is formed and it increases as the flame propagates through the combustion chamber. At this moment, spray combustion and combustion that is governed by the flame propagation through the premixed mixture occur at the same time. Since now the flame propagation has started, spray zones are engulfed with the propagating flame (Figure 21), and new interactions between the zones are formed (Figure 22 and Figure 23).

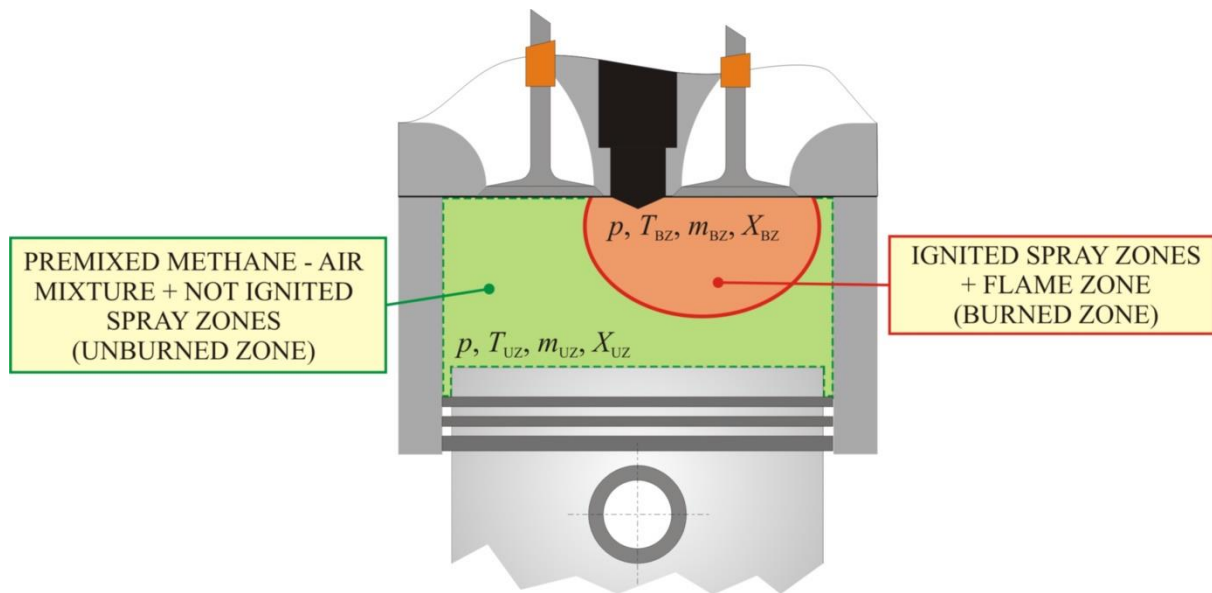


**Figure 21. Schematic presentation of the zones inside the cylinder during spray combustion and flame propagation through the premixed charge**

The interactions between the zones after the flame propagation has started are presented in Figure 23. The spray zones exchange mass and energy with both the flame and unburned zone, while the flame zone exchanges mass and energy with the unburned zone. Energy transfer is connected to the enthalpy of the transferred mass. The mass transfer between the unburned and flame zone is governed by the flame propagation process, while the mass transfer between the flame and spray and the spray and unburned zone is governed by the entrainment of new mass into the spray zone. Flame propagation lasts until either the entire unburned zone has been consumed, or flame has quenched. The spray combustion on the other hand lasts until either the entire fuel mass inside the spray zone has been burned, or there is no more air

The diagram illustrates a three-stage thermodynamic cycle (SZ, FZ, UZ) with a central gray control volume. The stages are represented by different background colors: SZ (gray), FZ (yellow), and UZ (green). The central gray circle represents the control volume. Red stars indicate combustion heat input ( $dQ_{\text{COMB}}$ ).

**Mass Flows ( $dm$ ):**

- Input:**  $dm_{\text{ENTR,UZ}}$  enters the UZ stage from the left.
- Output:**  $dm_{\text{INJ,SZ}}$  exits the SZ stage from the top.
- Internal Flows:**  $dm_{\text{ENTR,FZ}}$  and  $dm_{\text{FP}}$  flow from the UZ stage to the FZ stage.  $dm_{\text{EVAP,SZ}}$  flows from the SZ stage to the central control volume.

**Work Flows ( $dW$ ):**

- Input:**  $dW_{\text{SZ,1}}$  enters the SZ stage from the bottom.
- Output:**  $dW_{\text{SZ,2}}$  exits the SZ stage to the left,  $dW_{\text{SZ,3}}$  exits to the right, and  $dW_{\text{FZ,1}}$  enters the FZ stage from the bottom.
- Internal Flows:**  $dW_{\text{FZ,2}}$  and  $dW_{\text{FZ,3}}$  flow from the FZ stage to the UZ stage.  $dW_{\text{UZ,2}}$  and  $dW_{\text{UZ,3}}$  flow from the UZ stage to the left.

**Heat Flows ( $dQ$ ):**

- Input:**  $dQ_{\text{COMB,SZ}}$  and  $dQ_{\text{COMB,FZ}}$  enter the central control volume from the bottom and right, respectively, indicated by red stars.
- Internal Flows:**  $dQ_{\text{EVAP,SZ}}$  and  $dQ_{\text{EVAP,FZ}}$  flow from the central control volume to the SZ and FZ stages, respectively.
- External Flows:**  $dQ_{\text{WHT,SZ}}$ ,  $dQ_{\text{WHT,FZ}}$ , and  $dQ_{\text{WHT,UZ}}$  exit the SZ, FZ, and UZ stages to the bottom, respectively, indicated by red arrows.

**State Variables:**

- SZ Stage:**  $p, T_{\text{SZ}}, m_{\text{SZ}}, X_{\text{SZ}}$
- FZ Stage:**  $p, T_{\text{FZ}}, m_{\text{FZ}}, X_{\text{FZ}}$
- UZ Stage:**  $p, T_{\text{UZ}}, m_{\text{UZ}}, X_{\text{UZ}}$

Figure 1 illustrates the combustion process in a diesel engine, showing the progression from compression to the end of combustion. The diagram is divided into six stages, each represented by a horizontal bar indicating the state of the fuel and the combustion zones.

**Legend:**

- AIR + EGR
- METHANE
- LIQUID DIESEL
- VAPORIZED DIESEL
- COMBUSTION PRODUCTS

**Combustion Zones:**

- UZ - UNBURNED ZONE
- SZ - SPRAY ZONES
- FZ - FLAME ZONE
- BZ - BURNED ZONE

**Stages of Combustion:**

- COMPRESSION:** The initial state shows a mixture of AIR + EGR (white) and METHANE (green) in the UNBURNED ZONE (UZ).
- DIESEL FUEL INJECTION:** LIQUID DIESEL (black) is injected into the UNBURNED ZONE (UZ), forming the SPRAY ZONES (SZ).
- SPRAY IGNITION & COMBUSTION:** The injected fuel begins to vaporize, forming VAPORIZED DIESEL (grey) within the SPRAY ZONES (SZ).
- SPRAY COMBUSTION & FLAME INITIATION:** The process continues with the formation of COMBUSTION PRODUCTS (dark grey) within the SPRAY ZONES (SZ). The UNBURNED ZONE (UZ) transitions into the FLAME ZONE (FZ).
- SPRAY COMBUSTION & FLAME PROPAGATION:** The flame propagates through the UNBURNED ZONE (UZ), converting it into the FLAME ZONE (FZ). The SPRAY ZONES (SZ) continue to form COMBUSTION PRODUCTS (dark grey).
- END OF COMBUSTION:** The final state shows the entire mixture converted into COMBUSTION PRODUCTS (dark grey), forming the BURNED ZONE (BZ).

---

38

After all interactions between the zones have been presented, it is possible to formulate the total mass, species  $j$  and energy fluxes for all zones. The total mass, species  $j$  and energy fluxes for a given  $i$ -th spray zone are given with the following equations:

$$\left(\frac{dm}{dt}\right)_{SZ,i} = \frac{dm_{\text{evap},SZ,i}}{dt} + \frac{dm_{\text{entr},UZ,i}}{dt} + \frac{dm_{\text{entr},FZ,i}}{dt} \quad (2.30)$$

$$\left(\frac{dm_{\text{liq}}}{dt}\right)_{SZ,i} = \left(\frac{dm_{\text{inj}}}{dt}\right)_{SZ,i} - \left(\frac{dm_{\text{evap}}}{dt}\right)_{SZ,i} \quad (2.31)$$

$$\left(\frac{dm_j}{dt}\right)_{SZ,i} = \frac{dm_{j,\text{evap},SZ,i}}{dt} + \frac{dm_{j,\text{entr},UZ,i}}{dt} + \frac{dm_{j,\text{entr},FZ,i}}{dt} + S_{j,i} \quad (2.32)$$

$$\begin{aligned} \left(\frac{dQ}{dt}\right)_{SZ,i} &= \frac{dQ_{\text{COMB},SZ,i}}{dt} + \frac{dQ_{\text{ZHT},SZ,i}}{dt} - \frac{dQ_{\text{EVAP},SZ,i}}{dt} - \frac{dQ_{\text{WHT},SZ,i}}{dt} + \\ &\frac{dm_{\text{evap},SZ,i}}{dt} h_{\text{evap}} + \frac{dm_{\text{entr},UZ,i}}{dt} h_{\text{UZ}} + \frac{dm_{\text{entr},FZ,i}}{dt} h_{\text{FZ}} \end{aligned} \quad (2.33)$$

In the equations given above,  $(dm/dt)_{SZ,i}$  (kg/s) represents the total mass flux for the  $i$ -th spray zone (gaseous phase),  $(dm_{\text{liq}}/dt)_{SZ,i}$  (kg/s) represents the total mass flux for the liquid fuel inside the  $i$ -th spray zone,  $(dQ/dt)_{SZ,i}$  (J/s) represents the total energy flux for the  $i$ -th spray zone,  $h_{\text{inj}}$  (J/kg) represents the liquid fuel enthalpy,  $h_{\text{UZ}}$  (J/kg) represents the enthalpy of the unburned zone mixture,  $h_{\text{evap}}$  (J/kg) represents the enthalpy of the evaporated fuel, while  $h_{\text{FZ}}$  (J/kg) represents the enthalpy of the flame zone mixture. Subscript  $j$  in the equation (2.32) denotes the  $j$ -th species. The source term  $S_{j,i}$  in equation (2.32) is associated with the spray combustion. The following expressions in equations (2.30, 2.31, 2.32 and 2.33) represent:

1.  $(dm_{\text{evap},SZ,i}/dt)$  (kg/s) represents the mass flux due to the fuel evaporation process for  $i$ -th spray zone. The expression for the mass flux due to the fuel evaporation process for  $i$ -th spray zone is given in the equation 3.73 (chapter 3.3.3).
2.  $(dm_{\text{entr},UZ,i}/dt)$  (kg/s) represents the mass flux due to mass entrainment from the unburned zone for  $i$ -th spray zone, while  $(dm_{\text{entr},FZ,i}/dt)$  (kg/s) represents the mass flux due to mass entrainment from the flame zone for  $i$ -th spray zone. The expression for the mass flux due to the fuel entrainment for  $i$ -th spray zone is given in the equations 3.59 and 3.60 (chapter 3.3.3).

3.  $(dm_{inj,SZ,i}/dt)$  (kg/s) represents the mass flux due to direct fuel injection (Diesel fuel) for  $i$ -th spray zone. This expression is calculated from the normalized injection rate which is an input to the model.
4.  $(dQ_{COMB,SZ,i}/dt)$  (J/s) represents the energy flux associated with the spray combustion process for  $i$ -th spray zone. The expression for energy flux associated with the spray combustion process  $i$ -th spray zone is given in the equation 3.106 (chapter 3.3.3).
5.  $(dQ_{EVAP,SZ,i}/dt)$  (J/s) represents the energy flux associated with the fuel evaporation process for  $i$ -th spray zone. The expression for energy flux associated with the fuel evaporation process for  $i$ -th spray zone is given in the equation 3.75 (chapter 3.3.3).
6.  $(dQ_{WHT,SZ,i}/dt)$  (J/s) represents the energy flux associated with the wall heat transfer for  $i$ -th spray zone. The expression for energy flux associated with the wall heat transfer for  $i$ -th spray zone is given in the equation 3.34 (chapter 3.2.3).
7.  $\frac{dQ_{ZHT,SZ,i}}{dt}$  (J/s) represents the sum of the heat supplied/taken away from the specified spray zone due to the heat transfer with the surrounding spray zones. The expression for energy flux associated with the zone heat transfer process for  $i$ -th spray zone is given in the equation 3.38 (chapter 3.2.4).

The overall energy flux due to spray combustion (J/s) can be expressed as:

$$\frac{dQ_{COMB,SZ}}{dt} = \sum_i \frac{dQ_{COMB,SZ,i}}{dt} \quad (2.34)$$

The total mass (2.35), species  $j$  (2.36) and energy (2.37) flux for the unburned zone is given with the following equations:

$$\left( \frac{dm}{dt} \right)_{UZ} = - \sum \frac{dm_{entr,UZ,i}}{dt} - \frac{dm_{FP}}{dt} - \frac{dm_{BB,UZ}}{dt} \quad (2.35)$$

$$\left( \frac{dm_j}{dt} \right)_{UZ} = - \sum \frac{dm_{j,entr,UZ,i}}{dt} - \frac{dm_{j,FP}}{dt} - \frac{dm_{j,BB,UZ}}{dt} + S_{j,UZ} \quad (2.36)$$

$$\left( \frac{dQ}{dt} \right)_{UZ} = \frac{dQ_{COMB,UZ}}{dt} - \frac{dQ_{WHT,UZ}}{dt} - \frac{dQ_{EVAP,UZ}}{dt} - \sum \frac{dm_{j,entr,SZ,i}}{dt} h_{UZ} - \frac{dm_{j,FP}}{dt} h_{UZ} - \frac{dm_{j,BB,UZ}}{dt} h_{UZ} \quad (2.37)$$

The total mass (2.38), species  $j$  (2.39) and energy (2.40) flux for the flame zone is given with the following equations:

$$\left(\frac{dm}{dt}\right)_{FZ} = -\sum \frac{dm_{entr,FZ,i}}{dt} + \frac{dm_{FP}}{dt} - \frac{dm_{BB,FZ}}{dt} \quad (2.38)$$

$$\left(\frac{dm_j}{dt}\right)_{FZ} = -\sum \frac{dm_{j,entr,FZ,i}}{dt} + \frac{dm_{j,FP}}{dt} - \frac{dm_{j,BB,FZ}}{dt} + S_{j,FZ} \quad (2.39)$$

$$\left(\frac{dQ}{dt}\right)_{FZ} = \frac{dQ_{COMB,FZ}}{dt} - \frac{dQ_{WHT,FZ}}{dt} - \frac{dQ_{EVAP,FZ}}{dt} - \sum \frac{dm_{entr,FZ,i}}{dt} h_{FZ} + \frac{dm_{FP}}{dt} h_{UZ} - \frac{dm_{BB,FZ}}{dt} h_{FZ} \quad (2.40)$$

During the compressions and flame propagation process, blow-by only affects the unburned zone (equations 2.41 and 2.42). After the flame has propagated through the unburned zone, the blow-by only affects the flame zone (equations 2.43 and 2.44):

$$\frac{dm_{BB,UZ}}{dt} = \frac{dm_{BB}}{dt} \quad (2.41)$$

$$\frac{dm_{BB,FZ}}{dt} = 0 \quad (2.42)$$

$$\frac{dm_{BB,UZ}}{dt} = 0 \quad (2.43)$$

$$\frac{dm_{BB,FZ}}{dt} = \frac{dm_{BB}}{dt} \quad (2.44)$$

In the equations given above,  $(dm/dt)_{UZ}$  (kg/s) represents the total mass flux for the unburned zone;  $(dm/dt)_{FZ}$  (kg/s) represents the total mass flux for the flame zone,  $\sum \frac{dm_{entr,UZ,i}}{dt}$  (kg/s) represents the overall entrainment flux from the unburned zone to the spray zones,  $\sum \frac{dm_{entr,FZ,i}}{dt}$  (kg/s) represents the overall entrainment flux from the flame zone to the spray

zones,  $(dQ/dt)_{UZ}$  (J/s) represents the total energy flux for the unburned zone, while  $(dQ/dt)_{FZ}$  (J/s) represents the total energy flux for the flame zone. Subscript  $j$  in the equations (2.34 and 2.37) denotes the  $j$ -th species. In case of the unburned zone, the source term  $S_{j,UZ}$  in equation (2.34) is associated with the knock combustion (occurs in the unburned zone), while the source term  $S_{j,FZ}$  in equation (2.37) is associated with the combustion that is governed by the flame propagation through the premixed mixture (occurs in the flame zone). The following expressions in equations (2.35, 2.36, 2.37, 2.38, 2.39 and 2.40) represent:

1.  $(dm_{FP}/dt)$  (kg/s) represents the mass flux associated with the flame propagation process. The expression for the mass flux associated with the flame propagation process is given in the equation 3.163 (chapter 3.5).
2.  $dQ_{COMB,UZ}/dt$  (J/s) represents the energy flux associated with the combustion in the unburned zone. The expression for the energy flux associated with the combustion in the unburned zone is given in the equation 3.308 (chapter 3.9.2).
3.  $dQ_{WHT,UZ}/dt$  (J/s) represents the energy flux associated with the wall heat transfer for the unburned zone. The expression for the energy flux associated with the wall heat transfer for the unburned zone is given in the equation 3.35 (chapter 3.2.3).
4.  $dQ_{EVAP,UZ}/dt$  (J/s) represents the energy flux associated with the evaporation process for the unburned zone (energy for the liquid fuel evaporation taken from the unburned zone). The expression for the energy flux associated with the evaporation process for the unburned zone is given in the equation 3.76 (chapter 3.3.3).
5.  $dQ_{COMB,FZ}/dt$  (J/s) represents the energy flux associated with the combustion in the flame zone. The expression for the energy flux associated with the combustion in the flame zone is given in the equation 3.166 (chapter 3.5).
6.  $dQ_{WHT,FZ}/dt$  (J/s) represents the energy flux associated with the wall heat transfer for the flame zone. The expression for the energy flux associated with the wall heat transfer for the flame zone is given in the equation 3.36 (chapter 3.2.3).
7.  $dQ_{EVAP,FZ}/dt$  (J/s) represents the energy flux associated with the evaporation process (energy for the liquid fuel evaporation taken from the flame zone). The expression for the energy flux associated with the evaporation process for the flame zone is given in the equation 3.77 (chapter 3.3.3).

The energy flux for the entire in-cylinder content due to combustion (J/s) can be expressed as:

$$\frac{dQ_{COMB}}{dt} = \frac{dQ_{COMB,SZ}}{dt} + \frac{dQ_{COMB,FZ}}{dt} + \frac{dQ_{COMB,UZ}}{dt} \quad (2.45)$$

### **3. Sub-models of 0-D dual fuel combustion model**

In this section, the sub-models of the presented 0-D combustion model (DFMZCM) for the calculation of the combustion process in the conventional dual fuel engines are presented. Each of these sub-models is used for calculating the specific physical phenomenon that occurs in a conventional dual fuel IC engine. It is important to appropriately describe these phenomena as they have a profound effect on the combustion process in the dual fuel engines. As most of these phenomena have a 3-D character, their reduction to 0-D environment requires an excellent knowledge of the physics and engine operation, since some simplifications have to be applied. The physical phenomena which have a profound effect on the combustion process in the conventional dual fuel engines are:

1. the in-cylinder flow and turbulence;
2. the heat transfer (both between the specific zones and between the entire cylinder content and the cylinder walls);
3. the fuel spray processes;
4. the autoignition chemistry (modeled with ignition delay and the chemical reaction rate);
5. the flame propagation process;
6. the multiple flame phenomenon;
7. the occurrence of knock in the end gas.

In the following chapters each of these physical phenomena together with the modeling approach in the 0-D environment is both schematically and mathematically presented and described. Also, as the emission modeling is becoming an industry standard, the physics behind emissions formation, as well as their modeling in the 0-D environment is presented and described.

#### **3.1. In-cylinder flow and turbulence**

The following chapters present the in-cylinder turbulence phenomenon and its modeling in 0-D environment.

##### **3.1.1. Physical background**

Fluid flows can be divided into two major groups, laminar flow and turbulent flow. In laminar flow, fluid flows in an organized, smooth and layered (laminar) manner [62]. Contrary, in the case of a turbulent flow, fluid flows in a chaotic, disorganized and unsteady manner [63] and

is characterized by the high levels of vorticity. All flows can be characterized by a specific Reynolds number; laminar flows are flows characterized by the low Reynolds numbers, while the turbulent flows are characterized by the high values of the Reynolds number [53]. Most of the flows that are encountered in the real life situations are turbulent in their nature [53], [63], where some of the typical examples include flow around a car or a building. Some of the types of turbulent flows which are encountered in the nature and engineering practice are shown in Figure 24.

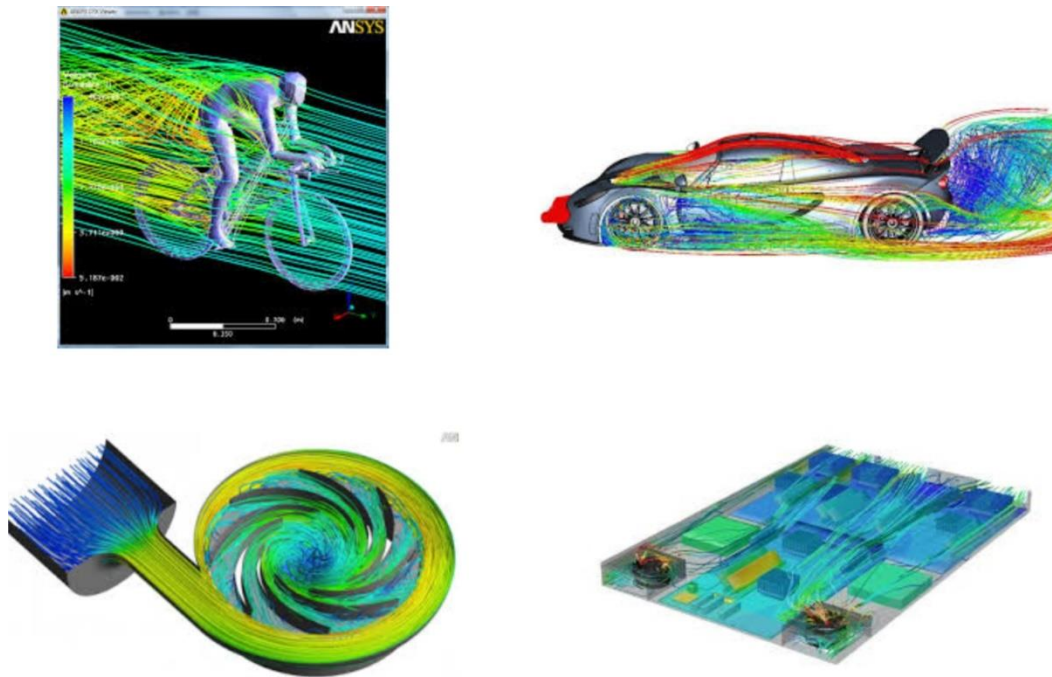


**Figure 24. Various types of turbulent flows in real life and engineering applications (flow around a cyclist, flow around a car, flow in the compressor, flow that cools various hardware components); figures taken from [64]**

Turbulence has no strict definition, but it can best be described as a complex 3-D phenomenon that is characterized by the random behavior and the velocity, pressure and temperature fields that vary both in space and time [63]. The level of turbulence is defined by the velocity fluctuations, which are referred to as the turbulence intensity [53]. Turbulent flow is always three-dimensional and unsteady [65], and in a typical turbulent fluid motion, eddies of different sizes (length scales) can be seen. Besides characteristic length scales, these eddies have characteristic velocities and time scales. The presence of eddies of different length scales and their motion leads to an effective mixing, thus increasing mass, heat and momentum transfer in the turbulent flows. Turbulence is generated from the kinetic energy of the mean flow through the phenomena known in the literature as the energy cascade mechanism [53], in



which the kinetic energy is progressively transferred from the large scale mean flow structures to the turbulent eddies of smaller and smaller sizes, where the energy is finally dissipated into the heat [53] (Figure 25).

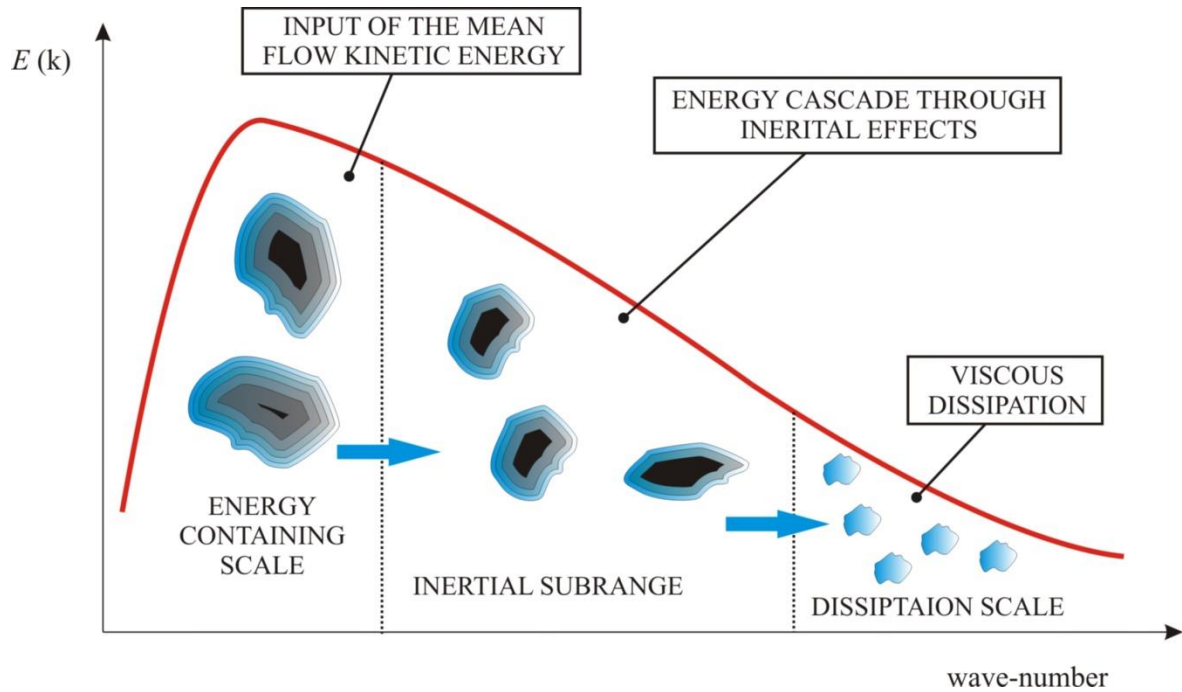


**Figure 25. The schematic presentation of the energy cascade mechanism; reproduced from [32]**

The large scale (energy containing) eddies interact and draw the energy from the main flow and transfer it through the inertial subrange to the stable small-scale eddies, where the kinetic energy is dissipated into the heat through the effects of viscous forces [53]. The inertial subrange, which can also be referred to as the energy transfer region simply acts as a road through which the energy is transferred [65].

The flow of the mixture inside the cylinder is turbulent in its nature and is considered to be one of the major factors that controls the mixture preparation and hence the combustion process in the IC engines [66]. The turbulent motion of the in-cylinder mixture is set-up by the intake process [66] and later influenced and modified by the combustion chamber geometry and direct fuel injection. There are 3 main types of the in-cylinder charge motion: tumble, swirl and squish. Presentation of these three characteristic in-cylinder charge motions can be seen in Figure 26. The in-cylinder charge is said to be in tumbling motion when it rotates around one of the horizontal axes of the cylinder. Swirl is the motion of the charge around the vertical axis of the cylinder. Squish is the radial, inward motion of the in-cylinder charge. Tumble and swirl can be induced by both the intake port geometry and combustion chamber geometry, while squish, is induced during the compression stroke. During the

compression stroke, turbulence level inside the combustion chamber increases as both the velocity gradients and density inside the mixture increase. This leads to high levels of viscous forces and consequently high rate of kinetic energy dissipation.

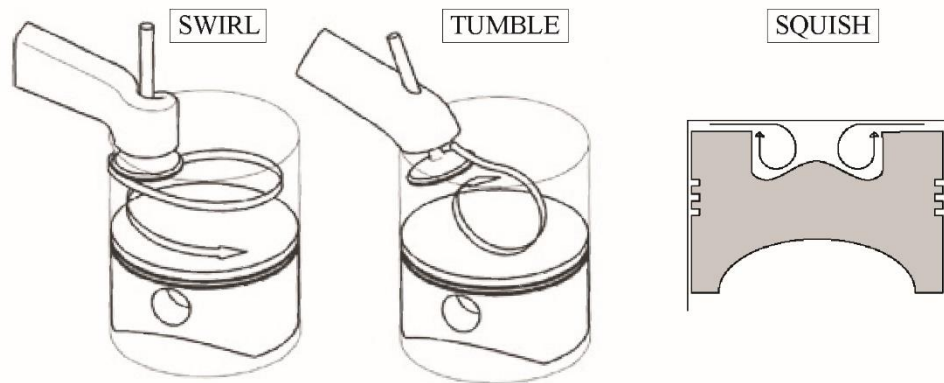


**Figure 26. Types of in-cylinder charge motion; images taken from [67], [68]**

Direct injection of the fuel during the high-pressure cycle also has a profound effect on the in-cylinder turbulent flow; additional mass is supplied to the cylinder at high velocity levels, which increase the in-cylinder kinetic energy. Additionally, since the fuel spray has high velocity, high velocity gradients at the spray/charge interface are present which lead to an increase in the turbulence production, especially in the fuel spray region. To summarize, the level of turbulence intensity inside the cylinder of an internal combustion engine significantly depends on the combustion chamber geometry, engine speed and load, valve timing, direct fuel injection and the governing of the combustion process [32].

The influence of the turbulence on combustion is a known fact [30], [50]–[52]. Since turbulence has a profound influence on the mixing rate it is responsible for fuel/air mixing and hence the combustible charge preparation. Contrary to the DI-CI and SI engines, in the HCCI engines, where combustion is primarily controlled by the kinetic chemistry of the combustible charge, the influence of the in-cylinder turbulent flow on the combustion process is not straight forward. However, as turbulence is responsible for charge mixing, it influences the kinetically-controlled combustion rate through the temperature and composition stratification of the in-cylinder charge. In the DI-CI engine, where combustion is primarily controlled by the process of fuel-air mixing (i.e. mixing-controlled combustion), the in-cylinder turbulent flow is responsible for the fuel/air mixing. In the SI engines, where combustion is controlled by the flame propagation through the premixed mixture, turbulence is responsible for wrinkling of the flame front [32], which increases its surface area thus increasing the overall burning rate. Turbulence is also modified by combustion as there is a

sharp temperature dependent jump in the viscosity at the burned/unburned region interface [50]. Moreover, high levels of turbulence may lead to local flame extinctions [51].

Since the combustion in the conventional dual fuel engines is a blend of the mixing-controlled combustion and combustion governed by the flame propagation through the premixed mixture, turbulence has a profound effect on the occurrence of the combustion process. Therefore, appropriate modeling of the in-cylinder turbulence is very important in modeling of the combustion in conventional dual fuel engines.

In the 0-D combustion model presented in this thesis, all turbulence quantities are calculated with a two zone  $k$ - $\epsilon$  turbulence model, which was developed and validated in [32]. In this thesis, the  $k$ - $\epsilon$  turbulence model was extended to include the effects of injection on the in-cylinder turbulence level. The entire process of the reduction of 3-D CFD  $k$ - $\epsilon$  turbulence model to 0-D space can be found in [30], [32], where detail explanation of this process has been presented. In this thesis only the 0-D  $k$ - $\epsilon$  equations and their explanation, as well as the derivation of the effect of injection on the in-cylinder turbulence level, will be given.

### 3.1.2. Overview of the $k$ - $\epsilon$ turbulence model in 0-D environment

The standard  $k$ - $\epsilon$  turbulence model features two transport equations, one that models the turbulent kinetic energy and one that models the dissipation rate [32]. As the 0-D approach does not directly (mathematically) account for the combustion chamber geometry, the effect of various in-cylinder flow types as well as the intake and the injection process on the turbulent kinetic energy level and its scales has to be modeled. The first assumption in the creation of the 0-D turbulence model is the isotropic and homogeneous in-cylinder turbulent flow field [30], [32] which means that the convection and diffusion terms in the equations are equal to zero [32].

Since it has been shown that the turbulence and its scales in front of the flame are the ones that affect the burning rate during the flame propagation process [32], [50], [66], a two-zone turbulence model is applied. The switch from the single to the two-zone turbulence model is made at the moment when the flame propagation is triggered. The turbulence level and its characteristic scales prior to the start of the flame propagation process and after the flame has propagated through the premixed mixture are calculate with the single zone approach. This means that turbulence is modeled with a single-zone approach during the intake, exhaust, compression and part of the expansion process, while during the flame propagation process the two-zone approach in modeling of the in-cylinder turbulence is used (Figure 27).

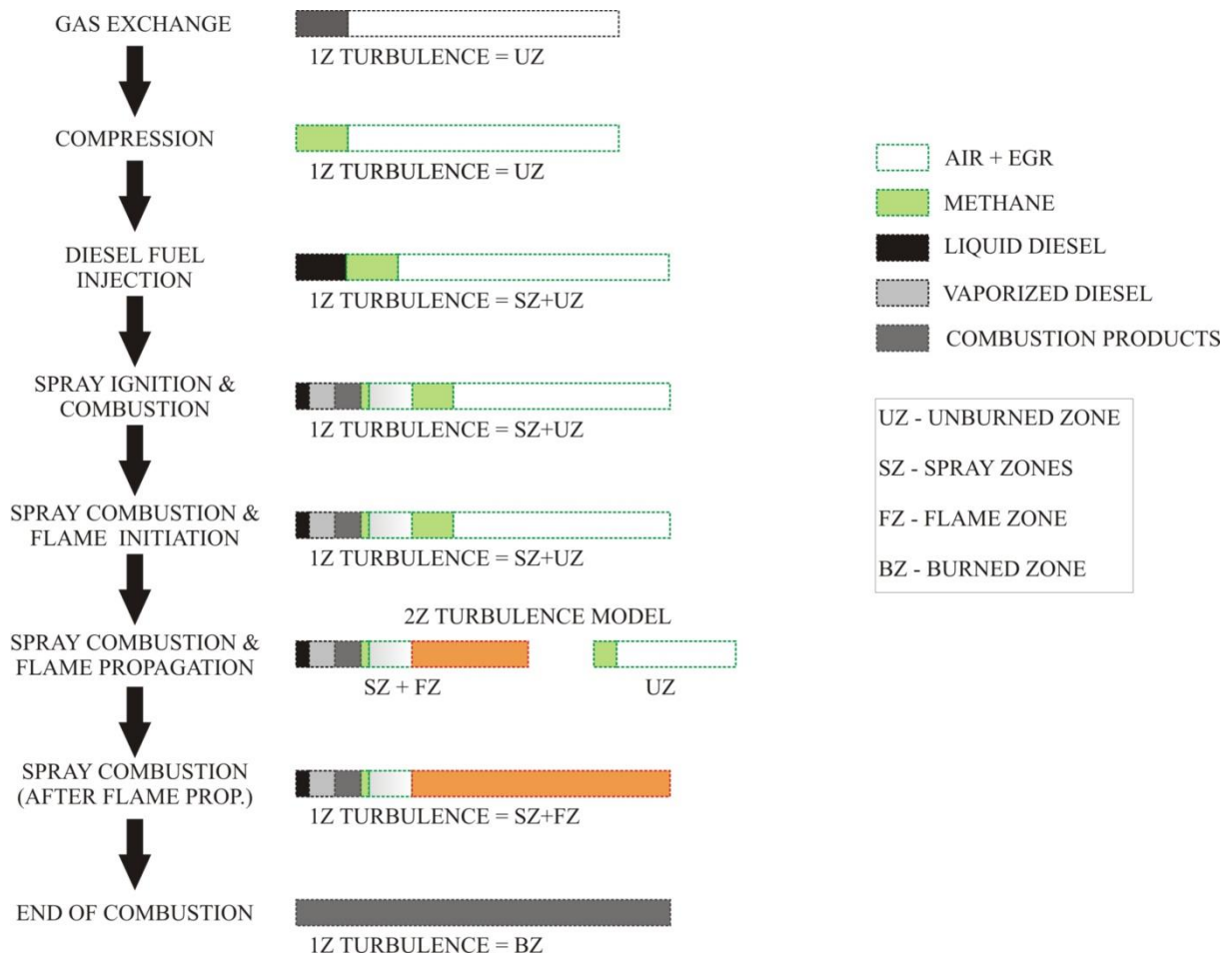


Figure 27. Scheme of the zone evolution in the turbulence model

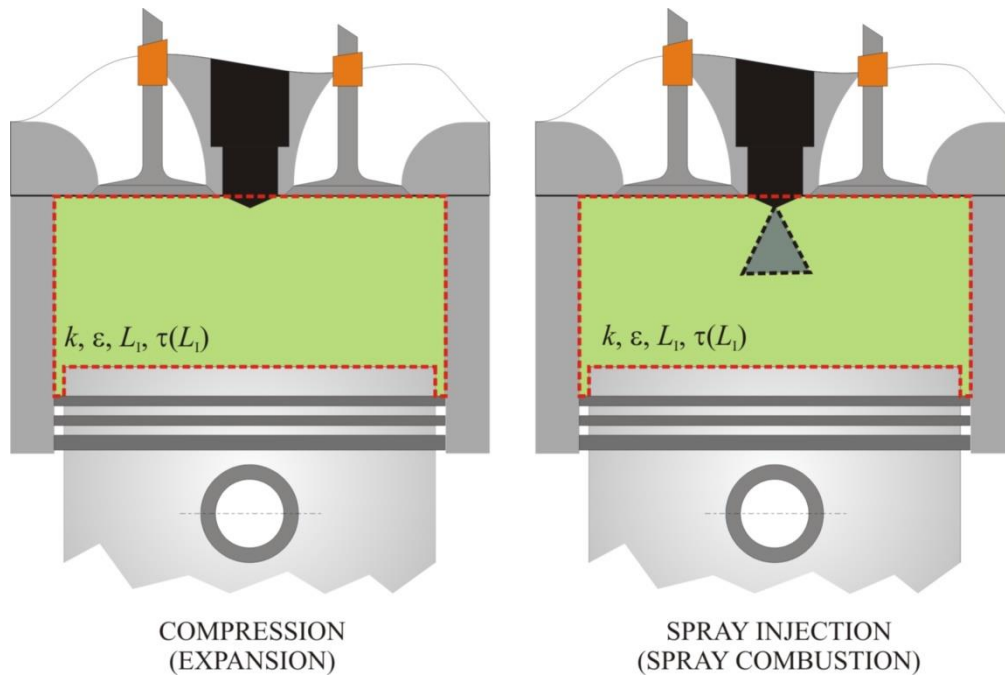


Figure 28. Presentation of the single zone turbulence approach

In the single zone turbulent modeling approach, the entire cylinder content is treated as one zone that has the same level of turbulence and dissipation as well as a single integral length scale and turbulence time scale (Figure 28). The 0-D  $k$ - $\varepsilon$  turbulence equations are based on the 3-D  $k$ - $\varepsilon$  turbulence equations. Since the 0-D modeling approach presumes homogeneous and isotropic turbulent flow field, convection and diffusion terms present in the 3-D  $k$ - $\varepsilon$  turbulence equations can be neglected [32]. The differential equations that describe the rate of turbulent kinetic energy and its dissipation can be written as [32]:

$$\frac{dk}{dt} = S_{in} \cdot \left( \frac{q_{m,in}}{m} u_{in}^2 \right) + \max \left( 0, \frac{2}{3} \frac{k}{\rho} \frac{d\rho}{dt} \right) - \frac{2}{3} \frac{k}{\nu} \frac{d\nu}{dt} - \varepsilon \quad (3.1)$$

$$\frac{d\varepsilon}{dt} = C_{in} \cdot \left( \frac{4}{3} \frac{q_{m,in}}{m} \varepsilon \right) + \max \left( 0, C_{\varepsilon} \cdot \left( \frac{4}{3} \frac{\varepsilon}{\rho} \frac{d\rho}{dt} \right) \right) + \frac{5}{12} \frac{\varepsilon}{\nu} \frac{d\nu}{dt} - C_2 \frac{\varepsilon^2}{k} \quad (3.2)$$

In the equations given above,  $k$  ( $m^2/s^2$ ) represents the turbulent kinetic energy,  $\varepsilon$  ( $m^2/s^3$ ) represents the turbulent kinetic energy dissipation,  $\rho$  ( $kg/m^3$ ) represents the density of the in-cylinder mixture and  $\nu$  ( $m^2/s$ ) represents the kinematic viscosity of the in-cylinder mixture. Model parameter  $C_{\varepsilon}$  (-) is used to calibrate the turbulent kinetic energy in the model with results calculated by 3-D CFD calculation [32], while the model parameter  $C_2$  (-) is usually set to 1.92 [32].

The first terms on the right hand side (RHS) of equations (3.1) and (3.2) represent the intake source terms. Intake process has a great impact on the in-cylinder flow [66], and consequently on the in-cylinder turbulence level [32], and hence its influence is included in the model in the same manner as in [32]. In the equations given above,  $q_{m,in}$  ( $kg/s$ ) represents the mean intake mass flow,  $m$  ( $kg$ ) represents the total in-cylinder mass, while  $u_{in}$  ( $m/s$ ) represents the mean cross flow velocity at the intake valve. The intake source term in the equations given above represents additional production term as a result of the intake process and creation of turbulence as the mixture flows around the intake valve, enters the cylinder and interacts with the combustion chamber geometry [32].  $S_{in}$  (-) and  $C_{in}$  (-) represent the model constants that are used to appropriately account for the effect of the intake process on the level of in-cylinder turbulence. These model constants are necessary since anisotropy and inhomogeneity of the turbulent flow field is not accounted for [32].

The second terms on the RHS represent production of turbulent kinetic energy and its dissipation, respectively [32]. The third term in these equations represent the diffusion term

which describes the rate of change of turbulent kinetic energy and its dissipation due to combustion [32], while the last terms in both equations represent the destruction of turbulent kinetic energy and its dissipation, respectively [32]. The production term was modeled according to the rapid distortion theory [69], [70], while the diffusion term was added as a boundary flux between the burned and the unburned zone [30], [70]. It can be noticed that the production term in equations (3.1 and 3.2) can only be positive. This is due to the energy cascade mechanism, which states that turbulence production can only be positive [32]. Negative turbulent kinetic energy production would mean that a few smaller eddies merge into a larger eddy which is not in accordance with the energy cascade mechanism. All neglected spatial effects, such as convective and diffusion changes of the turbulent kinetic energy and its dissipation and shear effects are accounted for with appropriate modeling of production, diffusion and destruction effect of the turbulence properties [32].

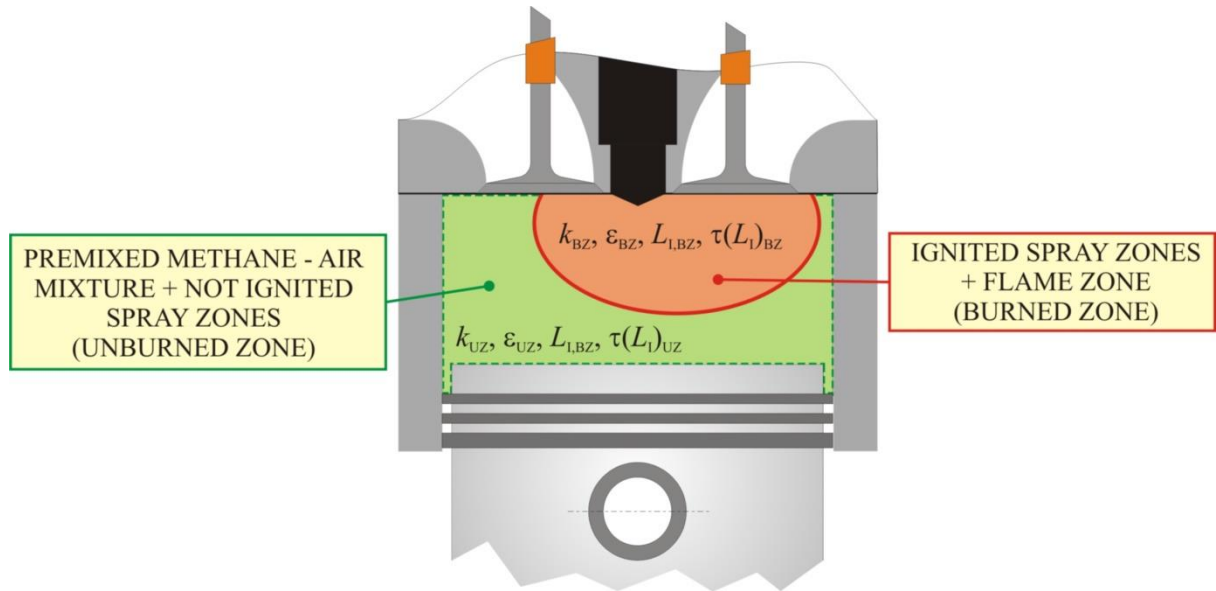


**Figure 29. Presentation of the two-zone turbulence approach**

The two-zone approach in turbulence modeling is applied during the flame propagation process (Figure 27). In the two-zone turbulence modeling approach, the in-cylinder content is divided into two zones:

1. Burned zone (spray zones + flame zone)
2. Unburned zone (fresh charge)

The mixture inside each of the zones has the same level of turbulence and dissipation as well as a single integral length scale and turbulence time scale (Figure 29). The assumptions of the 0-D two zone  $k$ - $\epsilon$  turbulence model are that the total value of the turbulent kinetic energy, the

total production and the total dissipation are equal to the sum of the respective values in the burned and unburned zone [32]. The differential equations that describe the rate of turbulent kinetic energy and its dissipation for the entire cylinder content (so called total values) are given in equations 3.1 and 3.2. The differential equations that describe the rate of turbulent kinetic energy and its dissipation for the unburned zone can be written as [32]:

$$\frac{dk_{UZ}}{dt} = \max \left( 0, \frac{2}{3} \frac{k_{UZ}}{\rho_{UZ}} \frac{d\rho_{UZ}}{dt} \right) - \frac{2}{3} \frac{k_{UZ}}{\nu_{UZ}} \frac{d\nu_{UZ}}{dt} - \varepsilon_{UZ} \quad (3.3)$$

$$\frac{d\varepsilon_{UZ}}{dt} = \max \left[ 0, C_{\varepsilon,UZ} \cdot \left( \frac{4}{3} \frac{\varepsilon_{UZ}}{\rho_{UZ}} \frac{d\rho_{UZ}}{dt} \right) \right] + \frac{5}{12} \frac{\varepsilon_{UZ}}{\nu_{UZ}} \frac{d\nu_{UZ}}{dt} - C_2 \frac{\varepsilon_{UZ}^2}{k_{UZ}} \quad (3.4)$$

The difference between the total and unburned zone turbulent kinetic energy traces is presented in Figure 30. The subscript UZ in the above equations indicates that these quantities refer to the unburned zone. Model parameters  $C_{\varepsilon,UZ}$  (-) is used to adjust the level of the turbulent kinetic energy of the unburned zone in the model with the level calculated with 3-D CFD calculation [32].

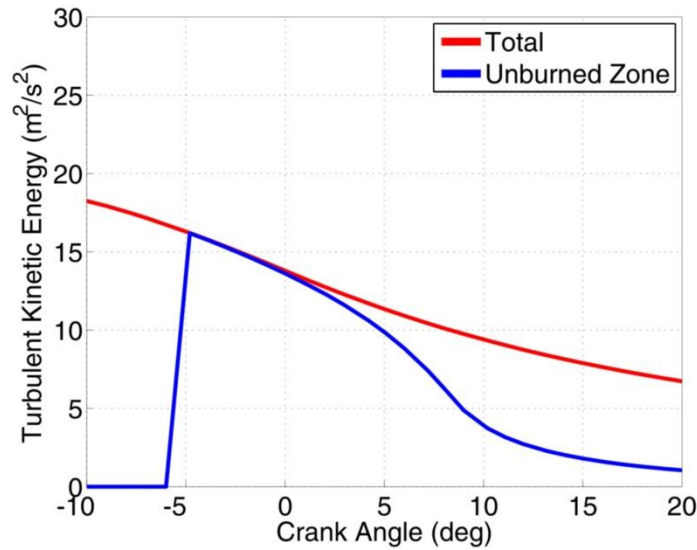


**Figure 30. Turbulent kinetic energy (Total and Unburned Zone)**

When the two-zone turbulence model is applied, the total and the unburned zone turbulence values (turbulent kinetic energy and its dissipation) are directly calculated, while the burned zone turbulence values can be calculated by subtracting the unburned zone turbulence values from the turbulence values of the entire in-cylinder charge (total turbulence values).

The details regarding the derivation of equations 3.1, 3.2, 3.3 and 3.4 can be found in [32].

### ***Extension and modification of the turbulence model***

In order to enable a good prediction of the turbulence level and calculation of the turbulent burning rate in conventional dual fuel engines, the 0-D  $k$ - $\varepsilon$  turbulence model which has been developed and validated in [32] was extended and slightly modified. The modifications that were made include:

1. Modeling of the injection effect on the rate of turbulent kinetic energy and its dissipation
2. Introduction of geometry effects in the calculation of the characteristic turbulence values (turbulent length scale and turbulence time scale)

#### **3.1.3. Modeling of the injection effect on in-cylinder turbulence level**

Since it was found that fuel injection has a significant effect both on the main (convective) in-cylinder flow and the level of turbulence [71], it is important to account for the direct fuel injection in the 0-D turbulence model. The authors in [71] presented a comparison between the cases with and without direct fuel injection, and it was found that in the case when the fuel was injected into the cylinder, the level of turbulence increased after the injection process and remained higher than in the case without the direct fuel injection. The influence of the injection on the turbulence level, was modeled with the same approach as the influence of intake in [32]. From [32], [72] it follows that the total velocity divergence in the case of the 0-D calculation approach can be expressed as [32]:

$$S_{ij}^{\text{tot}} = u_{i,j}^{\text{tot}} = -\frac{1}{\rho} \frac{d\rho}{dt} \quad (3.5)$$

By adding an additional source (injection) into the initial continuity equations (the same process as in [32]), the equation 3.7 is extended to:

$$S_{ij}^{\text{tot}} = u_{i,j}^{\text{tot}} = -\frac{1}{\rho} \left( \frac{d\rho}{dt} + \frac{q_{m,\text{in}}}{V_{\text{cyl}}} + \frac{q_{m,\text{inj}}}{V_{\text{cyl}}} \right) \quad (3.6)$$

In the equation given above,  $\rho$  ( $\text{kg}/\text{m}^3$ ) represents the density of the in-cylinder mixture, while  $V_{\text{cyl}}$  ( $\text{m}^3$ ) represent the total cylinder volume. The first term on the RHS represents the influence of the temporal density change on the total velocity divergence, while the second and the third term on the RHS represent the influence of the intake and injection processes on



the total velocity divergence. If the new source term is inserted into the turbulent kinetic energy and its dissipation transport equations the following equations are obtained:

$$\frac{dk}{dt} = S_{in} \cdot \left( \frac{q_{m,in}}{m} u_{in}^2 \right) + S_{inj} \cdot \left( \frac{q_{m,inj}}{m} u_{inj}^2 \right) + \max \left( 0, \frac{2}{3} \frac{k}{\rho} \frac{d\rho}{dt} \right) - \frac{2}{3} \frac{k}{\nu} \frac{d\nu}{dt} - \varepsilon \quad (3.7)$$

$$\frac{d\varepsilon}{dt} = C_{in} \cdot \left( \frac{4}{3} \frac{q_{m,in}}{m} \varepsilon \right) + C_{inj} \cdot \left( \frac{4}{3} \frac{q_{m,inj}}{m} \varepsilon \right) + \max \left( 0, C_{\varepsilon} \cdot \left( \frac{4}{3} \frac{\varepsilon}{\rho} \frac{d\rho}{dt} \right) \right) + \frac{5}{12} \frac{\varepsilon}{\nu} \frac{d\nu}{dt} - C_2 \frac{\varepsilon^2}{k} \quad (3.8)$$

In the equations given above,  $q_{m,inj}$  (kg/s) represents the mean injection mass flow, while  $u_{inj}$  (m/s) represents the mean cross flow velocity at the injector nozzle. The injection source term in the equations given above (second term on the RHS) represents an additional production term as a result of the injection process and generation of turbulence due to the shear effects inside the fuel spray and at the fuel spray/surrounding mixture interface.  $S_{inj}$  (-) and  $C_{inj}$  (-) represent the model constants which are used to appropriately account for the effect of the injection process on the level of in-cylinder turbulence.

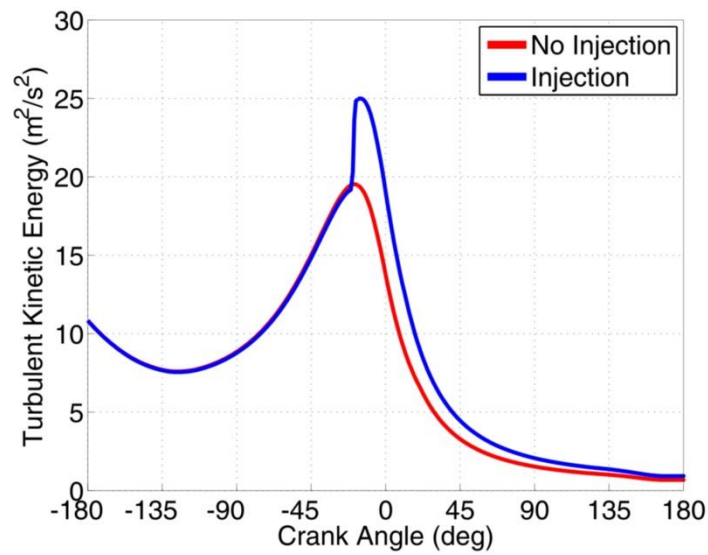


**Figure 31. Difference in turbulent kinetic energy level between a case with and without direct fuel injection**

Figure 31 presents the difference in the turbulent kinetic energy traces between a case with and without direct fuel injection. On this figure (Figure 31) it can be seen that in the case of the direct fuel injection turbulent kinetic energy increases after the injection process and remains higher during the entire expansion stroke compared to the case without the direct fuel injection. The effect is the same as reported in [71].

### 3.1.4. Characteristic turbulence scales calculation

In the  $k$ - $\varepsilon$  turbulence modeling approach, the turbulent integral length scale can be calculated by the following equations [30], [32], [66]:

$$L_{I,turb} = \frac{\sqrt{k^3}}{\varepsilon} \quad (3.9)$$

$$L_{I,UZ,turb} = \frac{\sqrt{k_{UZ}^3}}{\varepsilon_{UZ}} \quad (3.10)$$

In the equations given above,  $L_{I,turb}$  (m) represent the characteristic turbulent integral length scale for the entire cylinder, while  $L_{I,UZ,turb}$  (m) represent the characteristic turbulent integral length scale for the unburned zone. Since the isotropic and homogeneous turbulent flow field was assumed during the turbulence model derivation, Kolmogorov length scale can be calculated by the following equations [32], [66]:

$$l_k = \frac{L_I}{Re_T^{3/4}} \quad (3.11)$$

$$l_{k,UZ} = \frac{L_{I,UZ}}{Re_{T,UZ}^{3/4}} \quad (3.12)$$

$$Re_T = \frac{u_T \cdot L_I}{\nu} \quad (3.13)$$

$$Re_{T,UZ} = \frac{u_{T,UZ} \cdot L_{I,UZ}}{\nu_{UZ}} \quad (3.14)$$

$$u_T = \sqrt{\frac{2}{3} \cdot k} \quad (3.15)$$

$$u_{T,UZ} = \sqrt{\frac{2}{3} \cdot k_{UZ}} \quad (3.16)$$

In the equations given above,  $l_k$  (m) represents the Kolmogorov length scale for the entire cylinder,  $l_{k,UZ}$  (m) represents the Kolmogorov length scale for the unburned zone,  $Re_T$  (-)

represents the Reynolds turbulent number for the entire cylinder,  $Re_{T,UZ}$  (-) represents the Reynolds turbulent number for the unburned zone,  $\nu$  ( $m^2/s$ ) represents the viscosity of the mixture inside the cylinder,  $\nu_{UZ}$  ( $m^2/s$ ) represents the viscosity of the mixture in the unburned zone,  $u_T$  ( $m/s$ ) represents the turbulence intensity of the entire cylinder, while  $u_{T,UZ}$  ( $m/s$ ) represents the turbulence intensity of the unburned zone.

The additional new feature of the turbulence model compared to the one presented in [32] is the introduction of the controls for the size of the integral length scale in the entire cylinder and in the unburned zone. This improves the calculation of the characteristic turbulence time scales in the entire cylinder and in the unburned zone, which are used in the calculation of the heat transfer process and the flame propagation process. Moreover, such approach improves the calculation of the transition time from laminar to fully turbulent flame (linked to the turbulence), and the calculation of the final stage of the flame propagation process, as it accounts for the geometry effects on the integral length scale size.

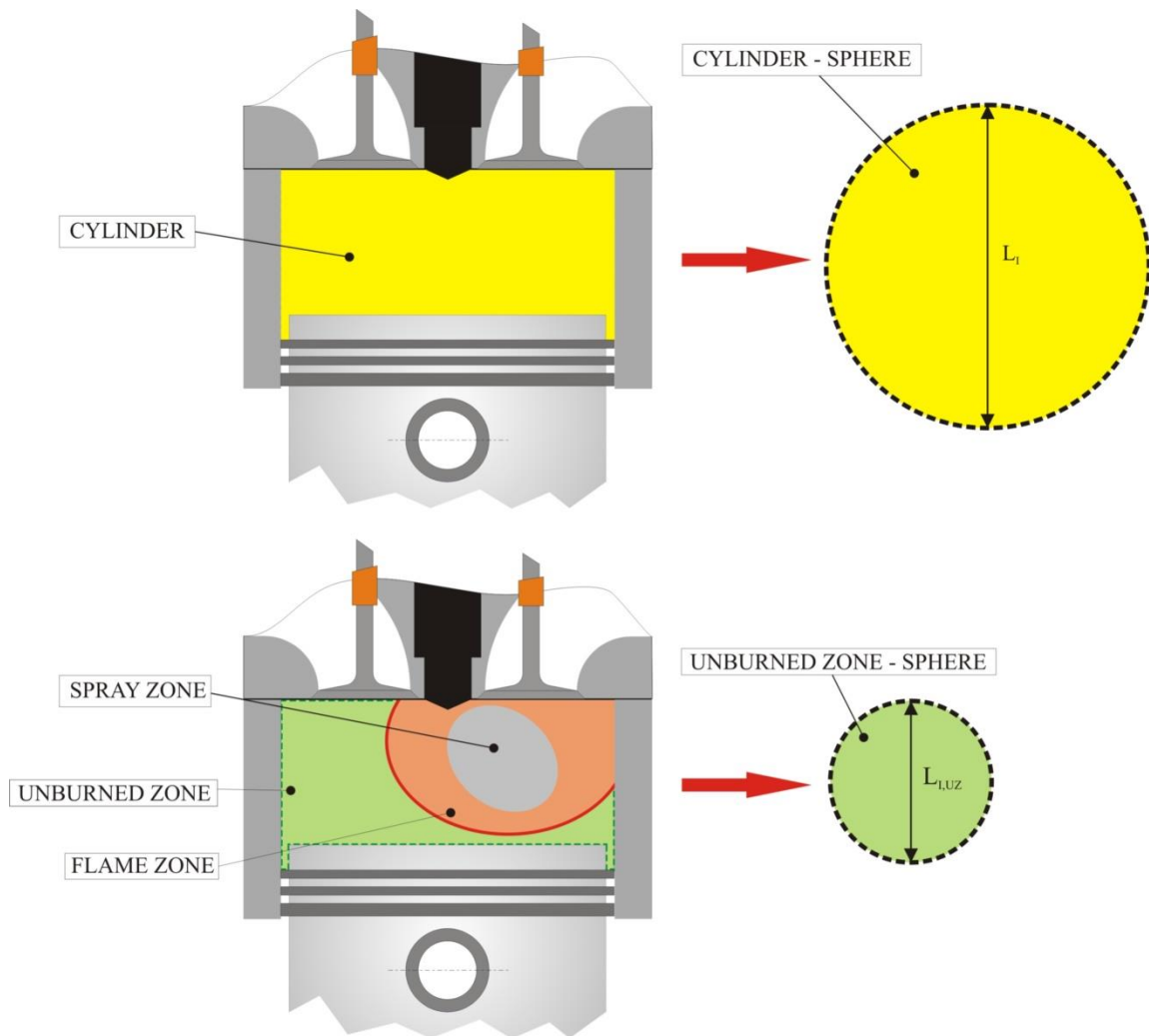


**Figure 32. Schematic presentation of the turbulent integral length scale in particular zones**

Since in the 0-D approach, there is no strict zone orientation or shape, in the calculation of the characteristic dimensions of the zones they are assumed to be spherical (Figure 32). This means that the maximum turbulent integral length scale that can be present inside a zone is equal to the diameter of the sphere that represents the respective zone (Figure 32).

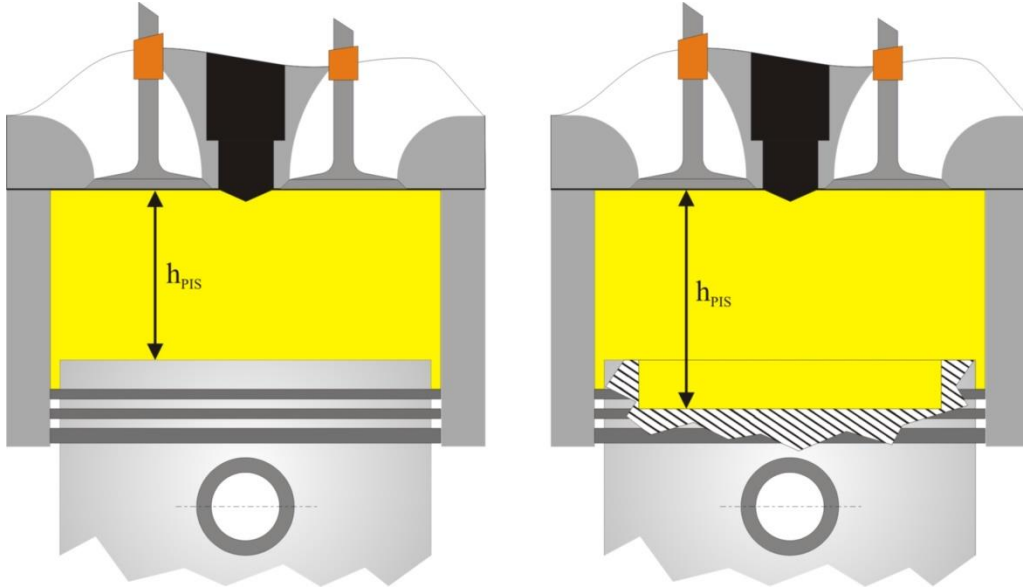


**Figure 33. Distance between piston and cylinder head for two considered combustion chamber geometries**

As the turbulent integral length scale is limited by the combustion chamber geometry (distance between the cylinder head and piston crown), the geometry effects have also been included in its calculation with the following expressions (Figure 33):

$$L_{I,limit} = C_L \cdot \left\{ MIN \left[ h_{PIS}, \left( 2 \cdot \sqrt[3]{\frac{3 \cdot V_{cyl}}{4 \cdot \pi}} \right) \right] \right\} \quad (3.17)$$

$$L_{I,limit,UZ} = C_L \cdot \left\{ MIN \left[ h_{PIS}, \left( 2 \cdot \sqrt[3]{\frac{3 \cdot V_{UZ}}{4 \cdot \pi}} \right) \right] \right\} \quad (3.18)$$

In the equations given above,  $L_{I,limit}$  (m) represents the maximum value of the turbulent integral length scale in the entire cylinder content,  $L_{I,limit,UZ}$  (m) represents the maximum value of the turbulent integral length scale in the unburned zone,  $h_{PIS}$  (m) represents the distance of the piston from the cylinder head (Figure 33),  $V_{cyl}$  (m<sup>3</sup>) represents the cylinder volume, while  $V_{UZ}$  (m<sup>3</sup>) represents the volume of the unburned zone. In order to control the size of the

integral length scales in the entire cylinder and in the unburned zone an additional correction,  $C_L$  (-) parameter was derived:

Finally, the integral length scale in the entire cylinder and in the unburned zone, as well as the eddy turnover time (turbulence time scale) for the entire cylinder content can be expressed with the following equations:

$$L_I = MIN(L_{I,turb}, L_{I,limit}) \quad (3.19)$$

$$L_{I,UZ} = MIN(L_{I,UZ,turb}, L_{I,limit,UZ}) \quad (3.20)$$

$$\tau_T = \frac{L_I}{u_T} \quad (3.21)$$

In the equations given above,  $L_I$  (m) represents the integral length scale size for the entire cylinder,  $L_{I,UZ}$  (m) represents the integral length scale size for the unburned zone, while  $\tau_T$  (s) represents the eddy turnover time for the entire cylinder. This characteristic time is used in the calculation of the heat transfer between the spray zones and in the calculation of the transition from laminar to fully developed turbulent flame propagation.

## 3.2. Heat transfer

The following chapters present the heat transfer phenomenon and its modeling in 0-D environment.

### 3.2.1. Physical background

From the thermodynamical point of view, the in-cylinder mixture is a system that exchanges energy with its surrounding. This energy exchange occurs in two forms, work and heat that are either supplied or taken away from the system (in-cylinder mixture). Heat is thermal energy in transit due to a spatial temperature difference and occurs whenever there is a temperature difference between a system and its surrounding, or between different parts of the system [73]. There are three main modes of heat transfer:

1. Conduction
2. Convection
3. Radiation

## Conduction

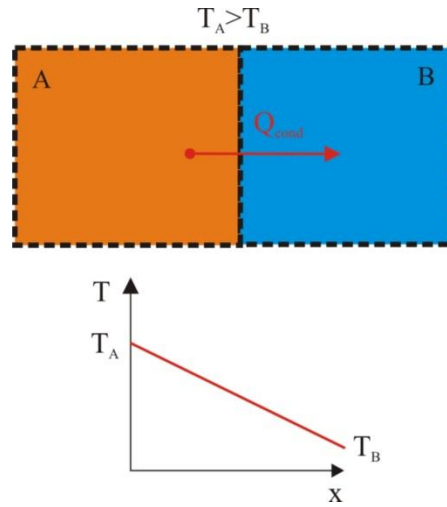


**Figure 34. 1-D conductive heat transfer between two neighboring regions**

Conduction, which is often referred to as heat diffusion is a heat transfer mode that occurs between two neighboring regions in a stationary medium that are at different temperature (Figure 34), where heat flows from a region that is at a higher temperature to the region that is at a lower temperature [73].

The conductive heat transfer is associated with the molecular collisions, where molecules of the higher energy (higher temperature) transfer energy to the molecules of the lower energy (lower temperature) [73]. The heat flux associated with conductive heat transfer can be expressed by the Fourier's law [73]:

$$\frac{dQ_{cond}}{dt} = -\lambda \cdot A_s \cdot \frac{dT}{dx} \quad (3.22)$$

In the equation given above,  $Q_{cond}$  (J) represents the conductive heat transfer;  $\lambda$  (W/mK) represents the thermal conductivity of the referent medium,  $A_s$  ( $m^2$ ) represents the contact surface area between the two neighboring regions, while  $\frac{dT}{dx}$  (K/m) represents the temperature gradient.

## Convection

Convection is a heat transfer mode which is driven by heat conduction and by the bulk flow, called advection (Figure 35) [73]. Bulk flow moves the fluid energy (heat) from one point in the space to the other, while conduction is responsible for the heat transfer between the two neighboring regions that are at different temperature and are in relative quiescence.

Convective heat transfer may be classified by the nature of the flow to forced convection driven by an external source, and natural convection driven by the buoyancy forces [73].

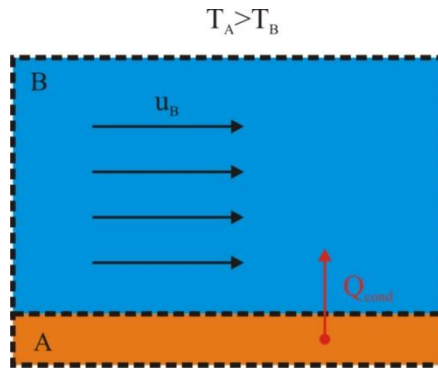


**Figure 35. Schematic of the convective heat transfer**

The heat flux associated with the convective heat transfer can be expressed in the following form (differential) [73]:

$$\frac{dQ_{\text{conv}}}{dt} = h_{\text{HT}} \cdot A_s \cdot \Delta T \quad (3.23)$$

In the equation given above,  $Q_{\text{conv}}$  (J) represents the convective heat transfer,  $h_{\text{HT}}$  (W/m<sup>2</sup>K) represents the convection heat transfer coefficient, while  $\Delta T$  (K) represents the temperature difference between the fluid in motion and warm or cold surface.

### ***Radiation***

Radiation (Figure 36) is a heat transfer mode that is driven by the emission and absorption of the electromagnetic waves [66].

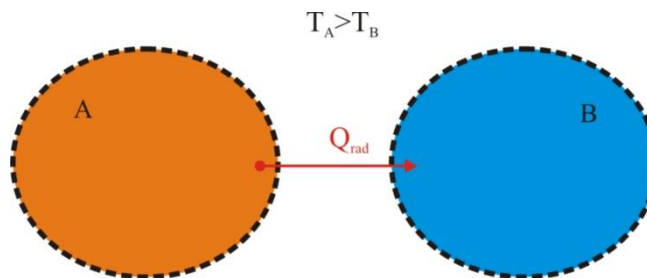


**Figure 36. Schematic of the radiative heat transfer**

All forms of matter emit radiation and contrary to conduction and convection, radiation does not require the presence of a material medium [73]. Radiative heat transfer can be expressed in the following way (differential) [73]:

$$\frac{dQ_{\text{rad}}}{dt} = \varepsilon_{\text{HT}} \sigma A (T_A^4 - T_B^4) \quad (3.24)$$

In the equation given above,  $Q_{\text{rad}}$  (J) represents the radiative heat transfer,  $\varepsilon_{\text{HT}}$  (-) represents the emissivity of the radiation source, which is a measure of how effectively a radiation source emits energy compared to a blackbody [73],  $\sigma$  ( $\text{W/m}^2\text{K}^4$ ) represents Stefan – Boltzmann constant,  $T_A$  (K) represents the temperature of the radiation source, while  $T_B$  (K) represents the temperature of the medium that absorbs radiation.

### 3.2.2. Heat transfer in IC engines

Since between 16% to 35% [66] of the fuel energy supplied to the in-cylinder mixture is taken away for the in-cylinder mixture by the process of heat transfer to the combustion chamber walls, appropriate modeling of the wall heat transfer is necessary for the correct modeling of the combustion process. As the heat transfer influences the in-cylinder temperature and pressure it has a huge effect on the engine performance and harmful exhaust gas emissions, regardless of the combustion type [74]. In the IC engines the heat transfer from the in-cylinder mixture to the combustion chamber walls is dominated by two heat transfer modes, convection and radiation [66]. In the IC engines there are two sources of radiation, glowing soot particles and high temperature burned gas region [66]. Contrary to gaseous burned gas region, glowing soot particles are a significant source of radiative heat transfer. For instance in Diesel engines, radiative heat transfer accounts for 20% - 35% of the overall wall heat transfer [66].

Since the ignition and combustion process and consequently the engine performance and harmful exhaust gas emissions significantly depend on the temperature field inside the in-cylinder mixture, it is also important to model the heat transfer between the zones which is again dominated by the convection and radiation. Modeling of the zone heat transfer in the spray region enables better description of the temperature field inside the fuel spray. This leads to more accurate modeling of the spray ignition process, which significantly depends on the temperature inside each spray zone. Moreover, this leads to more accurate modeling of the combustion process inside the spray zones since the reaction rate also depends on the spray zone temperature.

Since in the conventional dual fuel engines small amount of fuel burns in a mixing-controlled combustion mode, which is a predominant mode that forms soot, radiative heat transfer was



neglected in the modeling of both wall and zone heat transfer process. Wall and zone heat transfer models are presented in the next two chapters.

### 3.2.3. Wall heat transfer model

There are a large number of heat transfer correlations that have been derived for modeling of the wall heat transfer process in the IC engines. In this thesis the heat transfer from the in-cylinder mixture to the combustion chamber walls (Figure 37) during the high pressure cycle is modeled with a well-known Woschni's correlation for the convective heat transfer [75] that is already available in the AVL cycle simulation software [57]. This model is an extension to the previous Woschni's heat transfer model that was presented in [76].

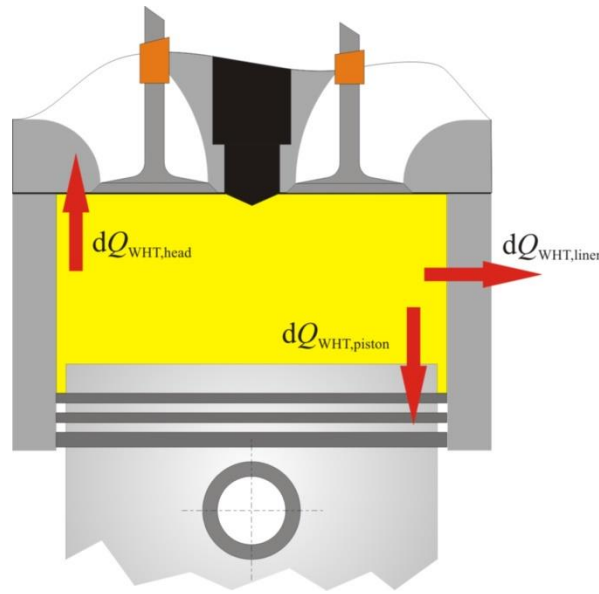


**Figure 37. Wall heat transfer**

Head, liner and piston wall heat transfer is calculated separately by the following expressions (differential form):

$$\frac{dQ_{\text{WHT,head}}}{dt} = h_{\text{W}} A_{\text{head}} (T - T_{\text{head}}) \quad (3.25)$$

$$\frac{dQ_{\text{WHT,liner}}}{dt} = h_{\text{W}} A_{\text{liner}} (T - T_{\text{liner}}) \quad (3.26)$$

$$\frac{dQ_{\text{WHT,piston}}}{dt} = h_{\text{W}} A_{\text{piston}} (T - T_{\text{piston}}) \quad (3.27)$$

$$\frac{dQ_{\text{WHT}}}{dt} = \frac{dQ_{\text{WHT, head}}}{dt} + \frac{dQ_{\text{WHT, liner}}}{dt} + \frac{dQ_{\text{WHT, piston}}}{dt} \quad (3.28)$$

In the equations given above,  $Q_{\text{WHT, head}}$  (J) represents the heat transferred to the cylinder head,  $h_w$  (W/m<sup>2</sup>K) represents the heat transfer coefficient,  $A_{\text{head}}$  (m<sup>2</sup>) represents the cylinder head surface area,  $T$  (K) represents the in-cylinder mixture temperature,  $T_{\text{head}}$  (K) represents the average cylinder head surface temperature,  $Q_{\text{WHT, liner}}$  (J) represents the heat transferred to the cylinder liner,  $A_{\text{liner}}$  (m<sup>2</sup>) represents the cylinder liner surface area,  $T_{\text{liner}}$  (K) represents the average cylinder liner surface temperature,  $Q_{\text{WHT, piston}}$  (J) represents the heat transferred to the piston,  $A_{\text{piston}}$  (m<sup>2</sup>) represents the piston surface area,  $T_{\text{piston}}$  (K) represents the average piston surface temperature, while  $Q_{\text{WHT}}$  (J) represents the overall wall heat transfer. From the equations given above it can be noticed that the mean cylinder temperature is used in the wall heat transfer calculation.

Woschni's heat transfer coefficients are given with the following two expressions. Expression given in (3.33) is the one that was presented in [76], while the one given in (3.34) is the one that was presented in [75], and both can be used in the present model.

$$h_w = 130 \cdot D^{-2} \cdot p^{0.8} \cdot T^{-0.53} \cdot \left[ c_1 \cdot c_m + c_2 \cdot \frac{V_D \cdot T_{\text{IVC}}}{p_{\text{IVC}} \cdot V_{\text{IVC}}} \cdot (p - p_{\text{mot}}) \right]^{0.8} \quad (3.29)$$

$$h_w = 130 \cdot D^{-2} \cdot p^{0.8} \cdot T^{-0.53} \cdot \left\{ c_1 \cdot c_m \cdot \left[ 1 + 2 \cdot \left( \frac{V_{\text{TDC}}}{V} \right)^2 \cdot IMEP^{-0.2} \right] \right\}^{0.8} \quad (3.30)$$

In the equations given above,  $D$  (m) represents the cylinder diameter,  $p$  (Pa) represents the in-cylinder pressure,  $c_1$  (-) and  $c_2$  (-) represent the model constants [57],  $V_D$  (m<sup>3</sup>) represents the cylinder displacement volume,  $T_{\text{IVC}}$  (K) represents the in-cylinder temperature at the intake valve closure moment,  $p_{\text{IVC}}$  (Pa) represents the cylinder pressure at the intake valve closure moment,  $V_{\text{IVC}}$  (m<sup>3</sup>) represents the cylinder volume at the intake valve closure moment,  $p_{\text{mot}}$  (Pa) represents the cylinder pressure in the motoring case,  $V_{\text{TDC}}$  (m<sup>3</sup>) represents the cylinder volume at the top dead center, while  $IMEP$  (Pa) represents the indicated mean effective pressure.

Once the overall heat transfer is calculated, it is divided to the zones according to the zone mass and temperature, same as in [33]. The specific zone's wall heat transfer factor is calculated with the following expressions; [33]:

$$w_{\text{WHT},\text{SZ},i} = m_{\text{SZ},i} \cdot T_{\text{SZ},i}^{0.53} \cdot R_{\text{SZ},i} \cdot [C_{\text{piston}} \cdot A_{\text{piston}} \cdot (T_{\text{SZ},i} - T_{\text{piston}}) + C_{\text{head}} \cdot A_{\text{head}} \cdot (T_{\text{SZ},i} - T_{\text{head}}) + C_{\text{liner}} \cdot A_{\text{liner}} \cdot (T_{\text{SZ},i} - T_{\text{liner}})] \quad (3.31)$$

$$w_{\text{WHT},\text{UZ}} = m_{\text{UZ}} \cdot T_{\text{UZ}}^{0.53} \cdot R_{\text{UZ}} \cdot [C_{\text{piston}} \cdot A_{\text{piston}} \cdot (T_{\text{UZ}} - T_{\text{piston}}) + C_{\text{head}} \cdot A_{\text{head}} \cdot (T_{\text{UZ}} - T_{\text{head}}) + C_{\text{liner}} \cdot A_{\text{liner}} \cdot (T_{\text{UZ}} - T_{\text{liner}})] \quad (3.32)$$

$$w_{\text{WHT},\text{FZ}} = m_{\text{FZ}} \cdot T_{\text{FZ}}^{0.53} \cdot R_{\text{FZ}} \cdot [C_{\text{piston}} \cdot A_{\text{piston}} \cdot (T_{\text{FZ}} - T_{\text{piston}}) + C_{\text{head}} \cdot A_{\text{head}} \cdot (T_{\text{FZ}} - T_{\text{head}}) + C_{\text{liner}} \cdot A_{\text{liner}} \cdot (T_{\text{FZ}} - T_{\text{liner}})] \quad (3.33)$$

In the equations given above,  $w_{\text{WHT},\text{SZ},i}$  ( $\text{Jm}^2\text{K}$ ) represents the wall heat transfer factor for the  $i$ -th spray zone,  $m_{\text{SZ},i}$  (kg) represents the mass of the  $i$ -th spray zone,  $T_{\text{SZ},i}$  (K) represents the temperature of the  $i$ -th spray zone,  $R_{\text{SZ},i}$  (K) represents the gas constant of the mixture inside the  $i$ -th spray zone,  $C_{\text{piston}}$  (-) represents the piston surface area scaling factor,  $C_{\text{head}}$  (-) represents the cylinder head surface area scaling factor,  $C_{\text{liner}}$  (-) represents the liner surface area scaling factor,  $w_{\text{WHT},\text{UZ}}$  ( $\text{Jm}^2\text{K}$ ) represents the wall heat transfer factor for the unburned zone,  $m_{\text{UZ}}$  (kg) represents the mass of the unburned zone,  $T_{\text{UZ}}$  (K) represents the temperature of the unburned zone,  $R_{\text{UZ}}$  (K) represents the gas constant of the mixture inside the unburned zone,  $w_{\text{WHT},\text{FZ}}$  ( $\text{Jm}^2\text{K}$ ) represents the wall heat transfer factor for the flame zone,  $m_{\text{FZ}}$  (kg) represents the mass of the flame zone,  $T_{\text{FZ}}$  (K) represents the temperature of the flame zone, while  $R_{\text{FZ}}$  (K) represents the gas constant of the mixture inside the flame zone. Now, the wall heat transfer for a specific zone can be calculated from the following expressions:

$$\frac{dQ_{\text{WHT},\text{SZ},i}}{dt} = \frac{dQ_{\text{WHT}}}{dt} \cdot \frac{w_{\text{WHT},\text{SZ},i}}{\sum_i w_{\text{WHT},\text{SZ},i} + w_{\text{WHT},\text{UZ}} + w_{\text{WHT},\text{FZ}}} \quad (3.34)$$

$$\frac{dQ_{\text{WHT},\text{UZ}}}{dt} = \frac{dQ_{\text{WHT}}}{dt} \cdot \frac{w_{\text{WHT},\text{UZ}}}{\sum_i w_{\text{WHT},\text{SZ},i} + w_{\text{WHT},\text{UZ}} + w_{\text{WHT},\text{FZ}}} \quad (3.35)$$

$$\frac{dQ_{\text{WHT},\text{FZ}}}{dt} = \frac{dQ_{\text{WHT}}}{dt} \cdot \frac{w_{\text{WHT},\text{FZ}}}{\sum_i w_{\text{WHT},\text{SZ},i} + w_{\text{WHT},\text{UZ}} + w_{\text{WHT},\text{FZ}}} \quad (3.36)$$

### 3.2.4. Zone heat transfer model

In order to improve the prediction of the spray temperature field heterogeneity and consequently improve the ignition and combustion calculation and hence the calculation of performance and of harmful exhaust gas emissions, a zone heat transfer model was derived. As was already mentioned the zone heat transfer is only calculated between the spray zones. The reason why there is no explicit zone heat transfer modeling between the other zones is that the other zones exchange mass and therefore exchange the energy as well.

The model is based on the approach that has been presented in [34] and is based on the assumption that after a sufficient amount of time passes, two zones in question (Figure 38) will be at the same temperature as a result of a mixing process due to mass diffusion, bulk flow and turbulence, and convective heat transfer.

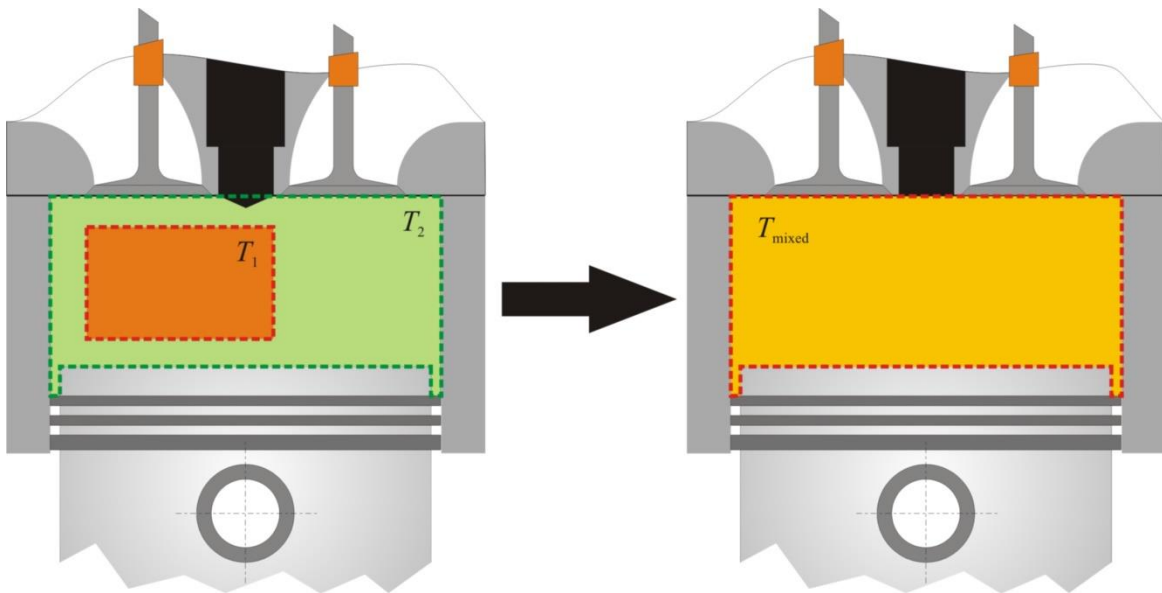


**Figure 38. Zone heat transfer principle**

Zone heat transfer is calculated through the following equations. Let's assume that the two zones (1 and 2 in Figure 38) that have corresponding temperatures  $T_1$  (K) and  $T_2$  (K) will be completely mixed after the characteristic heat transfer time  $t_{ZHT}$  (s) passes. The new (mixed) zone will have the temperature  $T_{mixed}$  (K). The temperature of the new (mixed) zone can easily be calculated assuming that the mixing occurs at constant volume, which means that the internal energy of the mixed zone equals the sum of the internal energies of the zones that were mixed together. The energy (heat) that needs to be supplied to or taken away from each of the zones (subscript  $i$  – denotes the  $i$ -th zone) so that their new temperature would be equal to  $T_{mixed}$  can be expressed by the following equations [34]:

$$Q_{ZHT,SZ,i} = m_{SZ,i} \cdot [u_{SZ}(T_{\text{mixed}}) - u_{SZ,i}(T_i)] \quad (3.37)$$

In the equation given above,  $Q_{ZHT,SZ,i}$  (J) represents the energy supplied to or taken away from  $i$ -th spray zone due to the zone heat transfer. With the spray zone heat transfer energy calculated, the spray zone heat transfer derivative for a given  $i$ -th spray zone can be expressed in the following way:

$$\frac{dQ_{ZHT,SZ,i}}{dt} = \frac{Q_{ZHT,SZ,i}}{t_{ZHT}} \quad (3.38)$$

In the equation given above,  $t_{ZHT}$  (s) represents the characteristic zone heat transfer time. Contrary to the approach presented in [34] where this characteristic time was directly set as an input parameter, in the model presented in here the characteristic zone heat transfer time is linked to the characteristic turbulence time scale:

$$t_{ZHT} = C_{ZHT,SZ} \cdot \tau_T \quad (3.39)$$

In the equation given above,  $C_{ZHT,SZ}$  (-) represents zone heat transfer model parameter for the spray zones. Zone heat transfer between the spray zones is calculated during the entire period from start of injection till exhaust valve opening.

### 3.3. Diesel fuel spray development process and combustion

Since dual fuel combustion process features the direct injection of Diesel fuel into the combustion chamber, it also features the process of the liquid fuel break-up into droplets, evaporation and mixing with the surrounding natural gas/ air/ combustion products (EGR) mixture and consequent ignition and combustion. Therefore, it is important to account for all of these physical phenomena in a conventional dual fuel combustion model. In the case of DI-CI engines, fuel – surrounding gas mixing and combustion need to be accounted for at the same time and cannot be treated separately [59]. Since the combustion in DI-CI engines significantly depends on the mixing process, such combustion process can be referred to as the mixing-controlled combustion process or the diffusion flame [66]. In the next two chapters of this thesis, the details regarding the physical phenomena of the Diesel fuel combustion and the method of its modeling in the presented DFMZCM are given.

### 3.3.1. Physical background

The following chapters present Diesel fuel spray phenomenon; its development and consequent combustion.

#### *Diesel fuel spray development*

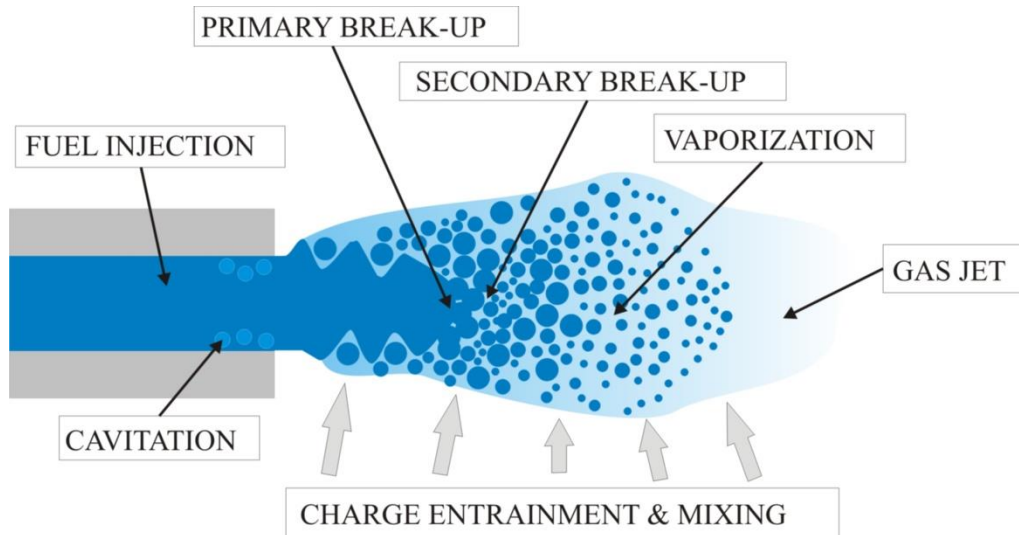


**Figure 39. Fuel spray development process**

Diesel fuel is injected into the combustion chamber during the high-pressure part of the engine cycle, and its utilization significantly depends on the mixing process with the surrounding mixture. During the Diesel fuel injection process a jet-like structure, often referred to as the Diesel fuel spray is formed. From the physics point of view, term spray is used only for the cylinder region that features the liquid fuel droplets. The region that features evaporated fuel mixed with the surrounding natural gas/ air/ EGR mixture is called jet. However, to simplify the terminology, in this thesis term spray will be used for the region of the cylinder that features Diesel fuel, either in liquid or in the evaporated state. In general, the Diesel fuel spray process can be divided into the following stages (Figure 39):

1. Liquid fuel injection.
2. Liquid fuel break-up into droplets.
3. Liquid fuel evaporation and mixing with the surrounding charge.

In the modern DI-CI engines, Diesel fuel is injected at high injection pressure (>2000 bar [59]) through an injector that features a number of small nozzles. As the increase of the injection pressure leads to an increase of the injection velocity, such high injection pressures are used to ensure adequate liquid fuel penetration depth ensuring appropriate mixing of the fuel with the surrounding charge. Moreover, high injection pressure aids in the break-up of

the liquid fuel enabling faster evaporation and mixing rates. This leads to the fact that the spray development and consequent spray combustion process (mixing-controlled combustion process, or diffusion flame) depends on the injection process [77].

Second important phenomenon in the spray development process is the break-up of the liquid fuel into the droplets. Liquid fuel break-up can be divided into two distinctive phases:

1. Primary break-up process (fuel atomization).
2. Secondary break-up process.

During the primary break-up process, coherent liquid fuel structure (liquid fuel column) breaks up (atomizes) into a number of droplets [78]. In the modern DI-CI engines which feature high pressure direct injection systems, the main mechanisms that lead to the initial formation of the liquid fuel droplets are cavitation and turbulence [59], [79], [80].

During the secondary break-up process, large liquid fuel droplets that have been created during the primary break-up process are broken into a number of smaller droplets [81]. Secondary break-up is induced by the aerodynamic forces caused by the relative differences in the velocity between the droplet and the surrounding gas mixture [59]. As the Diesel fuel droplets can also coalesce into a larger droplet, the size of the droplets is defined from the balance of the droplet coalescence and droplet break-up [82]. The stable droplet size is reached further away from the Diesel fuel injector in the coarse region of the spray, since in this region droplets are far away from each other so there is no more coalescence of the droplets [82]. Moreover, as in this region the relative velocity difference between the droplets and the surrounding gas mixture is negligible, droplet break-up process ceases [82].

The momentum of the spray causes the entrainment of the surrounding gas mixture into the spray region [59]. As the spray entrains air it decelerates [66]. Part of the deceleration is due to the aerodynamic drag effects, while the other part is a result of the momentum transfer to the quiescent surrounding gas mixture [71] and its acceleration and entrainment into the spray region. Energy for heating and evaporation of the liquid fuel droplets is supplied by the surrounding gas mixture. Evaporation is controlled by two mechanisms, heat transfer from the surrounding gas mixture to the liquid fuel droplet and mass diffusion from the droplet surface to the surrounding gas mixture. Finally, once the Diesel fuel has evaporated it mixes with the surrounding gas mixture, and thus an ignitable mixture is created.

This brief description of the spray development shows that injection plays a vital role in the spray development process, from supplying the adequate fuel mass to controlling the entire liquid column break-up, evaporation and entrainment processes.

### ***Diesel fuel spray combustion***

In order for the Diesel fuel to start burning, at least a part of the spray region has to be mixed within the flammability limits. Even though from the physics stand point of view, the correct terminology to use in the case of combustion in DI-CI IC engines is mixing-controlled combustion [66], in this thesis the combustion which occurs in the spray region will be simply referred to as the spray combustion process.

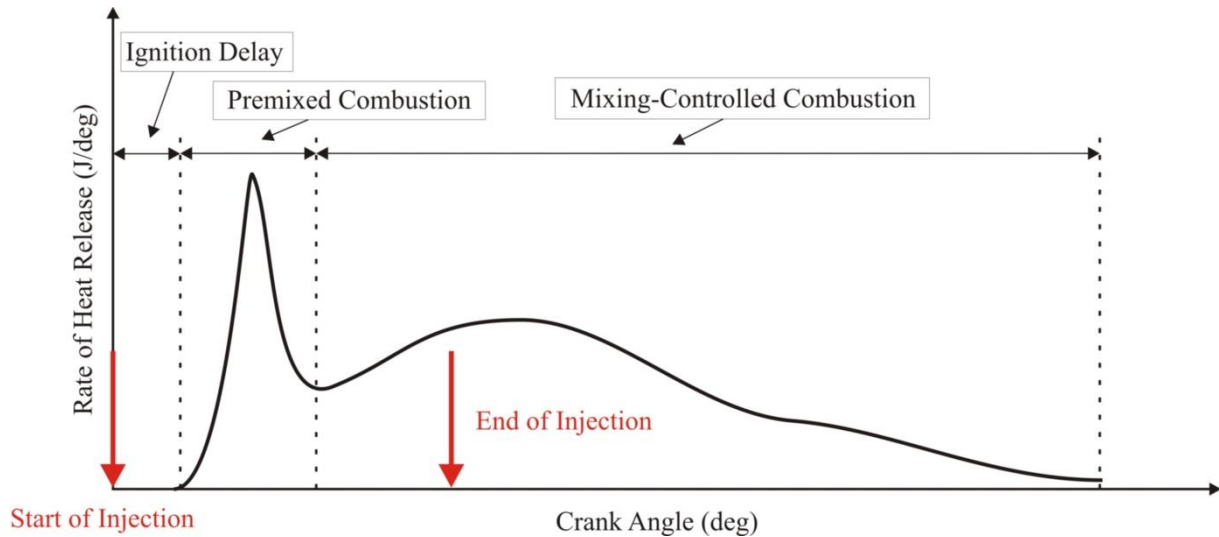


**Figure 40. DI CI engine rate of heat release curve**

The following stages can be identified in the Diesel fuel spray combustion process (Figure 40) [66]:

1. Initial ignition delay stage.
2. Premixed combustion stage.
3. Mixing-controlled combustion stage (diffusion flame).

According to [83], [84], the ignition delay stage is comprised of the physical ignition delay and chemical ignition delay. Physical ignition delay can be viewed as the time it is necessary for the combustible mixture to be created and it features fuel injection, liquid fuel break-up and evaporation and evaporated fuel mixing with the surrounding gas mixture. Chemical ignition delay on the other hand can be viewed as the time it is necessary for the prepared ignitable mixture to ignite, and it is governed by the chemical kinetics of the prepared ignitable mixture.

The premixed combustion stage is the initial stage in the spray combustion process. In this combustion stage the mixture that has been prepared and mixed within the flammability limits during the ignition delay phase ignites and burns. From the fundamental point of view, this



combustion stage is similar to the combustion in the HCCI engines and the burning rate is solely controlled by the chemical kinetics of the prepared mixture and by the mass of the mixture that has been prepared for combustion [59], [66].

The final part of the spray combustion process is called the mixing –controlled combustion stage, and in the fundamental combustion literature it is often referred to as the diffusion flame [50], [51], [85]. Diffusion flame, also called a non-premixed flame [51], [85], is a combustion process which occurs when the fuel and oxidizer are not mixed prior to the combustion process. In such applications fuel enters the reaction zone from one side, while the oxidizer enters the reaction zone from the other side (Figure 41) and for combustion to occur fuel and oxidizer have to mix.

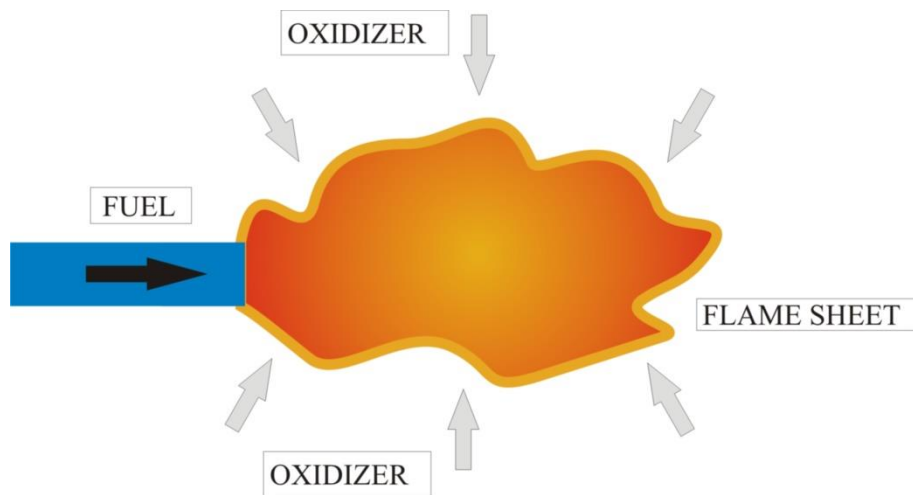


**Figure 41. Schematic of the non-premixed (diffusion) flame**

That's why such combustion process is limited by the fuel/oxidizer mixing process and is referred to as the mixing-controlled combustion process [59]. Contrary to the premixed flames, the diffusion flames do not exhibit a reference flame speed [50]. According to [51], diffusion flame consists of three zones (Figure 42):

1. Fuel rich zones, which is close to the fuel source (injector).
2. Oxidizer rich zone, which is away from the fuel source (injector).
3. Reaction zone (diffusion flame).

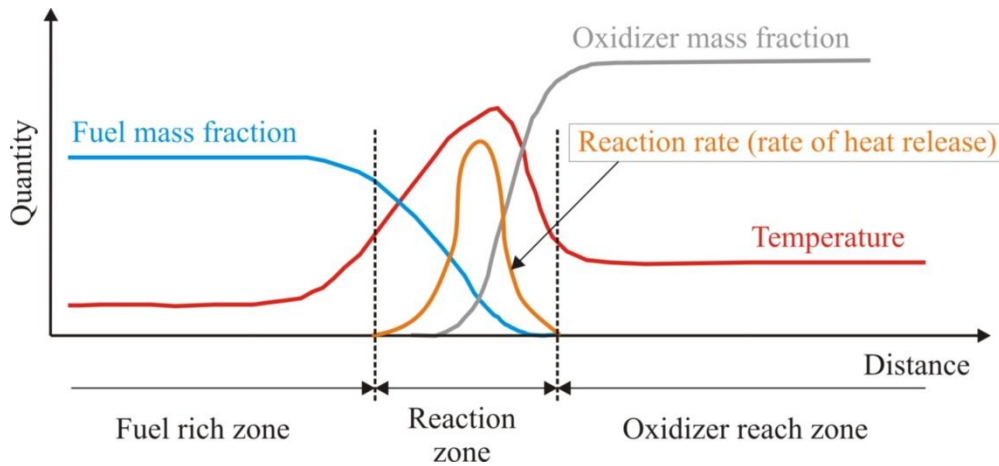


**Figure 42. Non-premixed (diffusion) flame structure; reproduced from [50], [51]**

As the turbulence increases heat and mass transfer, it increases the mixing rate thus increasing the mixing-controlled combustion rate. During the mixing-controlled combustion process in the DI-CI engines, entire spray process (injection, break-up, entrainment, mixing and evaporation) and combustion occur simultaneously [59]. Contrary to the conventional DI-CI engines, which usually operate with the Diesel fuel/ air/ EGR mixtures, conventional dual fuel engines operate with the Diesel fuel/ natural gas/ air/ EGR mixtures. Consequently, during the spray combustion process in the conventional dual fuel engines Diesel fuel has to mix with the natural gas leading to the combustion of the fuel mixture. This leads to an additional degree of complexity of the combustion process as now in addition to the pressure, temperature and equivalence ratio, reaction rate in the reaction zone is also determined by the relative content of the natural gas in the fuel mixture.

### 3.3.2. Overview of the 0-D spray combustion model

There are two basic principles how the spray development process and the spray combustion process can be calculated predictively in the 0-D environment [30]:

1. Models based on the free gas jet theory.
2. So-called packet models.

In the literature [30], [31], models based on both principles are often referred to as phenomenological models as in this models the burning rate can be calculated (predicted) based on the various sub-models which calculate physical and chemical phenomena that occur in the DI-CI engine combustion chamber.

Spray combustion models based on the free gas jet theory are based on the equations that were developed in [86]. In these models evaporation is not taken directly into account and the main limiting factor in the combustion calculation is the air entrainment into the spray region

[31], while the spray penetration is either calculated through an empirical correlation or through the spray momentum conservation. Some of the spray combustion models that are based on the free gas jet theory were presented in [87], [88].

Spray combustion model based on the packet approach was developed in [42], and later used and modified by a number of authors, i.e. [33]. The spray model used in this thesis is based on the model presented in [33] that was integrated within the AVL cycle simulation software, and it features:

1. the calculation of liquid fuel injection,
2. modeling of the liquid fuel break-up (only primary break-up of the liquid column into droplets is considered),
3. the spray development calculation (zone velocity and position tracking),
4. the calculation of entrainment of the gas mixture into the spray zones,
5. the calculation of the liquid fuel evaporation,
6. the calculation of the spray ignition and combustion,
7. the calculation of harmful exhaust gas emissions ( $\text{NO}_x$ , CO and soot) from the spray zones.

### ***Extension and modification of the spray combustion model***

Contrary to the conventional DI-CI engines which operate with Diesel fuel/ air/ EGR mixtures the conventional dual fuel engine operates with Diesel fuel/ natural gas/ air/ EGR mixtures. Therefore, in the spray model presented in this thesis natural gas is also entrained into the spray zones which means that at the ignition moment a Diesel fuel/ natural gas fuel mixture ignites and burns. Consequently, some modifications to the existing spray model which was presented in [33] had to be made. The modifications that were made, and that are given in details in the next sections include:

1. the new species balance as two fuels are present in each of the spray zones,
2. the modification of the injection velocity calculation,
3. tracking of the zone position,
4. the heat transfer calculation between the spray zones,
5. the new approach to calculation of spray ignition delay,
6. the new approach to calculation of spray combustion.

The details regarding the species balance are not given again in the following chapters since the general species mass balance when the engine is operated with two fuels was presented in

chapter 2. Also, the details regarding the heat transfer process between the spray zones are not given in the following chapters since they were already presented in the chapter 3.2.4.

### 3.3.3. Spray zone evolution modeling

In the next chapters the spray zone evolution modeling is presented. The spray zone evolution is the collective name for the following phenomena which occur in the liquid fuel sprays:

1. the liquid fuel injection,
2. the liquid fuel break-up process and the charge entrainment into the spray zones,
3. the liquid fuel evaporation,
4. the spray zones position tracking.

#### ***Injection***

The liquid fuel injection process is calculated same as in [33]. Since the liquid fuel injection rate and injection details (injection pressure, number of nozzle holes and nozzle hole diameter, and discharge coefficient) are inputs to the model, the injection velocity is calculated in the following way [33]:

$$v_{inj,SZ,i} = C_v \cdot v_{inj,id,SZ,i} \quad (3.40)$$

$$v_{inj,id,SZ,i} = \sqrt{\frac{2 \cdot \Delta p_{inj,SZ,i}}{\rho_{fuel}}} \quad (3.41)$$

$$C_D = C_v \cdot C_A \quad (3.42)$$

$$\Delta p_{inj,SZ,i} = MAX \left[ \frac{p_{rail}}{2}, \Delta p_{SZ,i} \cdot C_{rail} + p_{rail} \cdot (1 - C_{rail}) \right] \quad (3.43)$$

$$\Delta p_{SZ,i} = \left[ \frac{\left( \frac{dm_{inj}}{dt} \right)_{SZ,i}}{C_D \cdot A_n} \right]^2 \cdot \frac{1}{2 \cdot \rho_{fuel}} \quad (3.44)$$

$$A_n = \frac{d_n^2 \cdot n_n \cdot \Pi}{4} \quad (3.45)$$

Same as in [33], the injection velocity is calculated according to the Bernoulli's principle.

In the equations given above,  $v_{inj,SZ,i}$  (m/s) represents the real velocity at the nozzle hole exit cross section for the  $i$ -th spray zone, while  $v_{inj,id,SZ,i}$  (m/s) represents the ideal velocity at the nozzle exit cross section for the  $i$ -th spray zone.

The discharge coefficient is equal to the product of the so-called area and velocity coefficients [89], where  $C_v$  (-) represents the velocity coefficient and it relates the ideal velocity to the average velocity at the nozzle hole exit cross section [89],  $C_A$  (-) represents the cross section area coefficient and it relates the geometrical cross section area to the real flow cross section area that may contract due to cavitation or hydraulic flip [89]. The pressure drop across the nozzle for  $i$ -th spray zone,  $\Delta p_{inj,SZ,i}$  (Pa) is calculated with the equations 3.43, 3.44 and 3.45. In these equations,  $p_{rail}$  (Pa) represents the pressure in the rail of the fuel delivery system (usually common rail system),  $\Delta p_{SZ,i}$  (Pa) represents the pressure drop for the  $i$ -th spray zone that is calculated from the injection rate,  $C_{rail}$  (-) represents the injection weight factor,

$\left(\frac{dm_{inj}}{dt}\right)_{SZ,i}$  (kg/s) represents the mass flow at the nozzle hole exit cross section (injection mass rate) for the  $i$ -th spray zone,  $A_n$  (m<sup>2</sup>) represents the cross-section area of nozzle holes,  $\rho_{fuel}$  (kg/m<sup>3</sup>) represents the liquid fuel density,  $d_n$  (m) represents the nozzle hole diameter, while  $n_n$  (-) represents the number of the nozzle holes.

### ***Liquid fuel break-up and charge entrainment***

Before the equations for the liquid fuel break-up time and initial droplet diameter are presented, the equations for the spray zone velocity calculation have to be presented. Spray zone velocity is calculated with the same empirical expressions that were developed based on the turbulent jet theory by authors in [42] and used in [33]. Before the liquid fuel inside a given  $i$ -th spray zone breaks up into droplets,  $i$ -th spray zone velocity is calculated with the equation 3.40. After the liquid fuel inside a given  $i$ -th spray zone break-up into droplets, the corresponding  $i$ -th spray zone velocity is calculated with the following expressions [33]:

$$v_{SZ,i} = \frac{2.95}{2} \cdot \left( \frac{\Delta p_{inj,SZ,i}}{\rho} \right)^{0.25} \cdot d_n^{0.5} \cdot t_{inj,SZ,i}^{-0.5} \cdot C_{axial,SZ,i} \cdot C_{radial,SZ,i} \quad (3.46)$$

$$v_{SZ,i} = \frac{2.95}{2} \cdot \left( \frac{\Delta p_{inj,SZ,i}}{\rho} \right)^{0.25} \cdot d_n^{0.5} \cdot t_{inj,SZ,i}^{-0.75} \cdot t_{hit,SZ,i}^{0.25} \cdot C_{axial,SZ,i} \cdot C_{radial,SZ,i} \quad (3.47)$$

$$C_{\text{axial},\text{SZ},i} = 1 + 0.25 \cdot \left( \frac{i_{\text{axial}} - 1}{n_{\text{axial}} - 1} \right)^3 \cdot \frac{C_{\text{discr},\text{ax}} \cdot (i_{\text{axial}} - 1)}{\frac{6 \cdot n}{1000}} \quad (3.48)$$

$$C_{\text{radial},\text{SZ},i} = e^{\left[ \frac{\ln(0.5) \cdot (i_{\text{radial}} - 1)^2}{(n_{\text{radial}} - 1)^2} \right]} \quad (3.49)$$

The equation 3.46 is used for the spray tip velocity calculation before the spray tip has hit the combustion chamber wall, while the equation 3.47 is used for the spray tip velocity calculation after the spray tip has hit the combustion chamber wall. In the equations given above,  $\rho$  (kg/m<sup>3</sup>) represents the in-cylinder mixture density,  $t_{\text{inj},\text{SZ},i}$  (s) represents the time elapsed from the start of injection for the  $i$ -th spray zone, while  $t_{\text{hit},\text{SZ},i}$  (s) represents the time elapsed from the moment that the spray hit the combustion chamber wall for the  $i$ -th spray zone. Since the fuel droplets that were injected earlier have more intense interaction (momentum transfer) with the surrounding gas mixture and act as a slip stream for the droplets that are injected later, an axial correction function for the calculation of the spray zone velocities was applied in [33] and is presented with the equation 3.48. Also, as the outer spray zones have more intense interaction (momentum transfer) with the surrounding gas mixture compared to the inner spray zones, a radial correction function for the calculation of the spray zone velocities was also applied in [33] and is presented with the equation 3.49.

In the equations given above,  $v_{\text{SZ},i}$  (m/s) represents the velocity of  $i$ -th spray zone,  $C_{\text{axial},\text{SZ},i}$  (-) represents the axial correction parameter,  $C_{\text{radial},\text{SZ},i}$  (-) represents the radial correction parameter,  $i_{\text{radial}}$  (-) represents the number of the given spray zone in the radial direction. The number of the most inner zone is 1 and the number increase towards the edge of the spray;  $n_{\text{radial}}$  (-) represents the total number of spray zones in the radial direction, which depends on the radial discretization of the spray;  $i_{\text{axial}}$  (-) represents the number of the given spray zone in the axial direction. The axial parcel which was injected first has the number 1 and this number increases as the number of the injected parcels increases;  $n_{\text{axial}}$  (-) represents the total number of spray zones in the axial direction, which depends on the axial discretization of the spray and injection duration.

In [33] it was assumed that the liquid fuel column breaks up into droplets when the equations (3.40) and (3.46) give equal result; the equality of the injection and of the spray zone velocity. The break-up time for the given  $i$ -th spray parcel (a group of spray zones that have the same

axial number; i.e. the zones that were created in the same moment),  $t_{\text{break},i}$  (s) can be calculated with the following expression:

$$t_{\text{break},i} = \frac{2.95^2}{8} \cdot \frac{\rho_{\text{fuel}} \cdot d_n}{C_v^2 \cdot \sqrt{\Delta p_{\text{inj},\text{SZ},i}} \cdot \rho} \quad (3.50)$$

In the derivation of equation 3.50, it was assumed that both correction parameters ( $C_{\text{axial},\text{SZ},i}$  and  $C_{\text{radial},\text{SZ},i}$ ) are equal to one (1). Also, it was assumed that  $t_{\text{inj},\text{SZ},i}$  is actually  $t_{\text{break},i}$ . This equation is also slightly modified compared to the one used in [33] due to a modification in the injection velocity calculation. In order to account for more intense interaction of the outer spray zones with the gas mixture and consequently shorter break-up times in these zones, a radial correction function  $C_{\text{radial}}$  is also used in the break-up time calculation for a given  $i$ -th spray zone,  $t_{\text{break},\text{SZ},i}$  (s) [33]:

$$t_{\text{break},\text{SZ},i} = C_{\text{radial},\text{SZ},i} \cdot t_{\text{break},i} \quad (3.51)$$

In the break-up moment, the liquid fuel column breaks up into a number of droplets. Same as in [33], in this thesis the liquid fuel diameters (SMD) is calculated with the correlation that was given in [90]:

$$SMD_{\text{SZ},i} = \frac{12.392 \cdot d_n^{0.44} \cdot \rho_{\text{sauter}}^{0.42} \cdot (0.02 \cdot v_{\text{fuel}})^{0.28}}{\Delta p_{\text{inj},\text{SZ},i}^{0.42} \cdot \rho^{0.28}} \quad (3.52)$$

$$\rho_{\text{sauter}} = 840 - 0.55 \cdot (350 - 288) + 0.048 \cdot 10^{-5} \cdot p \quad (3.53)$$

In the equations given above,  $\rho_{\text{sauter}}$  represents the Sauter density, while  $v_{\text{fuel}}$  (m<sup>2</sup>/s) represents the fuel kinematic viscosity. Droplets are assumed to have a spherical shape and in the  $SMD$  calculation both primary and secondary break-up mechanisms are considered. The volume of a droplet,  $V_{\text{d},\text{SZ},i}$  (m<sup>3</sup>) and the number of droplets in a given  $i$ -th spray zone,  $n_{\text{d},\text{SZ},i}$  (-) are calculated with the following expressions [33]:

$$V_{\text{d},\text{SZ},i} = \frac{SMD_{\text{SZ},i}^3 \cdot \Pi}{6} \quad (3.54)$$

$$n_{d,SZ,i} = \frac{m_{liq,SZ,i}}{\rho_{droplets} \cdot V_{d,SZ,i}} \quad (3.55)$$

$$\rho_{droplets} = 2.77 \cdot 10^4 \cdot \left( 0.39992 \cdot 10^{-1} - 0.3869 \cdot 10^{-4} \cdot 630 + 0.3803 \cdot 10^{-7} \cdot 630^2 - 0.2035 \cdot 10^{-10} \cdot 630^3 \right) \quad (3.56)$$

In the equations given above,  $m_{liq,SZ,i}$  (kg) represents the liquid fuel mass inside the  $i$ -th spray zone, while  $\rho_{droplets}$  (kg/m<sup>3</sup>) represents the density of liquid fuel droplets (correlation for n-dodecane).

Once the liquid fuel inside the spray zone breaks up into droplets, spray zone starts to entrain the surrounding charge. The charge entrainment into the spray zone is governed by the momentum exchange between the liquid fuel droplets and the surrounding gas mixture. As the spray slows down, part of its deceleration is due to aerodynamic drag, while the other part is due to the entry of new mass into the spray zone. The mass entrained into the  $i$ -th spray zone,  $m_{entr,i}$  (kg) can be calculated with the following expression [33]:

$$m_{entr,SZ,i} = C_{entrain} \cdot \left( \frac{m_{fuel,SZ,i} \cdot v_{inj,SZ,i}}{v_{SZ,i}} \right) \quad (3.57)$$

In the equation given above,  $C_{entrain}$  (-) represents the entrainment model parameter, while  $v_{inj,SZ,i}$  (m/s) represents  $i$ -th spray zone injection velocity. The overall entrainment flux,  $\frac{dm_{entr,SZ,i}}{dt}$  (kg/s), and corresponding entrainment mass fluxes from the unburned and flame zone for  $i$ -th spray zone are calculated with the following equations:

$$\frac{dm_{entr,SZ,i}}{dt} = \frac{m_{entr,SZ,i} - m_{entr,SZ,i}(old)}{\Delta t} \quad (3.58)$$

$$\frac{dm_{entr,UZ,i}}{dt} = \frac{dm_{entr,SZ,i}}{dt} \cdot \frac{m_{UZ}}{m_{UZ} + m_{FZ}} \quad (3.59)$$

$$\frac{dm_{entr,FZ,i}}{dt} = \frac{dm_{entr,SZ,i}}{dt} \cdot \frac{m_{FZ}}{m_{UZ} + m_{FZ}} \quad (3.60)$$



In the equations given above,  $\frac{dm_{\text{entr,UZ},i}}{dt}$  (kg/s) represents the entrainment flux from the unburned zone for  $i$ -th spray zone,  $m_{\text{UZ}}$  (kg) represents the unburned zone mass,  $m_{\text{FZ}}$  (kg) represents the flame zone mass, while  $\frac{dm_{\text{entr,FZ},i}}{dt}$  (kg/s) represents the entrainment flux from the unburned zone for  $i$ -th spray zone.

### ***Liquid fuel evaporation***

The energy for the liquid fuel droplet heat-up is supplied from the surrounding gas mixture. The evaporation process is governed by the simultaneous heat transfer to the droplet surface and mass transfer away from the droplet surface.

The evaporation model used in this thesis was presented in [91] and integrated within the AVL simulation code by the authors in [33]. The following model assumptions and simplifications were made [91]:

1. droplet is spherical and does not deform,
2. the droplet is isolated from the other droplets,
3. the temperature field inside the droplet is uniform; in the literature, such model is called the infinite conductivity model,
4. the physical properties of the gas mixture surrounding the droplet are uniform,
5. the fuel a single component (n-dodecane),
6. turbulence has no effect on the boundary layer,
7. there are no chemical reactions inside the boundary layer.

The convective heat transfer and mass diffusion from the droplet surface are calculated separately in each of the spray zones, and they are calculated for only one droplet. In the case when the droplet temperature is below 702 K (boiling temperature), the following equations are used to calculate heat-up and evaporation processes for a single droplet [33]:

$$\frac{dQ_{\text{d,SZ},i}}{dt} = C_{\text{evap, HT}} \cdot SMD_{\text{SZ},i} \cdot \Pi \cdot \lambda_{\text{m,SZ},i} \cdot (T_{\text{SZ},i} - T_{\text{d,SZ},i}) \cdot Nu_{\text{SZ},i} \cdot \frac{z_{\text{SZ},i}}{e^{z_{\text{SZ},i}} - 1} \quad (3.61)$$

$$\frac{dT_{\text{d,SZ},i}}{dt} = \frac{\left( \frac{dQ_{\text{d,SZ},i}}{dt} - \frac{dm_{\text{evap,SZ},i}}{dt} \cdot h_{\text{lat,fuel}} \right)}{m_{\text{d,SZ},i} \cdot c_{\text{p,d,SZ},i}} \quad (3.62)$$

$$\frac{dm_{d, \text{evap}, \text{SZ}, i}}{dt} = C_{\text{evap}} \cdot SMD_{\text{SZ}, i} \cdot \Pi \cdot D_{\text{SZ}, i} \cdot \rho_{m, \text{SZ}, i} \cdot Sh_{\text{SZ}, i} \cdot \ln \left( 1 - \frac{p_{\text{sat}, \text{SZ}, i}}{p} \right) \quad (3.63)$$

In case when the droplet temperature is equal to or above 702 K (boiling temperature), the entire energy supplied to the droplet is used for the phase change (vaporization), and the following equations are used to calculate the vaporization processes for a single droplet [33]:

$$\frac{dQ_{d, \text{SZ}, i}}{dt} = 0 \quad (3.64)$$

$$\frac{dT_{d, \text{SZ}, i}}{dt} = 0 \quad (3.65)$$

$$\frac{dm_{d, \text{evap}, \text{SZ}, i}}{dt} = C_{\text{evap}} \cdot SMD_{\text{SZ}, i} \cdot \Pi \cdot 0.018 \cdot \left( \frac{p}{6} \right)^{-1.1} \quad (3.66)$$

The liquid droplet heat-up process is calculated from the energy balance inside the droplet, while the evaporation mass flux can be viewed as the mass leaving the droplet's surface. In the equations given above, subscript  $i$  denotes the  $i$ -th spray zone, while  $\frac{dQ_{d, \text{SZ}, i}}{dt}$  (J/s) represents the heat flux supplied to the droplet surface,  $C_{\text{evap}, \text{HT}}$  (-) represents the droplet heat-up model parameter,  $\lambda_{m, \text{SZ}, i}$  (W/mK) represents the boundary layer thermal conductivity,  $T_{\text{SZ}, i}$  (K) represents the spray zone temperature,  $T_{d, \text{SZ}, i}$  (K) represents the liquid droplet temperature,  $Nu_{\text{SZ}, i}$  (-) represents the spray zone Nusselt number, while the term  $\frac{z_{\text{SZ}, i}}{e^{z_{\text{SZ}, i}} - 1}$  (-) takes into account the boundary layer thickening [33].  $\frac{dT_{d, \text{SZ}, i}}{dt}$  (K/s) represents the droplet temperature flux due to droplet heat up process,  $h_{\text{lat}, \text{fuel}}$  (J/kg) represents the latent heat of vaporization,  $m_{d, \text{SZ}, i}$  (kg) represents the liquid fuel droplet mass, while  $c_{p, d, \text{SZ}, i}$  (J/kgK) represents the specific heat capacity of the liquid fuel droplet.  $\frac{dm_{\text{evap}, \text{SZ}, i}}{dt}$  (kg/s) represents the evaporated fuel mass flux,  $C_{\text{evap}}$  (-) represents the evaporation model parameter,  $D_{\text{SZ}, i}$  (m<sup>2</sup>/s) represents the binary diffusion coefficient,  $\rho_{m, \text{SZ}, i}$  (kg/m<sup>3</sup>) represents the boundary layer density,  $Sh_{\text{SZ}, i}$  (-) represents the spray zone Sherwood number, while  $p_{\text{sat}, \text{SZ}, i}$  (Pa) represents the spray zone saturation

pressure. The coefficient  $z$  (-) used in the boundary layer thickening effect calculation can be calculated from the following expression:

$$z_{SZ,i} = \frac{\frac{dm_{\text{evap},SZ,i}}{dt} \cdot c_{p,FV,SZ,i}}{SMD_{SZ,i} \cdot \Pi \cdot \lambda_{m,SZ,i} \cdot Nu_{SZ,i}} \quad (3.67)$$

In the equations given above,  $c_{p,FV,SZ,i}$  (J/kgK) represents the vaporized fuel heat capacity. The boundary layer properties are calculated in the following way:

$$\lambda_{m,SZ,i} = \left( \frac{1 - p_{\text{sat},SZ,i}}{2 \cdot p} \right) \cdot \lambda_{\text{charge},SZ,i} + \left( \frac{p_{\text{sat},SZ,i}}{2 \cdot p} \right) \cdot \lambda_{FV,SZ,i} \quad (3.68)$$

$$\rho_{m,SZ,i} = \frac{p \cdot M_{m,SZ,i}}{8.134472 \cdot T_{m,SZ,i}} \quad (3.69)$$

$$M_{m,SZ,i} = \left( \frac{1 - p_{\text{sat},SZ,i}}{2 \cdot p} \right) \cdot M_{\text{charge},SZ,i} + \left( \frac{p_{\text{sat},SZ,i}}{2 \cdot p} \right) \cdot M_{FV,SZ,i} \quad (3.70)$$

$$T_{m,SZ,i} = \frac{T_{SZ,i} + T_{d,SZ,i}}{2} \quad (3.71)$$

In the equations given above,  $\lambda_{\text{charge},SZ,i}$  (W/mK) represents the zone gas mixture thermal conductivity,  $\lambda_{FV,SZ,i}$  (W/mK) represents the liquid fuel vapor thermal conductivity,  $M_{m,SZ,i}$  (kg/kmol) represents the boundary layer molar mass,  $T_{m,SZ,i}$  (K) represents the boundary layer temperature,  $M_{\text{charge},SZ,i}$  (kg/kmol) represents the zone gas mixture molar mass, while  $M_{FV,SZ,i}$  (W/mK) represents the liquid fuel vapor molar mass. As the above equations are only for a single droplet evaporation process, the entire heat-up flux and evaporation flux for a given  $i$ -th spray zone is calculated from the following equations:

$$\frac{dQ_{\text{EVAP},SZ,i}}{dt} = -n_{d,SZ,i} \cdot \frac{dQ_{d,SZ,i}}{dt} \quad (3.72)$$

$$\frac{dm_{\text{evap},SZ,i}}{dt} = n_{d,SZ,i} \cdot \frac{dm_{d,\text{evap},SZ,i}}{dt} \quad (3.73)$$

The overall evaporation energy flux (J/s) for the spray can now be calculated from the following equation:

$$\frac{dQ_{\text{EVAP}}}{dt} = \sum_i \frac{dQ_{\text{EVAP},\text{SZ},i}}{dt} \quad (3.74)$$

The evaporation energy is taken from the entire cylinder content (all of the zones inside the cylinder). The evaporation energy is distributed to the zone inside the cylinder according to the following expressions:

$$\frac{dQ_{\text{EVAP},\text{SZ},i}}{dt} = \frac{dQ_{\text{EVAP}}}{dt} \cdot \frac{m_{\text{SZ},i} \cdot u_{\text{SZ},i}}{m_{\text{UZ}} \cdot u_{\text{UZ}} + m_{\text{FZ}} \cdot u_{\text{FZ}} + \sum_i m_{\text{SZ},i} \cdot u_{\text{SZ},i}} \quad (3.75)$$

$$\frac{dQ_{\text{EVAP},\text{UZ}}}{dt} = \frac{dQ_{\text{EVAP}}}{dt} \cdot \frac{m_{\text{UZ}} \cdot u_{\text{UZ}}}{m_{\text{UZ}} \cdot u_{\text{UZ}} + m_{\text{FZ}} \cdot u_{\text{FZ}} + \sum_i m_{\text{SZ},i} \cdot u_{\text{SZ},i}} \quad (3.76)$$

$$\frac{dQ_{\text{EVAP},\text{FZ}}}{dt} = \frac{dQ_{\text{EVAP}}}{dt} \cdot \frac{m_{\text{FZ}} \cdot u_{\text{FZ}}}{m_{\text{UZ}} \cdot u_{\text{UZ}} + m_{\text{FZ}} \cdot u_{\text{FZ}} + \sum_i m_{\text{SZ},i} \cdot u_{\text{SZ},i}} \quad (3.77)$$

In the equations given above,  $u_{\text{UZ}}$  (J/kg) represents the specific internal energy of the mixture inside the unburned zone,  $u_{\text{FZ}}$  (J/kg) represents the specific internal energy of the mixture inside the flame zone, while  $u_{\text{SZ},i}$  (J/kg) represents the specific internal energy of the mixture inside the  $i$ -th spray zone.

### ***Zone position tracking***

Tracking of a zone position is a new feature of the spray model that was developed and integrated within the AVL cycle simulation software within this thesis. Zone position tracking enables improved calculation of the moment when a particular spray zone hits the combustion chamber wall, consequently improving the charge entrainment calculation. Moreover, zone position tracking also improves the calculation of the location of the spray center, thus enabling more accurate calculation of the location from where the flame starts to propagate through the combustion chamber. In order to calculate the location of a given spray zone, following injector and spray geometry features have to be defined (Figure 43):

1. injector nozzle hole depth ( $z_{\text{tip}}$ ),

2. injector nozzle hole angle ( $\varphi_{\text{nozzle}}$ ),
3. number of injector nozzle holes,
4. spray angle ( $\varphi_{\text{spray}}$ ).

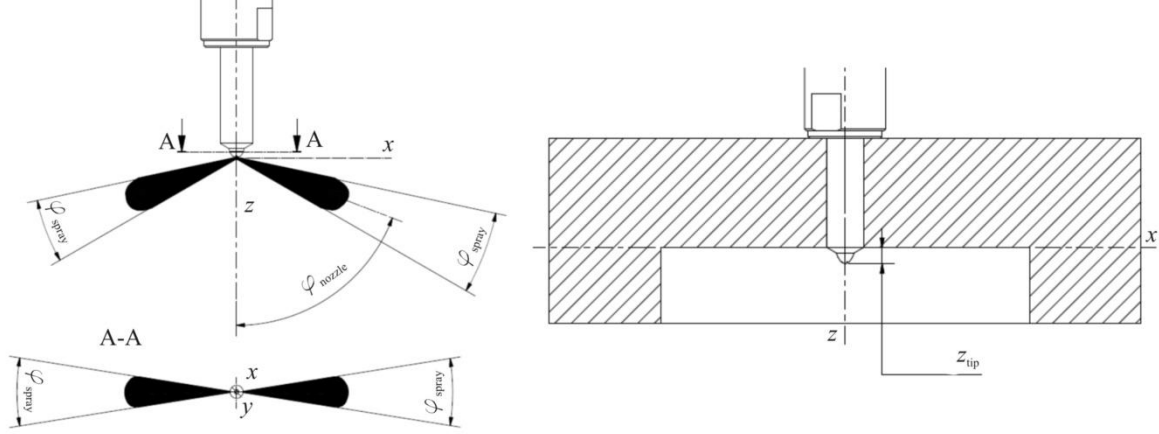


**Figure 43. Injector and spray geometry properties**

Number of injector nozzle holes is important for defining the number of flames that propagate through the combustion chamber, while the injector nozzle hole depth and angle are important for the calculation of each spray zone location. All of these three parameters are input parameters to the model. Spray zone angle on the other hand is calculated with the equation that was presented in [89]:

$$\frac{\varphi_{\text{spray}}}{2} = \tan^{-1} \left\{ 0.26 \cdot \left[ \left( \frac{\mu}{\rho_{\text{fuel}}} \right)^{0.19} - 0.0043 \cdot \left( \frac{\rho_{\text{fuel}}}{\mu} \right)^{0.5} \right] \right\} \quad (3.78)$$

The spray angle is calculated for every axial parcel in the moment it is created. Every spray zone has an inner, outer and medium angle; medium angle represents the angle of the spray zone's center of mass (Figure 44). The outer, inner and medium angle of the given  $i$ -th spray zone are calculated with the following expressions:

$$\varphi_{\text{SZ},i,\text{outer}} = \varphi_{\text{spray}} \cdot \frac{i_{\text{radial}}}{n_{\text{radial}}} \quad (3.79)$$

$$\varphi_{\text{SZ},i,\text{inner}} = \varphi_{\text{spray}} \cdot \frac{i_{\text{radial}} - 1}{n_{\text{radial}}} \quad (3.80)$$

$$\varphi_{SZ,i, \text{medium}} = \frac{\varphi_{SZ,i, \text{outer}} + \varphi_{SZ,i, \text{inner}}}{2} \quad (3.81)$$

In the equations given above,  $\varphi_{\text{spray}}$  (rad) represents the outer angle of the entire spray,  $\varphi_{SZ,i, \text{outer}}$  (rad) represents the outer angle of the  $i$ -th spray zone,  $\varphi_{SZ,i, \text{inner}}$  (rad) represents the inner angle of the  $i$ -th spray zone, while  $\varphi_{SZ,i, \text{medium}}$  (rad) represents the medium angle of the  $i$ -th spray zone. Also, the front, rear and medium position of  $i$ -th spray zone along its axis are tracked (Figure 44).

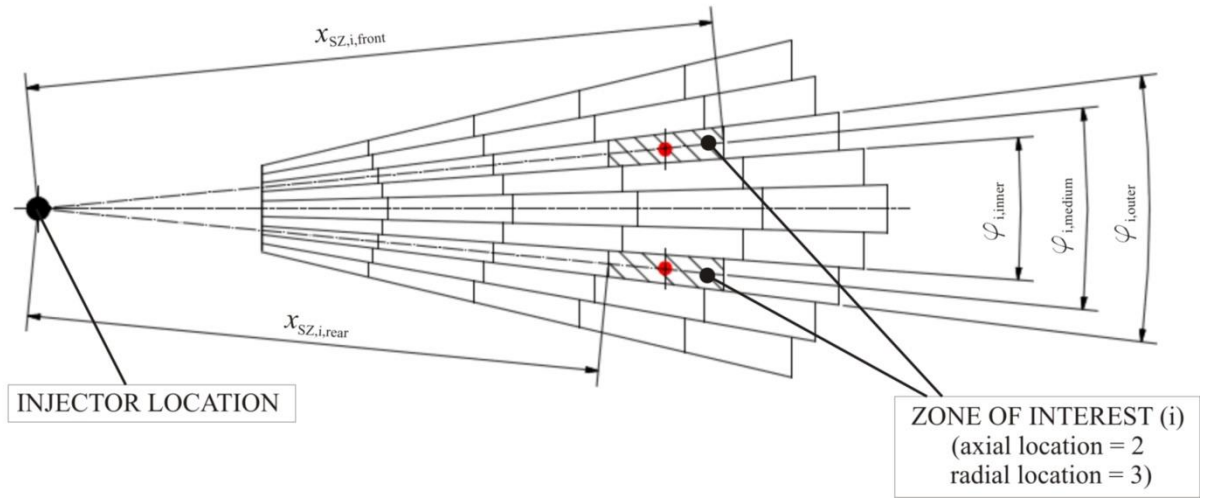


**Figure 44. Zone position tracking**

The front, rear and medium position of the given  $i$ -th spray zone along its axis are calculated with the following expressions:

$$x_{SZ,i, \text{front}} = \int_{t_{\text{SOI},SZ,i}}^t v_{SZ,i}(t) \cdot dt \quad (3.82)$$

$$x_{SZ,i, \text{rear}} = \int_{t_{\text{EOI},SZ,i}}^t v_{SZ,i}(t) \cdot dt \quad (3.83)$$

$$x_{SZ,i, \text{medium}} = \frac{x_{SZ,i, \text{front}} + x_{SZ,i, \text{rear}}}{2} \quad (3.84)$$

In the equations given above,  $x_{SZ,i, \text{front}}$  (m) represents the front position of the  $i$ -th spray zone,  $t_{\text{SOI},SZ,i}$  (s) represents the start of injection of the  $i$ -th spray zone,  $x_{SZ,i, \text{rear}}$  (m) represents the

rear position of the  $i$ -th spray zone,  $t_{EOI,SZ,i}$  (s) represents the end of injection of the  $i$ -th spray zone, while  $x_{SZ,i,medium}$  (m) represents the medium position of the  $i$ -th spray zone.

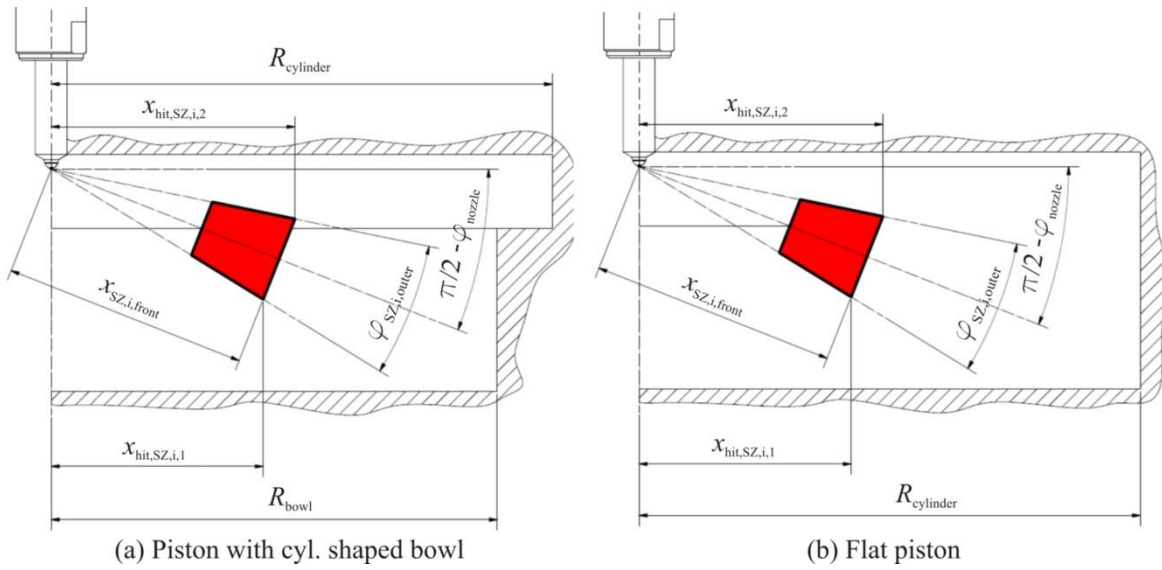


**Figure 45. Schematic presentation of the of the wall hit conditions**

In this model, it is considered that the spray zone truly slows down only when it hits the combustion chamber liner or a piston liner if the piston features a bowl, and the spray is located inside the piston bowl. The conditions when the spray zone slows down are calculated with the following expressions (Figure 45):

$$x_{hit,SZ,i,1} = x_{SZ,i,front} \cdot \cos\left(\frac{\pi}{2} - \varphi_{nozzle} + \frac{\varphi_{SZ,i,outer}}{2}\right) \quad (3.85)$$

$$x_{hit,SZ,i,2} = x_{SZ,i,front} \cdot \cos\left(\frac{\pi}{2} - \varphi_{nozzle} - \frac{\varphi_{SZ,i,outer}}{2}\right) \quad (3.86)$$

$$R_{bowl} \leq MIN(x_{hit,SZ,i,1}, x_{hit,SZ,i,2}) \quad (3.87)$$

$$R_{cylinder} \leq MIN(x_{hit,SZ,i,1}, x_{hit,SZ,i,2}) \quad (3.88)$$

In case when the piston features a bowl, a given  $i$ -th spray zone has hit the combustion chamber wall when condition (3.87) is satisfied. Otherwise it has hit the combustion chamber wall when the condition (3.88) is satisfied. In the equations given above,  $x_{hit,SZ,i,1}$  (m) and  $x_{hit,SZ,i,2}$  (m) represent the two points of the  $i$ -th spray zone that are potentially the closest to

the combustion chamber wall,  $R_{\text{bowl}}$  (m) represent the radius of the bowl inside the piston, while  $R_{\text{cylinder}}$  (m) represent the radius of the cylinder.

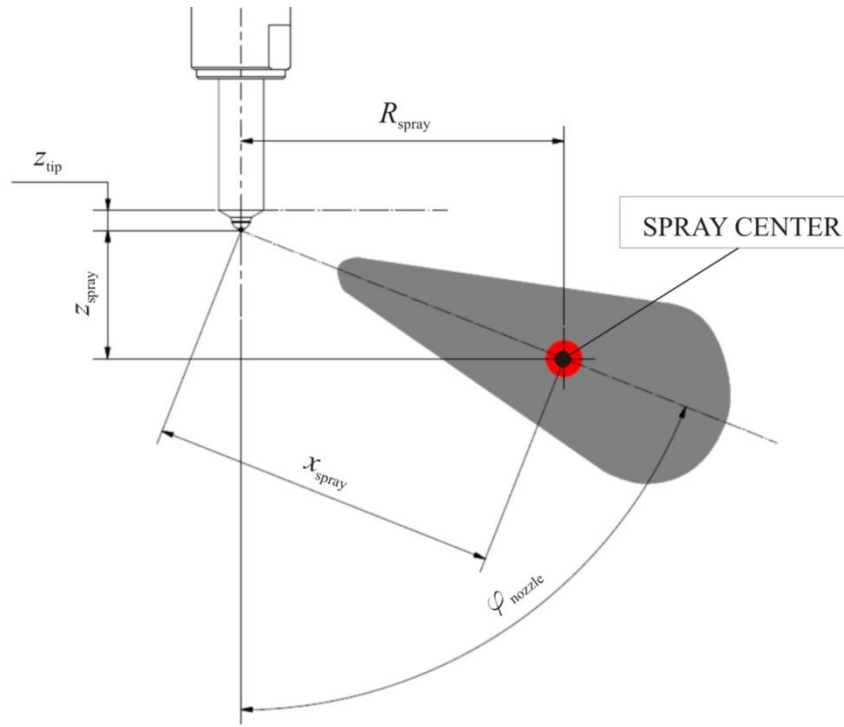


**Figure 46. Schematic presentation of the spray center location**

Since all details regarding the position of every spray zone have been defined, the position of the spray center (Figure 46) can be calculated with the following expressions:

$$x_{\text{spray}} = \frac{\sum_i m_{\text{SZ},i} \cdot x_{\text{SZ},i, \text{medium}}}{m_{\text{spray}}} \quad (3.89)$$

$$R_{\text{spray}} = x_{\text{spray}} \cdot \sin(\phi_{\text{nozzle}}) \quad (3.90)$$

$$z_{\text{spray}} = z_{\text{tip}} + x_{\text{spray}} \cdot \cos(\phi_{\text{nozzle}}) \quad (3.91)$$

### 3.3.4. Spray ignition and combustion model

Spray ignition and combustion is calculated with newly developed sub-models which are based on the lookup tables that feature low temperature and high temperature auto ignition delay times, percentage of the heat released in the low temperature ignition event and chemical reaction rate times. These are 5-D tables since they were made as functions of the



temperature, pressure, fuel vapor mass fraction, combustion products mass fraction and mass fraction of the methane in the fuel blend. Tables were made with a specially developed in-house code. More details regarding the code, the equations used and the method of table generation will be presented in the next chapter.

For every spray zone, low temperature and high temperature knock integrals introduced by Livengood and Wu [92] are calculated with its own temperature and mixture composition with the following equations:

$$KI_{LT, SZ, i} = \int_{t_{mj, i}}^t \frac{1}{C_{ignition} \cdot \tau_{LT, SZ, i}} dt \quad (3.92)$$

$$KI_{HT, SZ, i} = \int_{t_{mj, i}}^t \frac{1}{C_{ignition} \cdot \tau_{HT, SZ, i}} dt \quad (3.93)$$

$$\tau_{LT, SZ, i} = f(T_{SZ, i}, p, \phi_{SZ, i}, x_{CP, SZ, i}, x_{metFV, SZ, i}) \quad (3.94)$$

$$\tau_{HT, SZ, i} = f(T_{SZ, i}, p, \phi_{SZ, i}, x_{CP, SZ, i}, x_{metFV, SZ, i}) \quad (3.95)$$

In the equations given above,  $KI_{LT, SZ, i}$  (-) represents the low temperature knock integral in the  $i$ -th spray zone,  $KI_{HT, SZ, i}$  (-) represents the high temperature (main) knock integral in the  $i$ -th spray zone,  $\tau_{LT, SZ, i}$  (s) represents the low temperature ignition delay time in the  $i$ -th spray zone,  $\tau_{HT, SZ, i}$  (s) represents the high temperature ignition delay time in the  $i$ -th spray zone,  $T_{SZ, i}$  (K) represents the temperature inside the  $i$ -th spray zone,  $\phi_{SZ, i}$  (-) represents the equivalence ratio of the mixture inside the  $i$ -th spray zone,  $x_{CP, SZ, i}$  (-) represents the mass fraction of combustion products inside the  $i$ -th spray zone, while  $x_{metFV, SZ, i}$  (-) represents the mass fraction of the methane inside the fuel vapor, inside the  $i$ -th spray zone.

A given spray zone is considered as ignited once its knock integral exceeds the value of one and depending on which knock integral (high temperature or low temperature) crossed the value of one the corresponding heat release calculation is triggered.

Since the percentage of the low temperature heat released is also given in the chemistry tables, in the case that the low temperature heat release is triggered, a certain amount of heat is instantly released. The rate of the heat released due to low temperature heat release is calculated in the following way, with assumption that within every spray zone stoichiometric combustion occurs:

$$\frac{dQ_{LT, SZ, i}}{dt} = \frac{m_{FB, LT, SZ, i}}{dt} \cdot LHV_{SZ, i} \quad (3.96)$$

$$\frac{dm_{FB, LT, SZ, i}}{dt} = \frac{m_{FV, avail, SZ, i}}{\Delta t} \cdot LTHR_{SZ, i} \quad (3.97)$$

$$LTHR_{SZ, i} = f(T_{SZ, i}, p, \phi_{SZ, i}, x_{CP, SZ, i}, x_{metFV, SZ, i}) \quad (3.98)$$

$$m_{FV, avail, SZ, i} = MIN(m_{FV, SZ, i}, m_{FV, stoich, SZ, i}) \quad (3.99)$$

$$m_{FV, stoich, SZ, i} = \frac{m_{air, SZ, i}}{AFR_{stoich, SZ, i}} \quad (3.100)$$

In the equations given above,  $Q_{LT, SZ, i}$  (J) represents the heat released due to the low temperature combustion process inside the  $i$ -th spray zone,  $m_{FB, LT, SZ, i}$  (kg) represents the mass of fuel that burned due to the low temperature combustion event inside the  $i$ -th spray zone,  $m_{FV, avail, SZ, i}$  (kg) represents the mass of fuel vapor that is available for combustion inside the  $i$ -th spray zone,  $LHV_{SZ, i}$  (J) represents the lower heating value of the mixture inside the  $i$ -th spray zone,  $LTHR_{SZ, i}$  (-) represents the relative amount of energy that is released due to low temperature heat release (LTHR) process inside the  $i$ -th spray zone,  $m_{FV, SZ, i}$  (kg) represents the mass of fuel vapor inside the  $i$ -th spray zone,  $m_{FV, stoich, SZ, i}$  (kg) represents the mass of fuel vapor that is necessary for the stoichiometric combustion inside the  $i$ -th spray zone,  $m_{air, SZ, i}$  (kg) represents the mass of air inside the  $i$ -th spray zone, while  $AFR_{stoich, SZ, i}$  (-) represents the stoichiometric air to fuel ratio of the mixture inside the  $i$ -th spray zone.

The rate of heat release due to high temperature (main) combustion process and corresponding fuel burned masses inside  $i$ -th spray zone are calculated in the following way:

$$\frac{dQ_{HT, SZ, i}}{dt} = \frac{dm_{FB, HT, SZ, i}}{dt} \cdot LHV_{SZ, i} \quad (3.101)$$

$$\frac{dm_{FB, HT, SZ, i}}{dt} = MIN\left(\frac{m_{FV, avail, SZ, i}}{\Delta t}, \frac{m_{FV, avail, SZ, i}}{\tau_{reac, SZ, i}}\right) \quad (3.102)$$

$$\tau_{reac, SZ, i} = f(T_{SZ, i}, p, \phi_{SZ, i}, x_{CP, SZ, i}, x_{metFV, SZ, i}) \quad (3.103)$$

$$m_{\text{FV, avail, SZ, } i} = \text{MIN}(m_{\text{FV, SZ, } i}, m_{\text{FV, stoich, SZ, } i}) \quad (3.104)$$

$$m_{\text{FV, stoich, SZ, } i} = \frac{m_{\text{air, SZ, } i}}{\text{AFR}_{\text{stoich, SZ, } i}} \quad (3.105)$$

In the equations given above,  $Q_{\text{HT, SZ, } i}$  (J) represents the heat released due to high temperature (main) combustion process inside the  $i$ -th spray zone,  $m_{\text{FB, HT, SZ, } i}$  (kg) represents the mass of fuel that burned due to the high temperature combustion event inside the  $i$ -th spray zone, while  $\tau_{\text{reac, SZ, } i}$  (s) represents the chemical reaction rate time inside the  $i$ -th spray zone (tabulated). The overall rate of heat release (3.96) and the overall fuel burned flux (3.97) inside  $i$ -th spray zone are:

$$\frac{dQ_{\text{COMB, SZ, } i}}{dt} = \frac{dQ_{\text{LT, SZ, } i}}{dt} + \frac{dQ_{\text{HT, SZ, } i}}{dt} \quad (3.106)$$

$$\frac{dm_{\text{FB, SZ, } i}}{dt} = \frac{dm_{\text{FB, LT, SZ, } i}}{dt} + \frac{dm_{\text{FB, HT, SZ, } i}}{dt} \quad (3.107)$$

As can be seen from the equations presented above, combustion inside the spray is controlled by three mechanisms:

1. evaporation (amount of available Diesel fuel),
2. entrainment (amount of available methane and air),
3. chemical kinetics (reaction rate of the given mixture).

The evaporation mechanism controls the amount of Diesel fuel that is available for combustion, thus also controlling the mixture's reaction rate. On the other hand, entrainment mechanism controls the amount of fresh charge (methane/air/EGR) mixture that is entrained into the spray zone. In this way, entrainment controls the combustion rate through controlling the amount of air inside the zone. Combustion rate is determined from the slowest of these mechanisms.

### 3.4. Ignition delay and chemical reaction rate tabulation

Chemistry tables which are used in the ignition and reaction rate calculation of the spray combustion and the knock occurrence (detonation) were made with a specially developed in-house code. The code is based on a single zone, homogeneous, adiabatic constant volume 0-D reactor. In this code, the FORTRAN subroutine CHEMKIN<sup>TM</sup> was used to calculate the

thermodynamic properties of the gas mixture and production rates of the species involved in the chemical reaction process. The following data were stored in the chemistry tables:

1. Low temperature (cool flame) ignition delay time.
2. Percentage of the energy released in the cool flame event.
3. High temperature ignition delay time (autoignition delay).
4. Reaction rate time.

Low temperature ignition delay time and high temperature ignition delay time are used to initiate the corresponding combustion events, while the percentage of energy released in the cool flame event and the chemical reaction rate time are used to calculate the corresponding burning rates. The Diesel fuel/ natural gas chemical mechanism that features 654 species and 2827 reactions was used to generate the specified data. In these calculations, the fuel was set as n-heptane/ methane mixture. The data (initial mixture properties) used for the tabulation of the chemistry table are presented in the following table (Table 5).

**Table 5. Tabulation parameters (initial mixture properties) used for chemistry table generation**

Parameter	Values	Number
Temperature (K)	550, 600, 650, 700, 750, 800, 850, 900, 950, 1000, 1050, 1100, 1200, 1300, 1400, 1500, 1600, 1700, 1800, 2000	20
Pressure (bar)	3, 10, 20, 30, 50, 100, 150, 200	7
Mixture equivalence ratio (-)	0.2, 0.3, 0.5, 0.67, 1, 1.5, 2, 3, 5	9
Combustion products mass fraction (-)	0, 0.2, 0.4, 0.6, 0.8	5
Methane mass fraction in the fuel blend (-)	0, 0.1, 0.2, 0.4, 0.6, 0.8, 0.9, 1	8
		50400

At every time-step during the high pressure cycle calculation in the DFMZCM, depending on the combustion stage, either ignition delay time or chemical reaction rate time needs to be taken from the chemistry look-up tables. As these tables were made with 5 independent parameters, a 5-D interpolation needs to be performed. Therefore, during the work presented in this thesis a 5-D linear interpolation algorithm was implemented within the AVL cycle simulation software.

### 3.4.1. Physical background – chemical kinetics

Even though chemical kinetics is not directly a focus of this thesis, since it was used in the tabulation of chemistry, before presenting the 0-D tabulation code and the method and equations used in the tabulation process, a short introduction to this large and rather complex field is given.

Chemical kinetics in combustion can best be described as the field that deals with the rate at which species are produced and consumed and the rate at which heat of reaction is released or consumed [85]. Reactions depend on the concentration of species involved in it, and are sensitive to pressure, temperature and the presence of a catalyst [93].

In a combustion system, the initial and end mixture state is described by thermodynamics, while the rate at which this change occurs (burning rate) is described through chemical kinetics [51], [52].

From the equilibrium energy aspect, there are two main types of chemical reactions, exothermic and endothermic reactions. In an endothermic reaction, the energy of products is higher than the energy of reactants. On other hand, in an exothermic reaction, the energy of products is lower than the energy of reactants. From the global point of view, combustion process is an exothermic reaction in which combustion products are formed in a fuel/oxidizer reaction.

When dealing with the combustion process in an IC engines, the reactions occur in the gas phase. However, for a chemical reaction to occur the following two requirements have to be satisfied [94]:

1. Species have to collide
2. Species have to possess sufficient energy

According to [94], the reaction rate in the gaseous phase can be expressed as the product of the collision frequency and the number of collisions in which species have sufficient energy to cause a chemical reaction. From the chemistry point of view, a combustion process never starts directly from fuel and oxygen and it always features a number of steps (elementary reactions) which are collectively described by a global reaction (combustion) mechanism [85]. It was shown that complex chemical reactions involve very reactive intermediate species, called radicals [95]. There are four main types of elementary reactions [85], [96]:

1. Chain initiation, which describe the initiation of the combustion process
2. Chain branching, which describe the creation of the radicals
3. Chain terminating, which describe the formation of stable species

4. Chain propagating, which describes reactions where the number of radicals stays the same

Chemical reaction rate is expressed as a change in a particular species concentration in time [94]. First, let's consider a forward reaction which can be expressed as:



In the expression given above,  $r_j$  and  $p_k$  represent the reaction stoichiometry coefficients, while  $R_j$  and  $P_k$  represent the particular species which are involved in this specific reaction. The reaction rate is linked to the concentrations and stoichiometric coefficients of the species involved in the reaction, and can be expressed in the following way [51]:

$$\omega = -\frac{1}{r_j} \cdot \frac{dc_j}{dt} = \frac{1}{p_k} \cdot \frac{dc_k}{dt} \quad (3.109)$$

In the expression given above,  $\omega$  (kmol/m<sup>3</sup>s) represents the reaction rate, while  $c_j$ , and  $c_k$  (kmol/m<sup>3</sup>) represent molar concentrations of the corresponding species. The reaction rate law is usually represented as a function of the reactant concentrations [94]:

$$\omega = k_R \cdot \prod_j c_j^{n_j} \quad (3.110)$$

In the expression given above,  $k$  (-) represents the reaction rate constant, while  $n_j$  (-) represent the corresponding concentration exponent, which is usually equal to the species stoichiometric coefficient [51], [97]. The order of a given reaction is defined as a sum of the concentration exponents [94]. According to Arrhenius, for the major part of the chemical reactions the reaction rate constant can be expressed as:

$$k_R = A \cdot e^{-\frac{E_a}{R_m T}} \quad (3.111)$$

In the equation given above,  $A$  (-) represents the pre-exponential factor,  $E_a$  (J/kmol) represents the activation energy, and  $R_m$  (J/kmolK) represents the ideal gas constant, while  $T$  (K) represents the gas mixture temperature. The pre-exponential factor is a measure of the collision frequency, while the activation energy can be seen as the minimum energy the reactants must possess in order for the chemical reaction to occur [93] (Figure 47).

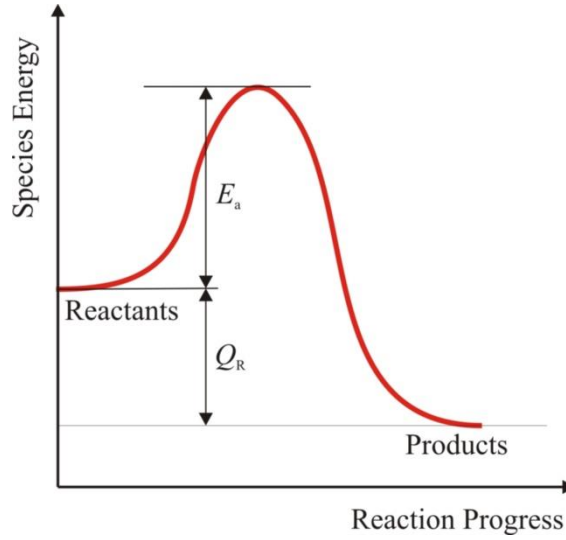


**Figure 47. Exothermic reaction energy profile; reproduced from [93]**

Since for many reactions the pre-exponential factor is a function of temperature, a modified Arrhenius expression can be written in the following form [51]:

$$k_R = B \cdot T^\beta \cdot e^{-\frac{E_a}{RT}} \quad (3.112)$$

In the equation given above,  $B$  (-) represents the temperature constant, while  $\beta$  (-) represents the temperature exponent. For reversible reactions, with every forward reaction there is a corresponding backward reaction [51]. This is due to the fact that the process of conversion of reactants into final equilibrium products occurs in several steps and in these steps; there is a simultaneous formation of the products from the reactants and reactants from the products. A reversible reaction that features  $j$  chemical species can be expressed as:

$$\sum_j r_j^f R_j \leftrightarrow \sum_j r_j^b R_j \quad (3.113)$$

In the expression given above,  $R_j$  represents the particular species which were involved in this specific reaction  $r_j^f$  (-) represents the stoichiometric coefficient of the  $j$ -th reactant species, while  $r_j^b$  (-) represents the stoichiometric coefficient of the  $j$ -th product species. Now, the reaction rate for a given reaction can be expressed as [51]:

$$\omega = k_f \cdot \prod_j c_j^{r_j^f} - k_b \cdot \prod_j c_j^{r_j^b} \quad (3.114)$$

In the equation given above,  $k_f$  (-) represents the forward reaction rate constant, while  $k_b$  (-) represents the backward reaction rate constant. According to [97], the forward and backward reaction rate constants are linked through equilibrium constant. As chemical kinetics is not the main focus of this thesis, the details regarding the equilibrium constant calculation, as well as specific reactions which are pressure dependent will not be given in this thesis and can be found in the literature [97].

### 3.4.2. 0-D tabulation code

In this chapter of the thesis, the overview of the in-house developed tabulation code and its equations is presented. The overall 0-D code for the tabulation of ignition delay time and reaction rate data features following sub-models:

1. Input data handling.
2. Calculation initialization.
3. Constant volume reactor calculations.
4. CHEMKIN<sup>TM</sup> subroutines.
5. Calculation data post-processing.
6. Code finish.

It is important to point out that in these calculations, the Diesel fuel is represented as n-heptane ( $C_7H_{16}$ ), while the natural gas is represented as methane ( $CH_4$ ). Gas mixture is considered to be ideal and the input combustion products are considered to consist of only nitrogen ( $N_2$ ), carbon dioxide ( $CO_2$ ) and water vapor ( $H_2O$ ). The input combustion products are considered to be a product of stoichiometric combustion process.

In the input data handling subroutine, specific input data regarding calculation duration, calculation time-step, choice between single and multi-calculation are read and stored. Moreover, in this subroutine the initial state and composition input parameters are stored and the appropriate vectors are initialized. There are two main calculation options:

1. Single-calculation.
2. Multi-calculation.

When single-calculation option is initiated, the calculation with only one set of the initial state and composition parameters is performed. On the other hand, in the case of multi-calculation option, multiple calculations with different sets of initial state and composition are performed. The number of calculations is defined by the number of the preset initial states and mixture compositions. For instance, if 5 temperature data, 4 pressure data, 8 equivalence ratio data, 3



combustion mass fraction data and 10 methane mass fractions in fuel blend data are set, the total of  $5 \times 4 \times 8 \times 3 \times 10 = 4800$  calculations will be performed.

In the initialization subroutine, new calculation is initialized. During this process, all calculation variables are re-set, and the initial species composition is calculated. As in the input file only equivalence ratio, combustion products mass fraction and mass fraction of methane in the fuel blend are given, the initial values of mass fractions of n-heptane, methane, oxygen, nitrogen, carbon dioxide and water vapor have to be calculated. These are calculated as follows; first the overall fuel mass fraction, as well as oxygen and nitrogen mass fraction in the fresh mixture is calculated (without combustion products included):

$$x_{\text{FV, fresh}} = \frac{1}{1 + \frac{1}{\phi} \cdot AF_{\text{stoich}}} \quad (3.115)$$

$$AF_{\text{stoich}} = \frac{O_{\text{min}} \cdot M_{O_2}}{M_{\text{FV}} \cdot 0.232} \quad (3.116)$$

$$O_{\text{min}} = y_{\text{methFV}} \cdot O_{\text{min, methane}} + (1 - y_{\text{methFV}}) \cdot O_{\text{min, n-heptane}} \quad (3.117)$$

$$O_{\text{min, i}} = c_i + \frac{h_i}{4} \cdot -\frac{o_i}{2} \quad (3.118)$$

$$x_{O_2, \text{fresh}} = (1 - x_{\text{FV, fresh}}) \cdot 0.232 \quad (3.119)$$

$$x_{N_2, \text{fresh}} = 1 - x_{\text{FV, fresh}} - x_{O_2, \text{fresh}} \quad (3.120)$$

In the equations given above,  $x_{\text{FV, fresh}}$  (-) represents the mass fraction of the fuel blend in the fresh charge (fresh means fuel + air),  $AF_{\text{stoich}}$  (kg/kg) represents the air to fuel ratio for a given fuel blend,  $O_{\text{min}}$  (kmol/kmol) represent the oxygen to fuel ratio for stoichiometric combustion for a given fuel blend,  $M_{O_2}$  (kg/kmol) represents the oxygen molar mass,  $M_{\text{FV}}$  (kg/kmol) represent the given fuel blend molar mass,  $y_{\text{methFV}}$  (-) represents the molar fraction of methane in the fuel blend, while  $O_{\text{min, methane}}$  (kmol/kmol) and  $O_{\text{min, n-heptane}}$  (kmol/kmol) represent the oxygen to fuel ratio for stoichiometric combustion of methane and n-heptane, respectively. These values are calculated based on the number of carbon, oxygen and hydrogen atoms in a given fuel species, as is presented for an arbitrary fuel species (denoted as  $i$ ) in the equation

3.118. In the equation 3.118,  $O_{\min,i}$  (kmol/kmol) represent the oxygen to fuel ratio for stoichiometric combustion for a given  $i$ -th fuel species,  $c_i$  (-) represents the number of carbon atoms in a given  $i$ -th fuel species,  $h_i$  (-) represents the number of hydrogen atoms in a given  $i$ -th fuel species, while  $o_i$  (-) represents the number of oxygen atoms in a given  $i$ -th fuel species. In the equations 3.119 and 3.120,  $x_{O_2, \text{fresh}}$  (-) represents the mass fraction of  $O_2$  in the fresh charge, while  $x_{N_2, \text{fresh}}$  (-) represents the mass fraction of  $N_2$  in the fresh charge. The mass fractions of  $N_2$ ,  $CO_2$  and  $H_2O$  in the combustion products can be calculated from the following equations:

$$x_{FV, \text{comb}} = \frac{1}{1 + AF_{\text{stoich}}} \quad (3.121)$$

$$x_{CO_2, CP} = (1 - x_{N_2, CP}) \cdot \left( \frac{n_{CO_2} \cdot M_{CO_2}}{n_{CO_2} \cdot M_{CO_2} + n_{H_2O} \cdot M_{H_2O}} \right) \quad (3.122)$$

$$x_{N_2, CP} = (1 - x_{FV, \text{comb}}) \cdot (1 - 0.232) \quad (3.123)$$

$$x_{H_2O, CP} = 1 - x_{N_2, CP} - x_{CO_2, CP} \quad (3.124)$$

In the equations given above,  $x_{FV, \text{comb}}$  (-) represents the mass fraction of fuel blend that is involved in the stoichiometric combustion process,  $x_{N_2, CP}$  (-) represents the mass fraction of  $N_2$  in the combustion products,  $x_{CO_2, CP}$  (-) represents the mass fraction of  $CO_2$  in the combustion products,  $n_{CO_2}$  (kmol) represents the overall amount of  $CO_2$  in the combustion products,  $M_{CO_2}$  (kg/kmol) represents the molar mass of  $CO_2$ ,  $n_{H_2O}$  (kmol) represents the overall amount of  $H_2O$  in the combustion products,  $M_{H_2O}$  (kg/kmol) represents the molar mass of  $H_2O$ , while  $x_{H_2O, CP}$  (-) represents the mass fraction of  $H_2O$  in the combustion products. The amount of  $CO_2$  and  $H_2O$  in the combustion products of a fuel blend are calculated with the following equations:

$$n_{CO_2} = y_{\text{methFV}} \cdot n_{CO_2, \text{methane}} + (1 - y_{\text{methFV}}) \cdot n_{CO_2, n\text{-heptane}} \quad (3.125)$$

$$n_{H_2O} = y_{\text{methFV}} \cdot n_{H_2O, \text{methane}} + (1 - y_{\text{methFV}}) \cdot n_{H_2O, n\text{-heptane}} \quad (3.126)$$

$$n_{CO_2, i} = c_i \quad (3.127)$$

$$n_{\text{H}_2\text{O},i} = \frac{h_i}{2} \quad (3.128)$$

In the equations given above,  $n_{\text{CO}_2,\text{methane}}$  (kmol) represents the amount of  $\text{CO}_2$  in the combustion products that is a result of stoichiometric combustion of methane,  $n_{\text{CO}_2,\text{n-heptane}}$  (kmol) represents the amount of  $\text{CO}_2$  in the combustion products that is a result of stoichiometric combustion of n-heptane,  $n_{\text{H}_2\text{O},\text{methane}}$  (kmol) represents the amount of  $\text{H}_2\text{O}$  in the combustion products that is a result of stoichiometric combustion of methane, while  $n_{\text{H}_2\text{O},\text{n-heptane}}$  (kmol) represents the amount of  $\text{H}_2\text{O}$  in the combustion products that is a result of stoichiometric combustion of n-heptane. These values are calculated based on the number of carbon or hydrogen atoms in a given fuel species, as is presented for an arbitrary fuel species (denoted as  $i$ ) in the equations 3.127 (for  $\text{CO}_2$ ) and 3.128 (for  $\text{H}_2\text{O}$ ). In the equations 3.127 and 3.128,  $n_{\text{CO}_2,i}$  (kmol) represent the amount of  $\text{CO}_2$  in the combustion products for a stoichiometric combustion of a given  $i$ -th fuel species, while  $n_{\text{H}_2\text{O},i}$  (kmol) represent the amount of  $\text{H}_2\text{O}$  in the combustion products for a stoichiometric combustion of a given  $i$ -th fuel species.

Now the mass fractions of the initial species can be calculated from the following equations:

$$x_{\text{FV},\text{n-heptane}} = (1 - x_{\text{methFV}}) \cdot x_{\text{FV},\text{fresh}} \cdot (1 - x_{\text{CP}}) \quad (3.129)$$

$$x_{\text{FV},\text{methane}} = x_{\text{methFV}} \cdot x_{\text{FV},\text{fresh}} \cdot (1 - x_{\text{CP}}) \quad (3.130)$$

$$x_{\text{O}_2} = x_{\text{O}_2,\text{fresh}} \cdot (1 - x_{\text{CP}}) \quad (3.131)$$

$$x_{\text{N}_2} = x_{\text{N}_2,\text{fresh}} \cdot (1 - x_{\text{CP}}) + x_{\text{N}_2,\text{CP}} \cdot x_{\text{CP}} \quad (3.132)$$

$$x_{\text{CO}_2} = x_{\text{CO}_2,\text{CP}} \cdot x_{\text{CP}} \quad (3.133)$$

$$x_{\text{H}_2\text{O}} = x_{\text{H}_2\text{O},\text{CP}} \cdot x_{\text{CP}} \quad (3.134)$$

In the equations given above,  $x_{\text{FV},\text{n-heptane}}$  (-) represents the mass fraction of  $\text{C}_7\text{H}_{16}$  in the gas mixture,  $x_{\text{CP}}$  (-) represents the mass fraction of combustion products in the gas mixture,  $x_{\text{FV},\text{methane}}$  (-) represents the mass fraction of  $\text{CH}_4$  in the gas mixture,  $x_{\text{O}_2}$  (-) represents the mass fraction of  $\text{O}_2$  in the gas mixture,  $x_{\text{N}_2}$  (-) represents the mass fraction of  $\text{N}_2$  in the gas

mixture,  $x_{\text{CO}_2}$  (-) represents the mass fraction of  $\text{CO}_2$  in the gas mixture, while  $x_{\text{H}_2\text{O}}$  (-) represents the mass fraction of  $\text{H}_2\text{O}$  in the gas mixture.

In the constant volume reactor calculation subroutine, thermodynamic state and species calculations are performed for every calculation time step and the following values are stored in the results vector at the end of the time step:

1. Time
2. Temperature
3. Pressure
4. Energy released
5. Species mass fractions ( $\text{C}_7\text{H}_{16}$ ,  $\text{CH}_4$ ,  $\text{O}_2$ ,  $\text{N}_2$ ,  $\text{CO}_2$ ,  $\text{H}_2\text{O}$ ,  $\text{CO}$ ,  $\text{HC}$ )
6. 1<sup>st</sup> derivative of temperature
7. 2<sup>nd</sup> derivative of temperature

Thermodynamic state (pressure and temperature) are calculated with the adiabatic constant volume reactor, which assumes that there is no heat transfer between the gaseous mixture and the surrounding and that the domain does not change in volume. This means there is no exchange in work between the domain and its surrounding.

Since this is a close system there is no mass transfer between the domain and its surrounding. The temperature derivative is derived from the energy balance equation (1<sup>st</sup> law of thermodynamics) in the following way:

$$\frac{dQ}{dt} = \frac{dU}{dt} + p \frac{dV}{dt} \rightarrow \frac{dU}{dt} = m \cdot \left( \sum_j \frac{dx_j}{dt} \cdot u_j + \sum_j x_j \cdot \frac{du_j}{dt} \right) = 0 \quad (3.135)$$

In the equation given above, subscript  $j$  denotes species. The change in a particular species  $j$  mass fraction and internal energy can be calculated from the following equations:

$$x_j = \frac{1}{\rho} \cdot M_j \cdot c_j \rightarrow \frac{dx_j}{dt} = \frac{1}{\rho} \cdot M_j \cdot \frac{dc_j}{dt} \quad (3.136)$$

$$u_j = u_j(T) \rightarrow \frac{du_j}{dt} = \frac{\partial u_j}{\partial T} \cdot \frac{dT}{dt} = c_{v,j} \cdot \frac{dT}{dt} \quad (3.137)$$

In the equations given above,  $M_j$  (kg/kmol) represents the molar mass of the  $j$ -th species,  $c_j$  (kmol/m<sup>3</sup>) represents the concentration of the  $j$ -th species, while  $c_{v,j}$  (J/kgK) represents the

specific heat capacity of the  $j$ -th species at constant volume. Finally, the temperature derivative can be calculated from the following equation:

$$\frac{dT}{dt} = \frac{1}{\rho \cdot c_{v,\text{mean}}} \cdot \sum_j M_j \cdot u_j \cdot \frac{dc_j}{dt} \quad (3.138)$$

$$c_{v,\text{mean}} = \sum_j x_j \cdot c_{v,j} \quad (3.139)$$

Term  $\frac{dc_j}{dt}$  (kmol/m<sup>3</sup>s) represents the total production rate of the  $j$ -th species. In the equations given above,  $c_{v,\text{mean}}$  (J/kgK) represents the specific heat capacity at constant volume of the entire mixture, while  $x_j$  (-) represents the mass fraction of the  $j$ -th species. The internal energy and production rates of the species, as well mixture density and its specific heat capacity at constant volume are calculated from the CHEMKIN<sup>TM</sup> subroutines. Thorough description of the equations used in calculating a particular thermodynamic property of the  $j$ -th species and the overall gaseous mixture thermodynamic properties, as well as equations used in the chemical reaction rate calculations can be found in [97]. In this thesis, only the calculation of important thermodynamic properties and species production rate calculation according to [97] will be presented.

All thermodynamic properties can be calculated from the standard state molar enthalpy, entropy and specific heat capacity at constant pressure, which are calculated from the following equations [97]:

$$\frac{h_{m,j}^o}{RT} = a_{1,j} + \frac{a_{2,j}}{2}T + \frac{a_{3,j}}{3}T^2 + \frac{a_{4,j}}{4}T^3 + \frac{a_{5,j}}{5}T^4 + \frac{a_{6,j}}{T} \quad (3.140)$$

$$\frac{s_{m,j}^o}{R} = a_{1,j} \ln T + a_{2,j}T + \frac{a_{3,j}}{2}T^2 + \frac{a_{4,j}}{3}T^3 + \frac{a_{5,j}}{4}T^4 + a_{7,j} \quad (3.141)$$

$$\frac{c_{p,m,j}^o}{R} = a_{1,j} + a_{2,j}T + a_{3,j}T^2 + a_{4,j}T^3 + a_{5,j}T^4 \quad (3.142)$$

In the equations given above,  $h_{m,j}^o$  (J/kmol) represents the standard state molar enthalpy of the  $j$ -th species,  $R$  (J/kmolK) represents the universal gas constant,  $s_{m,j}^o$  (J/kmol) represents the standard state molar entropy of the  $j$ -th species,  $c_{p,m,j}^o$  (J/kmolK) represents the standard state

molar heat capacity at constant pressure of the  $j$ -th species, while  $a_1, a_2, a_3, a_4, a_5, a_6$  and  $a_7$  represent the thermodynamic data coefficients and are given for every species through the input data. Internal energy and specific heat capacity at constant volume of the  $j$ -th species are calculated with the following equations [97]:

$$c_{v,j}^o = \frac{c_{v,m,j}^o}{M_j} \quad (3.143)$$

$$c_{v,m,j}^o = c_{p,m,j}^o - R \quad (3.144)$$

$$u_j^o = \frac{u_{m,j}^o}{M_j} \quad (3.145)$$

$$u_{m,j}^o = h_{m,j}^o - RT \quad (3.146)$$

In the equations given above,  $u_{m,j}^o$  (J/kmol) represents the standard state molar internal energy of the  $j$ -th species, while  $c_{v,m,j}^o$  (J/kmolK) represents the standard state molar heat capacity at constant volume of the  $j$ -th species. The production rate of the  $j$ -th species can be calculated from the following equation [97]:

$$\frac{dc_j}{dt} = \sum_k r_{j,k} \cdot \omega_k \quad (3.147)$$

The above equation presents the production rate of the  $j$ -th species (kmol/m<sup>3</sup>s), where  $r_{j,k}$  (-) represents the stoichiometric coefficient of the  $j$ -th species in  $k$ -th reaction, while  $\omega_k$  (kmol/m<sup>3</sup>s) represents the reaction rate of the  $k$ -th reaction. Released heat at the end of time step is calculated from the following expression:

$$Q_R = U_{\text{init}} - U(t) \quad (3.148)$$

In the equation given above,  $Q_R$  (J) represents the heat released at the end of the time step,  $U_{\text{init}}$  (J) represent the initial internal energy of the mixture, while  $U(t)$  (J) represent the internal energy of the mixture at time  $t$ . Temperature derivatives are calculated with the central difference scheme at the end of calculation.

The calculation duration and the time step are defined in the input file. Ignitable gaseous mixture that is at elevated pressure and temperature will eventually ignite and therefore the task of presetting the calculation duration and time step is rather challenging and ranges depending on the application. In this specific application, where this code was used to create the chemical tables (ignition delay times and reaction rate times) for the application in an IC engine combustion calculation, the calculation duration was set to  $0.2\text{ s}$ . Such calculation duration time was chosen as this is more than the high-pressure cycle (IVC to exhaust valve closure (EVO)) time at engine speed of 600 rpm, and in the IC engine calculations we are only interested if the mixture will ignite in this time span.

In order to speed-up the calculation process, the calculation cycle is stopped once equilibrium conditions are reached. In order for the calculation to be stopped the following two conditions have to be satisfied:

$$T(t) = T_{\text{init}} + 10 \quad (3.149)$$

$$\left[ \frac{T(t)}{T(t-\Delta t)} - 1 \right] \leq 1 \cdot 10^{-9} \quad (3.150)$$

The idea behind the stop criteria is:

1. for a combustion event to occur the temperature has to increase by at least 10 K (expression 3.149);
2. the temperature has remained approx. the same for two consecutive time steps thus indicating that the combustion event is finished (expression 3.150).

In the equations given above,  $T(t)$  (K) represent the temperature at the end of the current time step,  $T_{\text{init}}$  (K) represent the initial temperature of the mixture, while  $T(t-\Delta t)$  (K) represent the temperature at the end of the previous time step.

The initial time-step was set to  $1 \times 10^{-6}\text{ s}$ ; however, this code features a re-calculation option with even smaller time step if needed. The re-calculation with smaller time step (up to  $1 \times 10^{-9}\text{ s}$ ) is activated in the case when:

1. Ignition delay time is lower than the calculation time step.
2. An error occurred in the solver.

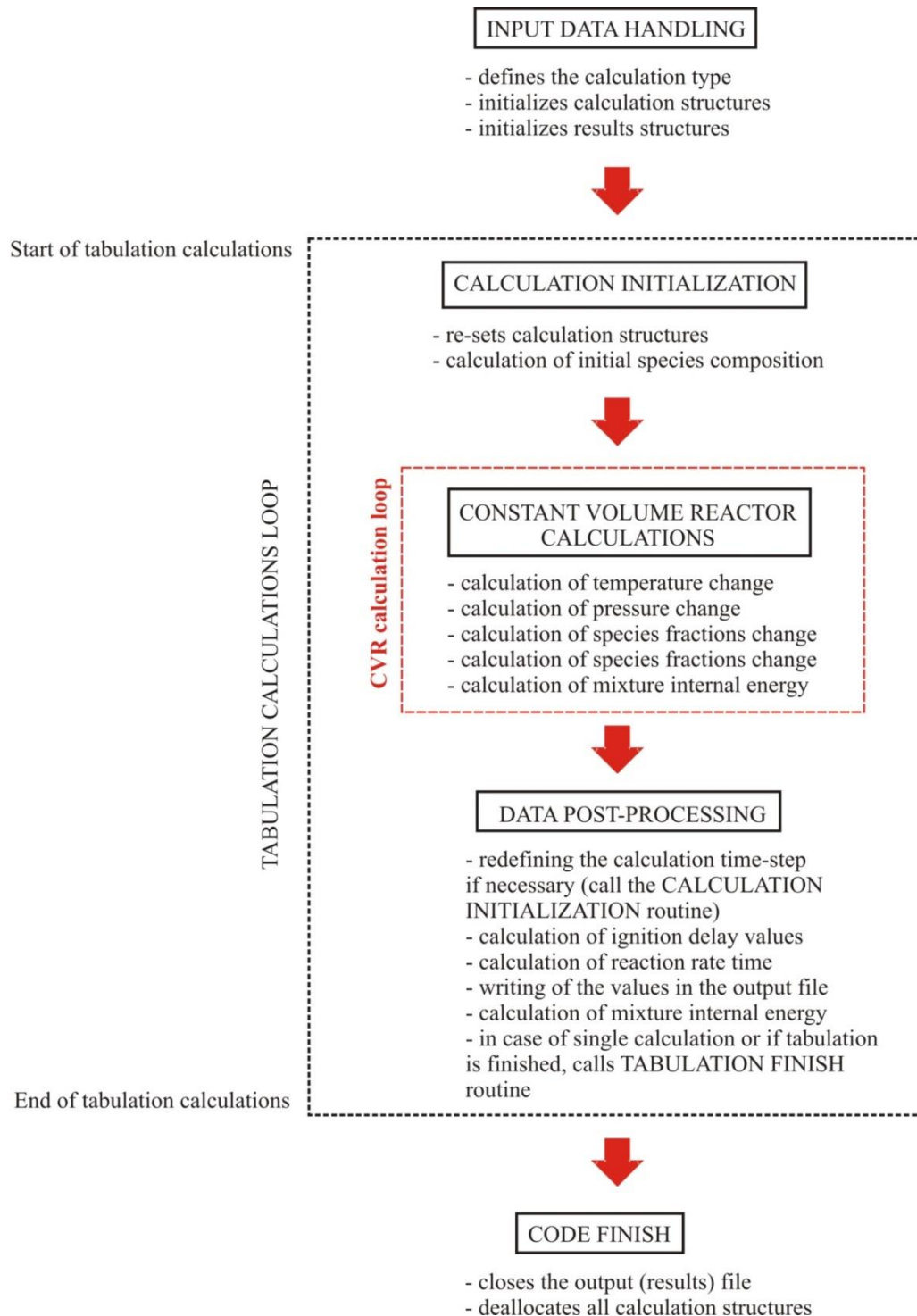


**Figure 48. Schematic of the 0-D chemistry tabulation code**

Once the gas mixture has reached its final state in which it is in chemical and thermodynamic equilibrium, the calculation is stopped and the post-processing sub-model is initiated. In this sub-model, the calculation results are analyzed and specific data regarding the ignition delay times and chemical reaction rate times are calculated and stored into the final output file.



Afterwards, in the case of multiple-calculations option, the procedure is repeated for every possible combination of the initial state and composition parameters, and in the end a chemical look-up table is created.

In the final subroutine (Code finish) the output file is closed and all opened structures are deallocated and tabulation code is exited. The schematic presentation of the 0-D tabulation code is given in Figure 48.

The methods of definition of the specific ignition delay times (low and high temperature), of the percentage of heat released in the low temperature combustion event and of the chemical reaction rate are presented in the next two chapters.

### 3.4.3. Autoignition times definition

The autoignition process has its own characteristic time, which is called the ignition delay time [84]. In DI-CI engines, ignition delay time is referred to as the time that elapses from the start of injection to the start of combustion and consists of a physical part and a chemical part. In the 0-D combustion model presented in this thesis, the physical part of the ignition delay is modeled with the spray development phenomena, while the chemical part of the ignition delay is calculated by using the specially developed chemistry tables. In this section of the thesis the method of calculating the low temperature ignition delay time, the percentage of energy released in the low temperature combustion event and the autoignition delay time (can be referred to as high temperature or main ignition event) is presented.

By comparing a combustion process that features the LTHR event (Figure 49), and a combustion process that does not feature the LTHR event (Figure 50), it can be seen that in the LTHR case energy and ROHR traces reveal a characteristic 2-stage ignition shape. In such case the initial bump in ROHR curve and a corresponding slight energy and temperature increase that occur at low temperatures are results of the LTHR event. The second, larger bump in the ROHR curve and corresponding significant temperature increase is a result of the main combustion event. Normalized released energy traces in Figure 49 and Figure 50 clearly show that LTHR event accounts for only a small fraction of the energy that is released in the entire combustion event.

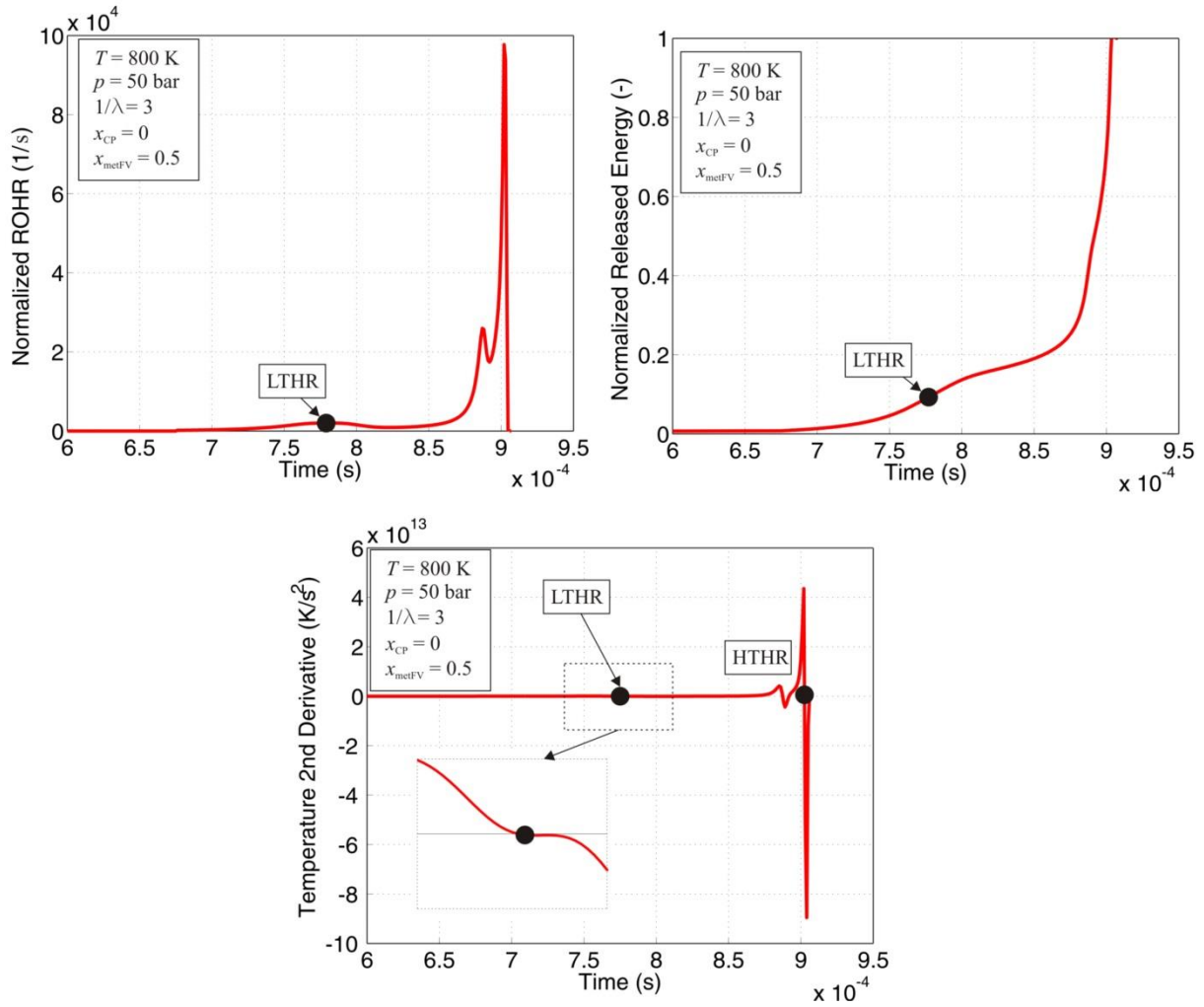


**Figure 49. Normalized released energy, ROHR and 2<sup>nd</sup> derivative of temperature traces for a case that exhibits LTHR**

Low temperature combustion event also referred to as the cool flame occurs at elevated pressures and in the temperature range from 500-910 K, depending on the fuel composition and pressure level [98], [99]. Even though cool flame event causes almost negligible heat release, followed by moderate temperature and pressure increase, it is important to appropriately account for this event as it can considerably accelerate the main ignition event. In this way, spray ignition (compression ignition phenomenon) and autoignition in the end gas which leads to engine knock can be appropriately modeled.

In order to appropriately determine the time when a combustible mixture ignites, an ignition expression had to be determined. In most of the literature, ignition is defined as the moment when the first flame is noticed [84]. From the mathematical point of view, this can be seen as the time when a considerable increase in the pressure and temperature occurs. According to [100], there are three basic approaches how ignition time can be determined:

1. Ignition occurs after a predefined temperature or pressure increase is reached.

2. Ignition occurs when temperature inflexion occurs.
3. Ignition occurs after a defined fraction of intermediate species has been formed.

In this thesis, both the LTHR and main ignition times are determined according to the approach that was taken in [127] and [128], where ignition time was determined according to the temperature inflection criteria that can be expressed as:

$$\text{sign}\left(\frac{d^2T}{dt^2}\right)_t = -\text{sign}\left(\frac{d^2T}{dt^2}\right)_{t-\Delta t} \quad (3.151)$$

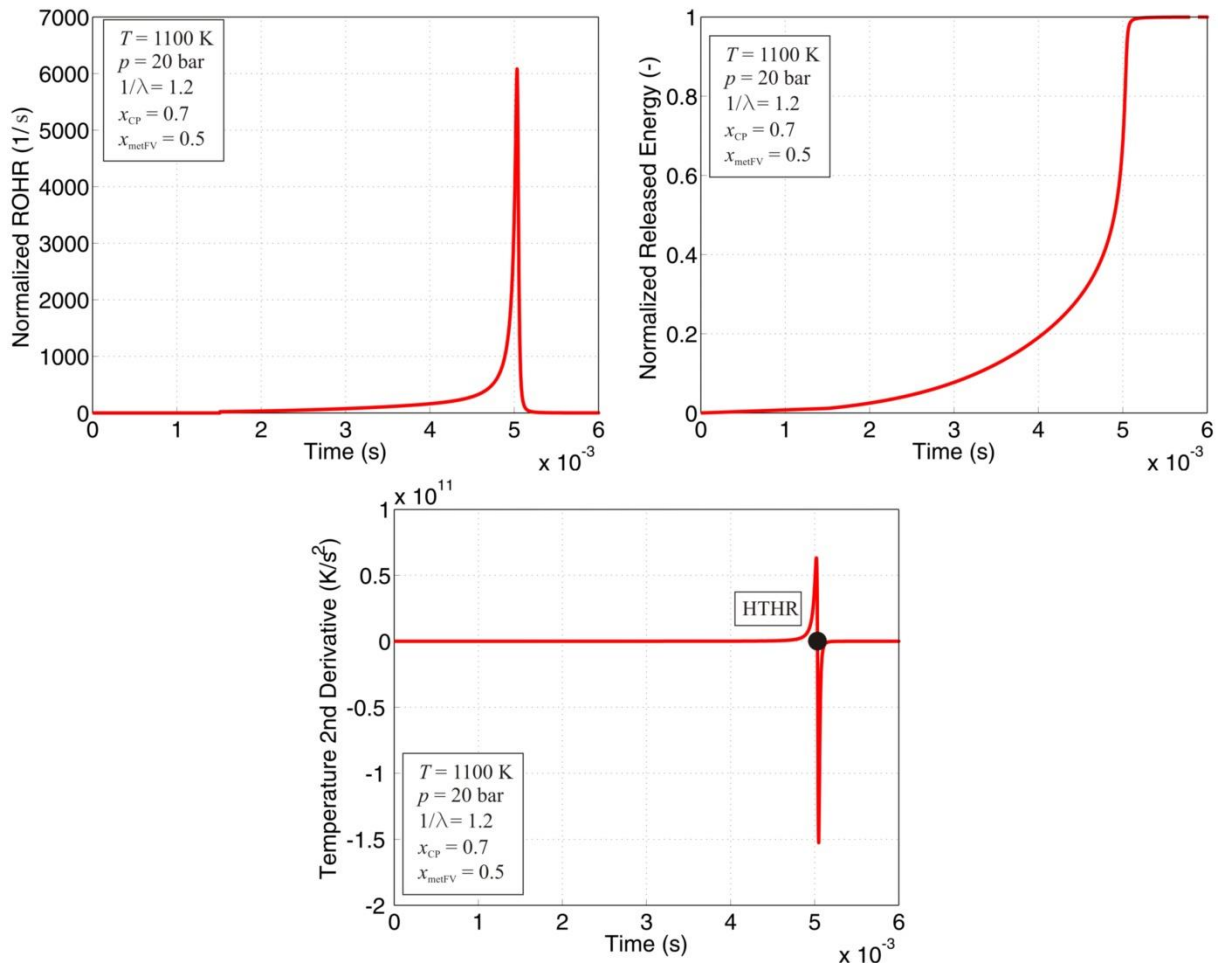


**Figure 50. Normalized released energy, ROHR and 2<sup>nd</sup> derivative of temperature traces for a case that does not exhibits LTHR**

Ignition times are defined during the post-processing step after the calculation, for a given case (set of initial conditions), is finished. The above criterion (equation 3.135) is used to examine the slope of the temperature curve and it triggers specific events once the slope changes. For a given case (for example Figure 49), temperature inflection event might be triggered a number of times. In case that the inflection has been triggered in the low

temperature range (set to the maximum value of 1100 K) and that its corresponding normalized released energy is below 15%, such ignition event is LTHR and its specific time and normalized released energy are stored as LTHR time and as the normalized energy released in the LTHR event. Main ignition event (HTHR) is marked as the first next inflection event that has occurred; first inflection event that cannot be characterized as the LTHR event.

### ***Influence of the initial state and composition on the autoignition***

In this chapter of the thesis, the influence of the initial homogeneous mixture state and charge composition on the autoignition process is presented. As chemical kinetics and mechanism development was not the primary focus of this work, only a brief overview of the major trends accompanied with a short discussion regarding the effects of the state and composition on the ignition delay time is given in this thesis.

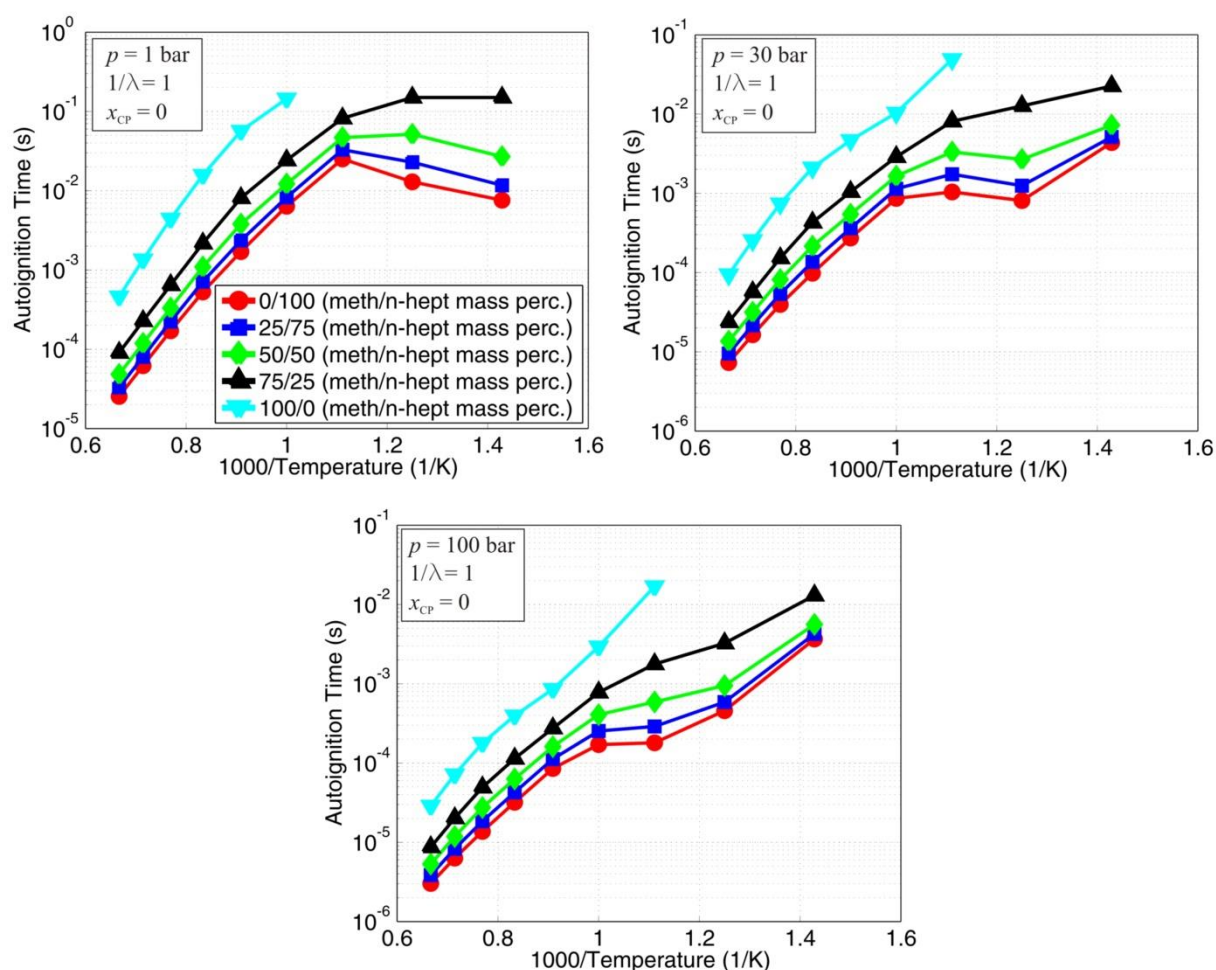


**Figure 51. Influence of temperature on autoignition time for various n-heptane/methane fuel blends at three different pressure levels**

The y-axis scale on all the figures presented in this section is logarithmic as this is characteristic for the autoignition delay time presentation.

The figure given above (Figure 51) presents the influence of temperature on the autoignition time for various methane/n-heptane fuel blends at three different pressure levels (1 bar, 30 bar and 100 bar), and at single equivalence ratio and combustion mass fraction levels.

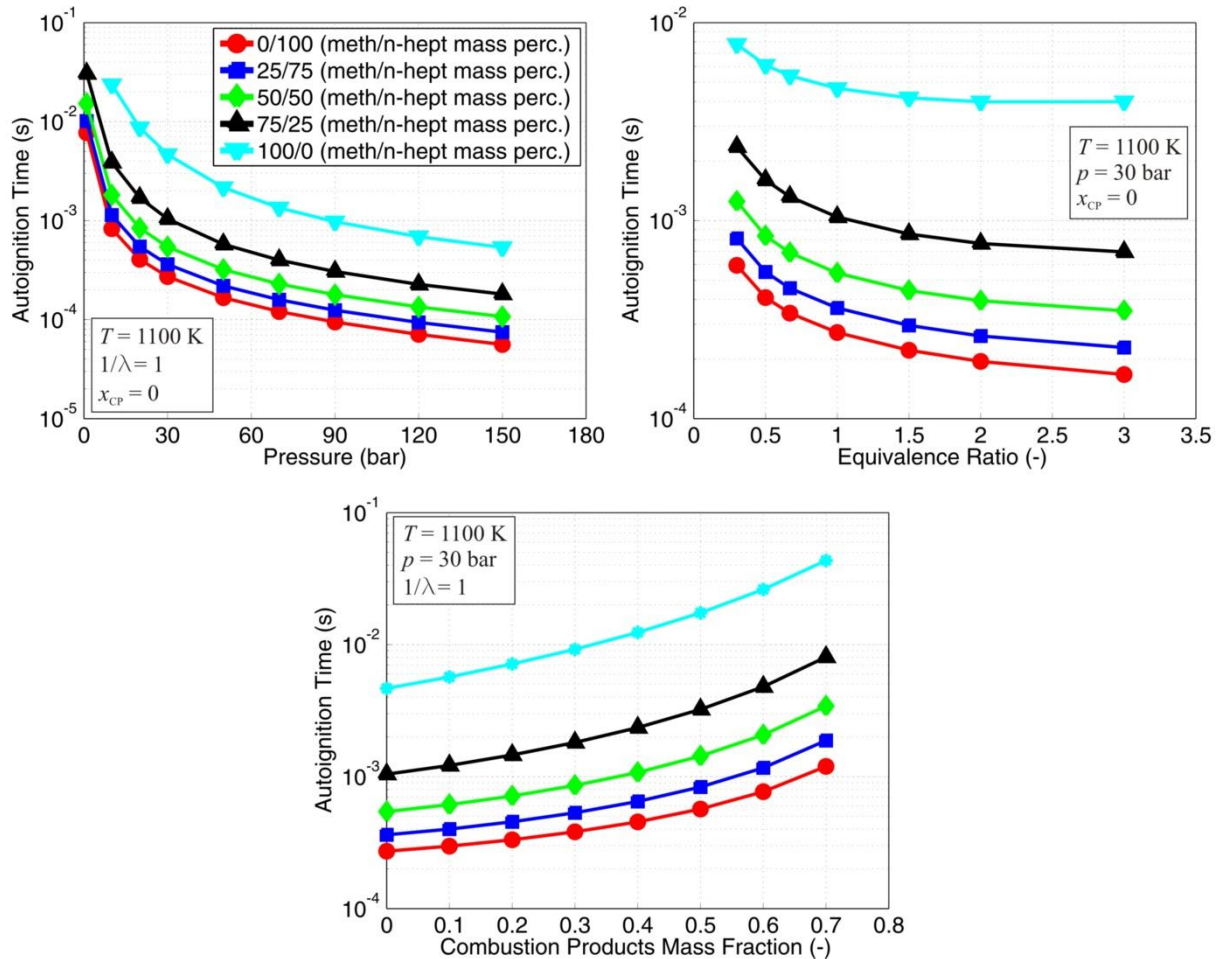


**Figure 52. Influence of pressure, equivalence ratio and combustion products mass fraction on autoignition time for various n-heptane/methane fuel blends**

It is evident that the autoignition time decreases as the n-heptane amount increases regardless of the pressure level. It can also be seen that the addition of n-heptane introduces the so called negative temperature coefficient (NTC) region which occurs at progressively lower n-heptane fractions in the blend as the pressure is increased. The NTC region is characteristic for more complex hydrocarbons [102], and is a result of the fact that their reaction mechanism includes low and high temperature branches [100], [102], [103].

Figure 52 presents the influence of the pressure, equivalence ratio and combustion products mass fraction on the autoignition time for various methane/n-heptane fuel blends, and at the temperature of 1100 K.

This figure reveals that the ignition time decreases as the n-heptane amount increases regardless of the pressure, equivalence ratio or combustion mass fraction level.

Autoignition time decreases as the pressure and equivalence ratio increase for all considered methane/n-heptane fuel blends. On the other hand, as the combustion products mass fraction is increased, autoignition time is increased for all considered methane/n-heptane fuel blends.

This is a result of the fact that the inert combustion products slow down chemical reactions.

#### 3.4.4. Reaction rate time definition

In the spray combustion calculation, the burned mass flux (expression 3.102) is defined by the availability of oxygen and fuel mass, and the size of the calculation time-step and chemical reaction rate time,  $\tau_{\text{reac}}$  (s). The chemical reaction rate time is taken from the chemistry look-up tables (expression 3.103), and its derivation will be explained in this chapter.

Chemical reaction rate time could be defined as the global characteristic reaction rate time; i.e. the time it takes for the current reactants to turn into the equilibrium state products. In the work presented in this thesis the chemical reaction rate time is defined as the time that elapses from 10%-90% of the fuel mass burned (energy released):

$$\tau_{\text{reac}} = \frac{\Delta t_{10-90}}{0.8} \quad (3.152)$$

$$\Delta t_{10-90} = t_{90} - t_{10} \quad (3.153)$$

In the equations given above,  $\tau_{\text{reac}}$  (s) represents the reaction rate time that is stored in the chemistry tables for specific conditions,  $\Delta t_{10-90}$  (s) represents the time elapsed between 10% and 90% of the fuel burned (energy released) for specific conditions,  $t_{90}$  (s) represents the time when 90% of the energy has been released for specific conditions, while  $t_{10}$  (s) represents the time when 10% of the energy has been released for specific conditions.

Figure 53 presents the normalized released energy traces for two cases; one that features LTHR event (left figure) and one that does not feature LTHR event (right figure). Also, in this figure (Figure 53), specific times and expressions have been marked. As can be seen (Figure 53), in the case that LTHR event occurs, corresponding 10% and 90% of the energy released is calculated for the remaining part of the released energy that corresponds to the main

combustion event. Since in the combustion model it is considered that if LTHR occurs, tabulated fraction of energy is released within a single time-step, only the characteristic reaction rate time of the main combustion event needs to be calculated and hence such approach was used.

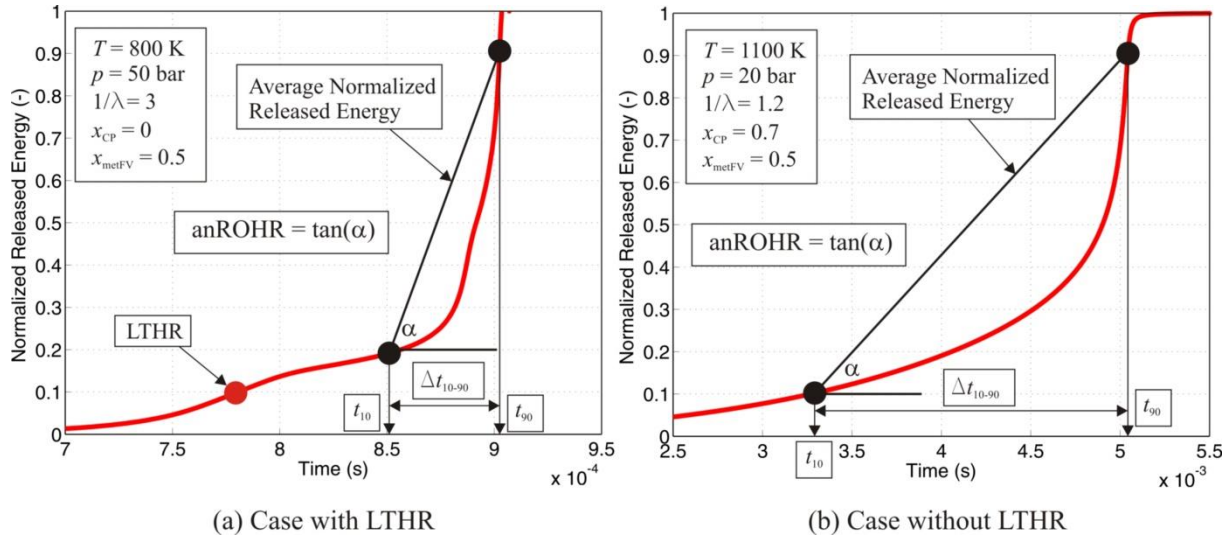


**Figure 53. Normalized released energy traces for a case with LTHR event (left figure) and a case without LTHR event (right figure)**

The average reaction rate; i.e. average normalized rate of heat release from 10% to 90% of energy released is denoted as *anROHR* (1/s), and can be calculated with the following equation:

$$anROHR = \frac{1}{\tau_{\text{reac}}} \quad (3.154)$$

The term *anROHR* is the gradient of the average normalized released energy curve (Figure 53). This term (*anROHR*) will be used in the verification of the presented reaction rate time definition. The approach that was used to verify the selected chemical reaction rate time definition is presented in Figure 54, while the data used in the verification process are given in Table 6. Chemical reaction rate time calculation was verified on 9 characteristic cases, which are presented in Table 6. For every case 3 characteristic points, one below 30% of energy released, one around 50% of energy released and one around or above 60% of energy released were selected (Table 6). Therefore, the final validation matrix consists of 27 points.

The definition of the chemical reaction rate time says that it represents the characteristic time during which initial reactants are converted into equilibrium state product. This means that if the combustion process is frozen at a particular point (left figure in Figure 54), the average



reaction rate of the remaining part of the combustion process has to be approximately similar to the average reaction rate of the entire combustion process when it is initiated with the conditions (state and mixture composition) at that point of interest (right figure in Figure 54).

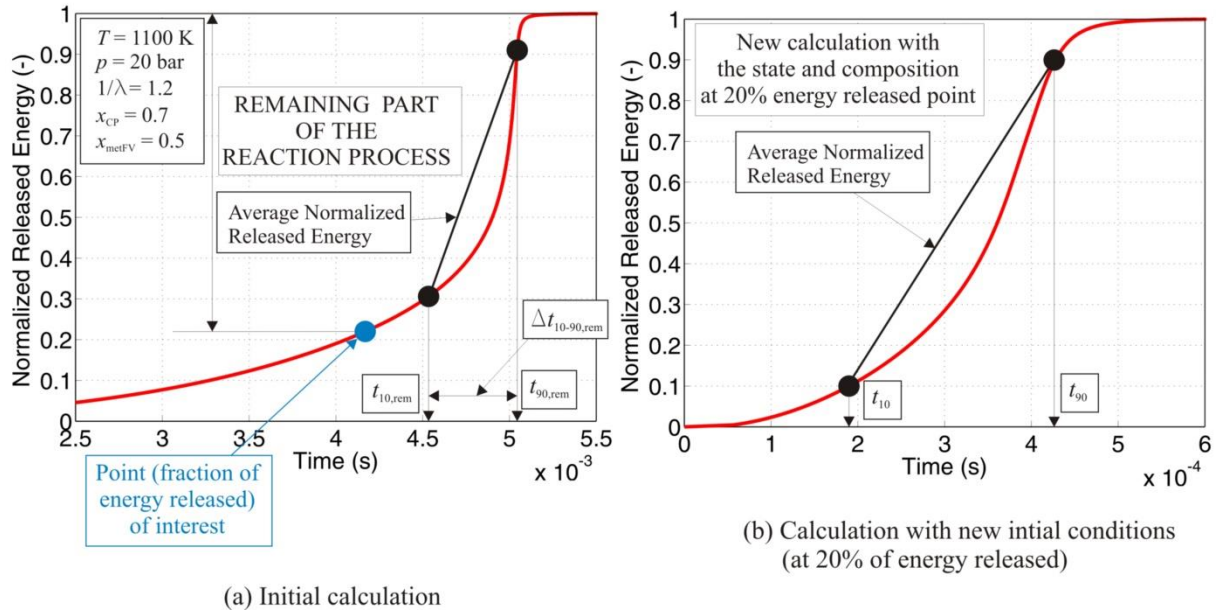


**Figure 54. Verification principle for the chemical reaction rate time calculation approach**

The calculation of the reaction rate time of the remaining part of the combustion (reaction) process can be described through the following steps (Figure 54):

1. Point of interest is chosen.
2. Fraction of energy released in the point of interest is defined.
3. 10% and 90% of energy released in the remaining process (right figure in Figure 54) are calculated and the reaction rate time of the remaining process is defined.

After that the average normalized ROHR,  $anROHR_{rem}$  (1/s) of the remaining combustion process is calculated in the following way:

$$anROHR_{rem} = \frac{1}{\tau_{reac, rem}} \quad (3.155)$$

$$\tau_{reac, rem} = \frac{\Delta t_{10-90, rem}}{0.8} \quad (3.156)$$

$$\Delta t_{10-90, rem} = t_{90, rem} - t_{10, rem} \quad (3.157)$$



In the equations given above,  $\tau_{\text{reac,rem}}$  (s) represents the characteristic reaction rate time of the remaining part of the combustion process,  $\Delta t_{10-90,\text{rem}}$  (s) represents the time elapsed from 10% to 90% of energy released in the remaining part of the combustion process,  $t_{90,\text{rem}}$  (s) represents the time when 90% of energy has been released in the remaining part of the combustion process, while  $t_{10,\text{rem}}$  (s) represents the time when 10% of energy has been released in the remaining part of the combustion process.

**Table 6. Data for verification of the chemical reaction rate time calculation approach**

Temperature (K)	Pressure (bar)	Equivalence ratio (-)	Combustion products mass fraction (-)	Methane mass fraction in the fuel blend (-)	Point of interest (energy released fraction)
<b>1100</b>	40	2.5	0	1	0.22
					0.4
					0.59
<b>1600</b>	70	1	0.4	1	0.19
					0.46
					0.82
<b>1300</b>	20	0.3	0.7	1	0.15
					0.43
					0.81
<b>800</b>	30	1.5	0	0	0.2
					0.45
					0.72
<b>1400</b>	35	1	0.2	0	0.15
					0.48
					0.79
<b>1200</b>	15	0.5	0.5	0	0.12
					0.5
					0.76
<b>800</b>	50	3	0	0.5	0.15
					0.5
					0.7
<b>1000</b>	30	1	0.5	0.5	0.2
					0.5
					0.74
<b>1100</b>	20	1.2	0.7	0.5	0.2
					0.5
					0.76

After the average normalized ROHR of the remaining combustion process is calculated, new calculation with the initial conditions (state and mixture composition) set according to the point of interest is performed and the average normalized ROHR,  $anROHR$  (1/s) for the corresponding combustion process is calculated; this is graphically presented in the Figure 54 (right figure). The procedure is performed for all 9 characteristic cases and corresponding 27 points. Finally,  $anROHR$  and  $anROHR_{rem}$  are compared for all considered 27 verification cases and the final verification results are presented in Figure 55.

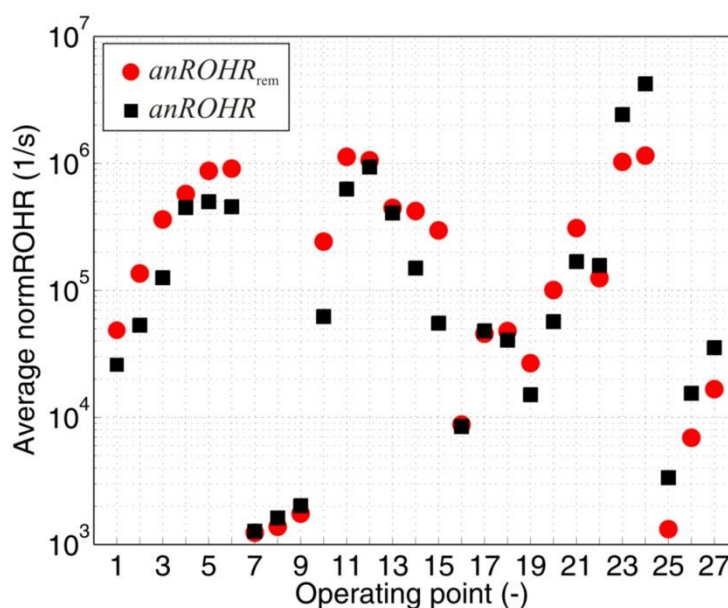


**Figure 55. Verification of the chemical reaction rate time calculation approach**

Figure 55 shows that there are slight differences between the corresponding  $anROHR_{rem}$  that describes the average progress of the reaction from the point of interest onwards, and  $anROHR$  that describes the average progress of the reaction for a calculation that was re-set with the initial conditions equal to the ones in the point of interest. Such small differences are expected and they are reasonable. One should bear in mind that by re-setting the initial conditions in the calculation of the corresponding  $anROHR$ , a pool of radicals that were created in the reaction process prior to the point of interest is completely neglected. These radicals can in some cases accelerate chemical reactions through chain branching & propagating reactions, while in the other they can decelerate chemical reactions through chain terminating reactions. The important conclusion that can be deduced from the verification process is that these differences are small and that the overall trends of change of average reaction rate times are well captured. This leads to the final conclusion that the approach is suitable for the calculation of the characteristic chemical reaction rate time.

### ***Influence of the initial state and composition on the chemical reaction rate***

In this chapter of the paper, the influence of the initial homogeneous mixture state and charge composition on the overall speed of the chemical reaction process is presented. As the chemical kinetics and mechanism development was not the primary focus of this work, only a brief overview of the major trends accompanied with a short discussion regarding the effects of the state and composition on the chemical reaction rate time is given in this thesis. The y-axis scale on all the figures presented in this section is logarithmic.

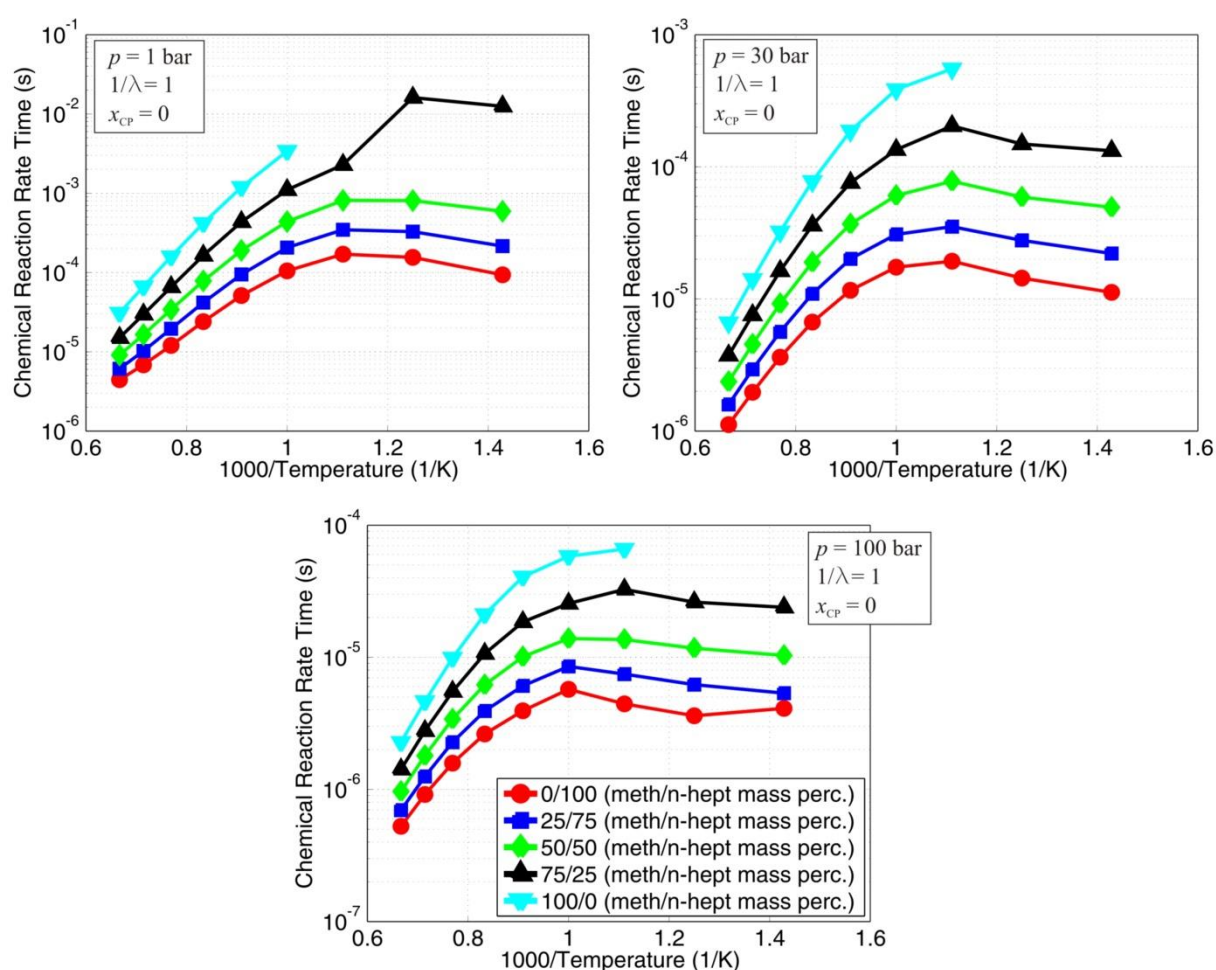


**Figure 56. Influence of temperature on chemical reaction rate time for various n-heptane/methane fuel blends at three different pressure levels**

Figure 56 presents the influence of temperature on the chemical reaction rate time for various methane/n-heptane fuel blends at three different pressure levels (1 bar, 30 bar and 100 bar), and at single equivalence ratio and combustion mass fraction levels. It is evident that the chemical reaction rate time decreases as the n-heptane amount increases regardless of the pressure level. It can also be seen that similarly as in the case with the autoignition time the

addition of n-heptane introduces the (NTC) region to the mixture. This is due to the occurrence of the LTHR event that leads to a shorter main combustion event that follows.

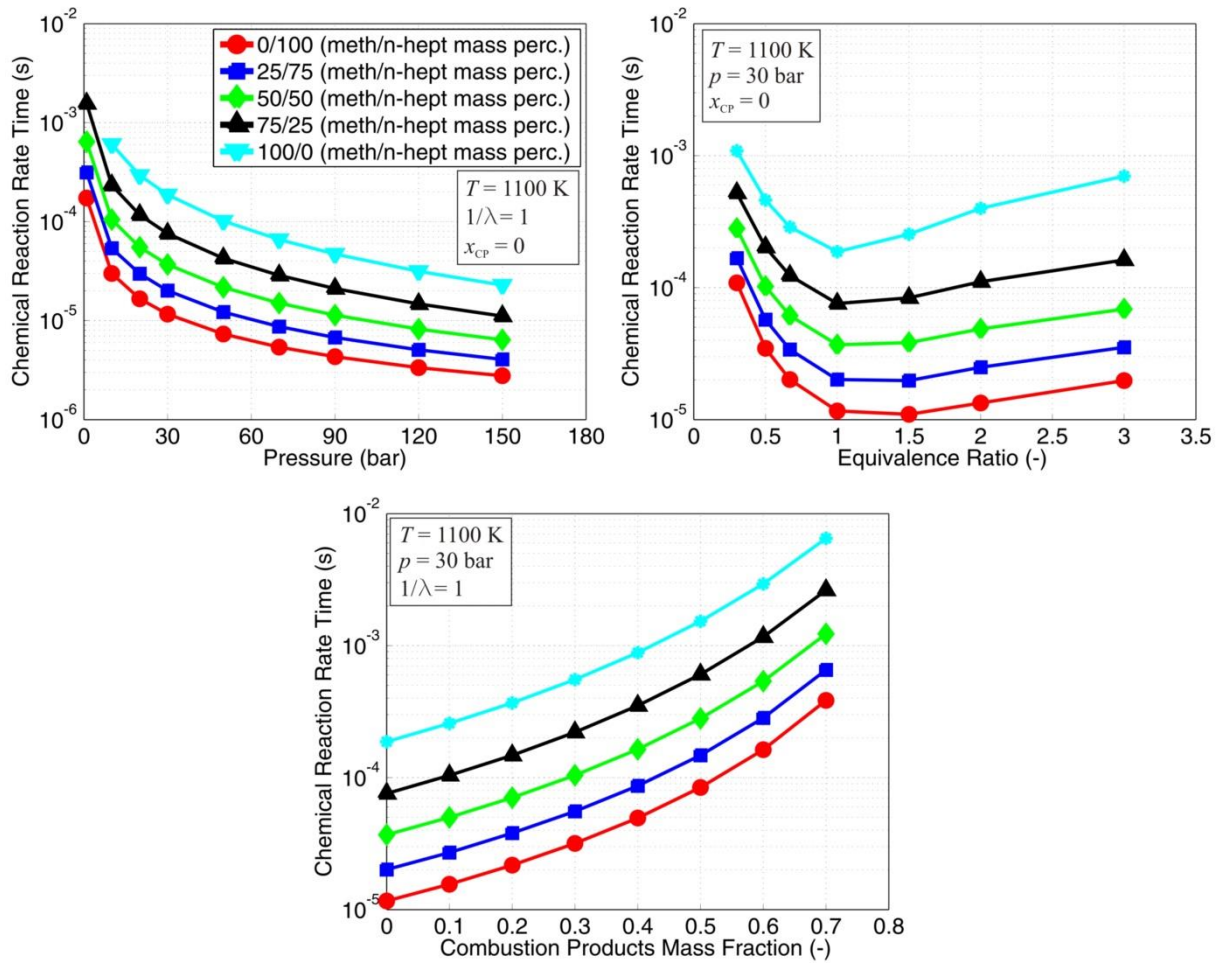


**Figure 57. Influence of pressure, equivalence ratio and combustion products mass fraction on chemical reaction rate time for various n-heptane/methane fuel blends**

Figure 57 presents the influence of pressure, equivalence ratio and combustion products mass fraction on the chemical reaction rate time for various methane/n-heptane fuel blends, and at the temperature of 1100 K. The figure reveals that the chemical reaction rate time decreases as the n-heptane amount increases regardless of the pressure, equivalence ratio or combustion mass fraction level. For all considered methane/n-heptane fuel blends, as the pressure increases, the chemical reaction rate time decreases, while as the combustion products fraction increases, the chemical reaction rate time increases. This increase is again a result of the fact that the inert combustion products slow down chemical reactions. For all considered methane/n-heptane fuel blends, as the equivalence ratio is increased from lean to stoichiometric region, the chemical reaction rate time is decreased and reaches a minimum

around stoichiometry. Afterwards as the equivalence ratio is further increased into the rich region, the chemical reaction rate time increases.

### **3.5. Flame propagation combustion modeling**

Since a considerable portion of the dual fuel combustion process is governed by the flame propagation through the premixed charge, it is important to appropriately model the flame propagation process. Moreover, as in the dual fuel combustion process flame is initiated at multiple locations within the combustion chamber, it is important to appropriately calculate the flame surface in the case when multiple flames propagate through the combustion chamber.

Since the flame propagates through the premixed mixture (fuel, air and combustion products), in the fundamental combustion literature [50]–[52], [85] such combustion process is referred to as the premixed combustion process and is typical for conventional SI engines. However, to distinguish between the initial premixed combustion phase which occurs in the spray combustion process and the premixed combustion driven by the flame propagation process, in this thesis term flame propagation will be used when describing combustion controlled by the flame propagation through the premixed mixture. In the next two sections, details regarding the physical phenomena of the flame propagation process and of the method of its modeling in 0-D conventional dual fuel combustion model are presented.

#### **3.5.1. Physical background**

According to [50], [51], turbulence is one of the most challenging problems in modern physics, and when turbulence and combustion are coupled the complexity of the entire problem rapidly increases. Therefore, in order to understand the physics behind a turbulent propagating flame, one first has to understand the physics behind a relatively simpler, but still complicated phenomenon called the laminar premixed flame.

##### ***Laminar propagating (premixed) flame***

The simplest way to describe the difference between a turbulent and a laminar flame would be that a laminar flame is a flame which occurs in a laminar flow field. From the physics standpoint, a laminar propagating flame (laminar premixed flame) can be viewed as a reaction wave that travels through the space (Figure 58). This wave propagates through the mixture with the laminar flame speed ( $S_L$  (m/s)), and the mixture that enters this wave consists of fuel and oxidizer (sometimes it also consists of a portion of combustion products), while the

mixture that exits the flame front consists of the burned and warm combustion products. Premixed laminar flame consists of the two characteristic zones [51], [85] (Figure 59):

1. Preheat zone.
2. Reaction zone.

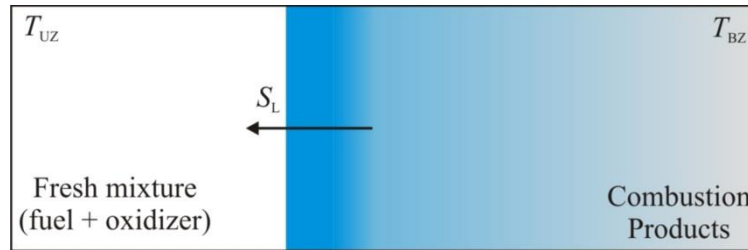


**Figure 58. Schematic of the laminar propagating (premixed) flame**

The laminar flame propagation process is controlled by two mechanisms [51], [85]:

1. Heat and mass transfer from the reaction zone upstream to the preheat zone which gradually increases the temperature in the preheat zone and eventually leads to the mixture ignition and burning in the reaction zone.
2. The chemical reactions in the reaction zone.

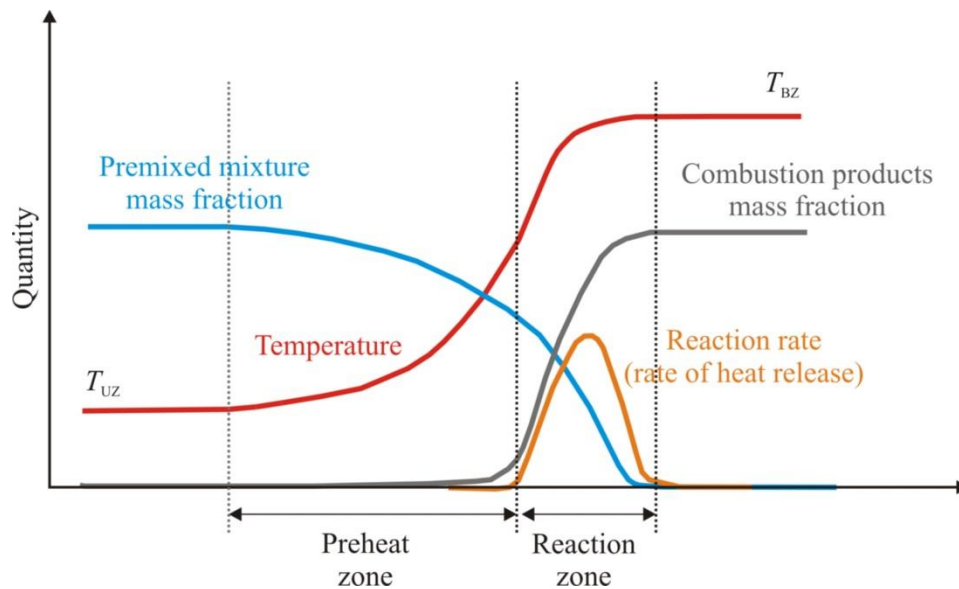


**Figure 59. Laminar propagating (premixed) flame structure; reproduced from [85]**

### ***Turbulent propagating (premixed) flame***

In the case of turbulent propagating flame, flame itself and consequently the burning rate are modified by the surrounding turbulent flow field, and likewise the turbulent flow field itself is modified by the combustion event. Combustion process is an energy source for the turbulent

flow field [50], [51], while at the same time it also decreases the level of turbulence as the Reynolds number decreases and viscosity increases (increase due to the temperature increase) [51]. Turbulent flow field, which is characterized by a large number of eddies of different sizes modifies the laminar flame structure. Smaller, more intense eddies enhance the mixing in the preheat zone [104] thus increasing the reaction rate, while larger eddies distort the flame front [104] causing it to have its characteristic “wrinkled” shape. By wrinkling the flame front, turbulence increases the overall flame front compared to the laminar flame thus increasing the burning rate. The mechanism that also leads to flame wrinkling is the local inhomogeneity in temperature and composition field in front of the propagating flame [32], [104].

The first explanation and conceptual model of the turbulent propagating (premixed) flame was given by Damkohler in 1940. According to Damkohler’s phenomenological model, in the case of a turbulent propagating flame, each point of the flame propagates with the laminar flame speed same as in the case of a laminar propagating flame. However, the difference between the two cases arises in the overall flame surface which is larger for the case of the turbulent flame due to its wrinkled shape.

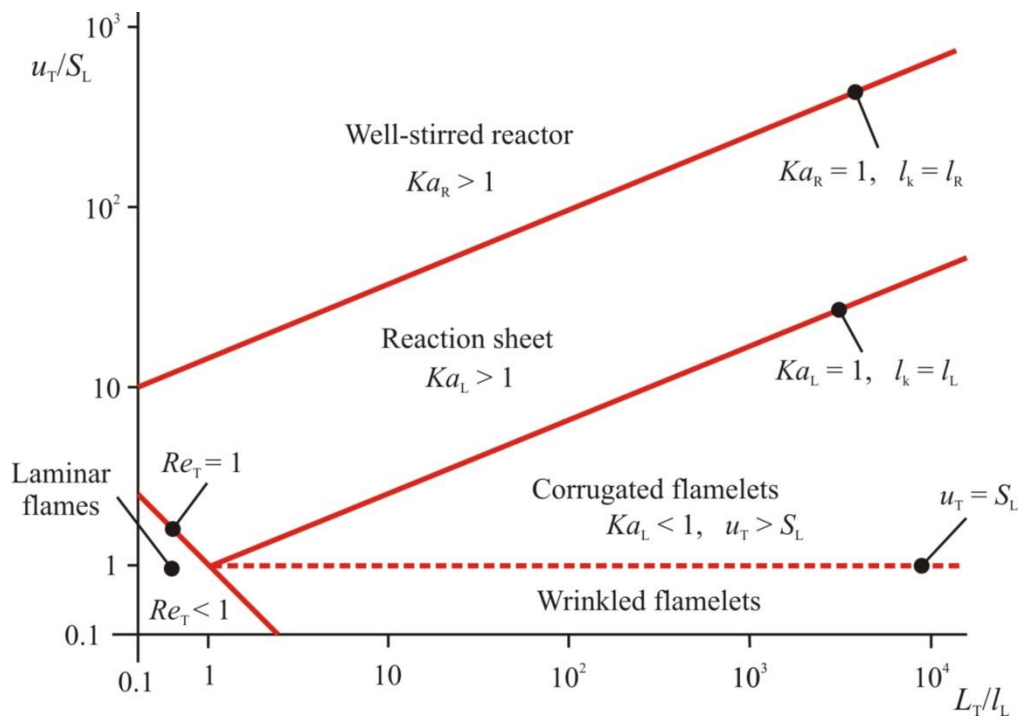


**Figure 60. Regime diagram for premixed turbulent combustion according to [105]; reproduced from [51]**

When modeling the turbulent combustion it is important to determine the combustion regime. The existence of different turbulent combustion regimes was first recognized by Damkohler



[51]. Figure 60 presents the types of premixed turbulent combustion regimes. The premixed turbulent combustion regime depends on the mixture reactivity and characteristics of the turbulent flow in the unburned zone. According to [105], [106], there are five (5) different regimes for the premixed combustion (Figure 60):

1. laminar flames,
2. wrinkled flamelets,
3. corrugated flamelets,
4. reaction sheet,
5. well-stirred reactor.

In order to understand the figure given above (Figure 60), it is necessary to define the Karlovitz number, turbulent Reynolds number and the characteristic flame and turbulent flow scales. Turbulent Reynolds number ( $Re_T$ ) has already been defined in the chapter 3.1.4.

Karlovitz number defines a relationship between the characteristic flow and reaction time scales [51]. In the figure given above, two Karlovitz numbers are defined. For the characteristic reaction time scale one of the Karlovitz numbers ( $Ka_L$ ) takes into account the characteristic flame scale, while the other ( $Ka_R$ ) takes into account the characteristic time scale of the reaction zone within the flame zone. It is important to stress out that the overall flame length consists of the reaction zone and preheat zone (Figure 59). Both of the Karlovitz numbers are defined for the smallest eddy encountered in the turbulent flow, Kolmogorov eddy [51]. Karlovitz numbers ( $Ka_L$  and  $Ka_R$ ) can be expressed in the following way [51]:

$$Ka_L = \left( \frac{l_L}{l_k} \right)^2 \quad (3.158)$$

$$Ka_R = \left( \frac{l_R}{l_k} \right)^2 \quad (3.159)$$

$$l_L = \frac{\nu}{S_L} \quad (3.160)$$

In the equations given above,  $l_L$  (m) represents flame thickness;  $l_R$  (m) represents the thickness of the reaction zone within the flame, while  $l_k$  (m) represents the Kolmogorov length scale.

The difference between the premixed combustion regimes lays in the structure and type of the reactive flow field and combustion process itself; laminar flame speed and its thickness. Out



of the above presented regimes, the turbulent premixed combustion in the IC engines falls in the flamelet regime category [85]. Therefore only this regime will be presented in more detail, while more information on other turbulent premixed flame regimes can be found in the specialized fundamental combustion literature [50]–[52], [105], [106].

Flamelet regime is the turbulent premixed combustion regime which occurs when the Karlovitz number is lower than unity, which means that the chemical time scale is shorter than the turbulent time scale and that flame thickness is smaller than the turbulent length scale [50]. This means that the flame front is thin and highly wrinkled by the turbulent eddies [50] (Figure 61).

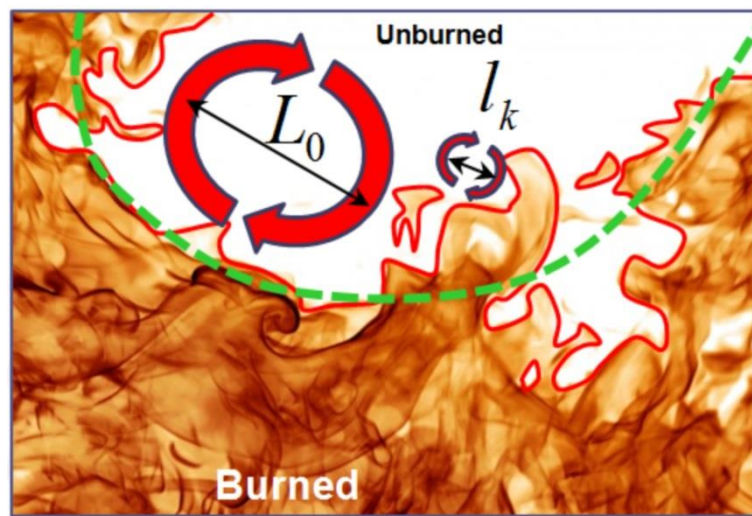


**Figure 61. Presentation of the flamelet regime, which is characteristic for turbulent premixed combustion in IC engine; picture taken from [32]**

The difference between the wrinkled flamelet regime and corrugated flamelet regime is in the ratio of turbulence intensity to laminar flame speed. In the case of large values of turbulence intensity (turbulence intensity larger than the laminar flame speed), eddies are able to wrinkle the flame front so strong that two sections of the flame front can become merged together and form pockets of fresh and burned gases [50]. Therefore, such turbulent premixed combustion regime is called the corrugated flamelet regime. Turbulent premixed combustion regime which will occur during IC engine combustion is determined by the engine operating characteristics. For example at high load and at high speed the turbulent flow field of SI engine becomes very intense and then the engine operates in the corrugated flamelet regime, with multiple pockets of fresh and burned gases [107]. However, in a major part of the IC engine operating conditions the turbulence intensity is lower than the laminar flame speed,

which means that the engine operates in a wrinkled flamelet regime [32], [104], [108], in which the flame front is a single highly wrinkled contour.

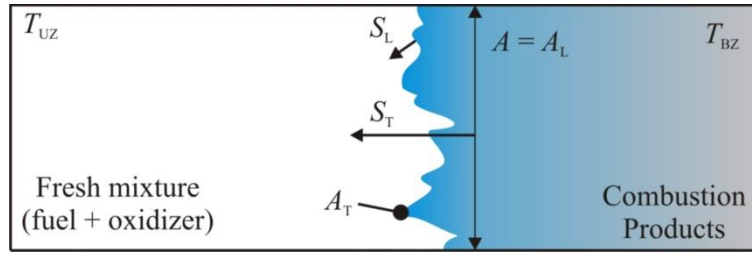


**Figure 62. Schematic of the turbulent propagating (premixed) flame**

From the Damkohler phenomenological model it follows that the mass flux through the flame contour equals [106] (Figure 62):

$$\frac{dm_{FP}}{dt} = \rho_{UZ} \cdot S_L \cdot A_T = \rho_{UZ} \cdot S_T \cdot A \quad (3.161)$$

In the equations given above,  $\frac{dm_{FP}}{dt}$  (kg/s) represents the mass flow through the flame contour, which is equivalent to the mass burning rate,  $\rho_{UZ}$  (kg/m<sup>3</sup>) represents the unburned zone density,  $S_L$  (m/s) represents the laminar flame speed,  $A_T$  (m<sup>2</sup>) represents the turbulent flame surface area,  $S_T$  (m/s) represents the turbulent flame speed, while  $A$  (m<sup>2</sup>) represents the characteristic surface of the incoming flow, which is essentially equal to the laminar surface area ( $A = A_L$ ). From the equation (3.145) it follows:

$$S_L \cdot A_T = S_T \cdot A_L \Rightarrow \frac{S_T}{S_L} = \frac{A_T}{A_L} \quad (3.162)$$

In the IC engine, turbulent propagating (premixed) flame is initiated by an energy source. In the conventional SI engines, this energy source comes from the spark plug, while in the conventional dual fuel IC engines flame propagation is triggered at multiple locations within the combustion chamber by the ignited Diesel fuel/ natural gas/ air/ combustion products mixture. A typical flame propagation mass fraction burned and normalized rate of the heat release traces are given in the Figure 63. Figure 63 reveals a bell like normalized rate of heat release trace which is typical for a combustion process which is governed by the flame propagation through the premixed mixture. On the other hand, the mass fraction burned (normalized energy released) trace reveals three (3) combustion stages which are typical for a

combustion process which is governed by the flame propagation through the premixed mixture [32]:

1. Initial (early) combustion stage, which is sometimes referred to as the flame kernel growth stage.
2. Developed turbulent propagating flame stage.
3. Wall-combustion stage.

According to [108], combustion chamber images reveal that in the initial phase the flame is smooth. Therefore, it is evident that in the initial phase of the flame propagation process, combustion proceeds in a laminar way. The reason for this is that in the initial phase flame kernel is very small, in fact it is smaller than the turbulent eddies that are encountered in the combustion chamber and therefore it cannot be instantaneously wrinkled.

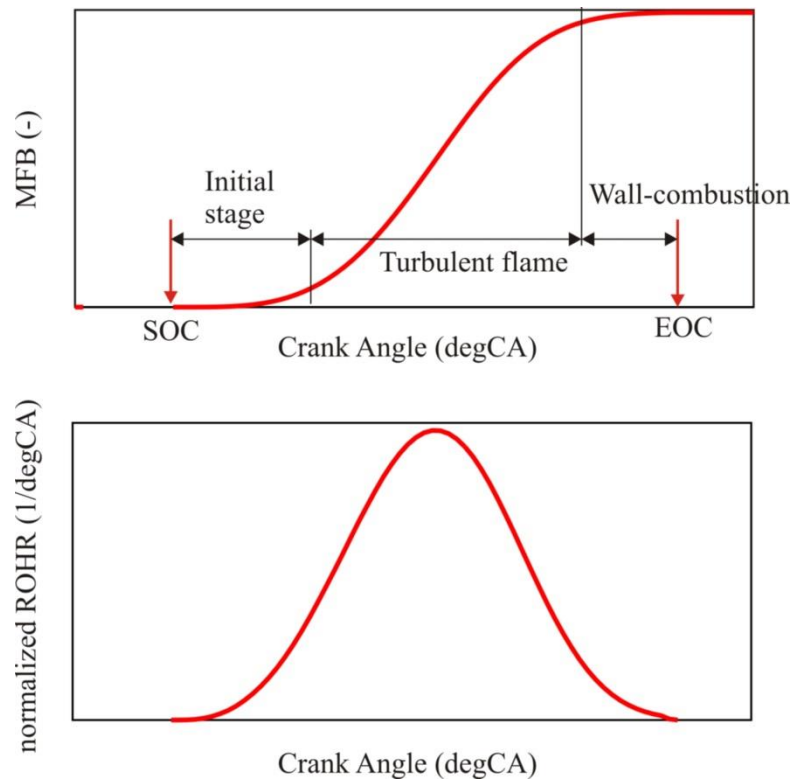


**Figure 63. Typical MFB and normalized ROHR traces for a combustion process which governed by the flame propagation through the premixed mixture**

As the combustion process progresses, flame gradually becomes larger and larger and when its size surpasses the size of the turbulent eddies, flame becomes wrinkled and the combustion process enters into the second stage called the fully developed turbulent flame. In this combustion stage the combustion process is much more intense than in the initial combustion stage which is evident from the normalized rate of heat release trace (Figure 63). Finally, as

the flame starts to approach the combustion chamber walls the combustion process enters its final stage, the so-called wall-combustion process. In this stage, the combustion rate is again significantly lower compared to the fully developed turbulent flame stage. There are three (3) main reasons for such behavior [108]:

1. Decrease in the turbulent flow length scale as the flame approaches the wall
2. The increased heat losses on the flame front
3. The decreased fresh mixture temperature in the regions close to the wall

It was already stated that the unburned zone turbulence and its eddies are responsible for wrinkling of the flame front [32]. As the flame approaches the combustion chamber walls, the unburned zone volume and hence the size of eddies inside the unburned zone decreases which leads to a decrease in the flame wrinkling (flame laminarization) and consequently to a decrease of the turbulent flame surface. Also, as the flame approaches the chamber walls, the heat losses from the flame front to the wall become more intense thus decreasing the energy that sustains the propagating flame, which leads to a decrease of the reaction rate in the reaction zone of the flame (decrease in the laminar flame speed). Moreover, as a consequence of the lower fresh mixture temperature in a region close to the combustion chamber walls, the reaction rate (laminar flame speed) additionally decreases.

After a brief review of the physics behind the phenomenon of the turbulent propagating (premixed) flame, an overview of the existing 0-D flame propagation models followed by the description of the flame propagation models used in this thesis are presented in the next chapters.

### 3.5.2. Overview of the 0-D flame propagation combustion models

In 0-D IC engine combustion modeling framework, combustion governed by the flame propagation through the premixed mixture is usually modeled with a multi-zone approach. In fact, a major part of the models in the literature are based on a two-zone approach where the entire cylinder content is divided into a burned and an unburned zone which are separated by an infinitely thin and highly wrinkled flame front. These models are quasi-dimensional in their nature because in the calculation of the burning rate the combustion chamber geometry is accounted for. There are a number of different flame propagation 0-D models in the literature and they can all be summarized in the following three (3) sets of models:

1. Turbulent entrainment models (in some literature referred to as the BK model)
2. Fractal combustion models
3. Turbulent flame speed models

Turbulent entrainment model is also known as the BK model. This is due to the authors that have first formulated it (Blizard and Keck) in [47]. The turbulent entrainment model was later upgraded and used in [70], [109]–[112]. The phenomenology behind the turbulent entrainment model is that a spherical flame entrains a portion of the unburned fresh charge with the specified mass entrainment rate and later the entrained mass burns behind the flame front during the characteristic time scale. This means that in the turbulent entrainment model combustion takes place in two steps [108]. In the first step, mass is entrained into the reaction (flame zone), while in the second step the entrained mass burns with a characteristic time constant that is a function of the turbulence and of the chemistry of the mixture.

Fractal description of the flame was proposed in [113], later refined for the use in the premixed combustion modeling in [55], [114], [115] and finally used by a number of authors in modeling of the SI engine combustion process [32], [36], [116]. The phenomenology behind the fractal combustion model (FCM) is that a highly wrinkled spherical flame travels through the combustion chamber with the laminar flame speed. The highly wrinkled flame surface is calculated through the fractal geometry approach. More on this approach will be presented in the following chapter of this thesis.

Turbulent flame speed models have also been used in modeling of the combustion process in SI engines by a number of authors [117]–[119]. The phenomenology behind the turbulent flame speed combustion model (TCM) is that a smooth spherical flame travels through the combustion chamber with the turbulent flame speed. More on the calculation of turbulent flame speed will be presented in the following chapters of this thesis.

In the 0-D combustion model presented in this thesis two different approaches were used in modeling of the flame propagation process which resulted in two different models:

1. Fractal combustion model.
2. Turbulent flame speed combustion model.

Both of these models are based on the wrinkled flamelet regime of the turbulent premixed flame. FCM model was already available in the AVL simulation tool and was purely modified during this study to satisfy the physics of the flame propagation in a conventional dual fuel IC engine. On the other hand, TCM model was developed and integrated within the AVL simulation software during this study. Both of these models use the same equation to specify the burning rate due to the flame propagation process:

$$\frac{dm_{FP}}{dt} = \rho_{UZ} \cdot S_L \cdot A_T = \rho_{UZ} \cdot S_T \cdot A_L \quad (3.163)$$

This is the well-known Damkohler's equation that has already been given in the previous chapter;  $\frac{dm_{FP}}{dt}$  (kg/s) represents the overall mass flow from the unburned to the burned (flame) zone as a result of the turbulent flame propagation mechanism. The fuel mass burning rate and the rate of heat release due to the flame propagation process can be expressed as:

$$\frac{dm_{FB,FP}}{dt} = \frac{dm_{FP}}{dt} \cdot x_{FV,UZ} \quad (3.164)$$

$$x_{FV,UZ} = x_{FV,UZ,M} + x_{FV,UZ,D} \quad (3.165)$$

$$\frac{dQ_{COMB,FZ}}{dt} = \frac{dQ_{FP}}{dt} = \frac{dm_{FB,FP}}{dt} \cdot LHV_{UZ} \quad (3.166)$$

$$LHV_{UZ} = x_{metFV,UZ} \cdot LHV_M + (1 - x_{metFV,UZ}) \cdot LHV_D \quad (3.167)$$

In the equations given above,  $\frac{dm_{FB,FP}}{dt}$  (kg/s) represents the fuel mass burning rate,  $x_{FV,UZ}$  (-) represents the mass fraction of the fuel vapor inside the unburned zone,  $x_{FV,UZ,M}$  (-) represents the mass fraction of the methane inside the unburned zone,  $x_{FV,UZ,D}$  (-) represents the mass fraction of the Diesel fuel vapor inside the unburned zone,  $\frac{dQ_{FP}}{dt}$  (J/s) represents rate of heat release due to the flame propagation,  $LHV_{UZ}$  (J/kg) represents the lower heating value of the fresh (unburned zone) mixture,  $x_{metFV,UZ}$  (-) represents the mass fraction of methane in the fuel vapor blend located in the fresh (unburned zone) mixture,  $LHV_M$  (J/kg) represents the lower heating value of methane, while  $LHV_D$  (J/kg) represents the lower heating value of the Diesel fuel.

Details on the turbulent flame surface calculation, in case of the FCM, and the turbulent flame speed calculations, in the case of TCM, are given in the next chapters.

### 3.5.3. Overview of the fractal combustion model

Images of the turbulent propagating (premixed) flame surface revealed that the flame has a highly wrinkled (irregular) shape (Figure 61) that cannot be described by standard (Euclidian) geometry [108]. It was already stated that the flame is wrinkled due to two effects:

1. Temperature and mixture in-homogeneities at the flame front
2. Turbulent flow field that exhibits a large number of length scales of various sizes

Therefore, the flame surface as an irregular shape will also exhibit a large number of length scales of different sizes, which are similar to those of the turbulent flow field. This means that the level of wrinkling of the flame surface depends on the character of the turbulent flow field; i.e. the range of different sizes of eddies in the fresh charge in front of the flame surface. Such an irregular geometry (highly wrinkled spherical surface) can be described through fractal approach that has been formulated in [113]. The mathematics behind the fractal approach is complicated and only a brief description will be given in this thesis; for more details one can refer to [113], [120]. A body or a curve that has irregular geometry has a fractal geometry properties if it has following features [55], [113], [120]:

1. Self-similarity at different scales
2. Power law between the measured dimension and measuring scale

Area of and irregular surface can be expressed with the following equation [113]:

$$A_s \cong N \cdot a^2 \quad (3.168)$$

In the above equation,  $A_s$  ( $m^2$ ) is the area of the measured surface,  $a$  (m) is the length of a side of a measuring square, while  $N$  (-) is the number of squares one can fit on the surface of interest (surface whose area is being measured). In a case of irregular surfaces, as the length  $a$  is decreased, surface area  $A$  increases as new levels of irregularity are encountered at smaller scales [51], [121]. However, if the surface is fractal (self-similarity behavior), the  $\log a - \log A$  plot will reveal a straight-line due to the power law dependence (Figure 64). The slope of the line in the case of surfaces will be  $2-D_3$  [55], where  $D_3$  is called the fractal dimension. For most geometries, the scaling law is expected to cease at sufficiently low and high measuring scale [51], called the inner and outer cutoffs.

The author in [121] has shown that the surfaces in a turbulent flow can be described by the fractal geometry approach. Likewise, since the turbulent flame surface is wrinkled due to turbulence, the turbulent flame surface can also be described by the fractal geometry approach as has been done in [55], where it was proposed that the scaling law breaks down at the turbulence integral scale (outer cutoff) and Kolmogorov scale (inner cutoff) (Figure 65).

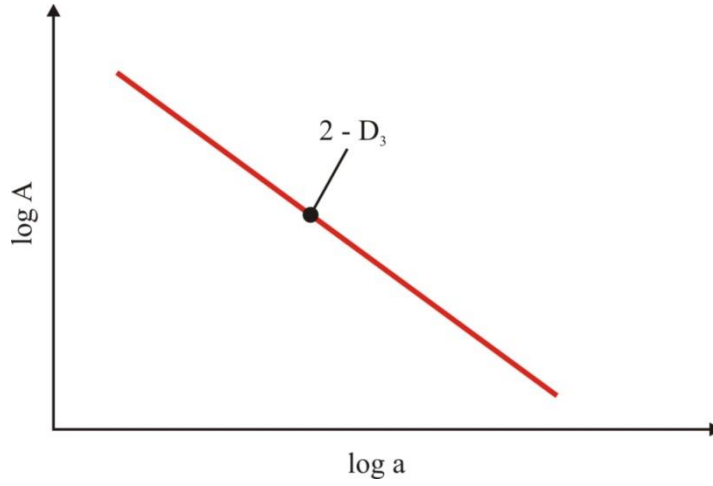


**Figure 64. Measured area vs. measuring scale for a surface that is fractal in its nature; reproduced from [55]**

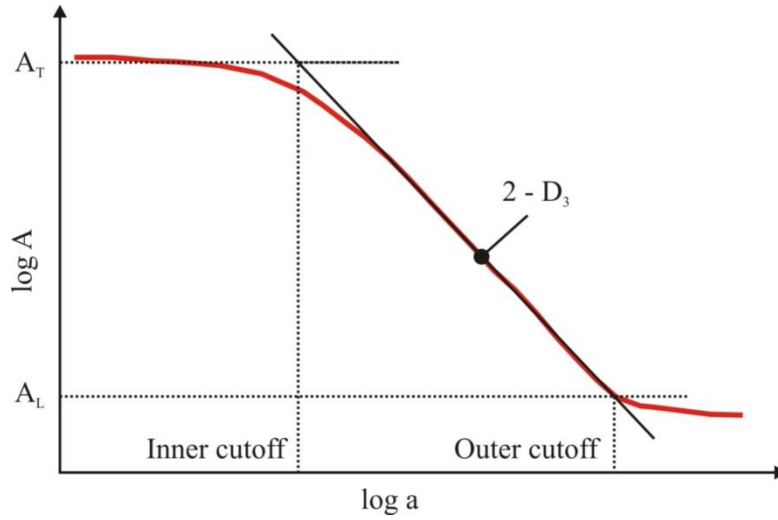


**Figure 65. Measured area vs. measuring scale for a surface that is fractal in its nature and has inner and outer cutoffs; Reproduced from [55]**

This proposal states that in the case of turbulent premixed flames, if the measuring scale is reduced all the way down to Kolmogorov scale the flame surface shape will result in a wrinkled turbulent flame surface, and on the other hand if the measuring scale is increased all the way up to the integral scale the flame surface shape will result in a smooth, laminar flame surface [55]. Such argument leads to the following expression for the flamelet regime in the turbulent premixed flames [114]:

$$\frac{S_T}{S_L} = \frac{A_T}{A_L} = \left( \frac{L_I}{l_k} \right)^{D_3-2} \quad (3.169)$$



Now, following the expression 3.153 which gives the ratio between the wrinkled turbulent and laminar flame surfaces, it is possible to calculate the burning rate as follows:

$$\frac{dm_{FP}}{dt} = \rho_{UZ} \cdot S_L \cdot A_L \cdot \left( \frac{L_t}{l_k} \right)^{D_3-2} \quad (3.170)$$

Since the unburned zone turbulent flow is responsible for the flame front wrinkling, the correct form in which the above equation should be written is [32]:

$$\frac{dm_{FP}}{dt} = \rho_{UZ} \cdot S_L \cdot A_L \cdot \left( \frac{L_{L,UZ}}{l_{k,UZ}} \right)^{D_3-2} \quad (3.171)$$

From the equation given above it can be seen that the correct prediction of the in-cylinder turbulence and its scales is imperative for the correct calculation of the flame propagation driven burning rate. Turbulent scales are calculated by the previously presented in-cylinder turbulence model that was presented in the chapter 3.1.4. The unburned zone density is calculated from the in-cylinder pressure and the unburned zone thermodynamic properties. In the original FCM laminar flame speed ( $S_L$ ) is calculated according to correlations presented in [122], while the laminar flame surface is calculated by the special calculation model which takes into account the combustion chamber geometry, spark plug location, piston position, current flame size and its interactions with the chamber boundaries. More on the geometries that can be used in the original FCM can be found in [57].

In the studies presented in [114], [115], [123] it has been shown that for a premixed turbulent flame, fractal dimension is a function of a ratio of the turbulence intensity to laminar flame speed (Figure 66).

According to [114], the convective process represented by the turbulence intensity wrinkles (distorts) the flame front, while smoothing of the flame surface is controlled by the laminar flame speed. Hence, for a premixed turbulent flame the following correlation for the fractal dimension was derived [114]:

$$D_3 = D_{3,min} \cdot \frac{S_L}{u_T + S_L} + D_{3,max} \cdot \frac{u_T}{u_T + S_L} \quad (3.172)$$

In the equation given above,  $D_{3,min}$  (-) represents the minimum value of the fractal dimension, while  $D_{3,max}$  (-) represents the maximum value of the fractal dimension. In the FCM model

that has already been integrated into the AVL cycle-simulation software, the minimum value of the fractal dimension is set to 2.05 which corresponds to the value for initial laminar flame, while the maximum value of the fractal dimension is set as an input parameter to the model.

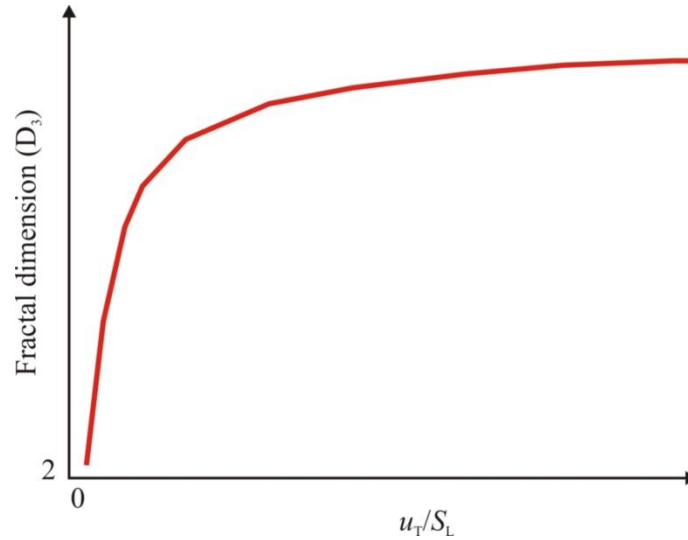


**Figure 66. Fractal dimension as a function of the ratio of turbulence intensity to laminar flame speed; reproduced from [115]**

As described earlier, in the IC engines, the initial laminar flame transitions to the fully developed turbulent flame and then gradually slows quenches due to wall effects. Therefore, appropriate sub-models need to be used to calculate the transition from the laminar to fully developed turbulent flame and to calculate the final wall-combustion burning rate.

In the original FCM details on the ignition and early phase of the flame propagation are not directly calculated. It is considered that the flame propagation process starts 200  $\mu$ s after the prescribed spark discharge and that the initial flame kernel is spherical and has an initial radius of 2 mm. This approach has been modified in [32], where a new flame kernel development model has been developed and integrated within the AVL cycle-simulation software. This model also considers that the flame kernel can be convected away from the spark plug location and it calculates the heat transfer between the flame kernel and spark plug which has a large impact on the actual start of the flame propagation process.

The transition from the laminar to the fully developed turbulent flame is in the original FCM model calculated with the following correlation [57]:

$$D_{3, \max} = D_{3, \min} \cdot (1 - I_f) + C_{\text{comb}} \cdot I_f \quad (3.173)$$

$$I_f = 1 - e^{-\gamma_{\text{wr}}} \quad (3.174)$$

$$\gamma_{wr} = \frac{r_f}{r_{f,ref}} \cdot \frac{n}{n_{ref}} \quad (3.175)$$

In the equation given above,  $I_f$  (-) represents an under-relaxation function,  $\gamma_{wr}$  (-) represents a non-dimensional flame wrinkling rate,  $r_f$  (m) represents the flame radius,  $r_{f,ref}$  (m) represents the flame radius at which flame is fully wrinkled by the fresh charge turbulent flow,  $n$  (rpm) represent the engine speed, while  $n_{ref}$  (rpm) represent the reference engine speed, while the parameter  $C_{comb}$  (-) represents the maximum value of fractal dimension (obtained when under-relaxation function reaches unity) and is set to 2.35.

In [32], a new transition model was developed and integrated within the AVL cycle-simulation software. This new model was derived with assumption that transition is linked to the in-cylinder turbulent flow field. In that context the wrinkling time ( $\Delta t$ ) was defined which represents the time it takes for the flame to transition from laminar to fully developed turbulent flame [32]:

$$t_{trans} = 0.55 \cdot C_{trans} \cdot \frac{L_I}{u_T} \quad (3.176)$$

In the equation given above,  $t_{trans}$  (s) represent the wrinkling time,  $L_I$  (m) represent the turbulence integral length scale, while  $C_{trans}$  (-) represent the wrinkling time model parameter. With this new approach, the non-dimensional flame wrinkling rate is calculated with the following equation [32], [57]:

$$I_f = 1 - e^{-\left(\frac{t}{\Delta t} \cdot \frac{n}{n_{ref}}\right)} \quad (3.177)$$

In the above equation,  $t$  (s) represents the time that has elapsed from the start of flame propagation.

### ***Extension and modification of the fractal combustion model***

Since in the conventional dual fuel IC engines flame propagation is initiated by the combustion of a Diesel fuel/ natural gas/ air/ EGR mixture a new flame propagation initiation model was derived. Moreover, since in the conventional dual fuel engine flame starts at multiple locations within the combustion chamber, a new multiple flame surface calculation model was also derived. The initial calculations revealed that both the original laminar to fully developed turbulent flame calculation as well as the one defined in [32] are not suitable

for the calculation of the transition process in a conventional dual fuel engine. Hence a new transition model was also derived. Similarly to the [32], the original wall-combustion model is excluded from the model. This is enabled by the fact that flame wrinkling is calculated with the unburned zone properties, which means that the ratio of turbulent scales decay as the unburned zone mass and hence unburned zone turbulence decay. Therefore, the effect of the decrease in the flame wrinkling is captured through a decrease in the ratio of the turbulence length scales. However, the initial calculations revealed that the final combustion phase cannot be adequately modeled as the CA90 and CA95 in simulations would always be more advanced compared to the experimental results. Therefore, a new wall-combustion model was also derived during the research that is also presented in this thesis. Finally since in the conventional dual fuel engines flame propagates through the lean mixture, instead of laminar flame speed correlations that have been derived in [122], the look-up tables were used for calculating the laminar flame speed in the premixed mixture. To summarize, within the research presented in this thesis following extensions and modifications were made to the FCM to enable its use in the calculation of the flame propagation process in the dual fuel engines:

1. new start of the flame propagation calculation model;
2. new model for the calculation of the transition from the laminar to fully developed turbulent flame;
3. new wall-combustion calculation model;
4. new multiple flame surface calculation model;
5. new laminar flame speed calculation model.

All of these modifications have been integrated within the AVL cycle-simulation code.

### 3.5.4. Overview of the turbulent flame speed combustion model

Turbulent flame speed combustion model (TCM) has been derived and integrated within the AVL cycle-simulation software during the research that is presented in this thesis. Same as the FCM, the TCM is also based on the wrinkled flamelet regime for the premixed turbulent flames. However, contrary to the FCM model that accounts for a turbulent surface that travels at the laminar flame speed, the TCM describes the turbulent flame propagation as a physical phenomenon where the flame with a smooth surface travels at a turbulent flame speed. Such approach is in agreement with the Damkohler phenomenological model of a premixed turbulent flame. From this equation, it follows that in the case when the TCM model is applied, the burning rate can be expressed with the following equation:

$$\frac{dm_{FP}}{dt} = \rho_{UZ} \cdot S_T \cdot A_L \quad (3.178)$$

Same as in the case when the FCM is applied, the unburned zone density is calculated from the state equation for the unburned zone, while the smooth, laminar flame surface is calculated by the specially developed multiple flame surface calculation model. However, in this case the challenge lies in the calculation of the turbulent flame speed.

Appropriate correlations for the turbulent flame speed have been published in numerous papers [105], [124]–[126] and in all the cases turbulent flame speed is a function of the laminar flame speed and the unburned zone state & turbulence characteristics.

For the TCM model, the turbulent flame speed correlation is taken from [56] (correlation that was derived by Frolov et. al), since this is the correlation that is used in the turbulent flame propagation modeling in AVL Fire, a 3-D CFD software specialized for the IC engine simulations. According to [56], turbulent flame velocity can be described with the following equation:

$$S_T = S_L \cdot F \quad (3.179)$$

$$F = -4.37 + 1.13 \cdot C_{comb} \cdot \left( \frac{u_{T,UZ}}{S_L} \right)^{0.5} \cdot \left( \frac{S_L \cdot L_{l,UZ}}{\nu_{UZ}} \right)^{0.25} \quad (3.180)$$

Finally, the burning rate in the case of the TCM can be expressed as:

$$\frac{dm_{FP}}{dt} = \rho_{UZ} \cdot S_L \cdot \left[ -4.37 + 1.13 \cdot C_{comb} \cdot \left( \frac{u_{T,UZ}}{S_L} \right)^{0.5} \cdot \left( \frac{S_L \cdot L_{l,UZ}}{\nu_{UZ}} \right)^{0.25} \right] \cdot A_L \quad (3.181)$$

The subscript *UZ* in the equations given above denotes that the appropriate quantities are taken for the unburned zone. This is due to the fact that the unburned zone turbulent flow is responsible for the flame wrinkling. Same as in the case of the FCM, in order to correctly predict the burning rate with the TCM it is necessary to correctly calculate the in-cylinder turbulence level and its scales. In the equations given above,  $\rho_{UZ}$  (kg/m<sup>3</sup>) represents the unburned zone density,  $S_T$  (m/s) and  $S_L$  (m/s) represent the turbulent and laminar flame speeds,  $C_{comb}$  (-) represents the model parameter for the turbulent flame speed correlation,  $u_{T,UZ}$  (m/s) represents the unburned zone turbulence intensity,  $L_{l,UZ}$  (m) represents the turbulence integral length scale inside the unburned zone,  $\nu_{UZ}$  (m<sup>2</sup>/s) represents the kinematic

viscosity of the mixture inside the unburned zone, while  $A_L$  ( $m^2$ ) represent the overall laminar flame surface.

### 3.5.5. Start of the flame propagation calculation

As was already mentioned at the beginning of the thesis, once the spray has ignited spray is viewed as the flame kernel from where the flame propagation through the premixed charge starts (Figure 67).

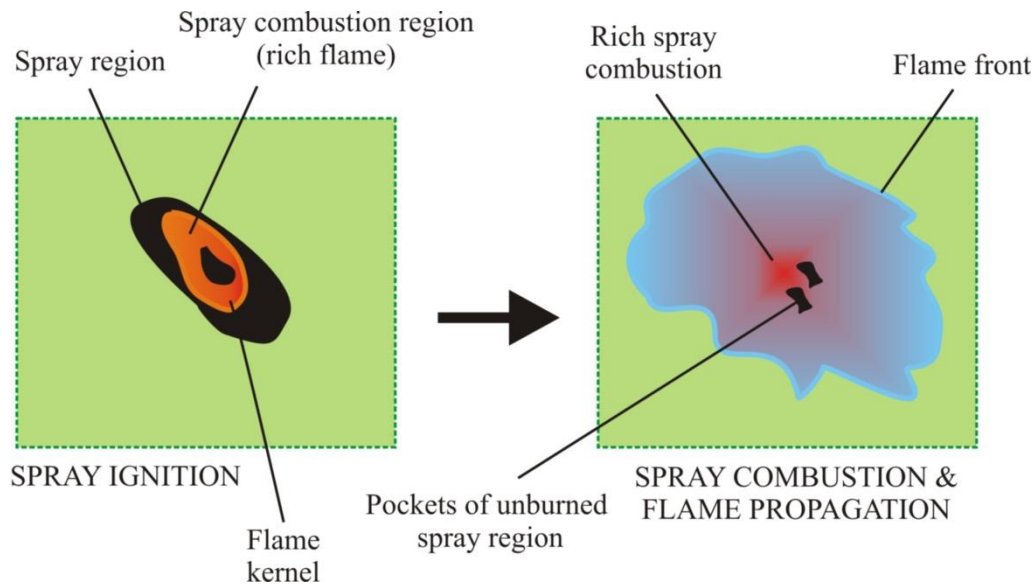


**Figure 67. Schematic of the early combustion phase (spray ignition) and later combustion phase (spray combustion & flame propagation that occur at the same time)**

The flame propagation can only be triggered if the unburned zone mixture is within the flammability limits; i.e. if the excess air ratio in the unburned zone is between 0.5 and 4. Essentially, if the unburned zone mixture is flammable the flame propagation is triggered one time-step after the spray combustion has been triggered. This is due to the fact that spray acts as a “spark plug” that initiates the flame propagation through the surrounding mixture.

Flame is considered to have a spherical shape from the beginning of the flame propagation process and it is considered that the center of the flame kernel is in the center of the spray. Since in the real-life application the flame starts from the outer surfaces of the patches within the spray that have ignited, flame will also propagate through a part of the other zones within the spray that have not yet ignited. That’s why in this model it is considered that at the moment when the flame propagation is initiated only a part of the prepared mixture from the spray zones is transferred to the unburned zone and instantaneously mixed with the mixture inside the unburned zone (Figure 68). It is important to point out that non-ignited spray zones

will partially burn in a flame propagation mode and partially in spray combustion mode. That's why only a part of the prepared mass is transferred to the unburned zone, and this mass transfer is controlled by a model parameter ( $C_{\text{ign,UZ,transf}}$ ).

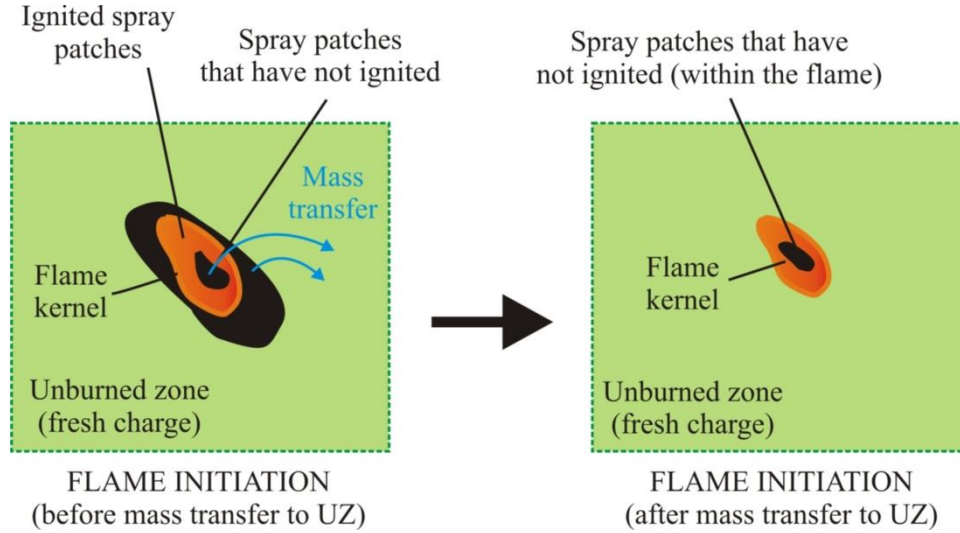


**Figure 68. Schematic of the flame initiation after the start of spray combustion; partial mass transfer from the non-ignited spray zones to the unburned zone**

The mass that is transferred is calculated with the following expression:

$$m_{\text{transf,UZ}} = C_{\text{ign,UZ,transf}} \cdot \sum_i m_{\text{SZ},i} \quad (3.182)$$

In the equation given above,  $m_{\text{transf,UZ}}$  (kg) represents the mass that is transferred from the spray to the unburned region at the flame initiation moment,  $C_{\text{ign,UZ,transf}}$  (-) represents the mass transfer model parameter that determines the amount of the spray region that will burn as a result of the flame propagation through the premixed mixture, while  $m_{\text{SZ},i}$  (kg) represents the mass of the  $i$ -th spray zone. The mass of the species  $j$  that is transferred at the flame initiation moment can be expressed by the following equations:

$$m_{j,\text{transf,UZ}} = C_{\text{ign,UZ,transf}} \cdot \sum_i m_{\text{SZ},i} \cdot x_{j,\text{SZ},i} \quad (3.183)$$

In the equation given above,  $m_{j,\text{transf,UZ}}$  (kg) represents the mass of the species  $j$  that is transferred from the spray to the unburned region at the flame initiation moment, while  $x_{j,\text{SZ},i}$  (-) represents mass fraction of the species  $j$  inside  $i$ -th spray zone.

### 3.5.6. Transition from laminar to fully developed turbulent flame calculation

After the flame initiation, flame surface is smooth (laminar) which means that the initial flame propagation process proceeds in a quasi-laminar way. This is due to the fact that the initial flame kernel is small compared to the length scales that are encountered in the surrounding turbulent flow field which means that the turbulence is not able to wrinkle the flame front. Since the correlations that are used to model the burning rate in both the FCM and the TCM are only applicable for the fully developed turbulent flame, it is necessary to somehow model the initial laminar burning rate and its gradual transition towards the fully developed turbulent flame (Figure 69).

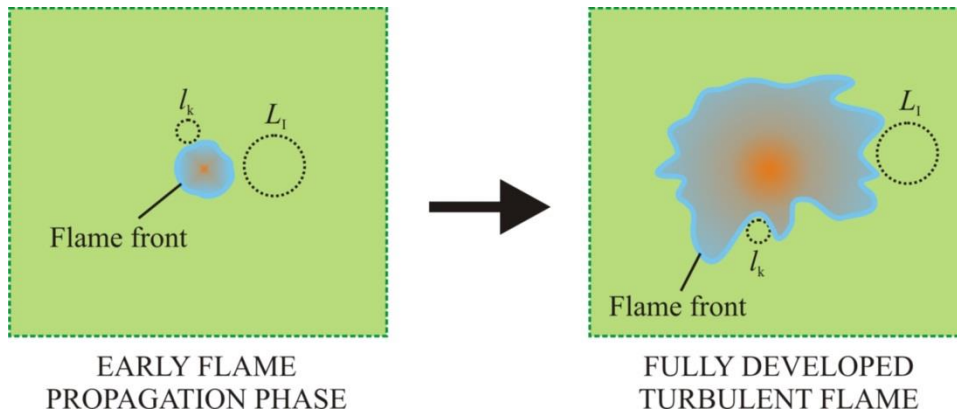


**Figure 69. Schematic of the transition from laminar to the fully developed turbulent flame**

After the initial calculations it was found that both the original transition model and the transition model developed in [32] are not suitable for describing the transition from laminar to fully developed turbulent flame in the conventional dual fuel engines. That's why a new transition model that is based on the in-cylinder turbulence similar to the one in [32] was developed. In the case of the FCM model, fractal dimension is calculated the same as in the case of the original model:

$$D_{3,\max} = D_{3,\min} \cdot (1 - I_f) + f_{D3,\max} \cdot I_f \quad (3.184)$$

$$I_f = 1 - e^{-\gamma_{wr}} \quad (3.185)$$

In the equations given above,  $D_{3,\max}$  (-) represent the maximum value of the fractal dimension,  $D_{3,\min}$  (-) represent the minimum value of the fractal dimension that is set to 2.05,  $I_f$  (-) represents an under-relaxation function,  $f_{D3,\max}$  (-) represent a user-defined maximum value of



the fractal dimension when flame becomes fully turbulent, while  $\gamma_{wr}$  (-) represents a non-dimensional flame wrinkling rate. The difference between the newly developed transition model, the original model and the model presented in [32] is in the calculation of the non-dimensional flame wrinkling rate. In the model presented in this thesis, the non-dimensional flame wrinkling rate is expressed with the following equation:

$$\gamma_{wr} = -7 \cdot \frac{t_{aSoFP}}{t_{trans}} \quad (3.186)$$

$$t_{trans} = C_{trans} \cdot \tau_T \quad (3.187)$$

In the equations given above,  $t_{aSoFP}$  (s) represents the time that has elapsed since the start of the flame propagation,  $t_{trans}$  (s) represents the transition time; i.e. the time it takes for the flame to transition from laminar to fully turbulent,  $C_{trans}$  (-) represents the transition model tuning parameter, while  $\tau_T$  (s) represents the eddy turnover time for the entire cylinder content that is calculated with the equation 3.22.

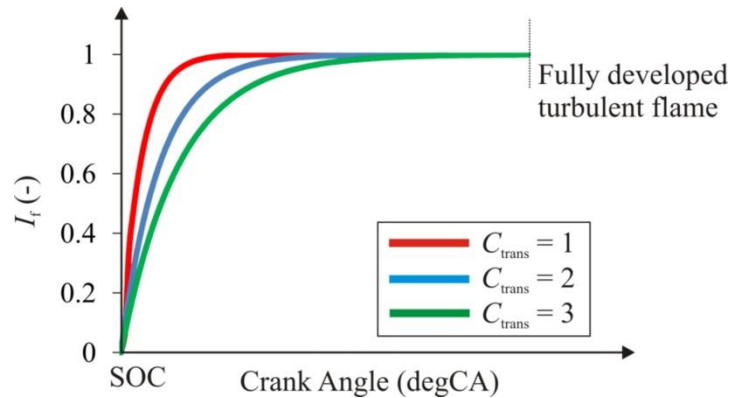


**Figure 70. Shape of the under-relaxation function that is used in modeling the transition from laminar to the fully developed turbulent flame**

In case of the TCM, the same under-relaxation function (3.202) is used to model the smooth transition from the laminar to fully developed turbulent flame. The instantaneous value of the turbulent flame speed in the case of the TCM can be expressed by the following equation:

$$S_T = S_L \cdot (1 - I_f) + S_T \cdot I_f \quad (3.188)$$

In the equations given above,  $S_T$  (m/s) represents the instantaneous turbulent flame speed, while  $S_L$  (m/s) represents the instantaneous laminar flame speed. The shape of the under-relaxation function used in both the FCM and the TCM is given in Figure 70.

### 3.5.7. Calculation of the wall-combustion phase

As the flame travels through the combustion chamber, the size of the unburned zone decreases. This decrease causes a decrease of the ratio of turbulent scales that wrinkle the flame front hence causing a decrease in the flame front area and a decrease in the burning rate. Same as in [32], this effect is captured with the application of a two zone turbulence model that is able to calculate the unburned zone turbulence decrease as its size decreases. Moreover, the application of the enhanced approach in the calculation of the turbulence integral length scale that has been derived and integrated within the AVL cycle-simulation software during this research additionally improves the prediction of the unburned zone turbulence scales.

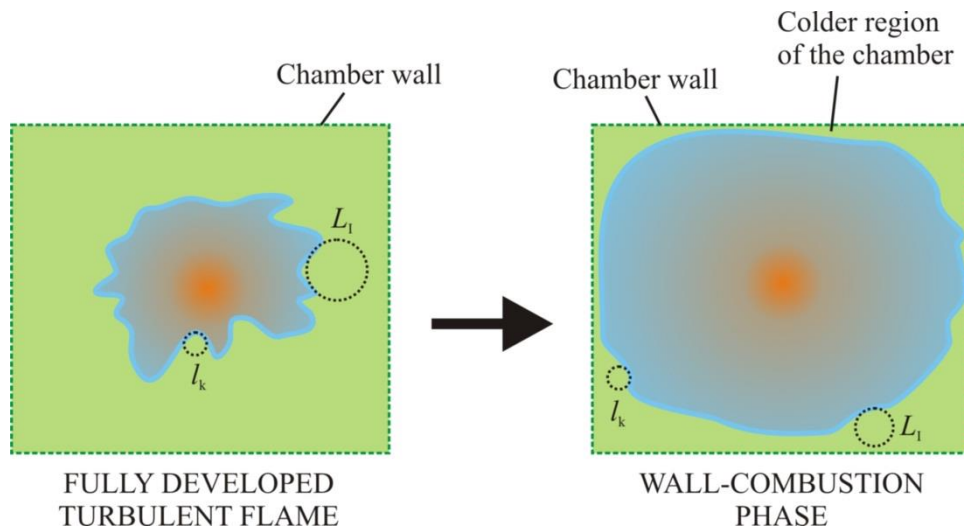


**Figure 71. Schematic of the transition from the fully developed turbulent flame to the wall-combustion phase**

Other two effects that cause a decrease in the burning rate as the flame approaches the combustion chamber walls are (Figure 71): increase in the heat transfer rate from the flame to the combustion chamber walls and decrease of the temperature in front of the flame. These effects were not taken into account neither with the original FCM nor with the enhanced FCM presented in [32].

In order to improve the calculation of the final (wall-combustion) stage, the effect of the unburned zone temperature decrease near the walls on the burning rate has been included with an exponential decay under-relaxation function. With the decrease of the unburned zone temperature the laminar flame speed also decreases. This decrease in the laminar flame speed leads to a decrease in the flame propagation burning rate.

The mass fraction burned at the start of the wall-combustion ( $C_{SOWC}$ ) is set as an input parameter to the model, and once the instantaneous mass fraction burned becomes larger than the input value, wall-combustion is initiated. During the wall combustion calculation, instantaneous unburned zone temperature is calculated by the following equations:

$$T_{UZ} = T_{UZ} \cdot I_T + (T_{wall} + 100) \cdot (1 - I_T) \quad (3.189)$$

$$I_T = e^{\gamma_{wall}} \quad (3.190)$$

$$\gamma_{wall} = -7 \cdot \left( \frac{MFB_{act} - C_{SOWC}}{C_{SOWC}} \right)^{C_{WC,shp}} \quad (3.191)$$

This model is the same for both the FCM and the TCM. In the equations given above,  $T_{UZ}$  (K) represent the unburned zone temperature,  $T_{wall}$  (K) represent the wall temperature,  $I_T$  (-) represents an under-relaxation function for the wall-combustion phenomenon,  $\gamma_{wall}$  (-) represents a non-dimensional temperature decrease rate,  $MFB_{act}$  (-) represents the instantaneous overall mass fraction burned (normalized heat released),  $C_{SOWC}$  (-) represents the mass fraction burned (normalized heat released) at the start of the wall-combustion, while  $C_{WC,shp}$  (-) represents the model parameter used to tune the shape of the non-dimensional temperature decrease rate and hence the shape of the under-relaxation function for the wall-combustion phenomenon. The shape of the under-relaxation function used in both the FCM and the TCM is given in Figure 72.

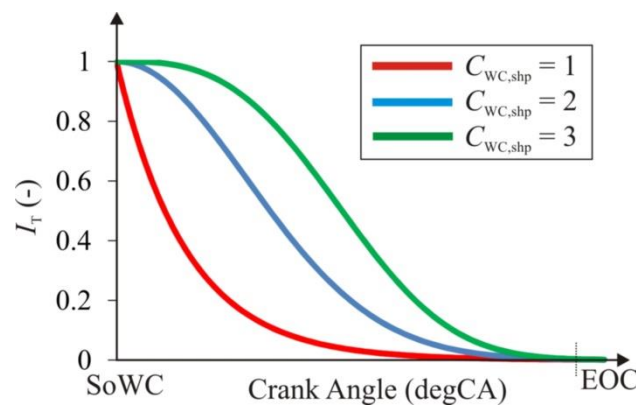


**Figure 72.** Shape of the under-relaxation function that is used in the wall-combustion phase modeling

In a real life situations, flame cannot fully propagate to all of the combustion chamber walls as it quenches; flame burns out and the combustion governed by the flame propagation through the premixed mixture is stopped. Flame quenching is primarily caused by two effects:

1. the heat transfer effects that decrease the flame's temperature,
2. cooler unburned zone regions in the vicinity of the combustion chamber walls.

As the result of the first effect the heat transfer rate to the preheat zone of the flame decreases. Additionally, due to lower heat transfer rate to the preheat zone and lower unburned zone temperature, the reaction rate in the reaction zone decreases, eventually leading to the termination of the reaction process and flame quenching (flame burn out).

Since the flame quenching is not directly calculated one more parameter,  $C_{EOP}$  (-) is added to this model. This parameter is used to tune the end of flame propagation and it represents the mass fraction burned at which the flame propagation ends.

### **3.6. Laminar flame speed calculation**

As it was already mentioned in the previous sections of this thesis, the instantaneous laminar flame speed of the flame front is calculated with a specially developed laminar flame speed tables, look-up tables. These tables were supplied by the partner in this research, AVL GmbH and therefore only a brief elaboration on the calculation method used in computing the laminar flame speed will be presented in this thesis. More detailed explanation on the methods and algorithms used can be found in [100].

Nowadays there are many commercial softwares that can be used to compute both ignition delay times as well as the laminar flame speed for a given fuel/ air mixture. However, a lot of researchers use the open source code that was developed by the researchers at Sandia National Laboratories in Livermore, California, called PREMIX. PREMIX is the software that computes the temperature and species profiles inside the domain, as well as the laminar flame speed for a given fuel/ oxidizer mixture.

Since the flame propagation is a phenomenon that is controlled by the transport process (energy and mass) and chemical reactions inside the reaction zone, PREMIX uses TRANSPORT and CHEMKIN codes to calculate transport and thermodynamic properties of the mixture as well as the reaction rate. In these calculations, flame is usually treated as a freely propagating one dimensional flame, as was done in [100]. For steady, isobaric, quasi one dimensional flame, the solution (temperature and species profiles, and laminar flame speed) is found by solving the equations of conservation of mass, species and energy, and the equation of state [100].

Since in a conventional dual fuel IC engine, most of the premixed fuel is methane, in the combustion model presented in this thesis (DFMZCM), laminar flame speed tables for pure methane are used. The list of data (initial mixture properties) that was used in the tabulation of the laminar flame speed tables is given in Table 7. In every time-step during the flame propagation calculation in a dual fuel combustion model, laminar flame speed needs to be computed from the look-up tables. As the table was made with 4 parameters, a 4-D interpolation needs to be performed. Therefore, during the work presented in this thesis a 4-D linear interpolation algorithm was implemented within the AVL cycle simulation software.

**Table 7. Tabulation parameters (initial mixture properties) used for the laminar flame speed table generation**

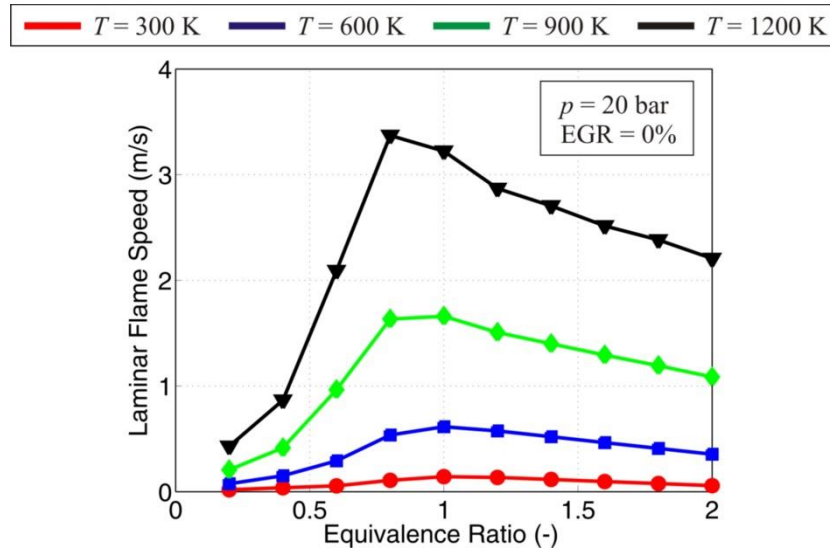
Parameter	Values
Temperature (K)	300, 500, 750, 900, 1250
Pressure (bar)	1, 5, 10, 15, 20, 50, 100
Mixture equivalence ratio (-)	0.2, 0.4, 0.6, 0.8, 1, 1.2, 1.4, 1.6, 1.8, 2, 5
EGR mass fraction (-)	0, 0.2, 0.4, 0.6

### 3.6.1. Influence of the initial state and composition on the laminar flame speed

In this chapter of the thesis, the influence of the initial homogeneous mixture state and charge composition on the laminar flame speed is presented. As chemical kinetics and mechanism development was not the primary focus of this work, only a brief overview of the major trends accompanied with a short discussion regarding the effects of state and composition on the laminar flame speed is given in this thesis.

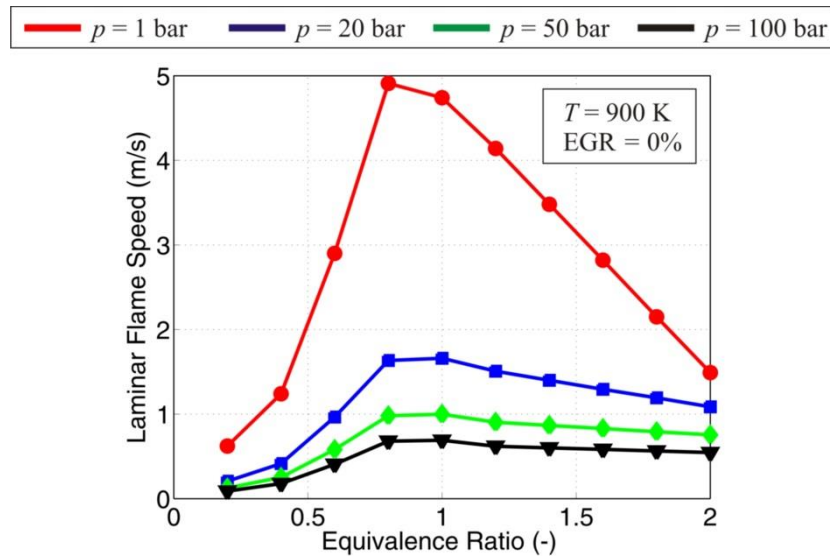
Figures given below present the influence of the equivalence ratio on the laminar flame speed at various temperatures (Figure 73), pressures (Figure 74) and mass fraction of EGR in the fresh mixture (Figure 75). As can be seen from this figure, the highest value of the laminar flame speed for all tested cases is in the narrow region around the stoichiometric mixture (Equivalence ratio = 1). The same occurrence has been observed in the numerous reported experimental [127] and numerical [128], [129] studies.

Figure 73 reveals that the laminar flame speed increases as the temperature increases. This is in the agreement with the behavior that has been reported in numerous laminar flame speed studies; i.e. [130].



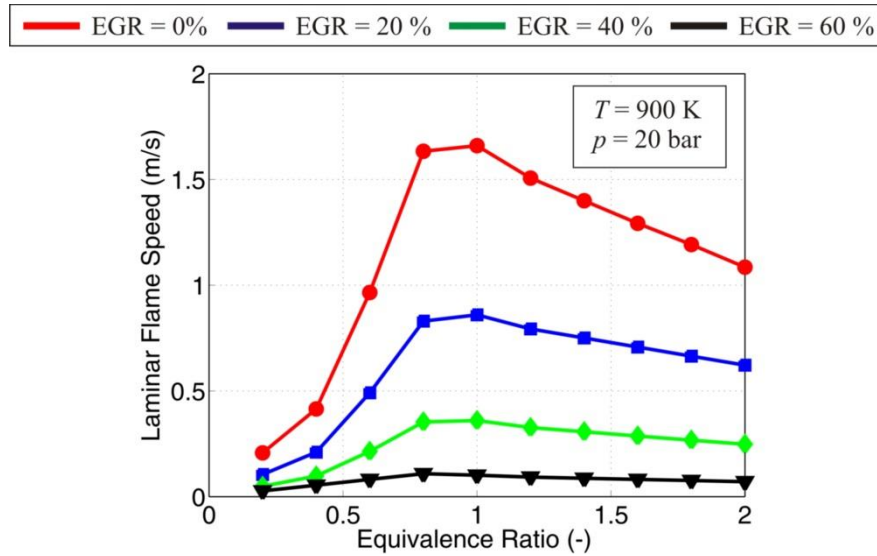
**Figure 73. Influence of the equivalence ratio and temperature on the laminar flame speed**

Figure 74 reveals that the laminar flame speed decreases as the pressure increases. This is in the agreement with the behavior that has been reported in numerous laminar flame speed studies; i.e. [127], [130].



**Figure 74. Influence of the equivalence ratio and pressure on the laminar flame speed**

Figure 75 reveals that the laminar flame speed decreases as the EGR mass fraction increases. This is in the agreement with the behavior that has been reported in numerous laminar flame speed studies; i.e. [131].



**Figure 75. Influence of the equivalence ratio and EGR mass fraction on the laminar flame speed**

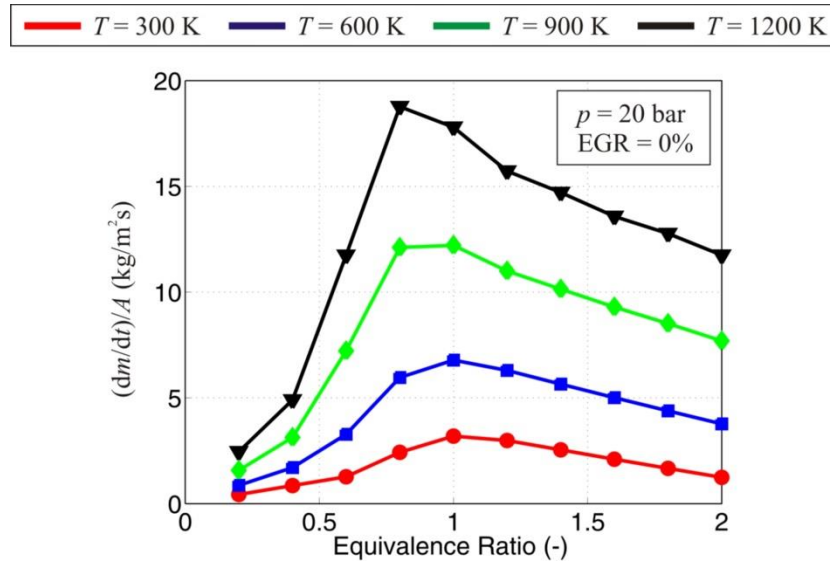
However, since the fuel mass burning rate also depends on the flame surface and density, to present the effects of mixture and thermodynamic properties of the fresh charge on the combustion rate, laminar flame speed was replaced with the area specific laminar mass burning rate. Area specific laminar mass burning rate ( $\text{kg/m}^2\text{s}$ ) can be expressed in the following way:

$$\frac{dm}{dt} = \rho \cdot S_L \cdot A_T \quad (3.192)$$

In the equation given above,  $\rho$  ( $\text{kg/m}^3$ ) represents the fresh charge density,  $S_L$  (m/s) represented the laminar flame speed, while  $A_T$  ( $\text{m}^2$ ) represents the flame surface.

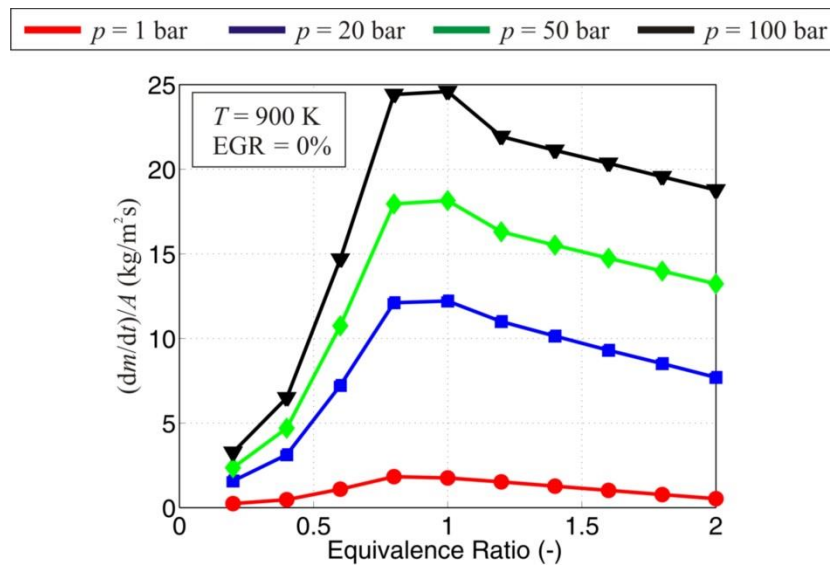
Figures given below present the influence of the equivalence ratio on the area specific laminar mass burning rate at various temperatures (Figure 76), pressures (Figure 77) and mass fraction of EGR in the fresh mixture (Figure 78). As can be seen from these figures, same as in the case of laminar flame speed, the highest value of the area specific laminar mass burning rate for all tested cases is in the narrow region around the stoichiometric mixture (equivalence ratio = 1).

Figure 76 and Figure 78 reveal that the area specific laminar mass burning rate exhibits the same behavior as the laminar flame speed when temperature and EGR mass fraction are increased. As temperature is increased, area specific laminar mass burning rate also increases, while as the EGR mass fraction is increased, area specific laminar mass burning rate decreases.



**Figure 76. Influence of the equivalence ratio and temperature on the surface area specific laminar mass burning rate**

On the other hand, Figure 77 reveals that the area specific laminar mass burning rate exhibits different behavior compared to the laminar flame speed as the pressure (density) is increased. As the pressure is increased, the area specific laminar mass burning rate also increases. This is in the agreement with the behavior that has already been reported in the literature [127].



**Figure 77. Influence of the equivalence ratio and pressure on the surface area specific laminar mass burning rate**



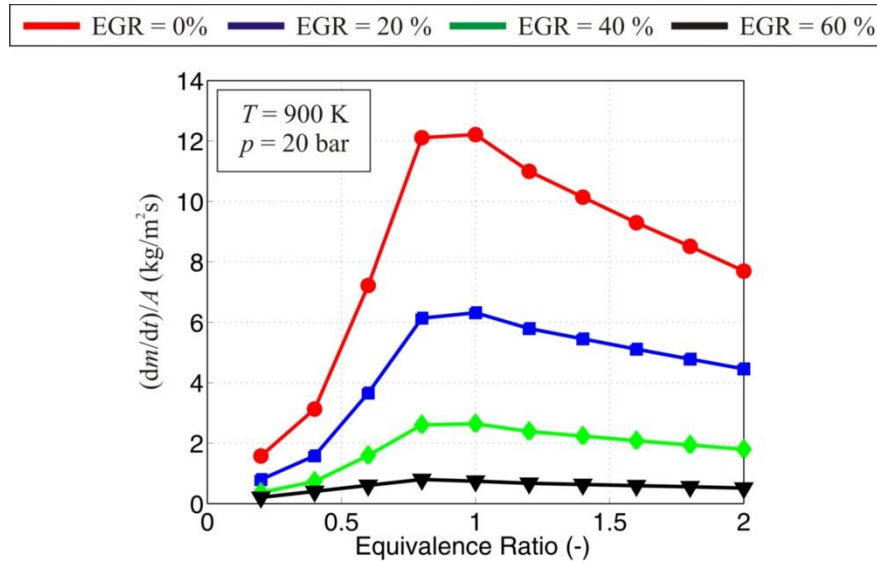


**Figure 78. Influence of the equivalence ratio and EGR mass fraction on the surface area specific laminar mass burning rate**

### 3.7. Flame surface area calculation model

In order to calculate the burning rate that is associated with the flame propagation through the premixed mixture, aside from the in-cylinder turbulence and state quantities, and laminar flame speed, it is also necessary to define the instantaneous smooth (laminar) flame surface area. As in the conventional dual fuel IC engines, flame propagation is initiated at multiple locations inside the cylinder, there are a number of flames that propagate through the cylinder at the same time [2], [18]. The number of these flames is equal to the number of the nozzles on the Diesel fuel injector [2], [18]. Since these flames propagate through the combustion chamber of the conventional dual fuel engines, they gradually merge into a single large single flame.

In the DMFZCM, laminar flame surface area is calculated with a newly developed multiple flame surface calculation model. With this model, it is possible to calculate the overall smooth flame surface area for any number of flames that propagate through the combustion chamber. Moreover, with this model it is possible to account for any viable position of the flame center inside the combustion chamber; the only limitation to the flame center location is that the flame center must be located within the combustion chamber.

In order to simplify the calculation model, similar approach to the one often used in the 3-D CFD simulations was used, where only one section of the combustion chamber is calculated (Figure 79 top two figures). The entire combustion chamber is split into  $n$  sections, where  $n$  equals the number of flame that propagate through the combustion chamber; and the entire flame surface data is calculated for just one slice. Additionally, two more simplifications were

made; as was mentioned before, the flame center is located in the center of the spray and the flame has a spherical shape. Also, as was already mentioned before, the presented flame surface calculation model features only two combustion chamber geometries (typical modern DI-CI engine geometries) that are shown in Figure 79 at bottom:

1. Flat cylinder head – flat piston top.
2. Flat cylinder head – piston that features a cylindrically shaped bowl.

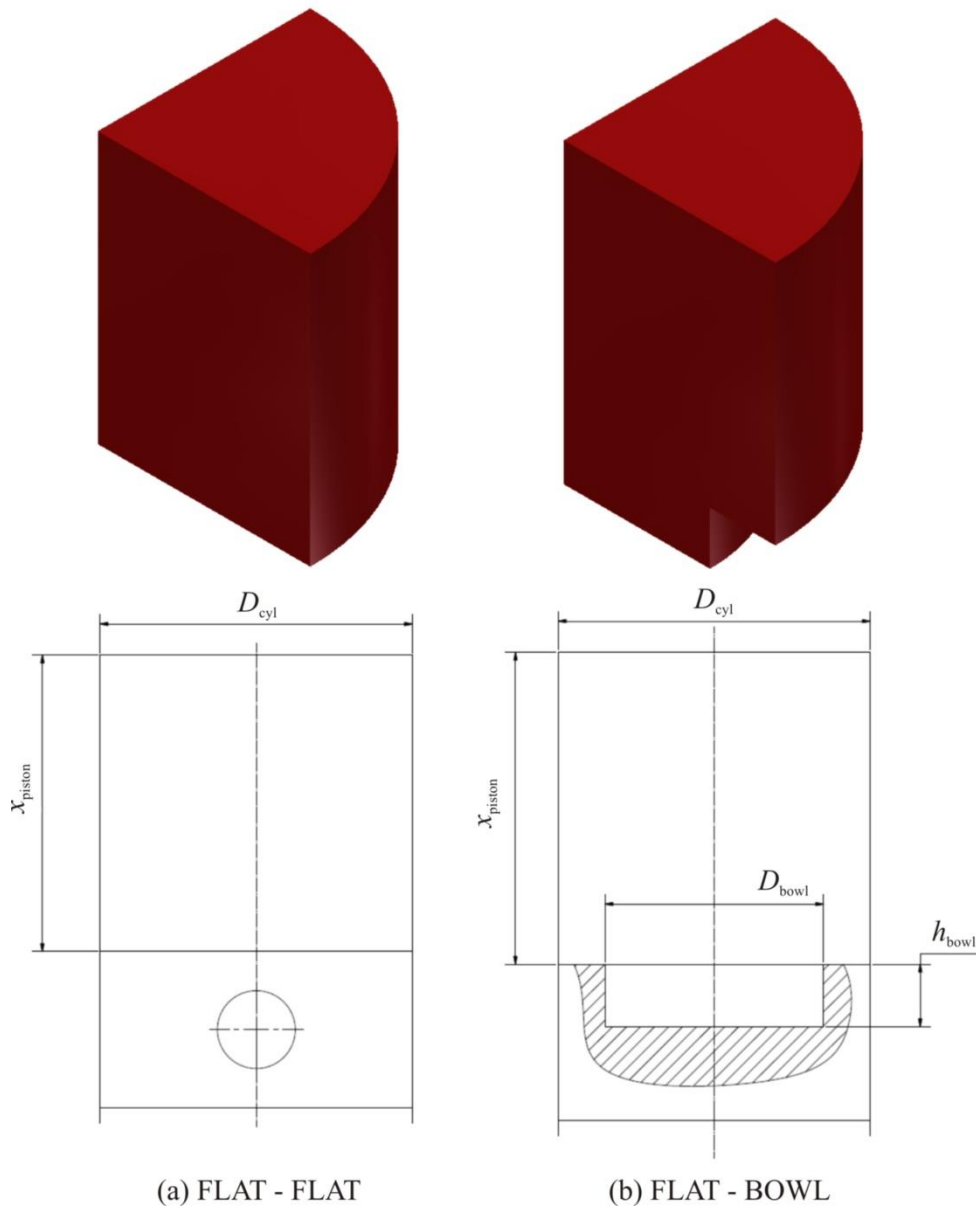


**Figure 79. Schematic presentation of the combustion chamber section (top two figures) and considered combustion chamber geometry types (bottom two figures)**

DI-CI engines usually feature an omega shaped bowl. However, to simplify the flame surface data calculation, a cylindrically shaped bowl (Figure 79 bottom right) is assumed in this multiple flame surface calculation model.

After all that was said, it is possible to sum up the limitations of the multiple flame surface calculation model:

1. Symmetrical combustion chamber (flame data for only one section are calculated).
2. Flame center is located in the spray center.
3. Flame has a spherical shape.
4. Two combustion chamber geometries are considered (flat-flat and flat-bowl).
5. The bowl in the piston has a cylindrical shape.

The multiple flame surface calculation model is run only once at the start of the flame propagation, and then all necessary flame data for all possible situations (all possible piston positions and corresponding flame sizes) are calculated and stored into the corresponding matrices. Within the calculation for a given flame center five (5) arrays are created. Three (3) of these arrays are 1D arrays (501 data points), while two (2) of the arrays are 2D arrays (501x501 data points):

1. Piston position array (1D)
2. Cylinder volume array (1D)
3. Flame radius array (1D)
4. Burned volume array (2D)
5. Flame surface area array (2D)

With these look-up tables, all possible situations (501 possible piston positions and 501 possible flame radii) are covered. Since the main flame data are stored in arrays 4 & 5 (burned volume and flame surface area), in the remaining part of this thesis these two (2) arrays will be referred to as the flame surface data matrices. Arrays 1 – 3 (piston position, cylinder volume and flame radii) are needed only for the calculation of the flame surface data matrices, and later during the extraction of the instantaneous flame data during each time-step of the DFMZCM.

All relevant flame data are calculated for only one flame and then at the end multiplied by the number of flames that propagate through the combustion chamber. The overall flame data can be calculated from the following equations:

$$V_{\text{flame, overall}}(n_{\text{pis}}, n_{\text{rad}}) = n_{\text{flames}} \cdot V_{\text{flame}}(n_{\text{pis}}, n_{\text{rad}}) \quad (3.193)$$

$$A_{\text{flame,overall}}(n_{\text{pis}}, n_{\text{rad}}) = n_{\text{flames}} \cdot A_{\text{flame}}(n_{\text{pis}}, n_{\text{rad}}) \quad (3.194)$$

In the equations given above,  $V_{\text{flame,overall}}$  ( $\text{m}^3$ ) represents the overall burned volume array,  $V_{\text{flame}}$  ( $\text{m}^3$ ) represents the burned volume array for one flame,  $n_{\text{pis}}$  (-) represents the number of possible piston positions, while  $n_{\text{rad}}$  (-) represents the number of possible flame radii.  $A_{\text{flame,overall}}$  ( $\text{m}^2$ ) represents the overall flame surface area array, while  $A_{\text{flame}}$  ( $\text{m}^2$ ) represents the flame surface area array for one flame.

### 3.7.1. Piston position matrix generation

Piston position; i.e. the distance between the cylinder head and the piston top depends on the IC engine geometry (compression ratio, combustion chamber geometry, cylinder bore and stroke). Since the piston has to be located between the top dead center (TDC) and the bottom dead center (BDC), the vector of possible piston positions is calculated with the following equation:

$$x_{\text{piston}}(i_{\text{pis}}) = r_{\text{crank}} \cdot \left[ 1 - \cos \varphi(i_{\text{pis}}) + \frac{1}{\lambda_{\text{crank}}} \cdot \left( 1 - \sqrt{1 - \lambda_{\text{crank}}^2 \cdot \sin^2 \varphi(i_{\text{pis}})} \right) \right] + h_{\text{TDC}} \quad (3.195)$$

In the equation given above,  $x_{\text{piston}}$  (m) represents the vector of possible piston positions (distance between the cylinder head and piston top),  $i_{\text{pis}}$  (-) represents the characteristic position of the piston (value inside the piston position vector),  $r_{\text{crank}}$  (m) represents the crank radius,  $\lambda_{\text{crank}}$  (-) represents the crank mechanism characteristic value,  $\varphi(i_{\text{pis}})$  (rad) represents the current crank angle for the given piston position (between TDC and BDC), while  $h_{\text{TDC}}$  (m) represents the distance between the cylinder head and piston top when piston is in the TDC. Characteristic crank mechanism parameters and the current crank angle are calculated with the following equations:

$$h_{\text{TDC}} = \frac{4 \cdot V_{\text{TDC,H-P}}}{D_{\text{cyl}}^2 \cdot \pi} \quad (3.196)$$

$$V_{\text{TDC,H-P}} = V_{\text{TDC,H-P}} - V_{\text{piston}} \quad (3.197)$$

$$r_{\text{crank}} = \frac{H}{2} \quad (3.198)$$

$$\lambda_{\text{crank}} = \frac{r_{\text{crank}}}{L_{\text{conrod}}} \quad (3.199)$$

$$\phi(i_{\text{pis}}) = \phi(i_{\text{pis}} - 1) + \Delta\phi \quad (3.200)$$

$$\Delta\phi = \frac{\pi}{(n_{\text{pis}} - 1)} \quad (3.201)$$

In the equations given above  $V_{\text{TDC,H-P}}$  ( $\text{m}^3$ ) represents the volume between the cylinder head and piston top when piston is in TDC,  $V_{\text{TDC}}$  ( $\text{m}^3$ ) represents the combustion chamber volume in TDC,  $V_{\text{piston}}$  ( $\text{m}^3$ ) represents the volume of the bowl inside the piston,  $D_{\text{cyl}}$  (m) represents the combustion chamber bore (diameter),  $H$  (m) represents the cylinder stroke,  $L_{\text{conrod}}$  (m) represents the conrod length,  $\phi_{\text{act}}$  (rad) represents the current crank angle,  $\phi_{\text{old}}$  (rad) represents the old crank angle, while  $\Delta\phi$  (rad) represents the crank angle step. For flat-flat combustion chamber geometry, the piston volume is zero (0). The volume of a piston that features a cylindrically shaped bowl is calculated with the following expression:

$$V_{\text{piston}} = \frac{D_{\text{bowl}}^2 \cdot \pi}{4} \cdot h_{\text{bowl}} \quad (3.202)$$

In the equation given above,  $D_{\text{bowl}}$  (m) represents the diameter of the bowl inside the piston, while  $h_{\text{bowl}}$  (m) represents the depth of the bowl inside the piston.

### 3.7.2. In-cylinder volume matrix generation

After the piston position matrix is generated it is possible to calculate the cylinder volume matrix, which is a function of the piston position matrix. For a given piston position, the cylinder volume,  $V_{\text{cyl}}$  ( $\text{m}^3$ ) is given with the following expression:

$$V_{\text{cyl}}(i_{\text{pis}}) = \frac{D_{\text{cyl}}^2 \cdot \pi}{4} \cdot x_{\text{piston}}(i_{\text{pis}}) + V_{\text{piston}} \quad (3.203).$$

### 3.7.3. Flame radius matrix generation

The minimum flame radius is zero (0), while the maximum flame radius is obtained when the piston is located in the BDC, and is calculated with the following equations:

$$R_{\text{flame}}(i_{\text{rad}}) = (i_{\text{rad}} - 1) \cdot \Delta R_{\text{flame}} \quad (3.204)$$

$$R_{\text{flame,max}} = \sqrt{H_{\text{flame,max}}^2 + W_{\text{flame,max}}^2} \quad (3.205)$$

$$\Delta R_{\text{flame}} = \frac{R_{\text{flame,max}}}{(n_{\text{rad}} - 1)} \quad (3.206)$$

In the equations given above  $R_{\text{flame,max}}$  (m) represents the maximum flame radius for a given flame center and piston position,  $H_{\text{flame}}$  (m) represents the maximum distance in the vertical direction (so-called flame height) between the flame center and combustion chamber wall,  $W_{\text{flame}}$  (m) represents the maximum distance in the radial direction (so-called flame width) between the flame center and combustion chamber wall,  $\Delta R_{\text{flame}}$  (m) represents the flame radius step, while  $R_{\text{flame}}$  (m) represents the flame radii matrix.

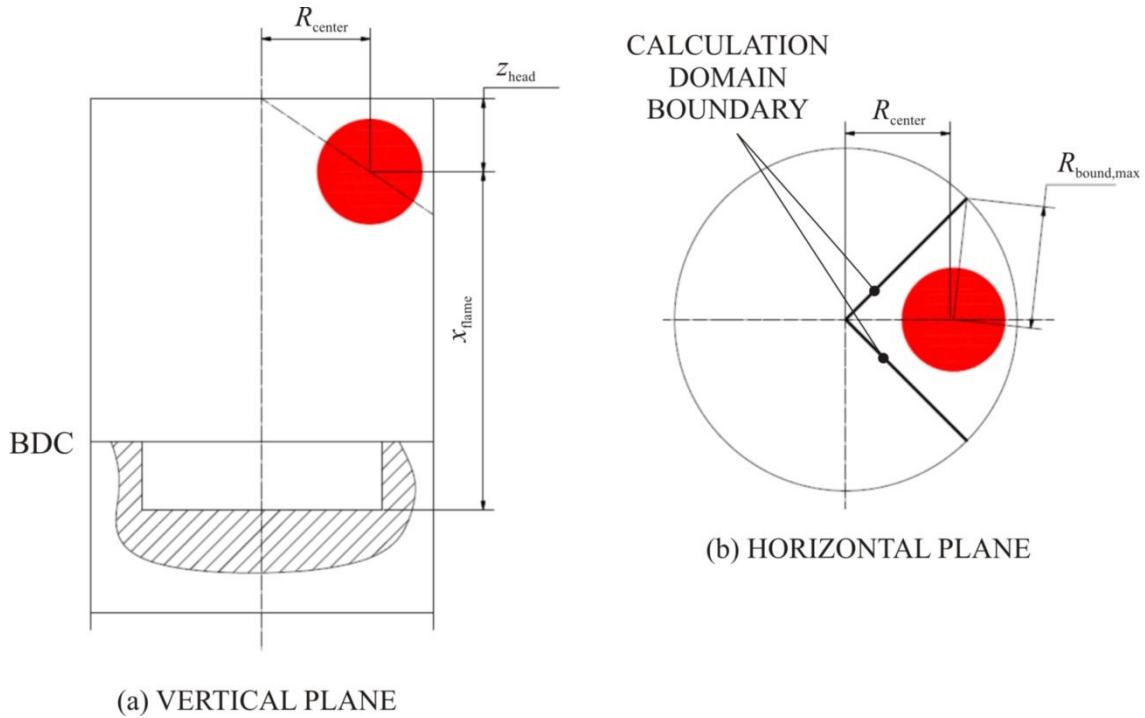


**Figure 80. Schematic of the flame location within the combustion chamber and its relative position to the combustion chamber walls and calculation domain boundaries**

Maximum flame distance in vertical and horizontal direction can be calculated with the following expression (Figure 80):

$$H_{\text{flame}} = \max[z_{\text{head}}, x_{\text{flame}}] \quad (3.207)$$

$$W_{\text{flame}} = \max(R_{\text{center}}, R_{\text{bound,max}}) \quad (3.208)$$

In the equations given above  $z_{\text{head}}$  (m) represents the distance between the cylinder head and flame center,  $x_{\text{flame}}$  (m) represents the distance from the flame center and the piston bottom (in this is piston top for flat piston geometry) when the piston is located in BDC,  $R_{\text{center}}$  (m) represents the distance from the cylinder axis to the flame center in the horizontal plane, while  $R_{\text{bound,max}}$  (m) represents the maximum distance from the flame center to the combustion chamber walls.

### 3.7.4. Flame surface data matrices generation

Finally, after the arrays that are necessary for the flame data generation have been defined it is possible to calculate the flame surface data arrays. As was already mentioned at the beginning of the chapter 3.7, in this thesis only the modeling approach for the more complicated combustion chamber (flat–bowl) is presented. In the case of the simpler combustion chamber geometry (flat – flat) all the data can easily be calculated in the same manner.

A spherical body; i.e. free, unbounded flame volume and surface area can numerically be calculated according to the approach that is presented in the Figure 81.

In this numerical approach the resulting sphere is sliced into a number of slices as shown in Figure 81. The incremental surface area and volume (area and volume of an infinitesimal element of a sphere) of each slice equals:

$$dV = R_{\text{slice}}^2 \cdot \pi \cdot dz \quad (3.209)$$

$$dA = 2 \cdot R_{\text{slice}} \cdot \pi \cdot dl = 2 \cdot R_{\text{flame}} \cdot \pi \cdot dz \quad (3.210)$$

$$R_{\text{slice}}(z) = \sqrt{R_{\text{flame}}^2 - z^2} \quad (3.211)$$

In the equations given above,  $dV$  (m<sup>3</sup>) represents the incremental volume of a given flame slice,  $R_{\text{slice}}$  (m) represents the radius of the flame slice,  $dA$  (m<sup>2</sup>) represents the incremental surface area of a given flame slice,  $R_{\text{flame}}$  (m) represents radius of the sphere (flame), while  $z$  (m) represents the vertical location of the slice.

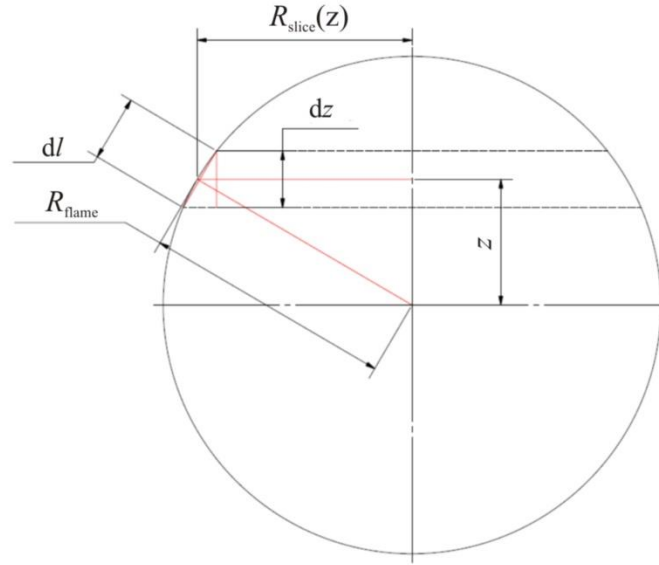


**Figure 81. Schematic of the division of the numerical calculation of the sphere volume and surface area (division into slices)**

The overall sphere (flame) volume and surface area can now be expressed in the following form:

$$V_{\text{flame}} = \int_{-R_{\text{flame}}}^{R_{\text{flame}}} R_{\text{slice}}(z)^2 \cdot \pi \cdot dz \quad (3.212)$$

$$A_{\text{flame}} = \int_{-R_{\text{flame}}}^{R_{\text{flame}}} 2 \cdot R_{\text{flame}} \cdot \pi \cdot dz \quad (3.213)$$

In the equations given above,  $V_{\text{flame}}$  ( $\text{m}^3$ ) represents the volume of the sphere (flame), while  $A_{\text{flame}}$  ( $\text{m}^2$ ) represents the surface area of the sphere (flame). In the first step of the flame surface data generation inside the cylinder of the engine (flame bounded by the combustion chamber walls), the flame body that is a result of the given flame center, piston position and flame radius is generated. A resulting flame can have several shapes (Figure 82):

1. The resulting flame interacts with all of the combustion chamber walls.
2. The resulting flame is fully spherical; flame does not interact with any of the chamber walls.
3. The resulting flame interacts only with the liner.
4. The resulting flame interacts with just two or three walls. In this case various different combinations are possible; i.e. the resulting flame interacts with the calculation domain, and with the piston and liner.



5. The resulting flame interacts only with the piston.
6. The resulting flame interacts only with the calculation domain (chamber symmetry surfaces). When the flame touches the calculation domain wall, the flames have merged into one larger flame.
7. The resulting flame interacts only with the cylinder head.

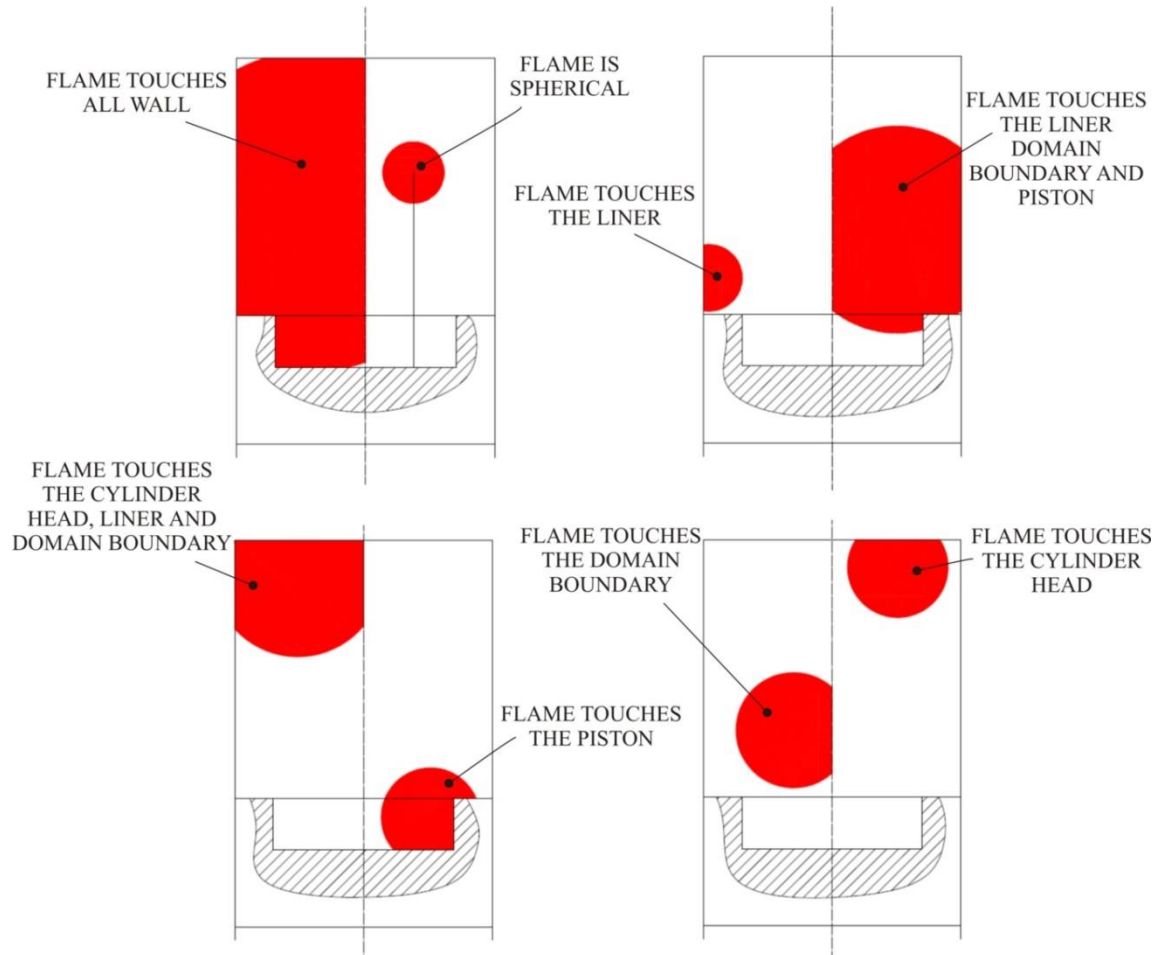


**Figure 82. Schematic of the possible flame – combustion chamber walls interactions**

To simplify the calculation approach, the combustion chamber was divided into two sections (Figure 83):

1. The main section of the combustion chamber
2. The bowl section of the combustion chamber

In the multiple flame surface calculation model the piston bowl section is considered as a small flat-flat combustion chamber. This enables the application of the same calculation approach for generating the flame data for the part of the flame that is in the main section as well as for the part of the flame that is in the piston section of the combustion chamber.

Therefore in the remaining part of the thesis only the interactions for the flat-flat geometry are presented.

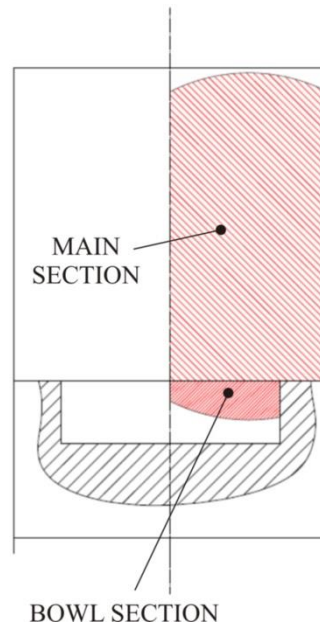


**Figure 83. Schematic of the sections within the combustion chamber**

For a given flame section (Figure 83 - main and bowl section), the flame body is divided into two parts, where the division surface is the surface perpendicular to the cylinder axis and goes through the flame center (see Figure 84):

1. Head flame
2. Piston flame

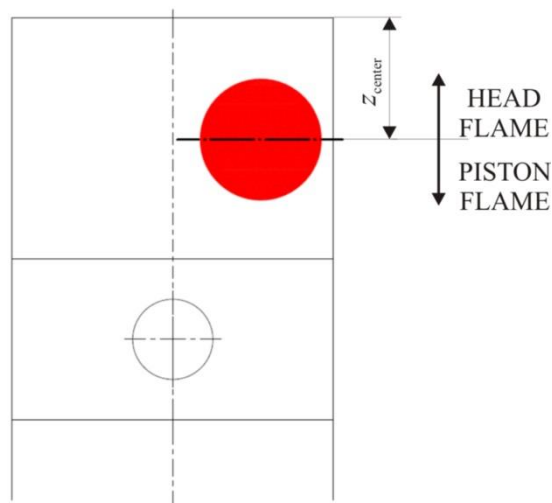


**Figure 84. Schematic of the division of the flame surface data calculation in two parts**

The head flame refers to the part of the flame that is located above the flame center axis, while the piston flame refers to the part of the flame that is located below the flame center axis (Figure 84). Once the flame was divided into two parts (head and piston flames) each of these parts is sliced into  $n$  slices; 101 slices have been applied in this model. After that for each flame slice its interactions with the walls are defined. According to these interactions for each flame slice the free flame arc and the flame slice surface area are calculated (Figure 85).

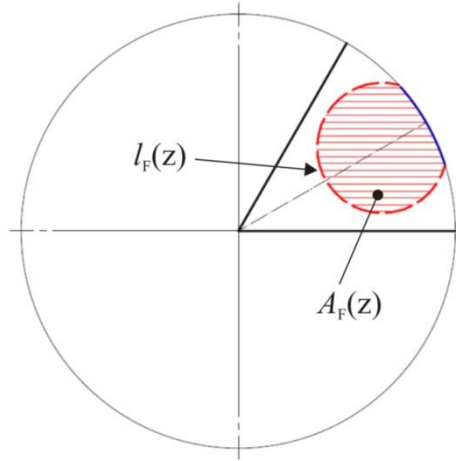


**Figure 85. Schematic of the free flame arc, interaction arc, flame slice surface area**

The free flame arc  $l_F$  (m) represents the arc of the flame slice which corresponds to the flame front. The flame slice surface area  $A_F$  (m<sup>2</sup>) represents the area of the slice that corresponds to the flame area. The part of the flame surface data that corresponds to head flame are calculated with the head calculation sub-model, while the second part is calculated with the piston calculation sub-model. For a given  $i$ -th part of the flame (head or piston calculation), the free flame surface and burned volume are calculated as follows:

$$V_{\text{flame},i} = \int_{z_1}^{z_2} A_F(z) \cdot dz \quad (3.214)$$

$$A_{\text{flame},i} = \int_{z_1}^{z_2} l_F(z) \cdot dz \quad (3.215)$$

In the equations given above,  $z_1$  (m) and  $z_2$  (m) represent the lower and upper flame vertical limits, respectively. Their respective derivation ( $z_1$  and  $z_2$ ) is presented in the next chapter. The final, overall flame surface data arrays (burned volume and free flame surface) for one flame are calculated with the following expressions:

$$V_{\text{flame}}(n_{\text{pis}}, n_{\text{rad}}) = \left[ V_{\text{flame,head}}(n_{\text{pis}}, n_{\text{rad}}) + V_{\text{flame,piston}}(n_{\text{pis}}, n_{\text{rad}}) \right]_{\text{main}} + \left[ V_{\text{flame,head}}(n_{\text{pis}}, n_{\text{rad}}) + V_{\text{flame,piston}}(n_{\text{pis}}, n_{\text{rad}}) \right]_{\text{bowl}} \quad (3.216)$$

$$A_{\text{flame}}(n_{\text{pis}}, n_{\text{rad}}) = \left[ A_{\text{flame,head}}(n_{\text{pis}}, n_{\text{rad}}) + A_{\text{flame,piston}}(n_{\text{pis}}, n_{\text{rad}}) \right]_{\text{main}} + \left[ A_{\text{flame,head}}(n_{\text{pis}}, n_{\text{rad}}) + A_{\text{flame,piston}}(n_{\text{pis}}, n_{\text{rad}}) \right]_{\text{bowl}} \quad (3.217)$$

In the equations given above, the subscript *head* refers to the head flame, while the subscript *piston* refers to the piston flame. In the case when the combustion chamber has a flat – bowl geometry, two sets of these data are calculated; one corresponds to the main section of the combustion chamber (subscript *main*), while the other corresponds to the bowl section of the combustion chamber (subscript *bowl*). Hence, in such case the overall flame surface data for each flame is calculated as a sum of the data that correspond to the main and bowl sections of the combustion chamber, respectively.

Generally, for a given piston position and flame radius the calculation proceeds in the following way:

1. Division of the flame body into two parts (main and bowl flame sections).
2. Division of each section into two parts (head and piston flame calculation).
3. Definition of the vertical limits and slicing of each of the corresponding part of the flame.
4. Definition of the cylinder head (in the case of head flame) or piston top (in the case of the piston flame) interaction slices and calculation of the wetted cylinder head or the wetted piston top surface areas (calculation of the corresponding flame slice – wall interactions and definition of the corresponding slice surface area). In this calculation cylinder head (or piston top) wetted surface area is generally the flame slice surface area.
5. Calculation of the flame – wall interaction for every flame slice (free flame arc, interaction arc and the flame slice surface area).
6. Generation of the overall flame surface data for the corresponding flame part.
7. Summation of the head flame data and piston flame data for each section.
8. Summation of the flame surface data for the main and bowl sections of the combustion chamber (if the piston features a bowl).

This procedure is performed for every possible combination of the piston positions and flame radii and then finally the overall flame surface data is generated (equations 3.193 and 3.194).

### ***Head and piston flame vertical limits calculation***

As can be seen from the previous elaboration, in order to slice the resulting flame body, it is necessary to prescribe the vertical flame limits. There are a few possible locations of the flame center relative to the combustion chamber geometry, i.e. domain walls, which are shown in Figure 86:

1. Flame center is both radially and vertically inside of the combustion chamber (**1<sup>st</sup> type**)
2. Flame center is both radially and vertically outside of the combustion chamber
  - a. Flame center is above the cylinder head (**2<sup>nd</sup> type**)
  - b. Flame center is below the piston top (**3<sup>rd</sup> type**)
3. Flame center is vertically inside the combustion chamber, while its radial position is outside of the combustion chamber (**4<sup>th</sup> type**)
4. Flame center is radially inside the combustion chamber, while its vertical position is outside of the combustion chamber
  - a. Flame center is above the cylinder head (**5<sup>th</sup> type**)
  - b. Flame center is below the piston top (**6<sup>th</sup> type**)

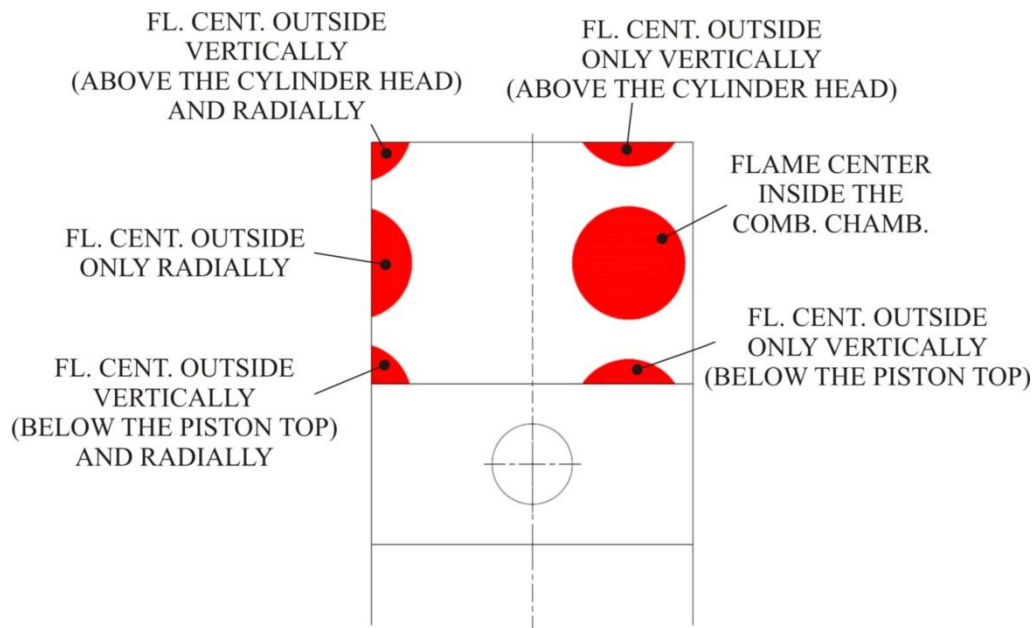


**Figure 86. Schematic of the flame center location relative to the combustion chamber geometry**

### 1<sup>st</sup> type of the relative location of the flame center to the domain walls

In this type of the relative position between the flame center and combustion chamber geometry, the flame center is located both radially and vertically inside of the combustion chamber (Figure 87).

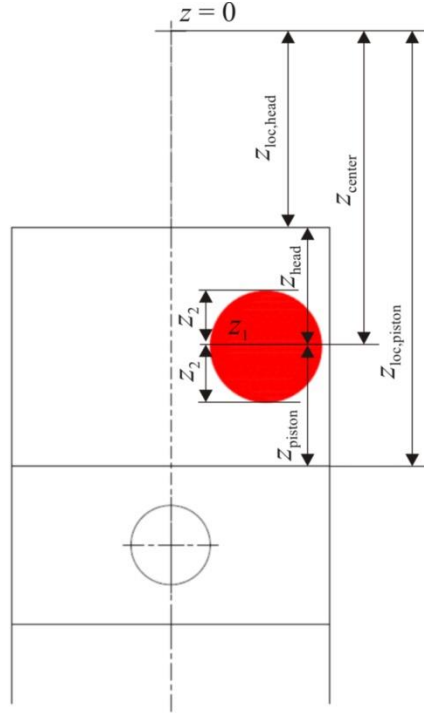


**Figure 87. Schematic of the specific interaction in the case of the 1<sup>st</sup> type of the relative location between the flame center and the domain walls**

For this flame center – combustion chamber interaction type, the lower flame vertical limits for both head and piston flame calculations is equal to zero (0). The upper flame vertical limit for the head flame calculation can be calculated from the following equations:

$$z_{\text{head}} = z_{\text{center}} - z_{\text{loc,head}} \quad (3.218)$$

$$z_2 = \min(R_{\text{flame}}(i_{\text{rad}}), z_{\text{head}}) \quad (3.219)$$

The upper flame vertical limit and the boundary vertical limit for the piston flame calculation can be calculated from the following equations:

$$z_{\text{piston}} = z_{\text{loc,piston}} - z_{\text{center}} \quad (3.220)$$

$$z_2 = \min(R_{\text{flame}}(i_{\text{rad}}), z_{\text{piston}}) \quad (3.221)$$

## 2<sup>nd</sup> type of the relative location of the flame center to the domain walls

In this type of the relative position between the flame center and combustion chamber geometry, the flame center is located both radially and vertically outside of the combustion chamber (above the cylinder head) (Figure 88).

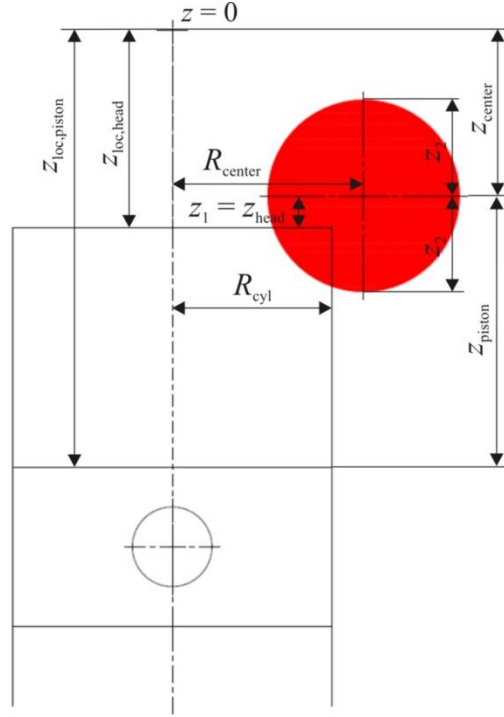


**Figure 88. Schematic of the specific interaction in the case of the 2<sup>nd</sup> type of the relative location between the flame center and the domain walls**

For this flame center – combustion chamber interaction type, there is no head flame as the flame center is above the cylinder head. The lower and upper flame vertical limit for the piston flame calculation can be calculated from the following equations:

$$z_{\text{head}} = z_{\text{loc,head}} - z_{\text{center}} \quad (3.222)$$

$$z_{\text{piston}} = z_{\text{loc,piston}} - z_{\text{center}} \quad (3.223)$$

$$z_1 = z_{\text{head}} \quad (3.224)$$

$$z_2 = \min(R_{\text{flame}}(i_{\text{rad}}), z_{\text{piston}}) \quad (3.225)$$

Also, if the flame radius is lower than the specific control value, flame does not enter the calculation domain and hence all relevant flame data are equal to zero (0). This control value,  $R_{\text{flame,control}}$  (m) can be calculated from the following equations:

$$R_{\text{flame,control}} = \sqrt{z_{\text{head}}^2 + (R_{\text{center}} - R_{\text{cyl}})^2} \quad (3.226)$$

### 3<sup>rd</sup> type of the relative location of the flame center to the domain walls

In this type of the relative position between the flame center and combustion chamber geometry, the flame center is located both radially and vertically outside of the combustion chamber (below the piston top) (Figure 89).

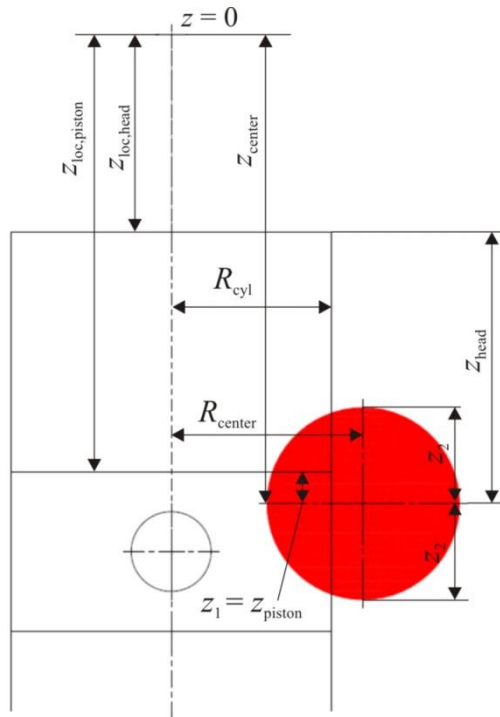


**Figure 89. Schematic of the specific interaction in the case of the 3<sup>rd</sup> type of the relative location between the flame center and the domain walls**

For this flame center – combustion chamber interaction type, there is no piston flame as the flame center is below the piston top. The lower and upper flame vertical limit for the head flame calculation can be calculated from the following equations:

$$z_{\text{head}} = z_{\text{center}} - z_{\text{loc,head}} \quad (3.227)$$

$$z_{\text{piston}} = z_{\text{center}} - z_{\text{loc,piston}} \quad (3.228)$$



$$z_1 = z_{\text{piston}} \quad (3.229)$$

$$z_2 = \min(R_{\text{flame}}(i_{\text{rad}}), z_{\text{head}}) \quad (3.230)$$

Also, if the flame radius is lower than the specific control value, flame does not enter the calculation domain and hence all relevant flame data are equal to zero (0). This control value,  $R_{\text{flame,control}}$  (m) can be calculated from the following equations:

$$R_{\text{flame,control}} = \sqrt{z_{\text{piston}}^2 + (R_{\text{center}} - R_{\text{cyl}})^2} \quad (3.231)$$

#### 4<sup>th</sup> type of the relative location of the flame center to the domain walls

In this type of the relative position between the flame center and combustion chamber geometry, the flame center is vertically inside the combustion chamber, while its radial position is outside the combustion chamber (Figure 90).

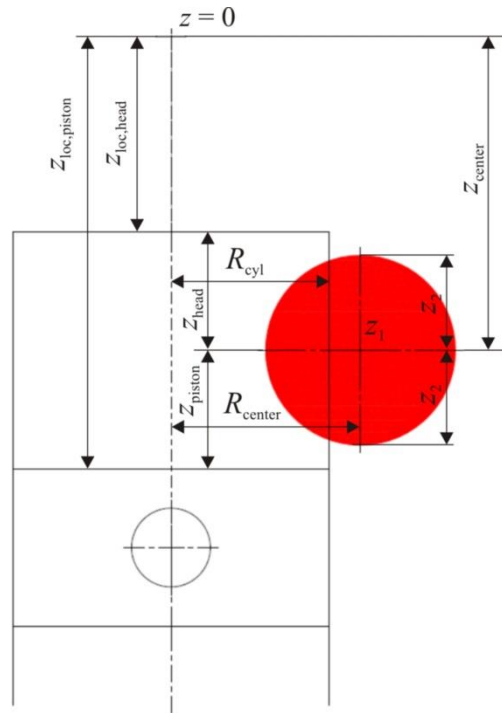


**Figure 90. Schematic of the specific interaction in the case of the 4<sup>th</sup> type of the relative location between the flame center and the domain walls**

For this flame center – combustion chamber interaction type, the lower flame vertical limits for both head and piston flame calculations is equal to zero (0). The upper flame vertical limit for the head flame calculation can be calculated from the following equations:

$$z_{\text{head}} = z_{\text{center}} - z_{\text{loc,head}} \quad (3.232)$$

$$z_2 = \min(R_{\text{flame}}(i_{\text{rad}}), z_{\text{head}}) \quad (3.233)$$

The upper flame vertical limit for the piston flame calculation can be calculated from the following equations:

$$z_{\text{piston}} = z_{\text{loc,piston}} - z_{\text{center}} \quad (3.234)$$

$$z_2 = \min(R_{\text{flame}}(i_{\text{rad}}), z_{\text{piston}}) \quad (3.235)$$

Also, if the flame radius is lower than the specific control value, flame does not enter the calculation domain and hence all relevant flame data are equal to zero (0). This control value,  $R_{\text{flame,control}}$  (m) can be calculated from the following equations:

$$R_{\text{flame,control}} = R_{\text{center}} - R_{\text{cyl}} \quad (3.236)$$

### 5<sup>th</sup> type of the relative location of the flame center to the domain walls

In this type of the relative position between the flame center and combustion chamber geometry, the flame center is radially inside the combustion chamber, while its vertical position is outside the combustion chamber (above the cylinder head) (Figure 91). For this flame center – combustion chamber interaction type, there is no head flame as the flame center is above the cylinder head. The lower and upper flame vertical limit for the piston flame calculation can be calculated from the following equations:

$$z_{\text{head}} = z_{\text{loc,head}} - z_{\text{center}} \quad (3.237)$$

$$z_{\text{piston}} = z_{\text{loc,piston}} - z_{\text{center}} \quad (3.238)$$

$$z_1 = z_{\text{head}} \quad (3.239)$$

$$z_2 = \min(R_{\text{flame}}(i_{\text{rad}}), z_{\text{piston}}) \quad (3.240)$$

Also, if the flame radius is lower than the specific control value, flame does not enter the calculation domain and hence all relevant flame data are equal to zero (0). This control value,  $R_{\text{flame,control}}$  (m) can be calculated from the following equations:

$$R_{\text{flame,control}} = z_{\text{head}} \quad (3.241)$$

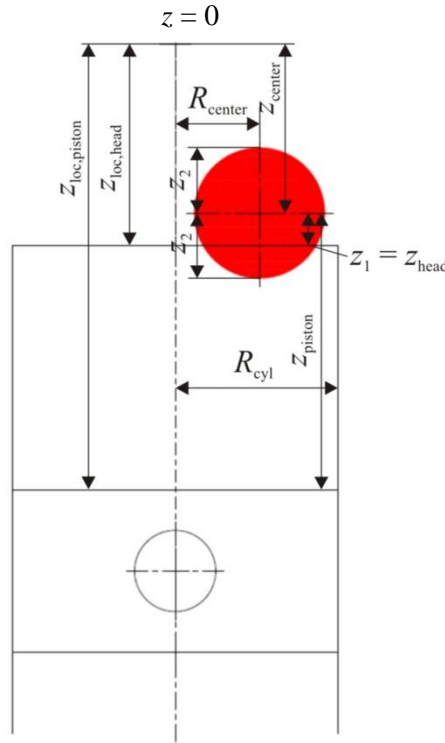


**Figure 91. Schematic of the specific interaction in the case of the 5<sup>th</sup> type of the relative location between the flame center and the domain walls**

### 6<sup>th</sup> type of the relative location of the flame center to the domain walls

In this type of the relative position between the flame center and combustion chamber geometry, the flame center is radially inside the combustion chamber, while its vertical position is outside of the combustion chamber (below the piston top) (Figure 92). For this flame center – combustion chamber interaction type, there is no piston flame as the flame center is below the piston top. The lower and upper flame vertical limit for the head flame calculation can be calculated from the following equations:

$$z_{\text{head}} = z_{\text{center}} - z_{\text{loc,head}} \quad (3.242)$$

$$z_{\text{piston}} = z_{\text{center}} - z_{\text{loc,piston}} \quad (3.243)$$

$$z_1 = z_{\text{piston}} \quad (3.244)$$

$$z_2 = \min(R_{\text{flame}}(i_{\text{rad}}), z_{\text{head}}) \quad (3.245)$$

Also, if the flame radius is lower than the specific control value, flame does not enter the calculation domain and hence all relevant flame data are equal to zero (0). This control value,  $R_{\text{flame,control}}$  (m) can be calculated from the following equations:

$$R_{\text{flame,control}} = z_{\text{piston}} \quad (3.246)$$

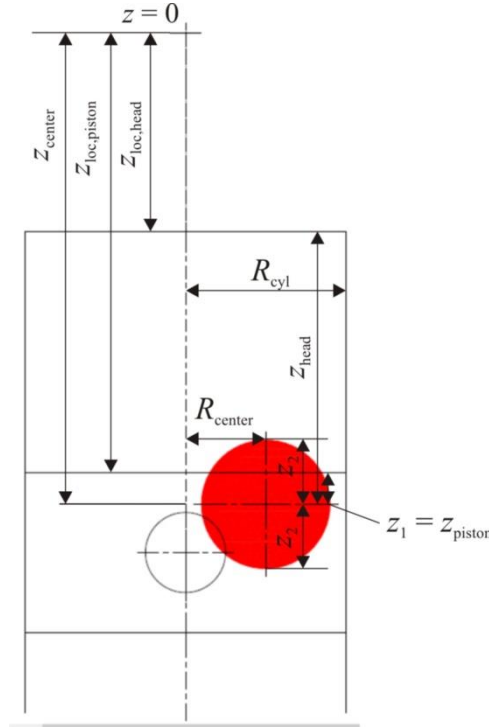


**Figure 92. Schematic of the specific interaction in the case of the 6<sup>th</sup> type of the relative location between the flame center and the domain walls**

### ***Flame slice – wall interaction calculation***

There are four (4) basic types of interactions between the flame slice and the walls:

1. Flame slice doesn't touch any walls (**1<sup>st</sup> interaction type**)
2. Flame slice touches the cylinder liner (**2<sup>nd</sup> interaction type**)
3. Flame slices touches the calculation domain boundary (**3<sup>rd</sup> interaction type**)
4. Flame slices touches both the cylinder liner and the calculation domain boundary
  - a. Flame slice only partially covers the boundaries (**4<sup>th</sup> interaction type**)
  - b. Flame slice completely covers both of the boundaries (**5<sup>th</sup> interaction type**)
  - c. Flame slice completely covers only the cylinder liner (**6<sup>th</sup> interaction type**)

It can be seen that the 4<sup>th</sup> interaction type features three (3) more sub-types. This means that there are a total of six (6) interaction types.

### 1<sup>st</sup> interaction type

As was already mentioned, in the case of this interaction type there is no interaction between the flame slice and the walls (Figure 93).

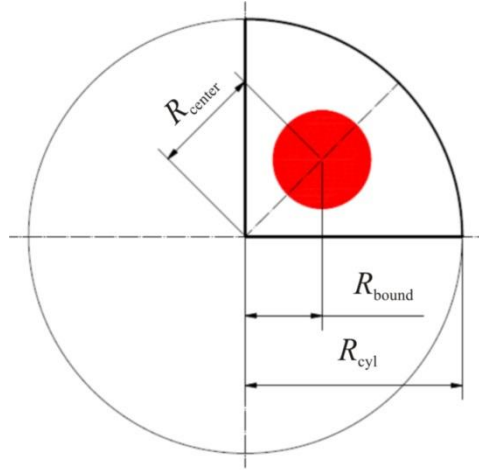


**Figure 93. Schematic of the 1<sup>st</sup> type of the flame slice – wall interaction**

For this interaction type, the free flame arc, wall interaction arc and flame slice surface area are calculated with the following equations:

$$l_F(z) = 2 \cdot R_{\text{flame}}(i_{\text{rad}}) \cdot \pi \quad (3.247)$$

$$A_F(z) = R_{\text{slice}}(z)^2 \cdot \pi \quad (3.248)$$

In the equations given above,  $R_{\text{cyl}}$  (m) represents the radius of the combustion chamber geometry;  $R_{\text{center}}$  (m) represents the distance between the vertical axis of the cylinder and the center of the flame (in the horizontal plane of the combustion chamber), while  $R_{\text{bound}}$  (m) represents the minimal distance between the domain boundary and the center of the flame (in the horizontal plane of the combustion chamber).

## 2<sup>nd</sup> interaction type

As was already mentioned, in the case of this interaction type the given flame slice touches the cylinder liner (Figure 94).

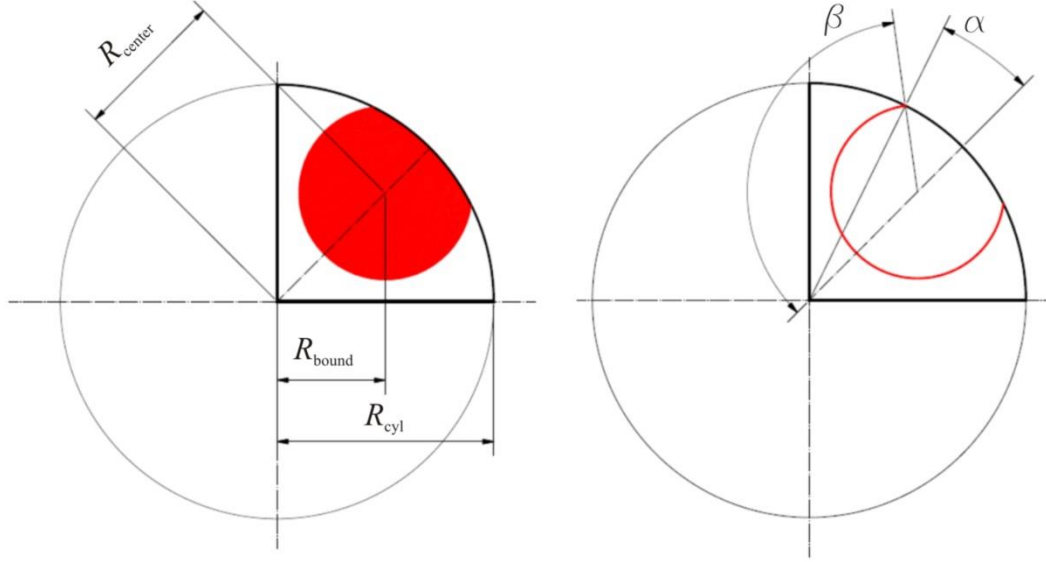


**Figure 94. Schematic of the 2<sup>nd</sup> type of the flame slice – wall interaction**

For this interaction type, the free flame arc, wall interaction arc and flame slice surface area are calculated with the following equations:

$$l_F(z) = 2 \cdot R_{\text{flame}}(i_{\text{rad}}) \cdot \beta \quad (3.249)$$

$$A_F(z) = R_{\text{cyl}}^2 \cdot \alpha + R_{\text{slice}}(z)^2 \cdot \beta - R_{\text{cyl}} \cdot R_{\text{center}} \cdot \sin \alpha \quad (3.250)$$

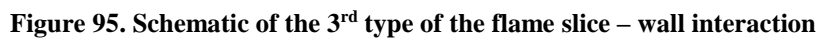
$$\alpha = \cos^{-1} \left( \frac{R_{\text{center}}^2 + R_{\text{cyl}}^2 - R_{\text{slice}}(z)^2}{2 \cdot R_{\text{center}} \cdot R_{\text{cyl}}} \right) \quad (3.251)$$

$$\beta = \cos^{-1} \left( \frac{R_{\text{center}}^2 + R_{\text{slice}}(z)^2 - R_{\text{cyl}}^2}{2 \cdot R_{\text{center}} \cdot R_{\text{slice}}(z)} \right) \quad (3.252)$$

In the equations given above, all angles are in radians.

## 3<sup>rd</sup> interaction type

As was already mentioned, in the case of this interaction type the given flame slice touches the calculation domain (Figure 95).


$$l_F(z) = 2 \cdot R_{\text{flame}}(i_{\text{rad}}) \cdot (\beta_1 + \beta_2) \quad (3.253)$$

$$A_F(z) = R_{\text{slice}}(z)^2 \cdot (\beta_1 + \beta_2) + 2 \cdot R_{\text{bound}} \cdot R_{\text{slice}}(z) \cdot \sin \gamma \quad (3.254)$$

$$\gamma = \cos^{-1} \left( \frac{R_{\text{bound}}}{R_{\text{slice}}(z)} \right) \quad (3.255)$$

$$R_{\text{bound}} = R_{\text{center}} \cdot \cos^{-1} \left( \frac{\varphi_{\text{bound}}}{2} \right) \quad (3.256)$$

$$\varphi_{\text{bound}} = \frac{2\pi}{n_{\text{flames}}} \quad (3.257)$$

$$\beta_1 = \pi - \left( \frac{\pi}{2} - \frac{\phi_{\text{bound}}}{2} \right) - \gamma \quad (3.258)$$

$$\beta_2 = \left( \frac{\pi}{2} - \frac{\varphi_{\text{bound}}}{2} \right) - \gamma \quad (3.259)$$

---

163

#### 4<sup>th</sup> interaction type

As was already mentioned, in the case of this interaction type the given flame slice touches both the cylinder liner and the calculation domain. In this specific interaction type the flame slices only partially covers the walls (Figure 96).

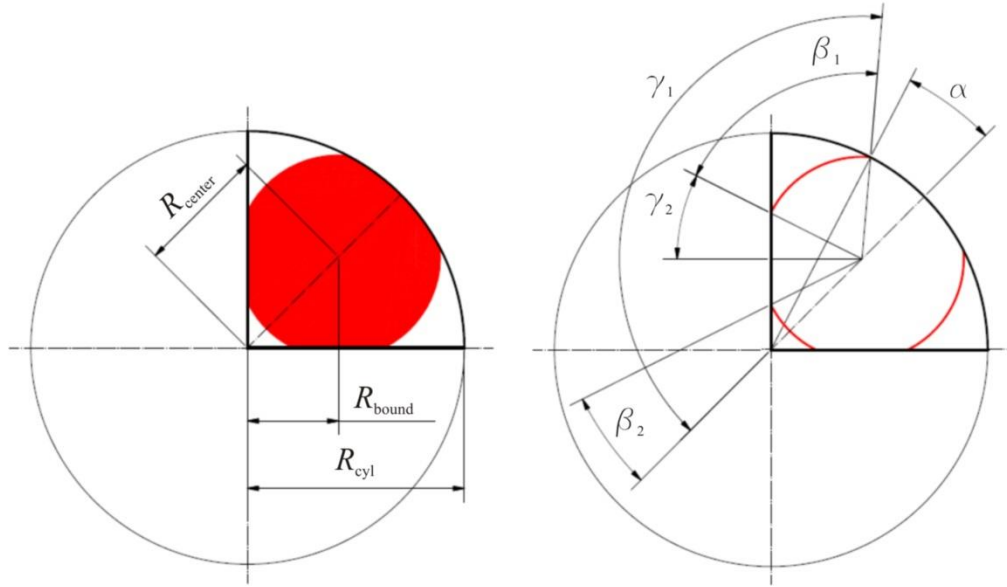


**Figure 96. Schematic of the 4<sup>th</sup> type of the flame slice – wall interaction**

For this interaction type, the free flame arc, wall interaction arc and flame slice surface area are calculated with the following equations:

$$l_F(z) = 2 \cdot R_{\text{flame}}(i_{\text{rad}}) \cdot (\beta_1 + \beta_2) \quad (3.260)$$

$$A_F(z) = R_{\text{cyl}}^2 \cdot \alpha + R_{\text{slice}}(z)^2 \cdot (\beta_1 + \beta_2) + 2 \cdot R_{\text{bound}} \cdot R_{\text{slice}}(z) \cdot \sin \gamma_2 - R_{\text{cyl}} \cdot R_{\text{center}} \cdot \sin \alpha \quad (3.261)$$

$$\alpha = \cos^{-1} \left( \frac{R_{\text{center}}^2 + R_{\text{cyl}}^2 - R_{\text{slice}}(z)^2}{2 \cdot R_{\text{center}} \cdot R_{\text{cyl}}} \right) \quad (3.262)$$

$$\gamma_1 = \cos^{-1} \left( \frac{R_{\text{center}}^2 + R_{\text{slice}}(z)^2 - R_{\text{cyl}}^2}{2 \cdot R_{\text{center}} \cdot R_{\text{slice}}(z)} \right) \quad (3.263)$$

$$\gamma_2 = \cos^{-1} \left( \frac{R_{\text{bound}}}{R_{\text{slice}}(z)} \right) \quad (3.264)$$



$$\beta_1 = \gamma_1 - \left( \frac{\pi}{2} - \frac{\varphi_{\text{bound}}}{2} \right) - \gamma_2 \quad (3.265)$$

$$\beta_2 = \left( \frac{\pi}{2} - \frac{\varphi_{\text{bound}}}{2} \right) - \gamma_2 \quad (3.266)$$

In the equations given above, all angles are in radians.

### 5<sup>th</sup> interaction type

As was already mentioned, in the case of this interaction type the given flame slice touches both the cylinder liner and the calculation domain. In this specific interaction type the flame slice fully covers the walls (Figure 97).

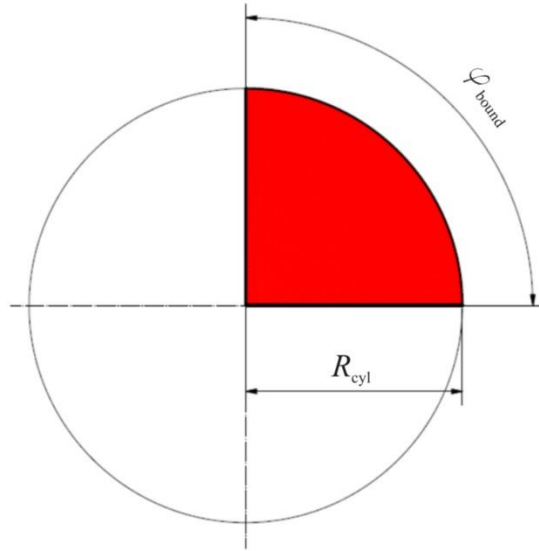


**Figure 97. Schematic of the 5<sup>th</sup> type of the flame slice – wall interaction**

For this interaction type, the free flame arc, wall interaction arc and flame slice surface area are calculated with the following equations:

$$l_F(z) = 0 \quad (3.267)$$

$$A_F(z) = \frac{R_{\text{cyl}}^2 \cdot \pi}{n_{\text{flames}}} \quad (3.268)$$

### 6<sup>th</sup> interaction type

As was already mentioned, in the case of this interaction type the given flame slice touches both the cylinder liner and the calculation domain. In this specific interaction type the flame slice fully covers only the cylinder liner (Figure 98).

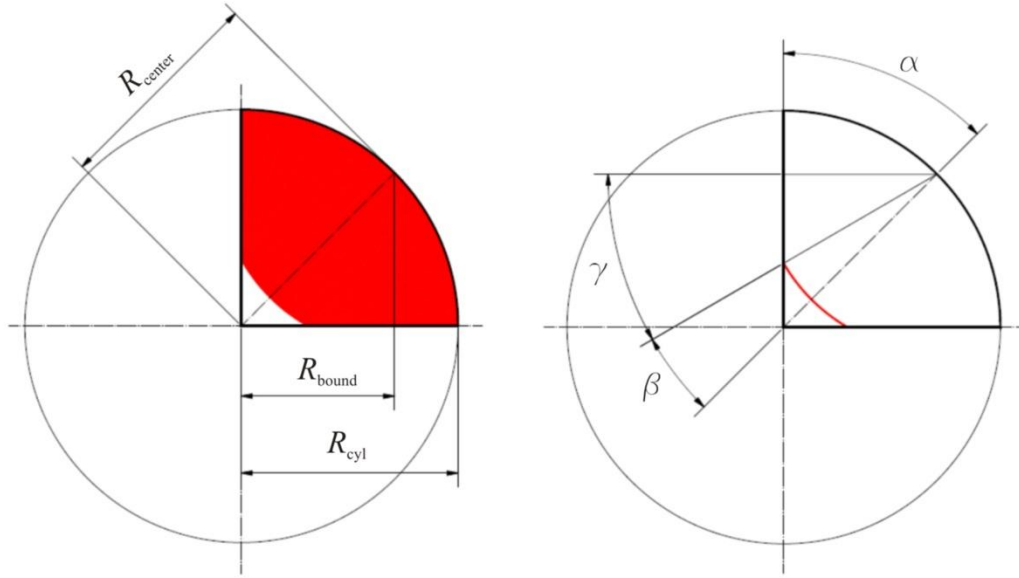


Figure 98. Schematic of the 6<sup>th</sup> type of flame slice – wall interaction

For this interaction type, the free flame arc, wall interaction arc and flame slice surface area are calculated with the following equations:

$$l_F(z) = 2 \cdot R_{\text{flame}}(i_{\text{rad}}) \cdot \beta \quad (3.269)$$

$$A_F(z) = R_{\text{cyl}}^2 \cdot \alpha + R_{\text{slice}}(z)^2 \cdot \beta - R_{\text{center}} \cdot R_{\text{slice}}(z) \cdot \sin \beta \quad (3.270)$$

$$\alpha = \frac{\varphi_{\text{bound}}}{2} \quad (3.271)$$

$$\gamma = \cos^{-1} \left( \frac{R_{\text{bound}}}{R_{\text{slice}}(z)} \right) \quad (3.272)$$

$$\beta = \left( \frac{\pi}{2} - \frac{\varphi_{\text{bound}}}{2} \right) - \gamma \quad (3.273)$$

In the equations given above, all angles are in radians.

### 3.7.5. Instantaneous flame surface values calculation

In the DFMZCM, the flame data (look-up tables) that have been made at the beginning of the calculation with multiple flame surface calculation model are used during the calculation of the flame propagation governed by fuel burning rate. In order to obtain the flame surface area value from the tables, the following procedure is performed:

1. Calculation of the instantaneous piston position location.
2. Calculation of the instantaneous burned volume.
3. Extraction of the instantaneous flame radius data from the tables (according to the calculated piston position location and burned volume).
4. Extraction of the instantaneous flame surface area from the tables (according to the extracted flame radius data and calculated piston position location).

## 3.8. Pollutants formation models

In the case of a complete combustion process of a hydrocarbon fuel, the exhaust gas will consist of nitrogen, carbon dioxide and water vapor, as well as oxygen if there was a surplus of air inside the fuel/air mixture. However, as no real combustion process occurs in a complete manner, depending on the combustion process, there will be some additional species present in the exhaust gases. These species can be summed up into 4 major categories [59], [66]:

1. carbon monoxide (CO),
2. unburned hydrocarbons (UHC),
3. nitrogen oxides (NO<sub>x</sub>),
4. particulate matter (PM).

As these species are harmful for both the environment and humans, they are referred to as pollutants. Since the formation of pollutants is a result of the combustion process, it is important that the combustion model is able to predict and calculate the pollutants formation process. Since for modeling of the phenomena of emission formation it is important to understand their origin, before presenting the models for calculating and predicting pollutants formation, a brief introduction into the physical and chemical background of the pollutant formation is given.

### 3.8.1. Pollutant formation background

As the combustion process in conventional dual fuel engine shares characteristics with both DI-CI and SI engines, the model in this thesis needs to be able to track and calculate the

harmful exhaust gas emissions that are characteristic for the conventional DI-CI engines (soot, CO and NO<sub>x</sub> emissions), and for the SI engines (HC, CO and NO<sub>x</sub> emissions). Generally, the pollutants formation is strongly dependent on the mixture equivalence ratio and associated in-cylinder temperature as well as on the fuel and air distribution inside the combustion chamber [66]. The background on the formation of each of these pollutants is presented in the next four chapters.

### ***CO emission***

CO emission is a pollutant whose formation is mainly controlled by the mixture equivalence ratio [66], [104]. In the process of hydrocarbon combustion, CO is an intermediate species before it is fully oxidized to CO<sub>2</sub> [59]. This means that CO is formed in a fuel rich regions where there is not enough air to oxidize CO to CO<sub>2</sub>. However, as this patch of gas mixes with the surrounding combustion products that still might feature some air, if the temperature is high enough this CO will oxidize into the CO<sub>2</sub>. This is supported by the results in [104], where it was shown that the CO concentration during the combustion process is actually higher than the CO concentration in the exhaust. This means that in order to model and predict the CO emission it is necessary to account for its creation and destruction.

It is important to keep in mind that if the temperature is not high enough (the necessary level depends on the in-cylinder pressure), even if there is significant surplus of air in the cylinder the process of oxidation of CO to CO<sub>2</sub> freezes, leaving behind a significant concentration of the CO in the exhaust gases.

### ***HC emissions***

HC emissions are characteristic for SI and HCCI engines that operate with the premixed mixture. Similarly to CO emissions, HC emissions are also mainly controlled by the mixture equivalence ratio [59], [66] and associated in-cylinder temperature. Assuming that the combustion of a hydrocarbon occurred in a stoichiometric way, in the burned gas region there is no evidence of the unburned HC concentration [59]. Same as in the case of the CO emission, HC emissions are formed due to incomplete combustion of hydrocarbon fuels. Since in the combustion of hydrocarbon there is no measurable concentration of the unburned HC in the burned gas region [59], HC emissions originate from the cylinder regions where flame cannot fully propagate. In [132], [133] the authors have identified the following sources of HC emissions in the SI engines:

1. Charge that entered the crevice volumes cannot burn as the flame is quenched at the crevice entrance.
2. Adsorption and later desorption of the fuel vapor from the oil layer at the combustion chamber walls.
3. Flame quenches as it approaches the combustion chamber walls, leaving patches of the mixture close to the walls unburned.
4. Local flame extinction that leads to only partial combustion of the premixed mixture due to either low temperature in the unburned zone, or overly lean mixture.
5. Complete misfire due to either low temperature in the unburned zone, or overly lean mixture.
6. A portion of the fuel did not completely vaporize and adequately mix with air.
7. Fuel slip directly into the exhaust as a result of the valve overlap during the intake stroke.

The sources of HC emissions in HCCI engines are similar to the ones in the SI engine [59] that have been presented above. In stratified SI engines and DI-CI engines, the sources of HC emissions are [59]:

1. Areas of the fuel spray where the fuel/air mixture is outside of the flammability limits.
2. Since modern DI engines operate with high injection pressure a part of the fuel can get in contact with the combustion chamber walls and adhere to it. Consequently, a part of the fuel condensates and cannot be completely burned during the combustion process.
3. Injector leakage, which causes a part of the fuel to be released into the combustion chamber during late expansion or even gas exchange stroke.
4. Misfires, which can occur in a case when either the mixture close to the spark plug is too lean, or the overall in-cylinder mixture is simply too lean to ignite in given pressure/temperature conditions.
5. Flame quenching due to rapid decrease of pressure and temperature in the expansion stroke.

### ***NO<sub>x</sub> emissions***

NO<sub>x</sub> emissions, which is common expression for a variety of nitrogen oxide species found in the exhaust (NO, NO<sub>2</sub>, etc.) are pollutants whose formation like in the case of CO emission is mainly controlled by the mixture equivalence ratio [66], [104]. However by observing the emissions – equivalence ratio diagram in [59], [66], [104] it can be seen that contrary to CO emissions, NO<sub>x</sub> emissions reach their peak close to stoichiometric mixture where the in-

cylinder temperatures are the highest. That's why even though DI-CI engine operate with globally lean mixtures, due to local patches of near stoichiometric high temperature regions, they exhibit high levels of NO<sub>x</sub> emissions, while CO and HC emissions are lower compared to the SI engines [66].

Since in the IC engines mainly NO is formed [59], [66], [134], the emphasis is put on the NO formation. Typical mechanisms of the NO formation that have been identified are [59], [104], [135]:

1. thermal NO,
2. prompt NO,
3. NO from N<sub>2</sub>O,
4. fuel NO.

Under major part of temperature/pressure conditions in which the IC engines operate, the dominant mechanism of NO formation is the thermal mechanism [59]. Thermal NO is created in the burned gas region behind the flame front [59], as a result of the reaction of atmospheric oxygen and nitrogen at elevated temperatures inside the combustion chamber. The thermal NO formation is described by the extended Zeldovich mechanism [136].

### ***PM emissions***

PM emissions are common term for a variety of particulates that are primarily formed during the combustion of the hydrocarbon fuels. Although PM emissions are characteristic for DI-CI engines, some particulates can be formed also in the SI engines, especially in ones that feature direct injection of fuel into the cylinder. The particulates formed during the combustion process can be divided into three main groups [59]:

1. soot (elementary carbon particles),
2. hydrocarbon particles,
3. sulfates.

The exact composition of the PM emissions vary with the engine operating strategy and load [59]. Usually, soot is used to indicate the PM emissions formed during the combustion process [5]. Modeling of soot is only partially understood and can be described in the following steps [59], [135]:

1. Chemical reduction of the fuel molecules to smaller hydrocarbons under rich mixture conditions. This process is called fuel pyrolysis and it leads to the creation of species that are precursors for the soot formation.

2. Formation of polycyclic aromatic hydrocarbons (PAH's) and a proportional increase of carbon atoms.
3. Condensation and formation of soot kernels. This is the process of nucleation during which the initial, small soot particles are formed.
4. Surface growth and coalescence of soot kernels into primary soot particles. During this phase, the mass of the initial soot particles is increased through the addition of gas phase species.
5. Coalescence of soot particle to long chain-like structures; essentially combination of various smaller soot particles to bigger ones.
6. Breaking down of large soot particles by oxidation with O<sub>2</sub> molecules and OH radicals. Through this mechanism (soot oxidation) the mass of soot in the exhaust gas is decreased.

The PM emissions (soot emissions) in the exhaust gases are controlled by 2 major mechanisms, soot formation and soot oxidation. In [137] the author derived the phenomenology of the spray flame and emissions development in DI-CI engine, and it was presented that the initial soot forms in the rich premixed combustion area. Afterwards it travels to the central flame region filled with soot and at the end it is oxidized at the diffusion flame layer.

### 3.8.2. Overview if the emissions models

The models which are used to predict and calculate pollutants formation are already available in the AVL cycle simulation software [57], and in this thesis the newly developed combustion model (DFMZCM) has simply been linked to these models.

#### ***CO emissions model***

In this thesis, the CO emissions are modeled with the model that has already been implemented in the AVL cycle-simulation software. This model is based on the CO formation model presented in [138] that accounts for the following 2 reactions [57]:



The final CO production/destruction rate,  $\omega_{CO}$  (mole/cm<sup>3</sup>s) rate can be calculated from the following expression: [57]:

$$\omega_{CO} = C_{CO,mult} \cdot (\omega_1 + \omega_2) \cdot (1 - \alpha_{CO}) \quad (3.276)$$

In the equation given above,  $C_{CO,mult}$  (-) represents the CO production/destruction rate parameter,  $\omega_1$  (mole/cm<sup>3</sup>s) and  $\omega_2$  (mole/cm<sup>3</sup>s) represent the reaction rates for the reactions given above (3.274 and 3.275), while  $\alpha_{CO}$  (-) represents an additional model parameter. More details regarding the CO production/destruction calculation can be found in [57]. The CO emission is calculated only in the spray zones and in the flame zone.

### ***HC emissions model***

In the previous chapters it was already mentioned that there are different sources of the HC emissions in the IC engines. In this thesis, the HC emissions are modeled with the model that was already implemented in the AVL cycle-simulation software, and accounts for [57]:

1. crevice mechanism,
2. HC absorption/desorption mechanism,
3. partial burn effects,
4. HC post oxidation.

All details regarding the HC emissions model can be found in [57]. Therefore, in this thesis only a brief description of the model will be given.

The crevice mechanism assumes that the flame cannot propagate into the crevice area and that after the combustion process stops, the mass trapped in the crevice region flows out of it and contributes to the overall HC emissions level [57].

HC absorption/desorption mechanism assumes that a fraction of the fuel will be absorbed in the oil film and later desorbed in the burned gas [57]. Only fuel desorbed in the burned gas affects the HC emissions level as the fuel that has been desorbed in the unburned zone will be burned during the process of flame propagation [57].

Partial burn effects cannot be physically described in a quasi-dimensional approach [57], so in this HC emissions model they are accounted for by a semi-empirical correlation that has been derived and proposed in [139]. Also, the process of HC post oxidation in the warm burned zone is modeled by an Arrhenius type expression that has been derived and proposed by the authors in [139]. HC emissions are calculated for the entire cylinder content. Additionally, to include the HC emissions as a result of the flame quenching, in a case that part of the fuel inside the spray zones or inside the unburned zone has not burned, the mass of this fuel is added to the overall HC emissions at the exhaust valve opening timing in the following way:



$$m_{\text{HC,tot}} = m_{\text{HC,crev}} + m_{\text{HC,absorb}} + m_{\text{HC,partburn}} + m_{\text{HC,postox}} + \sum_i m_{\text{FV,SZ,i}} + m_{\text{FV,UZ}} \quad (3.277)$$

In the equation given above,  $m_{\text{HC,tot}}$  (kg) represents the overall mass of the unburned hydrocarbons at the exhaust valve opening timing,  $m_{\text{HC,crev}}$  (kg) represents the mass of the unburned hydrocarbons that were formed due to crevice mechanism,  $m_{\text{HC,absorb}}$  (kg) represents the mass of the unburned hydrocarbons that were formed due to absorption/desorption mechanism,  $m_{\text{HC,partburn}}$  (kg) represents the mass of the unburned hydrocarbons that were formed due to partial burn effects,  $m_{\text{HC,postox}}$  (kg) represents the mass of the unburned hydrocarbons that were formed due to the post oxidation process,  $m_{\text{FV,SZ,i}}$  (kg) represents the overall mass of fuel vapor inside the  $i$ -th spray zone at the exhaust valve opening moment, while  $m_{\text{FV,UZ}}$  (kg) represents the overall mass of fuel vapor inside the unburned zone at the exhaust valve opening moment.

### ***NO<sub>x</sub> emissions model***

In this thesis, the NO<sub>x</sub> emissions are modeled with the model that has already been implemented in the AVL cycle-simulation software. This model is based on the NO<sub>x</sub> formation model presented in [140] that accounts for the following 6 reactions:



The final NO production/destruction rate,  $\omega_{\text{NO}}$  (mole/cm<sup>3</sup>s) rate can be calculated from the following expression: [57]:

$$\omega_{\text{NO}} = C_{\text{NO,postMult}} \cdot C_{\text{NO,kinMult}} \cdot 2 \cdot (1 - \alpha_{\text{NO}}^2) \cdot \frac{\omega_1}{1 + \alpha_{\text{NO}} \cdot \frac{\omega_1}{\omega_2 + \omega_3}} \cdot \frac{\omega_4}{1 + \alpha_{\text{NO}} \cdot \frac{\omega_4}{\omega_5 + \omega_6}} \quad (3.284)$$

In the equation given above,  $C_{\text{NO,postMult}}$  (-) represents the post-processing multiplier for NO production/destruction rate,  $C_{\text{NO,kinMult}}$  (-) represents the kinetic multiplier for NO production/destruction rate,  $\omega_1$  (mole/cm<sup>3</sup>s),  $\omega_2$  (mole/cm<sup>3</sup>s),  $\omega_3$  (mole/cm<sup>3</sup>s),  $\omega_4$  (mole/cm<sup>3</sup>s),  $\omega_5$  (mole/cm<sup>3</sup>s) and  $\omega_6$  (mole/cm<sup>3</sup>s) represent the reaction rates for the reactions given above (3.278, 3.279, 3.280, 3.281, 3.282 and 3.283), while  $\alpha_{\text{NO}}$  (-) represents an additional model parameter. More details regarding the NO production/destruction calculation can be found in [57]. The NO emission is calculated only in the spray zones and in the flame zone.

### ***Soot emissions model***

As the soot concentration in the exhaust gases is primarily controlled by two mechanisms, soot formation and soot oxidation, it is important to appropriately model them. In this thesis, the same approach to soot modeling as the one taken in [33] was used, where soot was modeled according to the equations first presented in [42]. In this approach, the net soot emissions are calculated as the difference between the formed and oxidized soot. Soot is calculated only in the spray zones:

$$\frac{dm_{\text{soot, form, SZ, i}}}{dt} = C_{\text{soot, form}} \cdot m_{\text{FV, SZ, i}} \cdot p^{0.5} \cdot e^{-\left(\frac{6250}{T_{\text{SZ, i}}}\right)} \quad (3.285)$$

$$\frac{dm_{\text{soot, oxd, SZ, i}}}{dt} = C_{\text{soot, oxd}} \cdot m_{\text{soot, SZ, i}} \cdot \frac{p_{\text{O}_2, \text{SZ, i}}}{p} \cdot p^{1.8} \cdot e^{-\left(\frac{7000}{T_{\text{SZ, i}}}\right)} \quad (3.286)$$

$$\frac{dm_{\text{soot, SZ, i}}}{dt} = \frac{dm_{\text{soot, form, SZ, i}}}{dt} - \frac{dm_{\text{soot, oxd, SZ, i}}}{dt} \quad (3.287)$$

$$\frac{dm_{\text{soot}}}{dt} = \sum_i \frac{dm_{\text{soot, SZ, i}}}{dt} \quad (3.288)$$

In the equation given above,  $m_{\text{soot, form, SZ, i}}$  (kg) represents the soot formed inside the  $i$ -th spray zone,  $C_{\text{soot, form}}$  (-) represents the soot formation model parameter,  $m_{\text{FV, SZ, i}}$  (kg) represents the fuel vapor mass inside the  $i$ -th spray zone,  $p$  (bar) represents the in-cylinder pressure,  $T_{\text{SZ, i}}$  (K)

represents the temperature inside the  $i$ -th spray zone,  $m_{\text{soot,oxd,SZ},i}$  (kg) represents the soot oxidized inside the  $i$ -th spray zone,  $C_{\text{soot,oxd}}$  (-) represents the soot oxidation model parameter,  $p_{\text{O}_2,\text{SZ},i}$  (bar) partial pressure of oxygen inside the  $i$ -th spray zone,  $m_{\text{soot,SZ},i}$  (kg) represents the net soot formed inside the  $i$ -th spray zone, while  $m_{\text{soot}}$  (kg) represents the net soot formed inside entire spray.

### 3.9. Knock calculation model

Knock is one of two major types of abnormal combustion that occur in the combustion process governed by the flame propagation through the premixed mixture, which is typical for the SI IC engines. Knock causes high in-cylinder pressure oscillations and can eventually lead to the damage of the vital engine components. The other type of abnormal combustion that occurs in the SI IC engines is called super-knock and usually occurs in the highly boosted direct injection SI engines at low engine speed and high load [141], [142]. In [141] it was found that contrary to knock which occur continuously, super-knock occurs randomly. The name super-knock has been suggested in order to distinguish this phenomenon from the conventional engine knock, as the occurrence of the super knock leads to excessive values of pressure and temperature inside the cylinder leading to the instantaneous engine damage [141]. Even though super knock is often regarded as preignition, this is not the case as the preignition does not necessarily have to lead to the occurrence of super knock, or even knock [141]. However, preignition is required for the super-knock to occur [141].

#### 3.9.1. Physical background

Both knock and super-knock are driven by the auto-ignition of the unburned premixed mixture. The process of auto-ignition in the unburned mixture can occur both before the combustion has started and after the combustion process has started. It can lead to the occurrence of knock and super knock, and thus to the damage of the vital engine components. Therefore, in modeling of the combustion process in engines that operate with the premixed charge, it is important to account for the auto-ignition and knock occurrence in the unburned mixture. And in order to appropriately model these phenomena, it is important to understand their physical background.

The process of auto-ignition in the unburned mixture occurs as a result of the high pressure and temperature generated during the compression and combustion process inside the internal combustion engine. Therefore in order to appropriately predict the knock in the end gas it is important to appropriately calculate the temperature stratification and chemistry inside the

unburned mixture. More details on the physics behind the engine knock phenomenon and knock theories can be found in the literature [96].

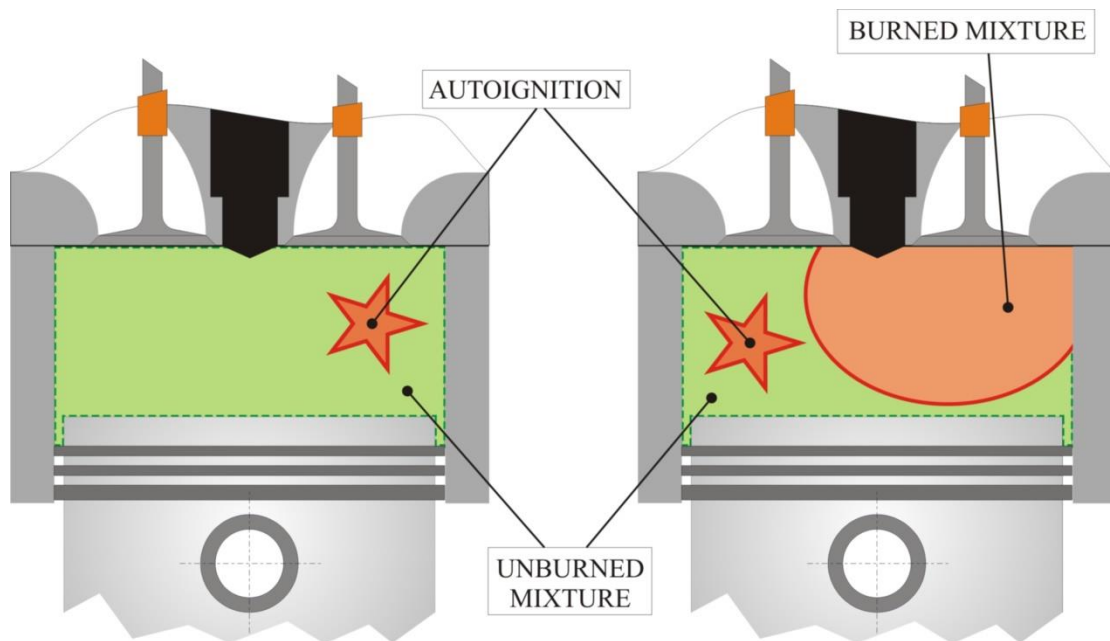


**Figure 99. The occurrence of autoignition in engines which operate with the premixed mixture**

### 3.9.2. Knock model

The knock model used in this thesis was derived, presented and integrated in the AVL cycle-simulation software in [58]. Contrary to a variety of models presented in the literature [143], which calculate ignition delay and hence the knock integral according to the empirical formulations based on the Arrhenius function, in the model presented in [58] whose main features are used to model knock in this thesis, the unburned zone is divided into a number of sub-zones and the ignition delay inside each of these zones is calculated through the specially developed ignition delay tables. In order to improve the physics of the model in terms of prediction of knock, during the research presented in this thesis this model has been extended and modified.

#### ***Extension and modification of the knock model***

The modifications to the knock model originally presented in [58] that have been made during the research presented in this thesis include:

1. Calculation of the low temperature and high temperature knock integral from the start of the high-pressure cycle. This enables inclusion of the effect of auto-ignition before the start of flame propagation.

2. New ignition delay tables (both low temperature and high temperature) which include the effect of two different fuels inside the zone have been used.
3. Chemical reaction rate tables are used in calculating knock combustion, which enable improvement of the calculation of heat release rate due to knock occurrence in the end gas.

### ***Features of the knock model***

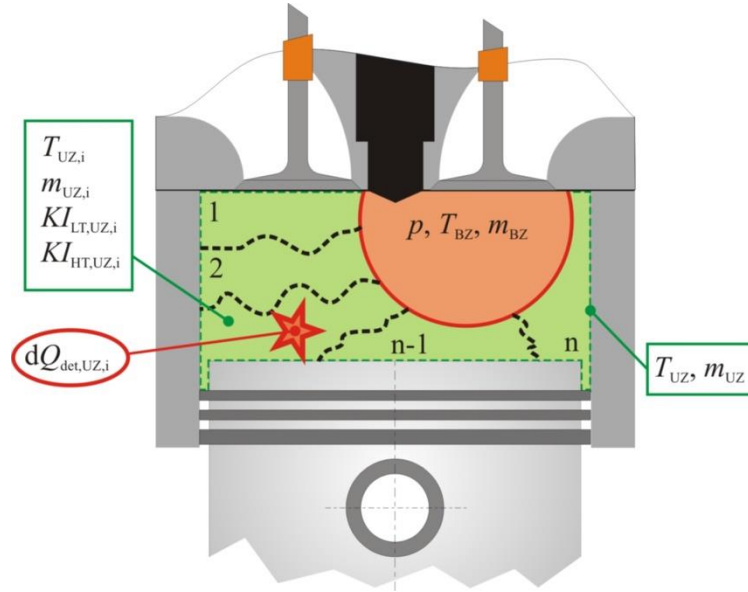


**Figure 100. Schematic presentation of the unburned zone temperature stratification sub-model**

In order to correctly predict the temperature stratification inside the unburned zone in [58] a temperature stratification sub-model has been derived. With this model, the unburned zone is divided into a user-defined number of zones with equal mass. Afterwards the temperature is assigned to each of the zones according to the distribution around the mean unburned temperature (Figure 100). Details regarding the temperature distribution inside the unburned zone can be found in [58]. Mass of the zones in the unburned mixture and low temperature and high temperature knock integrals are calculated with the following equations:

$$m_{UZ, i} = \frac{m_{UZ}}{n_{UZ, div}} \quad (3.289)$$

$$KI_{LT, UZ, i} = \int_{t_{SHP}}^t \frac{1}{\tau_{LT, UZ, i}} \quad (3.290)$$

$$KI_{HT, UZ, i} = \int_{t_{SHP}}^t \frac{1}{\tau_{HT, UZ, i}} dt \quad (3.291)$$

$$\tau_{LT, UZ, i} = f\left(T_{UZ, i}, p, x_{FV, UZ, i}, x_{CP, UZ, i}, x_{metFV, UZ, i}\right) \quad (3.292)$$

$$\tau_{HT, UZ, i} = f\left(T_{UZ, i}, p, x_{FV, UZ, i}, x_{CP, UZ, i}, x_{metFV, UZ, i}\right) \quad (3.293)$$

First two modifications; knock integral calculation from the start of the high-pressure cycle and new ignition delay tables are presented in the equations given above. These ignition delay tables are the same tables that are used in the spray ignition delay calculation, and the method of their calculation is presented in chapter 3.4. In the equations given above,  $m_{UZ, i}$  (kg) represents the mass inside the  $i$ -th zone of the unburned mixture,  $n_{UZ, div}$  (-) represents the user defined number of the zones inside the unburned mixture,  $KI_{LT, UZ, i}$  (-) represents the low temperature knock integral in a given zone inside the unburned mixture,  $KI_{HT, UZ, i}$  (-) represents the high temperature (main) knock integral in a given zone inside the unburned mixture,  $\tau_{LT, UZ, i}$  (s) represents the low temperature ignition delay time in a given zone inside the unburned mixture,  $\tau_{HT, UZ, i}$  (s) represents the high temperature ignition delay time in a given zone inside the unburned mixture,  $T_{UZ, i}$  (K) represents the temperature inside the  $i$ -th zone of the unburned mixture,  $x_{FV, UZ, i}$  (-) represents the mass fraction of fuel vapor inside the  $i$ -th zone of the unburned mixture,  $x_{CP, UZ, i}$  (-) represents the mass fraction of combustion products inside the  $i$ -th zone of the unburned mixture, while  $x_{metFV, UZ, i}$  (-) represents the mass fraction of methane inside the fuel vapor, inside the  $i$ -th zone of the unburned mixture.

It is important to state that there is no direct mass or heat transfer between the zones. However, if knock is triggered in one of the zones (knock integral becomes equal or larger than 1), the mixture inside this zone burns according to a given reaction rate, which raises the pressure inside the cylinder and temperature inside the entire unburned zone. Since the percentage of low temperature heat release is also given in the chemistry tables, in the case that the low temperature heat release has been triggered, a certain amount of heat is instantly released. The rate of heat release due to the low temperature heat release is calculated in the following way (same as in the case of spray combustion):

$$\frac{dQ_{LTknock, UZ, i}}{dt} = \frac{m_{FB, LT, UZ, i}}{dt} \cdot LHV_{UZ} \quad (3.296)$$

$$\frac{dm_{FB,LT,UZ,i}}{dt} = \frac{m_{FV,avail,UZ,i}}{\Delta t} \cdot LTHR_{UZ,i} \quad (3.297)$$

$$LTHR_{SZ,i} = f(T_{UZ,i}, p, \phi_{UZ}, x_{CP,UZ}, x_{metFV,UZ}) \quad (3.298)$$

$$m_{FV,avail,UZ,i} = MIN(m_{FV,UZ,i}, m_{FV,stoich,UZ,i}) \quad (3.299)$$

$$m_{FV,stoich,UZ,i} = \frac{m_{air,UZ,i}}{AFR_{stoich,UZ}} \quad (3.300)$$

In the equations given above,  $Q_{LTknock,UZ,i}$  (J) represents the heat released due to the low temperature combustion process inside the  $i$ -th zone of the unburned mixture,  $m_{FB,LT,UZ,i}$  (kg) represents the mass of fuel that burned due to the low temperature combustion event inside the  $i$ -th zone of the unburned mixture,  $m_{FV,avail,UZ,i}$  (kg) represents the mass of fuel vapor that is available for combustion inside  $i$ -th zone of the unburned mixture,  $LHV_{UZ}$  (J) represents the lower heating value of the unburned mixture,  $LTHR_{UZ,i}$  (-) represents the relative amount of energy that is released due to the low temperature combustion process,  $m_{FV,UZ,i}$  (kg) represents the mass of fuel vapor inside  $i$ -th zone of the unburned mixture,  $m_{FV,stoich,UZ,i}$  (kg) represents the mass of fuel vapor that can burn in stoichiometric conditions based on available air inside  $i$ -th zone of the unburned mixture,  $m_{air,UZ,i}$  (kg) represents the mass of air inside  $i$ -th zone of the unburned mixture, while  $AFR_{stoich,UZ}$  (-) represents the stoichiometric air to fuel ratio of the unburned mixture. The overall low temperature rate of heat release in the unburned zone is calculated from the following expression:

$$\frac{dQ_{LTknock,UZ}}{dt} = \sum_i \frac{dQ_{LTknock,UZ,i}}{dt} \quad (3.301)$$

The rate of heat release due to high temperature heat release is calculated in the following way (same as in the case of spray combustion):

$$\frac{dQ_{HTknock,UZ,i}}{dt} = \frac{dm_{FB,UZ,i}}{dt} \cdot LHV_{UZ} \quad (3.302)$$

$$\frac{dm_{FB,UZ,i}}{dt} = MIN\left(\frac{m_{FV,avail,UZ,i}}{\Delta t}, \frac{m_{FV,avail,UZ,i}}{\tau_{reac,UZ,i}}\right) \quad (3.303)$$

$$\tau_{\text{reac, UZ, } i} = f\left(T_{\text{UZ, } i}, p, \phi_{\text{UZ}}, x_{\text{CP, UZ}}, x_{\text{metFV, UZ}}\right) \quad (3.304)$$

$$m_{\text{FV, avail, UZ, } i} = \text{MIN}\left(m_{\text{FV, UZ, } i}, m_{\text{FV, stoich, UZ, } i}\right) \quad (3.305)$$

$$m_{\text{FV, stoich, UZ, } i} = \frac{m_{\text{air, UZ, } i}}{\text{AFR}_{\text{stoich, UZ}}} \quad (3.306)$$

In the equations given above,  $Q_{\text{HTknock, UZ, } i}$  (J) represents the heat released due to high temperature (main) combustion process inside  $i$ -th zone of the unburned mixture,  $m_{\text{FB, UZ, } i}$  (kg) represents mass of the burned fuel inside  $i$ -th zone of the unburned mixture, while  $\tau_{\text{reac, UZ, } i}$  (s) represents the chemical reaction rate time inside  $i$ -th zone of the unburned mixture. The overall high temperature (main) rate of heat release in the unburned zone, as well as the burning rate due to knock are calculated from the following expressions:

$$\frac{dQ_{\text{HTknock, UZ}}}{dt} = \sum_i \frac{dQ_{\text{HTknock, UZ, } i}}{dt} \quad (3.307)$$

$$\frac{dQ_{\text{COMB, UZ}}}{dt} = \frac{dQ_{\text{LTknock, UZ}}}{dt} + \frac{dQ_{\text{HTknock, UZ}}}{dt} \quad (3.308)$$

Finally, once the knock occurrence in a particular zone inside the unburned mixture has been triggered, knock intensity is calculated according to the expression presented in [144]:

$$IoK = K_1 \cdot \frac{m_{\text{FV, SOK}}}{m_{\text{FV, SOC}}} \cdot (CR - 1) \cdot \sqrt{1 - \frac{\phi_{\text{knock}}}{K_2}} \cdot n \quad (3.309)$$

In the equations given above,  $K_1$  (1/rpm) represents the overall knock intensity calculation parameter,  $m_{\text{FV, SOK}}$  (kg) represents mass of the fuel vapor inside the cylinder at the start of knock,  $m_{\text{FV, SOC}}$  (kg) represents mass of the fuel vapor inside the cylinder at the start of combustion process,  $CR$  (-) represents the engine compression ratio,  $\phi_{\text{knock}}$  (degCA) represents the crank angle at the start of knock,  $K_2$  (degCA) represents the latest crank angle at which the autoignition process will still lead to knock, while  $n$  (rpm) represents the engine speed.



## 4. Validation of the developed 0-D combustion model

In this chapter of the thesis the validation of the newly developed combustion model (DFMZCM) with the experimental results and comparison of the enhanced  $k-\varepsilon$  in-cylinder turbulence sub-model with the available 3-D CFD results is presented.

In the first part of this chapter the comparison between the results obtained with the enhanced  $k-\varepsilon$  in-cylinder turbulence sub-model and the available 3-D CFD results is presented. After that the validation of the entire DFMZCM at the so-called base operating point (experimentally obtained) is given. This is followed by the presentation of the sensitivity analysis of the DFMZCM to its modeling parameters and after that the validation of the DFMZCM at additional thirteen (13) operating points is presented. These experimentally obtained operating points feature two levels of engine speed and intake pressure and various different injection settings, loads and Diesel substitution ratios. Finally, at the end of this chapter the validation of the model with the single set of parameters is presented.

The DFMZCM has been validated with the experimental data that were obtained at the UC Berkeley, where the existing 2-liter Diesel engine was adjusted to operate in a conventional dual fuel mode. In order to validate the in-cylinder turbulence sub-model, specifically the extension that was made (inclusion of the injection effect on the turbulent kinetic energy level and its dissipation) the simulation that was performed with the DFMZCM was compared with the 3D-CFD simulation results.

### 4.1. Comparison between the 0-D and 3-D CFD turbulence results

In order to test the extensions to the  $k-\varepsilon$  in-cylinder turbulence sub-model that were made during the research that is presented in this thesis, a 3-D CFD simulation of an IC engine was performed at University of Zagreb (by. dr. Petranović) and the 0-D turbulence results were compared with the 3-D CFD turbulence results.

Since the 3-D CFD model of the UC Berkeley research engine was not available, in this part of the thesis a 3-D CFD model of an IC engine that has similar geometry was used (Table 8). Since the used 3-D CFD model represented a conventional Diesel engine the DFMZCM was used in simulating the combustion process of a conventional Diesel engine, and the obtained results were later compared to the available experimental and 3-D CFD results of the Diesel engine in question (Table 8). In this initial phase of the validation the main concern was to validate the extended in-cylinder turbulence sub-model. Therefore, the fact that the conventional Diesel engine combustion (spray combustion) was simulated, rather than the

conventional dual fuel engine combustion (spray combustion & flame propagation) was not an issue.

The corresponding experimental results of the Diesel engine that have been used to validate the 3-D CFD simulation model have been delivered by the partner in this research, AVL List GmbH.

**Table 8. Geometry and operating parameters of the engine used in the turbulence model validation**

Parameter	Value
Bore (mm)	84
Stroke (mm)	94
Compression Ratio (-)	16
Conrod Length (mm)	142
Engine Speed (rpm)	3000
SHP Pressure (bar)	2.29
SHP Temperature (K)	402
SHP Combustion Products Mass Fraction (-)	0.2
Start of Injection (degCA bTDC)	7
Injection Duration (degCA)	22
Injection Pressure (bar)	1200
Diesel Fuel Mass (mg)	27
Injector Nozzle Diameter ( $\mu\text{m}$ )	100
Injector Nozzle Number (-)	8
Injector Nozzle Depth (mm)	1
Injector Nozzle Angle (deg)	75
Discharge Coefficient (-)	0.7

#### 4.1.1. 3-D CFD simulation model

The 3-D CFD model of the Diesel engine in question was made in the AVL Fire; the engine geometry as well as the details regarding the simulated operating points can be found in Table 8. Since the details regarding the 3-D CFD model have already been presented in [145], only a brief description will be given in this thesis.

The 3-D CFD model is based on the Euler-Lagrangian approach, where the Lagrangian formulation is used to track the motion of the droplets, while the Eulerian approach is used to calculate the gas phase quantities. The liquid fuel break-up process is calculated with the well-known WAVE model [146], while the combustion process is calculated with the ECFM-

3Z model [147]. More details regarding the 3-D CFD modeling of the spray process, as well as the combustion process in the conventional Diesel engines can be found in [145], [148].

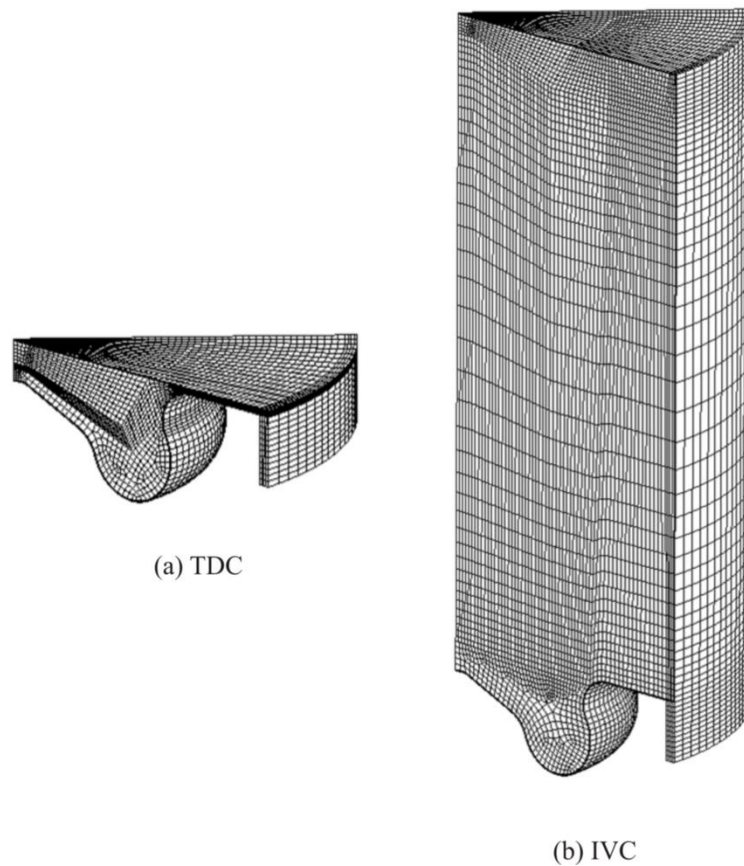
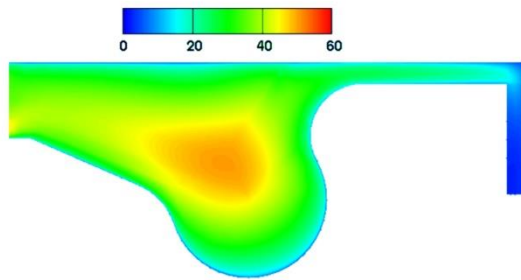


**Figure 101. Schematic of the mesh that was used in the 3-D CFD simulation**

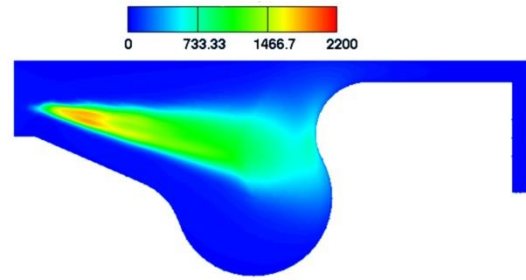
The 3-D CFD simulation was only performed for the closed part of the engine cycle (high pressure cycle). The mesh that was used in this 3-D CFD simulation is shown in Figure 101, where the left figure represents the mesh in TDC, while the right figure represents the mesh at the IVC. Since the dynamic mesh procedure was used the number of elements changes in time (as the size of the domain changes). Since the injector features 8 nozzles, in the 3-D CFD simulation symmetry was assumed. Therefore 1/8 of the combustion chamber was simulated; the number of elements in TDC equals 23834, while the number of elements in IVC equals 67558.

Figure 102 presents the turbulent kinetic energy (TKE) and temperature fields inside the cylinder at the specific crank angle before the start of injection (710 degCA) and at the specific crank angle after the start of injection (730 degCA). Figure 102 reveals that prior to injection and combustion processes both the temperature and the TKE fields are quite homogeneous. On the other hand, once injection and combustion processes have started, both

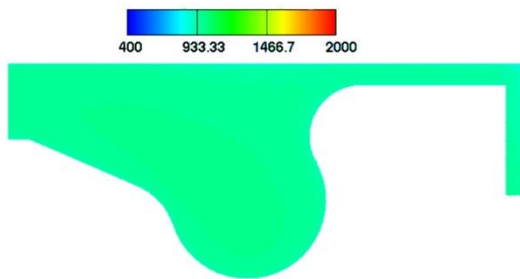
the TKE and temperature fields inside the cylinder become heterogeneous. Both quantities are significantly higher inside the fuel spray (jet) region where the combustion process occurs.



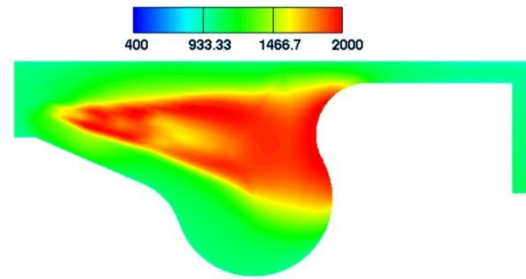
(a) In-cylinder Specific TKE; Crank Angle = 710 deg



(b) In-cylinder Specific TKE; Crank Angle = 730 deg



(c) In-cylinder Temperature; Crank Angle = 710 deg



(d) In-cylinder Temperature; Crank Angle = 730 deg

**Figure 102. Specific TKE and temperature fields inside the cylinder at two specific crank angle positions**

#### 4.1.2. 0-D simulation model

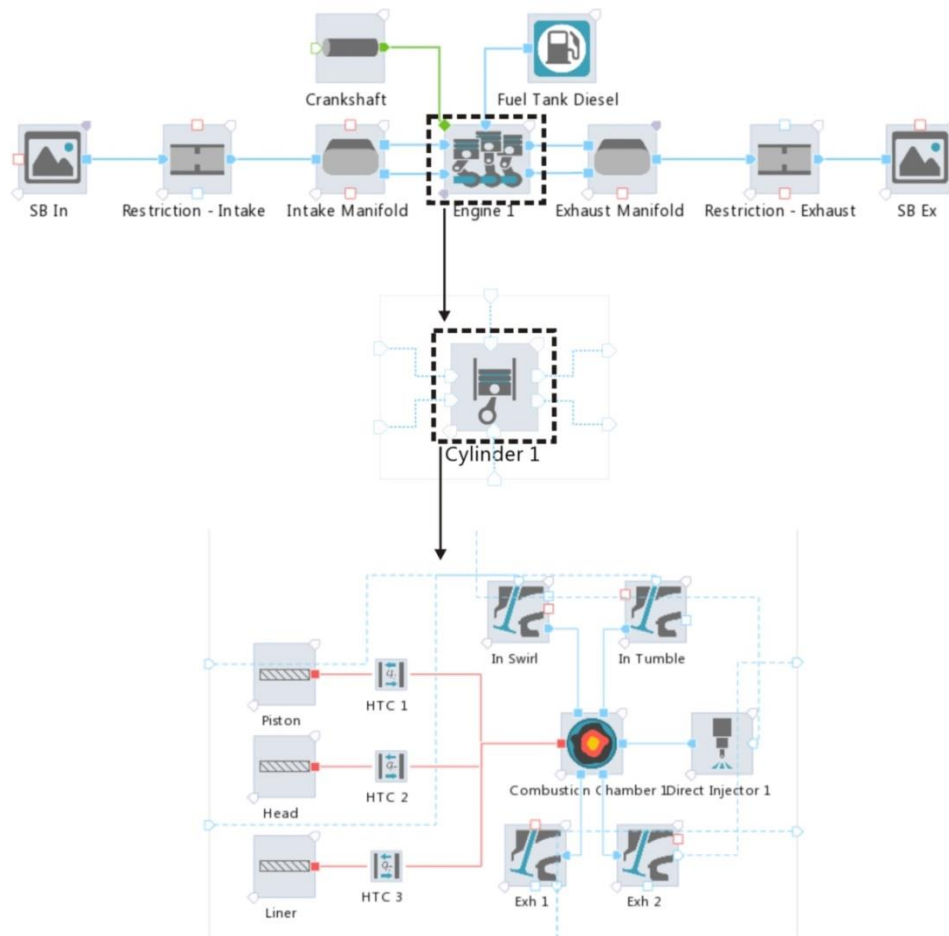


**Figure 103. Schematic of the single cylinder Diesel engine model created in the AVL CruiseM**

The newly developed 0-D conventional dual fuel combustion model (DFMZCM) is integrated within the AVL Boost code and linked to AVL CruiseM simulation tool. Therefore the 0-D simulation model was created in AVL CruiseM, which is a well-known simulation tool for the cycle-simulations of IC engines (Figure 103). The engine model is a single cylinder model that features the intake and the exhaust tracts, and direct fuel injection. In order to obtain the same in-cylinder state and mixture as in the 3-D CFD simulation, the 0-D simulation was run with the pre-set IVC conditions which were set to the same level as in the 3-D CFD simulation. The details on the engine geometry and the pre-set SHP conditions can be found in Table 8, while the in-cylinder turbulence and spray model parameters that were used in the simulation can be found in Table 9 and Table 10.

**Table 9. In-cylinder turbulence model parameters for turbulence validation model**

Model Parameter	Value
$S_{in}$ (-)	$1.5 \times 10^{-3}$
$C_{in}$ (-)	1.55
$S_{inj}$ (-)	$3.5 \times 10^{-2}$
$C_{inj}$ (-)	155
$C_2$ (-)	1.92
$C_\varepsilon$ (-)	2.35
$C_{\varepsilon,UZ}$ (-)	1
$C_L$ (-)	0.5

**Table 10. Spray and heat transfer model parameters for turbulence validation model**

Model Parameter	Value
$C_{evap,HT}$ (-)	1
$C_{evap}$ (-)	1
$C_{entrain}$ (-)	0.6
$C_{ignition}$ (-)	0.8
$C_{discr,ax}$ (-)	1
$C_{RZ}$ (-)	0.5
$C_{ZHT,SZ}$ (-)	1

### 4.1.3. Results

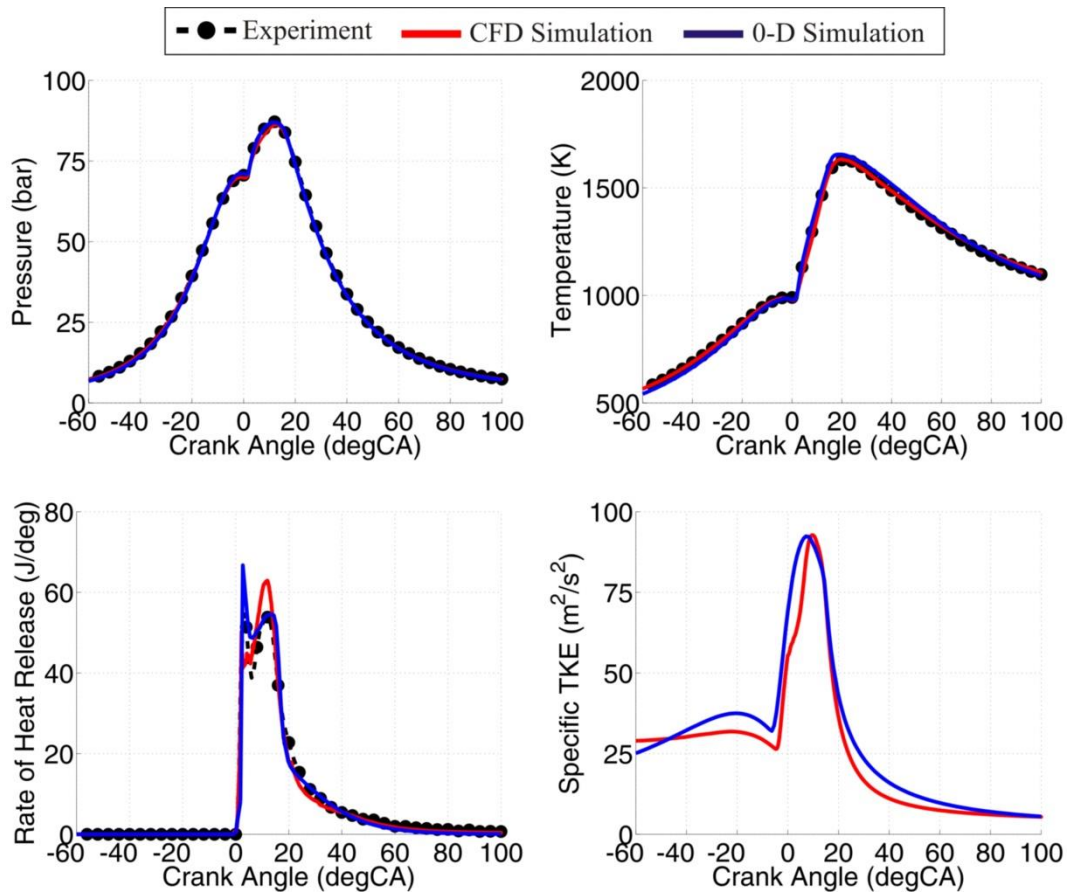


**Figure 104.** Comparison of pressure, temperature, ROHR and specific TKE results simulated with 3-D CFD and 0-D DFMZCM for the pure Diesel case; specific experimental results were also added to the charts for comparison

Figure 104 reveals that there is a good fit between the experimentally obtained results and the ones obtained with the 0-D DFMZCM simulation. Additionally, it can be seen that there is a good fit between the average cylinder TKE trace from 3-D CFD simulation and 0-D DFMZCM simulation (Figure 104 – bottom right). This means that the addition of new terms in the 0-D  $k-\varepsilon$  turbulence model enables the inclusion of injection effect on the turbulent kinetic energy level inside the IC engine combustion chamber.

## 4.2. Validation of the 0-D dual fuel combustion model

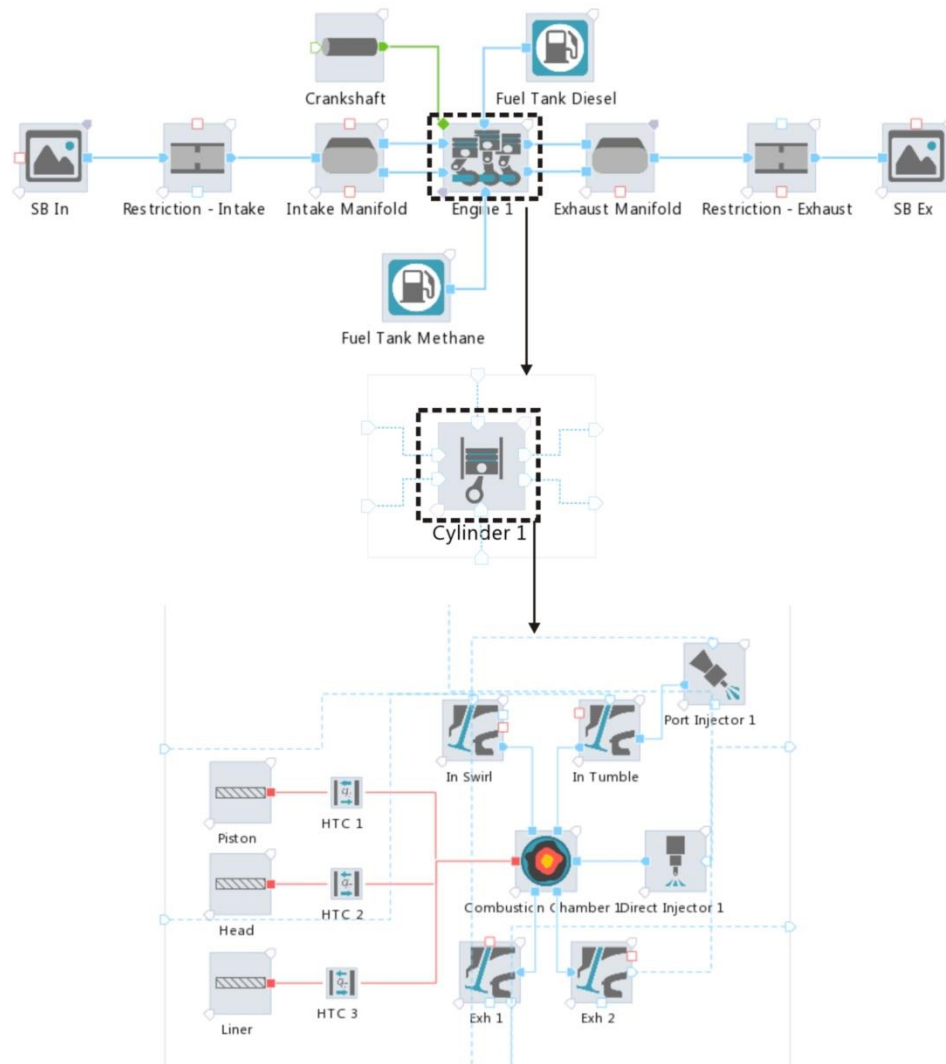


**Figure 105. Schematic of the single cylinder dual fuel IC engine model that was created in the AVL CruiseM**

The DFMZCM was validated with the experimental results that have been obtained at the UC Berkeley Combustion Analysis Laboratory. The UC Berkeley experimental engine was built on the basis of a 2.0 liter TDI VW Diesel engine from 2010 series VW Jetta. For combustion model validation purpose, the simulation model of the experimental engine was created in the AVL CruiseM (Figure 105).

The simulation model was made as a single cylinder model that features the intake and exhaust tracts, ports and direct fuel injection. In order to obtain the same in-cylinder state and mixture composition at the start of high pressure cycle as in the experiment, the 0-D simulation was run with the pre-set IVC conditions which have been set to the same level as



the ones that were obtained in the experiment. The details regarding the IC engine geometry can be found in the following table (Table 11).

**Table 11. Engine geometry parameters**

Parameter	Value
Bore (mm)	81
Stroke (mm)	95.5
Compression Ratio (-)	15.5
Conrod Length (mm)	144
Piston Bowl Bore (mm)	56
Piston Bowl Depth (mm)	10.1
Injector Nozzle Diameter ( $\mu\text{m}$ )	100
Injector Nozzle Number (-)	8
Intake Valve Closure, Swirl/Tumble (degCA bTDC)	154.5/112
Exhaust Valve Opening, Swirl/Tumble (degCA aTDC)	133.5/108
Injector Nozzle Depth (mm)	1
Injector Nozzle Angle (deg)	75
Discharge Coefficient (-)	0.7

The first step in the measurement process was to convert the existing experimental IC engine to a conventional dual fuel IC engine. Before that quite extensive modifications to the engine were already made by some other researchers. Various original engine components (turbocharger, intake and exhaust manifolds, etc.) were dismantled. Completely different pistons were installed in each of the cylinders and an entirely new intake and exhaust tracts were built (the air flows to the cylinders were separated), which in the end enabled precise intake air and fuel mass flow metering of the cylinder of interest. Finally, with all these modifications a single cylinder research platform was established which enabled the study of various different compression ignition combustion modes.

As this is not primarily an experimental thesis, only a short description of the experimental setup will be given in the next chapter. For more information on the entire experimental setup one can refer to [149], [150].

#### 4.2.1. Experimental setup

In the conventional dual fuel combustion experiments, methane was used as a premixed fuel instead of natural gas. As can be seen from Figure 106, the experimental setup features intake air compressor, intake air flow meter, intake air heater, various pressure and temperature

sensors, port (methane) and high pressure direct (Diesel fuel) fuel injection and emissions measurement.

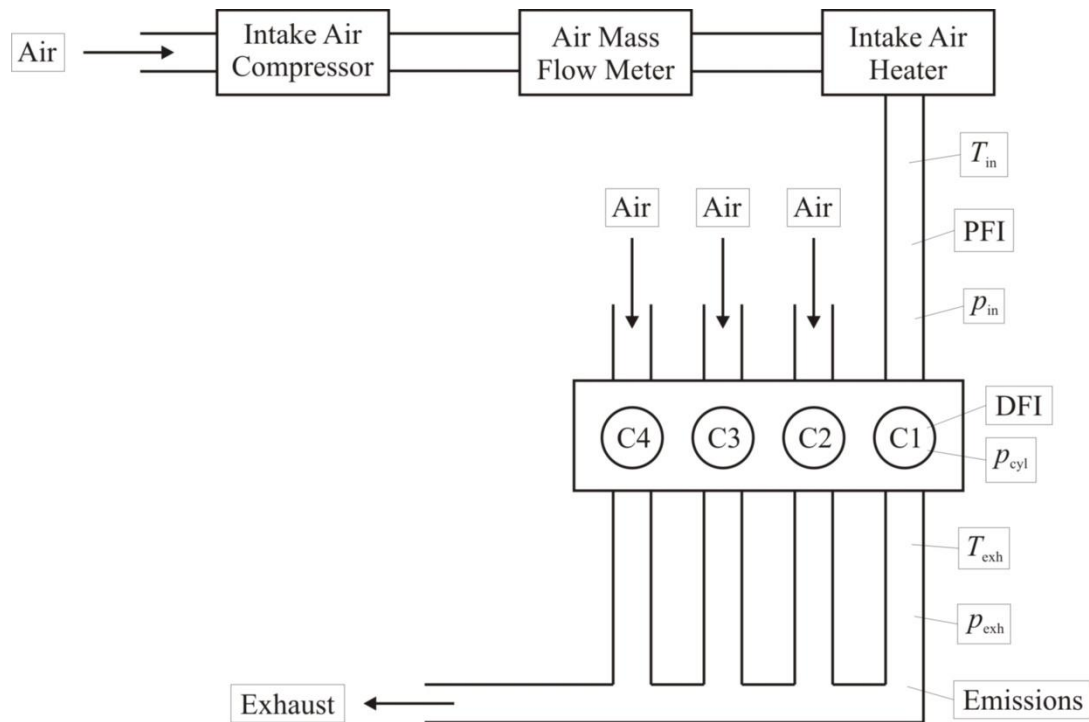
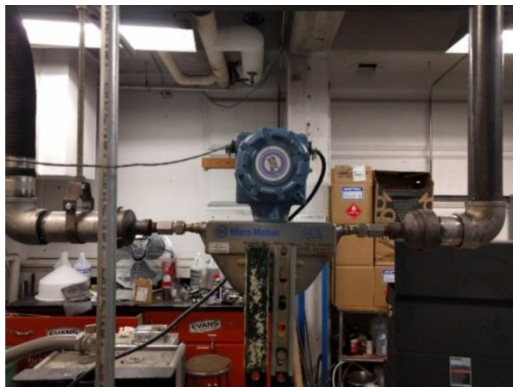


**Figure 106. Schematic of the UC Berkeley IC engine experimental setup**



(a) AIR FLOW METER



(b) METHANE FLOW METER

**Figure 107. Micro-Motion Coriolis mass flow meters; figures taken from [150]**

Intake charge conditioning (pressure and temperature) is controlled by the intake air compressor and heater. To control the amount of injected fuel, the experimental setup features a high precision scale and the Coriolis flow meter. The high precision scale was used to monitor the Diesel fuel tank mass, while the Coriolis flow meter was used to measure the methane mass flow. Likewise, the intake air mass flow was also measured with a Micro-Motion Coriolis mass flow meter (Figure 107).

When operating the engine in a conventional dual fuel mode, combustion chamber one (C1), which features the original piston geometry (Figure 108) was used.

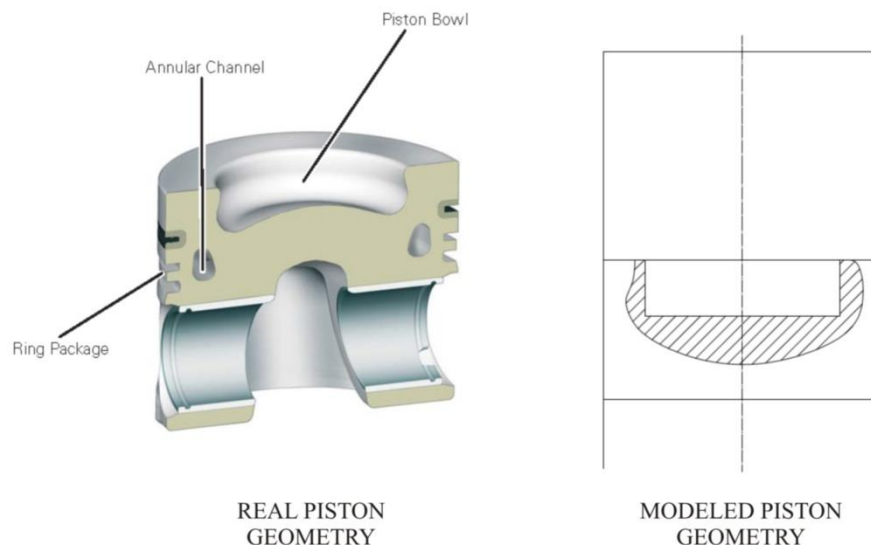


**Figure 108. Real piston geometry (figure taken from [151]) vs. modeled piston geometry**

The cylinder head (Figure 109) features the two intake and two exhaust valves. The interesting thing is that the intake tract features fill and swirl channels, which ensures the appropriate charge motion inside the cylinder in the original engine.

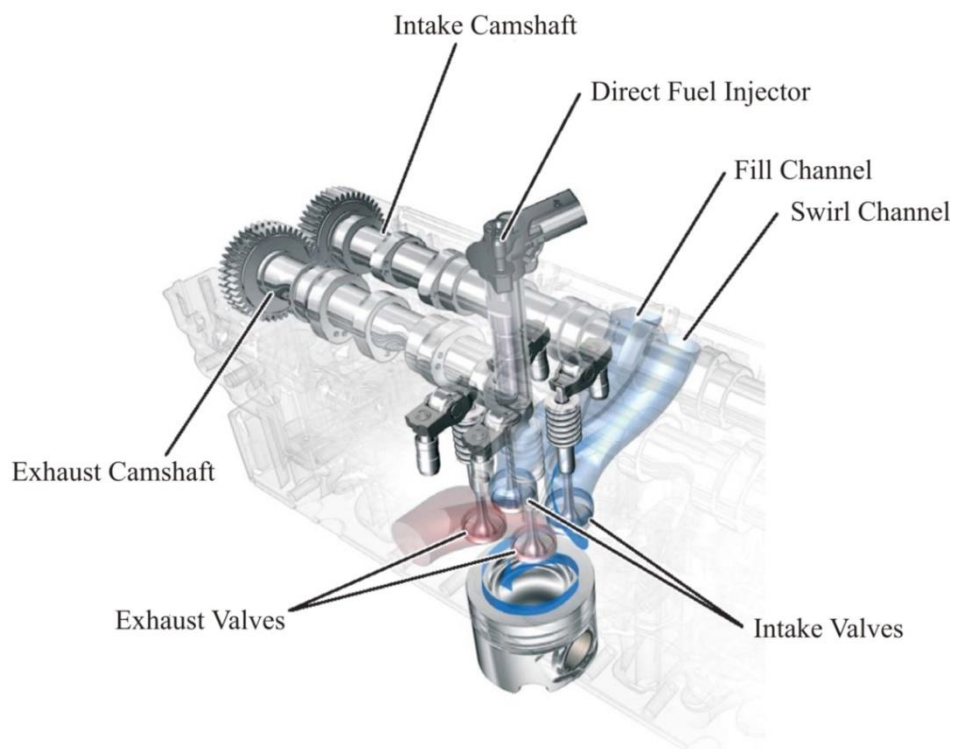


**Figure 109. VW IC engine cylinder head; figure taken from [151]**

The original engine featured a valve that could close the fill channel and thus ensure a higher level of swirling motion at given engine load and speed, but this valve was removed from the engine. As can be seen from Figure 110, the two intake as well as the two exhaust valves differ in the total valve lift as well as in the lift phase.

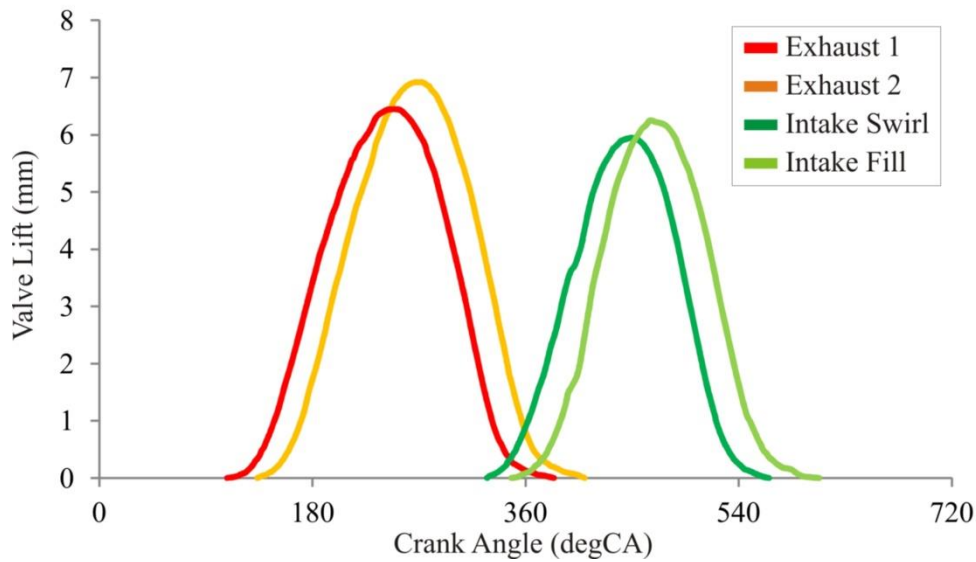


**Figure 110. Intake and exhaust valve lift profiles**

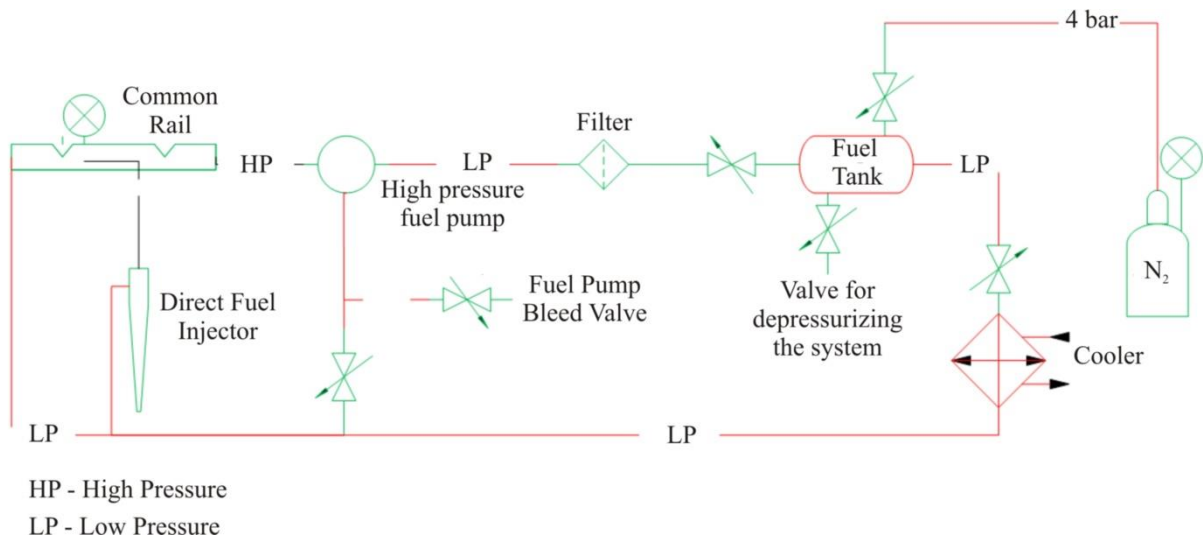


**Figure 111. Schematic of the high pressure fuel (Diesel fuel) delivery system; figure taken from [150]**

The engine was operated with the original common rail direct injection system and a piezoelectric injector. However, contrary to the original engine just one direct injector (on C1) was mounted, while the others were taken off and their supply lines were adequately closed. Also, the fuel delivery line was slightly different compared to the real engine. The original IC engine features a fuel delivery pump that provides fuel to the high-pressure pump. However,

on the experimental engine this pump was taken off and the pressurized fuel tank with the nitrogen at 4 barg was used instead (Figure 111).

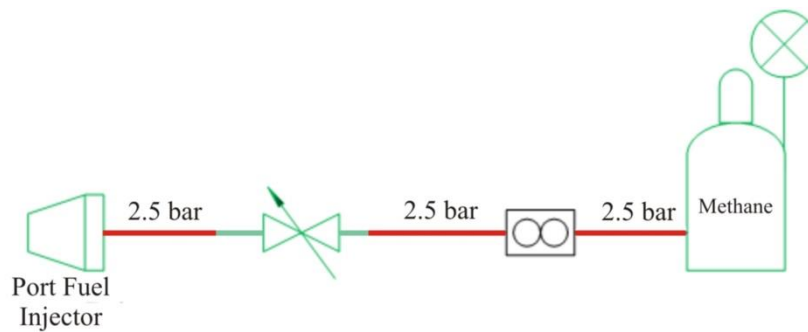


**Figure 112. Schematic of the port fuel injection system; figure taken from [150]**

Port fuel injector was mounted into the intake pipe (Figure 106), and as was already mentioned, the conventional dual fuel experiments were run with the methane as the primary fuel. The schematic of the PFI system is shown in the Figure 112 and it reveals that the methane was supplied from the high-pressure vessel which features a pressure regulator. Methane was injected with a gaseous fuel injector Peak & Hold Injector PQ2-3200, which had a maximum flow rate of 2 g/s and the maximum operating pressure of 3 barg. Therefore, the pressure in the fuel supply line was kept at roughly 2.5 barg.

The absolute intake pressure was measured with a Kulite XTEL 190(M) sensor, while the temperature was measured using a K-Type thermocouple [1]. The in-cylinder pressure was measured using a glow plug-mounted AVL GH14D sensor [1]. Harmful exhaust gas emissions (HC, CO and NO<sub>x</sub>, as well as O<sub>2</sub>) were measured with the Horiba gas analyzer FIA-220.

Port and direct fuel injection, as well as the pressure in the common rail was controlled through the Natural Instruments Drivers. The other operating parameters (engine speed and load) were monitored and controlled through a specially designed program that was developed in the LabVIEW. This program was also used as a data acquisition tool through which all important operating parameters were stored:

1. Engine speed and load
2. In-cylinder pressure
3. Intake pressure
4. PFI mass flow
5. DFI mass
6. Diesel fuel substitution ratio (both energy and mass based)

7. Total and premixed fuel air excess ratio
8. Temperatures in various places on the experimental setup (intake, exhaust, cooling liquid, etc.)
9. Etc.

### ***Rate of heat release re-calculation code***

The important operating parameters that cannot be directly measured (gross indicated mean effective pressure (IMEPg), indicated and gross indicated thermal efficiency), as well as the in-cylinder temperature and the rate of heat release (ROHR), were calculated with the in-house developed rate of heat release re-calculation code. Each experimental point was recorded at the steady-state conditions for the 300 consecutive cycles [1]. After that the in-cylinder and intake pressures are averaged and the respective mean traces are filtered with a Savitzky-Golay filter [152].

For each operating point the mean in-cylinder temperature trace and the mean ROHR are calculated from the state equation and from the energy conservation law (1<sup>st</sup> law of thermodynamics), respectively. The in-cylinder gas properties (temperature and species dependent) are calculated with the equations that have already been presented in the chapter 3.4.2 (equations 3.140 through 3.146).

In the first re-calculation step the combustion profile and hence the species traces are unknown. Therefore, a predefined combustion profile is assumed and according to that profile the species traces and hence the corresponding mixture gas constant and specific heat capacity traces are calculated. Such pre-set profiles are then used in the in-cylinder temperature and ROHR calculation. In the next step the combustion profile that was calculated in the previous step is used to calculate the species and gas mixture properties traces and after that the new in-cylinder temperature and ROHR traces are calculated. Such iterative approach is employed until convergence of the start of combustion timing is achieved. The instantaneous value of the in-cylinder temperature and the rate of heat release are calculated with the following equations:

$$T_{\text{cyl}} = \frac{p_{\text{cyl}} \cdot V_{\text{cyl}}}{m_{\text{cyl}} \cdot R_{\text{cyl}}} \quad (4.1)$$

$$\frac{dQ_{\text{COMB}}}{d\phi} = m_{\text{cyl}} \cdot c_{v,\text{cyl}} \cdot \frac{dT_{\text{cyl}}}{d\phi} + p_{\text{cyl}} \cdot \frac{dV_{\text{cyl}}}{d\phi} \cdot \frac{\kappa_{\text{cyl}}}{\kappa_{\text{cyl}} - 1} + \frac{V_{\text{cyl}}}{m_{\text{cyl}}} \cdot p_{\text{cyl}} \cdot \frac{dm_{\text{cyl}}}{d\phi} + \frac{dQ_{\text{wall}}}{d\phi} \quad (4.2)$$

In the equations given above,  $T_{cyl}$  (K) represents the in-cylinder temperature,  $p_{cyl}$  (Pa) represents the in-cylinder pressure,  $V_{cyl}$  (m<sup>3</sup>) represents the in-cylinder volume,  $m_{cyl}$  (kg) represents the in-cylinder mass,  $R_{cyl}$  (m<sup>3</sup>) represents the in-cylinder gas mixture constant,  $Q_{comb}$  (J) represents the released energy,  $\kappa_{cyl}$  (m<sup>3</sup>) represents the ratio of the specific heats of the mixture inside the cylinder, while  $Q_{wall}$  (J) represents the energy that has been transferred to the cylinder walls. The instantaneous cylinder volume is calculated with the following equation:

$$V_{cyl} = \frac{D_{cyl}^2 \cdot \pi}{4} \cdot \left[ \frac{H}{(CR-1)} + x_{piston} \right] \quad (4.3)$$

In the equations given above,  $D_{cyl}$  (m) represents the cylinder bore,  $H$  (m) represents the engine stroke,  $CR$  (-) represents the compression ratio, while  $x_{piston}$  (m) represents the instantaneous piston position. The in-cylinder mass is calculated according to the measured intake mass flow, measured fuel flows, internal EGR (assumed to be 5%). The wall heat transfer is calculated according to the equations that have already been presented in the chapter 3.2.3 (with the well-known Woschni's correlation for the overall heat transfer coefficient).

#### 4.2.2. Sensitivity analysis of the DFMZCM to its parameters

At the beginning of this chapter the DFMZCM is validated with the experimental results that were obtained at the so-called base operating point, whose parameters are given in the Table 12. After that the sensitivity of the DFMZCM to its parameters is presented.

The list of the turbulence, spray and flame propagation model parameters used in calculating the base operating point can be found in Table 13, Table 14 and Table 15 respectively. The in-cylinder turbulence model parameters (Table 13) that were used in all of the conventional dual fuel simulation are the same as the ones that were used in the pure Diesel simulation (presented in the chapter 4). The reason for such approach is that the 3-D CFD results that would reveal the level of in-cylinder turbulence and its profile were not available for the UC Berkeley VW engine and since the two engines in questions (engine used in the 3-D CFD simulation and the UC Berkeley VW engine) have quite similar geometries, same constants as the ones used in the pure Diesel simulations were taken in the validation of the entire DFMZCM.

**Table 12. Base operating point parameters**

Parameter	Value
Engine Speed (rpm)	1000
SHP Pressure (bar)	1.33
SHP Temperature (K)	396
SHP Combustion Products Mass Fraction (-)	0.02
Start of Injection (degCA bTDC)	20
Injection Duration (degCA)	1.5
Injection Pressure (bar)	500
Diesel Fuel Mass (mg)	1.4
Methane Fuel Mass (mg)	18.04
Total Excess Air Ratio (-)	1.34
IMEPg (bar)	7.003

**Table 13. Turbulence model parameters for the base operating point**

Model Parameter	Value
$S_{in}$ (-)	$1.5 \times 10^{-3}$
$C_{in}$ (-)	1.55
$S_{inj}$ (-)	$3.5 \times 10^{-2}$
$C_{inj}$ (-)	155
$C_2$ (-)	1.92
$C_\varepsilon$ (-)	2.35
$C_{\varepsilon,UZ}$ (-)	1
$C_L$ (-)	0.5

**Table 14. Spray and heat transfer model parameters for the base operating point**

Model Parameter	Value
$C_{evap,HT}$ (-)	1.1
$C_{evap}$ (-)	1
$C_{entrain}$ (-)	0.5
$C_{ignition}$ (-)	1
$C_{discr,ax}$ (-)	0.6
$C_{discr,rad}$ (-)	6
$C_{ZHT,SZ}$ (-)	1

Most of the spray model parameters (Table 14) used in the validation of the DFMZCM were also kept at the same level as the parameters that were used in the pure Diesel simulation. The only parameter that was altered from case to case is the parameter that controls the amount of



heat that is supplied to the liquid fuel droplet for its evaporation ( $C_{\text{evap,HT}}$ ). This parameter was used to adjust the ignition time in the 0-D simulation.

**Table 15. Flame propagation model parameters for the base operating point**

Model Parameter	Value – Fractal Combustion Model	Value – Turbulent Combustion Model
$C_{\text{ign,UZ,transf}} (-)$	0.95	0.95
$C_{\text{trans}} (-)$	2.2	4.5
$C_{\text{SOWC}} (-)$	0.8	0.8
$C_{\text{WC,shp}} (-)$	3	3
$C_{\text{comb}} (-)$	2.44	1
$C_{\text{EOFP}} (-)$	1	1

Similarly, to the spray model parameters, some of the flame propagation model parameters (Table 15) had to be adjusted from case to case. These parameters include the parameter used to tune the transition time from laminar to fully turbulent flame ( $C_{\text{trans}}$ ), parameter that controls the onset of the wall combustion ( $C_{\text{SOWC}}$ ), the parameter that controls the maximum value of the fractal dimension in FCM or turbulent flame speed level in the case of TCM ( $C_{\text{comb}}$ ), and the parameter that defines the mass fraction burned at which the flame propagation ends ( $C_{\text{EOFP}}$ ).

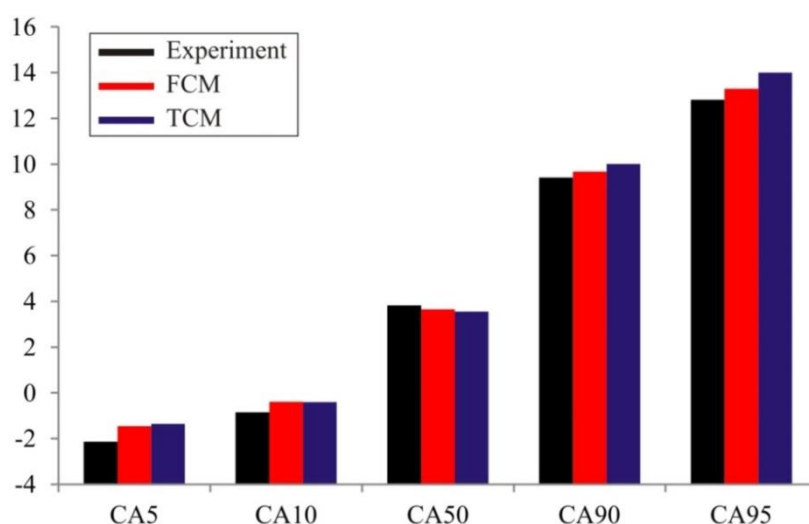


**Figure 113. Comparison between the measured and simulated CA5, CA10, CA50, CA90 and CA95 values for the base operating point**

The comparison between the measured and simulated indicators that present crank angles at which 5%, 10%, 50%, 90% and 95% of energy has been released (CA5, CA10, CA50, CA90

and CA95) is presented in Figure 113, and it reveals that there is only a slightest difference between the measured and simulated combustion profile.

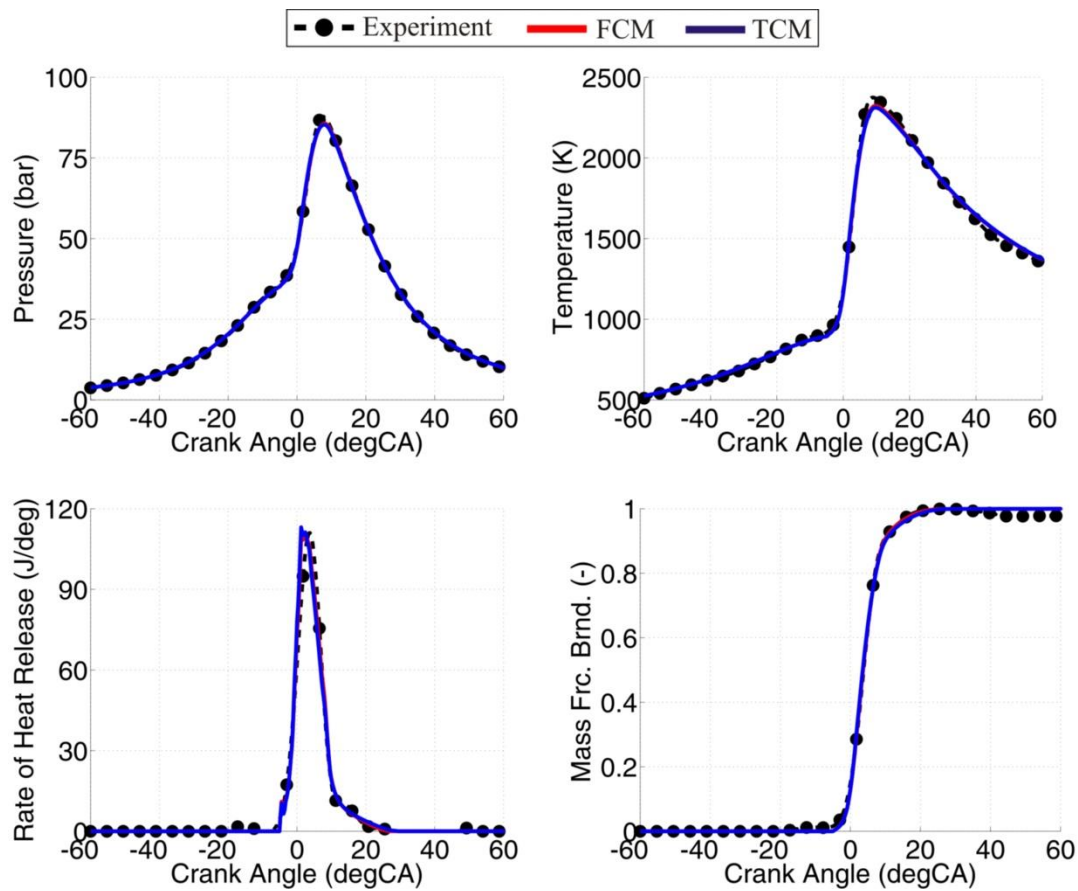


**Figure 114. Comparison between the measured and simulated in-cylinder pressure, temperature, ROHR and MFB traces for the base operating point**

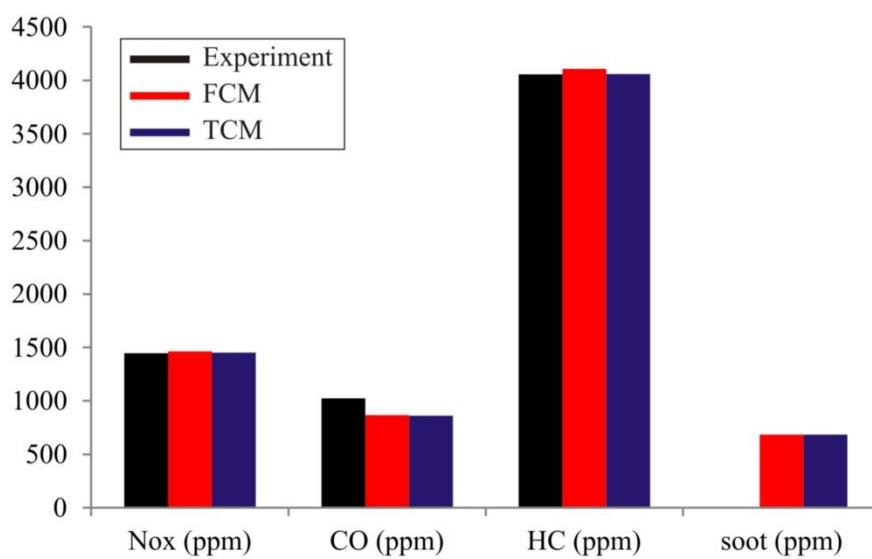


**Figure 115. Comparison between the measured and simulated NO<sub>x</sub>, CO, HC and soot emissions for the base operating point**

As can be seen from the comparison between the experimentally obtained and simulated in-cylinder pressure, temperature, ROHR and MFB traces (Figure 114), there is a good fit between the experiment and simulation for both flame propagation models.

**Table 16. Comparison between the specific measured and simulated parameters for the base operating point**

Parameter	Value – Experiment	Value – FCM	Value – TCM
IMEPg (bar)	7.003	6.998	6.999
Peak Cylinder Pressure (bar)	88.18	87.39	87.22
Peak Cylinder Pressure Crank Angle (degCA)	6.75	7.2	7.2

Finally, Figure 115 and the Table 16 reveal that there is a good correspondence between the measured and simulated emissions as well as between the measured and simulated IMEPg, peak cylinder pressure (PCP) and crank angle at PCP.

Once the model had been tuned and its validation at the base operating case has been performed, the sensitivity of the model to its tuning parameters was performed. Generally, the model parameters can be divided into three main groups:

1. In-cylinder turbulence model parameters
2. Spray model parameters
3. Flame propagation model parameters

### ***Sensitivity on in-cylinder turbulence model parameters***

**Table 17. The list of the varied turbulence model parameters**

Parameter	Base Value	Low Value	High Value
$S_{in}$ (-)	$1.5 \times 10^{-3}$	$0.75 \times 10^{-3}$	$3 \times 10^{-3}$
$C_{in}$ (-)	1.55	0.775	3.1
$S_{inj}$ (-)	$3.5 \times 10^{-2}$	$1.75 \times 10^{-2}$	$7 \times 10^{-2}$
$C_{inj}$ (-)	155	77,5	310
$C_2$ (-)	1.92	0.96	3.84
$C_\varepsilon$ (-)	2.35	1.175	4.7
$C_{\varepsilon, UZ}$ (-)	1	0.5	2
$C_L$ (-)	0.5	0.25	1

The list of the varied in-cylinder turbulence model parameters and their respective values are given in Table 17. As can be seen in Table 17, for all turbulence model parameters the low value is 2x lower than the base value, while the high value is 2x larger than the base value. The sensitivity on in-cylinder turbulence model parameters is performed for both flame

propagation models and the main conclusions are obtained by analyzing the results of in-cylinder pressure and rate of heat release. Additionally, tornado plot which clearly shows the influence of a given in-cylinder turbulence model parameter on the simulated combustion process (CA10, CA50 and CA90) is given at the end of this chapter.

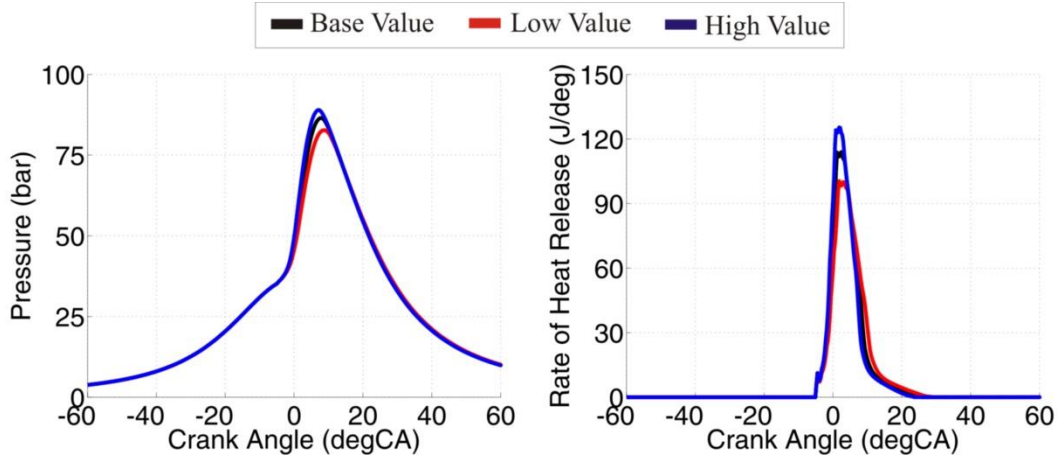


**Figure 116. Influence of the  $S_{in}$  model parameter on the in-cylinder pressure and ROHR traces; FCM flame propagation model**

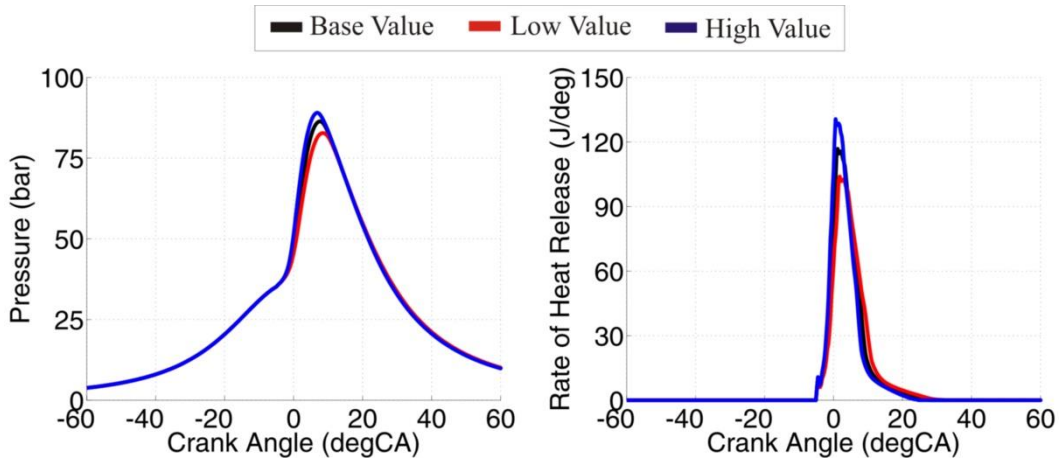


**Figure 117. Influence of the  $S_{in}$  model parameter on the in-cylinder pressure and ROHR traces; TCM flame propagation model**

$S_{in}$  is the in-cylinder turbulence model parameter which is used to appropriately account for the effect of the intake process on the specific TKE level. Figure 116 presents the influence of the  $S_{in}$  turbulence model parameter on the in-cylinder pressure and ROHR traces in the case when the flame propagation is modeled with the FCM, while in Figure 117 the same results are presented but now for the case when the flame propagation is modeled with the TCM. Figure 118 presents the influence of the  $S_{in}$  turbulence model parameter on the in-cylinder turbulence quantities when the flame propagation is modeled with the FCM. The in-cylinder

turbulence quantities exhibit the similar behavior when the flame propagation is modeled with the TCM. Figure 119 presents the influence of the  $S_{in}$  model parameter on fractal dimension (the flame propagation is modeled with FCM) and on the turbulent flame velocity (the flame propagation is modeled with TCM).

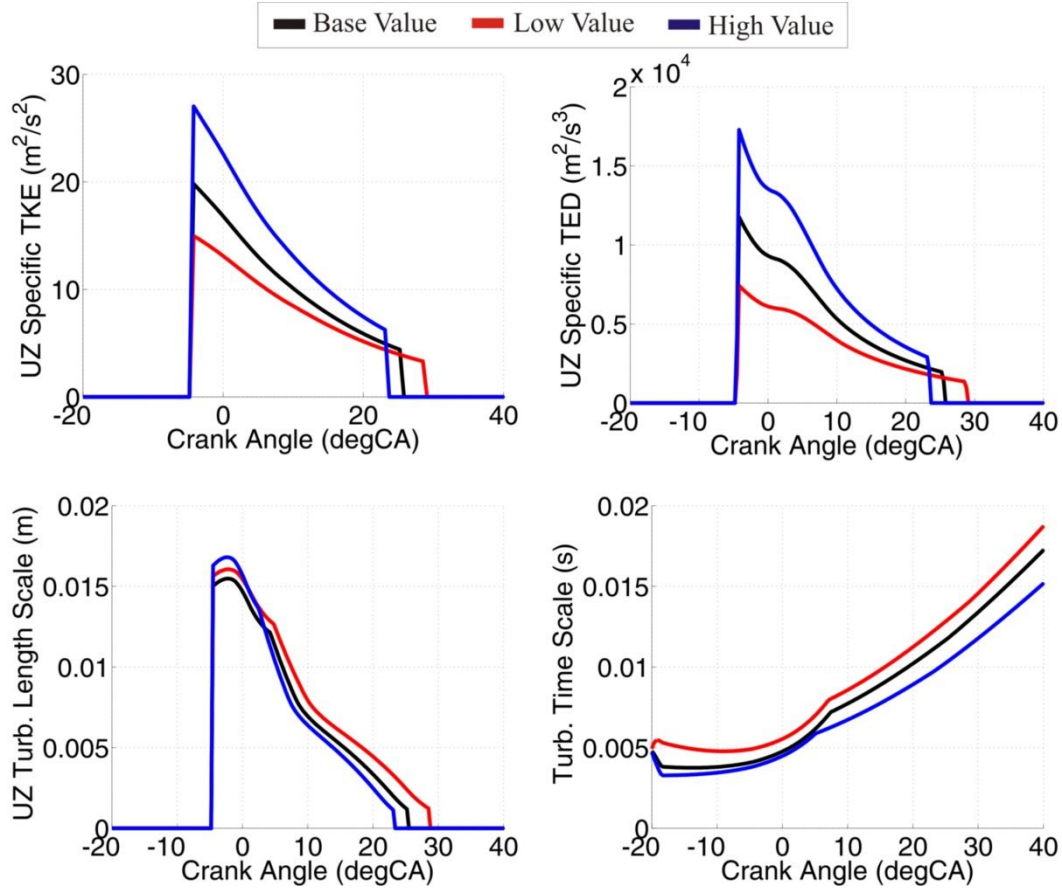


**Figure 118. Influence of the  $S_{in}$  model parameter on the in-cylinder turbulence quantities**

The in-cylinder turbulence quantities traces (Figure 118) reveal that the  $S_{in}$  has a significant influence on the in-cylinder turbulence levels. As  $S_{in}$  is increased, both specific TKE and turbulent energy dissipation (TED) increase. The trend in the integral length scale level is not that straight forward since the integral length scale is a function of the specific TKE to specific TED ratio. Moreover, the integral length scale is also a function of the geometry; specifically, the size of the unburned zone. The same applies for the turbulence time scale which is a function of the integral length scale to the turbulence intensity ratio.

Since the flame propagation and the in-cylinder turbulence are coupled, the change in the in-cylinder turbulence leads to the change in the part of the combustion process that is governed by the flame propagation. As the  $S_{in}$  is increased the entire combustion (CA10, CA50 and CA90) is advanced, combustion intensity (peak ROHR) increases and combustion duration is

shortened (Figure 116 and Figure 117). The reason for such effect can be seen in the Figure 119; as  $S_{in}$  parameter is increased, the peak values of fractal dimension (FCM case) and turbulent flame velocity (TCM case) are advanced (occur earlier) and increased. Therefore, combustion is more rapid, which leads to an increase in the peak ROHR value and shorter combustion duration.

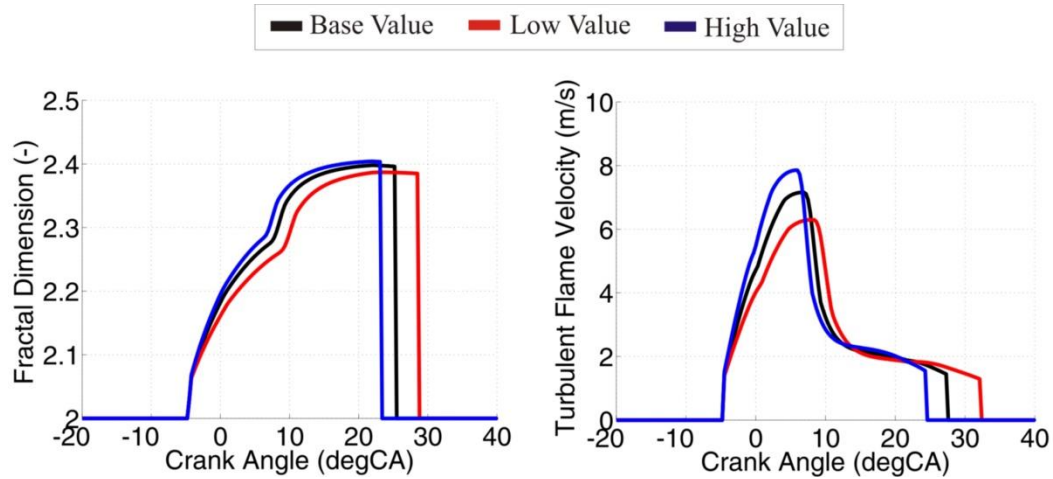


**Figure 119. Influence of the  $S_{in}$  model parameter on fractal dimension (FCM) and on the turbulent flame velocity (TCM)**

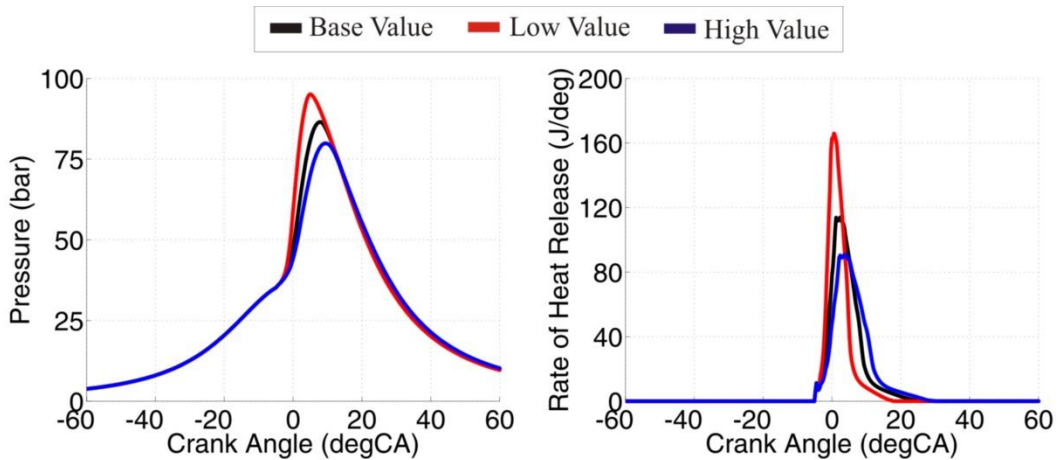


**Figure 120. Influence of the  $C_{in}$  model parameter on the in-cylinder pressure and ROHR traces; FCM flame propagation model**

Figure 120 and Figure 121 show the influence of the  $C_{in}$  turbulence model parameter on the in-cylinder pressure and ROHR traces in the case when the flame propagation is modeled with the FCM and TCM, respectively.  $C_{in}$  is the in-cylinder turbulence model parameter which is used to appropriately account for the effect of the intake process on the specific TED level. Figure 122 represents the influence of the  $C_{in}$  turbulence model parameter on the in-



cylinder turbulence quantities when the flame propagation is modeled with the FCM while in the case when TCM is used the in-cylinder turbulence quantities exhibit similar behavior.

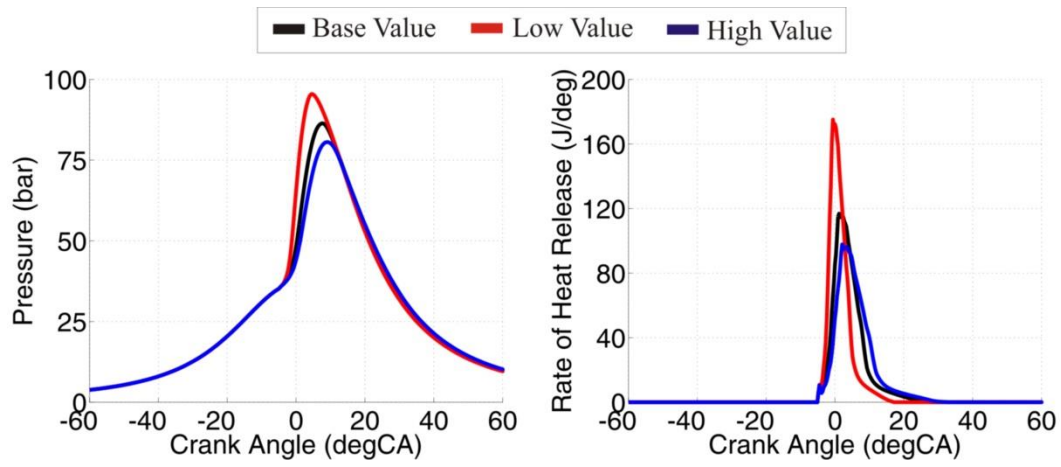


**Figure 121. Influence of the  $C_{in}$  model parameter on the in-cylinder pressure and ROHR traces; TCM flame propagation model**

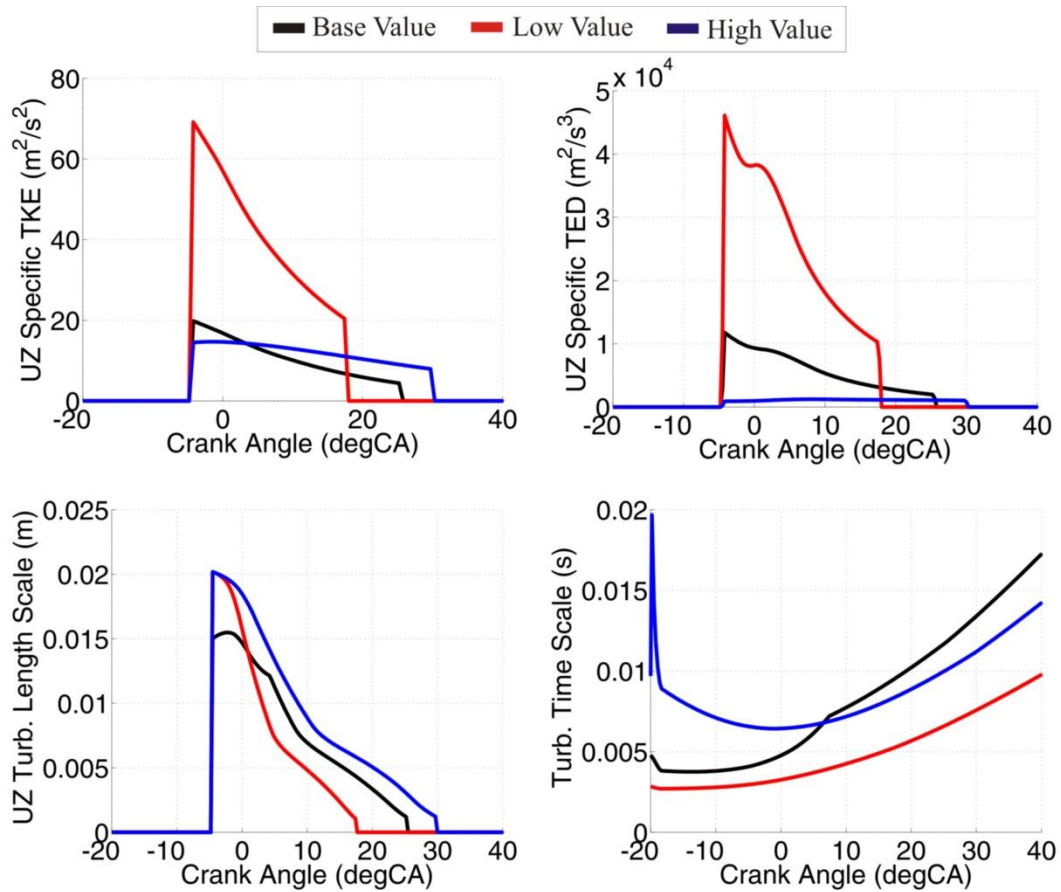
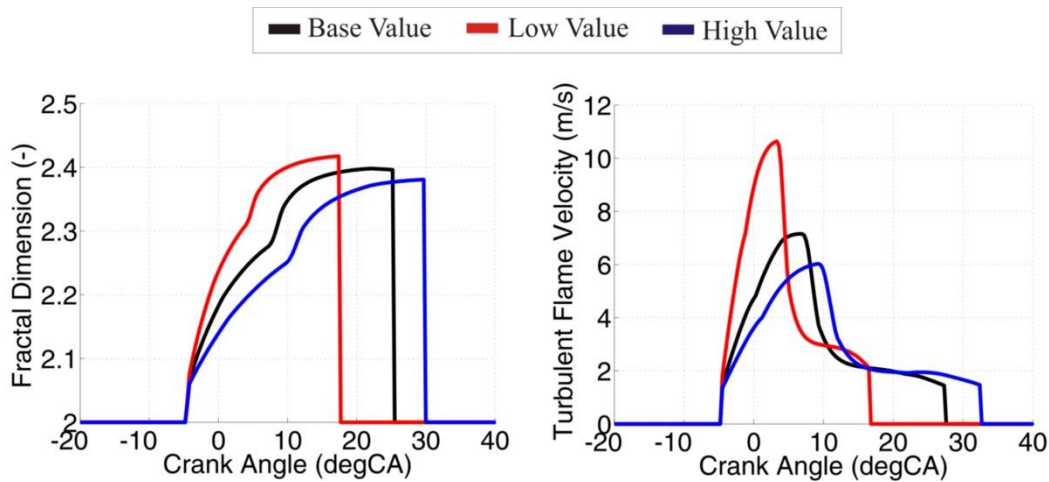


**Figure 122. Influence of the  $C_{in}$  model parameter on the in-cylinder turbulence quantities**

The results of the in-cylinder turbulence quantities (Figure 122) reveal that the  $C_{in}$  has a significant influence on the turbulence levels. As  $C_{in}$  is increased, both the specific TKE and

TED decrease. It can be seen that at one point the specific UZ TKE for the high-level case actually become higher than the base case specific UZ TKE. This is simply a result of the fact that in the high level  $C_{in}$  case the flame propagation is slower compared to the base level case, which means that at the same crank angle point the UZ mass in the high-level case will be higher leading to a higher value of the specific UZ TKE. Again, the trend in the integral length scale and the turbulence time scale levels is not that straight forward and depends on the in-cylinder turbulence quantities and on the combustion progress.

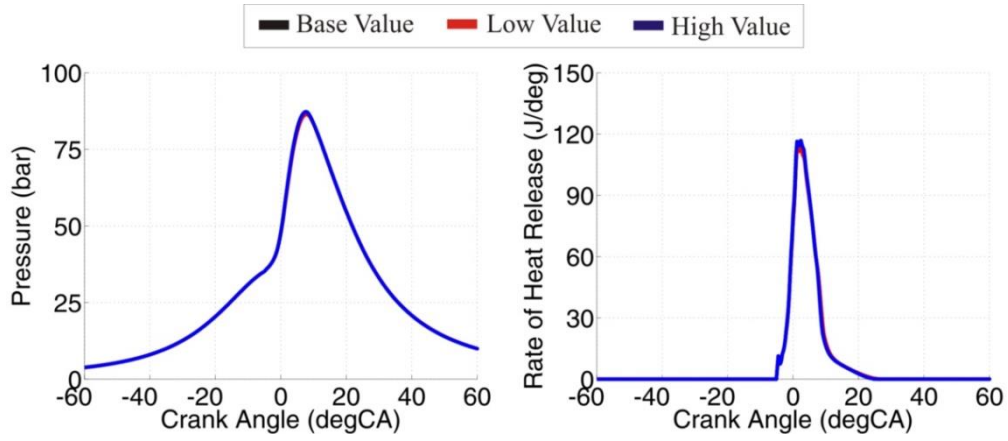
As  $C_{in}$  is increased the entire combustion (CA10, CA50 and CA90) is retarded, combustion intensity (peak ROHR) decreases and combustion duration is prolonged (Figure 120 and Figure 121). The reason for such effect can be seen in Figure 123, which presents the influence of  $C_{in}$  turbulence model parameter on fractal dimension (the flame propagation is modeled with FCM) and on the turbulent flame velocity (the flame propagation is modeled with TCM). As  $C_{in}$  is decreased (Figure 123), the peak values of fractal dimension (FCM case) and turbulent flame velocity (TCM case) are advanced (occur earlier) and increased. Therefore, combustion is more rapid, which leads to an increase in the peak ROHR value and shorter combustion duration.



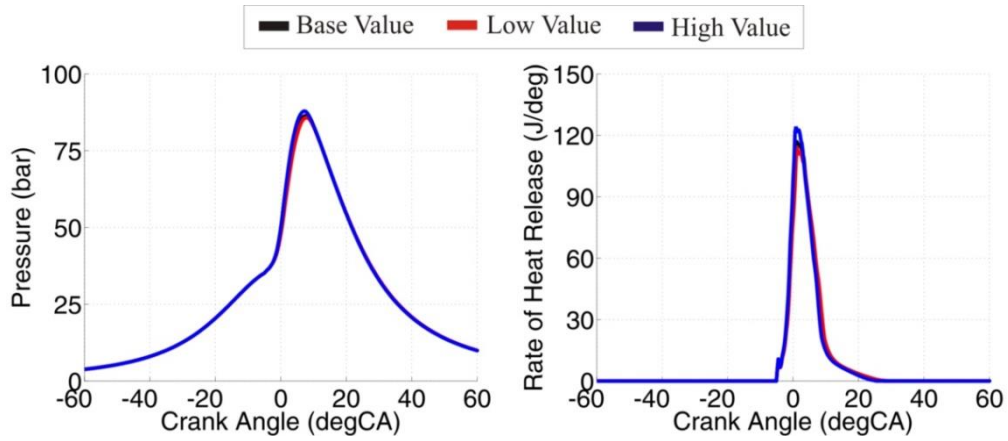
**Figure 123. Influence of the  $C_{in}$  model parameter on fractal dimension (FCM) and on the turbulent flame velocity (TCM)**

Figure 124 and Figure 125 represent the influence of the  $S_{inj}$  turbulence model parameter on the in-cylinder pressure and ROHR traces in the case when the flame propagation is modeled with FCM and TCM, respectively, and the same set of results but now for the influence of  $C_{inj}$  turbulence model parameter are shown in Figure 126 and Figure 127.  $S_{inj}$  and  $C_{inj}$  are the in-cylinder turbulence model parameters which are used to appropriately account for the effect of the direct fuel injection process on the specific TKE and TED level, respectively.





**Figure 124. Influence of the  $S_{inj}$  model parameter on the in-cylinder pressure and ROHR traces; FCM flame propagation model**



**Figure 125. Influence of the  $S_{inj}$  model parameter on the in-cylinder pressure and ROHR traces; TCM flame propagation model**

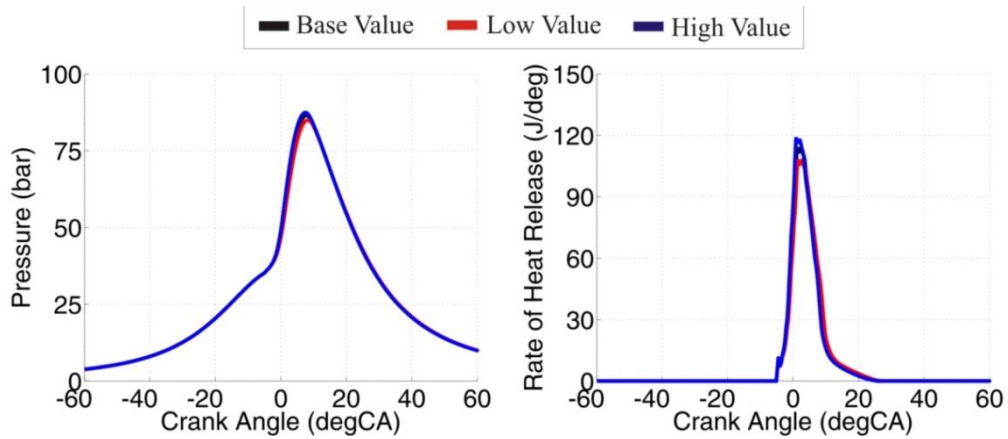


**Figure 126. Influence of the  $C_{inj}$  model parameter on the in-cylinder pressure and ROHR traces; FCM flame propagation model**

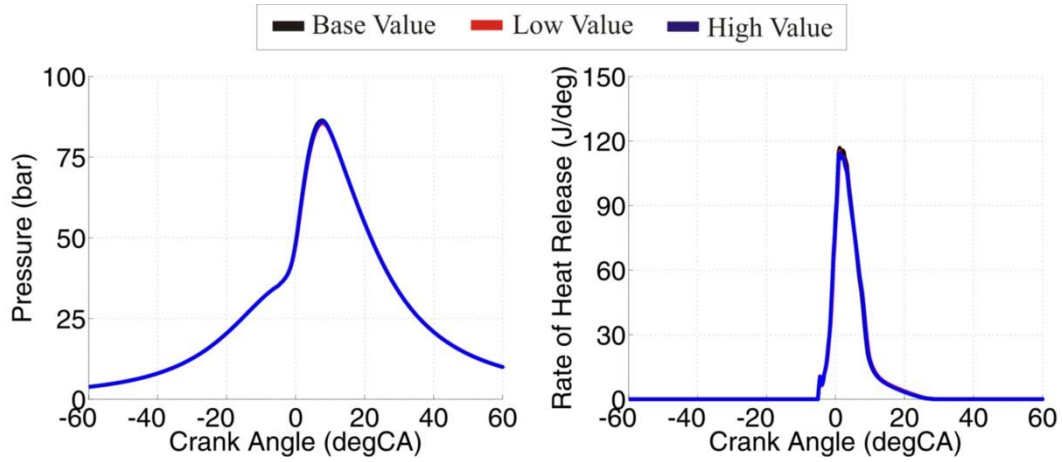


**Figure 127. Influence of the  $C_{inj}$  model parameter on the in-cylinder pressure and ROHR traces; TCM flame propagation model**

The influence of the  $S_{inj}$  and of the  $C_{inj}$  turbulence model parameters on the in-cylinder turbulence quantities for the FCM flame propagation model is shown in Figure 128 and Figure 129, respectively. The in-cylinder turbulence quantities exhibit a similar behavior when the flame propagation is modeled with TCM.

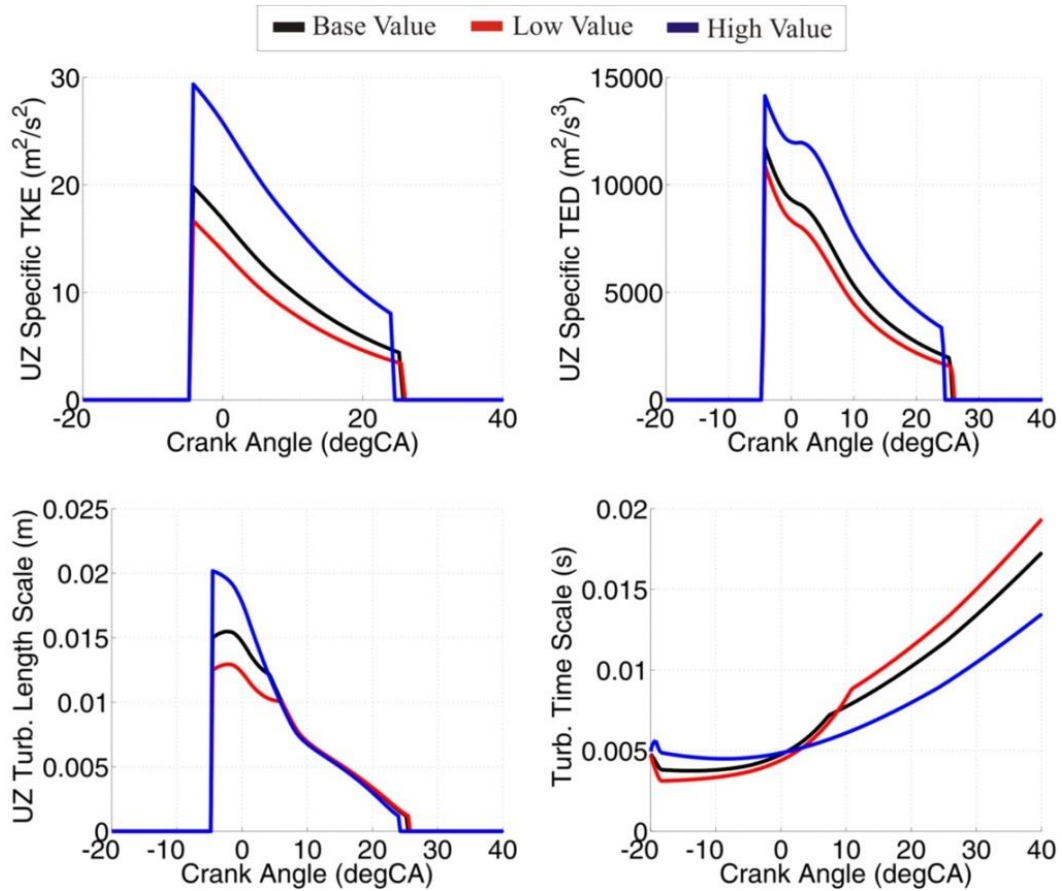


**Figure 128. Influence of the  $S_{inj}$  model parameter on the in-cylinder turbulence quantities**

As can be seen from Figure 128, as  $S_{inj}$  is increased, the specific TKE, specific TED and the integral length scale all increase. Interesting thing to note is that the integral length scale obtains roughly the similar value for all three cases around 10 degCA after top dead center (aTDC). This is a result of the integral length scale geometry limit which starts to control the integral length scale size as the flame approaches the walls. It can also be seen (Figure 128) that the turbulent time scale at some stages increases, while at the other decreases as the  $S_{inj}$  is increased. This is due to the fact that the turbulent time scale is a function of the specific TKE and the integral length scale which also change at the different stages of the combustion process.

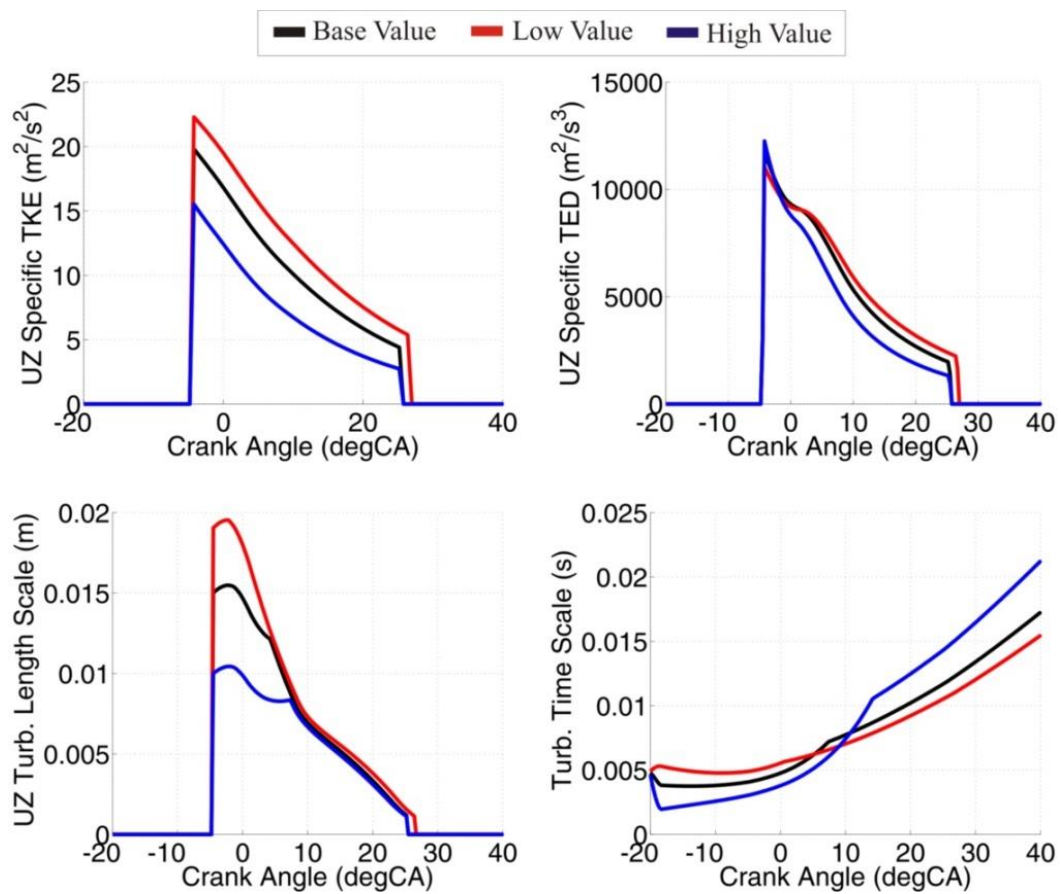


**Figure 129. Influence of the  $C_{inj}$  model parameter on the in-cylinder turbulence quantities**

On the other hand, the Figure 129 reveals that as the  $C_{inj}$  is increased, the specific TKE, specific TED and the integral length scale all decrease. Same as in the previous case, the integral length scales obtain roughly the same value around 10 degCA aTDC (Figure 129). Moreover, similarly to the previous case, the turbulent time scale at some stages increases, while at the other decreases as the  $C_{inj}$  is increased (Figure 129).

It is interesting to note that even though the change in the injection parameters has a large influence on the in-cylinder turbulence quantities (Figure 128 and Figure 129), the overall effect on combustion (ROHR) trace is negligible (Figure 126 and Figure 127). The reason for such effect can be seen in Figure 130 and Figure 131, which present the influence of the  $S_{inj}$  and  $C_{inj}$  model parameters on fractal dimension (the flame propagation is modeled with FCM) and on the turbulent flame velocity (the flame propagation is modeled with TCM).

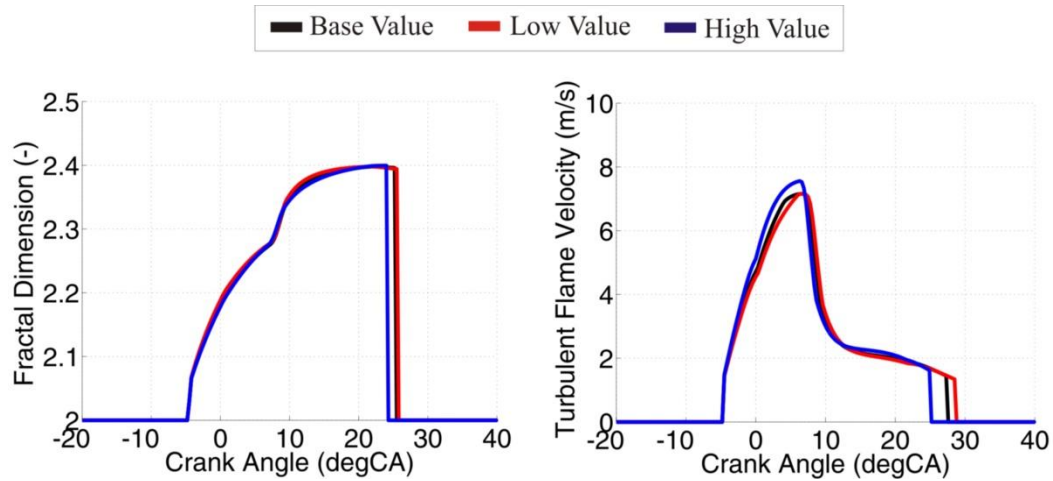


**Figure 130. Influence of the  $S_{inj}$  model parameter on fractal dimension (FCM) and on the turbulent flame velocity (TCM)**

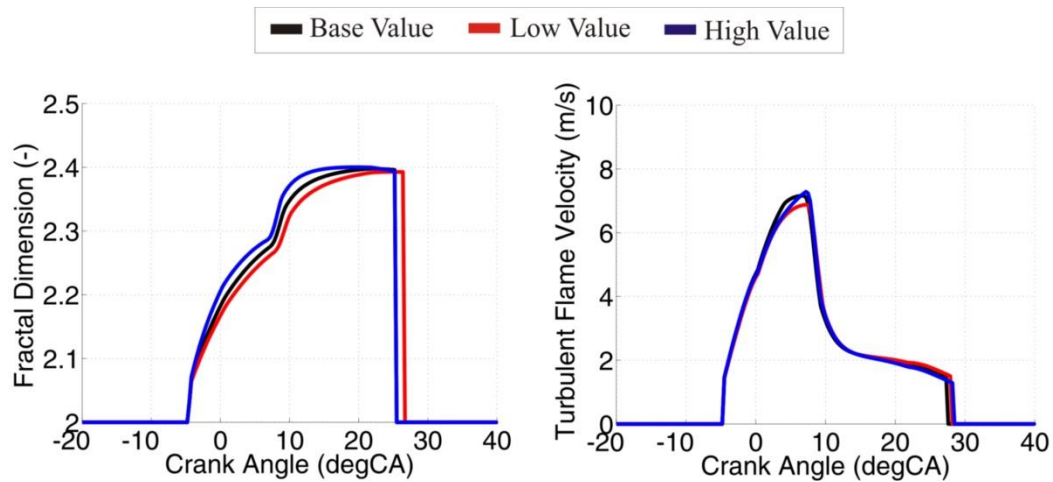


**Figure 131. Influence of the  $C_{inj}$  model parameter on fractal dimension (FCM) and on the turbulent flame velocity (TCM)**

Both of these figures reveal that as  $S_{inj}$  and  $C_{inj}$  are increased, the fractal dimension traces (FCM case) and turbulent flame velocity traces (TCM case) stay approximately the same. The reason for such effect is that fractal dimension and turbulent flame velocity are influenced by integral length scale and turbulence intensity (during the entire combustion phase), and by

turbulent time scale (its value in the start of combustion moment defines the laminar to turbulent flame transition).

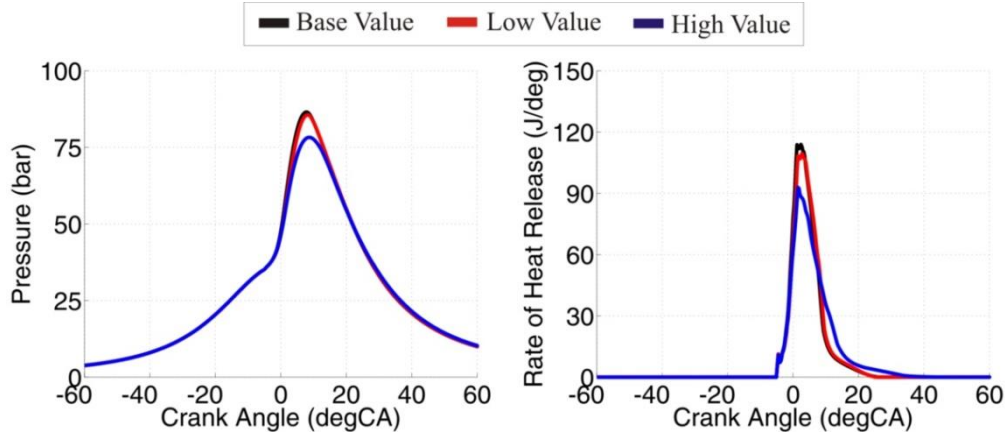
As  $S_{inj}$  parameter is increased turbulence intensity and integral length scale are increased (Figure 128) which leads to an increase in the maximum fractal dimension value and turbulent flame speed, respectively. However, Figure 128 also reveals that as  $S_{inj}$  parameter is increased, the turbulent time scale in the start of the flame propagation moment increases, which leads to longer transition from laminar to fully developed turbulent flame. The cumulative effect is that the combustion rate (ROHR) stays approximately the same even though there is a significant difference in the in-cylinder turbulence quantities.

As  $C_{inj}$  parameter is increased, turbulence intensity and integral length scale decrease (Figure 129) which leads to a decrease in the maximum fractal dimension value and turbulent flame speed, respectively. However, Figure 129 also reveals that as  $C_{inj}$  parameter is increased, the turbulent time scale in the start of the flame propagation moment decreases, which leads to shorter transition from laminar to fully developed turbulent flame. Again, the cumulative effect is that the combustion rate (ROHR) stays approximately the same even though there is a significant difference in the in-cylinder turbulence quantities.

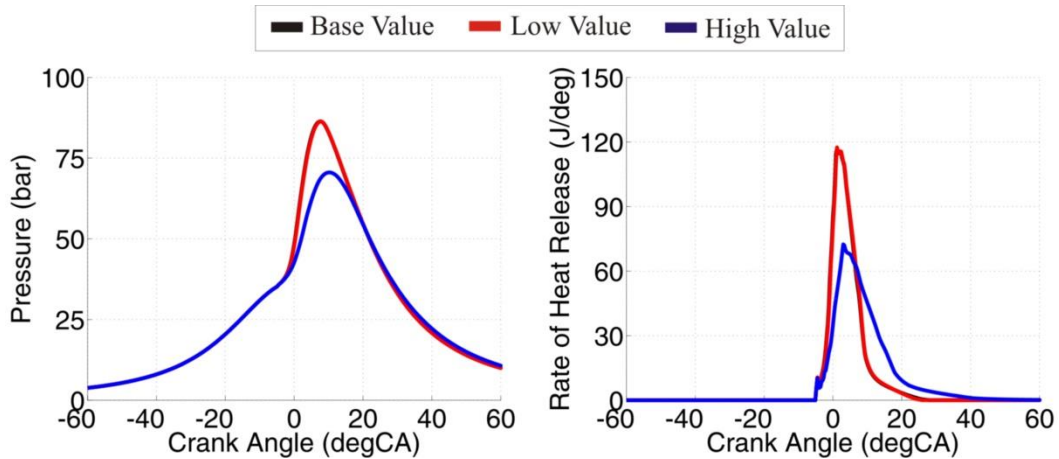
The ROHR traces also reveal that  $S_{inj}$  has more pronounced influence on the TCM; in this case as it is increased, combustion intensity increases and vice versa (Figure 125). On the other hand,  $C_{inj}$  has more pronounced influence on the FCM; in this case the combustion intensity increases with the increase of  $C_{inj}$  and vice versa (Figure 126). The reason for such effects can be found in the fractal dimension and turbulent flame velocity traces (Figure 130 and Figure 131). Figure 130 reveals that as  $S_{inj}$  parameter is increased, fractal dimension traces (FCM case) stays the same thus leading to approximately same ROHR traces (Figure 124). On the other hand, as  $S_{inj}$  parameter is increased, the peak value of turbulent flame velocity (TCM case) is slightly advanced (occur earlier) and increased thus leading to a slight increase in the peak ROHR value (Figure 125). Likewise, Figure 131 reveals that as  $C_{inj}$  parameter is increased, turbulent flame velocity traces (FCM case) stays approximately the same thus leading to approximately same ROHR traces (Figure 127). On the other hand, as  $C_{inj}$  parameter is increased, the peak value of fractal dimension (FCM case) is slightly advanced (occurs earlier) and increased thus leading to a slight increase in the peak ROHR value (Figure 126).

Figure 132 and Figure 133 show the influence of the  $C_\varepsilon$  turbulence model parameter on the in-cylinder pressure and ROHR traces in the case when the flame propagation is modeled with the FCM and TCM, respectively.  $C_\varepsilon$  is the in-cylinder turbulence model parameter which is

used to adjust the specific TED production level. Figure 134 represents the influence of the  $C_\varepsilon$  turbulence model parameter on the in-cylinder turbulence quantities in the case when the flame propagation is modeled with the FCM, while in the case when TCM is used the in-cylinder turbulence quantities exhibit similar behavior.



**Figure 132. Influence of the  $C_\varepsilon$  model parameter on the in-cylinder pressure and ROHR traces; FCM flame propagation model**



**Figure 133. Influence of the  $C_\varepsilon$  model parameter on the in-cylinder pressure and ROHR traces; TCM flame propagation model**

Figure 134 reveals that as the  $C_\varepsilon$  increases the specific TKE and the integral length scale decrease. As in the previous few cases, the turbulent time scale at some stages increases, while at the other decreases as  $C_\varepsilon$  is increased. The in-cylinder turbulence model parameter  $C_\varepsilon$  has an interesting influence on both the FCM and TCM. In both cases there is almost negligible difference in the combustion rate between the low and base case, while as the constant is further increased (base case to high case) the combustion phase is retarded, the combustion intensity is decreased, while the combustion duration is prolonged (Figure 132 and Figure 133). The reason for such effect can be seen in Figure 135, which presents the



influence of  $C_\varepsilon$  model parameter on fractal dimension (the flame propagation is modeled with FCM) and on the turbulent flame velocity (the flame propagation is modeled with TCM).

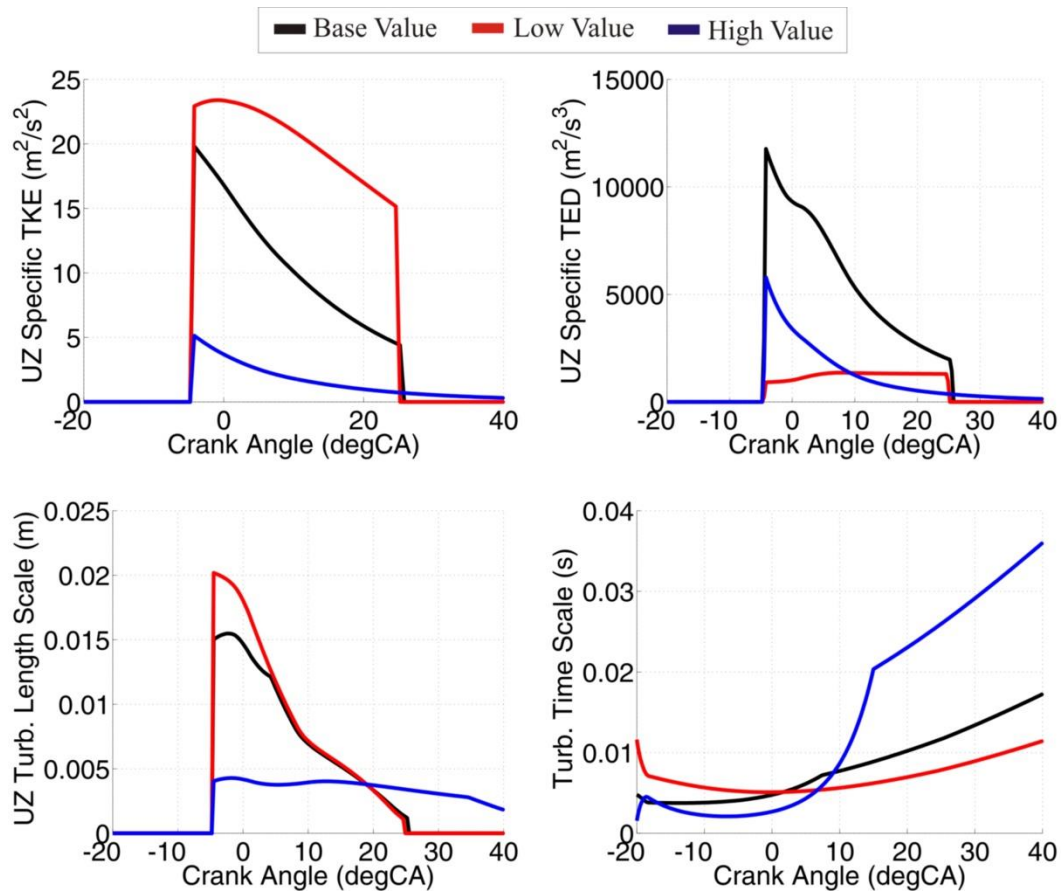


Figure 134. Influence of the  $C_\varepsilon$  model parameter on the in-cylinder turbulence quantities

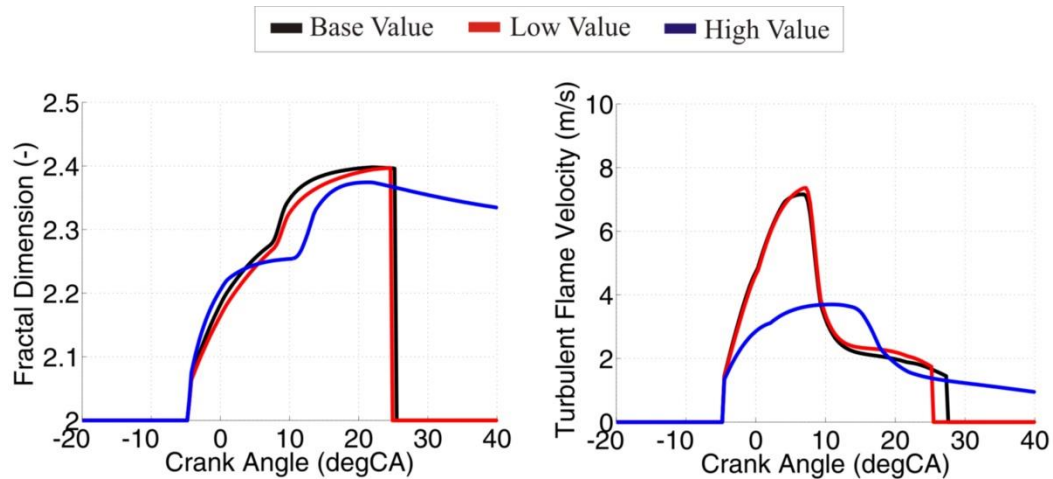


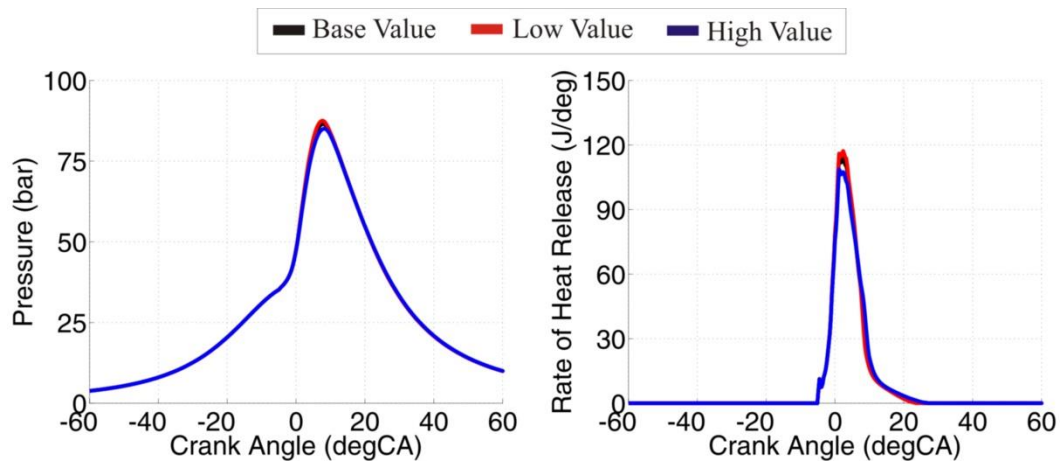
Figure 135. Influence of the  $C_\varepsilon$  model parameter on fractal dimension (FCM) and on the turbulent flame velocity (TCM)

Figure 135 reveals that for  $C_\varepsilon$  parameter there is only a slight difference in fractal dimension traces (FCM case), as well as turbulent flame velocity traces (TCM case) between the base

value case and low value case. Therefore, these two cases have similar combustion rates (Figure 132 and Figure 133). On the other hand, high value case has retarded (occurs later) and lower peak value of fractal dimension and turbulent flame velocity compared to the other two cases. Therefore, this case has lower combustion rate than the other two cases (Figure 132 and Figure 133).

Interesting thing to note is that even though the low and base value case exhibit similar combustion rates (Figure 132 and Figure 133), their respective in-cylinder turbulence quantities, are significantly different (Figure 134). This is a result of their respective turbulence intensity and integral length scale traces, and turbulent time scale values in the start of the flame propagation moment (Figure 134). Compared to the base value case, low value case has higher turbulence intensity and integral length scale values which leads to an increase in the maximum fractal dimension value and turbulent flame speed. On the other hand, its turbulent time scale in the start of the flame propagation is also higher, which leads to longer transition from laminar to fully developed turbulent flame. The cumulative effect is that the combustion rate (ROHR) stays approximately the same even though there is a significant difference in the in-cylinder turbulence quantities.

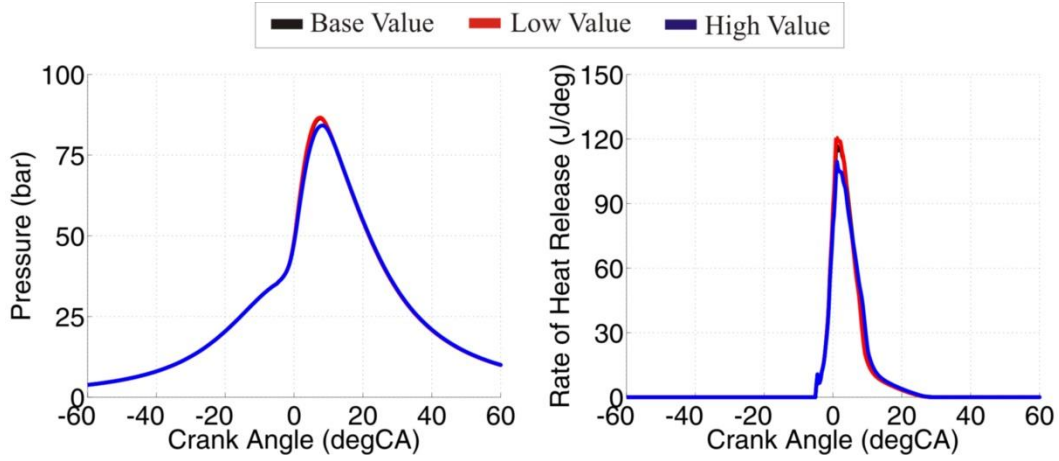
Figure 136 and Figure 137 show the influence of the  $C_{\epsilon, \text{UZ}}$  turbulence model parameter on the in-cylinder pressure and ROHR traces in the case when the flame propagation is modeled with FCM and TCM, respectively.  $C_{\epsilon, \text{UZ}}$  is the in-cylinder turbulence model parameter which is used to adjust the specific unburned zone (UZ) TED production level.



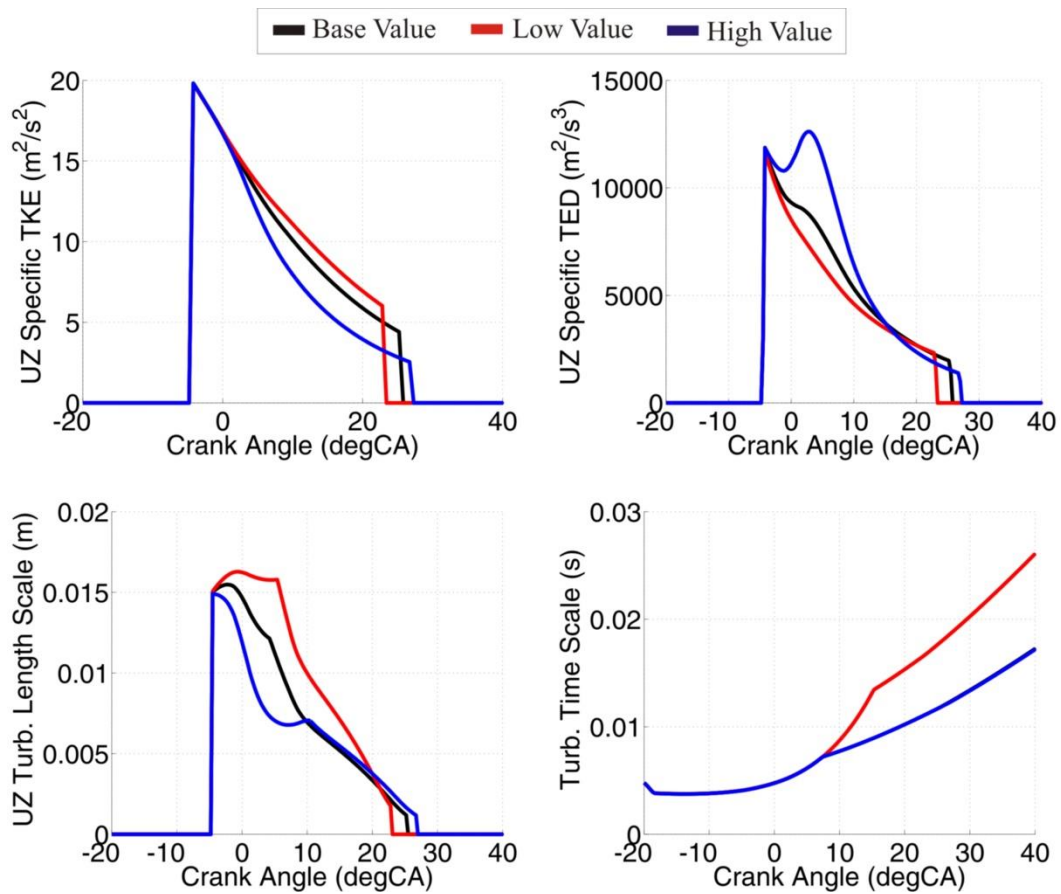
**Figure 136. Influence of the  $C_{\epsilon, \text{UZ}}$  model parameter on the in-cylinder pressure and ROHR traces; FCM flame propagation model**



Figure 138 represents the influence of  $C_{\epsilon, \text{UZ}}$  turbulence model parameter on the in-cylinder turbulence quantities in the case when the flame propagation is modeled with FCM, while in the case when TCM is used the in-cylinder turbulence quantities exhibit similar behavior.



**Figure 137. Influence of the  $C_{\epsilon, \text{UZ}}$  model parameter on the in-cylinder pressure and ROHR traces; TCM flame propagation model**

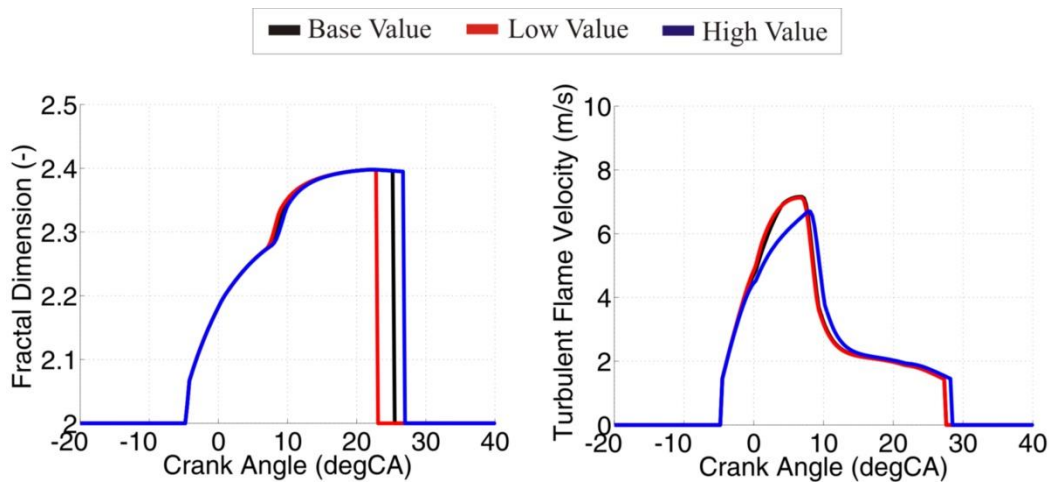


**Figure 138. Influence of the  $C_{\epsilon, \text{UZ}}$  model parameter on the in-cylinder turbulence quantities**

Figure 138 reveals that as the  $C_{\epsilon, \text{UZ}}$  is increased, the specific TKE and the integral length scale decrease, while the specific TED increases. Similarly, to the other in-cylinder turbulence model parameters, as the  $C_{\epsilon, \text{UZ}}$  is increased the turbulent time scale at some stages increases, while at the other it decreases.

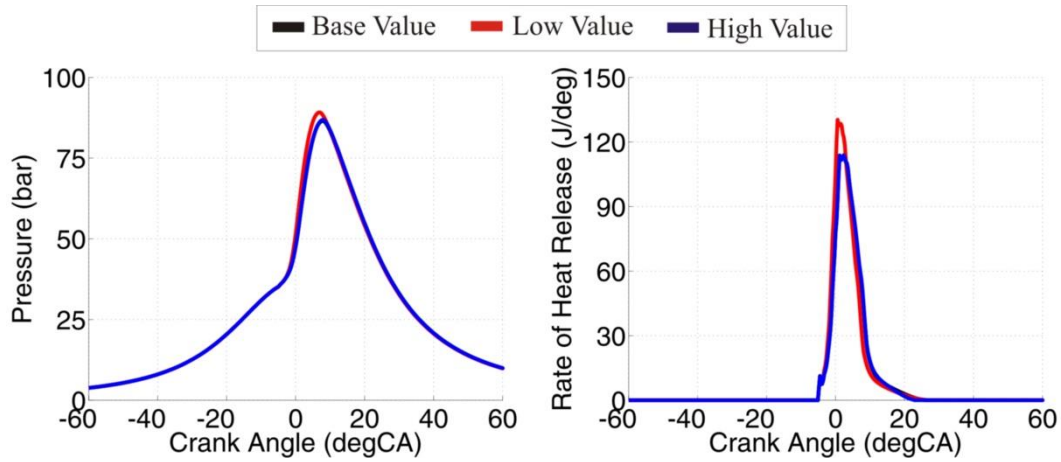
For both flame propagation models (FCM and TCM),  $C_{\epsilon, \text{UZ}}$  does not have a large influence on neither the combustion phasing, or the combustion intensity and its duration. As can be seen in Figure 136 and Figure 137, as  $C_{\epsilon, \text{UZ}}$  is increased from base to high value, the combustion phasing is slightly retarded. Moreover, as it is increased, the combustion intensity is slightly decreased, while the combustion duration is slightly increased. This effect is more pronounced for the TCM case. The reason for such effect can be seen in Figure 139, which presents the influence of  $C_{\epsilon, \text{UZ}}$  model parameter on fractal dimension (the flame propagation is modeled with FCM) and on the turbulent flame velocity (the flame propagation is modeled with TCM).

Figure 139 reveals that the low and base value cases have quite similar fractal dimension (FCM case) and turbulent flame velocity traces (TCM case) and therefore exhibit similar combustion rates. In the FCM case, high value case has slightly retarded fractal dimension trace which leads to slightly decreased combustion rate and longer combustion duration compared to the other two cases (Figure 136). In the TCM case, in addition to retarded turbulent flame velocity trace, high value case has lower peak value of the turbulent flame velocity compared to the other two cases (Figure 138). Therefore, it exhibits lower combustion rate and longer combustion duration compared to low and base value case (Figure 137).



**Figure 139. Influence of the  $C_{\epsilon, \text{UZ}}$  model parameter on fractal dimension (FCM) and on the turbulent flame velocity (TCM)**

Figure 140 and Figure 140 show the influence of the  $C_L$  turbulence model parameter on the in-cylinder pressure and ROHR traces in the case when the flame propagation is modeled with the FCM and TCM, respectively.  $C_L$  is the in-cylinder turbulence model parameter which is used to adjust the level of the turbulent integral length scale.



**Figure 140. Influence of the  $C_L$  model parameter on the in-cylinder pressure and ROHR traces; FCM flame propagation model**

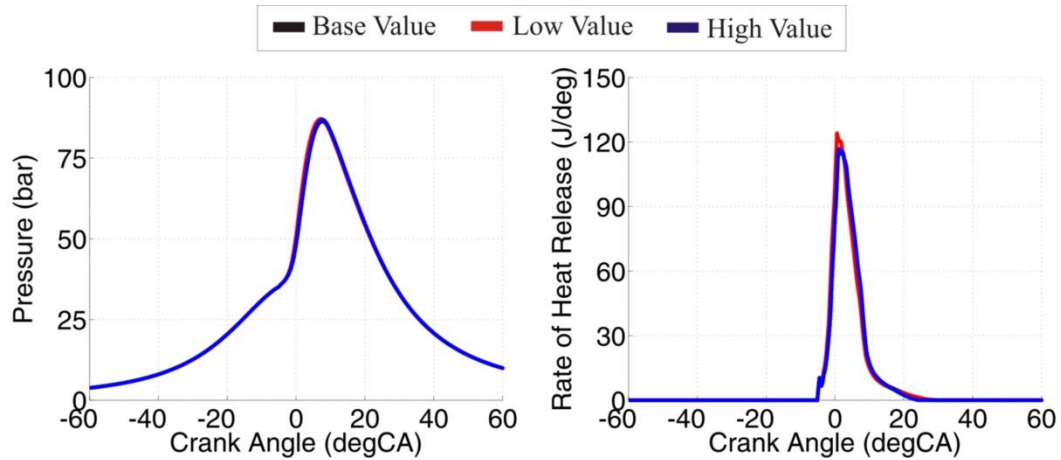


**Figure 141. Influence of the  $C_L$  model parameter on the in-cylinder pressure and ROHR traces; TCM flame propagation model**

Figure 142 represents the influence of  $C_L$  turbulence model parameter on the in-cylinder turbulence quantities in the case when the flame propagation is modeled with FCM, while in the case when TCM is used the in-cylinder turbulence quantities exhibit similar behavior.

Figure 140 and Figure 141 reveal that the  $C_L$  turbulence model parameter has more profound influence on the in-cylinder pressure and ROHR when the flame propagation is modeled with the FCM. Interesting thing to note is that as  $C_L$  is increased from base to high value, there is almost no effect on the combustion intensity. On the other hand, as  $C_L$  is decreased from base

value to low value, the combustion phasing is slightly advanced and the combustion intensity is slightly increased. This effect is more pronounced for the FCM case. Interesting thing to note is that as  $C_L$  parameter is increased, combustion duration is shortened.

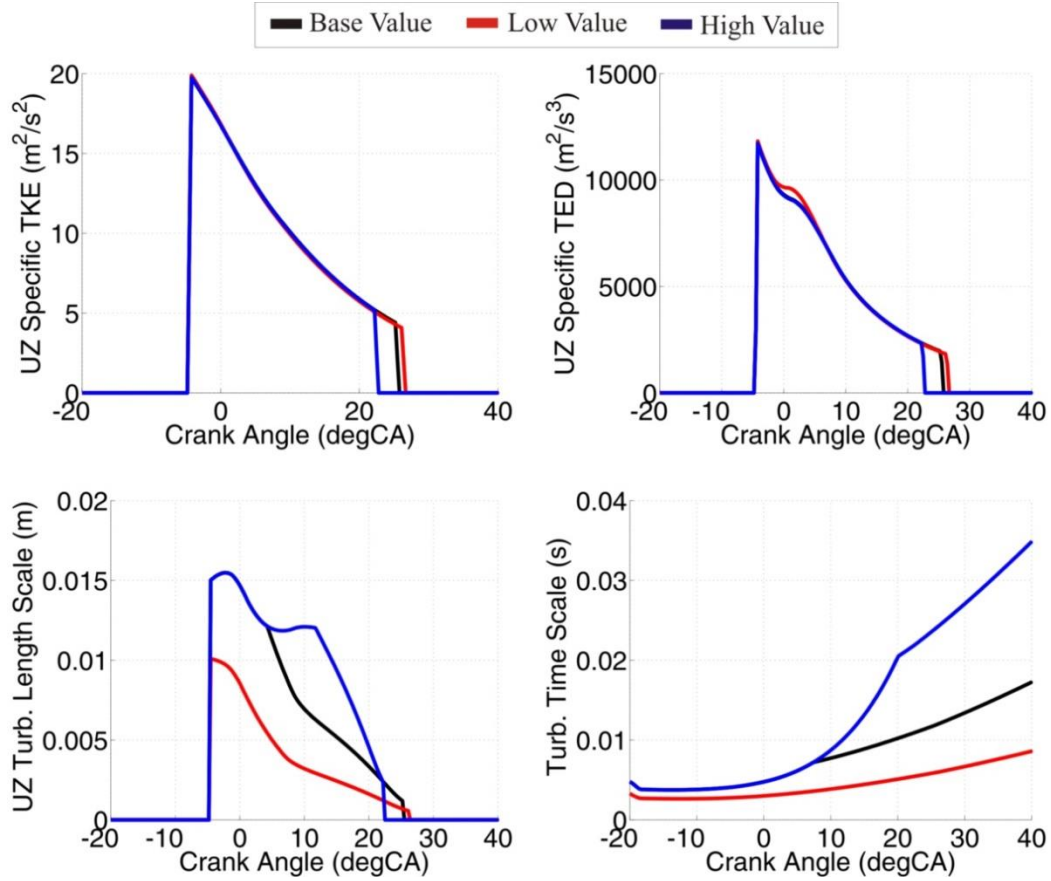


Figure 142. Influence of the  $C_L$  model parameter on the in-cylinder turbulence quantities

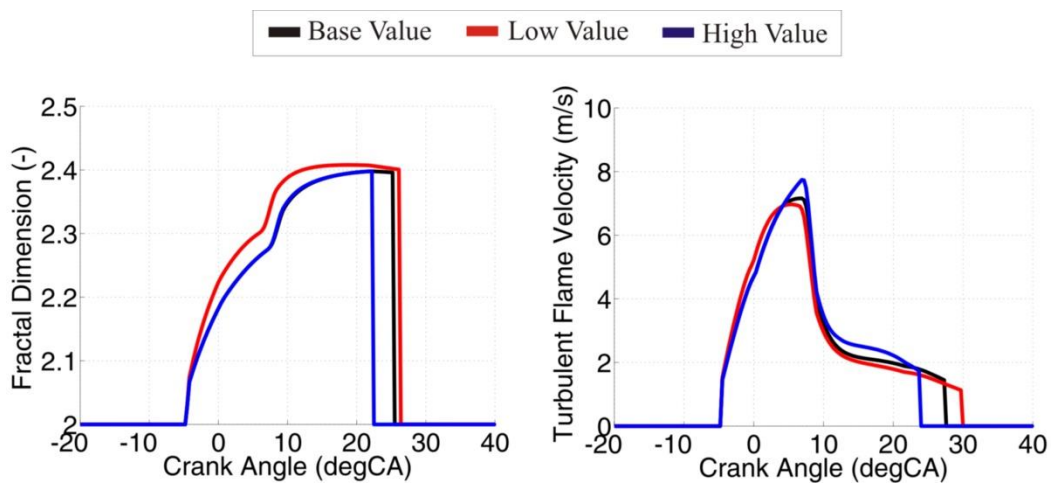


Figure 143. Influence of the  $C_L$  model parameter on fractal dimension (FCM) and on the turbulent flame velocity (TCM)

The reason for these effects can be seen in Figure 142 and Figure 143, which presents the influence of  $C_L$  model parameter on fractal dimension (the flame propagation is modeled with FCM) and on the turbulent flame velocity (the flame propagation is modeled with TCM). Figure 143 reveals that the base and high value cases have quite similar fractal dimension (FCM case) and turbulent flame velocity traces (TCM case) thus resulting in the similar combustion rates. In the TCM case, low value case has slightly advanced turbulent flame velocity trace which leads to slightly increased combustion rate compared to the other two cases (Figure 141). In the FCM case, in addition to advanced fractal dimension trace, low value case has higher peak value of the fractal dimension compared to the other two cases (Figure 143). Therefore, it exhibits higher combustion rate and longer combustion duration compared to base and high value cases (Figure 140).

Such fractal dimension (FCM case) and turbulent flame velocity (TCM case) trend, and hence combustion rate trends are a combined result of the turbulence intensity, integral length scale and turbulence time scale in the start of the flame propagation values. Even though compared to other two cases, low value case has lower integral length scale values, due to lower turbulence time scale in the start of the flame propagation, it exhibits higher combustion rate.

As the  $C_L$  parameter is decreased the combustion duration is prolonged due to the integral length scale effect. In the final stage of flame propagation (wall-combustion), lower integral length scales (Figure 142) lower the combustion rate thus leading to the longer combustion duration (Figure 140 and Figure 141).

From all reviewed cases ( $S_{in}$ ,  $C_{in}$ ,  $S_{inj}$ ,  $C_{inj}$ ,  $C_e$ ,  $C_{e,UZ}$ ,  $C_L$ ), it is evident that the in-cylinder turbulence model parameters have a profound influence on the turbulence quantities, which is expected. Also, since the flame propagation is coupled with the in-cylinder turbulence these parameters have a profound effect on the part of the combustion process which is governed by the flame propagation through the premixed mixture.

Since the start of the combustion and the start of flame propagation are not directly linked to the in-cylinder turbulence, the changes in its modeling parameters has no effect on neither the start of the combustion nor start of the flame propagation.

Figure 144 presents the tornado plot which clearly shows the influence of a given in-cylinder turbulence model parameter on the simulated combustion process (CA10, CA50 and CA90).

In the tornado plot, given in Figure 144, the effect of a decrease of the respective in-cylinder turbulence model parameter is marked with the red color, while the effect of an increase of the respective in-cylinder turbulence model parameter is marked with the green color. For all turbulence model parameters, the low value is 2x lower than the base value, while the high

value is 2x higher than the base value. In both cases (FCM and TCM) the intake parameters have the largest and straight forward influence on the modeled flame propagation process. An interesting thing to note is that the injection parameters have a negligible influence on the combustion profile. Also, an interesting thing to note is the large influence of the  $C_\epsilon$  model parameter on the CA50 and CA90; especially its increase which causes a considerable increase in the CA50 and CA90.

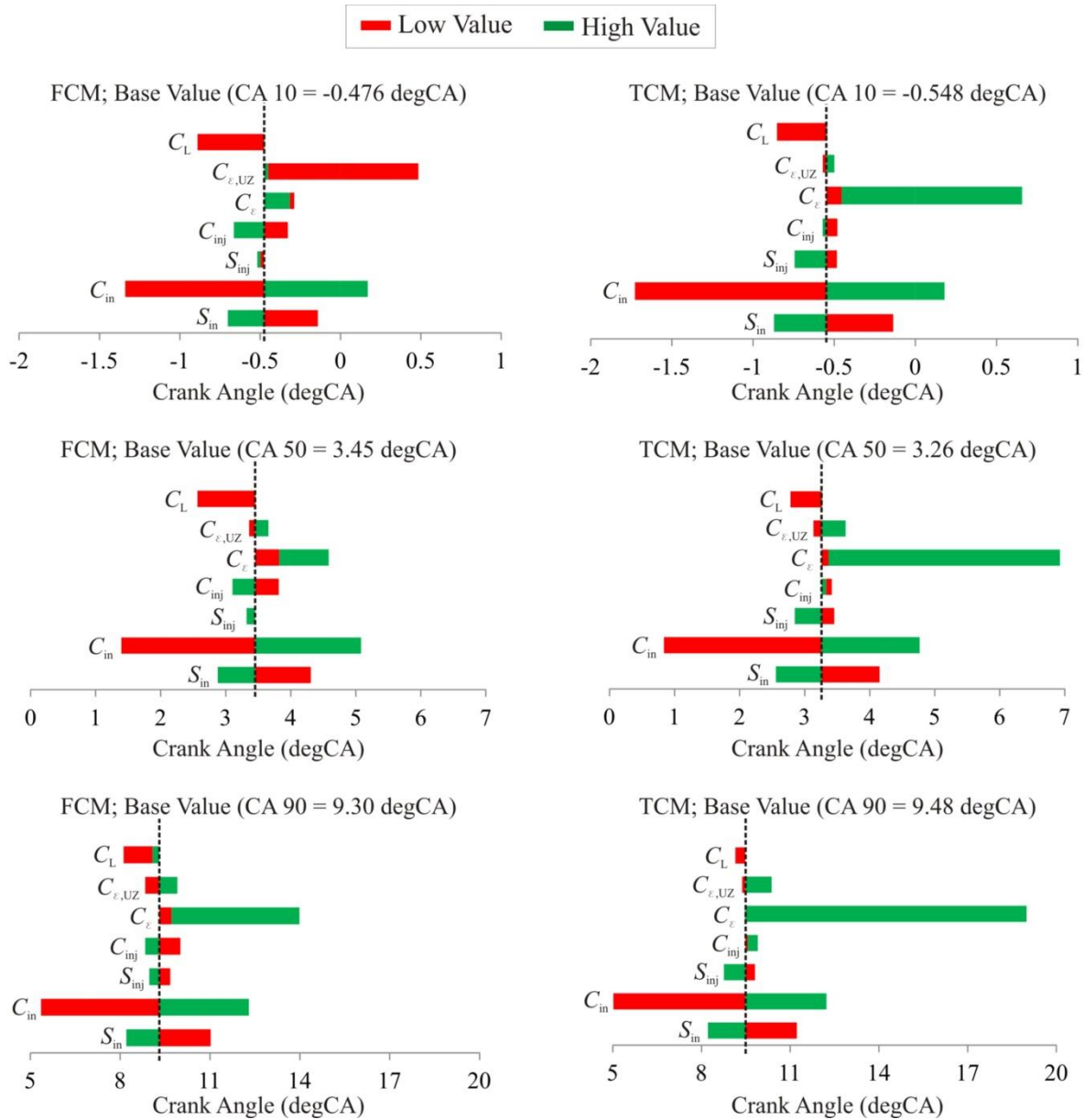


**Figure 144. Influence of the turbulence model parameters on the CA10, CA50 and CA90 for both flame propagation models**

The general conclusion on the overall influence of the in-cylinder turbulence model parameters on the DFMZCM is that these parameters have a profound influence on the in-

cylinder turbulence quantities. Therefore, since the in-cylinder turbulence and flame propagation process are coupled, these parameters have a profound influence on the flame propagation calculation.

Generally, the in-cylinder turbulence parameters are used to adjust the calculated turbulence levels (TKE, TED, integral length scale and turbulence time scale) with the ones obtained from the 3-D CFD simulation. This adjustment is performed in the following way (through the following model parameters):

1. Turbulence intake parameters ( $S_{in}$  and  $C_{in}$ ) are used to adjust the effect of intake on the in-cylinder turbulence level. As  $S_{in}$  is increased, turbulence intensity inside the cylinder increases, while as  $C_{in}$  is increased, turbulence intensity inside the cylinder decreases.
2. Turbulence injection parameters ( $S_{inj}$  and  $C_{inj}$ ) are used to adjust the effect of injection on the in-cylinder turbulence level. As  $S_{inj}$  is increased, turbulence intensity inside the cylinder increases, while as  $C_{inj}$  is increased, turbulence intensity inside the cylinder decreases.
3. Turbulence dissipation parameters ( $C_\epsilon$  and  $C_{\epsilon,UZ}$ ) are used to adjust the effect of TED production rate on the in-cylinder turbulence level.  $C_\epsilon$  influences the level of total turbulence intensity; as  $C_\epsilon$  is increased, the total turbulence intensity inside the cylinder decreases.  $C_{\epsilon,UZ}$  influences the level of turbulence intensity inside the unburned zone; as  $C_{\epsilon,UZ}$  is increased, the unburned zone turbulence intensity decreases.
4. Integral length scale parameter ( $C_L$ ) is used to adjust the average integral length scale size and average integral time scale value inside the cylinder. As  $C_L$  is increased, both the average integral length scale size and average integral time scale value increase.

The in-cylinder turbulence model parameters can also be used to slightly tune the flame propagation calculation; i.e. increase or decrease the combustion rate through tuning the intake ( $S_{in}$  and  $C_{in}$ ) or TED production ( $C_\epsilon$ ) model parameters that have a profound effect on the combustion intensity. Also, the in-cylinder turbulence model parameters can be used to fine tune the flame propagation duration; i.e. through the adjustment of the integral length scale parameter ( $C_L$ ).



## ***Sensitivity of the spray combustion model parameters***

**Table 18. List of the varied spray model parameters**

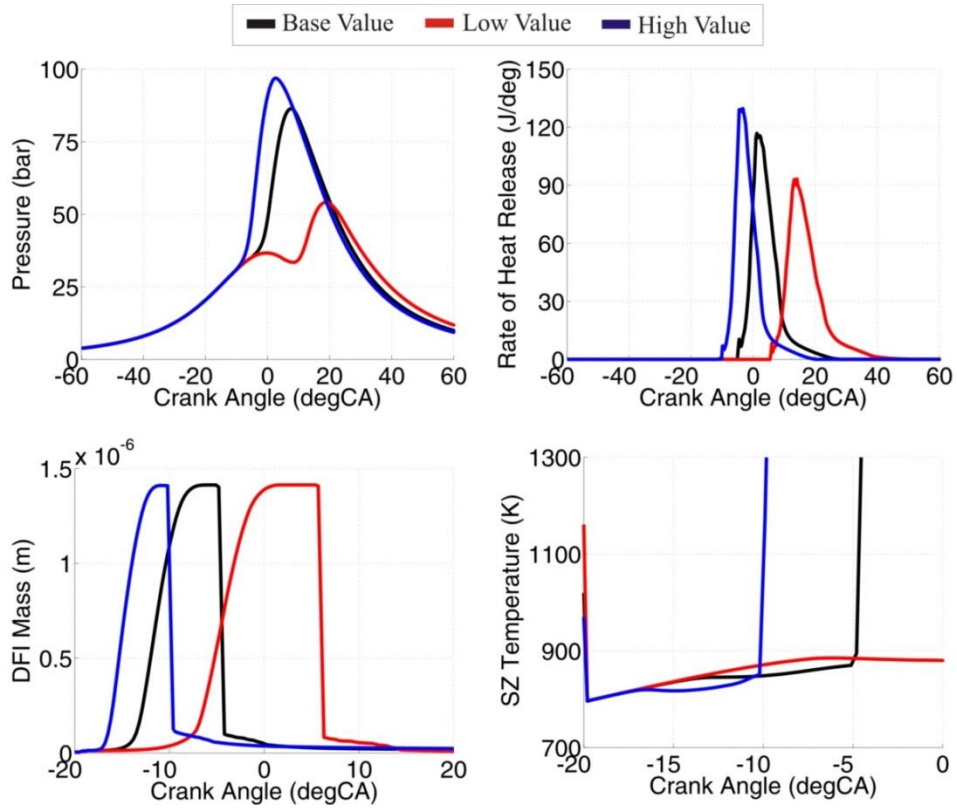
Parameter	Base Value	Low Value	High Value
$C_{\text{evap,HT}} (-)$	1.1	0.55	2.2
$C_{\text{evap}} (-)$	1	0.5	2
$C_{\text{centrain}} (-)$	0.5	0.25	1
$C_{\text{ignition}} (-)$	1	0.5	2
$C_{\text{discr,ax}} (-)$	0.6	0.3	1.2
$C_{\text{discr,rad}} (-)$	6	3	12
$C_{\text{ZHT,SZ}} (-)$	1	0.5	2

The list of varied spray combustion model parameters and their respective values are given in Table 18. The sensitivity to the spray combustion model parameters is performed for TCM flame propagation model and the main conclusions are obtained by analyzing the results of in-cylinder pressure and rate of heat release. As can be seen in Table 18, for all spray combustion model parameters the low value is 2x lower than the base value, while the high value is 2x larger than the base value. A tornado plot which clearly shows the influence of a given spray combustion model parameter on the simulated combustion process (ignition delay, CA10, CA50 and CA90) is given at the end of this chapter.

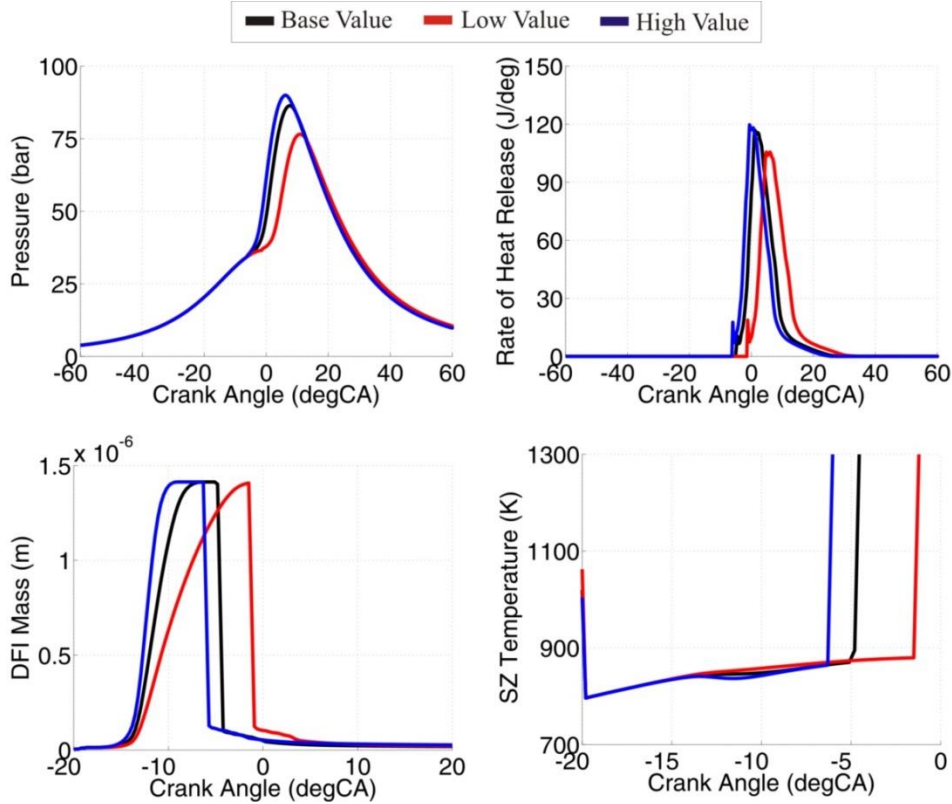
Figure 145 presents the influence of the  $C_{\text{evap,HT}}$  spray combustion model parameter on the in-cylinder pressure and ROHR traces, as well as on the DFI mass (the mass of the available Diesel fuel in the spray region) and SZ temperature (mean temperature in the spray region).  $C_{\text{evap,HT}}$  is a spray combustion model parameter that controls the amount of heat that is supplied to the liquid fuel droplet for its evaporation.

Figure 145 reveals that  $C_{\text{evap,HT}}$  parameter has a profound influence on governing of the combustion process. It can be seen that as  $C_{\text{evap,HT}}$  parameter is increased, the ignition delay time decreases and hence the combustion phasing is advanced, combustion intensity is increased, while the combustion duration is shortened. The reasons for such phenomena can clearly be seen from the Figure 145 – bottom two figures. As  $C_{\text{evap,HT}}$  parameter is increased, the amount of heat supplied to the liquid fuel droplet significantly increases, which lead to a temperature drop in the spray region (evaporation cooling effect). However, more significantly as  $C_{\text{evap,HT}}$  parameter is increased, the evaporation rate increases significantly (Figure 145 – bottom left), and hence the mass of the Diesel fuel vapor increases as well. Although temperature decreases slightly, the increase of the Diesel fuel vapor mass advances the ignition and hence advances the entire combustion phasing (Figure 145 – top right).





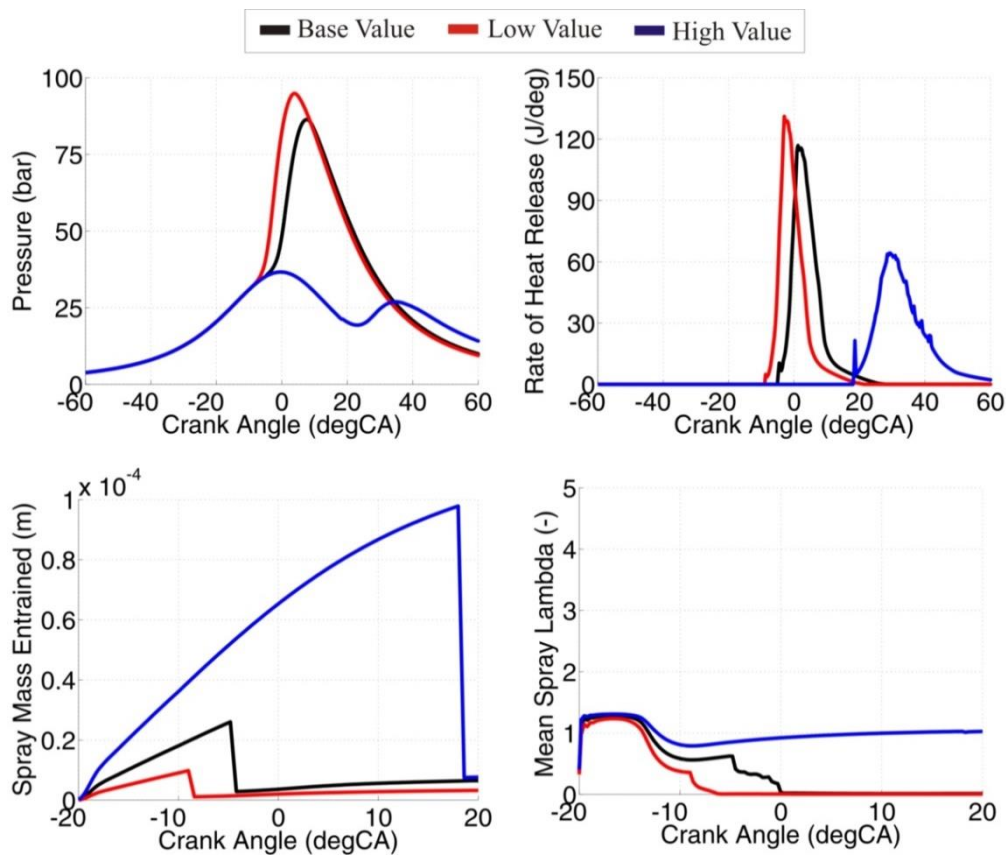
**Figure 145. Influence of the  $C_{evap,HT}$  model parameter on the in-cylinder pressure and ROHR traces, as well as on the DFI mass and SZ temperature traces**



**Figure 146. Influence of the  $C_{evap}$  model parameter on the in-cylinder pressure and ROHR traces, as well as on the DFI mass and SZ temperature traces**

Figure 146 presents the influence of the  $C_{\text{evap}}$  spray combustion model parameter on the in-cylinder pressure and ROHR traces, as well as on the DFI mass (the mass of the available Diesel fuel in the spray region) and SZ temperature (mean temperature in the spray region).  $C_{\text{evap}}$  is a model parameter that controls the Diesel fuel evaporation rate.

Figure 146 reveals that the  $C_{\text{evap}}$  spray combustion model parameter has a profound influence on governing of the combustion process. It can be seen that as the  $C_{\text{evap}}$  parameter is increased, the ignition delay decreases and hence the combustion phasing is advanced, combustion intensity is increased, while the combustion duration is shortened. The reasons for such phenomena can clearly be seen from the Figure 146 – bottom two figures. As the  $C_{\text{evap}}$  parameter is increased, the evaporation rate increases, while the SZ temperature decreases slightly (cooler Diesel fuel vapor enters the spray gas zones). Even though the temperature decreases, the significant increase in the evaporation rate (Figure 146 – bottom left) leads to advanced ignition that advances the entire combustion phasing (Figure 146–top right).



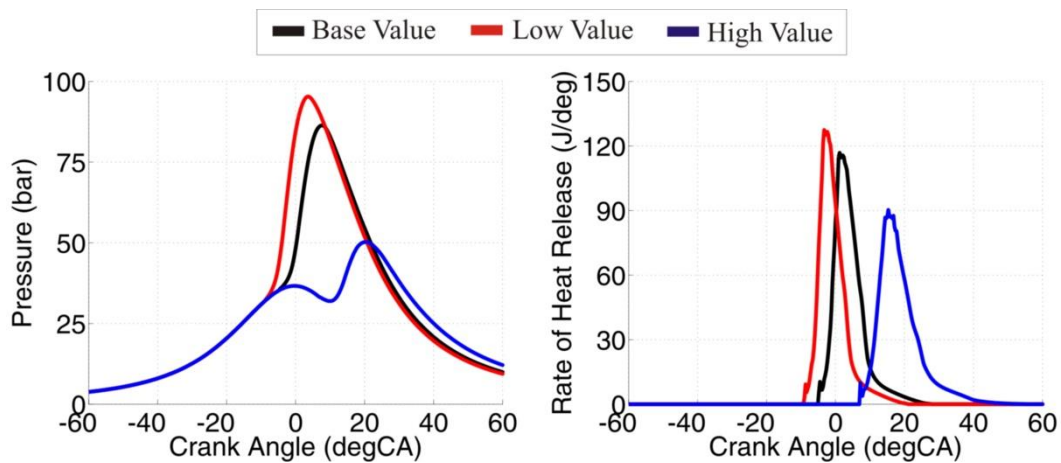
**Figure 147. Influence of the  $C_{\text{entrain}}$  model parameter on the in-cylinder pressure and ROHR traces, as well as on the mass entrained into the spray region and on the excess air ratio inside the spray region**

Figure 147 presents the influence of  $C_{\text{entrain}}$  spray combustion model parameter on the in-cylinder pressure and ROHR traces, as well as on the mass entrained into the spray region and

on the excess air ratio inside the spray region.  $C_{\text{entrain}}$  is a model parameter that controls the amount of mass from the unburned zone that is entrained into the spray region.

Figure 147 reveals that  $C_{\text{entrain}}$  spray combustion model parameter has a profound influence on governing of the combustion process. It can be seen that as  $C_{\text{entrain}}$  parameter is decreased, the ignition delay decreases and hence the combustion phasing is advanced, combustion intensity is increased, while the combustion duration is shortened. The reasons for such phenomena can clearly be seen from Figure 147 – bottom two figures. As  $C_{\text{entrain}}$  parameter is decreased, the mass entrainment rate decreases which lead to an increase in the Diesel fuel to methane ratio and a decrease in the excess air ratio inside the spray region. These two effects lead to advanced ignition that advances the entire combustion phasing (Figure 147–top right).

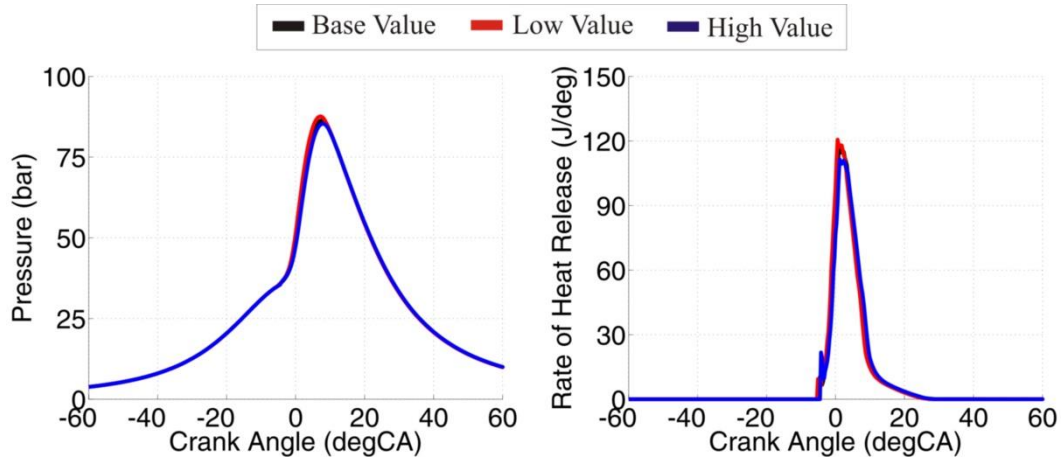
Figure 148 presents the influence of  $C_{\text{ignition}}$  spray combustion model parameter on the in-cylinder pressure and ROHR traces.  $C_{\text{ignition}}$  is a model parameter that controls the ignition delay time value. The ignition delay time is taken from the look-up tables and then it can be additionally modified through the  $C_{\text{ignition}}$  parameter.



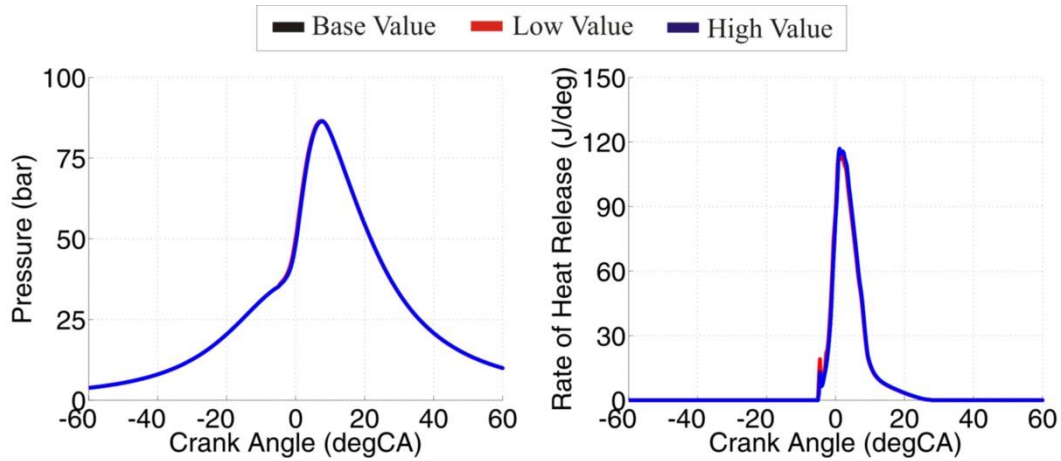
**Figure 148. Influence of the  $C_{\text{ignition}}$  model parameter on the in-cylinder pressure and ROHR traces**

Figure 148 reveals that the  $C_{\text{ignition}}$  spray combustion model parameter has a profound influence on governing of the combustion process. It can be seen that as  $C_{\text{ignition}}$  parameter is decreased, the ignition delay decreases and hence the combustion phasing is advanced, combustion intensity is increased, while the combustion duration is shortened.

Figure 149 presents the influence of the  $C_{\text{discr,ax}}$  spray combustion model parameter on the in-cylinder pressure and ROHR traces, while Figure 150 presents the influence of the  $C_{\text{discr,rad}}$  spray combustion model parameter on the in-cylinder pressure and ROHR traces.  $C_{\text{discr,ax}}$  is a model parameter that controls the spray discretization in the axial direction, while  $C_{\text{discr,rad}}$  is a model parameter that controls the spray discretization in the radial direction.



**Figure 149.** Influence of the  $C_{discr,ax}$  model parameter on the in-cylinder pressure and ROHR traces



**Figure 150.** Influence of the  $C_{discr,rad}$  model parameter on the in-cylinder pressure and ROHR traces

As can be seen from Figure 149 and Figure 150, both of these parameters have a negligible effect on the ignition delay as well as on the entire combustion profile. However, it can be noticed that as  $C_{discr,ax}$  parameter is increased, the ignition delay is slightly shortened and hence the combustion phasing advances, combustion intensity increases, while the combustion duration shortens. On the other hand,  $C_{discr,rad}$  parameter has absolutely no influence on the ignition delay. However, as it is decreased, the initial spray combustion increases, which advances the combustion phasing and shortens the combustion duration, but decreases the overall ROHR peak.

Figure 151 presents the influence of  $C_{ZHT,SZ}$  spray combustion model parameter on the in-cylinder pressure and ROHR traces, as well as on the spray ROHR and on the standard deviation of the temperature inside the spray region.  $C_{ZHT,SZ}$  is a model parameter that controls the heat transfer time (calculated from the turbulence time scale) and thus affects the heat transfer between the spray zones.

As can be seen from Figure 151 – top right,  $C_{ZHT,SZ}$  parameter has absolutely no influence on the ignition delay time, while it has only a minor influence on the entire combustion profile. However, as  $C_{ZHT,SZ}$  parameter is decreased, the standard deviation of the temperature inside the spray region decreases., which means that  $C_{ZHT,SZ}$  parameter has an influence on the temperature stratification inside the spray region. Through the influence on the temperature stratification,  $C_{ZHT,SZ}$  parameter has an effect on the combustion in the spray region (Figure 151 – bottom left).

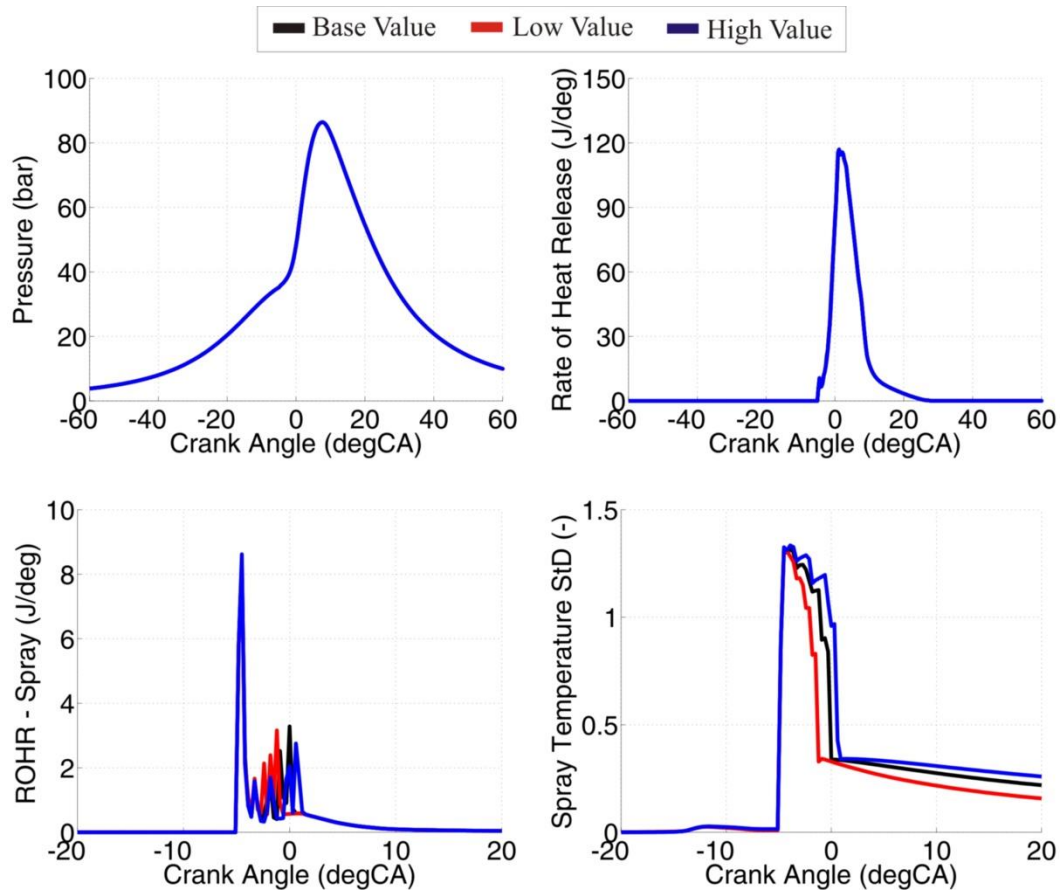


**Figure 151. Influence of the  $C_{ZHT,SZ}$  model parameter on the in-cylinder pressure and ROHR traces, as well as on the spray ROHR and SZ temperature standard deviation traces**

From all reviewed cases ( $C_{evap,HT}$ ,  $C_{evap}$ ,  $C_{entrain}$ ,  $C_{ignition}$ ,  $C_{discr,ax}$ ,  $C_{discr,rad}$ ,  $C_{ZHT,SZ}$ ), it is evident that the majority ( $C_{evap,HT}$ ,  $C_{evap}$ ,  $C_{entrain}$ ,  $C_{ignition}$ ) of the spray combustion model parameters have a profound effect on the ignition delay and hence a profound effect on the entire combustion profile; its phasing, intensity and duration.

Figure 152 presents the tornado plot which clearly shows the influence of a given spray combustion model parameter on the simulated combustion process (ignition delay, CA10, CA50 and CA90). In the tornado plot, which is given below (Figure 152), the effect of a



decrease of the respective spray combustion model parameter is marked with the red color, while the effect of an increase of the respective spray combustion model parameter is marked with the green color. For all spray combustion model parameters the low value is 2x lower than the base value, while the high value is 2x higher than the base value.

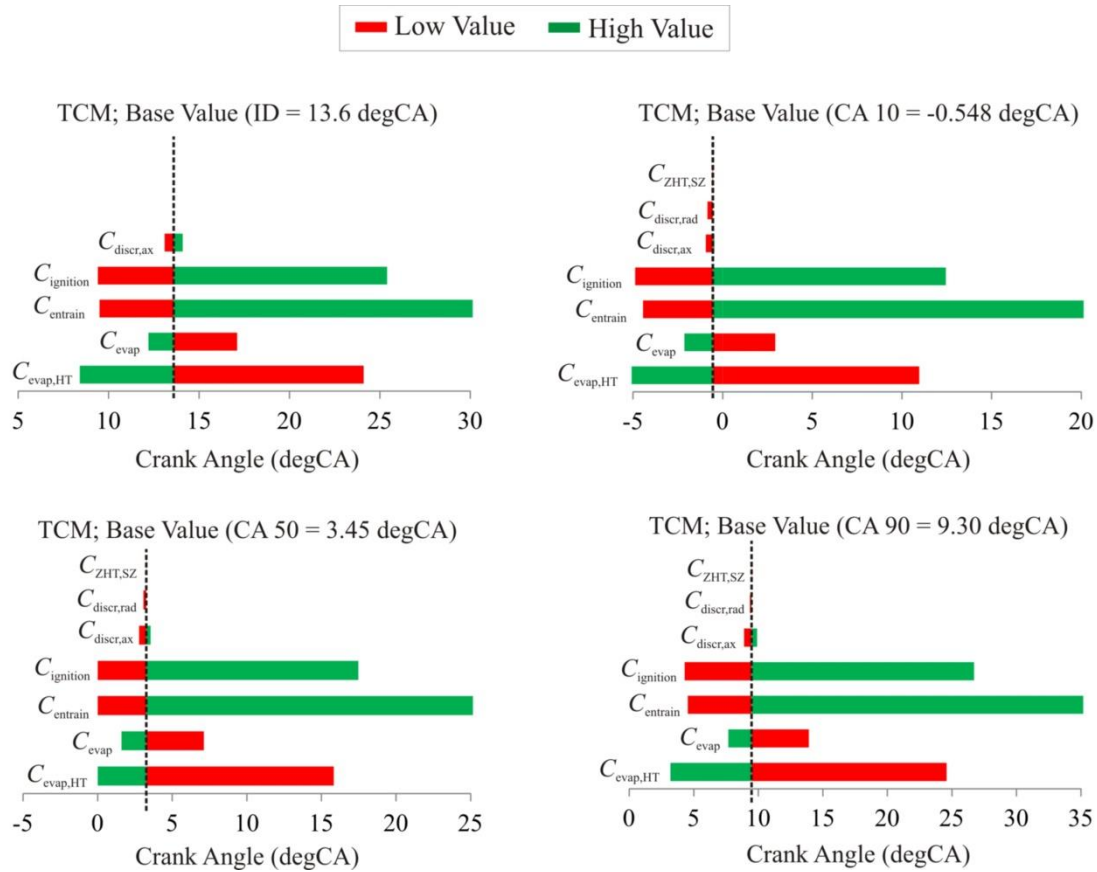


**Figure 152. Influence of the spray model parameters on the ignition delay, CA10, CA50 and CA90**

Figure 152 reveals that the entrainment ( $C_{entrain}$ ) and the ignition delay time parameter ( $C_{ignition}$ ) have the largest influence on the start of combustion and its phasing. As these parameters are decreased, the start of combustion and its phasing are advanced and vice versa. Also, it can be seen that the evaporation parameters ( $C_{evap,HT}$  and  $C_{evap}$ ) have a profound effect on the start of combustion and its phasing. As these parameters are increased, the start of combustion and its phasing are advanced and vice versa. All other spray combustion model parameters ( $C_{discr,ax}$ ,  $C_{discr,rad}$  and  $C_{ZHT,SZ}$ ) have a negligible effect on the start of combustion and its phasing.

The general conclusion on the overall influence of the spray combustion model parameters on the DFMZCM is that these parameters have a profound influence on the processes inside the spray, thus influencing the ignition moment as well as the initial combustion phase. Through

their influence on the initial combustion phase these parameters have a profound influence on the entire combustion process (combustion phasing, intensity and duration).

Generally, the spray combustion model parameters are used to adjust the calculated spray process (spray formation and evolution, and spray combustion), and combustion timing with the one obtained from the experiment. This adjustment is performed in the following way (through the following model parameters):

1. Evaporation parameters ( $C_{\text{evap,HT}}$ , and  $C_{\text{evap}}$ ) are used to adjust the evaporation process and thus control the air/fuel ratio and temperature inside the spray region. As these parameters are increased, the evaporation rate increases thus increasing the Diesel fuel mass that is prepared for ignition and/or combustion. The increase of these parameters leads to earlier ignition and therefore advanced combustion phasing.
2. Entrainment parameter ( $C_{\text{entrain}}$ ) is used to adjust the entrainment process (fresh charge mass that is entrained in the spray region) and thus controls the air/fuel ratio and temperature inside the spray region. As this parameter is increased, the entrainment rate increases thus increasing the mass of the fresh charge in the spray region. The increase of this parameter leads to later ignition and therefore retarded combustion phasing.
3. Ignition parameter ( $C_{\text{ignition}}$ ) is used to adjust ignition delay time and thus controls pre-ignition reactivity inside the spray region. As this parameter is increased, the pre-ignition reactivity is decreased thus leading to later ignition and retarded combustion phasing.
4. Discretization parameters ( $C_{\text{discr,ax}}$  and  $C_{\text{discr,rad}}$ ) are used to adjust the spray zone number and thus control the mixture and temperature stratification inside the spray region. As these parameters are increased, the number of spray zones increases. These parameters have a minor effect on the ignition delay and combustion phasing.
5. Zone heat transfer parameter ( $C_{\text{ZHT,SZ}}$ ) is used to adjust the zone heat transfer rate and thus controls the temperature stratification inside the spray region. As this parameter is decreased, the zone heat transfer rate increases thus homogenizing the temperature field inside the spray region. This parameter has a minor effect on the ignition delay and combustion phasing, however it can be used to slightly tune the spray combustion intensity.

### ***Sensitivity of the flame propagation model parameters***

In the DFMZCM two different flame propagation models were used to model the part of the combustion process that is governed by the flame propagation through the premixed mixture:

1. The modified Fractal Combustion Model (FCM)
2. The newly developed Turbulent Flame Speed Combustion Model (TCM)

Therefore, in this chapter the sensitivity of both of these models to their respective model parameters is presented.

**Table 19. List of the varied FCM parameters**

Parameter	Base Value	Low Value	High Value
$C_{ign,UZ,transf}$ (-)	0.475	0.2375	0.95
$C_{trans}$ (-)	2.2	1.1	4.4
$C_{SOWC}$ (-)	0.4	0.2	0.8
$C_{WC,shp}$ (-)	2	1	4
$C_{comb}$ (-)	2.44	2.05	3
$C_{EOF}$ (-)	0.5	0.25	1

**Table 20. List of the varied TCM parameters**

Parameter	Base Value	Low Value	High Value
$C_{trans}$ (-)	4.5	2.25	9
$C_{ign,UZ,transf}$ (-)	0.475	0.2375	0.95
$C_{SOWC}$ (-)	0.4	0.2	0.8
$C_{WC,shp}$ (-)	3	1.5	4
$C_{comb}$ (-)	1	0.5	2
$C_{EOF}$ (-)	0.5	0.25	1

The list of varied FCM parameters and their respective values are given in Table 19, while the list of varied TCM parameters and their respective values are given in Table 20. As can be seen in the tables given above (Table 19 and Table 20), for all FCM and TCM parameters the low value is 2x lower than the base value, while the high value is 2x larger than the base value.

Figure 153 represents the influence of  $C_{trans}$  flame propagation model parameter on the in-cylinder pressure and ROHR traces in the case when the flame propagation is modeled with the FCM, while Figure 154 represents the influence of the same flame propagation model parameter but now for the case when the flame propagation is modeled with the TCM.  $C_{trans}$  is



a model parameter that controls the transition time from the laminar to fully developed turbulent flame.

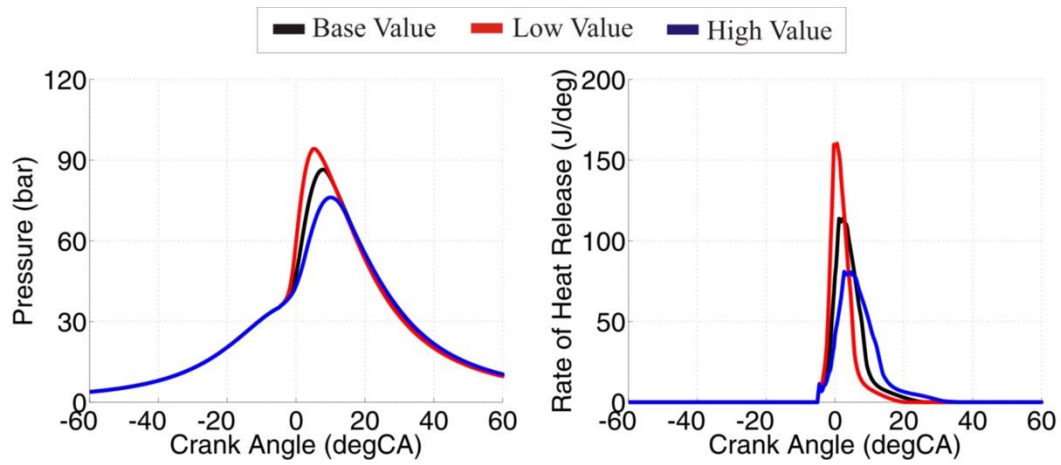


**Figure 153. Influence of the  $C_{trans}$  model parameter on the in-cylinder pressure and ROHR traces; FCM flame propagation model**

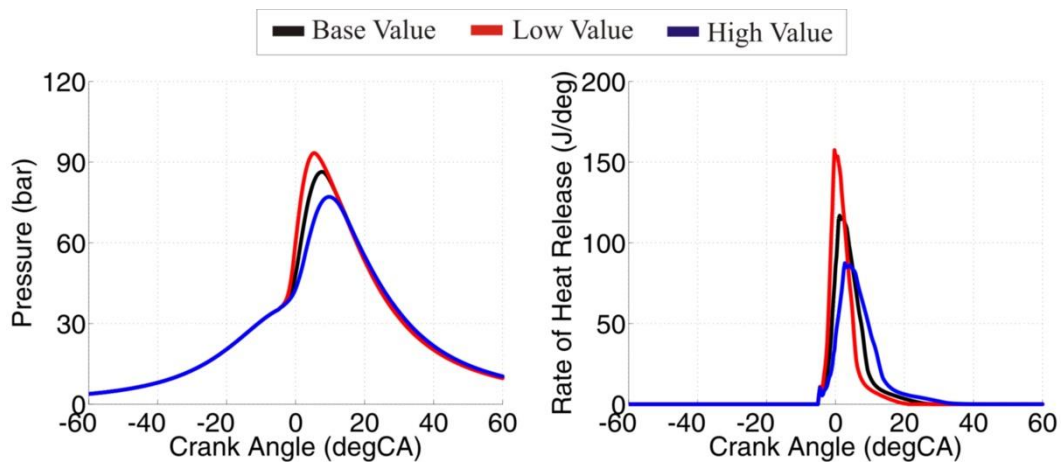
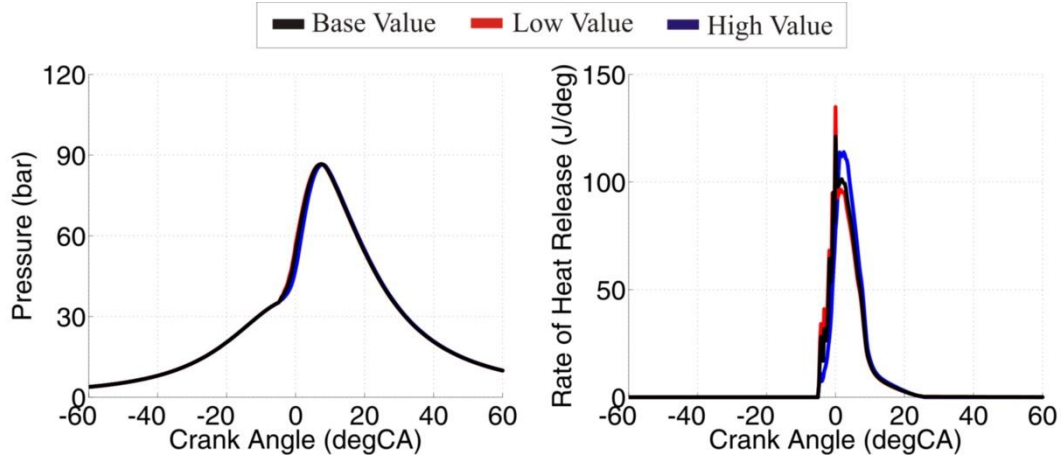


**Figure 154. Influence of the  $C_{trans}$  model parameter on the in-cylinder pressure and ROHR traces; TCM flame propagation model**

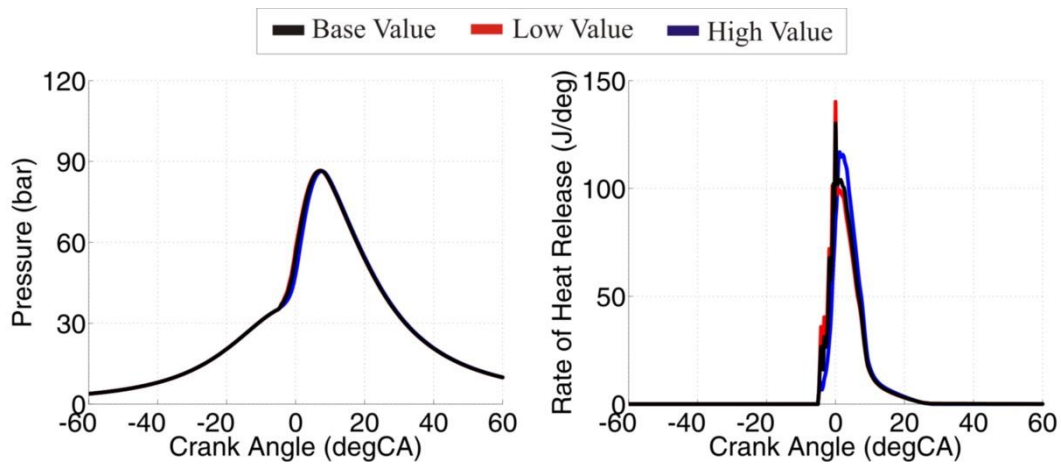
Figure 153 and Figure 154 reveal that the  $C_{trans}$  flame propagation model parameter has a profound influence governing of the combustion process in both the FCM and TCM case. It can be seen that as the  $C_{trans}$  parameter is increased, the combustion phasing is advanced; combustion intensity is increased, while the combustion duration is shortened. The reason for such phenomena is the faster shift from the laminar to fully developed turbulent flame as the  $C_{trans}$  parameter is increased.

Figure 155 represents the influence of the  $C_{ign,UZ,transf}$  flame propagation model parameter on the in-cylinder pressure and ROHR traces in the case when the flame propagation is modeled with the FCM, while Figure 156 represents the influence of the same flame propagation

model parameter but now for the case when the flame propagation is modeled with the TCM.  $C_{ign,UZ,transf}$  is a model parameter that controls the amount of the unburned spray mass that is transferred to the unburned zone in the start of the flame propagation moment.



**Figure 155. Influence of the  $C_{ign,UZ,transf}$  model parameter on the in-cylinder pressure and ROHR traces; FCM flame propagation model**



**Figure 156. Influence of the  $C_{ign,UZ,transf}$  model parameter on the in-cylinder pressure and ROHR traces; TCM flame propagation model**

As in the original base value case the model parameter  $C_{ign,UZ,transf} = 0.95$ , and the maximum allowed (physically)  $C_{ign,UZ,transf} = 1$ , in this sensitivity analysis, the base value case parameter  $C_{ign,UZ,transf} = 0.475$ , while the “original” base value case parameter is set as the high value case parameter.

Figure 155 and Figure 156 reveal that  $C_{ign,UZ,transf}$  flame propagation model parameter has an influence on governing of the combustion process in both the FCM and TCM case. This parameter changes the ratio of the spray combustion to the combustion that is controlled by the flame propagation through the premixed mixture. As  $C_{ign,UZ,transf}$  parameter is decreased,

the premixed spray combustion stage increases and hence the ROHR peak associated with this stage increases. Therefore, the second ROHR peak (ROHR peak due to the flame propagation process) decreases as the  $C_{ign,UZ,transf}$  parameter is decreased. Table 21 presents the influence of  $C_{ign,UZ,transf}$  parameter on the main combustion process (CA 10, CA50, and CA90). The data given in Table 21 reveal that as the  $C_{ign,UZ,transf}$  parameter is decreased, the entire combustion phase is advanced.

**Table 21. Influence of  $C_{ign,UZ,transf}$  model parameter on the main combustion parameters**

Model Parameter	CA10 (degCA)	CA50 (degCA)	CA90 (degCA)
FCM – LOW	-1.834	2.04	8.88
FCM – BASE	-1.519	2.28	8.81
FCM – HIGH	-0.476	3.45	9.48
TCM – LOW	-1.84	2.35	9.27
TCM – BASE	-1.54	2.57	9.26
TCM – HIGH	-0.548	3.26	9.30

Figure 157 represents the influence of the  $C_{sowc}$  flame propagation model parameter on the in-cylinder pressure and ROHR traces in the case when the flame propagation is modeled with the FCM, while Figure 158 represents the influence of the same flame propagation model parameter but now for the case when the flame propagation is modeled with the TCM.

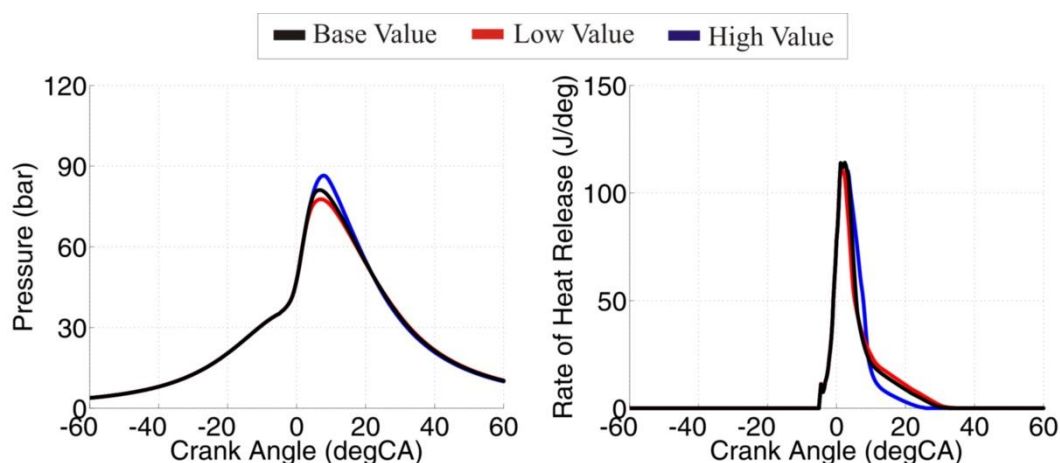


**Figure 157. Influence of the  $C_{sowc}$  model parameter on the in-cylinder pressure and ROHR traces; FCM flame propagation model**

$C_{sowc}$  is a model parameter that defines the mass fraction burned at which the wall flame propagation mode starts. Same as in the previous sensitivity analysis, since in the original base value case the model parameter  $C_{sowc} = 0.8$ , and the maximum allowed (physically)  $C_{sowc} = 1$ , in this sensitivity analysis the base value case parameter  $C_{sowc} = 0.4$ , while the

“original” base value case parameter is set as the high value case parameter. Figure 157 and Figure 158 reveal that  $C_{sowc}$  flame propagation model parameter has an influence on governing of the combustion process in both the FCM and TCM case. As  $C_{sowc}$  parameter is decreased, the start of the wall combustion stage is advanced which causes a faster decrease of the ROHR traces from its peak value and increases the final tail-like combustion stage.

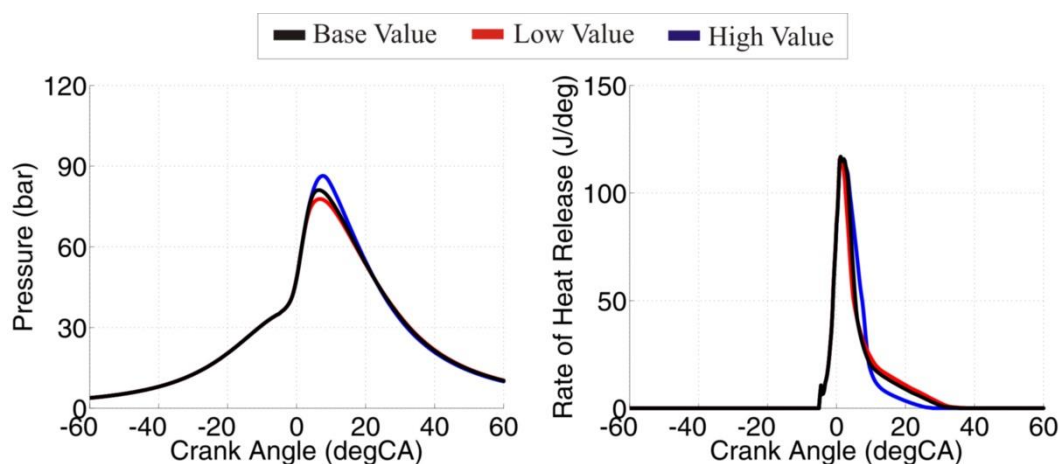


**Figure 158. Influence of the  $C_{sowc}$  model parameter on the in-cylinder pressure and ROHR traces; TCM flame propagation model**

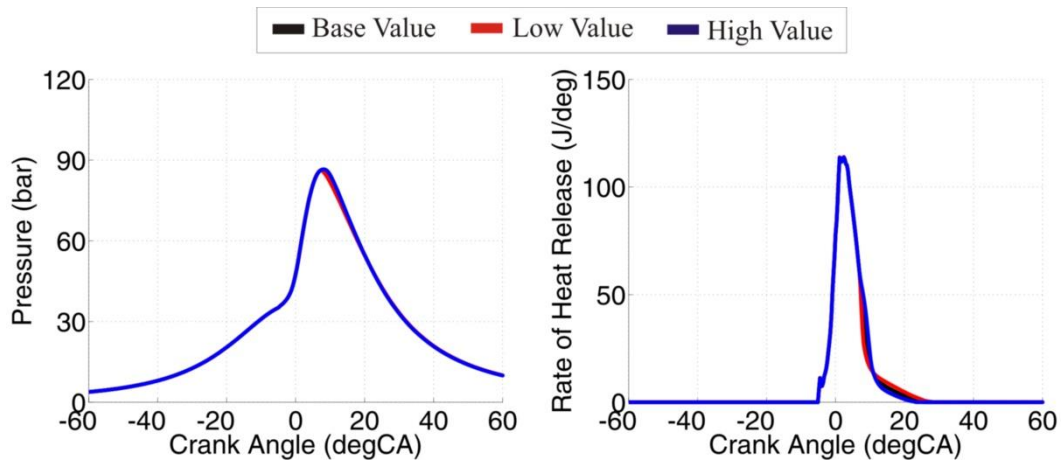
**Table 22. Influence of  $C_{sowc}$  model parameter on the main combustion parameters**

Model Parameter	CA10 (degCA)	CA50 (degCA)	CA90 (degCA)
FCM – LOW	-0.479	3.64	17.05
FCM – BASE	-0.48	3.45	15.07
FCM – HIGH	-0.476	3.45	9.48
TCM – LOW	-0.562	3.47	17.71
TCM – BASE	-0.553	3.26	15.66
TCM – HIGH	-0.548	3.26	9.30

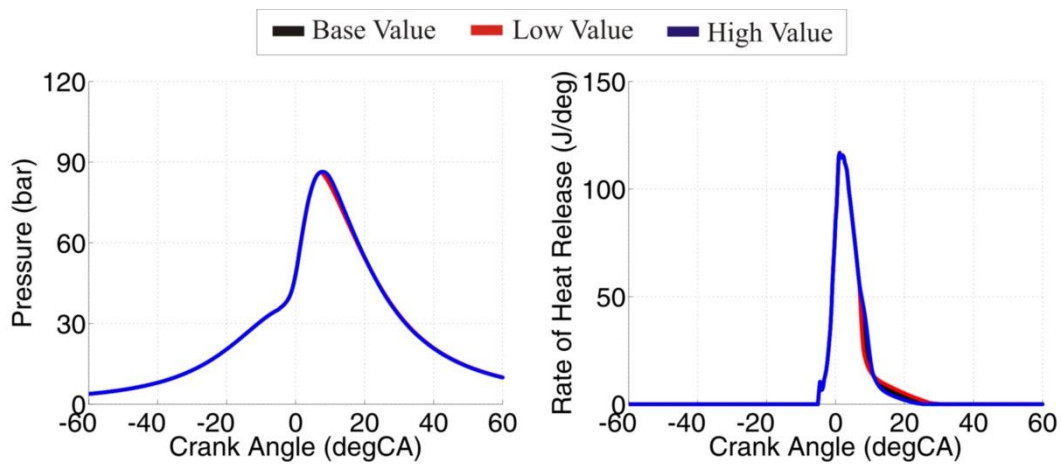
Table 22 presents the influence of  $C_{sowc}$  parameter on the main combustion process (CA 10, CA50, and CA90). The data given in Table 22 reveal that as the  $C_{sowc}$  parameter is decreased, the earlier combustion stages (CA10) and the combustion phase (CA50) stays approximately the same, while the later combustion stages (CA90) are retarded.

Figure 159 represents the influence of  $C_{wc,shp}$  flame propagation model parameter on the in-cylinder pressure and ROHR traces in the case when the flame propagation is modeled with the FCM, while Figure 160 represents the influence of the same flame propagation model parameter but now for the case when the flame propagation is modeled with the TCM.  $C_{wc,shp}$

is a model parameter that defines the shape of the non-dimensional temperature decrease rate and hence the shape of the under-relaxation function for the wall-combustion phenomenon.



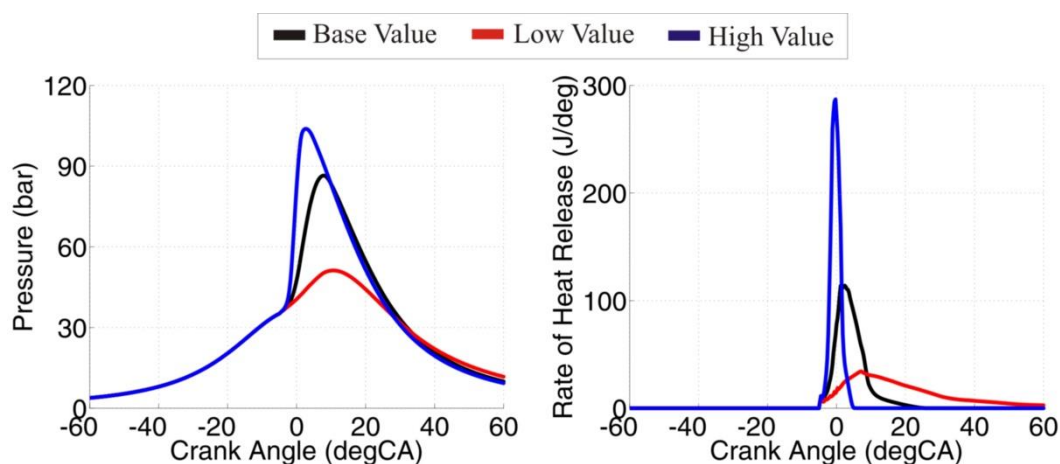
**Figure 159. Influence of the  $C_{WC,shp}$  model parameter on the in-cylinder pressure and ROHR traces; FCM flame propagation model**



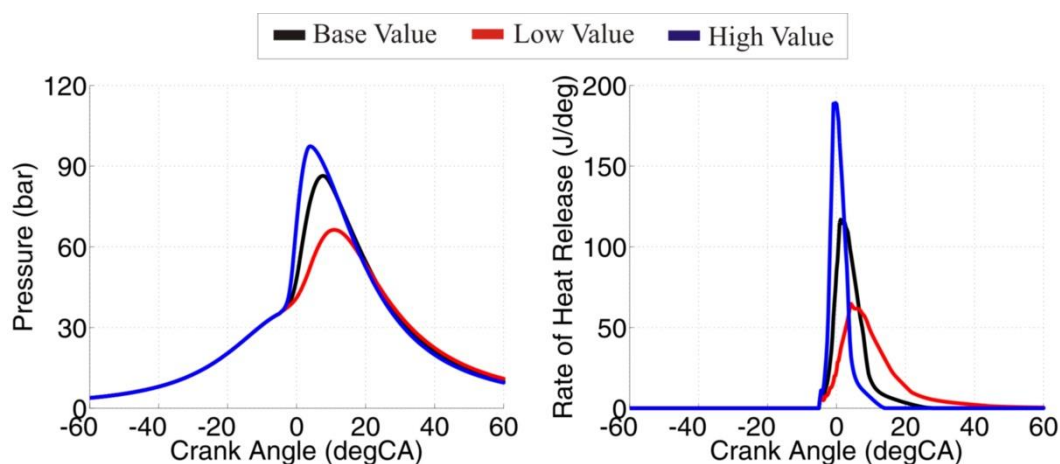
**Figure 160. Influence of the  $C_{WC,shp}$  model parameter on the in-cylinder pressure and ROHR traces; TCM flame propagation model**

Figure 159 and Figure 160 reveal that  $C_{WC,shp}$  flame propagation model parameter has a minor influence on governing of the combustion process in both the FCM and TCM case. It can also be seen that this parameter has a minor influence on the combustion phasing as well as on its intensity, while it has only a bit more profound influence on the final stages of the combustion process and hence on its duration. As  $C_{WC,shp}$  parameter is decreased, the initial ROHR decrease from the start of the wall combustion phenomenon moment is more rapid, while the final tail-like combustion stage increases, which slightly retards the final combustion stage (CA90).

Figure 161 represents the influence of  $C_{comb}$  flame propagation model parameter on the in-cylinder pressure and ROHR traces in the case when the flame propagation is modeled with the FCM, while Figure 162 represents the influence of the same flame propagation model parameter but now for the case when the flame propagation is modeled with the TCM. In the FCM,  $C_{comb}$  is a model parameter that defines the maximum value of the fractal dimension, while in the TCM  $C_{comb}$  is a model parameter that controls the value of the turbulent flame speed and is used in the TCM.



**Figure 161. Influence of the  $C_{comb}$  model parameter on the in-cylinder pressure and ROHR traces; FCM flame propagation model**



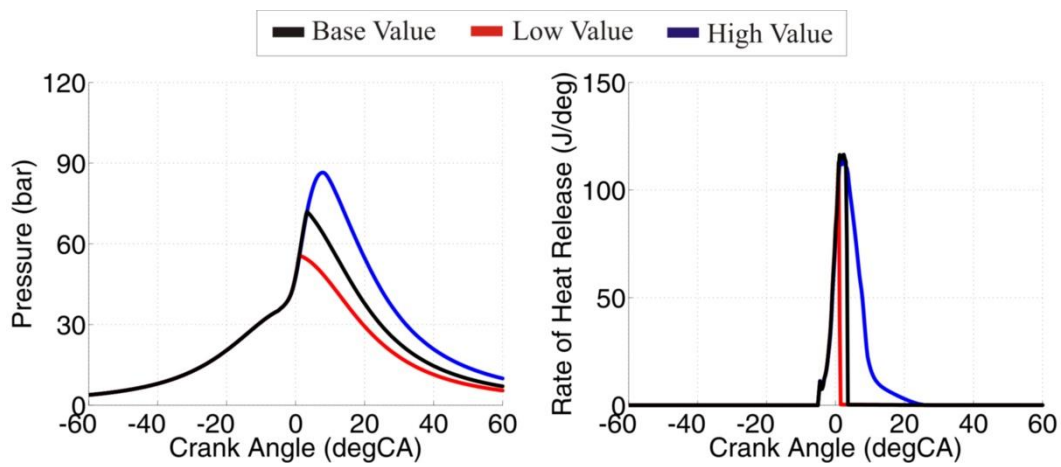
**Figure 162. Influence of the  $C_{comb}$  model parameter on the in-cylinder pressure and ROHR traces; FCM flame propagation model**

Figure 161 and Figure 162 reveal that  $C_{comb}$  flame propagation model parameters has a major influence on the combustion profile in both the FCM and TCM case, respectively. As this parameter is increased, the combustion phasing advances, combustion intensity increases and the combustion duration shortens. In the FCM, the reason for such phenomenon is the



increase of the overall turbulent flame surface as the  $D_{3,max}$  parameter is increased. In the TCM, the reason for such phenomenon is the increase of the turbulent flame speed as the  $C_{comb}$  parameter is increased.

Figure 163 represents the influence of  $C_{EOF}$  flame propagation model parameter on the in-cylinder pressure and ROHR traces in the case when the flame propagation is modeled with the FCM, while Figure 164 represents the influence of the same flame propagation model parameter but now for the case when the flame propagation is modeled with the TCM. Table 23 presents the influence of  $C_{EOF}$  parameter on the main combustion process (CA 10, CA50, and CA90).



**Figure 163. Influence of the  $C_{EOF}$  model parameter on the in-cylinder pressure and ROHR traces; FCM flame propagation model**

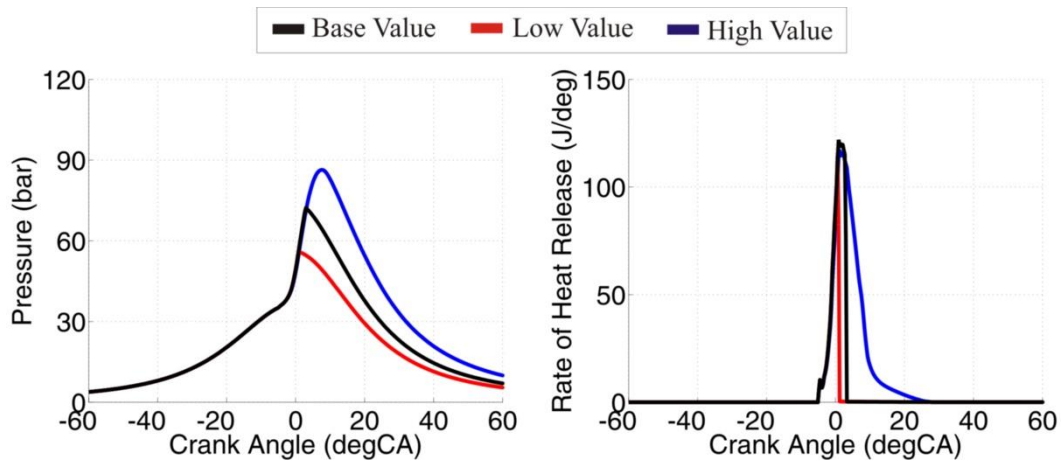


**Figure 164. Influence of the  $C_{EOF}$  model parameter on the in-cylinder pressure and ROHR traces; TCM flame propagation model**

$C_{EOF}$  is a model parameter that is used to tune the end of the flame propagation and it represents the mass fraction burned at which the flame propagation ends. Since in the original

base value case the model parameter  $C_{EOF} = 1$ , and the maximum allowed (physically)  $C_{EOF} = 1$ , in this sensitivity analysis the base case parameter  $C_{SOWC} = 0.5$ , while the “original” base case parameter is set as the high value case parameter.

**Table 23. Influence of  $C_{EOF}$  model parameter on the main combustion parameters**

Model Parameter	CA10 (degCA)	CA50 (degCA)	CA90 (degCA)
FCM – LOW	-2.50	-0.098	1.06
FCM – BASE	-1.53	1.19	2.96
FCM – HIGH	-0.476	3.45	9.48
TCM – LOW	-2.46	-0.24	0.85
TCM – BASE	-1.58	0.95	2.66
TCM – HIGH	-0.548	3.26	9.30

Figure 163 and Figure 164 reveal that the  $C_{EOF}$  flame propagation model parameter has a major influence on governing of the combustion process, in both the FCM and TCM case. It can also be seen that this parameter has a minor influence on peak ROHR value, while it has a profound influence on the final stages of the flame propagation and hence on the combustion phasing and its duration. As  $C_{EOF}$  parameter is decreased, the flame propagation ends at the earlier crank angles thus causing a decrease in the flame propagation duration and an advance in the entire combustion phasing, which is supported by the results that are presented in the Table 23. It is important to point out that such small values of  $C_{EOF}$  (0.25 and 0.5, respectively) are not expected.

From all reviewed cases ( $C_{trans}$ ,  $C_{ign,UZ,transf}$ ,  $C_{SOWC}$ ,  $C_{WC,shp}$ ,  $C_{comb}$ ,  $C_{EOF}$ ), it is evident that the two (2) ( $C_{trans}$  and  $C_{comb}$ ) of the flame propagation model parameters have a profound effect on the entire combustion profile; its phasing, intensity and duration.

Figure 165 presents the tornado plot which clearly shows the influence of a given flame propagation model parameter on the simulated combustion process (CA10, CA50 and CA90). In the tornado plot, which is given below (Figure 165), the effect of a decrease of the respective flame propagation model parameter is marked with the red color, while the effect of an increase of the respective spray combustion model parameter is marked with the green color. For all flame propagation model parameters the low value is 2x lower than the base value, while the high value is 2x higher than the base value.

The general conclusion on the overall influence of the flame propagation model parameters on the DFMZCM is that these parameters have a profound influence on part of the combustion process that is governed by the flame propagation through the premixed mixture.



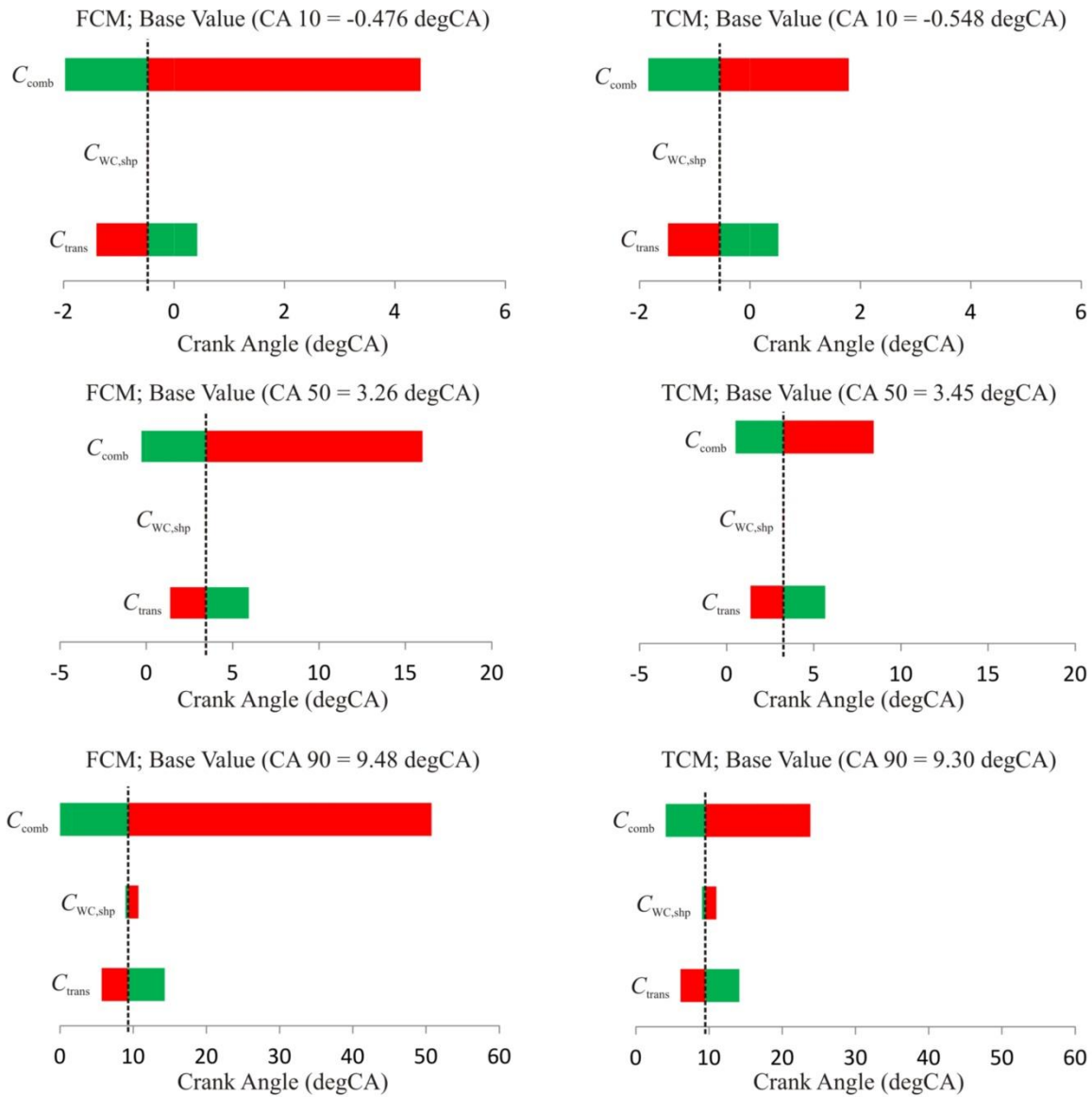


**Figure 165. Influence of the flame propagation model parameters ( $C_{trans}$ ,  $C_{WC,shp}$ ,  $C_{comb}$ ) on the CA10, CA50 and CA90 for both flame propagation models**

Generally, the flame propagation model parameters are used to adjust the calculated flame propagation process (main combustion event) with the one obtained from the experiment. This adjustment is performed in the following way (through the following model parameters):

1. Start of the flame propagation parameter ( $C_{ign,UZ,transf}$ ) is used to adjust the amount of mass that is transferred from the non-ignited spray zones to the unburned zone in the start of the flame propagation moment. This parameter controls the ratio of the spray combustion to the combustion that is controlled by the flame propagation through the premixed mixture and thus governs the way how the conventional dual fuel

combustion process is governed (controls the shape of the ROHR curve). As  $C_{ign,UZ,transf}$  is decreased, spray combustion stage increases.

2. The initial flame parameter ( $C_{trans}$ ) is used to adjust the duration of transition from laminar to fully premixed turbulent flame. This is one of the two important flame propagation parameters. As  $C_{trans}$  is decreased, the transition to the fully premixed turbulent flames speeds-up, which advances the combustion phasing, shortens the combustion duration and increases the combustion intensity.
3. Combustion parameter ( $C_{comb}$ ) is used to adjust the maximum value of fractal dimension (FCM case) and the maximum value of the turbulent flame speed (TCM case). This is the second important flame propagation parameter. As  $C_{comb}$  is increased, the maximum fractal dimension (FCM case) and the maximum turbulent flame speed (TCM case) increase, which advances the combustion phasing, shortens the combustion duration and increases the combustion intensity.
4. Wall combustion parameters ( $C_{SOWC}$ ,  $C_{WC,shp}$ ) are used to adjust the start and shape of the wall combustion burning rate. The overall influence of these parameters on the overall burning rate is negligible. However, these parameters can be used to fine tune the final combustion stage (around CA90) and combustion duration. As  $C_{SOWC}$  and  $C_{WC,shp}$  are decreased, CA 90 is retarded and combustion duration is prolonged.
5. Flame propagation end parameter ( $C_{EOF}$ ) is used to adjust the end of combustion (mass fraction burned at which the combustion ends). This parameter controls the end of combustion moment and thus has an influence on the combustion efficiency. The influence of  $C_{EOF}$  on the overall combustion profile is negligible; as  $C_{EOF}$  is decreased the final combustion stage (around CA90) is advanced.

#### 4.2.3. Validation of the model with the measured data

In this section of the thesis, the newly developed DFMZCM is validated at the additional thirteen (13) operating points. These operating points were measured at two different engine speeds, two different intake pressure levels and at various different loads, injection settings (injection timing and pressure), excess air ratios and Diesel fuel substitution ratios.

At the beginning of the section, the DFMZCM validation with the operating points that were measured at the engine speed of 1000 rpm is presented. This is followed by the validation of the model with the operating points that were measured at the engine speed of 1800 rpm. This initial validation was conducted with the single set of in-cylinder turbulence model parameters, while one spray combustion model parameter and four flame propagation model

parameters were varied in order to achieve a good fit between the measured and simulated in-cylinder pressure, temperature and ROHR traces.

After this the application of a single set of the flame propagation parameters at few different operating points is presented. Finally, at the end of this section the application of a single set of all model parameters (in-cylinder turbulence, spray combustion and flame propagation) at different operating points is presented.

The list of in-cylinder turbulence model parameters that were used in all cases is given in Table 13. In the following chapters (Operating points at 1000 rpm and Operating points at 1800 rpm), only a few spray combustion and flame propagation model parameters had to be adjusted from case to case. The only spray combustion model parameter that was altered from case to case is the parameter that controls the amount of heat that is supplied to the liquid fuel droplet for its evaporation ( $C_{\text{evap,HT}}$ ). This parameter was used to adjust the ignition time in the 0-D simulation. To appropriately model the flame propagation process (main combustion event), four (4) flame propagation model parameters had to be adjusted from case to case:

1.  $C_{\text{trans}}$  was used to appropriately model transition shape from laminar to fully premixed turbulent flame (the initial shape of the ROHR curve), and the peak ROHR crank-angle.
2.  $C_{\text{comb}}$  was used to appropriately model the combustion intensity (peak ROHR value).
3.  $C_{\text{SOWC}}$  was used in some cases to slightly adjust the final combustion event (around CA90).
4.  $C_{\text{EOF}}$  was used in some cases to slightly adjust the final combustion event (around CA90).

### ***Operating points at 1000 rpm***

At the engine speed of 1000 rpm, the DFMZCM was validated at the four (4) additional operating points. The characteristic operating parameters of each of these points is given in the table below (Table 24).

The list of the spray combustion and zone heat transfer model parameters is given in Table 25. The list of the flame propagation model parameters (FCM case) is given in Table 26, while the list of the flame propagation model parameters (TCM case) is given in Table 27.

**Table 24. Operating parameters for the points at 1000 rpm**

Parameter	OP1	OP2	OP3	OP4
Engine Speed (rpm)	1000			
SHP Pressure (bar)	1.31	1.49	1.49	2.31
SHP Temperature (K)	384	435	442	367
SHP Combustion Products Mass Fraction (-)	0.02			
Start of Injection (degCA bTDC)	20	13.5	20	25
Injection Duration (degCA)	2.5	2.5	2	2
Injection Pressure (bar)	250	750	500	500
Diesel Fuel Mass (mg)	1.71	2.73	2.92	4.19
Methane Mass (mg)	22.25	11.8	10.8	19.99
Total Excess Air Ratio (-)	1.09	1.9	2.01	2.11
IMEPg (bar)	7.85	4.54	4.46	8.18

**Table 25. Spray and zone heat transfer model parameters for the points at 1000 rpm**

Model Parameter	OP1	OP2	OP3	OP4
$C_{evap,HT}$ (-)	4.5	4	1.2	8
$C_{evap}$ (-)	1			
$C_{entrain}$ (-)	0.8			
$C_{ignition}$ (-)	1			
$C_{discr,ax}$ (-)	0.6			
$C_{discr,rad}$ (-)	6			
$C_{ZHT,SZ}$ (-)	1			

**Table 26. Flame propagation model parameters for the points at 1000 rpm; the FCM flame propagation model**

Model Parameter	OP1	OP2	OP3	OP4
$C_{trans}$ (-)	2.8	0.4	0.6	0.35
$C_{comb}$ (-)	2.46	2.31	2.32	2.37
$C_{ign,UZ,transf}$ (-)	0.95			
$C_{SOWC}$ (-)	0.8			
$C_{WC,shp}$ (-)	3			
$C_{EOFP}$ (-)	1			

Table 25, Table 26 and Table 27 reveal that at the engine speed of 1000 rpm only three parameters had to be adjusted between the different operating cases. The spray model parameter  $C_{evap,HT}$  had to be adjusted to tune the start of the combustion (ignition moment). The flame propagation model parameters  $C_{SOWC}$  and  $C_{comb}$  had to be adjusted in order to tune the combustion phasing and its intensity.

**Table 27. Flame propagation model parameters for the points at 1000 rpm; the TCM flame propagation model**

Model Parameter	OP1	OP2	OP3	OP4
$C_{trans}$ (-)	5.5	1	1.2	0.8
$C_{comb}$ (-)	1	0.6	0.6	0.7
$C_{ign,UZ,transf}$ (-)	0.95			
$C_{SOWC}$ (-)	0.8			
$C_{WC,shp}$ (-)	3			
$C_{EOFP}$ (-)	1			

There are a few reasons why these model parameters needed to be adjusted from case to case:

1. Uncertainty in the in-cylinder turbulence levels and the value of its quantities as there were no referent 3-D CFD simulations of the UC Berkeley engine available.
2. Uncertainty in the spray details (rate of evaporation, rate of entrainment, temperature and mixture stratification inside the spray region) as there were no referent 3-D CFD simulations of the UC Berkeley engine available.
3. Uncertainty in some of the measured values.

Regarding the necessity to tune the flame propagation model; it was already mentioned that the in-cylinder turbulence model was validated with the 3-D CFD data of an IC engine that has similar geometry to the UC Berkeley VW engine. Since there is a strong coupling between the in-cylinder turbulence and the flame propagation models, with the application of the turbulence model parameters that were obtained in such manner it was necessary to slightly tune the flame propagation model parameters from case to case. Moreover, in [32] it was shown that in order to be able to apply a single set of flame propagation model parameters it is necessary to adequately tune the in-cylinder turbulence model. So, it is expected that if the details regarding the in-cylinder turbulence quantities were available, it would be possible to tune the flame propagation model in a better way.

Regarding the necessity to tune the spray combustion model, there are multiple reason why this model had to be adjusted from case to cases:

1. In 0-D environment it is impossible to capture the entire spectrum of physical phenomena that occur in a real spray. Therefore, such reduced description of the physical processes leads to the necessity of the application of appropriate tuning parameters.

2. During the experiment, the injection rate was not directly measured. This means that the injection profile used in the simulation (simple rectangular shape) is not identical to the actual injection profile.
3. Since the injection rate was not directly measured, the actual injection timing could have been slightly advanced or retarded compared to one used in the simulation. Likewise, the actual injection duration could have been slightly longer or shorter compared to one used in the simulation.

Moreover, the sensitivity analysis has shown that the flame propagation is driven by the spray combustion, since the spray ignition and combustion triggers the flame propagation through the premixed mixture. Moreover, the location where the spray ignites has a profound influence on the combustion profile as it determines the shape of the flame front. Therefore, it is expected that a part of the necessity to tune the flame propagation model actually originates from the uncertainties regarding the actual spray process.

The figures given below (Figure 166 – Figure 169) represent the comparison between the measured and simulated in-cylinder pressure, temperature, ROHR and MFB traces for the four (4) simulated operating points at 1000 rpm.

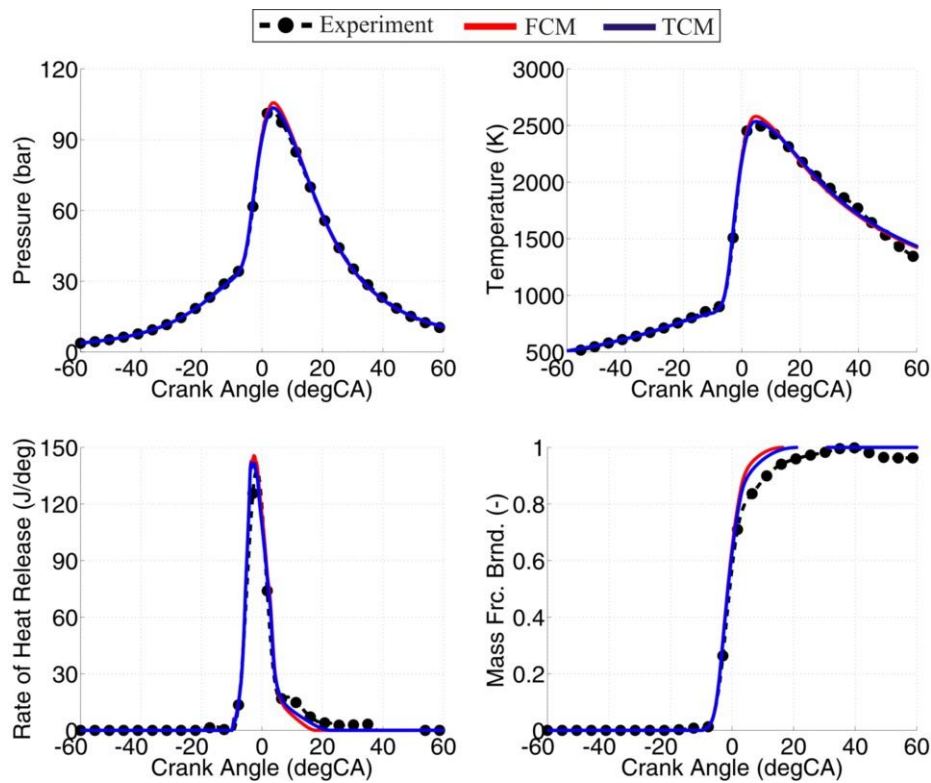


**Figure 166. Comparison between the measured and simulated in-cylinder pressure, temperature, ROHR and MFB traces for OP1 at 1000 rpm**

By looking at these figures one can clearly see that the fit between the experiment and simulation is very good for all four operating points. At some operating points (OP1 - Figure 166 and OP4 - Figure 169) there is a slight discrepancy between the measurement and simulation in the final stage of the combustion (after CA80). This is attributed to the inability of the model to appropriately capture the final wall combustion stage due to simplified description of the combustion chamber geometry and some of the aforementioned uncertainties. Moreover, this is also attributed to the inability of the model to predict the flame quenching phenomenon (3D).

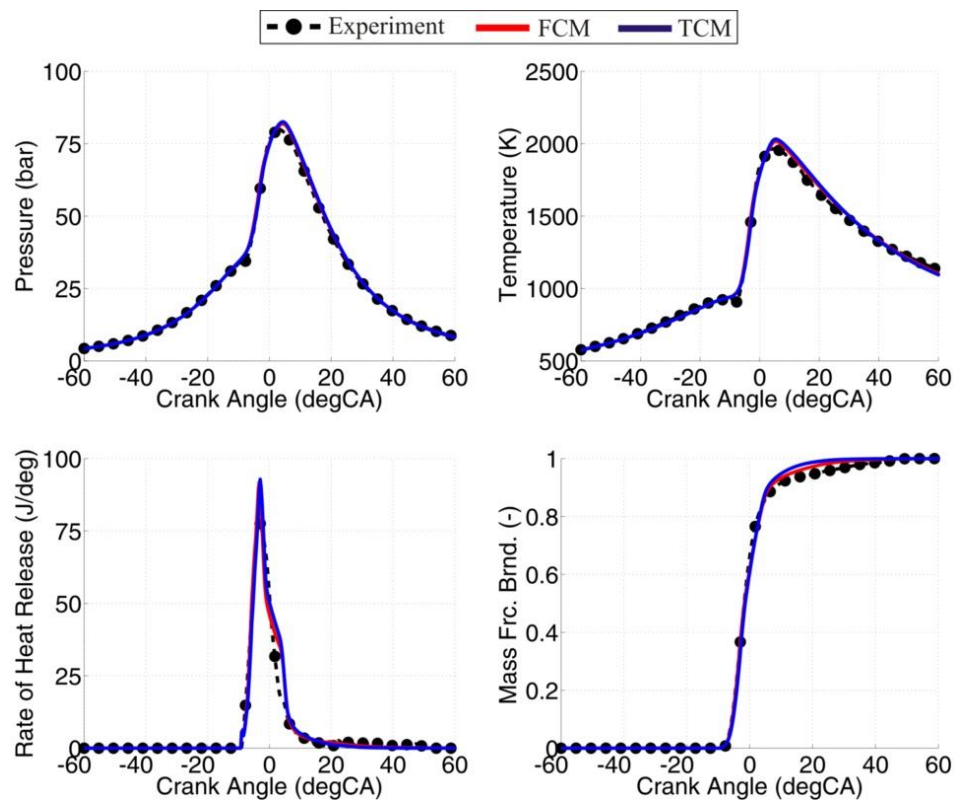


**Figure 167. Comparison between the measured and simulated in-cylinder pressure, temperature, ROHR and MFB traces for OP2 at 1000 rpm**

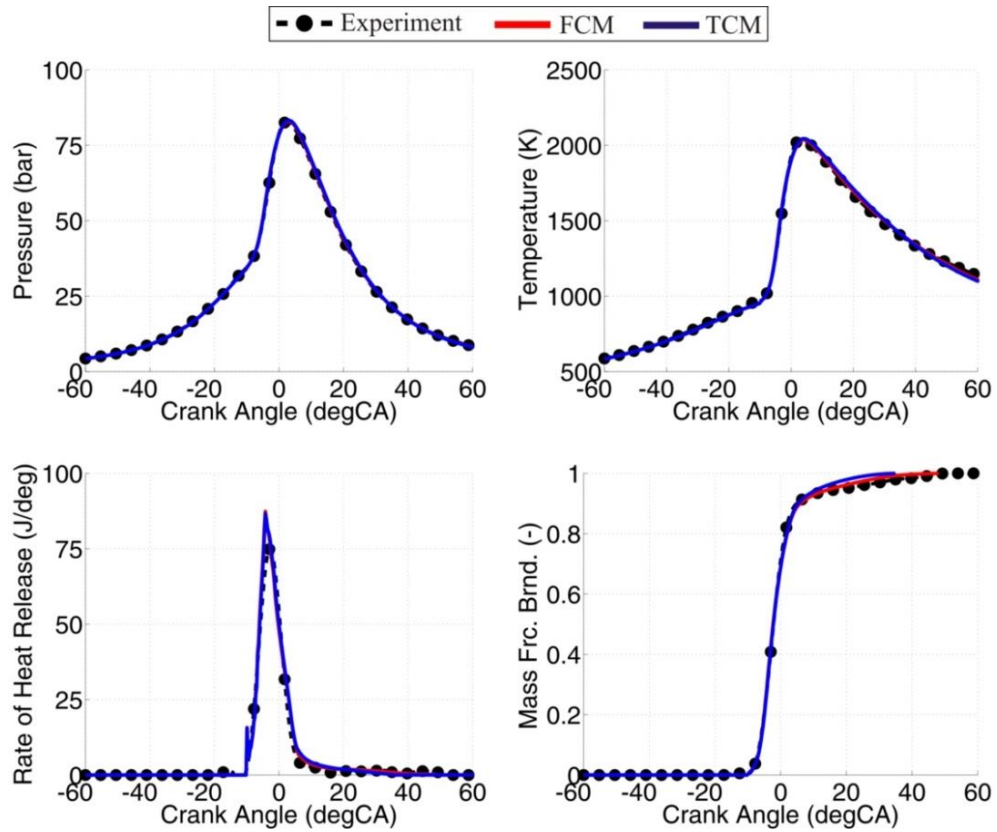


Figure 168. Comparison between the measured and simulated in-cylinder pressure, temperature, ROHR and MFB traces for OP3 at 1000 rpm

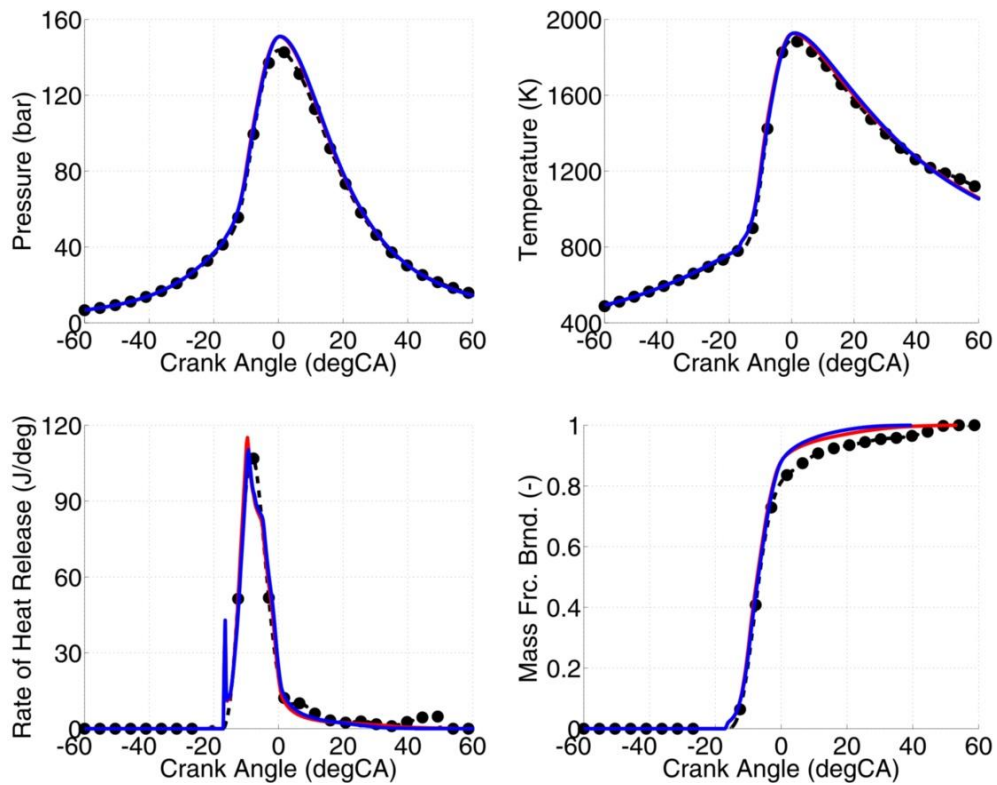
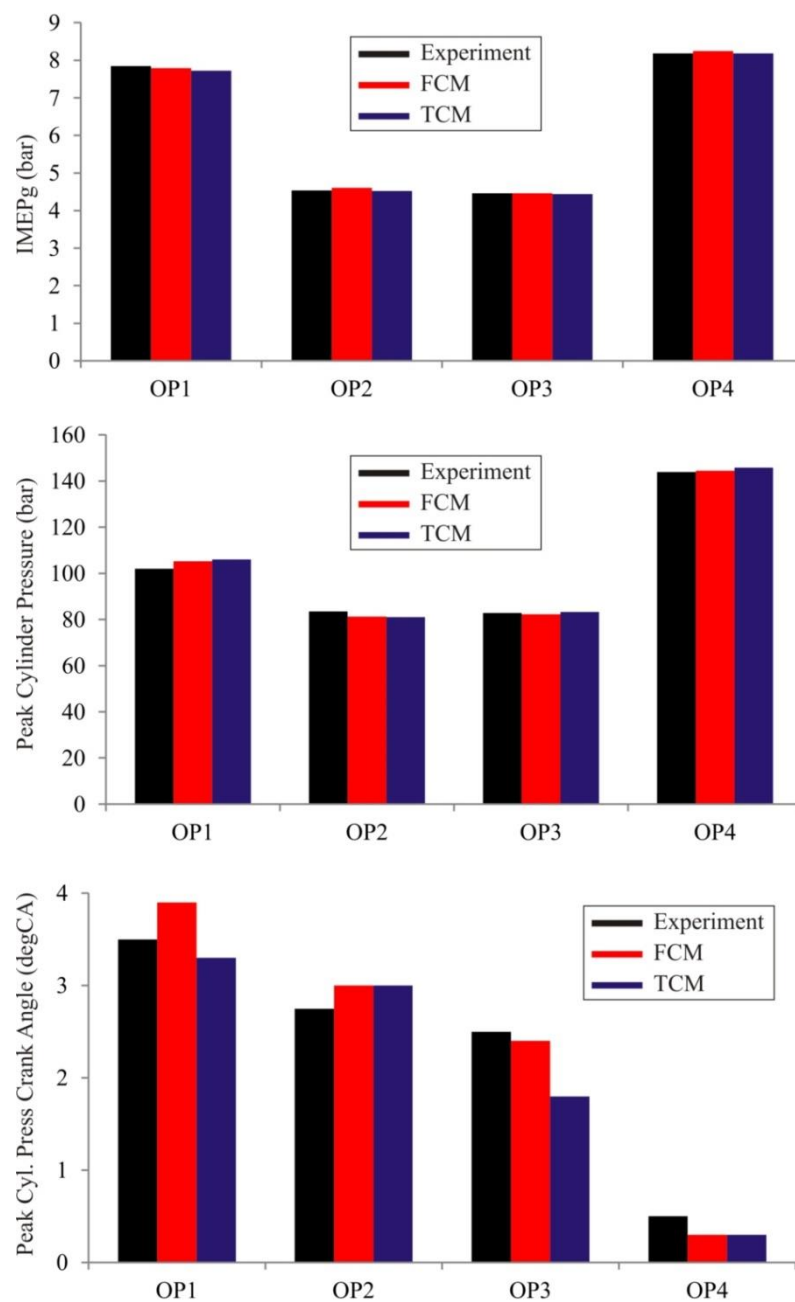


Figure 169. Comparison between the measured and simulated in-cylinder pressure, temperature, ROHR and MFB traces for OP4 at 1000 rpm



Figure 170 represents the comparison between the measured and simulated IMEPg, peak cylinder pressure and the crank angle at which the peak cylinder pressure occurred for the four (4) simulated operating points at 1000 rpm. For all four (4) simulated operating points the fit between the experiment and simulation is very good for all three (3) observed parameters. This behavior is expected since there is a good fit between the measured and simulated in-cylinder pressure for all four (4) simulated operating points (top left figure in Figure 166 – Figure 169).



**Figure 170. Comparison between the measured and simulated IMEPg, peak cylinder pressure and the crank angle at the peak cylinder pressure for all operating points at 1000 rpm**

### ***Operating points at 1800 rpm***

At the engine speed of 1800 rpm, the DFMZCM was validated at nine (9) operating points. The characteristic operating parameters of each of these points are given in Table 28.

**Table 28. Operating parameters for the points at 1800 rpm**

Parameter	OP1	OP2	OP3	OP4	OP5	OP6	OP7	OP8	OP9
Engine Speed (rpm)	1800								
SHP Pressure (bar)	1.48	1.48	1.48	1.47	1.5	1.58	2.5	1.49	1.49
SHP Temperature (K)	414.5	404	413	401	409.5	429.5	396	415	412
SHP Combustion Products Mass Fraction (-)	0.02								
Start of Injection (degCA bTDC)	20					40	30		20
Injection Duration (degCA)	4			3.5				4.5	
Injection Pressure (bar)	500			750	1000		800	500	
Diesel Fuel Mass (mg)	4.05	5	5.47	5.02	5.08	4.83	5.67	5.29	5.68
Methane Mass (mg)	9.43	7.53	9.29	8.61	7.73	16.9	13.9	8.63	9.45
Total Excess Air Ratio (-)	2.19	2.48	2.04	2.26	2.42	1.35	2.69	2.17	2.01
IMEPg (bar)	4.6	4.6	4.69	4.71	4.38	8.64	6.41	4.68	5.02

The list of the spray combustion and zone heat transfer model parameters is given in Table 29. The list of the flame propagation model parameters (FCM case) is given in Table 30, while the list of the flame propagation model parameters (TCM case) is given in Table 31.

**Table 29. Spray and zone heat transfer model parameters for the points at 1000 rpm**

Model Parameter	OP1	OP2	OP3	OP4	OP5	OP6	OP7	OP8	OP9
$C_{\text{evap,HT}}$ (-)	3.5	2.3	4	1.2	0.9	1.2	2		
$C_{\text{evap}}$ (-)	1								
$C_{\text{entrain}}$ (-)	0.8								
$C_{\text{ignition}}$ (-)	1								
$C_{\text{discr,ax}}$ (-)	0.6								
$C_{\text{discr,rad}}$ (-)	6								
$C_{\text{ZHT,SZ}}$ (-)	1								

Similarly, to the cases at 1000 rpm, in the tested cases at 1800 rpm the only spray parameter that had to be tuned is the  $C_{\text{evap,HT}}$ , which was used to adjust the ignition moment. The detailed elaboration on the necessity to tune the ignition timing has already been given in the previous chapters.

**Table 30. Flame propagation model parameters for the points at 1000 rpm; the FCM flame propagation model**

Model Parameter	OP1	OP2	OP3	OP4	OP5	OP6	OP7	OP8	OP9
C <sub>trans</sub> (-)	0			0.1	0.2	2	0	0.4	0
C <sub>comb</sub> (-)	2.45	2.51	2.5	2.42	2.41	2.32	2.45	2.43	2.35
C <sub>ign,UZ,transf</sub> (-)	0.95								
C <sub>SOWC</sub> (-)	0.5					0.8	0.5	0.6	
C <sub>WC,shp</sub> (-)	3								
C <sub>EOFP</sub> (-)	0.94					1	0.94		

**Table 31. Flame propagation model parameters for the points at 1000 rpm; the TCM flame propagation model**

Model Parameter	OP1	OP2	OP3	OP4	OP5	OP6	OP7	OP8	OP9
$C_{trans}$ (-)	0				0.5	5.5	0	0.5	0
$C_{comb}$ (-)	1.05	1.45	1.35	0.9	0.84	0.75	1		0.7
$C_{ign,UZ,transf}$ (-)	0.95								
$C_{SOWC}$ (-)	0.5					0.7	0.5	0.6	0.7
$C_{WC,shp}$ (-)	3								
$C_{EOFP}$ (-)	0.94					1	0.94		

In the 1800 rpm cases, the flame propagation model parameters  $C_{trans}$  and  $C_{comb}$  had to be adjusted in order to tune the combustion phasing and its intensity. The other two flame propagation model parameters  $C_{SOWC}$  and  $C_{EOFP}$  were used to tune the start of the wall combustion phase and to tune the flame quenching moment, respectively.

When looking at the flame propagation parameters; it can be seen that the combustion parameter ( $C_{comb}$  for the FCM and  $C_{comb}$  for the TCM) do not differ much from case to case. The parameters that control the wall combustion and flame quenching,  $C_{SOWC}$  and  $C_{EOFP}$  also had to be adjusted just slightly from case to case. As has already been mentioned a few times, the reason for this is the inability of the model to appropriately capture the final wall combustion stage due to simplified description of the combustion chamber geometry and the well-known drawback of the 0-D approach; the inability to adequately account for the temperature, mixture and turbulence stratification inside the cylinder. Even though the DFMZCM is based on the multizone approach, only the content inside the spray is divided into a number of zones which improves the calculation of the ignition and consequently combustion inside the spray. This means that with the DFMZCM, it is not possible to account for the inhomogeneities inside the premixed zone through which the flame propagates.

As the previously presented validation has revealed (validation with the data measured at 1000 rpm), the parameter that controls the time it takes for the flame to become fully turbulent,  $C_{trans}$  can significantly oscillate from case to case. There are a few reasons for such behavior:

- 1 The flame transition time is calculated from the turbulence time scale and there is uncertainty in modeling results of the turbulence model because of lack of 3-D CFD data of the experimental VW engine.
- 2 The real flame becomes fully turbulent once it has a sufficiently large size so that the turbulent eddies can make full wrinkles. This means that the transition can also depend on the location of the flame front as the in-cylinder turbulence is inhomogeneous. Unfortunately, these inhomogeneities cannot be captured with the 0-D approach.
- 3 There is an uncertainty if the prediction of the spray quantities (stratification inside the spray and the actual spray size) is fully correct for all of the validation cases. The elaboration on the uncertainty of the measurement details has already been given in the previous chapter. Since the spray ignition and combustion triggers the flame propagation, if the predictions of the spray location and size are inaccurate the prediction of the initial flame location and the initial flame kernel is also going to be inaccurate. Therefore, if the spray size is smaller than in the real-life operation, the initial flame kernel will be smaller which means that it will take longer time for the flame to become fully turbulent and vice versa. Also, if the spray center location is miscalculated, the flame (kernel) center will also be miscalculated leading to the wrong calculation of the flame front shape.

Figures (Figure 171 – Figure 179) represent the comparison between the measured and simulated in-cylinder pressure, temperature, ROHR and MFB traces for the nine (9) simulated operating points at 1800 rpm. By looking at these figures one can clearly see that the fit between the experiment and simulation is very good for all nine (9) operating points.

At some operating points (OP2 - Figure 172, OP7 - Figure 177 and OP9 - Figure 179) there is a slight discrepancy in the final stage of the combustion process (after CA75) between the measurement and simulation. This is again due to the inability of the 0-D approach to capture the fine 3D details, such as geometry and temperature, mixture and turbulence stratifications inside the cylinder.

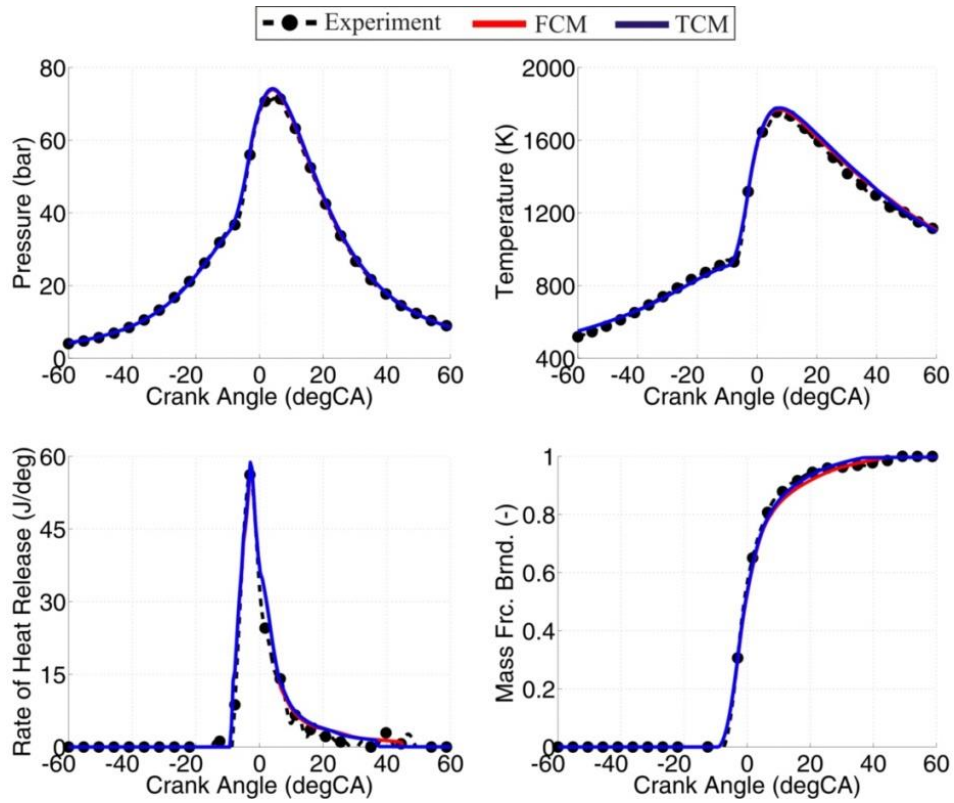


**Figure 171. Comparison between the measured and simulated in-cylinder pressure, temperature, ROHR and MFB traces for OP1 at 1800 rpm**

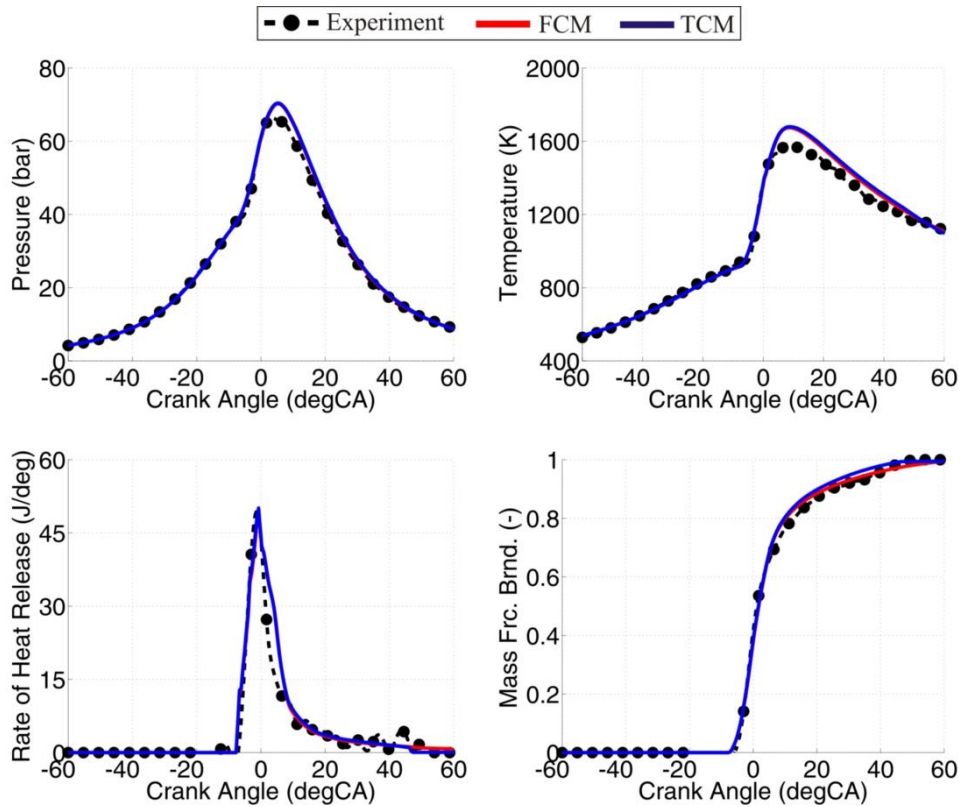


**Figure 172. Comparison between the measured and simulated in-cylinder pressure, temperature, ROHR and MFB traces for OP2 at 1800 rpm**

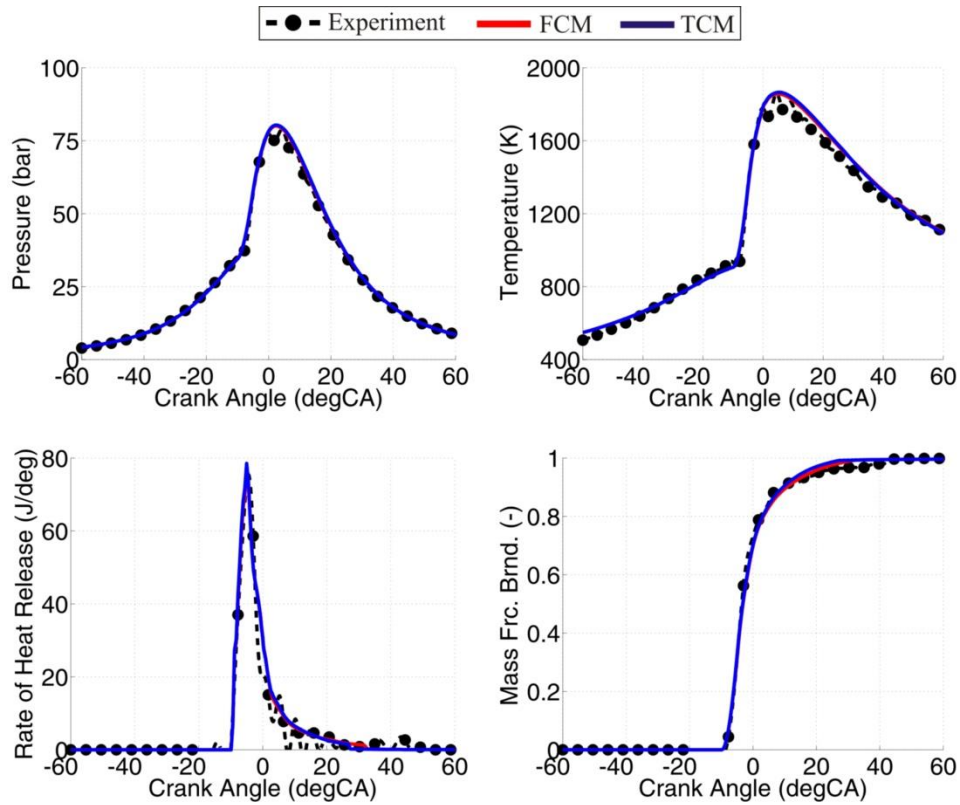


**Figure 173. Comparison between the measured and simulated in-cylinder pressure, temperature, ROHR and MFB traces for OP3 at 1800 rpm**

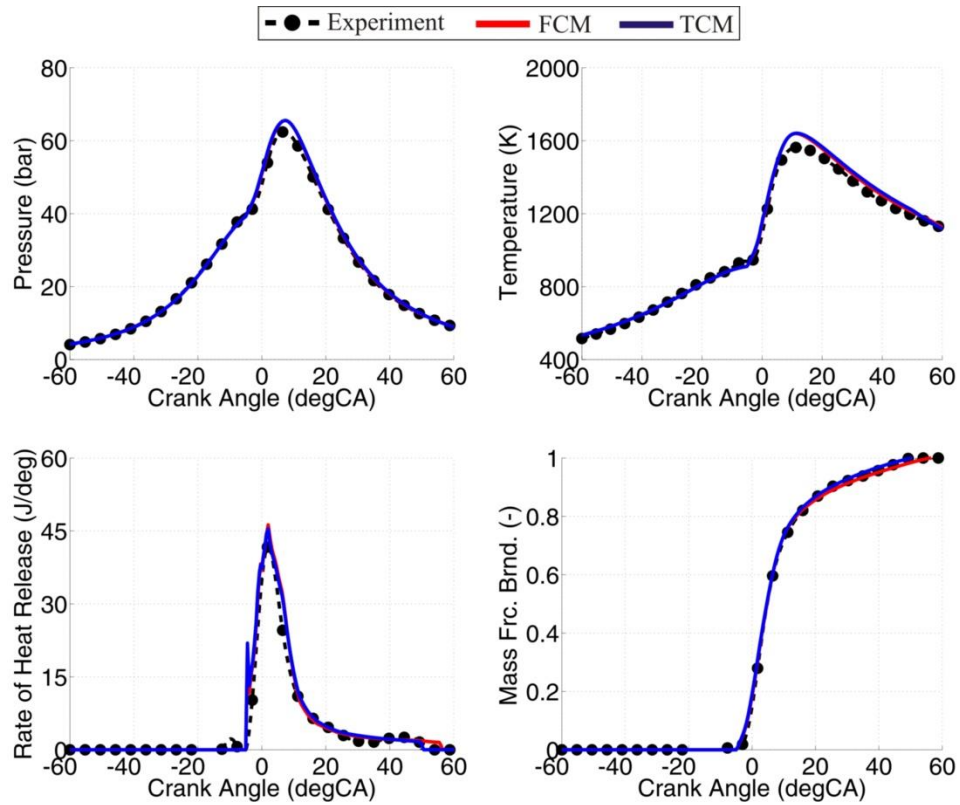


**Figure 174. Comparison between the measured and simulated in-cylinder pressure, temperature, ROHR and MFB traces for OP4 at 1800 rpm**

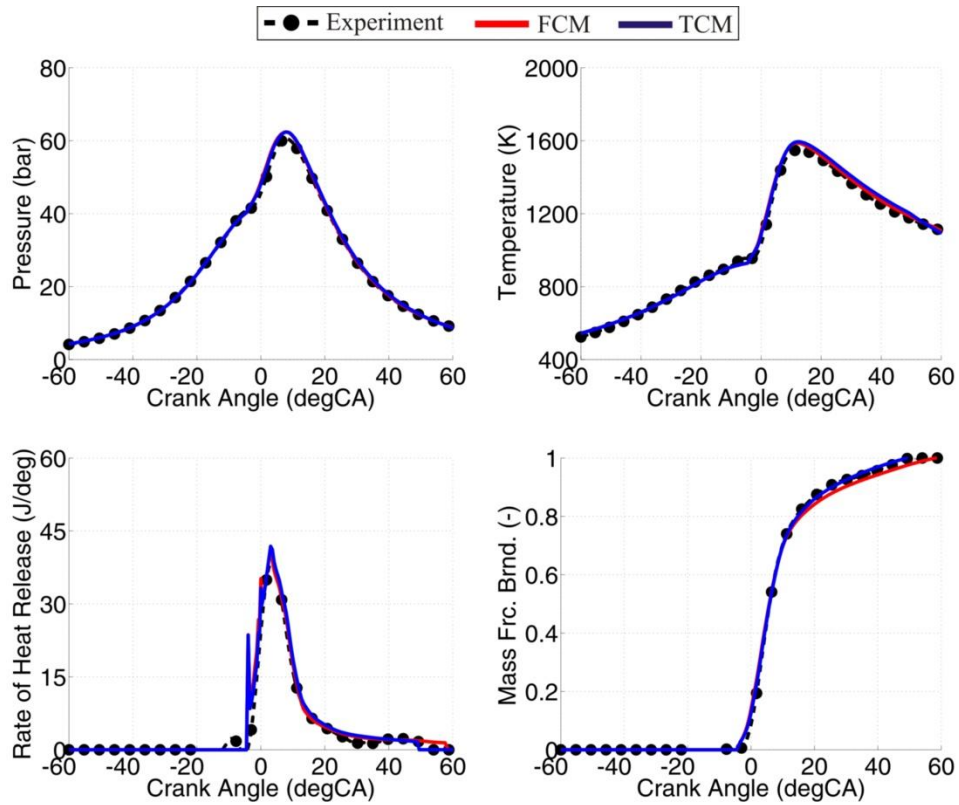


**Figure 175 Comparison between the measured and simulated in-cylinder pressure, temperature, ROHR and MFB traces for OP5 at 1800 rpm**

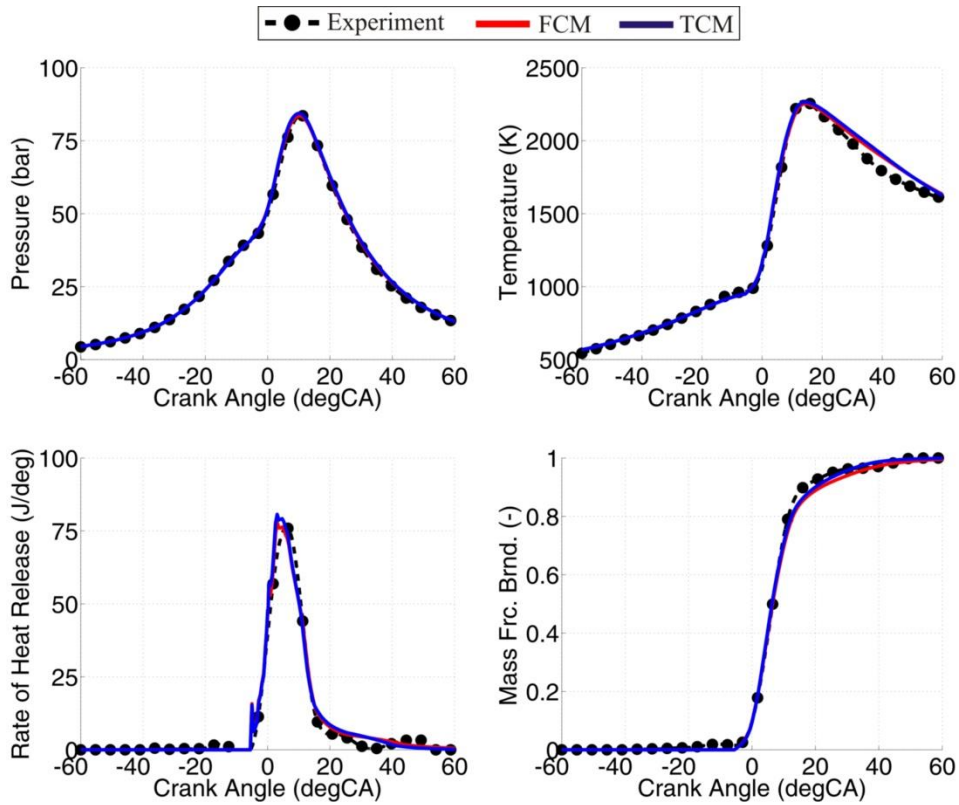


**Figure 176. Comparison between the measured and simulated in-cylinder pressure, temperature, ROHR and MFB traces for OP6 at 1800 rpm**



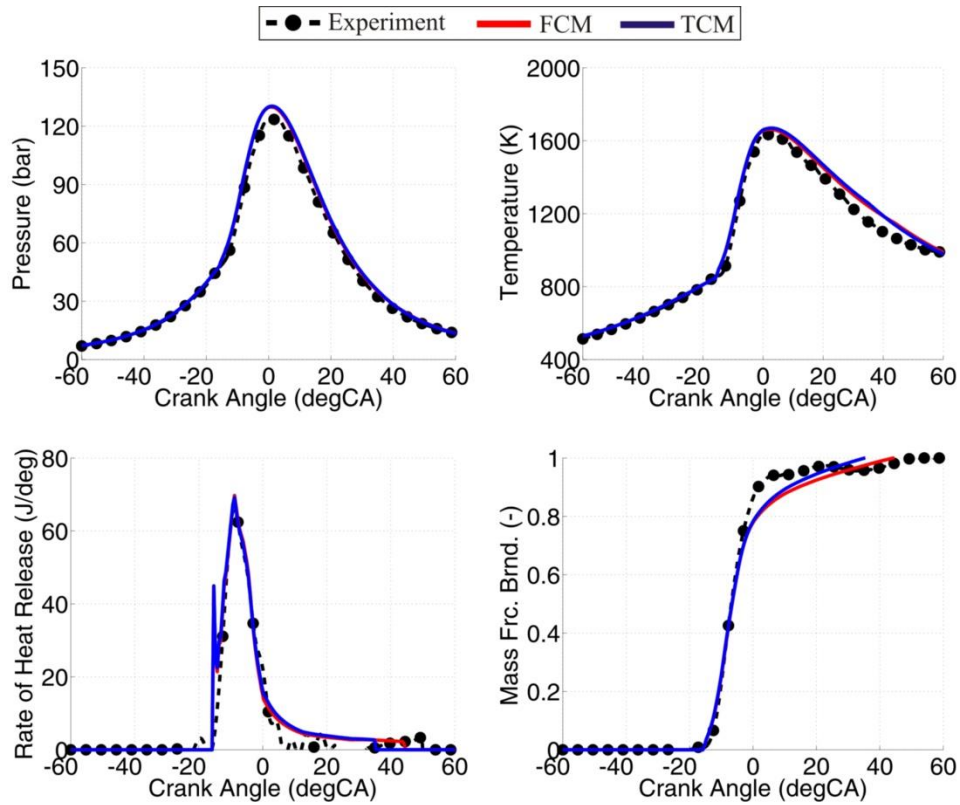


**Figure 177. Comparison between the measured and simulated in-cylinder pressure, temperature, ROHR and MFB traces for OP7 at 1800 rpm**

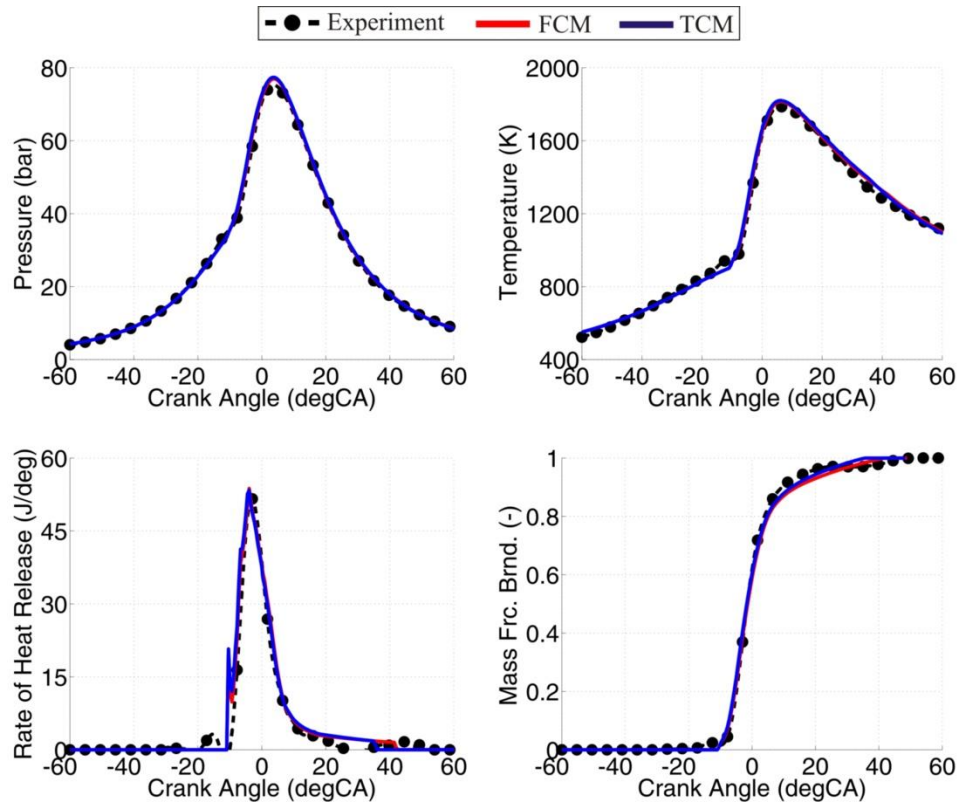


**Figure 178. Comparison between the measured and simulated in-cylinder pressure, temperature, ROHR and MFB traces for OP8 at 1800 rpm**



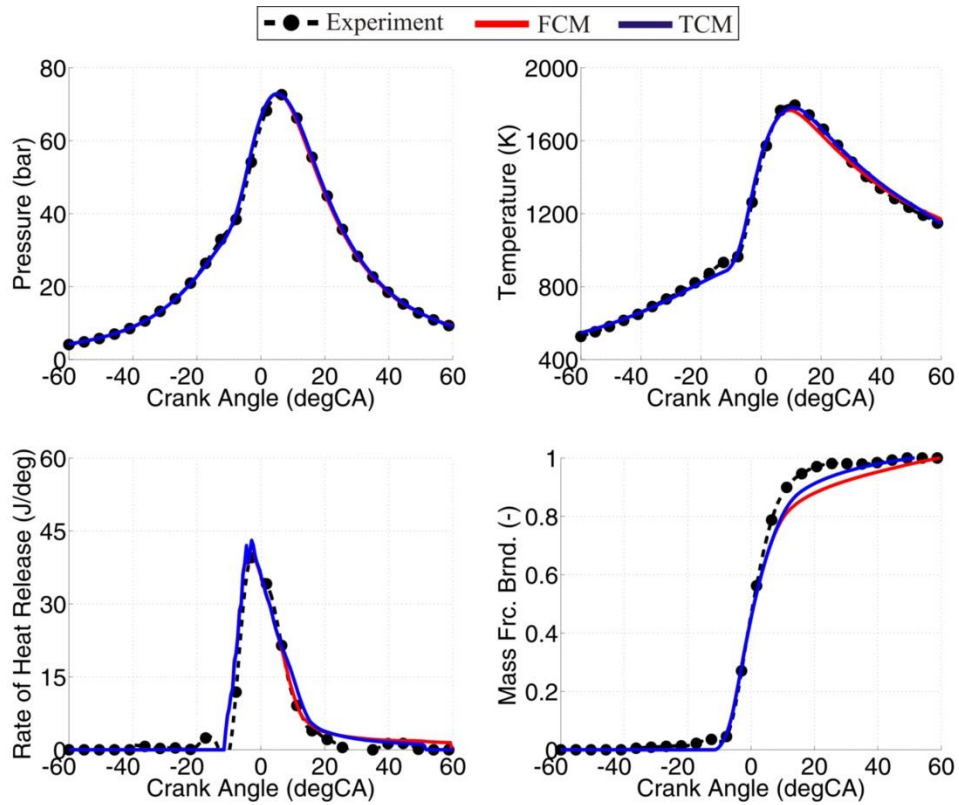


**Figure 179. Comparison between the measured and simulated in-cylinder pressure, temperature, ROHR and MFB traces for OP9 at 1800 rpm**

Figure 180 represents the comparison between the measured and simulated IMEPg, peak cylinder pressure and the crank angle at which the peak cylinder pressure occurred for the nine (9) simulated operating points at 1800 rpm. For all nine (9) simulated operating points the fit between the experiment and simulation is very good for all three (3) observed parameters. This behavior is expected since there is a good fit between the measured and simulated in-cylinder pressure for all nine (9) simulated operating points (top left figure in Figure 171 – Figure 179).

The validation that has been presented so far clearly shows that the newly developed DFMZC is capable of describing the conventional dual fuel combustion process. All of the measurement – simulation comparisons results show that there is a good fit between the measured and simulated in-cylinder pressure, temperature, ROHR and MFB traces. However, since this is a 0-D approach where the spatial details are not resolved and since the combustion and flow have a 3D character, there is a need to slightly tune some of the model parameters from case to case.

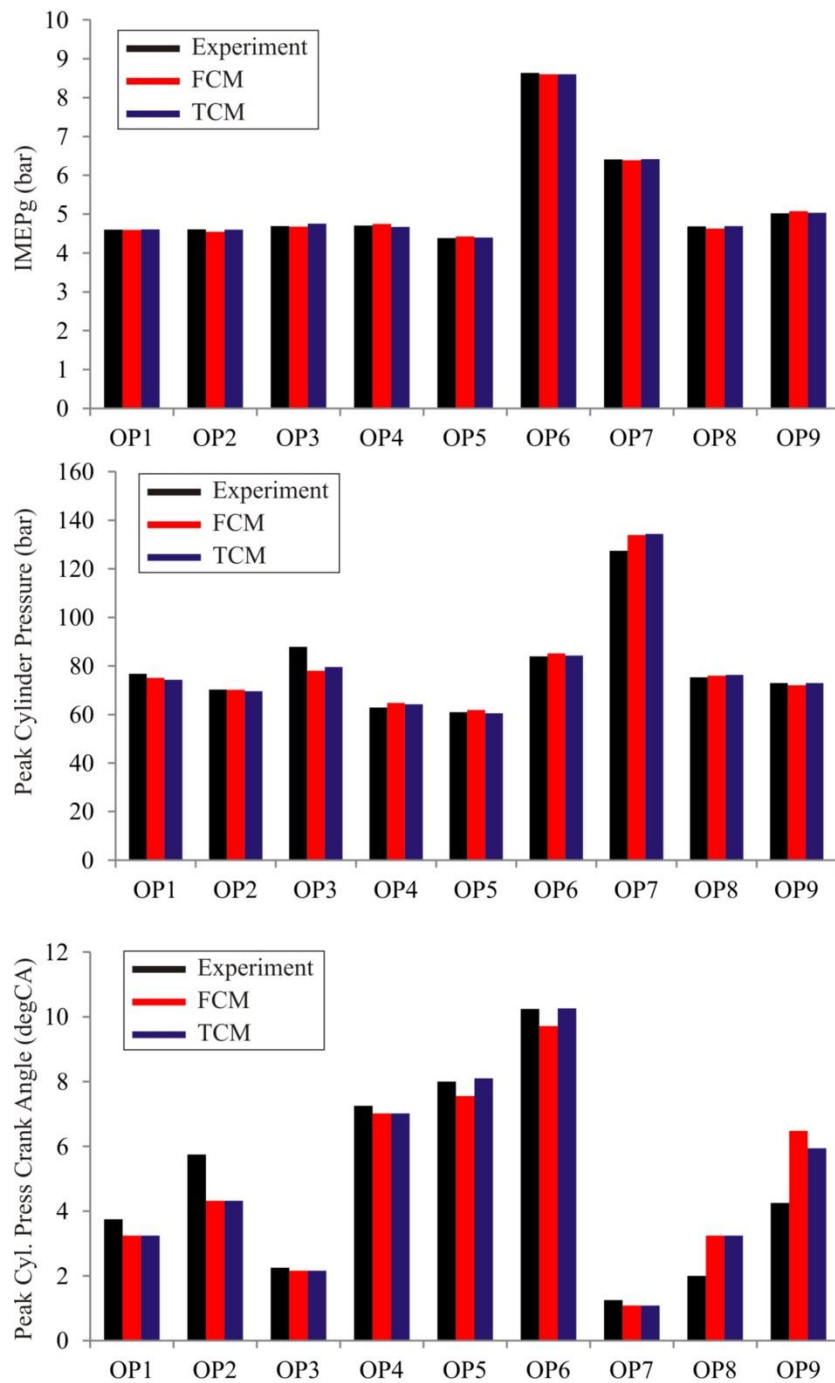


**Figure 180. Comparison between the measured and simulated IMEPg, peak cylinder pressure and the crank angle at the peak cylinder pressure for all operating points at 1800 rpm**

#### 4.2.4. Validation with a single set of model parameters

**Table 32. Operating parameters for the points that were used in the single set of the model parameters simulations**

Parameter	OP1	OP2	OP3	OP4	OP5	OP6	OP7	OP8	OP9
Engine Speed (rpm)	1000		1800						
SHP Pressure (bar)	1.49	1.49	1.48	1.48	1.48	1.47	1.5	1.49	1.49
SHP Temperature (K)	435	442	414.5	404	413	401	409.5	415	412
SHP Combustion Products Mass Fraction (-)	0.02								
Start of Injection (degCA bTDC)	13.5	20						30	40
Injection Duration (degCA)	2.5	2	4			3.5		4.5	
Injection Pressure (bar)	750	500				750	1000	500	
Diesel Fuel Mass (mg)	2.73	2.92	4.05	5	5.47	5.02	5.08	5.29	5.68
Methane Mass (mg)	11.8	10.8	9.43	7.53	9.29	8.61	7.73	8.63	9.45
Total Excess Air Ratio (-)	1.9	2.01	2.19	2.48	2.04	2.26	2.42	2.17	2.01
IMEPg (bar)	4.54	4.46	4.6	4.6	4.69	4.71	4.18	4.68	5.02

After the initial validation was performed a few operating points at each engine speed were selected and simulated with the single set of model parameter. It is important to point out that the single set of parameters was applied for the operating points at the same engine speed:

1. For OP1 and OP2 that have the engine speed of 1000 rpm (Table 32).
2. For OP3 – OP9 that have the engine speed of 1800 rpm (Table 32).

In the first step the single set of flame propagation parameters for each of these two sets was applied, and after that the single set of all model parameters was applied for each set of the operating points. The list of operating points along with the operating details for each of these points is given in Table 32.

#### ***Single set of flame propagation model parameters***

The full list of the spray combustion model parameters that were used in this simulation set is given in Table 33. As can be seen, in these simulations only the spray model parameter  $C_{\text{evap,HT}}$  is varied from case to case. As was already started a few times, this is the parameter that tunes the amount of heat that is supplied to the liquid fuel droplet and thus controls the evaporation rate. Through the control of the evaporation rate, this parameter can be used to control the ignition timing. The full list of flame propagation parameters is given in Table 34.

The figures (Figure 181 – Figure 189) represent the comparison between the measured and simulated in-cylinder pressure, temperature, ROHR and MFB traces for the nine (9) operating points that are presented in this chapter.

**Table 33. The list of the spray combustion model parameters**

Model Parameter	OP1	OP2	OP3	OP4	OP5	OP6	OP7	OP8	OP9
$C_{\text{evap,HT}} (-)$	4	1.2	3.5	2.3	4	1.2	0.9	2	2
$C_{\text{evap}} (-)$	1								
$C_{\text{entrain}} (-)$	0.5								
$C_{\text{ignition}} (-)$	1								
$C_{\text{discr,ax}} (-)$	0.6								
$C_{\text{discr,rad}} (-)$	6								
$C_{\text{ZHT,SZ}} (-)$	1								

**Table 34. The list of the flame propagation model parameters**

Model Parameter	OP1	OP2	OP3	OP4	OP5	OP6	OP7	OP8	OP9
$C_{\text{ign,UZ,transf}} (-)$	0.95								
$C_{\text{trans}} (-)$ TCM/FCM	1.1/0.5		0.125/0.1						
$C_{\text{SOWC}} (-)$	0.8		0.5						
$C_{\text{WC,shp}} (-)$	3		3						
$C_{\text{comb}} (-)$ ; TCM/FCM	0.6/2.31		1/2.44						
$C_{\text{EOFP}} (-)$	1		0.94						

As can be seen from the figures that are given in this chapter (Figure 181 – Figure 189) when the single set of the flame propagation parameters is applied for multiple operating points that are at the same engine speed (OP1 and OP2 at 1000 rpm; OP3 – OP9 at 1800 rpm) the fit between the measured and simulated traces is not as good as the one that was obtained when a few of the flame propagation model parameters were adjusted from cases to case. However, the fit between the measured and simulated traces is still reasonable and all of the trends are adequately captured. Combustion phasing is reasonable for all of the cases, just in some of the cases the combustion process is either too intense or it is too weak compared to the measured cases. The main reason for the differences between the calculation/experiment results when the single set of the flame propagation model parameters for the operating points that are at the same engine speed, are the uncertainties regarding the in-cylinder turbulence model parameters (single set in all of the cases) as well as the uncertainties regarding the spray processes. A detailed elaboration on these issues has already been given in the previous chapters.

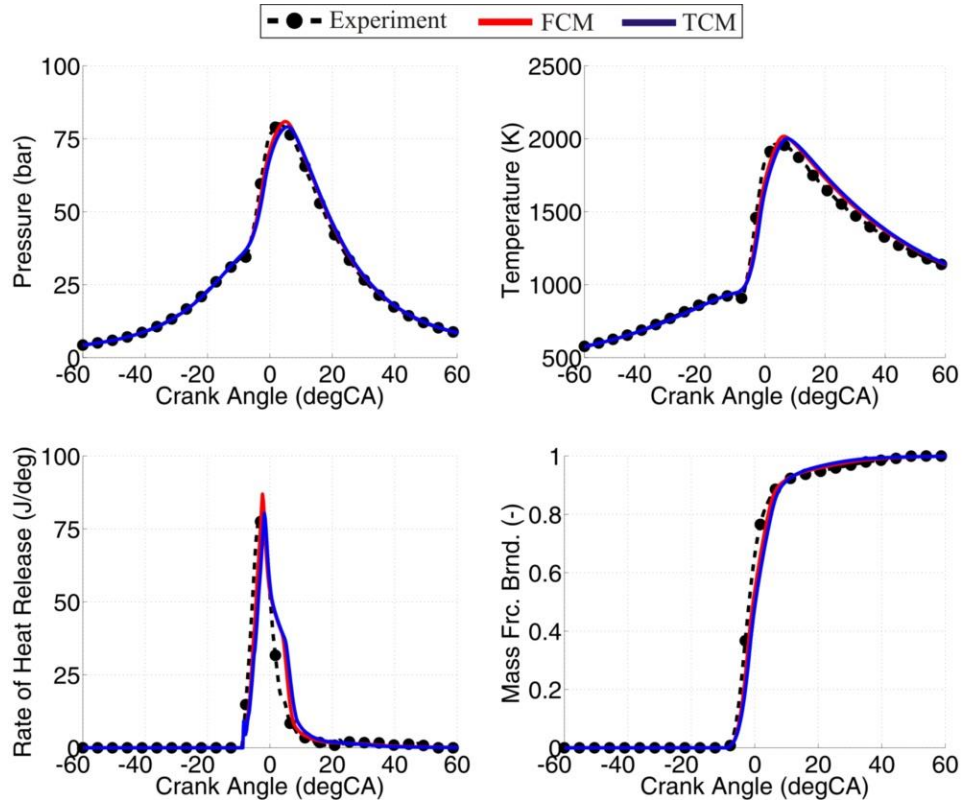


**Figure 181.** Comparison between the measured and simulated in-cylinder pressure, temperature, ROHR and MFB traces for OP1 at 1000 rpm and the single set of the flame propagation model parameters

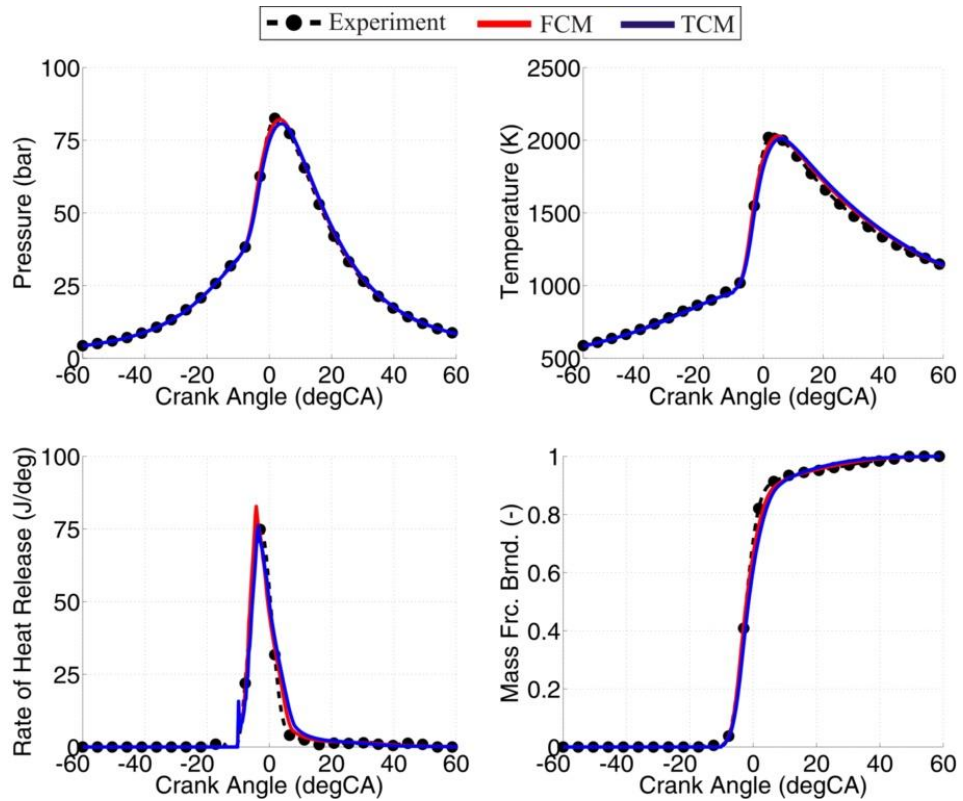


**Figure 182.** Comparison between the measured and simulated in-cylinder pressure, temperature, ROHR and MFB traces for OP2 at 1000 rpm and the single set of the flame propagation model parameters

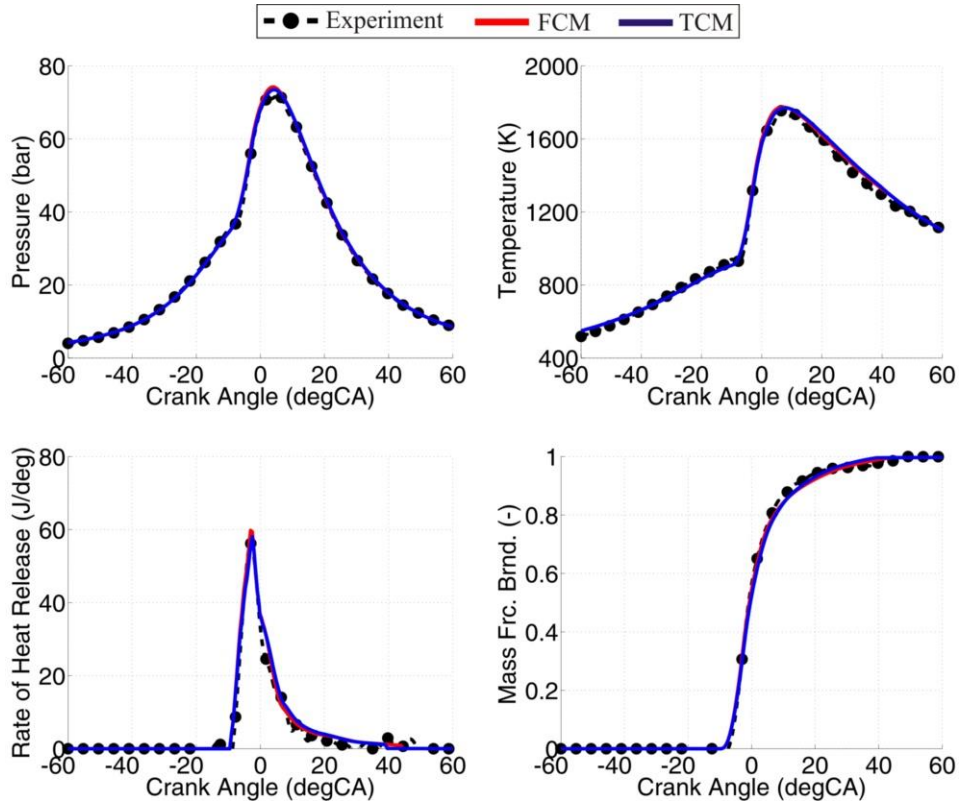


**Figure 183.** Comparison between the measured and simulated in-cylinder pressure, temperature, ROHR and MFB traces for OP3 at 1800 rpm and the single set of the flame propagation model parameters

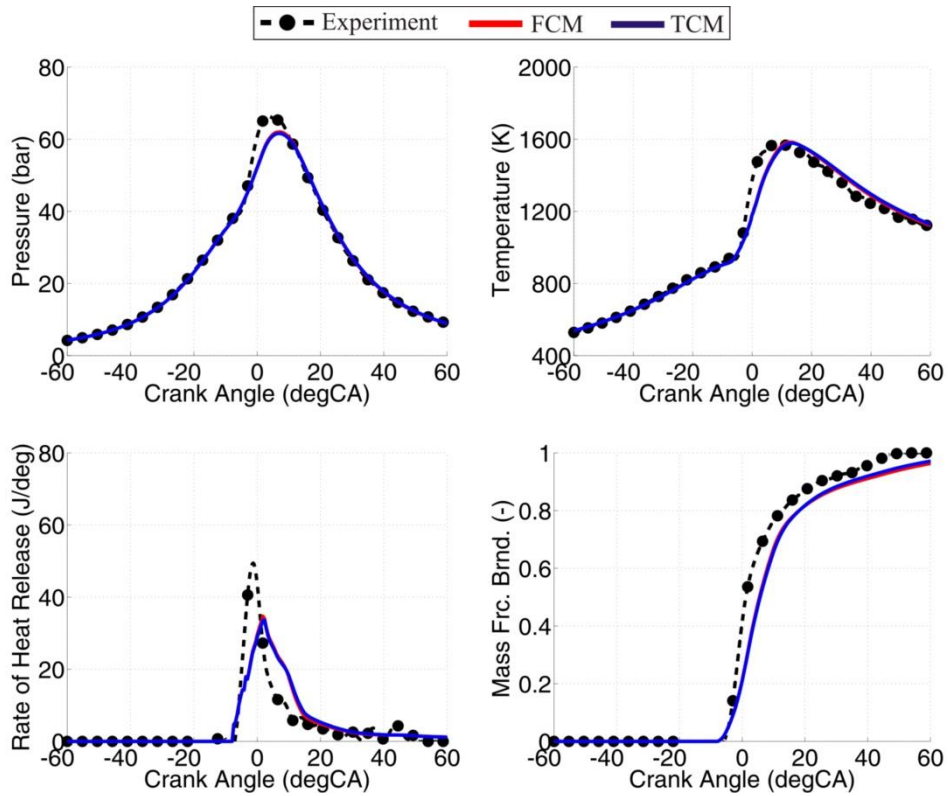


**Figure 184.** Comparison between the measured and simulated in-cylinder pressure, temperature, ROHR and MFB traces for OP4 at 1800 rpm and the single set of the flame propagation model parameters

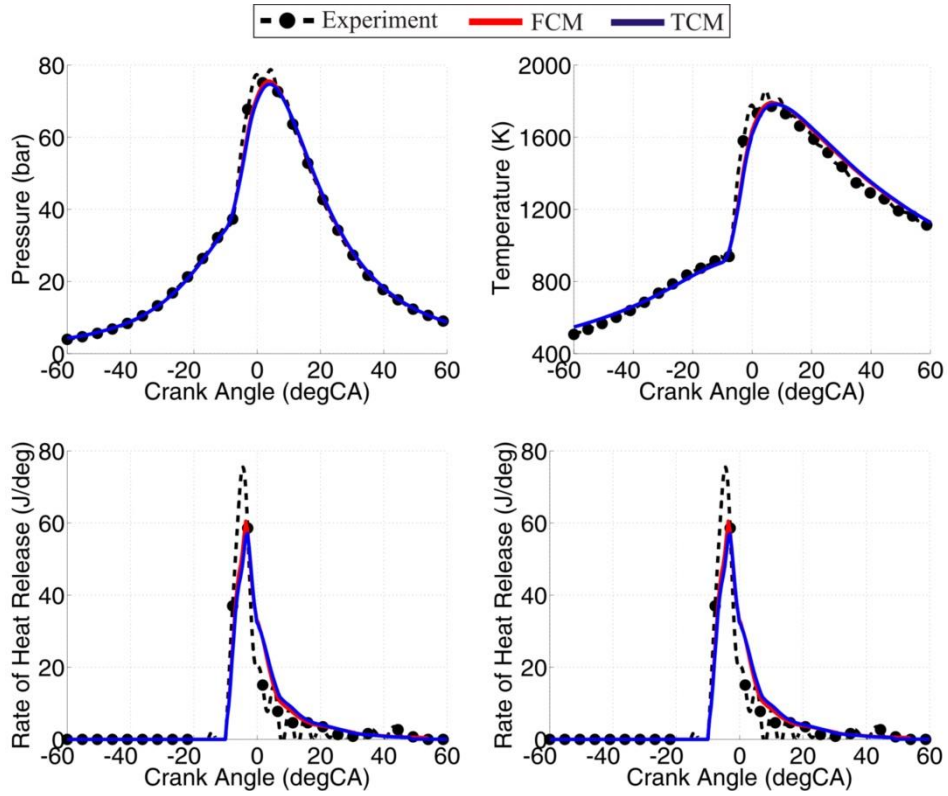


**Figure 185.** Comparison between the measured and simulated in-cylinder pressure, temperature, ROHR and MFB traces for OP5 at 1800 rpm and the single set of the flame propagation model parameters

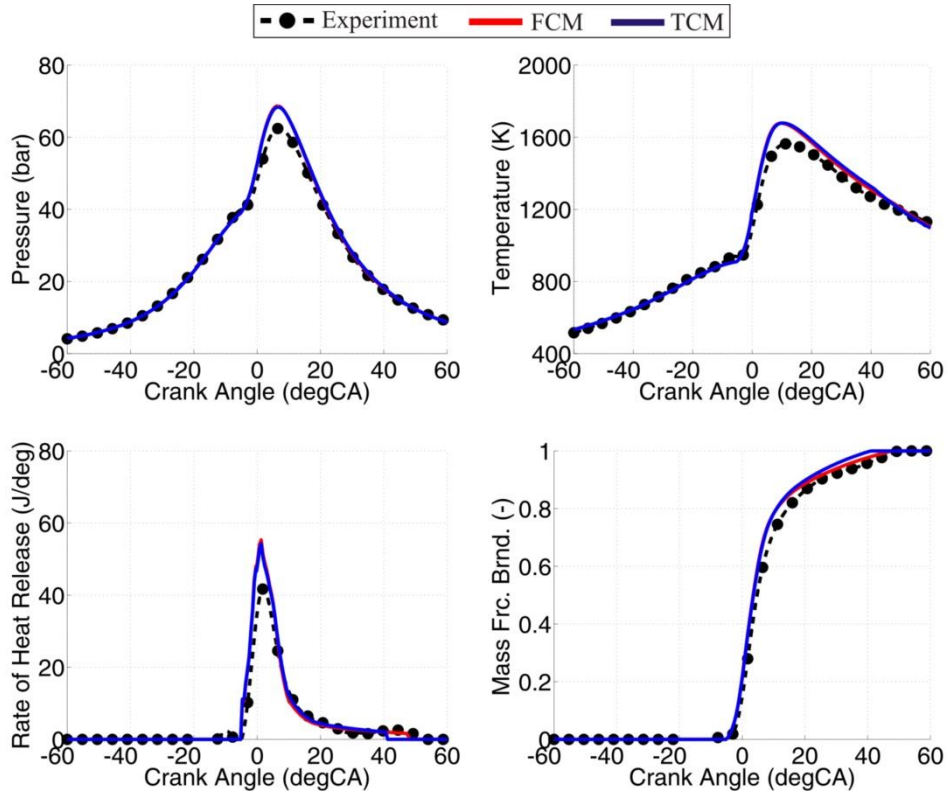


**Figure 186.** Comparison between the measured and simulated in-cylinder pressure, temperature, ROHR and MFB traces for OP6 at 1800 rpm and the single set of the flame propagation model parameters



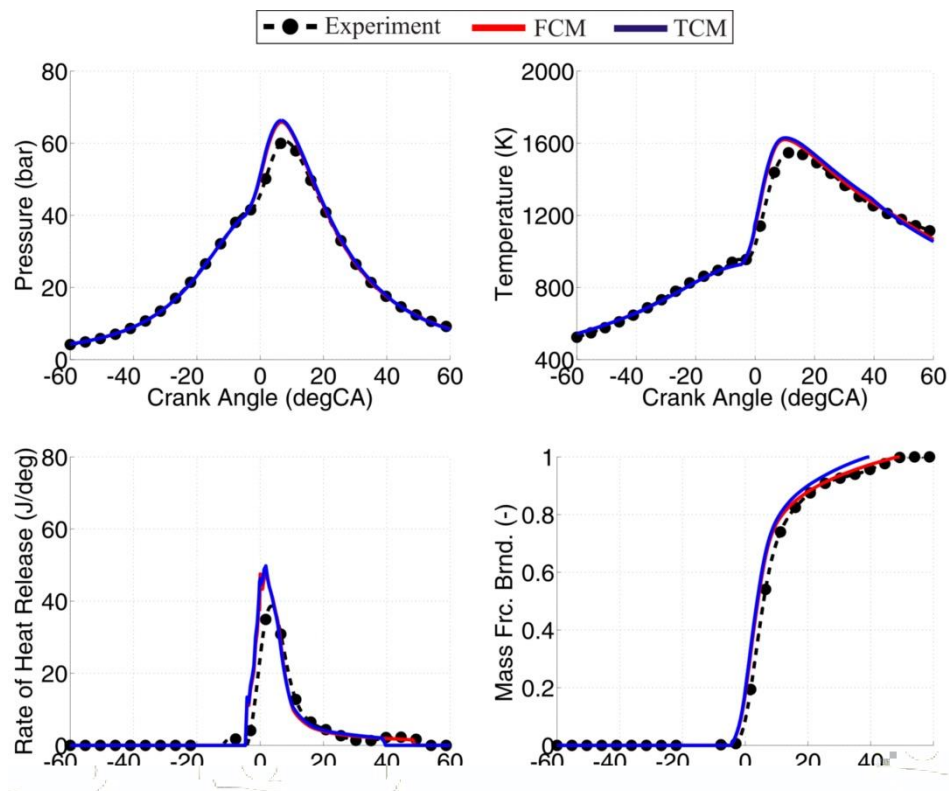


Figure 187. Comparison between the measured and simulated in-cylinder pressure, temperature, ROHR and MFB traces for OP7 at 1800 rpm and the single set of the flame propagation model parameters

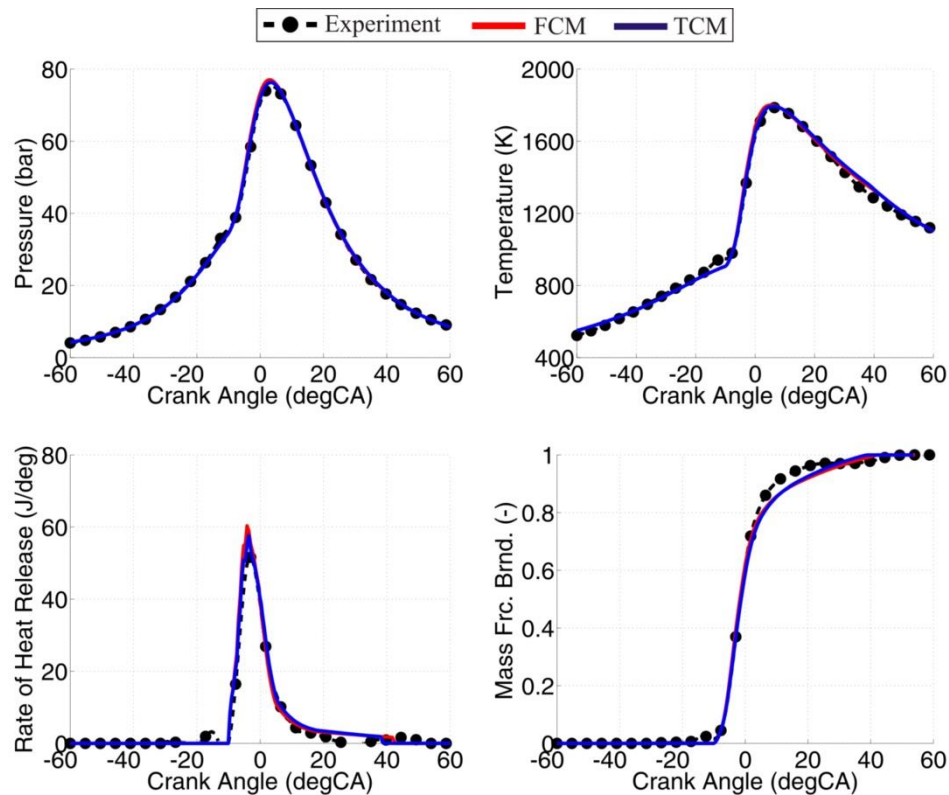
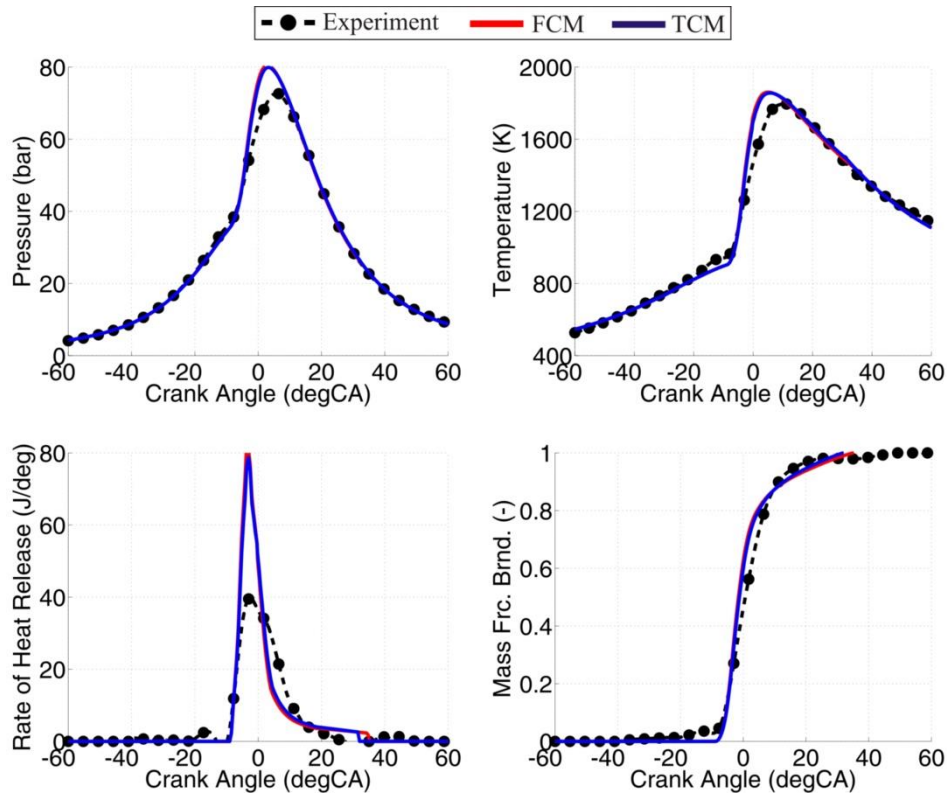
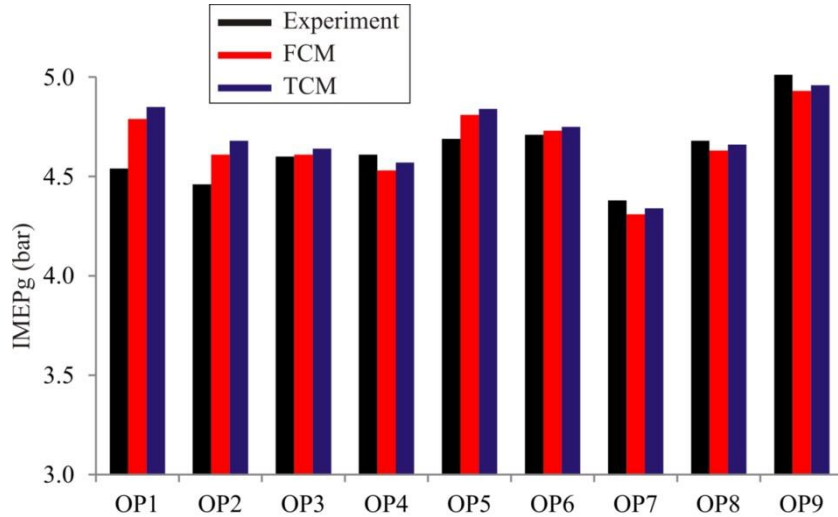


Figure 188. Comparison between the measured and simulated in-cylinder pressure, temperature, ROHR and MFB traces for OP8 at 1800 rpm and the single set of the flame propagation model parameters





**Figure 189.** Comparison between the measured and simulated in-cylinder pressure, temperature, ROHR and MFB traces for OP9 at 1800 rpm and the single set of the flame propagation model parameters



**Figure 190.** Comparison between the measured and simulated IMEPg for the operating points that were simulated with the single set of the flame propagation model parameters

Figure 190 represents the comparison between the measured and simulated IMEPg, for the nine (9) operating points that are presented in this chapter. For all nine (9) simulated operating points the fit between the measured and simulated IMEPg is very good and it can be seen that the trends in the IMEPg are reasonably captured.

The reasons for somewhat different constants between the two engine speeds lies in the different temperature and mixture stratification inside the cylinder as the engine speed changes. It is a well-known that as the engine speed is changed, the in-cylinder temperature and composition field change as well. With the multizone 0-D approach that is applied in the DFMZCM it is possible to account for the temperature and mixture inhomogeneities inside the spray zone. However, it is not possible to account for the heterogeneities inside the premixed zone through which the flame propagates. Therefore, these spatial effects that are not directly modeled can only be captured by tuning the model parameters.

### ***Single set of all parameters***

The full list of the spray combustion model parameters that were used in this simulation set is given in Table 35. As can be seen, in this simulation set the operating points that are at the same engine speed have been calculated with the single set of the spray combustion model parameters which means that the operating points that are at the same engine speed have been calculated with a single set of all model parameters. Flame propagation was modeled with the same parameters that were used in the previous simulation set (Table 34), while the in-cylinder turbulence was modeled with the parameters that were used in all of the simulations that are presented in this thesis (Table 13). The figures (Figure 191 – Figure 199) represent the comparison between the measured and simulated in-cylinder pressure, temperature, ROHR and MFB traces for the nine (9) operating points that are presented in this chapter.

**Table 35. The list of the spray combustion model parameters**

Model Parameter	OP1	OP2	OP3	OP4	OP5	OP6	OP7	OP8	OP9
$C_{\text{evap,HT}} \text{ (-)}$	2		2.6						
$C_{\text{evap}} \text{ (-)}$	1								
$C_{\text{entrain}} \text{ (-)}$	0.5								
$C_{\text{ignition}} \text{ (-)}$	1								
$C_{\text{discr,ax}} \text{ (-)}$	0.6								
$C_{\text{discr,rad}} \text{ (-)}$	6								
$C_{\text{ZHT,SZ}} \text{ (-)}$	1								

As can be seen from the figures that are given in this chapter (Figure 191 – Figure 199) when the single set all model parameters is applied for multiple operating points that are the same engine speed (OP1 and OP2 at 1000 rpm; OP3 – OP9 at 1800 rpm) the fit between the measured and simulated traces is not as good as the one that was obtained only the single set of the flame propagation model parameters was used.

However, the measurement – simulation comparison figures reveal that the fit between the measured and simulated traces is still reasonable and most of the trends are adequately captured. Combustion phasing is reasonable for all of the cases; in some cases, it is almost perfect (OP2 and OP8), while in others it is slightly off (OP6 and OP7). Also, in some of the cases the combustion process is either too intense or it is too weak compared to the measured cases. The main reason for the inability to apply the single set of all model parameters for the operating points that are at the same engine speed are the uncertainties regarding the in-cylinder turbulence model parameters as well as the uncertainties regarding the spray processes; a detailed elaboration on these issues has already been given in the previous chapters. Again, the reasons for somewhat different constants between the two engine speeds lie in the different temperature and mixture stratification inside the cylinder as the engine speed changes.

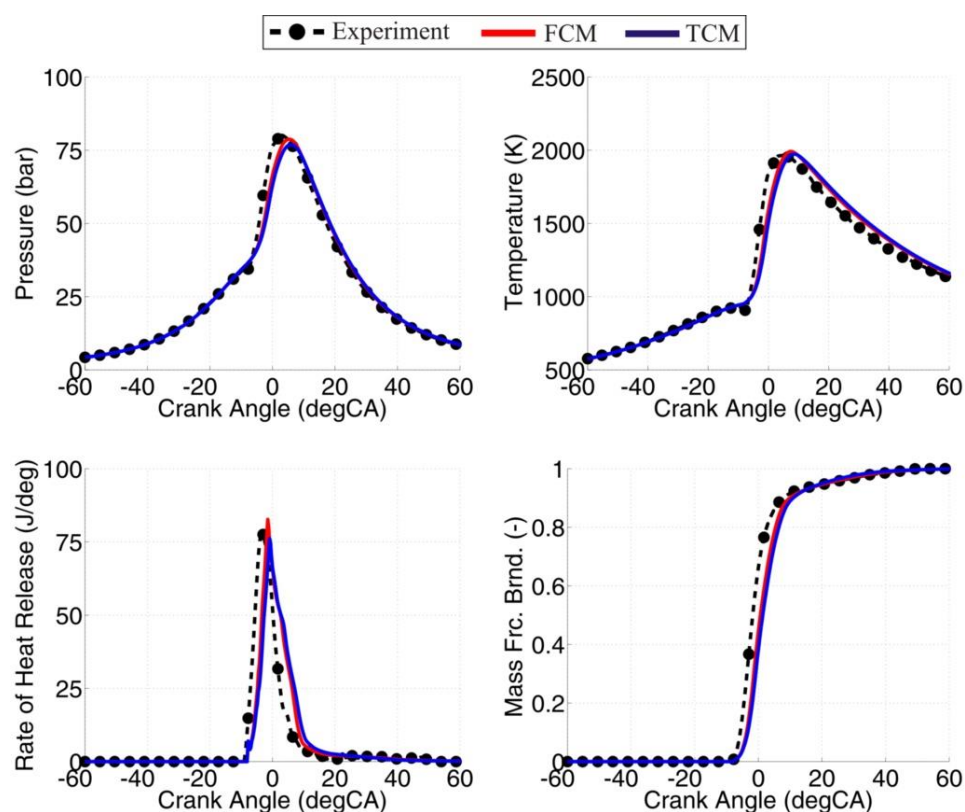


**Figure 191. Comparison between measured and simulated pressure, temperature, ROHR and MFB traces for OP1 at 1000 rpm and the single set of all model parameters**

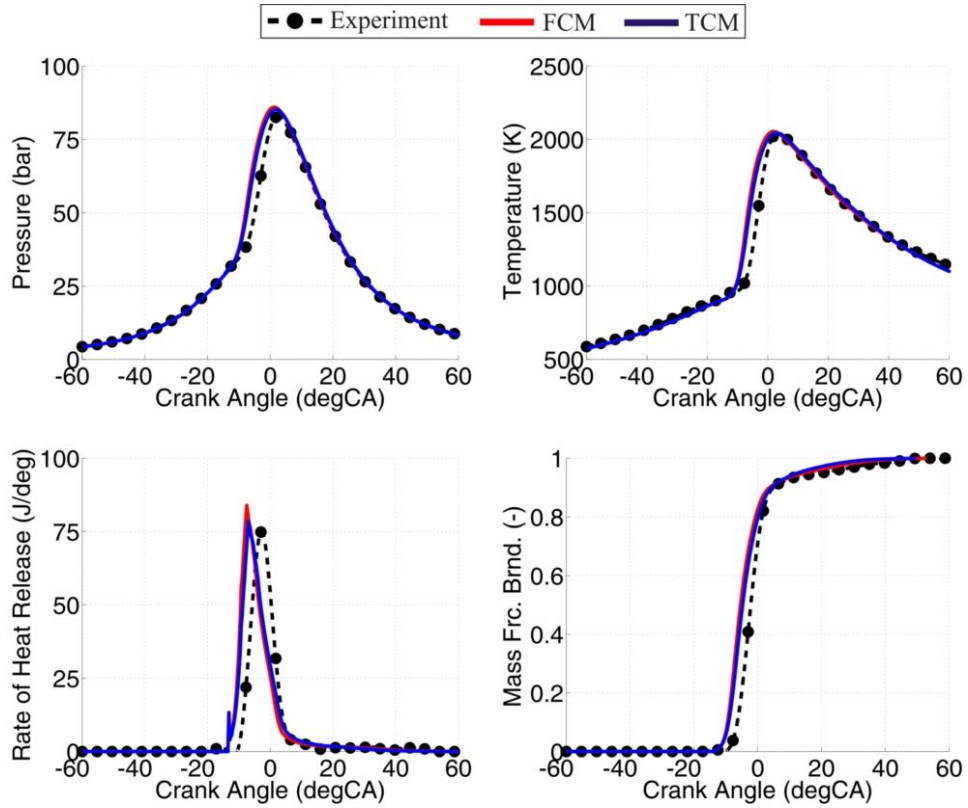


**Figure 192.** Comparison between the measured and simulated in-cylinder pressure, temperature, ROHR and MFB traces for OP2 at 1000 rpm and the single set of all model parameters

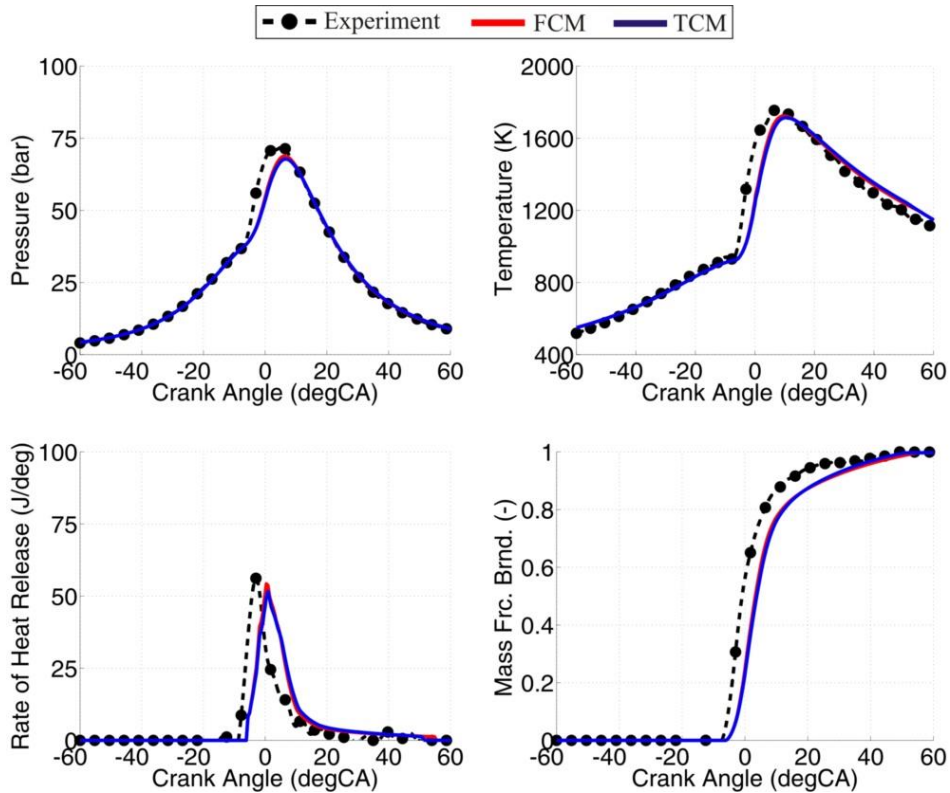


**Figure 193.** Comparison between the measured and simulated in-cylinder pressure, temperature, ROHR and MFB traces for OP3 at 1800 rpm and the single set of all model parameters

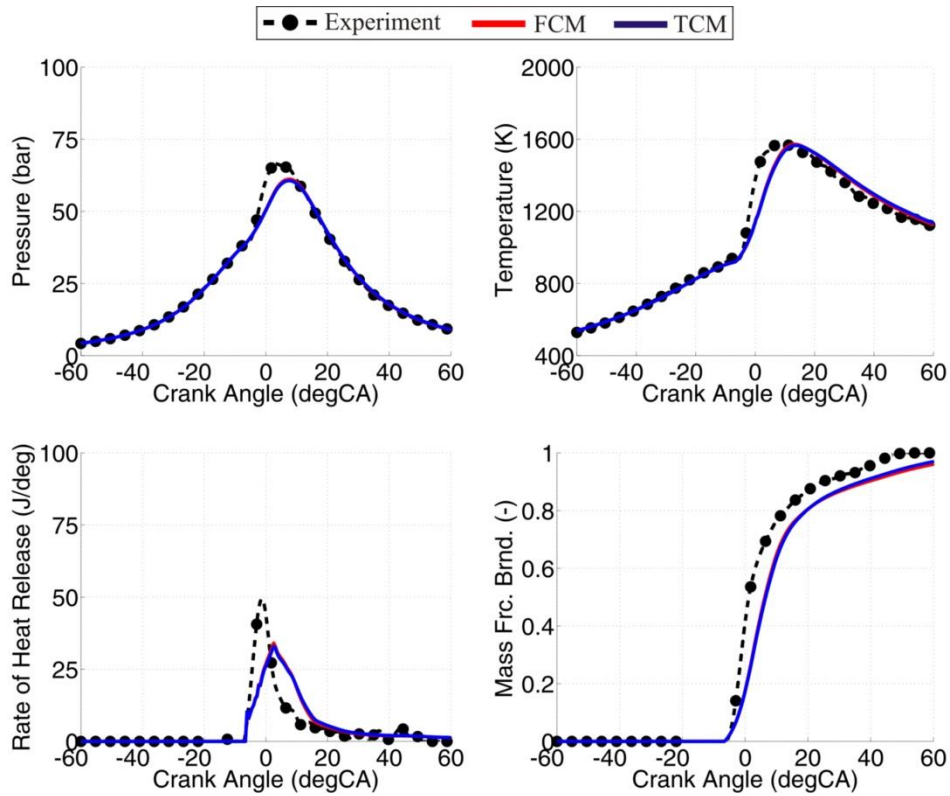


**Figure 194.** Comparison between the measured and simulated in-cylinder pressure, temperature, ROHR and MFB traces for OP4 at 1800 rpm and the single set of all model parameters

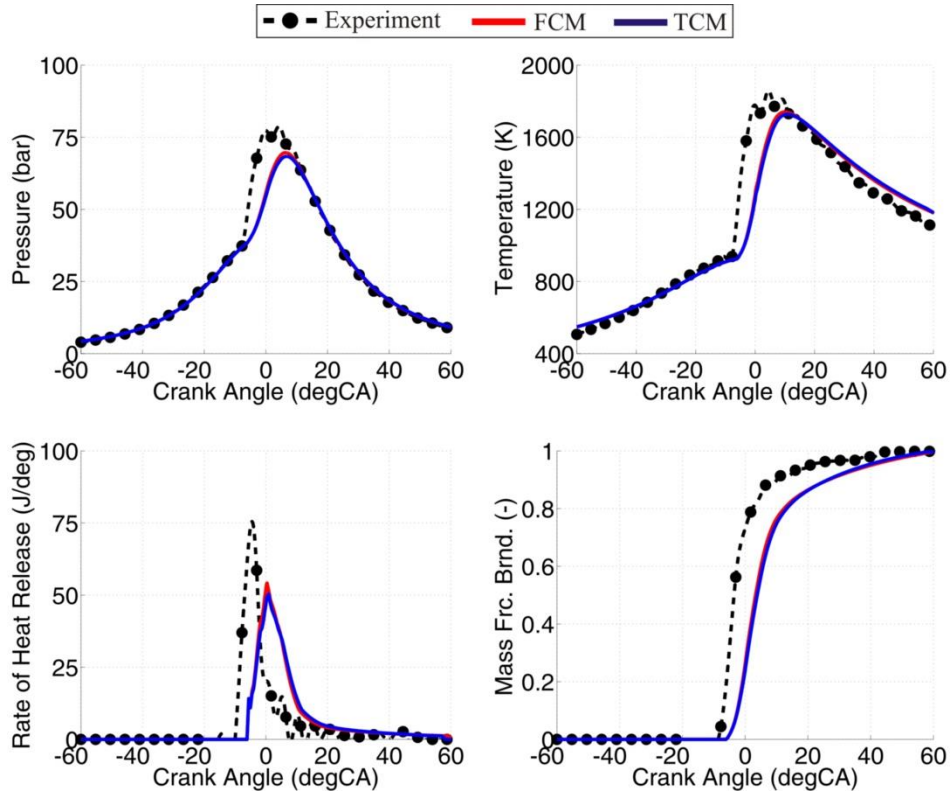


**Figure 195.** Comparison between the measured and simulated in-cylinder pressure, temperature, ROHR and MFB traces for OP5 at 1800 rpm and the single set of all model parameters



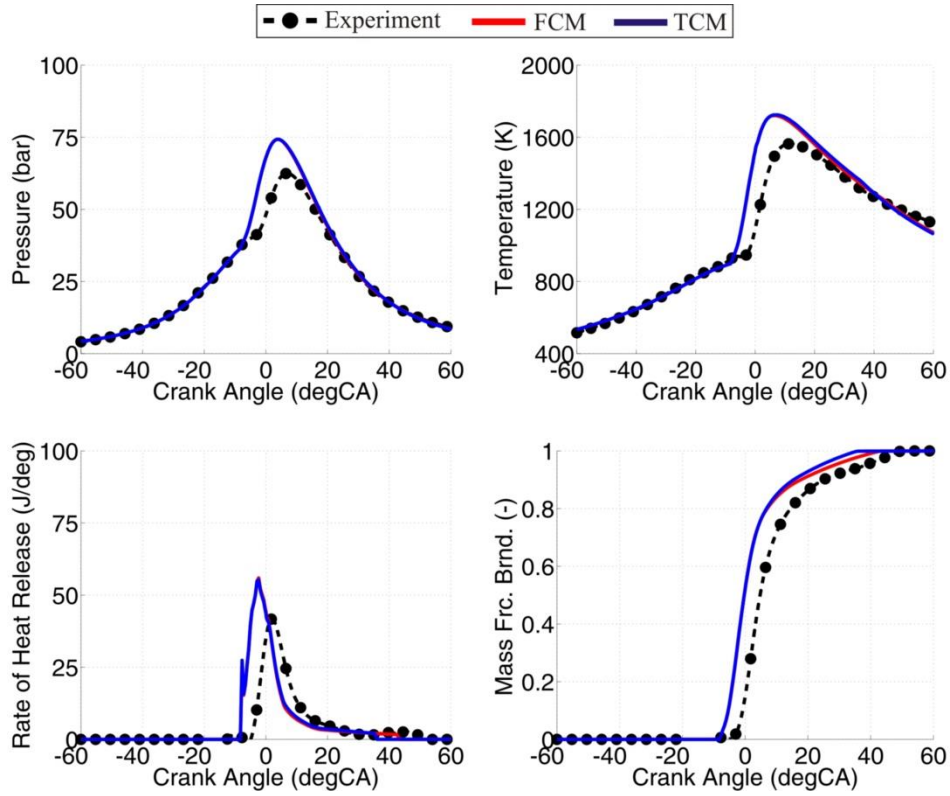


**Figure 196.** Comparison between the measured and simulated in-cylinder pressure, temperature, ROHR and MFB traces for OP6 at 1800 rpm and the single set of all model parameters

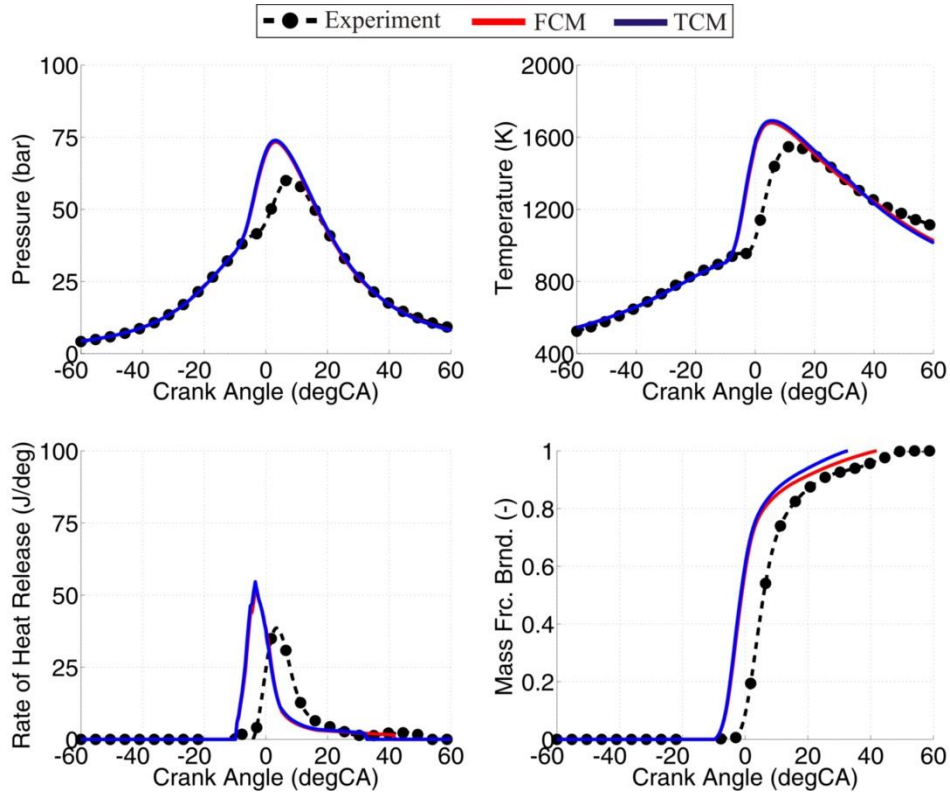


**Figure 197.** Comparison between the measured and simulated in-cylinder pressure, temperature, ROHR and MFB traces for OP7 at 1800 rpm and the single set of all model parameters

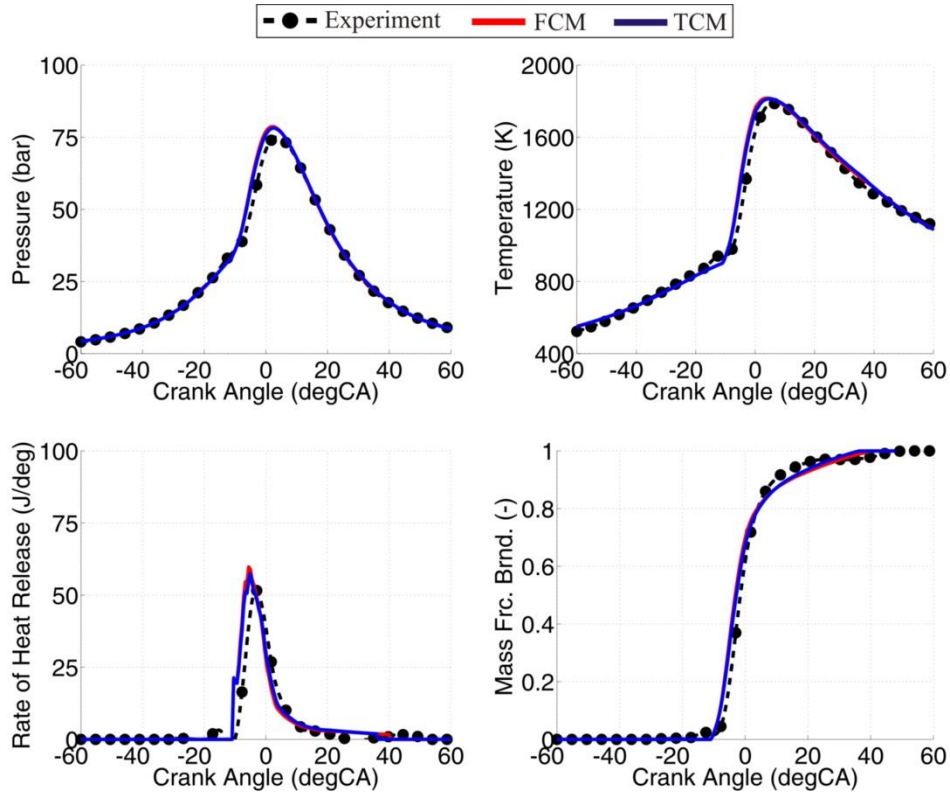


**Figure 198.** Comparison between the measured and simulated in-cylinder pressure, temperature, ROHR and MFB traces for OP8 at 1800 rpm and the single set of all model parameters

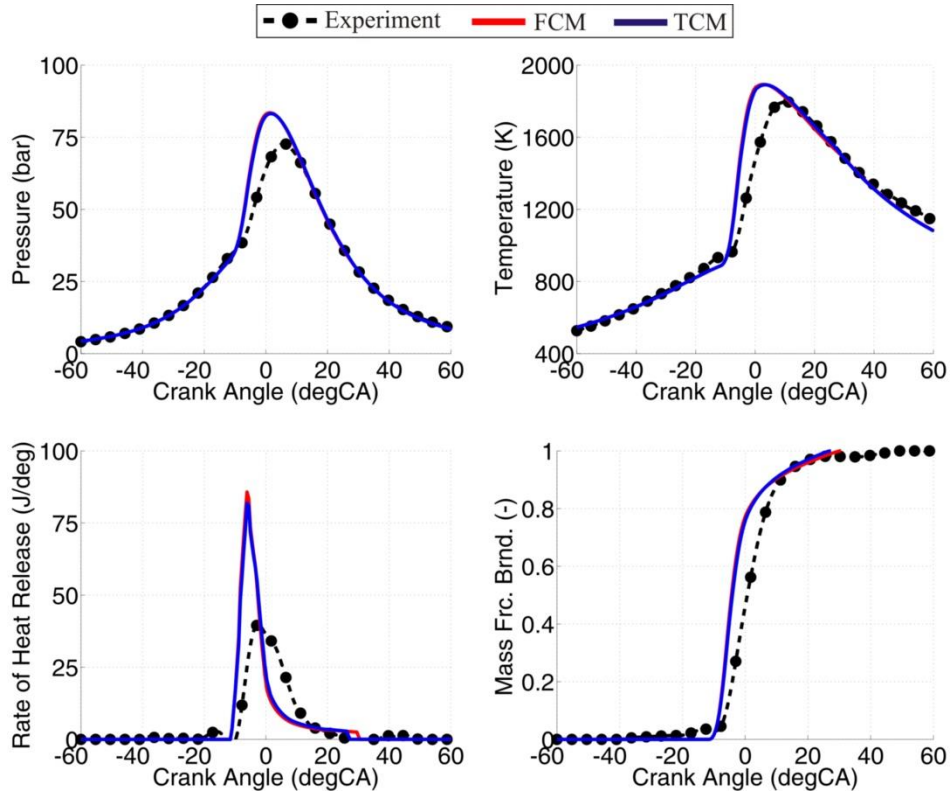


**Figure 199.** Comparison between the measured and simulated in-cylinder pressure, temperature, ROHR and MFB traces for OP9 at 1800 rpm and the single set of all model parameters

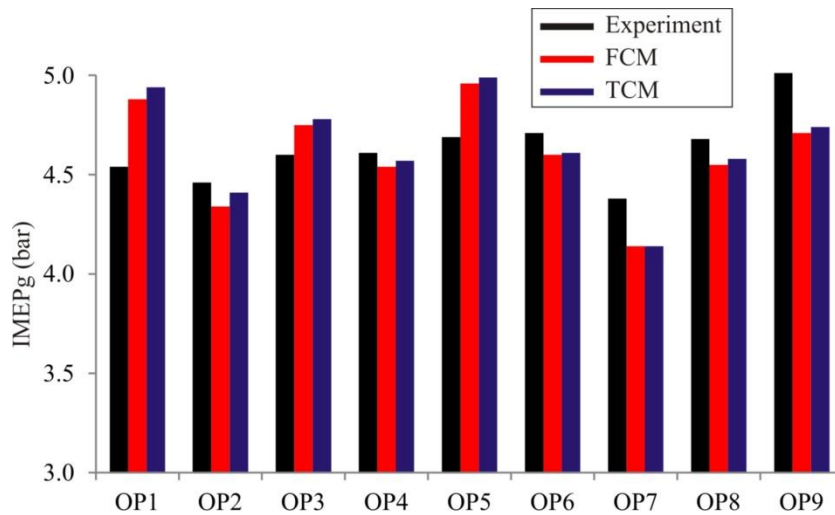


**Figure 200. Comparison between the measured and simulated IMEPg for the operating points that were simulated with the single set of all model parameters**

Figure 200 represents the comparison between the measured and simulated IMEPg, for the nine (9) operating points that are presented in this chapter. For all nine (9) simulated operating points the fit between the measured and simulated IMEPg is reasonable and it can be seen that most of the trends in the IMEPg are reasonably captured.

It is interesting to notice that the results that were obtained at 1000 rpm (OP1 and OP2) are considerably better than the results that were obtained at 1800 rpm (OP3 – OP9). Part of the reason for this could lie in the more pronounced overall temperature and mixture stratification at 1800 rpm. Temperature and mixture stratification inside the premixed (unburned) zone has a profound influence on both the flame propagation and spray processes. The premixed zone heterogeneity influences the spray through the premixed mass entrainment into the spray region. For instance, slightly warmer and fuel richer mass that is entrained into the spray region could lead to a shorter ignition delay and advanced ignition and combustion phasing. Such a change could also have a profound influence on the location where the flame propagation starts. Moreover, this could also have a profound influence on the size of the initial flame kernel thus changing the duration of the transition to the fully premixed turbulent flame.



## 5. Application of the 0-D dual fuel model

In this chapter, the application of the newly developed DFMZCM is presented. The DFMZCM can be applied to study the phenomenon of the conventional dual fuel combustion. Specifically, to study the effect of various geometry and operating parameters on the combustion profile and on the harmful exhaust gas emissions from a conventional dual fuel engine.

The DFMZCM can also be used in the IC engine performance analysis simulations. In these simulations (cycle-simulations), the entire engine and its various systems are modeled in detail. These simulations are used to assess the entire engine cycle efficiency as well as to investigate the coupling between the various engine systems and the influence of the entire engine system on the combustion process itself. Moreover, cycle-simulations can be used to study various operating and control settings of the engine; the example of such analyses can be found in [21], [36], [37].

In the first part of this chapter a single-cylinder engine model (pre-set SHP conditions) was used to study the effect of the geometry and operating parameters on the conventional dual fuel engine performance and harmful exhaust gas emissions. In the second part of this chapter the analysis regarding the effect of the start of injection timing  $a$  on the cycle efficiency and exhaust gas emissions of a full conventional dual fuel engine is presented. In this analysis, the entire engine (full model) that features a detailed description of the entire intake and exhaust flow path, as well as the variable geometry turbocharger, and the intake air cooling was simulated. The full engine simulation model that features various control elements was created and calculated with the AVL Boost, while the conventional dual fuel combustion process in the cylinder was calculated with the AVL CruiseM.

Before presenting the simulation results it is important to stress out a couple of important notices regarding the exhaust gas emissions predictions. In this chapter only the exhaust gas emissions that are calculated with the predictive emission models will be given ( $\text{NO}_x$ , CO and soot). Since the CO and  $\text{NO}_x$  emissions were experimentally measured, the parameters of respective emission models were adjusted to obtain a good fit between the measured and simulated emissions. Since the soot emissions were not directly measured, soot emissions are modeled with a default set of parameters. The general trends (load, efficiency and emissions) that are reported in the next two chapters should be viewed in a qualitative way.

## **5.1. The effect of the engine geometry and of the operating settings on the performance and exhaust gas emissions**

In this chapter the effect of the conventional dual fuel engine geometry and operating parameters on the combustion, performance and harmful exhaust gas emissions is presented. These analyses and simulations were performed to assess the ability of the DFMZCM to follows certain geometrically and operationally defined combustion and harmful exhaust gas emissions trends.

Therefore, in this chapter the effect of the following parameters on the dual fuel combustion process is presented:

1. Compression ratio;
2. Intake pressure;
3. Intake temperature;
4. Direct fuel (Diesel fuel) injection rail pressure;
5. Direct fuel (Diesel fuel) injection timing;
6. Diesel fuel substitution ratio (Diesel fuel mass);
7. Mass fraction of the combustion products at the start of the high-pressure cycle (the intake valve closure moment).

In the simulation results presented in this chapter, the original base operating point whose operating parameters are given in Table 12 was used as the base case point. In all of the simulations that are presented in this chapter the single set of parameters was used. The in-cylinder turbulence was modeled with the parameters that are given in Table 13. The spray combustion model parameters that were used in these simulations are given in Table 14. The flame propagation through the premixed mixture was modeled TCM, and the flame propagation model parameters can be found in Table 15. The simulations were made on a single cylinder engine model that was created in the AVL CruiseM (Figure 105) with the pre-set SHP conditions (Table 12).

### **5.1.1. The effect of change in the compression ratio**

In this section, the effect of change in the engine's compression ratio on the base operating point of a conventional dual fuel engine is presented. The base engine model has a compression ratio of 15.5, while the two (2) additional simulations were performed with the compression ratio of 13 and 18. As the compression ratio changes, the mass of fresh charge that enters the combustion chamber changes as well. Therefore, to keep the same level of

input energy into the cylinder the methane mass as well as the Diesel fuel mass was kept at the same level (Table 12), which resulted in small changes in excess air ratio.

Figure 201 represents the comparison between the simulated in-cylinder pressure, temperature, ROHR and mass of the Diesel fuel vapor inside the spray region for the three (3) different compression ratios. Figure 202 represents the comparison between the simulated emissions, ignition delay and combustion phasing (CA50) for the three (3) different compression ratios. Table 36 represents the comparison between the engine output parameters for the three (3) different simulated compression ratios cases.

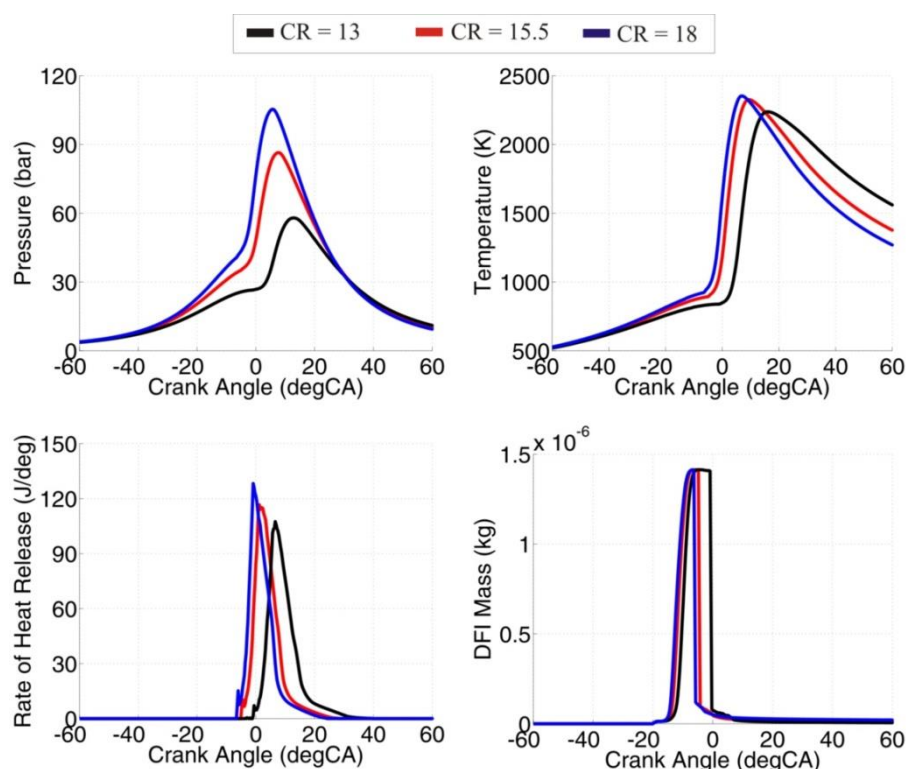


**Figure 201.** Comparison between the simulated in-cylinder pressure, temperature, ROHR and DFI mass traces for the three different compression ratios

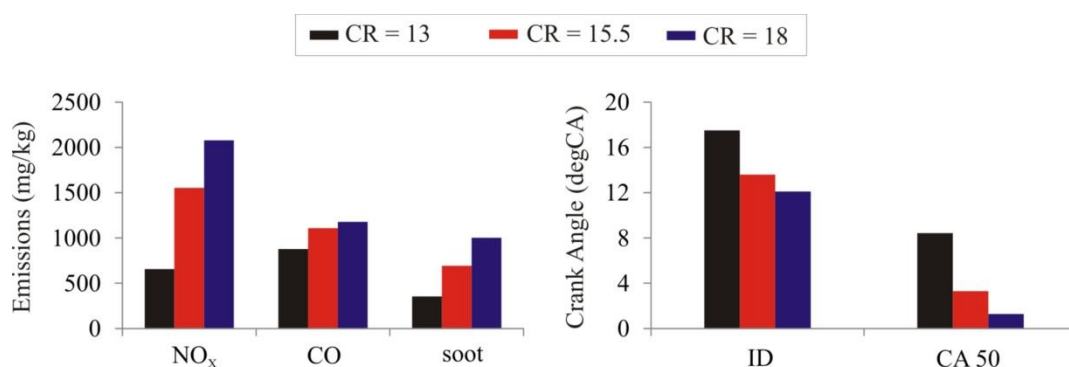


**Figure 202.** Comparison between the simulated emissions, ignition delay time and combustion phasing (CA50) for the three different compression ratios

**Table 36. Comparison between the engine output parameters for the three different simulated compression ratios cases**

Parameter	CR = 13	CR = 15.5	CR = 18
IMEPg (bar)	7.2	7	6.7
Indicated Efficiency (%)	35.4	34.7	33.1
Total Excess air Ratio (-)	1.29	1.26	1.24

As can be seen from the Figure 201, as the compression ratio is increased the pressure and temperature inside the cylinder increase, which enhances the fuel evaporation rate. As a result of the enhanced evaporation rate and the higher in-cylinder pressure and temperature the ignition delay (Figure 202) shortens. The combination of the shorter ignition delay and enhanced laminar flame speed due to the higher in-cylinder temperature (Figure 201) and lower excess air ratio (Table 36), lead to the advance in the combustion phasing (Figure 202). Since the higher compression ratio leads to an increase of the in-cylinder temperature, the NO<sub>x</sub> emissions increase. Likewise, due to a decrease of the excess air ratio the soot and CO emissions also increase with the increase of compression ratio.

As the compression ratio is increased the output load and efficiency decrease. This is a result of the advance of the combustion phasing which leads to the higher in-cylinder temperature and higher associated heat transfer losses, which then lower the final engine output power and efficiency.

### 5.1.2. The effect of the change in the intake pressure

In this section, the effect of the change in the intake pressure on the base operating point of the conventional dual fuel engine is presented. The base engine point has an intake pressure of 1 bar and therefore two (2) additional simulations with the intake pressure of 1.5 bar and 2 bar were performed. As the intake pressure changes, the mass of the fresh charge that enters the combustion chamber changes as well. Therefore, to keep the same amount of the input energy into the cylinder the methane mass as well as the Diesel fuel mass were kept at the same level (Table 12), which resulted in changes in excess air ratio, as can be seen in Table 37..

Figure 203 represents the comparison between the simulated in-cylinder pressure, temperature, ROHR, mass of Diesel fuel vapor inside the spray region, liquid fuel SMD inside the spray region and the laminar flame velocity for the three (3) different intake pressure levels. Figure 204 represents the comparison between the simulated emissions, ignition delay and combustion phasing (CA50) for the three (3) different intake pressure

levels. Table 37 represents the comparison between some of the engine output performance parameters for the three (3) different simulated intake pressure levels.

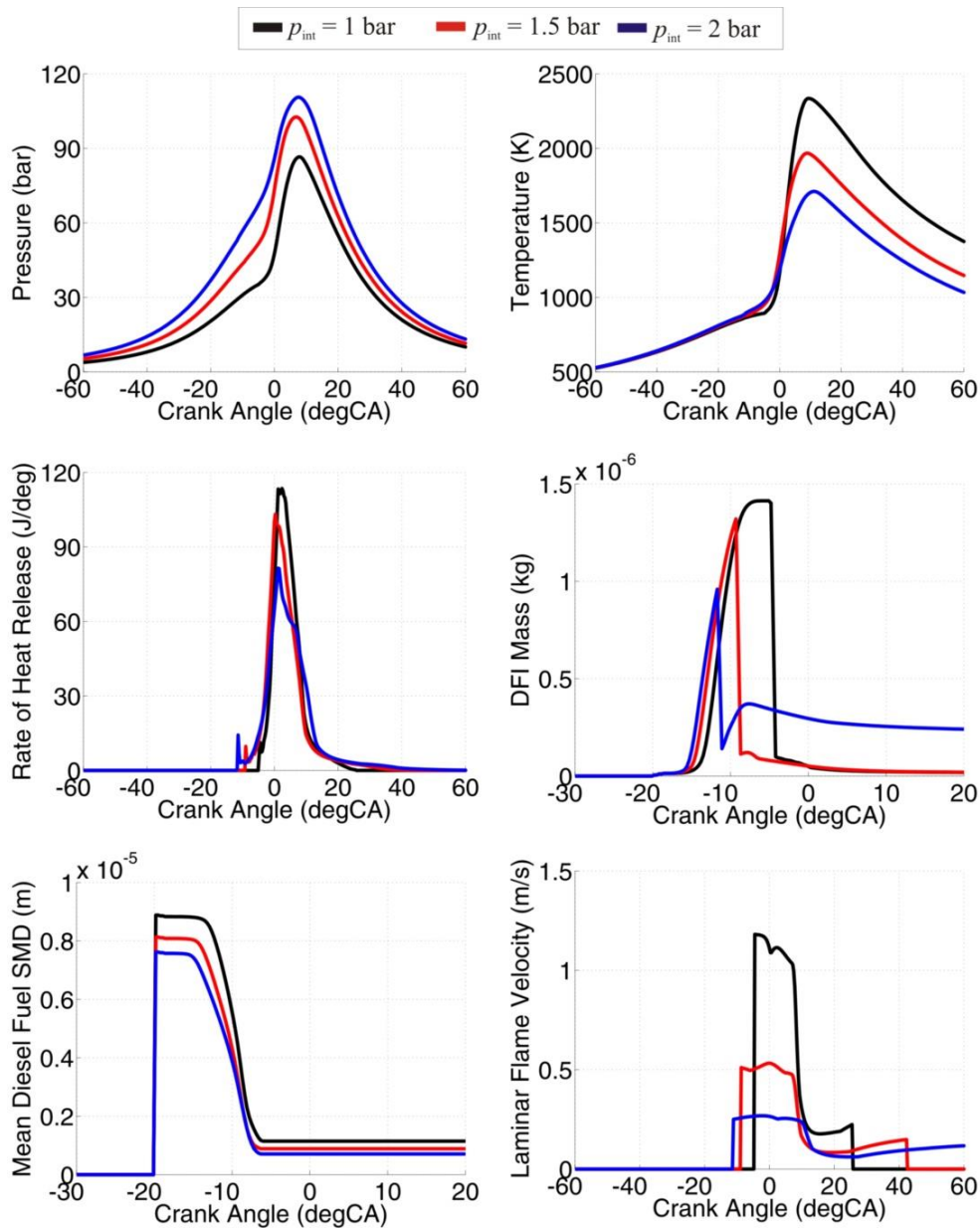


**Figure 203. Comparison between the simulated in-cylinder pressure, temperature, ROHR, DFI mass, liquid fuel SMD and laminar flame velocity traces for the three different intake pressure levels**

As can be seen from the Figure 203, as the intake pressures is increased, the pressure and density inside the cylinder increase, which enhances the liquid fuel break-up and hence increases the fuel evaporation rate. As the result of the enhanced evaporation rate and the higher in-cylinder pressure the ignition delay (Figure 204) decreases. Even though the start of combustion is advanced, due to the slightly slower flame propagation, the combustion intensity decreases and the combustion phasing (CA50) stays approximately the same, while

the combustion duration increases. Slower flame propagation is a result of the increase of the excess air ratio as the intake pressure is increased (Table 37), which also causes a decrease of the in-cylinder temperature (Figure 203).

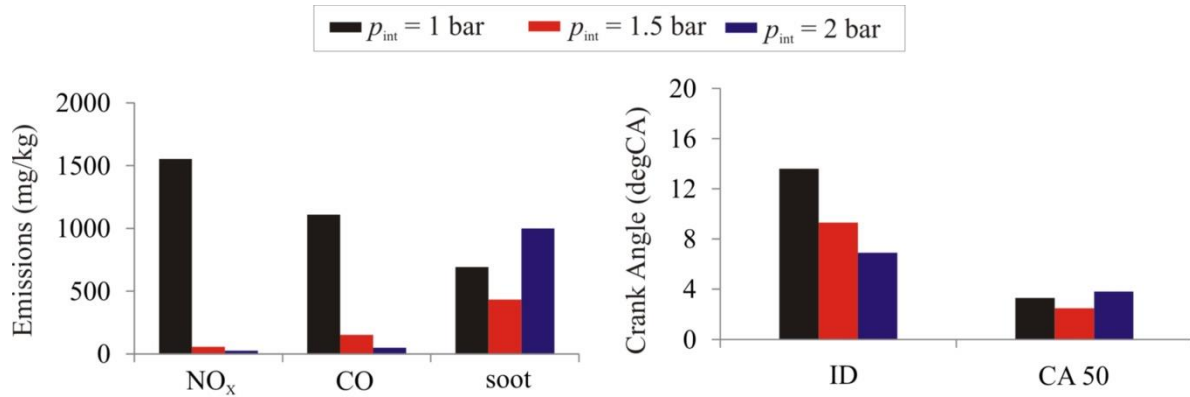


**Figure 204.** Comparison between the simulated emissions, ignition delay time and combustion phasing (CA50) for the three different intake pressure levels

**Table 37.** Comparison between the engine output parameters for the three different simulated intake pressure levels

Parameter	$p_{int} = 1 \text{ bar}$	$p_{int} = 1.5 \text{ bar}$	$p_{int} = 2 \text{ bar}$
IMEPg (bar)	7	7.07	7.13
Indicated Efficiency (%)	34.7	34.9	35.1
Total Excess air Ratio (-)	1.26	1.77	2.27
Premixed Charge (Methane) Excess air Ratio (-)	1.34	1.88	2.42

Since the in-cylinder temperature decreases as the intake pressure is increased, the NO<sub>x</sub> emissions decrease. Likewise, due to the increase of the excess air ratio the CO emissions also decrease as the compression ratio is increased. Interesting thing happens with the soot emissions. As the intake pressure increases from 1 bar to 1.5 bar, the soot emissions decrease due to the higher availability of the air inside the cylinder (increase of the excess air ratio). However, as the intake pressure is further increased to 2 bar, there is a sharp increase of the soot emissions. This is a result of the fact that at the moment of ignition, there is still relatively large quantity of the liquid fuel (Figure 203 – middle right). As this fuel evaporates it is surrounded by the combustion products of both spray combustion and flame propagation. Therefore, this Diesel fuel is surrounded by the mixture that has significantly smaller amount of available air, and hence it burns in a rich combustion mode which is favorable for the soot formation.

As the intake pressure is increased the output load and efficiency increase. This is mainly a result of the lower in-cylinder temperature and lower associated heat transfer losses, which increase the final engine output load and efficiency.

### 5.1.3. The effect of the change in the intake temperature

In this section, the effect of change in the intake temperature of the conventional dual fuel engine is presented, on the base operating point. The base engine operating point has an intake temperature of 45°C and therefore two (2) additional simulations with the intake temperature of 25°C and 65°C were performed. As the intake temperature changes, the mass of the fresh charge that enters the combustion chamber changes as well. Therefore, to keep the same amount of the input energy into the cylinder, the methane mass as well as the Diesel fuel mass was kept at the same level (Table 12), which resulted in changes in excess air ratio.

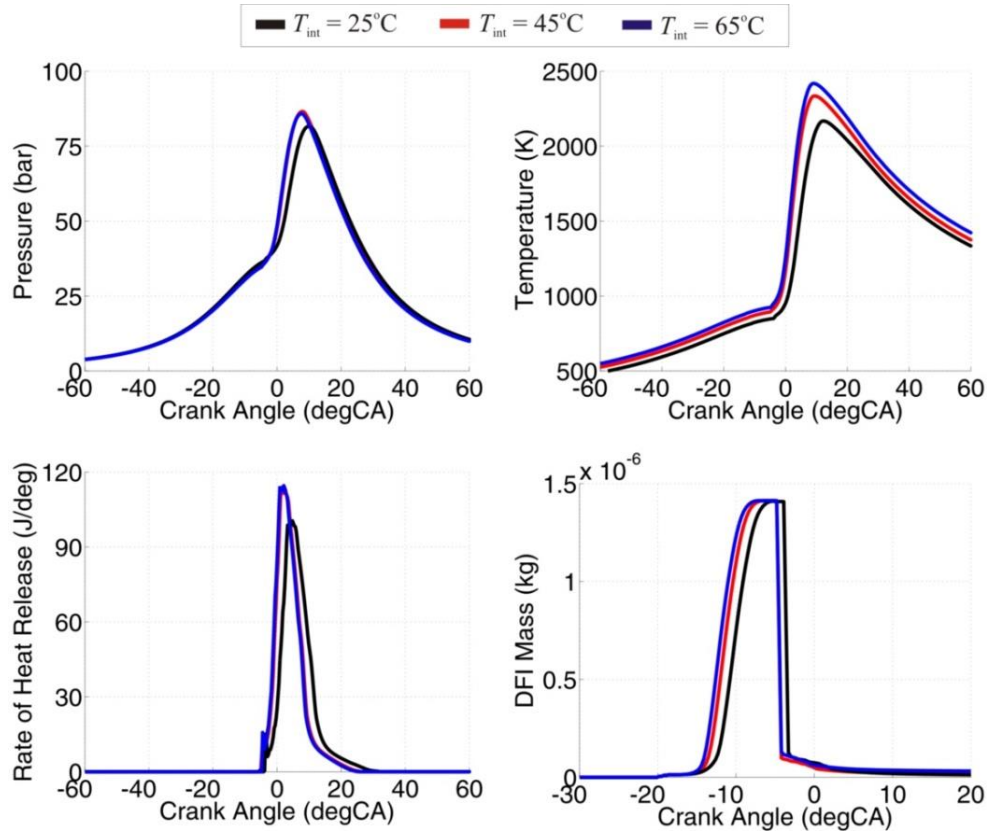


**Figure 205. Comparison between the simulated in-cylinder pressure, temperature, ROHR and DFI mass traces for the three different intake temperature levels**

Figure 205 represents the comparison between the simulated in-cylinder pressure, temperature, ROHR and mass of the Diesel fuel vapor inside the spray region for the three (3) different intake temperature levels. Figure 206 represents the comparison between the simulated emissions, ignition delay and combustion phasing (CA50) for the three different

intake temperature levels, while Table 38 represents the comparison between some of the engine output performance parameters for the three different simulated intake temperature levels.

**Table 38. Comparison between the engine output parameters for the three different simulated intake temperature levels**

Parameter	$T_{\text{int}} = 25^{\circ}\text{C}$	$T_{\text{int}} = 45^{\circ}\text{C}$	$T_{\text{int}} = 65^{\circ}\text{C}$
IMEPg (bar)	7.36	7	6.9
Indicated Efficiency (%)	36.3	34.7	34
Total Excess air Ratio (-)	1.37	1.26	1.19

As can be seen from the Figure 205, as the intake temperature is increased the temperature inside the cylinder increases, which enhances the fuel evaporation rate. As the result of the enhanced evaporation rate and higher in-cylinder temperature the ignition delay (Figure 206) decreases. The combination of the shorter ignition delay and enhanced laminar flame speed due to higher temperature (Figure 205) and lower excess air ratio (Table 38), leads to the advance of the combustion phasing (Figure 206). Figure 205 also reveals that this effect (evaporation rate enhancement) is more pronounced during the initial intake temperature increase (from  $25^{\circ}\text{C}$  to  $45^{\circ}\text{C}$ ). Therefore, the ignition delay decrease and combustion phase advancement is more pronounced for this initial intake temperature increase (from  $25^{\circ}\text{C}$  to  $45^{\circ}\text{C}$ ).

Since the increase of the intake temperature leads to an increase of the in-cylinder peak temperature, the  $\text{NO}_x$  emissions increase. Likewise, due to a decrease of the excess air ratio the soot and CO emissions also increase as the intake temperature is increased.

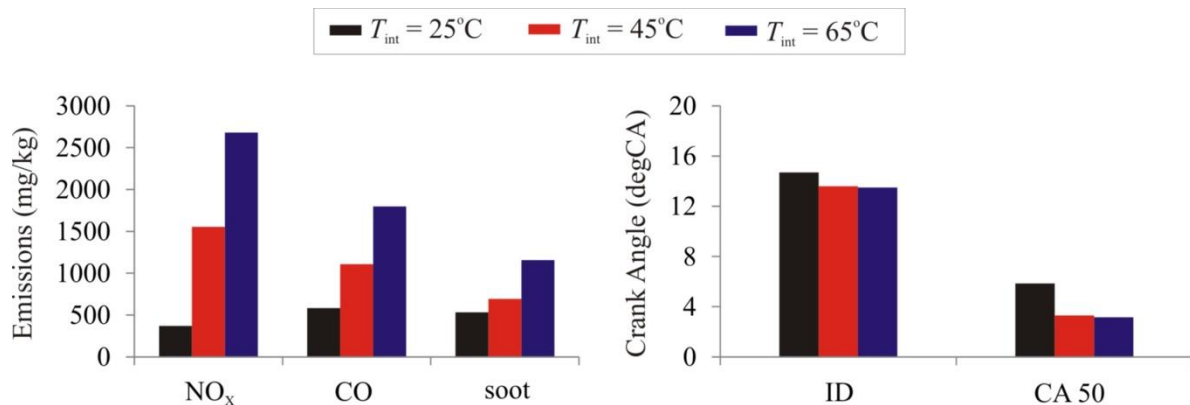


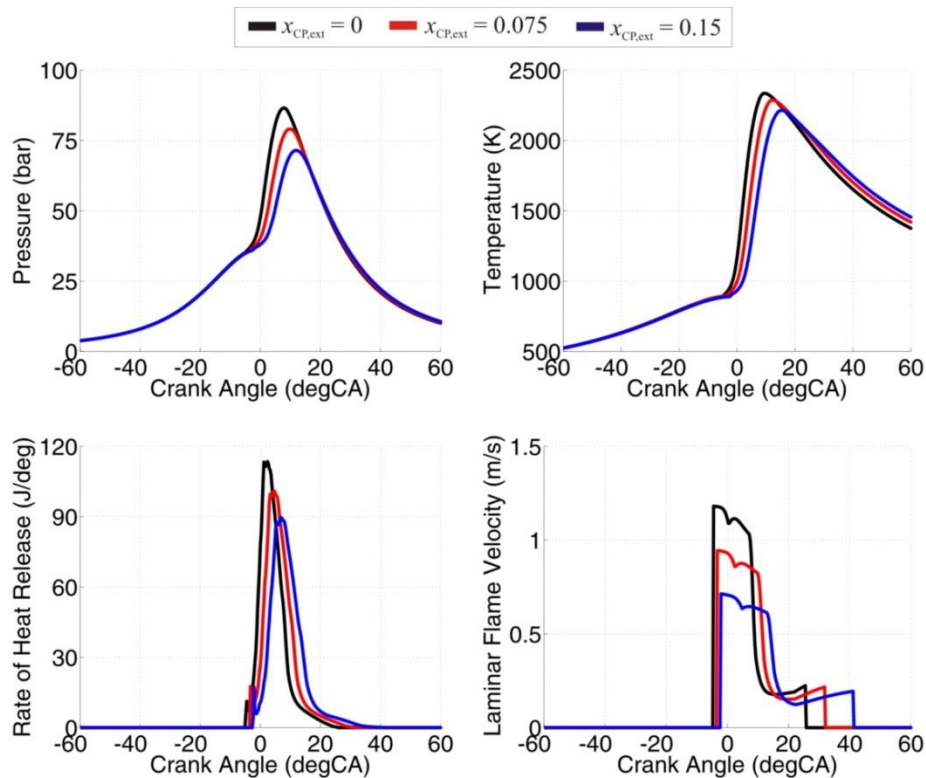
**Figure 206. Comparison between the simulated emissions, ignition delay time and combustion phasing (CA50) for the three different intake temperature levels**



As the intake temperature is increased the output load and efficiency decrease. This is a result of the advance of the combustion phasing which leads to higher in-cylinder temperature and higher associated heat transfer losses, which then lowers the final engine output power and efficiency.

#### 5.1.4. The effect of the change in the mass fraction of combustion products at the start of high pressure cycle

In this section, the effect of change in the mass fraction of the combustion products at the intake valve closure (IVC) on the conventional dual fuel engine, at base operating point, is presented. The base engine model has an external mass fraction of combustion products (can be seen as EGR) of 0 and therefore two (2) additional simulations with the external mass fraction of combustion products of 0.075 and 0.15 were performed. As the mass fraction of the combustion products at the IVC changes, the mass of fresh charge that enters the combustion chamber changes as well. Therefore, to keep the same amount of the input energy into the cylinder the methane mass as well as the Diesel fuel mass was kept at the same level (Table 12), which resulted in changes in excess air ratio.



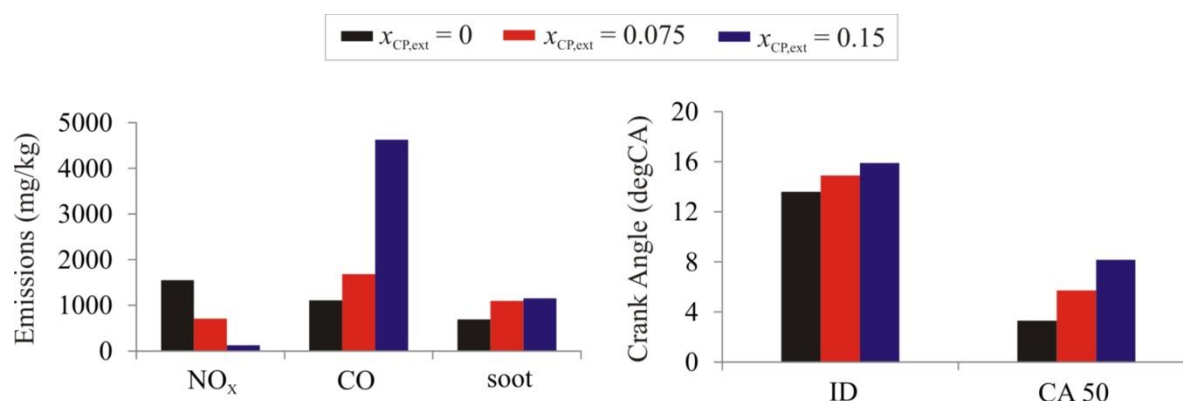
**Figure 207. Comparison between the simulated in-cylinder pressure, temperature, ROHR and the laminar flame velocity traces for the three cases that feature different mass fraction of the combustion products at the IVC**

Figure 207 represents the comparison between the simulated in-cylinder pressure, temperature, ROHR and the laminar flame velocity traces for the three (3) cases that feature different mass fractions of the combustion products at the IVC.

Table 39 represents the comparison between some of the engine output performance parameters for the three (3) cases that feature different mass fraction of the combustion products at the IVC. Figure 208 represents the comparison between the simulated emissions, ignition delay and combustion phasing (CA50) for the three (3) cases that feature different mass fraction of the combustion products at the IVC.

**Table 39. Comparison between the engine output parameters for the three cases that feature different mass fraction of the combustion products at the IVC**

Parameter	$x_{CP,ext} = 0$	$x_{CP,ext} = 0.075$	$x_{CP,ext} = 0.15$
IMEPg (bar)	7	7.12	7.21
Indicated Efficiency (%)	34.7	35.1	35.5
Total Excess air Ratio (-)	1.26	1.14	1.05



**Figure 208. Comparison between the simulated emissions, ignition delay time and combustion phasing (CA50) for the three cases that feature different mass fraction of the combustion products at the IVC**

As can be seen from the Figure 207, as the mass fraction of the combustion products at the IVC is increased the pressure and temperature around the TDC are slightly decreased. This decrease in combination with the decreased mixture reactivity due to an increase of the inert species inside the mixture, leads to an increase in the ignition delay (Table 39). The combination of the longer ignition delay and decreased laminar flame speed due to the decreased mixture reactivity (Figure 207), leads to the decrease in the combustion intensity and eventually to the prolonged combustion duration and retarded combustion phasing (Figure 207). Consequently, due to less intense combustion and the existence of larger quantity of inert gases inside the mixture, the in-cylinder temperature decreases and this

causes the decrease of the NO<sub>x</sub> emissions. On the contrary due to a decrease of the excess air ratio the soot and CO emissions increase as the mass fraction of the combustion products at the IVC is increased (Figure 208).

As the mass fraction of the combustion products at the IVC is increased the output power and efficiency increase. This is a result of the retarded combustion phasing and lower in-cylinder temperature which lead to the lower heat transfer losses. This in the end leads to the higher final engine output power and efficiency.

### 5.1.5. The effect of change in the direct fuel injection timing

In this section, the effect of change in the direct fuel injection timing of conventional dual fuel engine, at base operating point is presented. The base engine operating point has the direct fuel injection timing of 20 degCA before top dead center (bTDC) (SOI B). Therefore five (5) additional simulations with the direct fuel injection timing of 10 degCA bTDC (SOI 1), 30 degCA bTDC (SOI 2), 40 degCA bTDC (SOI 3), 50 degCA bTDC (SOI 4) and 60 degCA bTDC (SOI 5) were performed. The other operating parameters of the simulated cases can be found in the Table 12 (pressure and temperature at the IVC, direct injection pressure, referent fuel masses, etc.).

Figure 209 represents the comparison between the simulated emissions, ignition delay and combustion phasing (CA50) for the six (6) cases that feature different direct fuel injection timing. Table 40 represents the comparison between the engine output parameters for the six (6) cases that feature different direct fuel injection timing.

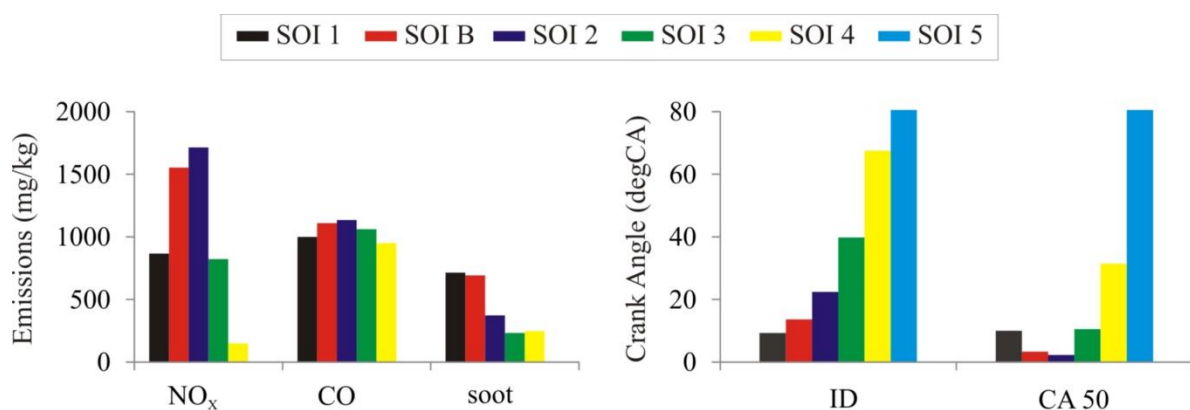


**Figure 209. Comparison between the simulated emissions, ignition delay time and combustion phasing (CA50) for the six cases that feature different direct fuel injection timing**

**Table 40. Comparison between the engine output parameters for the six cases that feature different direct fuel injection timing**

Parameter	<i>SOI 1</i>	<i>SOI B</i>	<i>SOI 2</i>	<i>SOI 3</i>	<i>SOI 4</i>	<i>SOI 5</i>
IMEPg (bar)	7.36	7	6.94	7.38	6.2	-0.5
Indicated Efficiency (%)	36.3	34.7	34.2	36.4	30.5	0
Total Excess air Ratio (-)	1.26	1.26	1.26	1.26	1.26	1.26

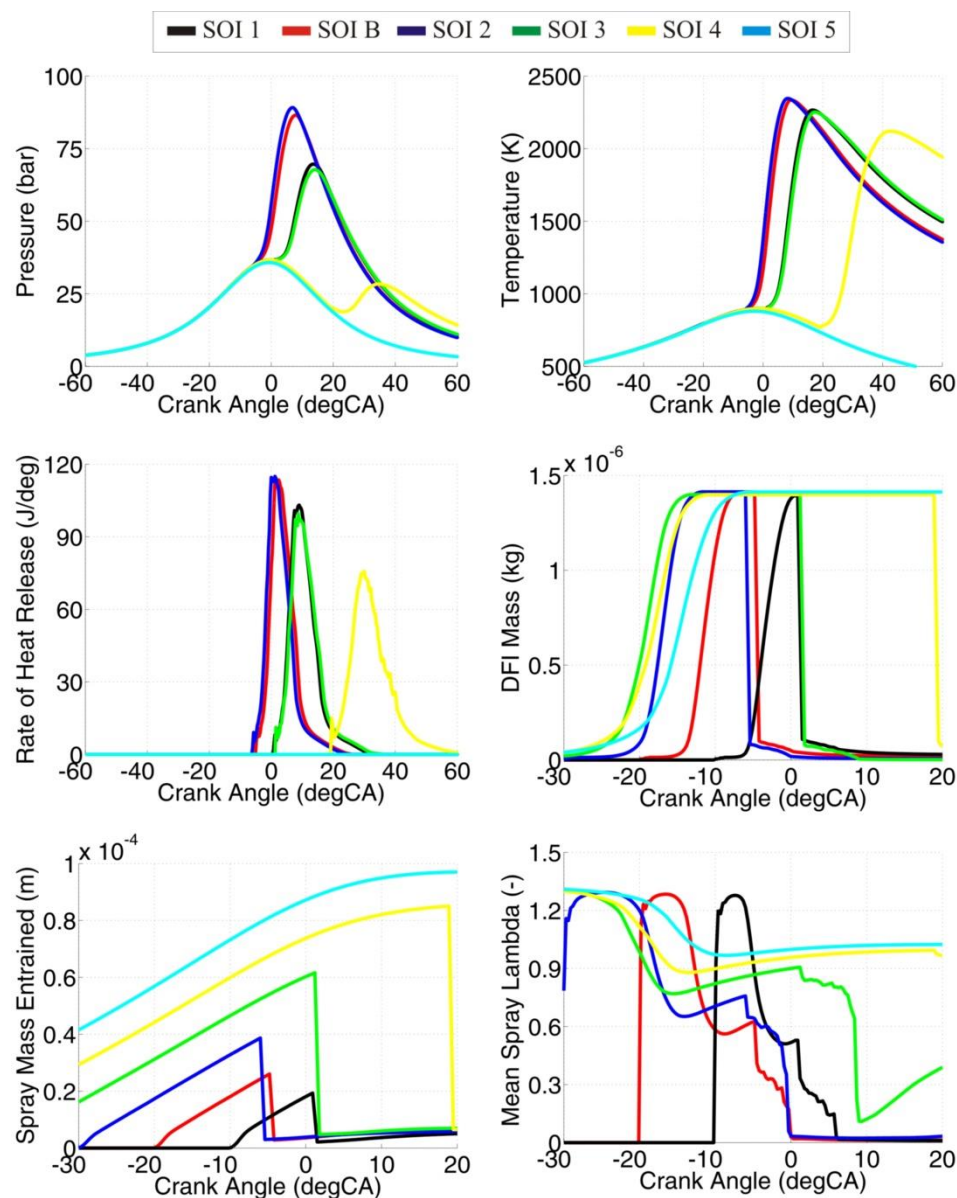


**Figure 210. Comparison between the simulated in-cylinder pressure, temperature, ROHR, DFI mass, entrained mass and mean spray excess air ratio traces for the six cases that feature different direct fuel injection timing**

Figure 210 represents the comparison between the simulated in-cylinder pressure, temperature, ROHR, mass of the Diesel fuel vapor inside the spray region, the premixed charge mass that has been entrained into the spray region and the excess air ratio inside the

spray region traces for the six (6) cases that feature different direct fuel injection timing. As can be seen from the Figure 210, the change in the direct fuel injection timing has a profound effect on the dual fuel combustion process as well as on the engine performance (Table 40) and on the harmful exhaust gas emissions (Figure 209).

As the direct fuel injection timing is retarded from the 20 deg CA bTDC (SOI B) to the 10 degCA bTDC (SOI 1), the ignition delay decreases as a result of the fact that the fuel is injected into the warmer mixture, which enhances the evaporation rate and increases the mixture reactivity. Due to a later injection timing, the combustion phasing is retarded which causes a decrease of the peak in-cylinder temperature and consequently lowers the NO<sub>x</sub> emissions (Figure 209). The CO emissions stay approximately the same, while the soot emissions increase slightly due to decreased excess air ratio inside the spray region. The excess air ratio inside the spray region decreases as the injection timing is retarded due to a shorter amount of the available mixing time prior to the ignition (shorter ignition delay).

As the direct fuel injection timing is retarded from the 20 deg CA bTDC (SOI B) to the 10 degCA bTDC (SOI 1) the output power and efficiency increase. This is a result of the retarded combustion phasing and lower in-cylinder temperature which lead to the lower heat transfer losses. This in the end leads to the higher final engine output power and efficiency.

As the combustion timing is advanced from 20 degCA bTDC to 30, 40, 50 and 60 degCA bTDC, the ignition delay gradually increases (Figure 209). The increase in the ignition delay is caused by the fact that the fuel is injected into the colder mixture which reduces the evaporation rate. As the spray process goes on, more and more premixed mixture is entrained into the spray region (Figure 209), which leads to an increase in the methane to Diesel fuel ratio inside the spray region and additional decrease of the mixture reactivity (longer ignition delay). It can be seen that eventually at 60 degCA bTDC (SOI 5) the mixture does not ignite at all.

It can also be seen (Figure 209) that the initial injection timing advance (from SOI B to SOI 2) slightly advances the combustion phasing, while further increase of the injection timing (from SOI 2 to SOI 3, SOI 4 and SOI 5) retards the combustion phasing. Advanced combustion phasing leads to the higher peak in-cylinder temperature and hence increases the NO<sub>x</sub> emissions and vice versa (Figure 209). CO emissions stay approximately the same for all injection timings. Slight oscillation is a result of the different mixture stratification inside the spray region from case to case. The soot emissions (Figure 209) generally decrease as the injection timing is advanced due to an increase in the ignition delay, which increases the

excess air ratio inside the spray region (Figure 210). Moreover, as the ignition delay is prolonged, larger amount of Diesel fuel is prepared for combustion in the ignition moment.

The engine output power and hence the engine output efficiency (Table 40) is a function of the combustion phasing. Generally, the load and efficiency increase as the combustion phasing is retarded. However, by pushing the combustion phasing too far into the expansion stroke the power and efficiency decrease.

#### 5.1.6. The effect of change in the direct fuel injection rail pressure

In this section, the effect of change in the direct fuel injection pressure of the conventional dual fuel engine for the base operating point is presented. The base engine operating point has the direct fuel injection pressure of 500 bar. Therefore, additional three (3) simulations with the direct fuel injection pressure of 250 bar, 750 bar and 1000 bar were performed. In order to keep the same amount of Diesel fuel mass that is directly injected into the cylinder, the injection duration was shortened as the injection pressure was increased (Table 41). It was assumed that the injection profile and discharge coefficient does not change with the injection pressure and therefore the fuel injection rate is the same for all injection pressures.

**Table 41. Duration of the direct fuel injection for a given direct fuel injection pressure**

Injection Pressure (bar)	Injection Duration (degCA)
250	2.1
500	1.5
750	1.2
1000	1

The other operating parameters of the simulated cases can be found in the Table 12 (pressure and temperature at the IVC, direct injection timing, referent fuel masses, etc.).

Figure 211 represents the comparison between the simulated in-cylinder pressure, temperature, ROHR, liquid fuel SMD inside the spray region, mass of the Diesel fuel vapor inside the spray region, the premixed charge mass that has been entrained into the spray region and the excess air ratio inside the spray region traces for the four (4) cases that feature different direct fuel injection pressure.

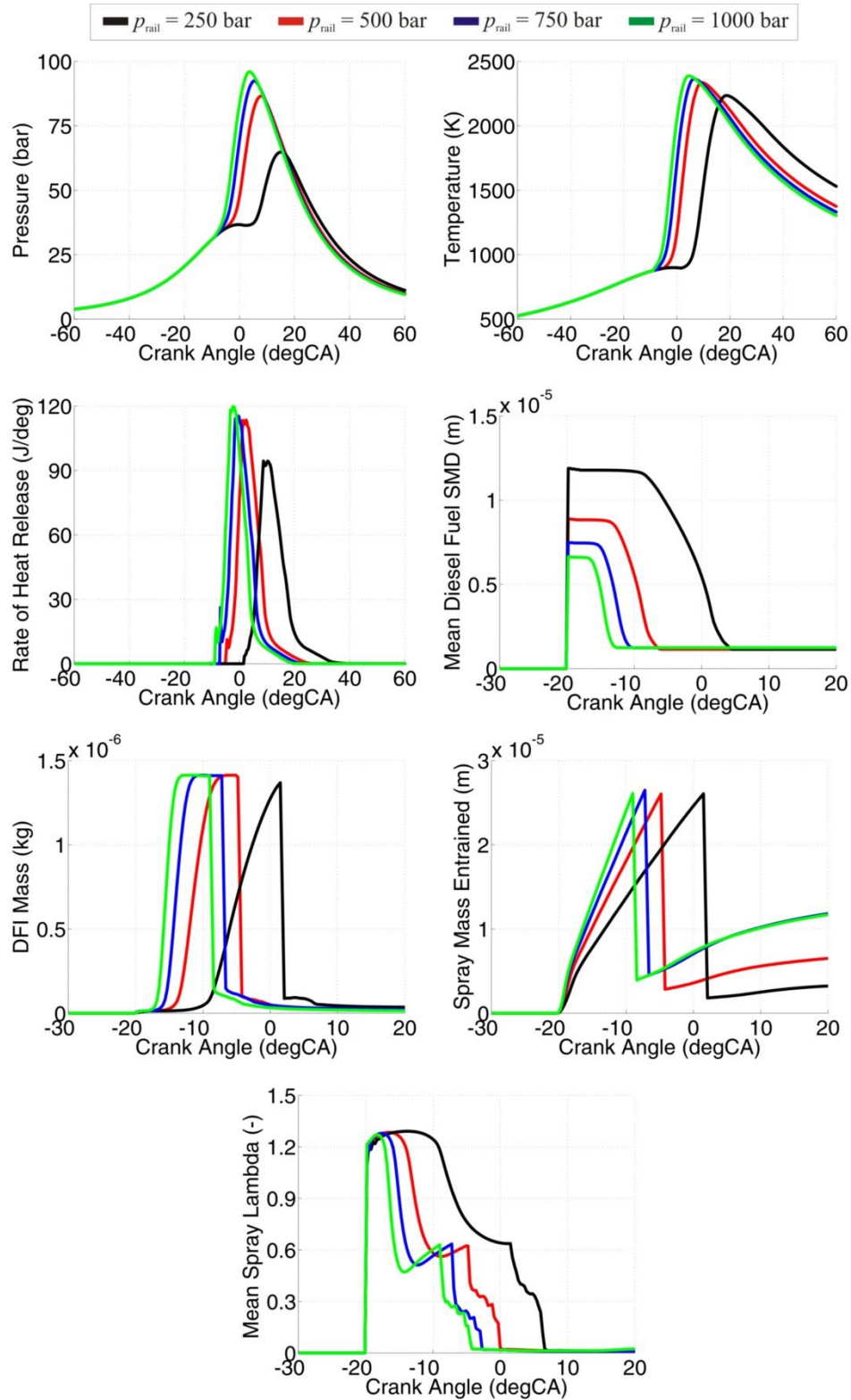


**Figure 211. Comparison between the simulated in-cylinder pressure, temperature, ROHR, liquid fuel SMD, DFI mass, entrained mass and mean spray excess air ratio traces for the four cases that feature different direct fuel injection pressure**

Figure 212 represents the comparison between the simulated emissions, ignition delay and combustion phasing (CA50) for the four (4) cases that feature different direct fuel injection



pressure, while Table 40 represents the comparison between some of the engine output performance parameters for the four cases that feature different direct fuel injection pressure.

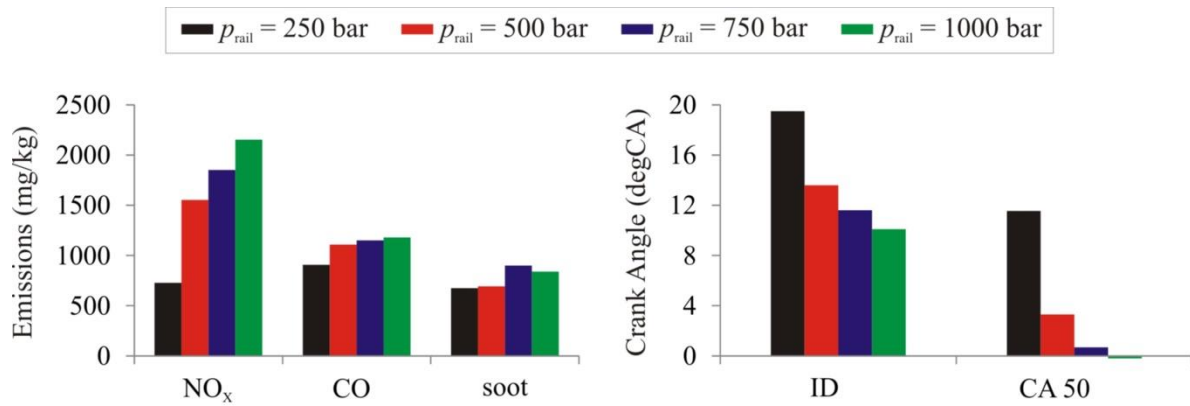


**Figure 212.** Comparison between the simulated emissions, ignition delay time and combustion phasing (CA50) for the four cases that feature different direct fuel injection pressure

**Table 42.** Comparison between the engine output parameters for the four cases that feature different direct fuel injection pressure

Parameter	$p_{\text{rail}} = 250$ bar	$p_{\text{rail}} = 500$ bar	$p_{\text{rail}} = 750$ bar	$p_{\text{rail}} = 1000$ bar
IMEPg (bar)	7.4	7	6.8	6.6
Indicated Efficiency (%)	36.3	34.7	33.4	32.3
Total Excess air Ratio (-)	1.26	1.26	1.26	1.26

As can be seen from the Figure 211, the change in the direct fuel injection pressure has a profound effect on the dual fuel combustion process as well as on the engine performance (Table 42) and harmful exhaust gas emissions (Figure 212).

As the direct fuel injection pressure is increased the liquid fuel break-up process is enhanced thus leading to the enhanced evaporation rate (Figure 211). Even though the premixed mass entrainment rate also increases as the injection pressure is increased, the more enhanced evaporation rate causes the ignition delay to decrease. It can be seen that the relative ignition delay decrease decreases as the injection pressure is increased (Figure 212). Shorter ignition delay pushes the combustion phasing to advanced crank angles thus increasing the peak in-cylinder temperature and NO<sub>x</sub> emissions (Figure 212).

Since the global excess air ratio is the same for all the cases, the CO emissions are roughly at the same level (Figure 212). Somewhat higher CO emissions for the higher injection pressure cases are a result of the faster temperature decrease in the expansion stroke (Figure 211) that freezes the CO to CO<sub>2</sub> oxidation process.



Soot emissions have an interesting trend. Even though the increase in the injection pressure increases the evaporation rate and should promote the mixture preparation, due to shorter ignition delay, at the moment of ignition the mean spray excess air ratio is roughly the same in all of the cases. Therefore, regardless of the injection pressure level the soot emissions are roughly the same. The oscillations in soot emissions (slightly higher for higher injection pressures) are merely a result of the slightly higher spray region that ignites in the first step which leads to more unburned fuel being trapped inside of the flame region where the fresh air availability is significantly lower. Moreover, as the injection pressure is increased the temperature decrease in the expansion stroke is more rapid (Figure 211) and therefore the soot oxidation process stops somewhat earlier.

The engine output power and hence the engine output efficiency (Table 42) is a function of the combustion phasing. For the given operating point, as the injection pressure is increased, combustion phasing advances and this leads to a decrease of the engine output power and efficiency.

#### 5.1.7. The effect of change in the Diesel fuel substitution ratio

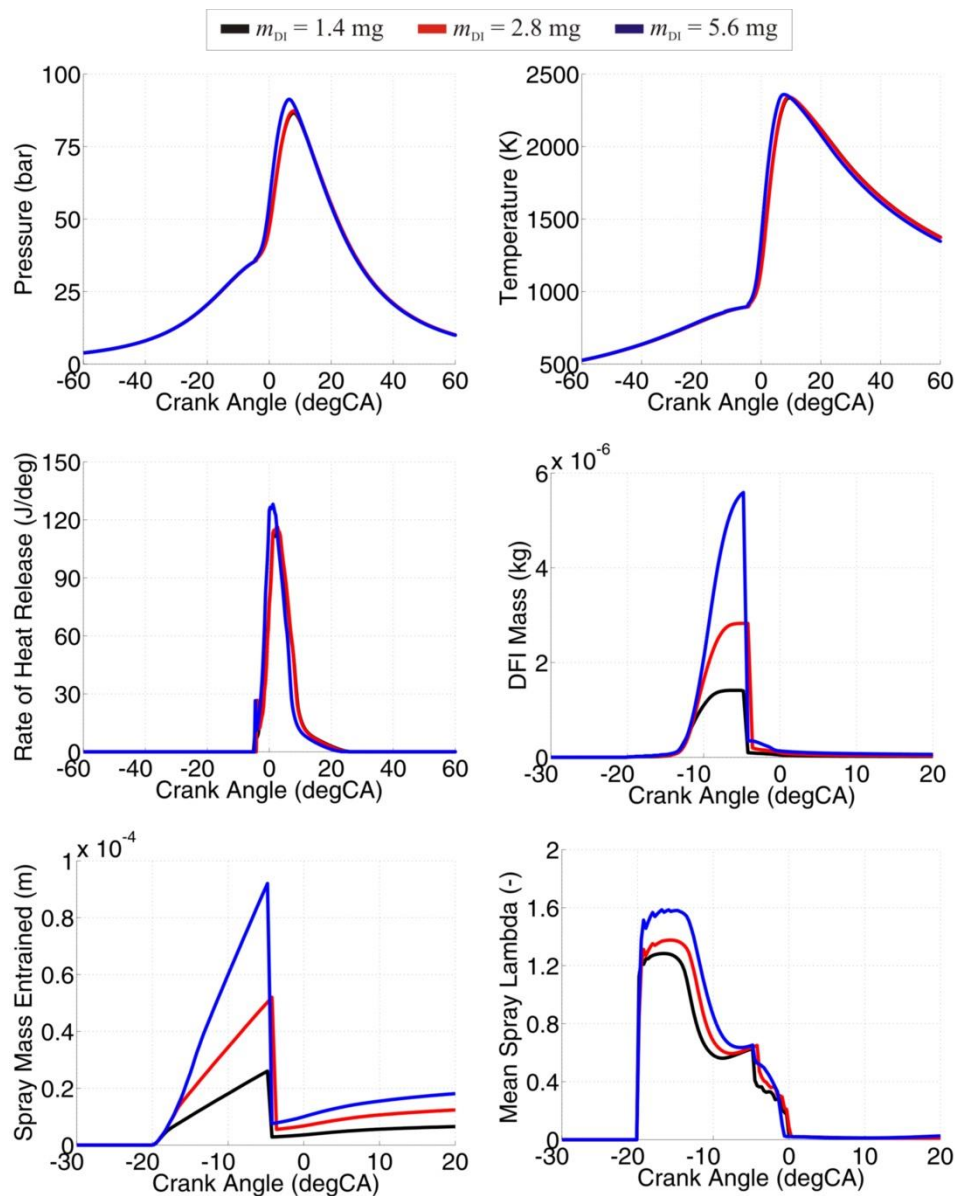
In this section, the effect of change in the Diesel fuel mass on the conventional dual fuel engine, at base operating point is presented. The base engine operating point has the Diesel fuel mass of 1.4 mg. Therefore two (2) additional simulations with the Diesel fuel mass of 2.8 mg and 5.6 mg were performed. In order to keep the same amount of the input energy into the cylinder and to keep the same injection rate (injection pressure), the injection duration was increased, while the methane mass was decreased (Table 43). It was assumed that the injection profile and discharge coefficient does not change with the Diesel fuel mass increase (injection duration increase).

**Table 43. Duration of the direct fuel injection for a given direct fuel injection pressure**

Diesel fuel mass (mg)	Injection Duration (degCA)	Methane mass (mg)	Diesel fuel substitution ratio – energy based (%)
1.4	1.5	18.76	94
2.8	3	17.58	88
5.6	6	15.19	76

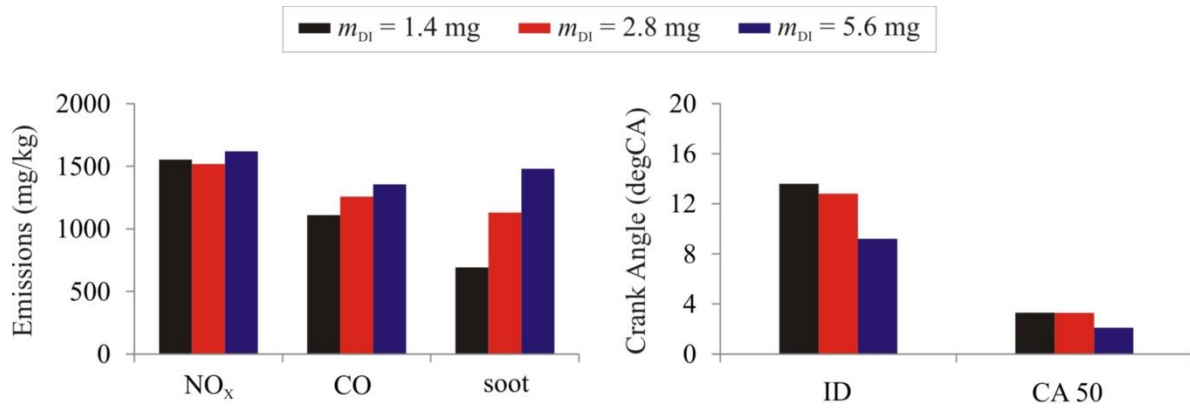
The other operating parameters of the simulated cases can be found in Table 12 (pressure and temperature at the IVC, direct injection pressure, referent fuel masses, etc.).

Figure 213 represents the comparison between the simulated in-cylinder pressure, temperature, ROHR, mass of the Diesel fuel vapor inside the spray region, the premixed charge mass that has been entrained into the spray region and the excess air ratio inside the spray region traces for the three (3) cases that feature different Diesel fuel substitution ratios.



**Figure 213. Comparison between the simulated in-cylinder pressure, temperature, ROHR, DFI mass, entrained mass and mean spray excess air ratio traces for the three cases that feature different Diesel fuel substitution ratio**

Figure 214 represents the comparison between the simulated emissions, ignition delay and combustion phasing (CA50) for the three (3) cases that feature different Diesel fuel substitution ratios. Table 44 represents the comparison between the engine output parameters for the three (3) cases that feature different Diesel fuel substitution ratios.



**Figure 214.** Comparison between the simulated emissions, ignition delay time and combustion phasing (CA50) for the three cases that feature different Diesel fuel substitution ratios

Figure 213 and Figure 214 reveals that the increase in the Diesel fuel substitution ratio leads to a slight increase of the premixed spray combustion phase. Moreover, the increase of the Diesel fuel substitution ratio leads to a slight earlier ignition and hence slightly advanced combustion phasing.

**Table 44.** Comparison between the engine output parameters for the three cases that feature different Diesel fuel substitution ratios

Parameter	$m_{DI} = 1.4$ mg	$m_{DI} = 2.8$ mg	$m_{DI} = 5.6$ mg
IMEPg (bar)	7	7.05	6.95
Indicated Efficiency (%)	34.7	34.8	34.2
Total Excess air Ratio (-)	1.26	1.26	1.27

As a result of the advanced combustion phasing, the peak in-cylinder temperature increases slightly which leads to a slight increase of the NO<sub>x</sub> emissions. Table 44 reveals that as the Diesel fuel substitution ratio is increased, excess air ratio slightly increases as well. This is a result of the lower stoichiometric air to fuel ratio of Diesel fuel compared to methane.

Spray region is the area where the in-cylinder mixture is the richest. Hence in relative terms this area is a main source of the soot and CO emissions in a conventional dual fuel engine when it is operated with lean mixtures. Therefore, as the Diesel fuel substitution ratio is increased, the mass of the Diesel fuel and hence the spray mass increase causing an increase in the CO and soot emissions.

The initial Diesel fuel substitution ratio increase leads to an increase in the engine's output load and efficiency. However, as the Diesel fuel substitution ratio is increased further, the power and efficiency slightly decrease.

## 5.2. Full conventional dual fuel IC engine simulation

In this chapter of the thesis the effect of the injection timing on the cycle efficiency and engine out (pre-catalyst) NO<sub>x</sub> emissions of a full conventional dual fuel engine is presented. The full model of the turbocharged engine was created in the AVL Boost, while the combustion process was calculated with a cylinder model that was created in the AVL CruiseM. This chapter presents the optimization of one operating point of conventional dual fuel engine in terms of engine efficiency, power and NO<sub>x</sub> emissions.

As was presented before, for a given input energy and engine speed, there are a number of operating parameters that can be optimized in conventional dual fuel engine:

1. Intake pressure, temperature and EGR;
2. Direct fuel injection pressure;
3. Direct fuel injection timing;
4. Diesel fuel substitution ratio.

Moreover, as the IC engine can feature various different systems, the number of overall operating and control parameters is significant. Some of the possible systems that can be installed on a modern IC engine are:

1. Turbocharging:
  - a. Single-stage or multi-stage
  - b. Electrically assisted
2. Exhaust gas recirculation (EGR):
  - a. High pressure EGR loop (HP-EGR)
  - b. Low pressure EGR loop (LP-EGR)
  - c. Mixed EGR loop (MP-EGR)
3. Intercooling:
  - a. Intake air
  - b. EGR
4. Exhaust gas treatment systems:
  - a. Diesel Particulate Filter (DPF)
  - b. Selective Catalytic Reduction (SCR)
  - c. Tri-component Catalyst

Therefore, instead of conducting extensive experimental research, the engine can be experimentally run at a few operating points and then the detailed optimization can be

performed through the numerical simulations, which is exactly where a simulation model such as the newly developed DFMZCM comes in handy.

The main goal of this thesis is not the optimization of the engine performance in terms of the entire possible set of operating and control parameters. Therefore, in this section only the injection timing of the selected operating point will be optimized. The selected operating point is optimized both in terms of the output power and efficiency, as well as in terms of the NO<sub>x</sub> emissions. The same procedure that is shown in this section can be used to optimize the engine with respect to all possible operating and control parameters.

### 5.2.1. Engine model and simulation settings

The operating parameters of the point whose optimization is presented in this chapter are given in the Table 45.

**Table 45. Base operating point parameters for the full engine simulation**

Parameter	Value
Engine Speed (rpm)	1600
Intake Pressure (bar)	$\approx 1.7$
SHP Pressure (bar)	2.38
SHP Temperature (K)	382
SHP Combustion Products Mass Fraction (-)	0.02
Start of Injection (degCA bTDC)	25
Injection Duration (degCA)	2.7
Injection Pressure (bar)	750
Diesel Fuel Mass (mg)	1.8
Methane Mass (mg)	19.75
Total Excess Air Ratio (-)	1.22
IMEPg (bar)	8.01

Before conducting the optimization simulations, it is necessary to find the right DMFZCM parameters; i.e. the right set of the model parameters so that there is a good fit between the measured and simulated results for the given operating point. Here, the same procedure as the one that was performed in the validation, sensitivity and engine geometry & operating parameters analyses, was performed. The combustion model parameterization was performed on a single cylinder engine model that was created in the AVL CruiseM (Figure 105), with the pre-set SHP conditions (Table 45).

In the simulations that are presented in this chapter, the flame propagation was calculated with the TCM. The list of the in-cylinder turbulence, spray and flame propagation model parameters can be found in the three tables given below. All of the in-cylinder turbulence model parameters (Table 46), as well as the most of the spray (Table 47) and flame propagation (Table 48) model parameters are the same as the ones that were used in the previous simulations.

**Table 46. In-cylinder turbulence model parameters for optimization model**

Model Parameter	Value
$S_{in}$ (-)	$1.5 \times 10^{-3}$
$C_{in}$ (-)	1.55
$S_{inj}$ (-)	$3.5 \times 10^{-2}$
$C_{inj}$ (-)	155
$C_2$ (-)	1.92
$C_\varepsilon$ (-)	2.35
$C_{\varepsilon,UZ}$ (-)	1
$C_L$ (-)	0.5

**Table 47. Spray and heat transfer model parameters for optimization model**

Model Parameter	Value
$C_{evap,HT}$ (-)	1
$C_{evap}$ (-)	1
$C_{entrain}$ (-)	0.5
$C_{ignition}$ (-)	1
$C_{discr,ax}$ (-)	0.6
$C_{discr,rad}$ (-)	6
$C_{ZHT,SZ}$ (-)	1

**Table 48. Flame propagation model parameters for optimization model**

Model Parameter	Value
$C_{ign,UZ,transf}$ (-)	0.95
$C_{trans}$ (-)	1
$C_{SOWC}$ (-)	0.7
$C_{WC,shp}$ (-)	3
$C_{comb}$ (-)	0.83
$C_{EOFP}$ (-)	0.94

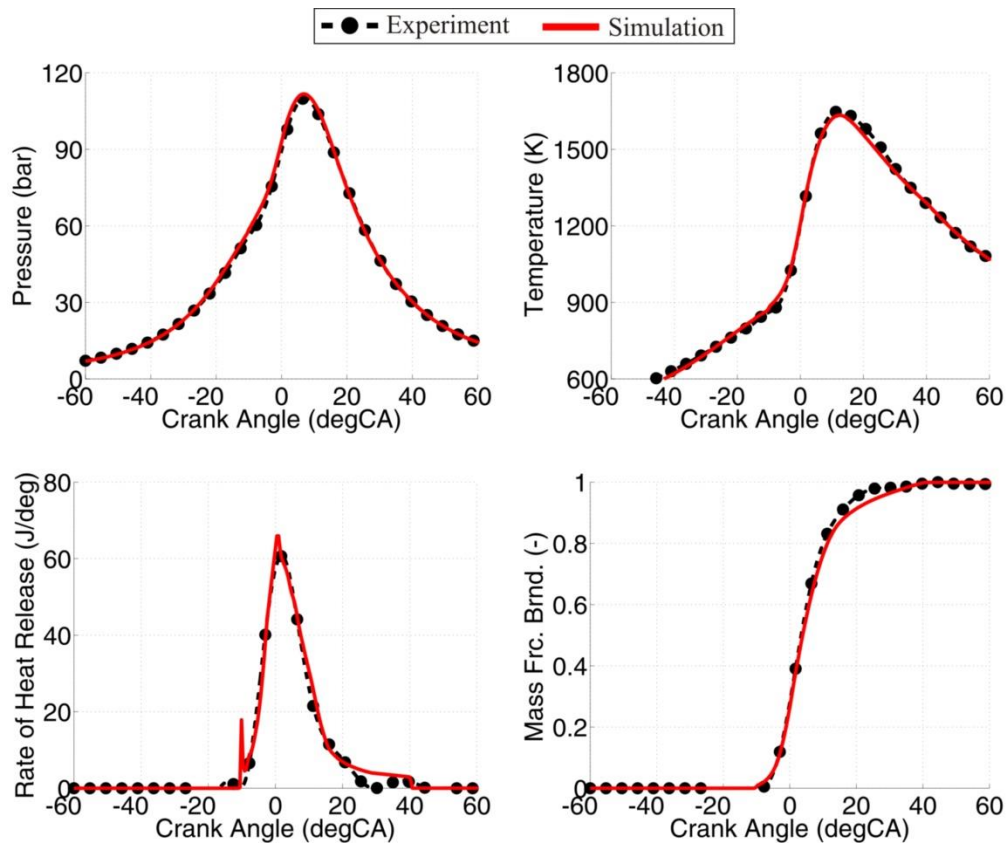


**Figure 215. Comparison between the measured and simulated in-cylinder pressure, temperature, ROHR and MFB traces**

As can be seen from the comparison between the experimentally obtained and simulated in-cylinder pressure, temperature, ROHR and MFB traces (Figure 215), there is a good fit between the experiment and simulation. The comparison between the measured and simulated CA5, CA10, CA50, CA90 and CA95 (Figure 216) reveals that there is only a slightest difference between the measured and simulated combustion profile. Likewise, the Table 49 reveals that there is a good fit between the experimentally obtained and simulated IMEPg, peak cylinder pressure, the crank angle at which the peak cylinder pressure occurred and the pre-catalyst NO<sub>x</sub> emissions.

**Table 49. Comparison between the specific measured and simulated parameters**

Parameter	Value – Experiment	Value – Simulation
IMEPg (bar)	8.01	7.97
Peak Cylinder Pressure (bar)	109.97	111.68
Peak Cylinder Pressure Crank Angle (degCA)	7	6.72
NO <sub>x</sub> Emissions (mg/kg)	66	61

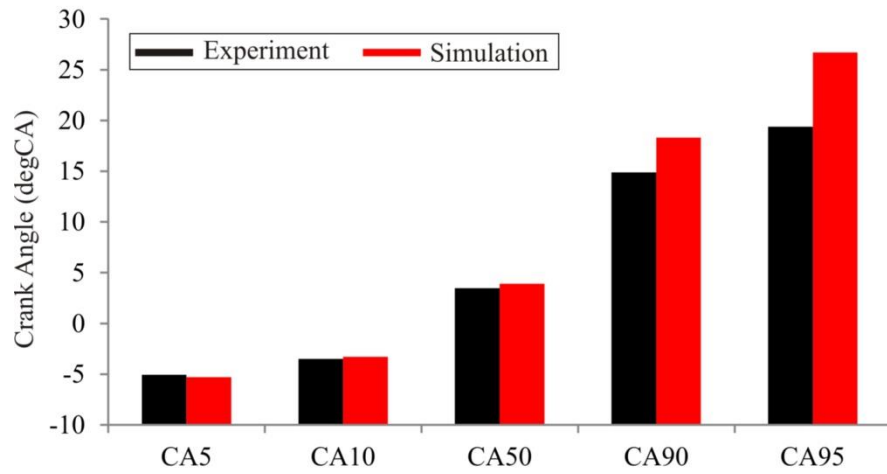


Figure 216. Comparison between the measured and simulated CA5, CA10, CA50, CA90 and CA95 values

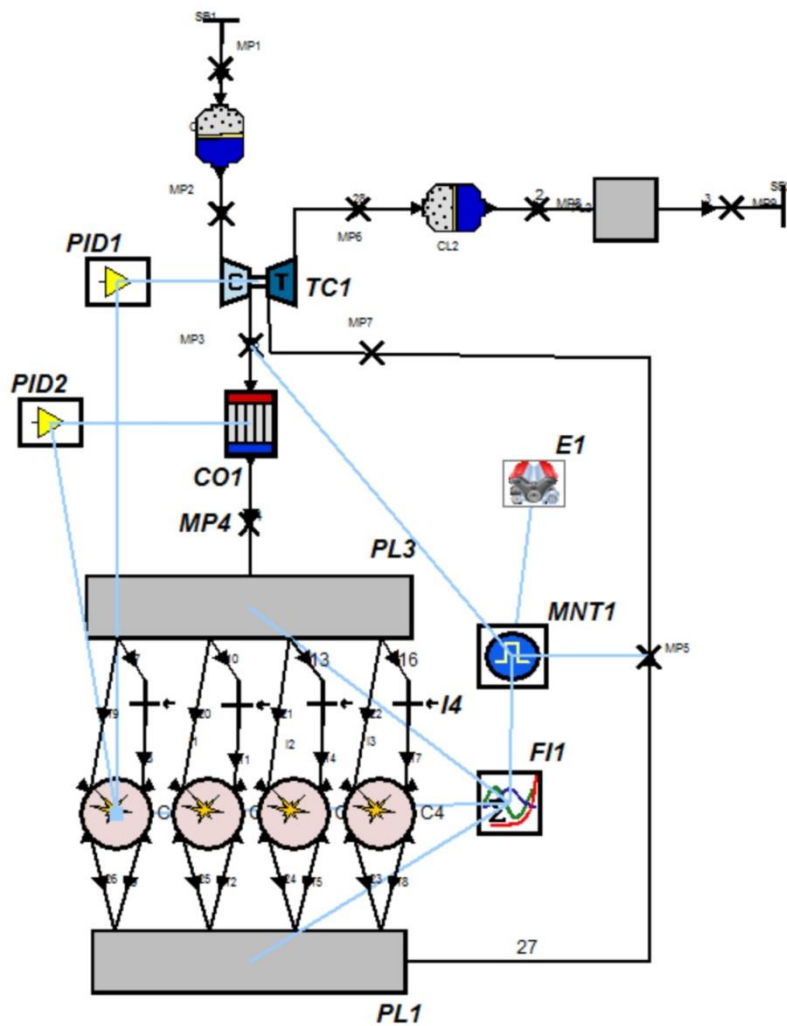


Figure 217. Schematic of the full conventional dual fuel IC engine model that was created in the AVL Boost



After the combustion model has been parameterized for the selected operating point, the full model analysis was conducted. In this analysis, the injection timing sweep was performed in order to optimize the selected operating point (Table 49) in terms of the engine output power, efficiency and NO<sub>x</sub> emissions. In these simulations, the combustion process was calculated by the single-cylinder model (pre-set SHP conditions) that was created in the AVL CruiseM, and then the normalized ROHR curves were simply fed to the full engine cycle—simulation model which was created in the AVL Boost simulation tool (Figure 217).

The full engine simulation model was made according to the 2.0 liter VW TDI engine geometry. As can be seen in Figure 217, the full engine model the model features:

1. Four cylinders.
2. Entire intake and exhaust system (pipes & plenums).
3. Intake air cleaner (CL1).
4. Variable geometry turbocharger (TC1); controlled through a PID regulator (PID1).
5. Intake air cooler (CO1); controlled through a PID regulator (PID2).
6. Exhaust gas filters (CL2).

Since the AVL Boost features a one-dimensional (1-D) calculation of the flow phenomena through the pipes, with such simulation tool it is possible to account for the gas dynamics inside the IC engine system.

The variable geometry turbocharger has a set of the stator blades that can be used to control the flow through the turbine, thus increasing or decreasing the pressure drop and hence the work at the turbine. As the turbine is connected to the compressor with the shaft, this work is then transferred to the compressor (intake) side where it is used to increase the intake pressure level. The adequate level of temperature at the SHP was achieved with the intake air cooler (CO1), through the appropriate control of the cooling liquid temperature. More information on the calculation of the phenomena inside the pipes and other engine systems can be found in [37], [57].

Since the base operating point that was used in these simulations (Table 45) has the injection timing of 25 degCA bTDC, the injection timing sweep was performed with a few earlier and a few later timings compared to the base point (Table 50). All other relevant operating parameters are the same and can be found in Table 45.

**Table 50. Simulated operating points (injection timings)**

Operating Point Name	SOI (degCA bTDC)
SOI 1	5
SOI 2	15
SOI 3	25
SOI 4	35
SOI 5	45
SOI 6	55
SOI 7	65

### 5.2.2. Simulation results

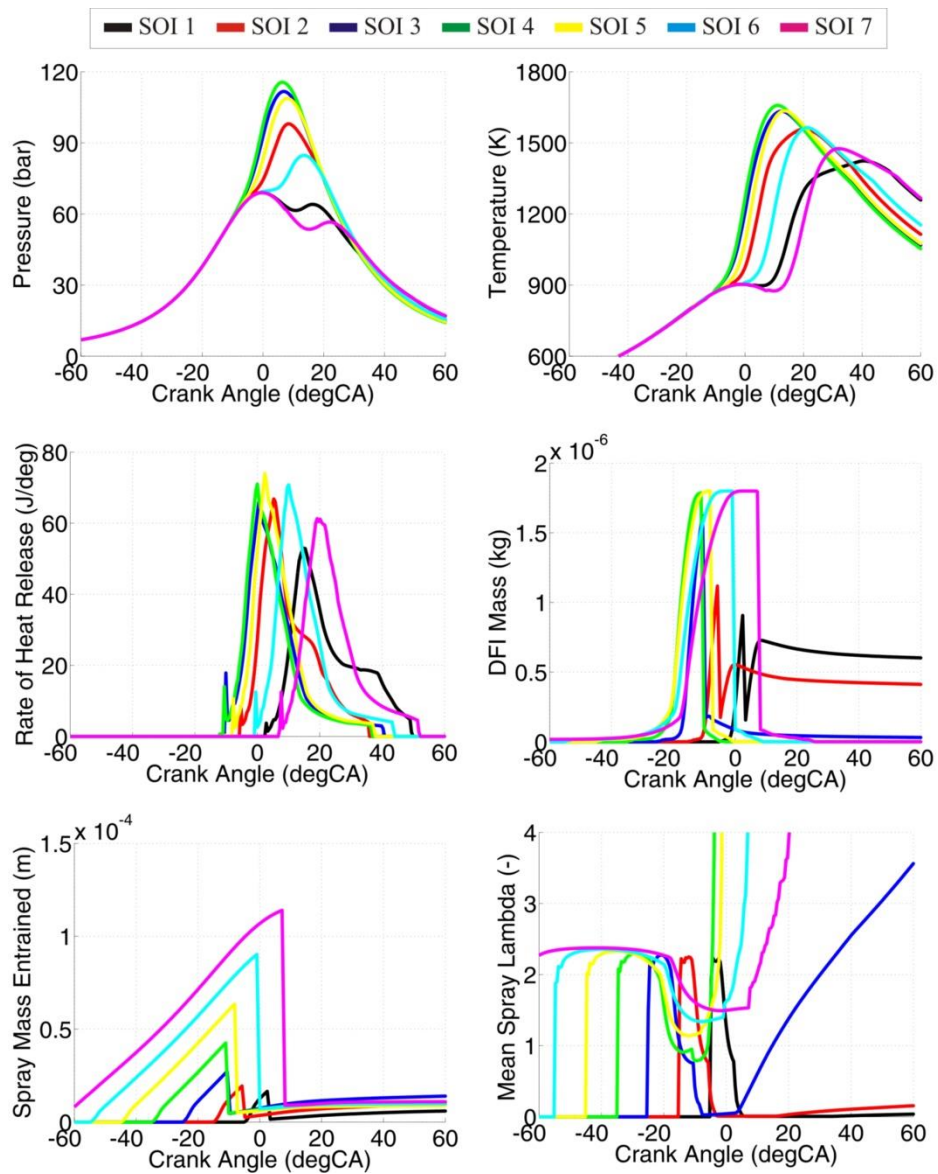


**Figure 218. Comparison between the simulated in-cylinder pressure, temperature, ROHR, DFI mass, entrained mass and mean spray excess air ratio traces for the seven full engine cases that feature different direct fuel injection timing**

Figure 218 presents the comparison between the simulated in-cylinder pressure, temperature, ROHR, mass of the Diesel fuel vapor inside the spray region, the premixed charge mass that has been entrained into the spray region and the excess air ratio inside the spray region traces for the seven (7) full engine cases that feature different direct fuel injection timing. Figure 219 represents the comparison between the ignition delay and combustion phasing (CA50) for the seven (7) full engine cases that feature different direct fuel injection timing. Figure 220 represents the engine load and NO<sub>x</sub> emissions for the seven full engine cases that feature different direct fuel injection timing.

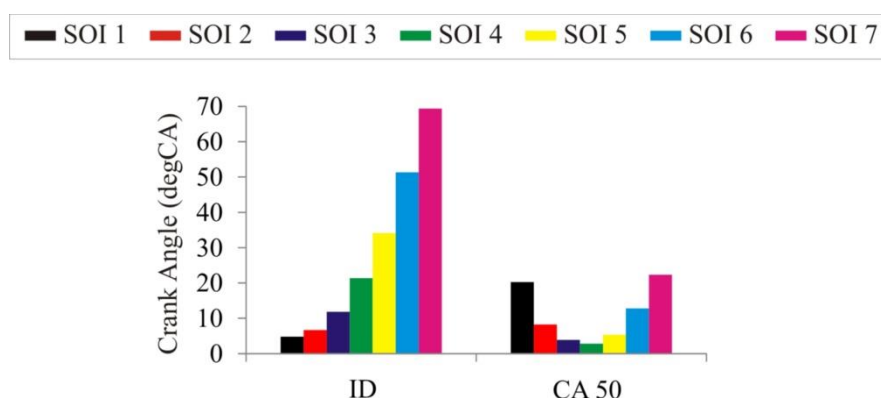


**Figure 219.** Comparison between the ignition delay time and combustion phasing (CA50) for the seven full engine cases that feature different direct fuel injection timing

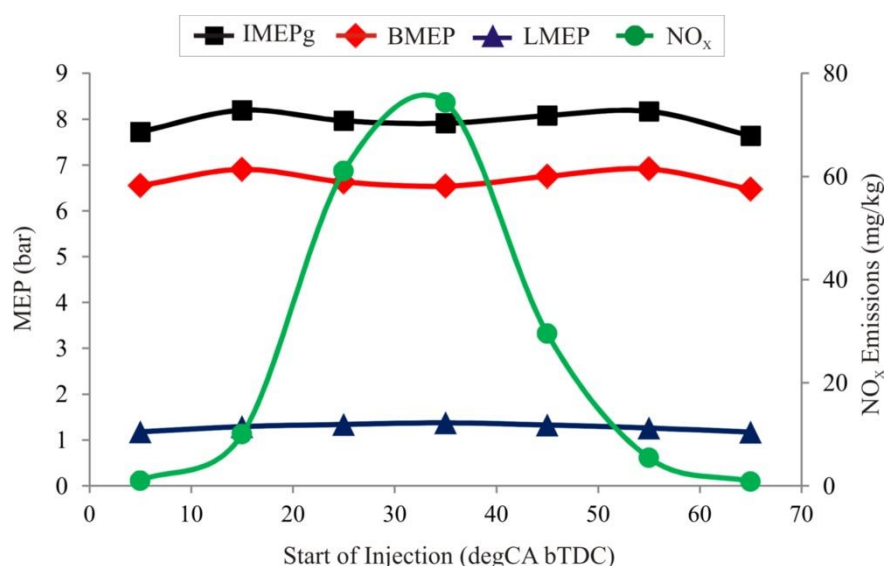


**Figure 220.** Engine load and NO<sub>x</sub> emissions for the seven full engine cases that feature different direct fuel injection timing

The same effect as in the chapter 5.1.4 has been noted in the full engine simulations (Figure 218 and Figure 219). As the direct fuel injection timing is advanced, the fuel is injected into the colder mixture, which decreases the evaporation rate and the mixture reactivity. Hence the

ignition delay increases. Again, the combustion phasing (CA50) has an interesting trend; as the injection timing is advanced, even though the ignition delay increases the CA50 initially also advances due to the earlier injection timing. However, as the ignition delay gets considerably prolonged the CA50 starts to retard as well (after SOI 4 = 35 degCA bTDC).

As the CA 50 is advanced, the peak in-cylinder temperature increases (Figure 219) and thus the NO<sub>x</sub> emissions increase as well (Figure 220). The NO<sub>x</sub> emission peaks at SOI 4 = 35 degCA bTDC, and since after this injection timing the combustion phasing retards, the peak in-cylinder temperature and the NO<sub>x</sub> emissions decrease.

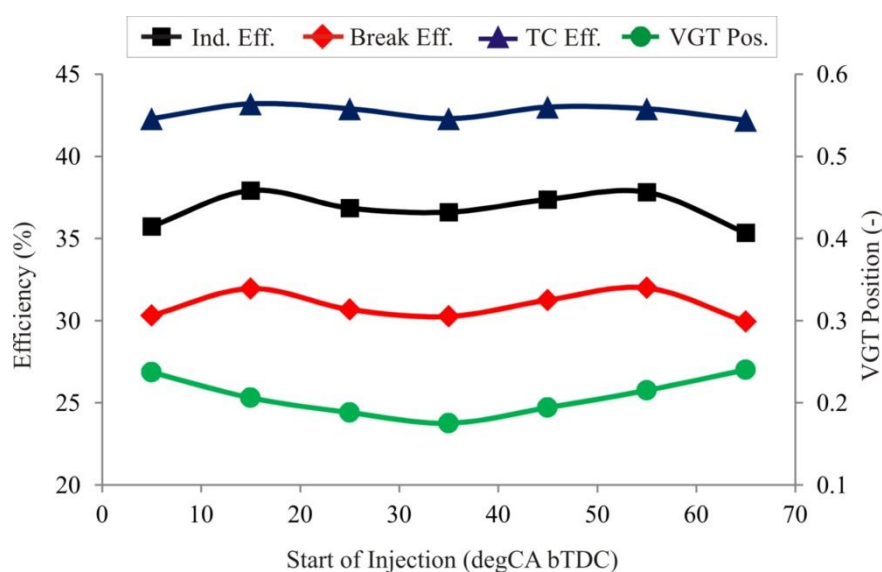


**Figure 221. Engine and turbocharger efficiencies and the VGT position for the seven full engine cases that feature different direct fuel injection timing**

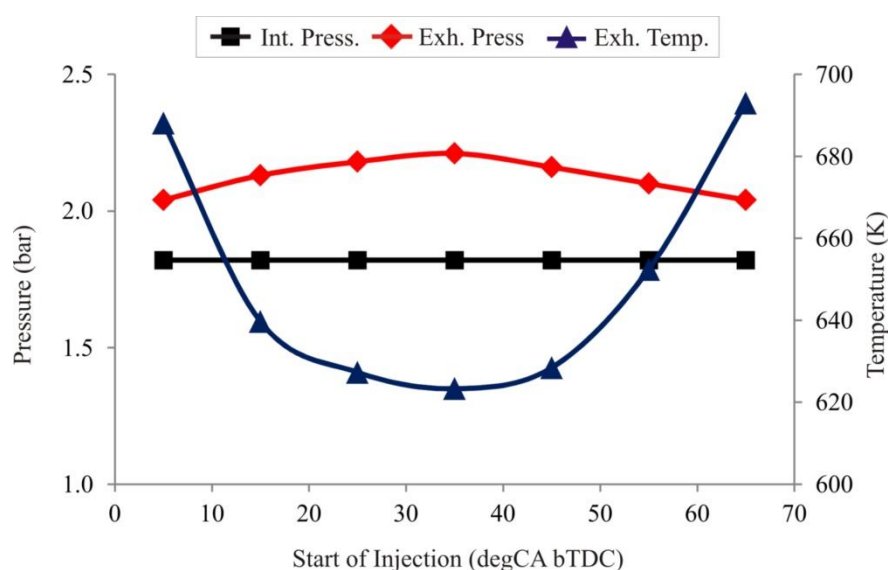


**Figure 222. Intake and exhaust pressure, and the exhaust temperature for the seven full engine cases that feature different direct fuel injection timing**

Figure 221 represents the engine and turbocharger efficiencies, and the turbine stator blades position for the seven (7) full engine cases that feature different direct fuel injection timing. Figure 222 represents the intake and exhaust pressure, and the exhaust temperature for the seven (7) full engine cases that feature different direct fuel injection timing.

It can be seen (Figure 221) that regardless of the injection timing, the turbocharger efficiency is roughly constant (approximately 43%). It can also be seen that the intake pressure (Figure 222) was the same in all simulations, while the exhaust pressure and temperature (Figure 222) as well as the VGT position (Figure 221) varied from case to case. As the combustion phasing is advanced, the peak-cylinder temperature increases, while the in-cylinder temperature at the EVO moment decreases. Therefore, in order to achieve the adequate level of turbine work and sufficient increase of the intake pressure, the VGT needs to be closed which increases the exhaust pressure and increases the pressure drop across the turbine.

The increase of the exhaust pressure causes an increase in the gas exchange losses (higher difference between the exhaust and intake pressure) and thus raises the Loss Mean Effective Pressure (LMEP). LMEP represents the sum of the gas exchange losses and friction losses. Nevertheless, it can be seen that the load and thus the efficiency are primarily a function of the combustion phasing. The optimal combustion phasing for the selected operating point is found to be around 10 degCA, which can be achieved with two different injection timings; SOI 2 = 15 degCA bTDC and SOI 6 = 55 degCA bTDC. Interesting thing to note is that the injection timing SOI 2 has slightly higher IMEPg; 8.19 bar to 8.17 bar, while the SOI 6 has a slightly higher brake mean effective pressure (BMEP; 6.91 bar to 6.9 bar. Since the soot emissions, unfortunately, could not be measured at the experimental setup there are no referent soot emissions for the given operating point. However, same as in the previous chapters, the soot was modeled with the pre-set model parameters and the soot simulation results are given in Figure 223.

Figure 223 reveals that the soot emissions decrease as the injection timing is advanced. This is due to an increase in the ignition delay which leads to longer mixing time resulting in the well-mixed, more homogeneous mixture at the ignition timing. For such mixtures (since the overall mixture is lean), there is little fuel vapor left inside of the flame once the flame propagation is initiated. Therefore, there is no source for the soot production inside the spray region.

This leads to the conclusion that the SOI 6 will have higher output load and efficiency as well as lower NO<sub>x</sub> and considerably lower soot emissions compared to the SOI 2 case. Moreover, as the overall mixture for the selected operating point is lean and the mixture inside the spray

for the SOI 6 case is more homogeneous at the ignition timing, compared to the SOI 2 case, the SOI 6 case should also have lower CO emissions. Finally, for the selected operating point (Table 45) the overall optimum case in terms of cycle-efficiency and NO<sub>x</sub> emissions is the SOI 6 case (SOI = 55 degCA bTDC).

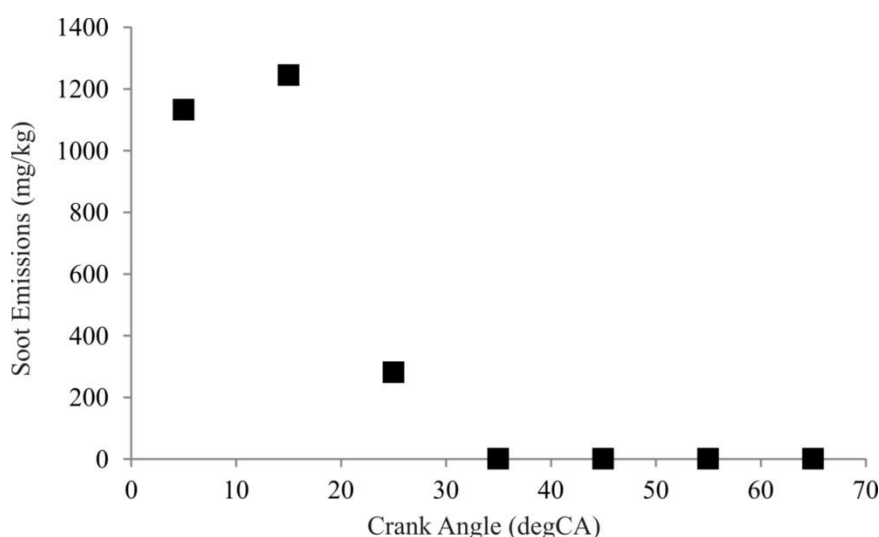


**Figure 223. Simulated soot emissions for the seven full engine cases that feature different direct fuel injection timing**

The best values of the selected performance results (output load, efficiency and NO<sub>x</sub> emissions) from the entire injection timing sweep together with the respective operating parameter for the operating point are given in the Table 51.

**Table 51. Optimum cases (injection timing) in terms of the load, efficiency and NO<sub>x</sub> emissions for the simulated operating point**

Parameter	Simulated Case	Value
IMEPg (bar)	SOI 2 = 15 degCA bTDC	8.19
Indicated Efficiency (%)	SOI 2 = 15 degCA bTDC	37.92
BMEP (bar)	SOI 6 = 55 degCA bTDC	6.91
Break Efficiency (%)	SOI 6 = 55 degCA bTDC	32
NO <sub>x</sub> Emissions (mg/kg)	SOI 7 = 65 degCA bTDC	0.8

Table 51, and the Figure 220 and Figure 221 reveal that there is a trade-off between the brake efficiency and NO<sub>x</sub> emissions, as the lowest NO<sub>x</sub> emissions (SOI 1 and SOI 7) were obtained in the cases that exhibit the lowest brake efficiency. The Figure 223 reveals that the major difference between the SOI 1 and SOI 7 cases is in the level of the soot emissions. Aside from having the lowest NO<sub>x</sub> emissions, the SOI 7 case also has the lowest simulated soot emissions.

## 6. General Overview and Conclusions

The research that is shown in this thesis presents the development, validation and application of a quasi-dimensional combustion model for the cycle-simulations in the conventional dual fuel engines (DFMZCM).

The conventional dual fuel IC engine is a term used for the dual fuel engines that operate with the premixed natural gas and directly injected Diesel fuel. The relative amount of the natural gas in the combustion process is usually defined as the Diesel fuel substitution ratio, which represents the ratio of energy supplied by natural gas to the total amount of energy supplied by both fuels [2].

The combustion process that occurs in a conventional dual fuel engine is a blend of the mixing-controlled combustion process (characteristic for the DI-CI engines) and the combustion process governed by the flame propagation through the premixed mixture (characteristic for SI engines) [2]. According to the experimental research that was conducted at the UC Berkeley, and reported combustion chamber images [23] and CFD studies [24], [38], [39], the following combustion stages are identified [2]:

1. Premixed (chemically controlled) combustion of the Diesel fuel/ natural gas/ air mixture. The products of this combustion phase trigger the flame propagation through the premixed mixture.
2. Combination of the mixing-controlled combustion of the Diesel fuel with the surrounding mixture and flame propagation through the premixed Diesel fuel/ natural gas/ air mixture.
3. Final, mixing-controlled combustion of the remaining Diesel fuel after the flame propagated through the entire combustion chamber.

The newly developed DFMZCM is a multi-zone, quasi-dimensional combustion model which can be used in the cycle-simulation analyses of the conventional dual fuel engines. Since the combustion in the conventional dual fuel IC engines is a blend of two fundamental combustion types which occur in DI-CI and SI engines DFMZCM features:

1. multi-zone approach to combustion modeling:
  - a) unburned zone,
  - b) n spray zones,
  - c) flame zone.
2. quasi-dimensional approach to combustion modeling:
  - a) description of the combustion chamber geometry,

- b) description of the injector nozzle orientation and spray angle (injector data),
  - c) tracking of the spray zone position (deflection of the chamber walls),
  - d) calculation of the location where flame start to propagate through the premixed mixture,
  - e) calculation of the multiple flames that propagate through the combustion chamber,
  - f) calculations of the interactions between the flames and between the flame and combustion chamber walls (cylinder head and liner, and piston).
- 3. in-cylinder turbulence modeling,
- 4. heat transfer modeling,
- 5. modeling of the spray processes:
  - a) injection,
  - b) liquid fuel break-up,
  - c) charge entrainment and heat transfer between the zones,
  - d) liquid fuel heat-up and evaporation,
  - e) spray ignition and combustion,
  - f) calculation of the harmful exhaust gas emissions inside each spray zone.
- 6. modeling of the flame propagation process:
  - a) calculation of the start of flame propagation,
  - b) calculation of the flame surface in a case when multiple flames propagate through the combustion chamber,
  - c) laminar flame speed calculation,
  - d) calculation of the turbulent burning rate,
  - e) calculation of the harmful exhaust gas emissions inside the flame zone,
- 7. calculation of the harmful exhaust gas emissions (HC emissions) in front of the flame (inside the unburned zone),
- 8. calculation of the knock occurrence and its intensity in front of the flame (inside the unburned zone).

By dividing the cylinder content into a number of zones (multi-zone approach to combustion modeling) it is possible to account for temperature and charge inhomogeneity, which improves ignition, burning rate and emissions calculations. By applying quasi-dimensional modeling approach, it is possible to account for the geometry effects on the spray development process and burning rate calculation.

In order to enable a good prediction of the turbulence level and calculation of the turbulent burning rate in conventional dual fuel engines, the 0-D  $k-\varepsilon$  turbulence model which has been



developed and validated in [32] was extended and slightly modified during the research that is presented in this thesis. The modifications that have been made include:

1. Modeling of the injection effect on the rate of turbulent kinetic energy and its dissipation.
2. Inclusion of the geometry effects in the calculation of the characteristic turbulence values (turbulent length scale and turbulence time scale).

The heat transfer from the in-cylinder mixture to the combustion chamber walls during the high pressure cycle is modeled with a well-known Woschni's correlation for the convective heat transfer [75] that is already available in the AVL cycle simulation software [57].

The zone heat transfer model is based on the approach that was presented in [34] and is based on the assumption that after sufficient time passes the entire cylinder content would be at the same temperature as a result of a mixing process due to mass diffusion, bulk flow and turbulence, and conductive heat transfer. However, contrary to the original model, the zone heat transfer model that is presented in this thesis has been linked to the in-cylinder turbulence quantities.

The spray combustion model is based on the packet approach that was developed by the authors in [42], and later used and modified by a number of authors, i.e. [33]. The spray model used in this thesis is based on the model presented in [33] that was integrated within the AVL cycle simulation software, and features:

1. the liquid fuel injection calculation,
2. the liquid fuel break-up modeling,
3. the spray development calculation (zone velocity and position tracking),
4. gas mixture entrainment into the spray zones calculation,
5. the calculation of liquid fuel evaporation,
6. the spray ignition and combustion calculation,

Since contrary to the conventional DI-CI engines which operate with Diesel fuel/ air/ EGR mixtures, the conventional dual fuel engines operate with Diesel fuel/ natural gas/ air/ EGR mixtures, in the spray model presented in this thesis natural gas is also entrained into the spray zones which means that at moment of ignition a Diesel fuel/ natural gas fuel mixture ignites and burns. Consequently, some modifications to the existing spray model which was presented in [33] had to be made. The modifications that were made include:

1. the new species balance as two fuels are present in each of the spray zones,
2. the modification of the injection velocity calculation,
3. the zone position tracking,

4. the heat transfer calculation between the spray zones,
5. the new approach to spray ignition delay calculation,
6. the new approach to spray combustion calculation.

Spray ignition and consequent combustion are calculated with newly developed sub-models that are based on the lookup tables that feature low temperature and high temperature (main) ignition delay times, percentage of the heat released in the low temperature ignition event and chemical reaction rate times.

The chemistry tables which are used in the ignition and reaction rate calculation of the spray combustion and the knock occurrence (detonation) were made with a specially developed in-house code. The code is based on a single zone, homogeneous, adiabatic constant volume 0-D reactor. In this code, the FORTRAN subroutine CHEMKIN<sup>TM</sup> was used to calculate the thermodynamic properties of the gas mixture and production rates of the species involved in the chemical reaction process.

In the DFMZCM, two different approaches were used in the flame propagation process modeling:

1. Fractal combustion model (FCM)
2. Turbulent flame speed combustion model (TCM)

Turbulent flame propagation calculation based on the fractal theory is a well-known calculation approach, while the other approach in turbulent flame propagation calculation was newly derived and implemented into the AVL cycle-simulation software during the research presented in this thesis. This model is based on the calculation of the turbulent flame velocity as proposed in [56], and applied in modeling of the flame propagation phenomena in 3-D CFD. Since the conventional dual fuel engine flame propagation phenomenon differs from the one that occurs in the SI engines, some further extensions and modifications had to be made:

1. new start of the flame propagation calculation model;
2. new model for the calculation of the transition from the laminar to fully developed turbulent flame;
3. new wall-combustion calculation model;
4. new multiple flame surface calculation model;
5. new laminar flame speed calculation model.

As the flame approaches the walls the combustion rate decreases. This decrease is caused by the three phenomena:

1. a decrease of the ratio of turbulent scales that wrinkle the flame front
2. an increase in the heat transfer rate from the flame to the combustion chamber walls

### 3. a decrease of the temperature in front of the flame

The first effect is captured through the application of a two-zone in-cylinder turbulence model that can describe the gradual decrease of the turbulent kinetic energy inside the unburned zone. The other two effects are modeled through an exponential decay under-relaxation function (wall-combustion model). The flame quenching phenomenon is accounted for with a model parameter that represents the mass fraction burned at which the flame propagation ends.

The instantaneous laminar flame speed of the flame front is calculated with a specially developed laminar flame speed tables (look-up tables). These tables were supplied by the partner in this research, AVL GmbH.

In the DMFZCM, laminar flame surface area is calculated with a newly developed multiple flame surface area calculation model. With this model, it is possible to calculate the overall flame surface area as well as the cylinder head, liner and piston wetted areas for any number of flames that propagate through the combustion chamber. Moreover, with this model it is possible to account for any viable position of the flame center inside the combustion chamber; the only limitation to the flame center location is that the flame center must be located within the combustion chamber.

The formation of soot (particles), unburned hydrocarbon (HC), carbon monoxide (CO) and nitrogen oxides (NO<sub>x</sub>) is accounted for with the appropriate emissions models. The formation of these harmful species is modeled with existing models that are available in the AVL Boost. The knock occurrence and its intensity is calculated with the model that was presented and integrated in the AVL Boost in [58]. In order to improve the number of effects that the model captures and the knock occurrence prediction capability, during the research presented in this thesis this model was extended and modified:

1. Calculation of the low temperature and high temperature knock integral from the start of the high-pressure cycle. This improves the auto-ignition event calculation.
2. New ignition delay tables (both low temperature and high temperature) which include the effect of two different fuels inside the zone on the knock occurrence calculation.
3. The use of the chemical reaction rate tables, which enable improvement of the calculation of heat release rate due to knock occurrence in the end gas.

In the validation part, both the extended in-cylinder turbulence model as well as the entire DMFZCM were compared and validated with the available 3-D CFD and experimental data.

In order to verify the extensions to the  $k$ - $\varepsilon$  in-cylinder turbulence sub-model that were made during the research that is presented in this thesis, a 3-D CFD simulation of an IC engine was

performed and the 0-D turbulence results were compared with the 3-D CFD turbulence results. Unfortunately, the 3-D CFD model of the experimental dual fuel engine was not available and therefore the 3-D CFD model of an IC engine that has similar geometry was used. The turbulence verification results reveal that there is a good fit between the experimentally obtained results (in-cylinder pressure and ROHR) and the ones obtained with the 3-D CFD and the 0-D DFMZCM simulations. It could be noticed that the fit between the experimentally obtained in-cylinder pressure and ROHR traces with the ones calculated with the DFMZCM was better than the fit between the experiment and 3-D CFD. Also, it could be seen that there is a good fit in the specific TKE trace between the 3-D CFD simulation and the 0-D DFMZCM simulation.

The DFMZCM was validated with the experimental data that were obtained at the UC Berkeley, where the existing 2-liter Diesel engine was adjusted to operate in a conventional dual fuel mode. The DFMZCM was validated at the total of fifteen (15) operating points. These operating points were measured at three different engine speeds, two different intake pressure levels and at various different loads, injection settings (injection timing and pressure), excess air ratios and Diesel fuel substitution ratios.

In the first step the DFMZCM was validated at the base engine point and the validation result revealed that there is a good fit between the measured and simulated in-cylinder pressure, temperature, ROHR and MFB traces. Likewise, there was a good fit between the measured and simulated engine load and exhaust gas emissions.

Once the model has been tuned and its validation at the base operating case has been performed, the sensitivity of the model to its tuning parameters was performed.

Generally, the in-cylinder turbulence parameters are used to adjust the calculated turbulence levels (TKE, TED, integral length scale and turbulence time scale) with the ones obtained from the 3-D CFD simulation.

The spray combustion model parameters are used to adjust the calculated spray process (spray formation and evolution, and spray combustion), and combustion timing with the one obtained from the experiment.

The flame propagation model parameters are used to adjust the calculated flame propagation process (main combustion event) with the one obtained from the experiment.

In the third part of the validation the DFMZCM was validated at additional thirteen (13) operating points. This validation process was conducted with the single set of the in-cylinder turbulence model parameters, while one spray combustion model parameter and four flame propagation model parameters were varied from case to case in order to achieve a good fit

between the measured and simulated in-cylinder pressure, temperature and ROHR traces. All of the measurement – simulation comparison results show that there is a good fit between the measured and simulated load and the in-cylinder pressure, temperature, ROHR and MFB traces.

In this validation set, the spray model parameter had to be adjusted to tune the start of combustion (ignition timing), while the flame propagation model had to be adjusted in order to tune the combustion phasing and its intensity. The reasons why these model parameters had to be adjusted from case to case are:

1. Uncertainty in the in-cylinder turbulence levels and the value of its quantities as there were no referent 3-D CFD simulations of the experimental engine available.
2. Uncertainty in the spray details (rate of evaporation, rate of entrainment, temperature and mixture stratification inside the spray region) as there were no referent 3-D CFD simulations of the experimental engine available.
3. Uncertainty in some of the measured values.
4. Inability to describe the stratification inside the premixed zone through which the flame propagates.

In the fourth part of the validation process, for the selected operating points at one engine speed the single set of the in-cylinder turbulence and of the flame propagation model parameters was applied, while a single spray combustion model parameter was varied from case to case. As can be seen from the measurement – simulation comparison figures, the fit between the measured and simulated traces is still reasonable and most of the trends are adequately captured. Combustion phasing is reasonable for all of the cases; in some cases, it is almost perfect (OP2 and OP8), while in others it is slightly off (OP6 and OP7). Also, in some of the cases the combustion process is either too intense or it is too weak compared to the measured cases. It is interesting to notice that the results that were obtained at 1000 rpm (OP1 and OP2) are considerably better than the results that were obtained at 1800 rpm (OP3 – OP9). Part of the reason for this could lie in the more pronounced overall temperature and mixture stratification at 1800 rpm.

Finally, in the fifth part of the validation process, for the selected operating points at one engine speed the full single set of model parameters was applied. The results reveal that when the single set of all model parameters is applied for multiple operating points that are at the same engine speed (OP1 and OP2 at 1000 rpm; OP3 – OP9 at 1800 rpm) the fit between the measured and simulated traces is not as good as the one that was obtained when only the

single set of the flame propagation model parameters was used, however it is still reasonable and the main combustion and performance trends are adequately captured.

The validation clearly showed that the newly developed DFMZC is capable of describing the conventional dual fuel combustion process. However, since this is a 0-D approach where the spatial details are not resolved, there is a need to slightly tune some of the model parameters from case to case.

After the validation, the DFMZCM was used to assess the effect of various geometry and performance parameters on the base engine operating point. These simulations reveal that with the DFMZC it is possible to appropriately account for the effect of geometry and of operating parameters on the conventional dual fuel combustion, performance and exhaust gas emissions. It is important to stress out that the HC model is not fully predictive, since the DFMZCM does not account for the flame quenching in a fully predictive way. Therefore, it is not possible to describe the HC emissions trends in an appropriate way. Even though the CO emissions also partially depend on the flame quenching process, since it is possible to account for the mixture composition quality and stratification inside the cylinder it is possible to account for most of the CO emission trends.

In the final chapter of the thesis the newly developed DFMZCM was used in the IC engine performance analysis simulations. In these simulations (cycle-simulations), the entire engine and its various systems were modeled in detail. In this chapter of the thesis the effect of the injection timing on the cycle efficiency and engine out (pre-catalyst) NO<sub>x</sub> emissions of a full conventional dual fuel engine is presented. The full model of the turbocharged engine was created in the AVL Boost, while the combustion process was calculated with a cylinder model created in the AVL CruiseM. This chapter presented the optimization of one conventional dual fuel engine operating point in terms of the engine efficiency, power and NO<sub>x</sub> emissions. The results show that the engine system performance (mainly turbocharger) impacts the overall output power and efficiency. At the end of the optimization process it was revealed that the two cases with significantly different injection timing have similar cycle efficiency (near the optimum). These two specific points also have similar NO<sub>x</sub>, but completely different soot emissions. Moreover, it was shown that the model is able to capture the tradeoff between the efficiency and NO<sub>x</sub> emissions.

The final conclusion is that the newly developed DFMZM enables the description of the combustion process that occurs in the conventional dual fuel engines. Also, the DFMZCM has reasonably short calculation time as it takes roughly 4 s to calculate one engine cycle. As such, the DFMZCM can be used to:

1. Study the specifics of the conventional dual fuel combustion phenomenon.
2. Study the influence of various geometry and operating parameters on the conventional dual fuel engine performance and exhaust gas emissions.
3. Study the performance of the entire, full engine system with its various components.

## **6.1. Original scientific contribution**

The original scientific contribution of this doctoral research, through which a new physically based 0-D combustion model for conventional dual fuel (diesel/natural gas) internal combustion engines was developed, are:

1. the new sub-models which calculate multiple flame propagation, diesel fuel spray and premixed flame interaction in the combustion chamber, ignition delay and a sub-model that calculates the rate of heat release of the diesel-natural gas mixture;
2. the integration of the developed sub-models in the new dual fuel combustion model;
3. the introduction of calculation of in-cylinder temperature and mixture in-homogeneity, which will enable a qualitative prediction of dual fuel engine emissions and the effect of change of operating parameters on the start of combustion and on the calculation of the duration and intensity of a particular dual fuel combustion phase;
4. the possibility to perform detailed numerical analysis and optimization of the dual fuel engine operating parameters, with respect to its emissions, efficiency and power.

## **6.2. Possible directions of further work**

The drawbacks of the newly developed DFMZCM have been presented in detail both in the validation and application chapters as well as in the final overview chapter. The further work should be directed in solving these drawbacks:

1. Creation of the 3-D CFD model of the experimental engine and conducting the conventional dual fuel combustion simulation. These simulations should enable a more thorough insight into the in-cylinder turbulence quantities, spray phenomena as well as the early flame growth, transition to the fully developed turbulent flame, start of wall-combustion and flame quenching phenomena. Moreover, these simulations should reveal the true level of stratification inside the premixed zone at different engine speeds, and its influence on the spray and flame propagation processes.
2. Derivation of the model that describes the stratification inside the premixed zone.

3. Derivation of the physically based flame quenching model which should significantly improve the wall-combustion stage calculation as well as the calculation of the HC and CO emissions.
4. Parameterization of the DFMZCM to enable the application of the single set of constants for one engine.
5. Application of the DFMZCM in full optimization of the engine performance, efficiency and exhaust gas emissions in a wide range of engine loads and speeds.



## References

- [1] I. Taritas, D. Kozarac, M. Sjerić, R. Tatschl, M. Sierra Aznar and D. Vuilleumier, "Development and Validation of a Quasi-Dimensional Dual Fuel (Diesel – Natural Gas) Combustion Model," *SAE Int. J. Engines*, vol. 10, no. 2, pp. 483–500, 2017.
- [2] I. Taritaš, M. Sremec, D. Kozarac, M. Blažić, and Z. Lulić, "The Effect of Operating Parameters on Dual Fuel Engine Performance and Emissions – An Overview," *Trans. FAMENA*, vol. 41, no. 1, pp. 1–14, 2017.
- [3] I. Taritaš, D. Kozarac, and Z. Lulić, "New Quasi-Dimensional Simulation Model for Conventional Dual Fuel Combustion," in *Digital Proceedings of the 10th Conference on Sustainable Development of Energy, Water and Environment Systems - SDEWES*, 2015.
- [4] I. Taritaš, D. Kozarac, M. Sjerić, R. Tomić, and Z. Lulić, "The Literature Review on Dual Fuel Diesel-Natural Gas Combustion, Emission and Performance," in *FUELS 2014*, 2014.
- [5] F. Perini, E. Mattarelli, and F. Paltrinieri, "Development and validation of predictive emissions schemes for quasi-dimensional combustion models," in *SAE Technical Paper 2010-01-0148*, 2010.
- [6] J. O. Anderson and J. G. Thundiyil, "Clearing the Air: A Review of the Effects of Particulate Matter Air Pollution on Human Health," *J. Med. Toxicol.*, vol. 8, pp. 166–175, 2012.
- [7] M. Kampa and E. Castanas, "Human health effects of air pollution," *Environ. Pollut.*, vol. 151, pp. 362–367, 2008.
- [8] K. Kim, S. Ara, E. Kabir, and R. J. C. Brown, "A review of airborne polycyclic aromatic hydrocarbons ( PAHs ) and their human health effects," *Environ. Int.*, vol. 60, pp. 71–80, 2013.
- [9] "<http://www.who.int/mediacentre/news/releases/2014/air-pollution/en/>"
- [10] "<https://www.epa.gov/ghgemissions/global-greenhouse-gas-emissions-data>"
- [11] "[https://en.wikipedia.org/wiki/Motor\\_vehicle](https://en.wikipedia.org/wiki/Motor_vehicle)"
- [12] "[https://ec.europa.eu/clima/policies/transport/vehicles/cars\\_en](https://ec.europa.eu/clima/policies/transport/vehicles/cars_en)"
- [13] "[https://en.wikipedia.org/wiki/European\\_emission\\_standards](https://en.wikipedia.org/wiki/European_emission_standards)"
- [14] T. V Johnson, "Review of Vehicular Emissions Trends," *SAE Int. J. Engines*, vol. 8, no. 3, pp. 1152–1167, 2015.
- [15] "[https://www.naesb.org/pdf2/wgq\\_bps100605w2.pdf](https://www.naesb.org/pdf2/wgq_bps100605w2.pdf)"
- [16] T. Korakianitis, A. M. Namasivayam, and R. J. Crookes, "Natural-gas fueled spark-ignition (SI) and compression-ignition (CI) engine performance and emissions," *Prog. Energy Combust. Sci.*, vol. 37, no. 1, pp. 89–112, 2011.
- [17] K. Bhandari, A. Bansal, A. Shukla, and M. Khare, "Performance and emissions of natural gas fueled internal combustion engine: A review," *J. Sci. Ind. Res.*, vol. 64, pp. 333–338, 2005.
- [18] F. Königsson, "Advancing the Limits of Dual Fuel Combustion," Licenciate thesis, Royal Institute of Technology, Stockholm, 2012.
- [19] D. Serrano and L. Bertrand, "Exploring the Potential of Dual Fuel Diesel-CNG Combustion for Passenger Car Engine," in *Proceedings of the FISITA 2012 World Automotive Congress*, 2012.
- [20] D. Goudie, M. Dunn, and S. R. Munshi, "Development of a Compression Ignition Heavy Duty Pilot-Ignited Natural Gas Fuelled Engine for Low NOx Emissions," in *SAE Technical Paper 2004-01-2954*, 2004.
- [21] D. Kozarac, I. Taritaš, D. Vuilleumier, S. Saxena, and R. W. Dibble, "Experimental

- and numerical analysis of the performance and exhaust gas emissions of a biogas/n-heptane fueled HCCI engine,” *Energy*, vol. 115, pp. 180–193, 2016.
- [22] G. McTaggart-Cowan, K. Mann, J. Huang, A. Singh, B. Patychuk, Z. X. Zheng and S. Munshi, “Direct Injection of Natural Gas at up to 600 Bar in a Pilot-Ignited Heavy-Duty Engine,” *SAE Int. J. Engines* 8(3):981-996, 2015.
  - [23] N. Dronniou, J. Kashdan, B. Lecointe, K. Sauve, and D. Soleri, “Optical Investigation of Dual-fuel CNG/Diesel Combustion Strategies to Reduce CO<sub>2</sub> Emissions,” *SAE Int. J. Engines*, vol. 7, no. 2, pp. 873–887, 2014.
  - [24] C. Abagnale, M. C. Cameretti, L. De Simio, M. Gambino, S. Iannaccone, and R. Tuccillo, “Numerical simulation and experimental test of dual fuel operated diesel engines,” *Appl. Therm. Eng.*, vol. 65, pp. 403–417, 2014.
  - [25] A. Shah *et al.*, “Literature Review and Simulation of Dual Fuel Diesel-CNG Engines,” in *SAE Technical Paper 2011-26-0001*, 2011.
  - [26] L. Wei and P. Geng, “A review on natural gas/diesel dual fuel combustion, emissions and performance,” *Fuel Process. Technol.*, vol. 142, pp. 264–278, 2016.
  - [27] M. S. Lounici, K. Loubar, L. Tarabet, M. Balistrrou, D. C. Niculescu, and M. Tazerout, “Towards improvement of natural gas-diesel dual fuel mode: An experimental investigation on performance and exhaust emissions,” *Energy*, vol. 64, pp. 200–211, 2014.
  - [28] R. G. Papagiannakis, C. D. Rakopoulos, D. T. Hountalas, and D. C. Rakopoulos, “Emission characteristics of high speed, dual fuel, compression ignition engine operating in a wide range of natural gas/diesel fuel proportions,” *Fuel*, vol. 89, no. 7, pp. 1397–1406, 2010.
  - [29] R. W. Dibble, “Better than a Fuel Cell an IC Engine that uses Argon as the Working Fluid.” Zagreb, 2017.
  - [30] J. I. Ramos, *Internal Combustion Engine Modeling*. Hemisphere Publishing Corporation, 1989.
  - [31] G. Stiesch, *Modeling Engine Spray and Combustion Processes*, 1st ed. Springer-Verlag, 2003.
  - [32] M. Sjerić, “New Physically Based Sub-Models for the Cycle-Simulation of Spark-Ignition Engine,” PhD thesis, University of Zagreb, 2014.
  - [33] C. Pötsch and H. Ofner, “Assessment of a Multi Zone Combustion Model for Analysis and Prediction of CI Engine Combustion and Emissions Author,” in *SAE Technical Paper 2011-01-1439*, 2011.
  - [34] D. Kozarac, Z. Lulic, and G. Sagi, “A six-zone simulation model for HCCI engines with a non-segregated solver of zone state,” *Combust. Theory Model.*, vol. 14, no. 3, pp. 425–451, 2010.
  - [35] D. T. Hountalas and R. G. Papagiannakis, “Development of a Simulation Model for Direct Injection Dual Fuel Diesel-Natural Gas Engines,” in *SAE Technical Paper 2000-01 0286*, 2000,.
  - [36] M. Sjerić, I. Taritaš, R. Tomić, M. Blažić, D. Kozarac, and Z. Lulić, “Efficiency improvement of a spark-ignition engine at full load conditions using exhaust gas recirculation and variable geometry turbocharger - Numerical study,” *Energy Convers. Manag.*, vol. 125, pp. 26–39, 2016.
  - [37] D. Vuilleumier, I. Taritaš, B. Wolk, D. Kozarac, S. Saxena, and R. W. Dibble, “Multi-level computational exploration of advanced combustion engine operating strategies,” *Appl. Energy*, vol. 184, pp. 1273–1283, 2016.
  - [38] S. Singh, S. Kong, R. D. Reitz, S. R. Krishnan, and K. C. Midkiff, “Modeling and Experiments of Dual-Fuel Engine Combustion and Emissions” in *SAE Technical Paper 2004-01-0092*, 2004.

- [39] S. Singh, L. Liang, S.-C. Kong, and R. D. Reitz, "Development of a Flame Propagation Model for Dual-Fuel Partially Premixed Compression Ignition Engines," *Int. J. Engine Res.*, vol. 7, no. 1, pp. 65–75, 2006.
- [40] P. Ouellette, P. L. Mtui, and P. G. Hill, "Numerical Simulations of Directly Injected Natural Gas and Pilot Diesel Fuel in a Two-Stroke Compression Ignition Engine," in *SAE Technical Paper 981400*, 1998.
- [41] P. Zoldak, A. Sobiesiak, D. Wickman, and M. Bergin, "Combustion Simulation of Dual Fuel CNG Engine Using Direct Injection of Natural Gas and Diesel," *SAE Int. J. Engines* 8(2):846-858, 2015.
- [42] H. Hiroyasu, T. Katoda, and M. Arai, "Development and Use of a Spray Combustion Modeling to Predict Diesel Engine Efficiency and Pollutant Emissions, Part 1: Combustion Modeling," *Bulletin of JSME*, vol. 26, no. 214, pp. 569–575, 1983.
- [43] D. T. Hountalas and R. G. Papagiannakis, "A Simulation Model for the Combustion Process of Natural Gas Engines with Pilot Diesel Fuel as an Ignition Source," in *SAE Technical Paper 2001-01-1245*, 2001, no. 724.
- [44] R. G. Papagiannakis, D. T. Hountalas, and P. N. Kotsiopoulos, "Experimental and Theoretical Analysis of the Combustion and Pollutants Formation Mechanisms in Dual Fuel DI Diesel Engines," in *SAE Technical Paper 2005-01-1726*, 2005.
- [45] R. G. Papagiannakis, "Study of air inlet preheating and EGR impacts for improving the operation of compression ignition engine running under dual fuel mode," *Energy Convers. Manag.*, vol. 68, pp. 40–53, 2013.
- [46] S. R. Krishnan and K. K. Inivasan, "Multi-zone modelling of partially premixed low-temperature combustion in pilot-ignited natural-gas engines," in *Proceedings of the Institution of Mechanical Engineers, Part D: Journal of Automobile Engineering*, 2010, vol. 224, no. 12, pp. 1597–1622.
- [47] N. Blizard and J. Keck, "Experimental and Theoretical Investigation of Turbulent Burning Model for Internal Combustion Engines," in *SAE Technical Paper 740191*, 1974.
- [48] M. Mikulski, S. Wierzbicki and A. Piętak, "Zero-dimensional 2-phase combustion model in a dual-fuel compression ignition engine fed with gaseous fuel and a divided diesel fuel charge," *Maintenance and Reliability*, vol. 17, no. 1, pp. 42–48, 2015.
- [49] F. Cernik, J. Macek, C. Dahnz, and S. Hensel, "Dual Fuel Combustion Model for a Large Low-Speed 2-Stroke Engine," in *SAE Technical Paper 2016-01-0770*, 2016.
- [50] T. Poinso and D. Veynante, *Theoretical and Numerical Combustion*. R.T. Edwards, Inc., 2001.
- [51] C. K. Law, *Combustion physics*. Cambridge University Press, 2006.
- [52] K. K. Kuo, *Principles of Combustion*, 2nd ed. John Wiley & Sons, 2005.
- [53] W. M. H.K.Versteeg, *An Introduction to Computational Fluid Dynamics*, 2nd ed. Pearson Education Limited, 2007.
- [54] B. E. Launder and D. B. Spalding, "The Numerical Computation of Turbulent Flows," *Comput. Methods Appl. Mech. Eng.*, vol. 3, pp. 269–289, 1974.
- [55] F. C. Gouldin, "An Application of Fractals to Modeling Premixed Turbulent Flames," *Combust. Flame*, vol. 68, pp. 249–266, 1987.
- [56] S. M. Frolov *et al.*, "Flame Tracking – Particle Method for 3D Simulation of Normal and Abnormal ( Knocking ) Operation of Spark-Ignition Automotive Engines," in *International Automotive Conference NUMV*, 2015, vol. 9, pp. 83–91.
- [57] "AVL BOOST - version 2010, Theory, Edition 11/2010." 2010.
- [58] D. Kozarac, R. Tomic, I. Taritas, J.-Y. Chen, and R. W. Dibble, "A Model for Prediction of Knock in the Cycle Simulation by Detail Characterization of Fuel and Temperature Stratification," *SAE Int. J. Engines*, vol. 8, no. 4, 2015.

- [59] G. P. Merker, C. Schwarz, and R. Teichmann, *Combustion Engines Development, Mixture Formation, Combustion, Emissions and Simulation*. Springer-Verlag, 2012.
- [60] J. A. Caton, *An Introduction to Thermodynamic Cycle Simulations for Internal Combustion Engines*. John Wiley & Sons, 2015.
- [61] E. Tomita and N. Fukatani, “Combustion in a supercharged biomass gas engine with micro-pilot ignition-effects of injection pressure and amount of diesel fuel,” *J. KONES Powertrain Transp.*, vol. 14, no. 2, pp. 513–520, 2007.
- [62] D. C. Wilcox, *Turbulence Modeling for CFD*, 3rd ed. DCW Industries, Inc., 2006.
- [63] S. B. Pope, *Turbulent Flows*, 10th ed. Cambridge University Press, 2013.
- [64] “<http://www.izeninc.com/events/ansys-cfd-workshop/>”
- [65] L. Davidson, “Fluid mechanics, turbulent flow and turbulence modeling.” p. 346, 2015.
- [66] J. B. Heywood, *Internal Combustion Engine Fundamentals*. McGraw-Hill, Inc., 1988.
- [67] M. Trzesniowski, *Rennwagenteknik - Grundlagen, Konstruktion, Komponenten, Systeme*, 4th ed. Springer Vieweg, 2014.
- [68] “<http://vegburner.co.uk/DIcombustion.html>”
- [69] V. W. Wong and D. P. Hoult, “Rapid Distortion Theory Applied to Turbulent Combustion,” in *SAE Technical Paper 790357*, 1979.
- [70] C. Borgnakke, V. Arpaci, and R. Tabaczynski, “A Model for the Instantaneous Heat Transfer and Turbulence in a Spark Ignition Engine,” in *SAE Technical Paper 800287*, 1980.
- [71] C. Arcoumanis and T. Kamimoto, *Flow and Combustion in Reciprocating Engines*. Springer-Verlag, 2009.
- [72] B. Ahmadi-Befrui and A. D. Gosman, “Assessment of variants of the  $k-\epsilon$  turbulence model for engine flow applications,” *Int. J. Numer. Methods Fluids*, vol. 9, no. 9, pp. 1073–1086, 1989.
- [73] T. L. Bergman, A. S. Lavine, F. P. Incropera, and D. P. Dewitt, *Fundamentals of Heat and Mass Transfer*, 7th ed. John Wiley & Sons, 2011.
- [74] N. P. Komninou and G. M. Kosmadakis, “Heat transfer in HCCI multi-zone modeling: Validation of a new wall heat flux correlation under motoring conditions,” *Appl. Energy*, vol. 88, no. 5, pp. 1635–1648, 2011.
- [75] G. Woschni, “Einfluß von Rußablagerungen auf den Wärmeübergang zwischen Arbeitsgas und Wand im Dieselmotor,” in *Der Arbeitsprozeß des Verbrennungsmotors*, 1991.
- [76] G. Woschni, “Universally Applicable Equation for the Instantaneous Heat Transfer Coefficient in the Internal Combustion Engine,” in *SAE Technical Paper 670931*, 1967.
- [77] M. Sjöberg, “The Rotating Injector as a Tool for Exploring DI Diesel Combustion and Emissions,” PhD thesis, Royal Institute of Technology, Stockholm, 2001.
- [78] G. M. Bianchi and P. Pelloni, “Modeling the Diesel Fuel Spray Breakup by Using a Hybrid Model,” in *SAE Technical Paper 1999-01-0226*, 1999, pp. 1–16.
- [79] C. Arcoumanis and M. Gavaises, “Linking nozzle flow with spray characteristics in a Diesel fuel injection system,” *At. Sprays*, vol. 8, no. 3, pp. 307–347, 1998.
- [80] N. Tamaki, M. Shimizu, and H. Hiroyasu, “Enhancement of the atomization of a liquid jet by cavitation in a nozzle hole,” *At. Sprays*, vol. 11, no. 2, p. 14, 2001.
- [81] C. Baumgarten, J. Stegemann, G. P. Merker, T. Verbrennung, and U. Hannover, “A New Model for Cavitation Induced Primary Break-Up of Diesel Sprays,” in *ILASS-Europe*, 2002, no. September, p. 7.
- [82] R. Reitz and R. Diwaker, “Effect of Drop Breakup on Fuel Sprays,” in *SAE Technical Paper 860469*, 1986.
- [83] C. Yin, “Modelling of heating and evaporation of n-Heptane droplets: Towards a

- generic model for fuel droplet/particle conversion,” *Fuel*, vol. 141, pp. 64–73, 2015.
- [84] S. K. Aggarwal, “A review of spray ignition phenomena: Present status and future research,” *Prog. Energy Combust. Sci.*, vol. 24, no. 95, pp. 565–600, 1998.
  - [85] S. McAllister, J.-Y. Chen, and A. C. Fernandez-Pello, *Fundamentals of Combustion Processes*. Springer, 2011.
  - [86] G. N. Abramovich, *The Theory of Turbulent Jets*. Cambridge: MIT Press, 1963.
  - [87] W. Chiu, S. Shahed, and W. Lyn, “A Transient Spray Mixing Model for Diesel Combustion,” in *SAE Technical Paper 760128*, 1976.
  - [88] G. Merker, B. Hohlbaum, and M. Rauscher, “Two-Zone Model for Calculation of Nitrogen-Oxide Formation in Direct-Injection Diesel Engines,” in *SAE Technical Paper 932454*, 1993.
  - [89] D. L. Siebers, “Scaling liquid-phase fuel penetration in diesel sprays based on mixing-limited vaporization,” in *SAE Paper 1999-01-0528*, 1999.
  - [90] K. Varde, D. Popa, and L. Varde, “Spray Angle and Atomization in Diesel Sprays,” in *SAE Technical Paper 841055*, 1984.
  - [91] G. L. Borman and J. H. Johnson, “Unsteady Vaporization Histories and Trajectories of Fuel Drops Injected into Swirling Air,” in *SAE Technical Paper 620271*, 1962.
  - [92] J. C. Livengood and P. C. Wu, “Correlation of autoignition phenomena in internal combustion engines and rapid compression machines,” *Symp. Combust.*, vol. 5, pp. 347–356, 1955.
  - [93] P. W. Atkins and J. de Paula, *Physical Chemistry*, 8th ed. Oxford University Press, 2006.
  - [94] J. E. House, *Principles of Chemical Kinetics*, 2nd ed. Elsevier, 2007.
  - [95] E. T. Denisov, O. M. Sarkisov, and G. I. Likhtenshtein, *Chemical Kinetics - Fundamentals and New Developments*. Elsevier, 2003.
  - [96] Z. Liu, “Chemical Kinetics Modelling Study on Fuel Autoignition in Internal Combustion Engines,” PhD thesis, Loughborough University, 2010.
  - [97] R. J. Kee, F. M. Rupley, E. Meeks, and J. A. Miller, “Chemkin-III: a fortran chemical kinetics package for the analysis of gas- phase chemical and plasma kinetics,” 1996.
  - [98] P. G. Lignola and E. Reverchon, “Cool flames,” *Prog. Energy Combust. Sci.*, vol. 13, pp. 75–96, 1987.
  - [99] J. F. Griffiths, P. A. Halford-Maw, and D. J. Rose, “Fundamental features of hydrocarbon autoignition in a rapid compression machine,” *Combust. Flame*, vol. 95, no. 3, pp. 291–306, 1993.
  - [100] M. Ban, “Numerical Modelling of Auto- Ignition Chemistry Kinetics in Computational Fluid Dynamics,” PhD thesis, University of Zagreb, 2011.
  - [101] M. Ban and N. Duić, “Adaptation of n-heptane autoignition tabulation for complex chemistry mechanisms,” *Therm. Sci.*, vol. 15, no. 1, pp. 135–144, 2011.
  - [102] H. J. Curran, P. Gaffuri, W. J. Pitz, and C. K. Westbrook, “A Comprehensive Modeling Study of n -Heptane Oxidation,” *Combust. Flame*, vol. 114, pp. 149–177, 1998.
  - [103] J. Yang and S. Wong, “On the suppression of negative temperature coefficient ( NTC ) in autoignition of n-heptane droplets,” *Combust. Flame*, vol. 132, pp. 475–491, 2003.
  - [104] S. Bougrine, “0-Dimensional Modeling of the Combustion of Alternative Fuels in Spark Ignition Engines,” PhD thesis, Ecole Centrale Paris, 2012.
  - [105] N. Peters, “The turbulent burning velocity for large-scale and small-scale turbulence,” *Journal of Fluid Mechanics*, vol. 384, pp. 107–132, 1999.
  - [106] N. Peters, *Turbulent Combustion*. Cambridge University Press, 2000.
  - [107] R. Matthews, M. Hall, W. Dai, and G. Davis, “Combustion Modeling in SI Engines with a Peninsula-Fractal Combustion Model,” in *SAE Technical Paper 960072*, 1996.
  - [108] S. Verhelst and C. G. W. Sheppard, “Multi-zone thermodynamic modelling of spark-

- ignition engine combustion - An overview,” *Energy Convers. Manag.*, vol. 50, no. 5, pp. 1326–1335, 2009.
- [109] Z. Filipi and D. N. Assanis, “Quasi-Dimensional Computer Simulation of the Turbocharged Spark-Ignition Engine and its Use for 2- and 4-Valve Engine Matching Studies,” in *SAE Technical Paper 910075*, 1991.
  - [110] A. Agarwal, Z. S. Filipi, D. N. Assanis, and D. M. Baker, “Assessment of Single- and Two-Zone Turbulence Formulations for Quasi-Dimensional Modeling of Spark-Ignition Engine Combustion,” *Combust. Sci. Technol.*, vol. 136, no. March 2015, pp. 13–39, 1998.
  - [111] R. J. Tabaczynski, F. H. Trinker, and B. A. Shannon, “Further refinement and validation of a turbulent flame propagation model for spark ignition engine,” *Combust. Flame*, vol. 39, pp. 111–121, 1980.
  - [112] R. Tabaczynski, C. Ferguson, and K. Radhakrishnan, “A Turbulent Entrainment Model for Spark-Ignition Engine Combustion,” in *SAE Technical Paper 770647*, 1997.
  - [113] B. B. Mandelbrot, *The Fractal Geometry of Nature*. New York: W.H. Freeman and Company, 1983.
  - [114] G. L. North and D. A. Santavicca, “The Fractal Nature of Premixed Turbulent Flames,” *Combust. Sci. Technol.*, vol. 72, pp. 215–232, 1990.
  - [115] F. Foucher and C. Mounaïm-Rousselle, “Fractal approach to the evaluation of burning rates in the vicinity of the piston in a spark-ignition engine,” *Combust. Flame*, vol. 143, no. 3, pp. 323–332, 2005.
  - [116] F. Bozza, G. Fontana, E. Galloni, and E. Torella, “3D-1D Analyses of the Turbulent Flow Field , Burning Speed and Knock Occurrence in a Turbocharged SI Engine 3D-1D Analyses of the Turbulent Flow Field , Burning Speed and Knock Occurrence in a Turbocharged SI Engine,” in *SAE Technical Paper 2007-24-0029*, 2007.
  - [117] H. Mathur, M. Gajendra Babu, and K. Reddi, “A Thermodynamic Simulation Model for a Methanol Fueled Spark Ignition Engine,” in *SAE Technical Paper 830333*, 1983.
  - [118] J. J. Fagelson, W. J. Mclean, and P. C. T. De Boer, “Performance and NO<sub>x</sub> Emissions of Spark Ignited Combustion Engines Using Alternative Fuels — Quasi One-Dimensional Modeling I . Hydrogen Fueled Engines,” *Combust. Sci. Technol.*, vol. 18, pp. 47–57, 1978.
  - [119] M. B. Rubin and W. J. Mclean, “Performance and NO<sub>x</sub> Emissions of Spark Ignited Combustion Engines Using Alternative Fuels — Quasi One-Dimensional Modeling II . Methanol Fueled Engines,” *Combust. Sci. Technol.*, vol. 18, pp. 199–206, 1978.
  - [120] K. Falconer, “Fractal Geometry: Mathematical Foundations and Applications.” John Wiley & Sons, New York, p. 288, 2003.
  - [121] B. B. Mandelbrot, “On the geometry of homogeneous turbulence , with stress on the fractal dimension of the iso-surfaces of scalars,” *J. Fluid Mech.*, vol. 72, pp. 401–416, 1975.
  - [122] M. Metghalchi and J. C. Keck, “Burning Velocities of Mixtures of Air with Methanol , Isooctane , and Indolene at High Pressure and Temperature,” *Combust. Flame*, vol. 48, pp. 191–210, 1982.
  - [123] O. L. Gulder *et al.*, “Flame Front Surface Characteristics in Turbulent Premixed Propane / Air Combustion,” *Combust. Flame*, vol. 120, pp. 407–416, 2000.
  - [124] V. L. Zimont, “Theory of Turbulent Combustion of a Homogeneous Fuel Mixture at High Reynolds Numbers,” *Combust. Explos. Shock Waves*, vol. 15, no. 3, pp. 305–311, 1979.
  - [125] O. L. Gulder, “Turbulent premixed flame propagation models for different combustion regimes,” *Proc. Combust. Inst.*, vol. 23, pp. 743–750, 1990.
  - [126] P. D. Ronney and V. Yakhot, “Flame Broadening Effects on Premixed Turbulent

- Flame Speed,” *Combust. Sci. Technol.*, vol. 24, pp. 305–311, 1992.
- [127] F. N. Egolfopoulos, P. Cho, and C. K. Law, “Laminar Flame Speeds of Methane-Air Mixtures Under Reduced and Elevated Pressures,” *Combust. Flame*, vol. 76, pp. 375–391, 1989.
  - [128] E. Hu *et al.*, “Laminar flame speeds and ignition delay times of methane – air mixtures at elevated temperatures and pressures,” *Fuel*, vol. 158, pp. 1–10, 2015.
  - [129] X. Shi, J. Chen, and Y. Chen, “Laminar flame speeds of stratified methane, propane, and n -heptane flames,” *Combust. Flame*, vol. 176, pp. 38–47, 2017.
  - [130] Y. Wu, V. Modica, B. Rossow, and F. Grisch, “Effects of pressure and preheating temperature on the laminar flame speed of methane / air and acetone / air mixtures,” *Fuel*, vol. 185, pp. 577–588, 2016.
  - [131] F. Halter, F. Foucher, L. Landry, and C. Mounaim-Rousselle, “Effect of Dilution by Nitrogen and / or Carbon Dioxide on Methane and Iso- Octane Air Flames,” *Combust. Sci. Technol.*, vol. 181, pp. 813–827, 2009.
  - [132] G. D’Errico, G. Ferrari, A. Onorat, and T. Cerri, “Modeling the Pollutant Emissions from a S.I. Engine,” in *SAE Technical Paper 2002-01-0006*, 2002.
  - [133] W. K. Cheng, D. Hamrin, J. B. Heywood, S. Hochgreb, K. Min, and M. Norris, “An overview of hydrocarbon emissions mechanisms in spark-ignition engines,” in *SAE Technical Paper 932708*, 1993.
  - [134] C. T. Bowman, “Kinetics of pollutant formation and destruction in combustion,” *Prog. Energy Combust. Sci.*, pp. 33–45, 2010.
  - [135] X. L. J. Seykens, “Development and validation of a phenomenological diesel engine combustion model,” PhD thesis, Technische Universiteit, Eindhoven, 2010.
  - [136] G. A. Lavoie, J. B. Heywood, and J. C. Keck, “Experimental and Theoretical Study of Nitric Oxide Formation in Internal Combustion Engines,” *Combust. Sci. Technol.*, vol. 1, pp. 313–326, 1970.
  - [137] J. Dec, “A Conceptual Model of DI Diesel Combustion Based on Laser Sheet Imaging,” in *SAE Technical Paper 970873*, 1997.
  - [138] A. Onorati, G. Ferrari, and G. D’Errico, “1D Unsteady Flows with Chemical Reactions in the Exhaust Duct-System of S.I. Engines: Predictions and Experiments,” in *SAE Technical Paper 2001-01-0939*, 2001.
  - [139] G. A. Lavoie and P. N. Blumberg, “A Fundamental Model for Predicting Fuel Consumption, NO<sub>x</sub> and HC Emissions of the Conventional Spark-Ignited Engine,” *Combust. Sci. Technol.*, vol. 21, no. 5–6, pp. 225–258, 1980.
  - [140] K. Pattas and G. Häfner, “Stickoxidbildung bei der ottomotorischen Verbrennung,” *MTZ*, vol. 12, pp. 397–404, 1973.
  - [141] Z. Wang *et al.*, “Relationship between super-knock and pre-ignition,” *Int. J. Engine Res.*, vol. 16, no. 2, pp. 166–180, 2015.
  - [142] Z. Wang *et al.*, “Investigation on Pre-ignition and Super-Knock in Highly Boosted Gasoline Direct Injection Engines,” in *SAE Technical Paper 2014-01-1212*, 2014, pp. 2014-01–1212.
  - [143] X. Zhen *et al.*, “The engine knock analysis - An overview,” *Appl. Energy*, vol. 92, pp. 628–636, 2012.
  - [144] S. Richard, S. Bougrine, G. Font, F. A. Lafossas, and F. le Berr, “On the Reduction of a 3D CFD Combustion Model to Build a Physical 0D Model for Simulating Heat Release, Knock and Pollutants in SI Engines,” *Oil Gas Sci. Technol.*, vol. 64, no. 3, pp. 223–242, 2009.
  - [145] Z. Petranović, M. Vujanović, and N. Duić, “Towards a more sustainable transport sector by numerically simulating fuel spray and pollutant formation in diesel engines,” *J. Clean. Prod.*, vol. 88, pp. 272–279, 2015.

- [146] A. Liu, D. Mather, and R. Reitz, "Modeling the Effects of Drop Drag and Breakup on Fuel Sprays," in *SAE Technical Paper 930072*, 1993.
- [147] O. Colin and A. Benkenida, "The 3-zones Extended Coherent Flame Model (ECFM3Z) for computing premixed/diffusion combustion," *Oil Gas Sci. Technol.*, vol. 59, no. 6, pp. 593–609, 2004.
- [148] Z. Petranović, "Numerical modelling of spray and combustion processes using the Euler Eulerian multiphase approach," PhD thesis, University of Zagreb, 2016.
- [149] D. M. Vuilleumier, "The Effect of Ethanol Addition to Gasoline on Low- and Intermediate- Temperature Heat Release under Boosted Conditions in Kinetically Controlled Engines," PhD thesis, UC Berkeley, 2016.
- [150] M. Blažić, "Testing and Performance Analysis of Dual Fuel Engine," Master thesis, University of Zagreb, 2016.
- [151] "Volkswagen of America, Inc.: Self study program: 2.0 Liter TDI Common Rail BIN5 ULEV Engine." USA, 2008.
- [152] A. Savitzky and M. J. E. Golay, "Smoothing and differentiation of data by simplified least squares procedures," *Anal. Chem.*, vol. 38, no. 8, pp. 1627–1639, 1964.



# Curriculum Vitae in English

## EDUCATION

- 2013 – 2017 PhD student, postgraduate study at Faculty of Mechanical Engineering and Naval Architecture, University of Zagreb, Direction: Theory of Construction
- 2010 – 2012 Master degree in mechanical engineering (MEng Mech), Faculty of Mechanical Engineering and Naval Architecture, University of Zagreb, Direction: Engineering Design, IC Engines and Motor Vehicles
- 2006 – 2010 Bachelor degree in mechanical engineering (BEng Mech), Faculty of Mechanical Engineering and Naval Architecture, University of Zagreb, Direction: Engineering Design, IC Engines and Motor Vehicles

## EMPLOYMENT

- 2017 – Current Senior Associate, KF Finance d.o.o., Zagreb
- 2013 – 2017 Junior Researcher, University of Zagreb, Faculty of Mechanical Engineering and Naval Architecture, Chair of IC Engines

### Research Topics:

- IC Engines Combustion Modeling
- Dual-Fuel (Diesel-Natural Gas) Combustion
- Operating Strategies of Advanced Internal Combustion Engine
- Analysis of the Entire Engine System (Cycle-Simulation)

### Conference Presentations:

- 2014 – SAE International World Congress & Exhibition, Detroit, USA
- 2014 – 47th Symposium FUELS 2014, Šibenik, Croatia
- 2015 – High-Pressure and High Reynolds Combustion Workshop, KAUST, Kingdom of Saudi Arabia
- 2015 – 10th Conference on Sustainable Energy, Water and Environment Systems, Dubrovnik, Croatia
- 2017 – SAE International World Congress & Exhibition, Detroit, USA

### Selected Publications:

- Taritaš I. Kozarac D. Sjerić M. Numerical Study of Boosting Configurations and Valve Strategies for High Load HCCI Engine in Wide Range of Engine Speed. SAE Technical Paper 2014-01.1267, Detroit, USA, 2014.

- Vuilleumier D., Taritaš I., Wolk B., Kozarac D., Saxena S., Dibble R.W. Multi-level computational exploration of advanced combustion engine operating strategies. *Applied energy*, Vol. 184, pp. 1273-1283, 2016.
- Sjerić M., Taritaš I., Tomić R., Blažić R., Kozarac D., Lulić Z. Efficiency improvement of a spark-ignition engine at full load conditions using exhaust gas recirculation and variable geometry turbocharger – Numerical study. *Energy conversion and management*, Vol.125, pp. 26-39, 2016.
- Kozarac D., Taritaš I., Vuilleumier D., Saxena S., Dibble R.W. Experimental and numerical analysis of the performance and exhaust gas emissions of a biogas/n-heptane fueled HCCI engine. *Energy*, Vol. 115, pp. 180-193, 2016.
- Taritaš, I., Sremec, M., Kozarac, D., Blažić, M., Lulić, Z. The effect of operating parameters on dual fuel performance and emissions – An overview. *Transactions of FAMENA*, Vol. 41, pp. 26-39, 2017.
- Taritaš, I., Kozarac, D., Sjerić, M., Sierra Aznar, M., Vuilleumier, D., Tatschl, R. Development and Validation of a Quasi – Dimensional Dual Fuel (Diesel – Natural Gas) Combustion Model. *SAE International Journal of Engines*, Vol. 10(2), pp. 483-500, 2017.

#### Bibliography:

- <http://bib.irb.hr/lista-radova?autor=340033>

#### **ADDITIONAL (SPORTS)**

##### Sailing – Laser (Single-Handed Olympic Dinghy)

- Youth Croatian National Team (2002 – 2005)
- Croatian National Team (2005 – 2013)

##### Selected Achievements:

- 2004 – 2<sup>nd</sup> place in the overall standings of the Youth Europa Cup
- 2005 – 1<sup>st</sup> place at the Youth European Championship, Split, Croatia
- 2005 – 3<sup>rd</sup> place at the Youth World Championship, Fortaleza, Brazil
- 2006 – 5<sup>th</sup> place at the U21 European Championship, Gdynia, Poland
- 2008 – 1<sup>st</sup> place in the overall standings of the Europa Cup
- 2011 – 9<sup>th</sup> place at the European Championship, Helsinki, Finland
- 2011 – 17<sup>th</sup> place at the World sailing rankings

# Curriculum Vitae in Croatian

## OBRAZOVANJE

2013. – 2017. Student na doktorskom studiju Fakulteta strojarstva i brodogradnje, Sveučilišta u Zagrebu, smjer: Teorija konstrukcija
2010. – 2012. Magistar inženjer strojarstva, Fakultet strojarstva i brodogradnje, Sveučilišta u Zagrebu, smjer: Konstrukcijski, motori i vozila
2006. – 2010. Prvostupnik strojarske struke, Fakultet strojarstva i brodogradnje, Sveučilišta u Zagrebu, smjer: Konstrukcijski, motori i vozila

## ZAPOSLENJE

- 2017 – Danas Viši stručni savjetnik, KF Finance d.o.o., Zagreb
2013. – 2017 Znanstveni novak, asistent na projektu , Fakultet strojarstva i brodogradnje, Sveučilište u Zagrebu

### Područje istraživanja:

- Modeliranje procesa izgaranja u motorima s unutarnjim izgaranjem
- "Dual-fuel" izgaranje
- Upravljanje radom suvremenih motora s unutarnjim izgaranjem
- Proračuni radnog ciklusa motora s unutarnjim izgaranjem

### Izlaganja na konferencijama:

- 2014 – SAE konferencija, Detroit, SAD
- 2014 – 47. međunarodni simpozij GORIVA, Šibenik, Republika Hrvatska
- 2015 – High pressure & High Reynolds Combustion, KAUST, Kraljevina Saudijska Arabija
- 2015 – 10. SDEWES konferencija, Dubrovnik, Republika Hrvatska
- 2017 – SAE konferencija, Detroit, SAD

### Odabrane publikacije:

- Taritaš I. Kozarac D. Sjerić M. Numerical Study of Boosting Configurations and Valve Strategies for High Load HCCI Engine in Wide Range of Engine Speed. SAE Technical Paper 2014-01.1267, Detroit, SAD, 2014.
- Vuilleumier D., Taritaš I., Wolk B., Kozarac D., Saxena S., Dibble R.W. Multi-level computational exploration of advanced combustion engine operating strategies. Applied energy, 2016.

- Sjerić M., Taritaš I., Tomić R., Blažić R., Kozarac D., Lulić Z. Efficiency improvement of a spark-ignition engine at full load conditions using exhaust gas recirculation and variable geometry turbocharger – Numerical study. Energy conversion and management, 2016.
- Kozarac D., Taritaš I., Vuilleumier D., Saxena S., Dibble R.W. Experimental and numerical analysis of the performance and exhaust gas emissions of a biogas fueled HCCI engine. Energy, 2016.
- Taritaš, I., Sremec, M., Kozarac, D., Blažić, M., Lulić, Z. The effect of operating parameters on dual fuel performance and emissions – An overview. Transactions of FAMENA, 2017.
- Taritaš, I., Kozarac, D., Sjerić, M., Sierra Aznar, M., Vuilleumier, D., Tatschl, R. Development and Validation of a Quasi – Dimensional Dual Fuel (Diesel – Natural Gas) Combustion Model. SAE International Journal of Engines, Vol. 10(2), pp. 483-500, 2017.

#### Bibliografija:

- <http://bib.irb.hr/lista-radova?autor=340033>

#### **DODATNO (SPORT)**

##### Laser – olimpijski jednosjed (jedrenje)

- Hrvatska juniorska reprezentacija (2002 – 2005)
- Hrvatska seniorska reprezentacija (2005 – 2012)

##### Značajniji rezultati:

- 2004 – 2. mjesto u ukupnom poretku juniorskom europskog kupa
- 2005 – 1. mjesto na europskom juniorskom prvenstvu, Split, Republika Hrvatska
- 2005 – 3. mjesto na svjetskom juniorskom prvenstvu, Fortaleza, Brazil
- 2006 – 5. mjesto na europskom U21 prvenstvu, Gdynia, Poljska
- 2008 – Ukupni pobjednik europskog kupa
- 2011 – 9. mjesto na europskom prvenstvu, Helsinki, Finska
- 2011 – 17 mjesto na svjetskoj jedriličarskoj ljestvici